Cold Gas Spraying of Copper and Tin onto Metallic and Non metallic substrates

The University of Nottingham

by

Eklavya Calla

Thesis submitted to the University of Nottingham for the degree of Doctor of Philosophy

November 2005

Contents

Abstract

Cold gas dynamic spraying (CGDS) is a recent development in the field of thermal spraying in which a powder feedstock can be deposited onto a substrate to form a coating without it being heated significantly. The aim of the present study was to investigate the potential for manufacturing electrical circuits for automobile applications by depositing copper tracks on non-metallic substrates. Powders were sprayed using He gas at room temperature and elevated temperatures onto a number of different polymers, ceramic and metal substrates to understand the factors controlling deposit formation and the development of adequate adhesion between track and substrate. The use of tin as an interlayer to improve adhesion was a novel development in this study.

The deposits were characterized by optical microscopy (OM), scanning electron microscopy (SEM), X-ray diffraction (XRD), profilometry, microhardness, tensile testing, adhesion testing and resistivity measurements. Investigations were also performed to study thermal stability since as sprayed deposits are in non-equilibrium state.

Copper could be deposited on aluminium for a wide range of deposition parameters. Sprayed copper had nanometre size grains and demonstrated high hardness and tensile strength. Annealing resulted in recrystallization and grain growth and decrease in hardness and tensile strength.

Copper could be deposited on polymers like nylon (PA66), glass reinforced nylon (PA6T) and poly (butylene terepthalate) (PBT). Copper could be deposited on a wide

range of polymers when a layer of tin was deposited as a bond coat. The use of tin bond coat improved the overall adhesion of tin + copper tracks.

Intermetallic compound formation was observed in tin – copper tracks after annealing at 343 K and 443 K. The formation of the intermetallic compound did not increase the resistance of tin – copper couples as the resistance of the couples after annealing were found to be below that of the as – sprayed couples where the intermetallic compound formation had not taken place. This effect is a result of the recovery/recrystallization taking place in copper which reduces the resistance.

Abbreviations/Nomenclature

Abbreviations

CGDS	Cold gas dynamic spraying
HVOF	High velocity oxy-fuel spraying
OM	Optical microscopy
SEM	Scanning electron microscopy
BSE	Back scattered electron
EDX	Energy dispersive x-ray
XRD	X-ray diffraction

Nomenclature

Al	Aluminium
Cu	Copper
Sn	Tin
PA66	Nylon 66
PA6T	Glass filled nylon
PBT	Poly butylene terepthalate
PE	Polyethylene
PPS	Polyphenylene sulfide
% wt	Weight percent
% at	Atomic percent
A	Cross-sectional area
V	Volume

C_d	Drag coefficient
C_P	Gas heat capacitance at constant pressure
C_V	Gas heat capacitance at constant volume
F_D	drag force on particle
$\dot{m}$	Mass flow rate
M	Mach number
P	Pressure
R	Universal gas constant
$\overline{R}$	Specific gas constant
T	Temperature
v	Velocity
m	Mass
ρ	Density
γ	Ratio of gas specific heats
P_f^m	Powder feed rate
P_f^t	Theoretical powder feed rate
P_s	Powder wheel speed
P_f	Powder feed rate
σ_y	Yield stress
σ_0	Friction stress
R	Resistance
t	time
B	X-ray peak broadening
λ	Wavelength of x-ray radiation

d_c	Crystallite size
θ	Bragg angle
h	Height of track
w	Width of track
η	Eta phase
ε	Epsilon phase

Subscripts and superscripts

*	Critical conditions
e_x	Nozzle exit conditions
p	Particle conditions
s	Post shock conditions
g	Gas conditions
0	Stagnation conditions

Chapter 1

Introduction

Surface coatings are utilized in engineering design and manufacture to modify/enhance properties of the surface or as a means to saving cost on expensive materials for manufacture of the whole component. There are different methods of surface coating and they differ in the manner in which the coatings are applied, thickness of coating, nature of bonding, materials coated and temperature during coating process. The choice of the surface coating process used for a particular engineering application depends upon factors such as [1]:

- The coating-surface treatment should not impair the properties of the bulk material. For example, there is little point in applying a coating for corrosion protection if the fatigue or mechanical properties of the bulk material are adversely affected.

- The deposition process must be capable of coating the component, in terms of both size and shape. For example, vacuum evaporation is partly a line of sight process and rotation of the component may be necessary to achieve a uniform coating. In contrast, chemical vapour deposition (CVD) and electroless nickel plating are noted for their ability to coat complex shaped components with a layer of uniform thickness.

- Some changes in material specification may be necessary to accommodate the coating. In some cases it is not sufficient to coat an existing component, but usually it will be advisable to redesign in order to realize the full engineering benefits of the surface treatment.
- The surface treatments must be cost-effective, but this judgment should include factors such as reduced downtime and improved product quality, in addition to the coating cost. For example, the improvement in surface finish, which occurs through the use of a coated tool, may give an additional benefit in that a subsequent finishing operation may be omitted.

The decision to use particular coating process therefore will depend upon the capabilities and limitations of the process and benefits versus cost analysis of the coating applied. A comparison of various coating processes is given in **Table 1.1** [1].

Yazaki Europe Limited is the Industrial Sponsor of this project. The overall aim of this research project is to investigate cold gas dynamic spraying (CGDS) also called as cold spraying, of copper to produce EDS (Circuit Patterns). The circuit patterns are to be deposited upon polymer substrates, which will be part of an automobile body. The circuit patterns are expected to be used to operate various features in the automobile, such as motorized seat adjustment, central locking etc. The present technology for this application is the use of circuits in the form of wire harnesses. These wire harnesses are carried between the metal body of the door and the inner upholstery. In the present project instead of using wire harnesses, it is proposed that

the circuit patterns are to be deposited on the inside of the car doors. This is expected to deliver the following benefits:

1. Reduced weight and the space occupied by the circuits (wire harnesses are bulky, heavy and take up a lot of space)
2. Reduce the time period from circuit design to manufacture as cold spray deposition can be rapidly carried out by mounting the cold spray gun on an industrial robot. (For wire harnesses this time is at least a few months, which is expected to be reduced to a few weeks by using a direct deposit circuit)

The characteristics expected from a coated track are;

1. Ability to deposit tracks on polymer substrates relatively quickly
2. Good electrical conductivity.
3. Sufficient adhesion and mechanical strength to withstand the environment of an automobile
4. Metallurgical stability in the conditions of operation of the automobile.

Cold spray deposited copper is expected to fulfill the above criteria; hence in this study the deposition of copper by cold spraying and the properties of the deposited copper were investigated. As cold spraying is a comparatively new coating process and many of the fundamental principles underlying the process are not clearly understood. The present project will investigate the influence of deposition conditions on the deposited tracks. The critical areas identified for investigation are:

1. Adhesion of the track on various substrates

2. Electrical conductivity of the track
3. Mechanical strength of the track
4. Use of a bond coat for deposition on various substrates and the effect of the bond coat on the adhesion of the track
5. Metallurgical stability of the track

Table 1.1: Comparison of different surfacing processes and deposits [1]

	Vapour deposition	Ion implantation	Sol-gel	Electro-deposition	Thermal spraying	Spray fusing	Welding
Thickness / mm	0.001-0.2	~ 0.005	0.002	0.02-0.5	0.1-1.0	0.5-1.5	>1.2
Component geometry	Versatile	-	-	Versatile	Line of sight		
Component size	Limited by chamber size		Limited by plating bath		No limit	Limited by fusing facility	No limit
Substrate temperature / K	30-1000	-	-	373	473	1323	1673
Pre-treatment	PVD-ion bombardment CVD-various	Chemical plus ion bombardment	Grit blast and/or chemical clean	Chemical cleaning and etching	Clean and roughen surface		Cleaning
Post-treatment	None/stress relief	None	High temperature calcine	None/stress relief	None	Nil	
Coating porosity / %	Nil to small	Low	Low	Nil to small	1-15	Nil	
Adhesion / MPa	High	High	High	100	20-140	High	
Adhesion mechanism	Atomic	-	Surface forces	Surface forces	Mechanical	Metallurgical	
Thickness control	Good	-	Good	Good	Low to good	Low	Low to good
Substrate distortion	Low	Low	Low	Low	Low	Moderate	Can be high
Phase change during coating	Controlled	Controlled	Controlled	Controlled	Uncontrolled	Partly controlled	

Chapter 2

Description of thermal spraying and cold spraying

2.1 Introduction

In this chapter the development of the thermal spray processes since its discovery approximately 85 years ago and the discovery and development of the cold spray process is described. This chapter consists of the following sections:

2.2 Brief history and description of thermal spray processes

2.3 Historical development of the cold spray process

2.4 Gas dynamic principles of cold spraying

2.5 Commercially available cold spray systems

2.6 Applications of cold sprayed deposits

2.7 Mechanism of deposit formation

2.8 Deposit microstructures and properties

2.2 Brief history and description of thermal spray processes

Thermal spraying is a process of particulate deposition in which the molten or semi-molten particles are deposited on to a substrate whereupon they solidify to form a coating. M. U. Schoop described the metallizing process and he is considered as the inventor of metal spraying technology [2, 3]. Since the first demonstration of the thermal spray process by Schoop there have been tremendous developments in the technology of thermal spray with respect to

- Heat source employed to heat the feed stock material
- Heating of the particles by the heat source
- Velocity attained by the particles
- Range of materials that can be deposited
- Properties of the coatings

Thermal spray processes may be broadly classified into two categories [4, 5]:

A. Those in which the material feedstock is rendered molten or semi molten by introduction into a region of intense heat such as flame, plasma or arc prior to propulsion onto the substrate.

B. Those, which exploit higher particle velocities, shorter transit times and overall lower temperatures, experienced by feedstock particles.

Classification and features of thermal spraying processes are given in **Table 2.1** [2, 6, 7].

Thermal spray methods are discussed in sections 2.2.1 to 2.2.6. The methods discussed in sections 2.2.1 to 2.2.3 [2] fall in category A and depend upon heating the sprayed material to form the coating. The philosophy here is that higher temperatures are preferred for enhanced coating properties due to enhanced softening/melting of the material, resulting in better flattening of the sprayed particles on the substrates. This increases contact between substrate and sprayed particle and improves bonding [2].

The methods discussed in section 2.2.4 and 2.2.6 are in category B and they depend upon the high velocity of the spray particles to create a dense and well adhering coating upon impact on the substrate. In these methods the spray particles are not very hot but they are travelling a lot faster. In the case of cold spraying, the particles may be sprayed even in the cold condition with no heating involved [8]. The coating is formed by the impact of the high velocity particles. Schematic diagrams of selected thermal spray process are shown in **Fig. 2.1** [9] and the comparative gas temperature and particle velocity for thermal spray processes are shown in **Fig. 2.2** [10].

The trend in thermal spraying is towards increasing particle velocity and decreasing particle temperature [4, 6, 11]. This offers many benefits namely:

- Less in-flight reactions of the sprayed particles and lower oxide content in the coatings

- Lower porosity and higher bond strength of coatings

The process development over the past few years has resulted in the increase in spray particle velocity (V_p) from 25 m s^{-1}, in flame spraying to ~ 750 m s^{-1} - 1500 m s^{-1} in cold spraying. The particle temperature has decreased from molten/semi-molten condition of the sprayed material, in thermal spraying, to solid state in cold spraying.

2.2.1 Arc spraying

In this process two wires of the material to be coated are brought together so as to propagate an arc between them, which continuously melts their tips. The molten metal is atomized and blown clear from the arc gap by compressed air. Feeding the wires together at a constant rate produces a steady stream of fine atomized particles which impact the substrate and form the coating [2].

2.2.2 Flame spraying

In this process the material to be sprayed is heated/melted in an oxy-fuel flame and these particles are then propelled on the substrate where they form the coating. Flame spraying equipment is available to use either wire or powder as feedstock [2].

2.2.3 Plasma spraying

In the plasma spraying process, gases like argon, helium and hydrogen are used to create high temperature plasma, wherein temperatures as high as 14000 K [2] can be generated. Ceramic, metal or cermet powder is injected in this high temperature region and the heated, melted or partially melted powder particles are propelled to the substrate where the coating is formed. The high temperatures generated in the plasma make it a very suitable method to coat ceramic materials creating coatings with typically 5 – 10 % porosity [2].

2.2.4 Detonation Technology

In the detonation spray system, a mixture of fuel and oxygen along with the powder is introduced into the combustion chamber. This gas mixture is ignited and an explosion/detonation wave is created. The powder particles are heated and accelerated to a very high velocity. A highly adhering low porosity coating is formed when the high velocity particles impact the substrate. The combustion chamber is purged by an inert gas after the detonation is over and the cycle is repeated again. Usually 1-15 cycles are carried out in one second. Due to the cyclic nature of the process deposition rates are usually low [2].

2.2.5 High Velocity Oxy-Fuel spraying (HVOF)

In the HVOF processes, oxygen and fuel are combusted and accelerated in a specially designed nozzle and combustion chamber. This creates supersonic velocity of the gases in the nozzle. The powder is injected in to the gas stream where it is accelerated to high velocity and also heated up to some extent. A highly adhering and low porosity coating is formed due to the high velocity impact of the particles [2]. The fuels can be gaseous such as hydrogen, propylene, or liquid such as kerosene. HVOF process is mainly used for metal and cermet powders but can also be used for selected ceramics.

2.2.6 Cold gas dynamic spraying (CGDS)

In the CGDS process, also known as cold spraying, a specially designed converging - diverging de Laval nozzle is used. The gas at a pressure of up to 3.5 MPa are fed to the de Laval nozzle and they attain supersonic velocity by virtue of the nozzle design. The powder, usually in the size range of 1 to 50 μm, is introduced into the flow by means of a high-pressure powder feeder, using a carrier gas to deliver the powder to the high-pressure converging part of the nozzle where it is entrained in the gas stream. The powder particles attain high velocity as the gas accelerates through the nozzle. Gases used are usually helium, nitrogen or air. The gases may be heated, although it is possible to form a coating without heating the gas [8, 12].

A schematic of the cold spray system is given in **Fig 2.3** [7].

2.3 Historical development of the cold spray process

The trend in thermal spray process development is towards increasing the particle velocity and decreasing the particle temperature [11]. In cold spraying the particles are deposited in the cold condition. In cold spraying the mechanism for acceleration of the feedstock particles results not from a combustion or detonation process, but rather through the control of the gas dynamics associated with a converging/diverging (de Laval) nozzle into which powder feedstock particles are introduced [4]. Cold spraying was developed in the mid 1980s at The Institute of Theoretical and Applied Mechanics of the Siberian Division of the Russian Academy of Science in Novosibirsk [13]. While performing supersonic wind tunnel tests with flows containing small tracer particles, scientists observed that above a critical particle velocity (V_p^*) which, depends upon the material being sprayed, there was a transition from particle erosion of target surfaces to rapidly increasing material deposition. Although this wind tunnel phenomenon had been observed by others, the Russian scientists developed the process as a coating technique. They successfully deposited a wide range of pure metals, metal alloys, polymers, and composites onto a variety of substrate materials. They also demonstrated that cold spray could rapidly apply coatings over large surface areas, up to 5 $m^2 min^{-1}$ in a pilot demonstration system for cold spray coating of pipe. A U.S. patent was issued in 1994 [8].

The actual mechanism by which the solid state particles deform and bond has not been well characterized. It is proposed that plastic deformation may disrupt thin

surface films, such as oxides, and provide intimate conformal contact under high local pressure, thus permitting bonding to occur. Though unproven, this hypothesis is consistent with the fact that wide ranges of ductile metals have been cold spray deposited. However experiments with non-ductile materials have not been successful unless they are co-deposited along with a ductile matrix material. This theory would also explain the observed minimum critical velocity necessary to achieve deposition, because sufficient kinetic energy must be available to plastically deform the solid material [13].

2.4 Gas dynamic principles of cold spraying

The following discussion about the one-dimensional isentropic flow is primarily based upon the text book "Compressible fluid flow" by Oosthuizen and Carscalen [14] and on the work done by Dykhuzien *et al.* [13] and Jodoin [15]. The nozzle exit velocity of the particle in a cold spray device is in principle, limited only by the gas velocity. High pressure gas flow, long nozzles, and small particles result in particles travelling at or near the gas velocity, and a particle acceleration model in cold spraying has been developed based upon the work by Gu *et al.* [16]

The gas flow in cold spraying may be studied as compressible gas flow under the following assumptions [13]:

i. The flow is one dimensional

ii. The gas flow is isentropic (adiabatic and frictionless)

iii. The gas is approximated as a perfect gas with constant specific heats

iv. The gas flow is calculated without considering the influence of the powder flux

The one dimensional flow ignores the small boundary layer present at the nozzle wall where the gas is traveling slower then the main body of the flow in middle of the nozzle. Thus, the gas flow rates calculated by the model are expected to be slightly higher than those obtained in practice. However, the area of the boundary layer is small as compared to the bulk of the flow thus it can be safely assumed that the bulk of the flow is largely one-dimensional. Also, the one-dimensional assumptions limit the application of the model to regions away from the jet impingement on the substrate.

The compressibility of a fluid is basically, a measure of the change in density that will be produced in the fluid by a specified change in pressure. Gases are in general, highly compressible whereas most liquids have a very low compressibility. In a fluid flow, changes in velocity will result in a change in pressure. These pressure changes will influence the density of the fluid, which will have an influence on the flow, i.e., the compressibility of the fluid involved will have an influence on the flow. If these density changes are significant, the temperature changes associated with the velocity changes also influence the flow, i.e., when compressibility is important, the temperature changes in the flow are usually important.

Compressibility effects are normally associated with gas flows in which the flow velocity is relatively high compared to the speed of sound in the gas. The basic assumptions regarding compressible flow, apart from those discussed above are:

i. The gas is continuous, i.e. the motion of individual molecules does not have to be considered, the gas being treated as a continuous medium. This is valid under most conditions, except under conditions of low pressure or vacuum

ii. No chemical changes occur in the flow

iii. The specific heats at constant pressure and constant volume, C_p and C_v are both constants. The ratio of two specific heats will be used extensively in the analyses of compressible gas flows and is given by:

$$\gamma = \frac{C_p}{C_v} \quad \text{---------- Equation 2.1}$$

It should also be recalled that

$$R = C_p - C_v \quad \text{---------- Equation 2.2}$$

Where, R is the universal gas constant.

This is valid if the gases are not subject to very large temperature changes.

iv. Gravitational effects on the gas flow field are negligible. This assumption is quite justified for gas flows.

v. Magnetic and electrical fields are negligible. These effects are important if the gas is electrically conducting, e.g. ionized gas. However in cold spraying this is not important.

vi. The effects of viscosity are negligible. This is never true close to a solid surface; however, for a nozzle, the overall effects of viscosity remain small.

When the above assumptions are adopted, the flow field is completely described by knowing the values of the following variables at all points of the flow field;

- Velocity vector, v
- Pressure, P
- Density, ρ
- Temperature, T

The equations describing the flow field are derived by applying the following principles,

- Conservation of mass (continuity equation)
- Conservation of momentum (Newton's Law)
- Conservation of energy (First law of thermodynamics)
- Equation of state

2.4.1 One-dimensional isentropic flow

The concept of control volume is used in the derivation and application of many equations of compressible flow. A control volume is an arbitrary imaginary volume of cross-section area A, fixed relative to the coordinate system being used bounded by a control surface through which fluid may pass.

Applying the law of conservation of mass over a control volume gives us the continuity equation, which is:

$$\frac{d\rho}{\rho}+\frac{dv}{v}+\frac{dA}{A}=0$$ ---------- **Equation 2.3**

Applying the law of conservation of momentum over a control volume gives:

$$\frac{-dP}{\rho}=VdV$$ ---------- **Equation 2.4**

The energy equation for an adiabatic steady flow is given by:

$$C_p dT+VdV=0$$ ---------- **Equation 2.5**

The equation of state applied on a control volume is given by:

$$\frac{dp}{p}-\frac{d\rho}{\rho}-\frac{dT}{T}=0$$ ---------- **Equation 2.6**

The compressibility effects are important in a gas flow when the velocity in the flow is high. In general it is taken that compressibility effects must be considered in

a flow $M > 0.3$, where Mach number, M = velocity of gas/velocity of sound in that gas;

$$M = \frac{v}{a} \text{ ---------- Equation 2.7}$$

Where a is the velocity of sound. When $M > 1$, the flow is called as supersonic flow and when, $M < 1$ the flow is considered subsonic.

The speed of sound in a perfect gas is given by

$$a = \sqrt{\gamma \overline{R} T} \text{ ---------- Equation 2.8}$$

Where, $\overline{R}$ is the specific gas constant and $\overline{R} = \frac{R}{m}$; m is the molecular weight of the gas.

The entropy remains constant in an isentropic flow, thus

$$P / \rho^{\gamma} = c \text{ (Constant) ---------- Equation 2.9}$$

If any two points 1 and 2, in an isentropic flow are considered, having the conditions of pressure, temperature, volume and density specified by P_1, T_1, V_1, ρ_1 and P_2, T_2, V_2, ρ_2. The cross-section areas at points 1 and 2 are A_1 and A_2.

Then from **Equation 2.9** it follows that:

$$\frac{P_2}{P_1} = \left(\frac{\rho_2}{\rho_1}\right)^{\gamma}$$ ---------- **Equation 2.10**

Combining equations 3.4 and the general equation of state $P = \rho RT$ gives:

$$\frac{a_2}{a_1} = \sqrt{T_2/T_1} = \left(\frac{\rho_2}{\rho_1}\right)^{\frac{\gamma-1}{2}} = \left(\frac{P_2}{P_1}\right)^{\frac{\gamma-1}{2\gamma}}$$ ---------- **Equation 2.11**

Applying the steady state adiabatic energy equation between points 1 and 2 gives,

$$\frac{T_2}{T_1} = \frac{1+\frac{1}{2}(\gamma-1)M_1^2}{1+\frac{1}{2}(\gamma-1)M_2^2}$$ ---------- **Equation 2.12**

For isentropic flow **Equations 2.12** and **2.11** can be combined, thus

$$\frac{P_2}{P_1} = \left(\frac{1+\frac{1}{2}(\gamma-1)M_1^2}{1+\frac{1}{2}(\gamma-1)M_2^2}\right)^{\frac{\gamma}{\gamma-1}}$$ ---------- **Equation 2.13**

$$\frac{\rho_2}{\rho_1} = \left(\frac{1+\frac{1}{2}(\gamma-1)M_1^2}{1+\frac{1}{2}(\gamma-1)M_2^2}\right)^{\frac{1}{\gamma-1}}$$ ---------- **Equation 2.14**

The continuity equation gives,

$\rho_1 V_1 A_1 = \rho_2 V_2 A_2$ This can be rearranged to give,

$$\left(\frac{\rho_2}{\rho_1}\right)\left(\frac{V_2}{V_1}\right)=\left(\frac{A_1}{A_2}\right)$$ ---------- **Equation 2.15**

The **Equations 2.12 - 2.15** can be used to adequately describe the characteristics of one-dimensional isentropic flow.

2.4.2 Stagnation conditions

Stagnation conditions are those that would exist if the flow at any point in a flow was isentropically brought to rest. If the velocity is zero at some point in an isentropic flow, then the conditions at the zero velocity point are considered as the stagnation conditions. The stagnation conditions are denoted by the subscript *0*. The stagnation P_0, ρ_0 and T_0 since M at stagnation conditions is 0, are related to P, ρ and T at some point in the flow by the following equations,

$$\frac{P_0}{P}=\left(1+\frac{\gamma-1}{2}M^2\right)^{\frac{\gamma}{\gamma-1}}$$ ---------- **Equation 2.16**

$$\frac{\rho_0}{\rho}=\left(1+\frac{\gamma-1}{2}M^2\right)^{\frac{1}{\gamma-1}}$$ ---------- **Equation 2.17**

$$\frac{T_0}{T}=\left(1+\frac{\gamma-1}{2}M^2\right)$$ ---------- **Equation 2.18**

2.4.3 Critical conditions

The conditions that would exist if the flow was isentropically accelerated or decelerated to **M** = 1 are known as critical conditions and they are denoted by an asterisk. The critical $\mathbf{p^*}$, $\boldsymbol{\rho^*}$ and $\mathbf{T^*}$ since $\mathbf{M_2}$ at stagnation conditions is 1, are given by,

$$\frac{T^*}{T} = \left(\frac{2}{(\gamma+1)} + \frac{\gamma-1}{\gamma+1} M^2 \right)$$ ---------- **Equation 2.19**

$$\frac{a^*}{a} = \sqrt{\left(\frac{2}{(\gamma+1)} + \frac{\gamma-1}{\gamma+1} M^2 \right)}$$ ---------- **Equation 2.20**

$$\frac{P^*}{P} = \left(\frac{2}{(\gamma+1)} + \frac{\gamma-1}{\gamma+1} M^2 \right)^{\frac{\gamma}{\gamma-1}}$$ ---------- **Equation 2.21**

$$\frac{\rho^*}{\rho} = \left(\frac{2}{(\gamma+1)} + \frac{\gamma-1}{\gamma+1} M^2 \right)^{\frac{1}{\gamma-1}}$$ ---------- **Equation 2.22**

The relation between the critical conditions and the stagnation conditions can be found by setting $M = 0$ in the above equations, thus

$$\frac{T^*}{T_0} = \frac{2}{\gamma+1}$$ ---------- **Equation 2.23**

$$\frac{a^*}{a_0} = \sqrt{\frac{2}{\gamma+1}}$$ ---------- **Equation 2.24**

$$\frac{P^*}{P_0} = \left(\frac{2}{\gamma+1}\right)^{\frac{\gamma}{\gamma-1}}$$ ---------- **Equation 2.25**

$$\frac{\rho^*}{\rho_0} = \left(\frac{2}{\gamma+1}\right)^{\frac{1}{\gamma-1}}$$ ---------- **Equation 2.26**

2.4.4 Shock waves

In a supersonic flow, under certain conditions sudden deceleration of the flow to subsonic flow can take place across a thin region. This deceleration of flow is accompanied by an increase in pressure. This extremely thin region where the change from a supersonic flow to subsonic flow takes place along with an increase in pressure is known as a shockwave. Shock waves are important in cold spray process because a shockwave occurring in the flow path will change the supersonic flow to a subsonic flow. Because the exit pressure calculated by **Equation 2.16** is typically less than ambient a simple check is required to ascertain that shocks do not form inside the nozzle. The following calculation yields a trial pressure for the design. P_s is the downstream shock pressure that would be obtained if a shock occurred at the nozzle exit when the pressure at nozzle exit is P_e [13]:

$$\frac{P_s}{P_e} = \frac{2\gamma}{\gamma+1}M^2 - \frac{\gamma-1}{\gamma+1}$$ ---------- **Equation 2.27**

If P_s is equal to ambient pressure, a shock occurs at the nozzle exit. If this pressure is less than the ambient pressure, a shock occurs somewhere inside the nozzle and subsequent subsonic flow occurs past the shock location so that the exit pressure is equal to ambient pressure. If P_s is greater than the ambient pressure, then the calculations as per the equations described in sections 2.4.1, 2.4.2 and 2.4.3 represent real conditions inside the nozzle. The gas stream then slows down outside of the nozzle exit as the pressure adjusts to the ambient. This gas deceleration upon exiting is not as significant in cold spraying due to short stand-off distances.

2.4.5 Flow in converging-diverging nozzle

The flow in a variable cross-sectional area is given by,

$$\frac{dA}{dv} = (M-1)\frac{A}{v}$$ ---------- **Equation 2.27**

As A and v are positive, it is seen from **Equation 2.27** that,

1. If $M < 1$, then dA has the opposite sign to dv, i.e., decreasing the area increases the velocity and vice versa.
2. If $M > 1$, then dA has the same sign as dv, decreasing the area decreases the velocity and vice versa.

3. If $M = 1$ then $\frac{dA}{dv} = 0$. From (1) and (2) it follows that when $M = 1$, A must be a minimum.

It follows from the above discussion that a converging divergent nozzle is required to accelerate the flow to supersonic. The convergent part accelerates the flow to $M = 1$ and the divergent portion accelerates the flow to supersonic velocity. At the throat since $dA = 0$ the Mach number, $M = 1$.

The critical nozzle area is given by,

$$A^* = \frac{\dot{m}}{\sqrt{\gamma P_0 \rho_0}} \left(\frac{2}{\gamma+1}\right)^{\frac{\gamma+1}{2(\gamma-1)}} \quad \text{---------- Equation 2.29}$$

$\dot{m}$ is the mass flow rate of the gas. This equation may be used to calculate the critical area needed to achieve supersonic flow in the divergent part of the nozzle, if the throat conditions are $M = 1$.

In a converging diverging nozzle the flow at any point down stream of the throat having cross-section area as A^* is related to the mach number of the flow by the equation,

$$\frac{A}{A^*} = \frac{1}{M}\left[\frac{2}{\gamma+1}\right]\left[1+\left(\frac{\gamma-1}{2}\right)M^2\right]^{\frac{\gamma+1}{2(\gamma-1)}} \quad \text{---------- Equation 2.30}$$

The **Equation 2.30** can be used to calculate the Mach number for a ratio of A/A^*. The conditions of flow depend upon the back pressure, which is the pressure in the downstream region of the nozzle. For a given stagnation conditions of P_0, ρ_0, T_0 there exists a back pressure where the gas pressure at throat is equal to the critical pressure, P^*. The gas velocity at throat will be $M = 1$ when the back pressure is decreased to P^*. Once the Mach number of 1 has been reached at the throat, further reduction in the back pressure can not affect the mass flow rate through the nozzle. The nozzle in this condition is considered as choked. If the back pressure is decreased further below P^*, a region of supersonic flow develops just downstream of the throat. This region of supersonic flow is terminated by a normal shockwave. The shock wave increases the pressure and reduces the velocity to subsonic. If the back pressure is further reduced the supersonic flow region is extended and the shockwave moves further downstream in the divergent part of the nozzle. As the back pressure is further reduced the shock wave will eventually be on the exit plane of the nozzle. When this condition is achieved the flow in the nozzle is isentropic and the **Equation 2.30** can be used to calculate the velocity of the gas. When the back pressure is decreased further the shockwave moves outside the nozzle and eventually, with further reduction in back pressure, a point is reached where the exit pressure and back pressure are equal. The nozzle is then known to operate at its design pressure ratio and there are no shock waves inside or outside the nozzle. When the back pressure is decreased below the exit plane pressure the exit pressure is expanded to the back pressure through a series of expansion waves and the nozzle is said to be in the under expanded condition. The above discussion was for a

condition of constant stagnation pressure and decreasing the back pressure. However, in the condition of operation of cold spray nozzle the back pressure is usually the atmospheric pressure and the stagnation pressure is increased to get supersonic flow in the divergent part of the nozzle. The area ratio of the nozzle is used to calculate the design Mach number of the nozzle using **Equation 2.30**. The **Equation 2.29** can be used to calculate the minimum stagnation pressure and mass flow rate required to achieve, critical conditions at the nozzle throat.

2.4.6 Particle acceleration model

Gu *et al.* [16] developed a computational fluid dynamics model for acceleration of particles in HVOF spraying. The model developed is presented here.

The momentum transport between the gas and particle can be solved directly from Newton's second law;

$$m_p \frac{dv_p}{dt} = F \quad \text{---------- Equation 2.31}$$

Where F is the force acting on the particle, N; m_p is the mass of particle, kg; v_p is the velocity of particle, m s^{-1} and t is time in seconds. The acting force in the particle could involve the drag force, force due to pressure gradients, force due to added mass, Basset history term, and external potential forces [2]. In principle, among the factors that affect the movement of particle during the HVOF process,

only the drag force plays a dominant role; other factors can be neglected in most cases [2]. Therefore, the aero-dynamic drag force can be used to represent the general force in the form;

$$F_D = \frac{1}{8} A_p \rho_g C_d \left| v_g - v_p \right| \left(v_g - v_p \right) \text{---------- Equation 2.32}$$

Where F_D is the drag force, N; A_p is the surface area of the particle, m^2; ρ_g is the density of the gas, kg m^{-3}; C_d is the drag factor, V_g is the velocity of gas, m s^{-1}.

The acceleration for a spherical particle is deduced as;

$$\frac{dv_p}{dt} = \frac{3\rho_g}{4 d_p \rho_p} C_d \left| v_g - v_p \right| \left(v_g - v_p \right) \text{---------- Equation 2.33}$$

Where d_p is the diameter of the particle, m; and ρ_p is the density of the particle, kg m^{-3}.

The drag factor C_d is related to the Reynolds number (R_e) as follows;

$$C_d = \frac{24}{R_e} \qquad (R_e < 1)$$

$$C_d = \frac{24}{R_e}\left(1 + 0.15 R_e^{0.67}\right) \qquad (1 < R_e < 10^3) \text{ ---------- Equation 2.34}$$

$$C_d = 0.44 \qquad (R_e > 10^3)$$

The Reynolds number is defined by;

$$R_e = \frac{\rho_g |v_g - v_p| d_p}{\mu_g} \quad \text{---------- Equation 2.35}$$

Where, μ_g is the dynamic viscosity of the gas, kg m^{-1} s^{-1}, which is assumed to be constant. The **Equations 2.31 – 2.35** were solved numerically by Thei, using the assumption of isentropic gas flow to obtain particle velocities for various nozzle lengths and expansion ratios [17].

If the value of particle diameter is provided, **Equation 2.33** can be used to calculate the velocity of a particle after a small time interval. The particle velocity can be calculated by inputting calculated gas velocity (**Equation 2.30**) and an initial value for particle velocity in **Equation 2.35** and thereafter using the Reynolds number to calculate the drag coefficient. The drag coefficient is then used in **Equation 2.33** to calculate the particle velocity. The density of gas to be used in **Equation 2.33** is obtained from the **Equation 2.17**. Further details of particle velocity calculation in cold spraying are available in [17].

2.4.7 Nozzle design

The one dimensional isentropic analysis shows that the nozzle geometry and the pressure ratio are important factors to consider when designing a cold spray nozzle operating at a specific Mach number [13-15]. The general geometry required to accelerate a subsonic flow to the supersonic regimen is a convergent-divergent nozzle. With this geometry, the fluid is continuously accelerated from low subsonic

to supersonic velocity. The flow passes through the sonic condition ($M = 1$) at the junction of the converging and the diverging parts, i.e. at the throat.

The maximum possible particle velocity is the gas velocity; this can be increased by using a lower molecular weight gas or by increasing the inlet gas temperature. **Equation 2.8** shows that heating the gas and using gas having lower molecular weight will achieve higher velocity of sound as it has higher specific gas constant ($\overline{R}$). Thus, as predicted by **Equation 2.30**, the exit Mach number does not depend upon the type of gas or the gas temperature, but the higher velocity of sound will result in higher gas velocities. **Equation 2.30** shows that the exit gas velocity can also be increased by using a nozzle with higher expansion ratio. However, it is seen from **Equation 2.17**; higher expansion ratio results in lower gas density in the divergent part. This decrease in gas density can be off-set by increasing the stagnation gas pressure, as this will increase the total gas mass flow and result in a denser gas.

The CGDS nozzles can have a rectangular cross-section of the throat and exit [12, 18-21] or a circular cross-section throat but rectangular cross-section of exit [22-24] and circular cross-section of throat and circular cross-section of exit [25-27].

2.5 Commercially available cold spray systems

Cold spray systems are available commercially from Cold Gas Technology (CGT), Ampfig, Germany and Ktech Corporation, USA. The photo of the CGT cold spray system is shown in **Fig. 2.4** [28]. The system consists of a nozzle, gas heater, powder feeder and a process controller. Various groups in Russia have come out with cold spray systems based upon their research into the two-dimensional gas dynamic model of the flow, heat and momentum transfer from gas to particles, particle impact and deformation theory, coating microstructural development, etc. These processes use compressed air, nitrogen and helium as the carrier gas at wide range of gas temperature and pressure to produce some coatings with acceptable characteristics. However, systems based on these processes are relatively cheap. These processes have been marketed with various brand names such as Rus Sonic, Tev Tech, Dymet, etc [29].

2.6 Applications of cold sprayed coatings

ASB Industries in USA has carried out extensive work on development of the cold spray process for thick coatings/freeform fabrication. Most applications developed by ASB industries and other workers are proprietary. Cold spray has produced protective coatings and performance enhancing layers, ultrathick coatings, freeforms, and near net shapes. Large sizes and shapes can be spray-fabricated, and geometrical features can be easily incorporated during spray preparation, and then

machine finished. When a robot is used to handle cold spray gun, CAD files can be used to control the spray pattern to produce near net shapes (NNS). Moreover, by controlling the feed stock composition, the deposit microstructure and composition can be varied to produce functionally gradient materials (FGM) and other special structures [30].

Some applications of cold sprayed deposits are listed below [30-32]:

- Copper coatings on aluminium heat sinks.
- Cold sprayed thermal management layers for the RL60 rocket engine.
- Copper-carbon MMC thermal management layers for NASA GRC.
- Cold spray fabrication of slabs and plates of high strength copper alloys.

Some of the potential applications of cold spray coatings are [32]:

- Nickel and nickel base alloys for corrosion and wear protection layers.
- Tantalum layers for chemically resistant layers in the chemical industry.
- Generation of solderable surfaces on materials with poor wettability (for example heat sinks, copper on aluminium)
- Deposition of electric screening coatings on plastics
- Deposition of conducting structures on non-metals
- Deposition of brazing and soldering alloys

Fig. 2.5 shows an example of soldered power transistor on an aluminium heat sink with a cold sprayed copper layer [32]. The industrial applications of cold sprayed

coatings can be further developed by research and development in the following areas [32]:

- Availability of low cost powder feed stocks with adequate processing properties (feeding properties, purity), which can produce coatings of the required quality.
- Improving reproducibility of the cold spray process.
- Integrating the complete manufacturing process; pre and post-treatment / machining processes / heat treatment and combination with other manufacturing processes.

2.7 Mechanism of deposit formation

2.7.1 Particle velocity and temperature during cold spraying

2.7.1.1 Concept of critical velocity and its estimation

The particles in cold spraying are accelerated by the drag force of the gas acting on them in the de Laval nozzle. There exists a critical impact velocity (V_p^*) for the sprayed particles, which, must be exceeded to induce particle deposition rather than erosion [4, 6, 12, 13, 21, 22, 26, 27, 33-36]. The value of V_p^* usually lies between 500 - 800 m s^{-1} for most metals [4, 27]. The variation of deposition efficiency with particle velocity in cold spraying is shown in **Fig. 2.6** [4]. The deposition efficiency is seen to increase with particle velocity, reaching values from 30% to 80% [4].

Stoltenhoff *et* al. [27] conducted experiments with four different nozzles having different geometries (expansion ratios, shape and length of the divergent section) to deposit copper on to aluminium. The diverging section of nozzle A had a length of 65 mm, an expansion ratio of 6 and a conical shape. Nozzle B has the same length and shape of the diverging section but the expansion ratio is 9. Nozzle C is a lengthened version of nozzle A by a factor of 1.5 with a bell shaped contour. The bell shaped nozzle D is lengthened by a factor of 1.8 with respect to nozzle B. All four nozzles were tested for spraying copper onto aluminium substrates. The particle impact velocity was computed using computational fluid dynamic (CFD) Code FLUENT. It was seen that not all copper particles adhered to the substrate. The fraction adhering is termed the deposition efficiency. Assuming that only particles above a certain critical velocity will form a coating, it is postulated that for the measured particle size distribution, this will only be the case for particles up to the diameter for which the cumulative mass fraction is equivalent to the deposition efficiency [27, 36]. The respective deposition efficiencies for each nozzle are shown in **Fig. 2.7(a)**. The maximum particle diameter corresponds to about 12.2 μm for nozzle A, 14.3 μm for nozzle B, 15.8 μm for nozzle C and 17.5 μm for nozzle D, as shown in **Fig. 2.7(b)**. For these maximum particle diameters, the calculated impact velocity is in the range of 550 m s^{-1} to 570 m s^{-1} with their respective nozzles. Therefore, this can be considered as a critical velocity but only for the particular powder used in that work [27, 36-38].

2.7.1.2 Particle velocity and temperature during cold spraying

Voyer *et al.* [27, 36] carried out numerical simulation of the gas and particle flow. The Computational Fluid Dynamic code (CFD-code) FLUENT was used to model the flows inside and outside of the nozzle. **Fig. 2.8** shows gas and particles flow calculations performed by the CFD-code FLUENT for a nozzle having expansion ratio of 9 using N_2 as process gas at an initial temperature of 593 K and initial pressure of 2.5 MPa and using copper particles having 15 μm diameter. It is clearly observed that gas acceleration takes place in the nozzle throat area and in the first third of the divergent section of the nozzle. As the gas accelerates, its temperature falls far below room temperature. In the free jet, after the nozzle exit, irregular changes of the gas properties are due to compression shocks. The velocity of the particles rises sharply in the first half of the divergent section of the nozzle. Since the gas velocity in the free jet is still higher than the particle velocity, acceleration of the powder particles is still taking place. The powder particles are injected upstream of the throat of the nozzle, where the gas is relatively hot and slow, therefore, the particles are heated up rapidly in this section. After the throat section, the particles cool down but they always remain at a temperature higher than the gas temperature.

The particle velocities and temperatures calculated by Voyer *et al.* using nitrogen as process gas are shown in **Fig. 2.9 – 2.10** and using helium gas is shown in **Fig. 2.11** [36]. The temperature and velocity of 15 μm copper particles at the exit of the nozzle as a function of inlet gas pressure for a fixed inlet gas temperature of 673 K

is shown in **Fig. 2.9(a)**. The particle temperature is almost independent of the gas inlet pressure. However, for the gas inlet pressure range shown in **Fig. 2.9(a)**, the particle velocity is dependent on the pressure and increases by a factor of 15 % approximately as the inlet gas pressure is doubled. **Fig. 2.9(b)** shows the temperature and velocity of 15 μm diameter copper particles at the exit of the nozzle as a function of the inlet gas temperature for a fixed inlet gas pressure of 2.5 MPa. Both particle temperature and velocity are strongly dependent on the inlet gas temperature. For the inlet gas temperature range shown in **Fig. 2.9(b)**, when the inlet gas temperature is doubled, the particle temperatures is approximately doubled and the particle velocity increases by a factor of 25 % approximately.

Fig. 2.10 shows temperature and velocity of copper particles at the exit of a nozzle as a function of particle diameter for an inlet gas pressure and temperature of 2.5 MPa and 673 K respectively. It is seen that smaller particles are accelerated to higher velocities due to their lower inertia and are cooled to much lower temperatures (due to gas expansion) than coarser particles.

Fig. 2.11 shows the effect of the process gas type (N_2 or He) on the temperature and velocity of 15 μm diameter MCrAlY particles at the exit of the nozzle as a function of either the inlet gas pressure (**Fig. 2.11(a)**) or the inlet gas temperature (**Fig. 2.11(b)**). The nozzles used in these experiments were optimized for N_2 and He. Therefore the dimensions of optimal nozzle for N_2 are different than the dimensions of the optimal nozzle for He. **Fig. 2.11** clearly shows that higher particles velocities by approximately 75 % are obtained when using He gas for either a fixed inlet gas

pressure or temperature. At the same time, the use of He as a process gas decreases the particle temperature by approximately 100 K for either a fixed inlet gas pressure or temperature.

Steenkiste *et al.* [24] used the one dimensional model to compute the gas and particle velocity and temperature along the length of the nozzle for copper particles of various sizes using a nozzle having throat diameter 2.8 mm and exit dimensions of 2 mm by 10 mm (expansion ratio of 3.25). They used air heated to 800 K for their deposition experiments. The velocity computation from their work is shown in **Figs. 2.12 & 2.13**. The results of their computations show that smaller particles (1 μm) are accelerated to higher velocities, and although smaller particles are heated to higher temperatures in the throat they also cool down rapidly along with the gas in the diverging part of the nozzle. They validated their computations by measuring particle velocities for known particle diameters. Reasonable agreement between the results of the measurements and the computations was obtained.

The particle velocity has been experimentally determined using techniques such as Laser two focus (L2F) Velocimetry and Particle Image Velocimetry (PIV) [21, 23, 39]. Shukla *et al.* used PIV to measure the velocity of copper particles (1, 5 and 18 μm in size) deposited using air at 288 K to 293 K, 3.1 MPa and nozzle having expansion ratio of 5.1. They measured velocities between 700 to 750 m s^{-1} [21]. L2F was used by Gilmore *et al.* to measure the velocity of 19 and 22 μm sized copper particles sprayed using air and helium as driving gas [39]. They observed that the measured variation of particle velocity with gas pressure and temperature was in

reasonable agreement with theoretical predictions. They concluded that helium can be used as the driving gas instead of air to achieve higher particle velocities for a given temperature and pressure. Coating deposition efficiencies were found to increase with particle velocity. A significant mass loading effect on the particle velocity was observed; particle velocities began to drop as the mass ratio of powder to gas flow rates exceeded 3 %.

2.7.1.3 Influence of heating the gas on substrate during cold spraying

The influence of gas heating on the substrate was investigated by Taeyung *et al.* [40]. They used CFD – code FLUENT to predict the particle and gas, temperature and velocity in cold spraying. They observed significant heating of the substrate due to high shear flow at the substrate. The formation of a bow shock near the substrate was observed by Morgan *et al.* and the image of the bow shock provided by them is given in **Fig. 2.14** [41]. They observed that larger particles deform the most even though they are not accelerated as much as smaller particles. This is due to the bow shock. When the gas jet impinges on the substrate, a high-pressure region is formed directly above the substrate, resulting in a shock wave opposing the flow from the nozzle. The particles have to penetrate the bow shock before impacting on the base material. While the larger particles have sufficient momentum to maintain the critical velocity, the smaller lighter particles are decelerated to the point where they will no longer undergo deformation on impact. Taeyung *et al.* [40] also studied the effect of presence of a bow shock region near the substrate on the particle velocity

for different particle diameters in aluminium. The results obtained by them are shown in **Fig. 2.15**. The velocity of 1 μm particles reduces drastically, due to the bow shock, from nearly 900 m s^{-1} to less than 400 m s^{-1}; the decrease in 5 μm size particle is much less, from ~ 850 m s^{-1} to just below 800 m s^{-1}. The effect of bow shock on particle velocities of particles larger than 10 μm was negligible.

2.7.2 Impact phenomenon in cold spraying

The coating deposition and growth is dependent upon the impact of high velocity particles and hence the impact phenomenon of the particles with the substrate has been investigated by many researchers [22, 35, 42-44].

Steenkiste *et al.* studied the particle substrate interaction for aluminum particles in the size range of –106 μm +63 μm [35]. For the particle to stick to the substrate or the underlying coating, all of its kinetic energy must be transformed into heat and strain energy of the coating and substrate. Such a plastic deformation was observed experimentally, with a roughly spherical aluminum particle flattening into a pancake like shape with an aspect ratio in the range of 3:1 to 5:1. The yield stress of the particle and/or the substrate must be exceeded during the collision, and for this reason powders and substrates usually employed in the cold spray process are metals with relatively low strength. Such deformation of deposited material has been observed by several other researchers for a variety of substrate-deposited material combination [6, 8, 19, 35, 41, 42, 44-51]. The microstructure images of

cold sprayed aluminium, Inconel 718, copper and Cu-W are shown in **Fig. 2.16(a-b)** [41], **Fig. 2.17(a-b)** [47], **Fig. 2.18(a-b)** [45] and **Fig. 2.19(a-b)** [46] respectively. A wide range of materials have been deposited by cold spraying. The microstructures show significant deformation of the sprayed particles.

Papyrin *et al.* [42] numerically studied the dynamics of aluminum particle deformation. They observed that a high speed radial jet of metal is formed at the contact zone. This effect is similar to the jet formed during explosive welding and it leads to corona shaped ejection of metal at the final stage of plastic deformation at the periphery contact zone. The formation of a metal jet has been suggested and it has been subsequently experimentally verified [43-45, 52]. The image showing jetting for the case of aluminium particle impacts upon aluminium substrate is shown in **Fig. 2.20** [43, 44] and for the case of copper particle impact on copper substrate is shown in **Fig. 2.21** [45].

2.7.3 Bonding mechanism for deposit formation

In cold spraying, a clean and oxide free interface between substrate and the sprayed particles as well as between previously deposited particles and oncoming particles is formed due to the plastic deformation and metal jetting observed during cold spraying [19, 22, 42]. The bonding mechanism in cold spraying can be compared to those in processes such as explosive cladding or shock wave powder compaction. In these processes metal jetting is observed and the microstructures show regions of

highly deformed material [45]. In explosive cladding as well as shock wave compaction successful bonding has been related to the critical conditions for extensive plastic deformation at the particle/particle interface [45]. Assadi *et al.* [45] modelled the deformation of particles upon impact using the finite element program ABAQUS/EXPLICIT. They chose two particle velocities for the impact of copper particles (-22 + 5 μm) on copper substrate in their model, namely 500 m s^{-1} and 600 m s^{-1}. The critical velocity was estimated according to the method described in section 2.7.1.1, for impact of copper particles on copper substrate was 570 m s^{-1}. The phenomenon at impact is shown in **Fig. 2.22**. The particles and substrates are initially at room temperature. The contours indicate temperature and the arrows represent the magnitude of velocity at the respective surfaces. The figure shows much localized heating near the particle/substrate interface for both impact velocities; this is more severe for the higher velocity impact. The figure also shows the formation of a jet-type flow of material at the interface at an early stage of impact. The formation of the jet is attributed to the localization of plastic deformation in cold spraying. The strain and stress profiles for a 10 μm particle, 5 ns after the beginning of the impact, for two initial velocities of 300 and 900 m s^{-1} are shown in **Fig. 2.23**. For the impact velocity of 300 m s^{-1}, there is a monotonic increase in flow stress as the interface is approached. This is a result of hardening effects due to high strains at the interface. The high plastic strain at the interface on the other hand results in softening due to adiabatic heating. At the higher particle velocities, the softening effect can dominate over the hardening effect thus leading to adiabatic shear instability at the interface. This effect is observed for an impact

velocity of 900 m s^{-1}. At this velocity, despite the high magnitude of plastic strain at the interface, the shear strength of material falls to values near zero due to dominance of thermal softening over hardening. **Fig. 2.24(a-c)** [45] shows the strain, stress and temperature rise during impact at various particle velocities. As shown in **Fig. 2.24(a)** strain rates of up to 0.5 x 10^9 s^{-1} and maximum strains of about 4 are observed for three velocities of 450, 500 and 550 m s^{-1}. For the velocity of 580 m s^{-1} the flow mechanism changes from plastic to viscous flow and strains of about 10 are achieved. **Fig. 2.24(b)** shows that heating rates for all impact velocities are around 10^9 K s^{-1}. For the impact velocity of 580 m s^{-1}, the temperature approaches the melting temperature of copper, whereas in other cases it remains well below it. **Fig. 2.24(c)** shows the temporal development of the equivalent stress. For lower or medium velocities of up to 550 m/s, there is a drop in stress after 0.05 μs, which can be attributed to the loading conditions from the substrate. For an impact velocity of 580 m s^{-1} the stress changes 0.3 μs after impact and wide fluctuations in stress are observed. This coincides with the increase in temperature and strain as seen in **Fig. 2.24(a-b)**. It is seen from the above analysis that rapid changes in variables like strain, temperature and stress take place in a narrow range of impact velocity between 550 and 580 m s^{-1}. This velocity range corresponds well with the estimated critical velocity for deposition (570 m s^{-1}). Assadi *et al.* [45] suggest that bonding takes place due to adiabatic shear instability upon impact. The occurrence of adiabatic shear instability depends upon the impact velocity; the critical velocity must be exceeded for adiabatic shear instability to occur. A similar model for bonding in cold spraying has been suggested by Grujicic *et al.* [53]. They

suggest that adiabatic shear localization and the associated formation of the interfacial jets during cold spraying can be expected to produce clean contacting surfaces. In addition, adiabatic softening of the material in the particle/substrate interfacial region combined with relatively high contact pressures promote formation of mutually conforming contacting surfaces via plastic deformation of the contacting surfaces.

2.8 Characterization of cold sprayed deposits

The properties of the cold sprayed deposits are highly dependent upon the spraying conditions employed [7, 19, 20, 24, 35, 54-57]. The wide range of spray parameters in terms of gas pressure, flow and temperature; particle morphology, size and route of manufacturing, etc that can be used to deposit coatings results in coatings with properties scattered over a wide range in terms of density, hardness, adhesion on substrate, electrical resistivity etc. **Table 2.2** describes some properties of cold spray coatings and the conditions used to deposit these coatings. The values for a typical bulk material are also given for comparison. It is seen that the hardness of all the cold sprayed materials are higher than those of a corresponding bulk material. This is attributed to the significant cold working during cold spray deposition. The coatings display porosity < 5 % and in some cases for copper the porosity is < 0.1 %. The porosity in aluminium shows dependence upon the powder feed rate used; higher powder feed rate (0.65 g s^{-1}) produces denser coatings (porosity 1.75 %) while lower powder feed rate produces coatings with higher

porosity (4 %) [35]. Similarly the adhesion of aluminium on brass for coatings produced using lower powder feed rate is lower (30.5 MPa) than the adhesion for coatings produced using higher powder feed rate (49 MPa). The authors attribute the lower porosity and higher adhesion to the peening effect of the impacting aluminium particles during spraying, which is greater for the higher powder feed rate. The adhesion strength of copper on aluminium substrate is greater than 70 MPa as at this strength the epoxy failure was observed [24].

The resistivity of bulk copper and copper produced by cold spraying as well as different thermal spray methods is shown in **Fig. 2.25** [54]. The resistivity of cold sprayed copper was seen to be close to the bulk value whereas thermal sprayed copper had high values of resistivity. The effect of heat treatment on the resistivity of cold sprayed copper is shown in **Fig. 2.26** [58]. As sprayed copper has resistivity of ~ 23 nΩ m. It is seen that annealing at 373 K does not affect the resistivity significantly but annealing at 473 K decreases the resistivity to ~ 19 nΩ m. In addition, the hardness values of copper annealed at different temperatures are shown in **Fig. 2.27** [58]. As-deposited copper has a hardness of 140 kgf mm^{-2}. The hardness does not start to significantly decrease until 473 K; following annealing at 673 K, the hardness decreases to ~ 95 kgf mm^{-2}. The authors attribute the decrease in electrical resistivity after annealing to recovery and recrystallization and the decreases in hardness to grain growth.

The properties of cold sprayed Ti were investigated by Marrocco *et al* [56, 59]. The hardness plot from their work is given in **Fig. 2.28** [59] and the porosity values are

shown in **Fig. 2.29** [56]. The hardness values are distributed in the range between 100 and 200 kgf mm^{-2}. The authors attribute the scatter in the hardness values to the porosity observed in the coatings. The porosity was 15 % to 22 % for coatings deposited at gas pressures between 15 bar to 29 bar. The adhesion strength of cold sprayed Ti on Ti6Al4V and steel substrates is shown in **Fig. 2.30** [56]. The adhesion on grit blasted substrate was ~ 10 MPa whereas on polished/ground surface it was ~ 20 MPa. The authors suggest that work hardening of the substrate during grit blasting hardens the substrate and decreases the deformation of the substrate during cold spraying. The decreased deformation of substrate hinders the formation of a metallurgical bond at the interface of coating-substrate.

2.9 Conclusions

The following areas can be identified in the science of cold spraying where gaps exist in the present knowledge.

1 Adhesion of cold sprayed deposits on non-metallic, particularly polymer substrates.

2 Mechanism by which the phenomenon of adiabatic shear instability promotes bonding in cold spray coatings, as it is seen that the adhesion strength of deposits are lower than their tensile strength.

3 Relation between the deposit microstructure and their properties like resistivity, hardness, tensile strength.

4 Microstructural stability of cold sprayed coatings has received only a little attention.

The present work will attempt to increase the understanding of the adhesion of deposits on non-metallic substrates, the relationship between the deposit microstructure and their properties and thermal stability in cold sprayed coatings.

Table 2.1: Processing conditions and deposit properties of thermal spray processes [2, 6, 7, 60].

Property	Wire flame spraying	Powder flame spraying	Wire arc spraying	Air plasma spraying	HVOF spraying	D-Gun spraying	Cold spraying
Effective temperature / K	< 3300	< 3300	< 5300	< 16000	< 3300	< 3300	< 800
Substrate temperature / K	323 - 423	373 – 423	323 – 400	370 – 400	370 – 400	370 -400	295 – 395
Particle velocity / m s^{-1}	150 – 240	25 – 35	150 – 400	300 – 500	800 – 1200	800 – 1500	400 – 1500
Materials sprayed	Metals, alloys and ceramics	Metals, alloys, ceramics, cermets & polymers	Metals, alloys and cermets	Metals, alloys, ceramics and cermets	Metals, alloys, ceramics and cermets	Metals, alloys, ceramics and cermets	Metals and alloys
Average spray rates / kgs hr^{-1}	2.5 - 30	3 – 9 metals 1.5 – 2.5 ceramics	4.5 – 55	3 – 9 metals 5.5 – 9 ceramics	4 – 5 cermets	0.9 – 2.4	0.3 – 3.
Adhesion values / MPa	6 - 10	6 - 10	10 - 20	20 - 70	> 70	> 70	30 - 35

Table 2.2: Properties of cold sprayed coatings deposited using various spraying conditions.

Powder				Cold spray conditions				Properties			Ref.
Composition	Size / μm	Morphology	Manufacturing route	Nozzle expansion ratio	Gas temperature / K	Gas pressure / bar	Powder feed rate / g s^{-1}	Hardness / kgf mm^{-2}	Porosity / %	Adhesion / MPa	
Cu	10 - 20	Convoluted	Direct reduction	NI	588 (air)	20 – 24	NI	140 ± 10	NI	NI	[20]
Cu	< 45	Angular	NI	3.25	800 (air)	20	NI	102 ± 8	0 – 0.1	~ 70 (Al substrate, epoxy failure)	[24]
Al	63 - 106	Spherical	Gas atomized	3.25	561[(1)] (air) 588[(2)] (air)	20	0.22[(a)] 0.65[(b)]	51[(2)] (air); powder feed rate not indicated	4[(1, a)] 1.75[(1, b)]	30.5[(1, a)] 49[(1, b)] (brass substrate)	[35]
Steel	< 45	Angular	Water atomized	NI	616 (He)	20	NI	193 ± 12	NI	NI	[19]
Nickel	5 - 35	Spherical	Gas atomized	3.23	773 (He)	24	NI	263	2	NI	[57]
38.4Co31.7Ni 21Cr8.1Al0.6 Y	5 - 25	spherical	Gas atomized	3.23	773 (He)	24	NI	551	4	NI	[57]
Cu (bulk)	-	-	-	-	-	-	-	64	-	-	[20]
Al (bulk)	-	-	-	-	-	-	-	37.5	-	-	[35]
Steel (bulk)	-	-	-	-	-	-	-	118 ± 13	-	-	[19]
Ni (bulk)	-	-	-	-	-	-	-	261	-	-	[57]
CoNiCrAlY	-	-	-	-	-	-	-	202			[57]

Note: NI means not indicated

a

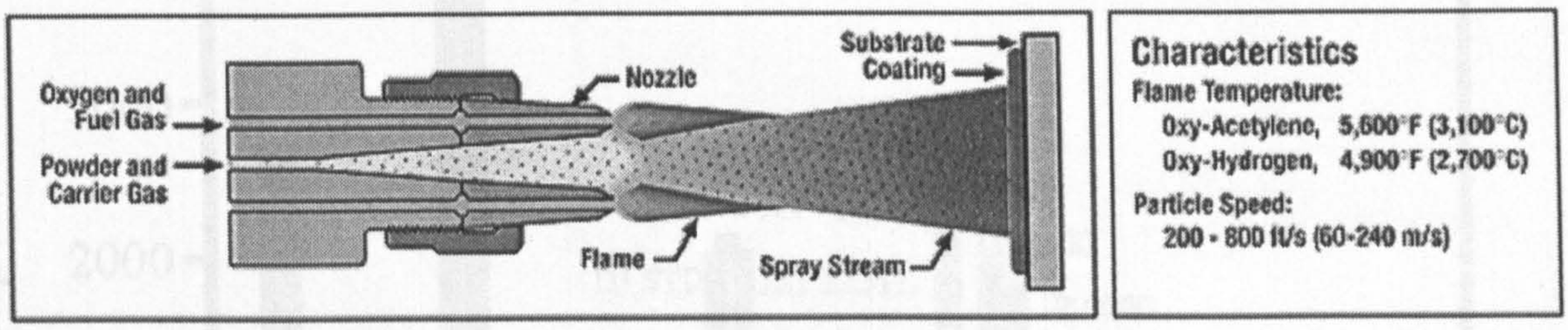

b

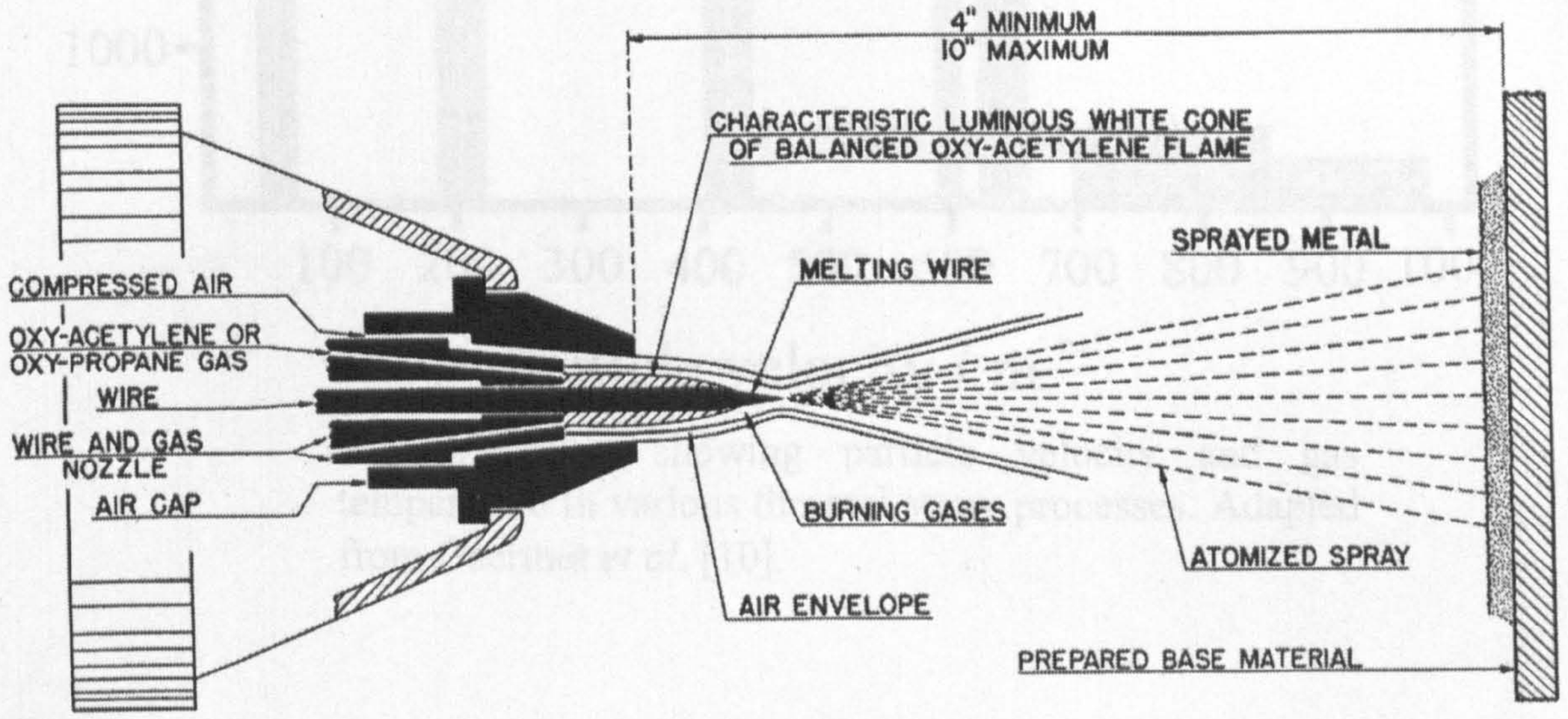

c

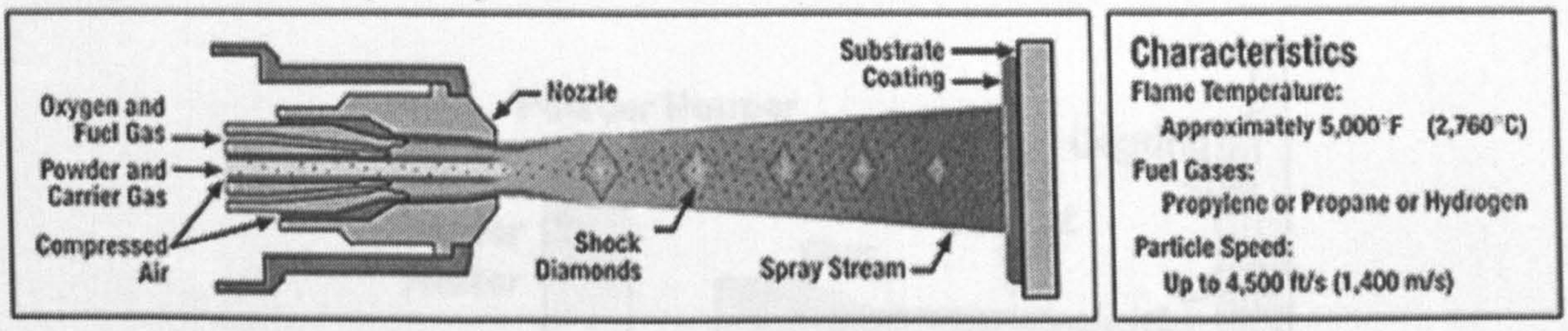

d

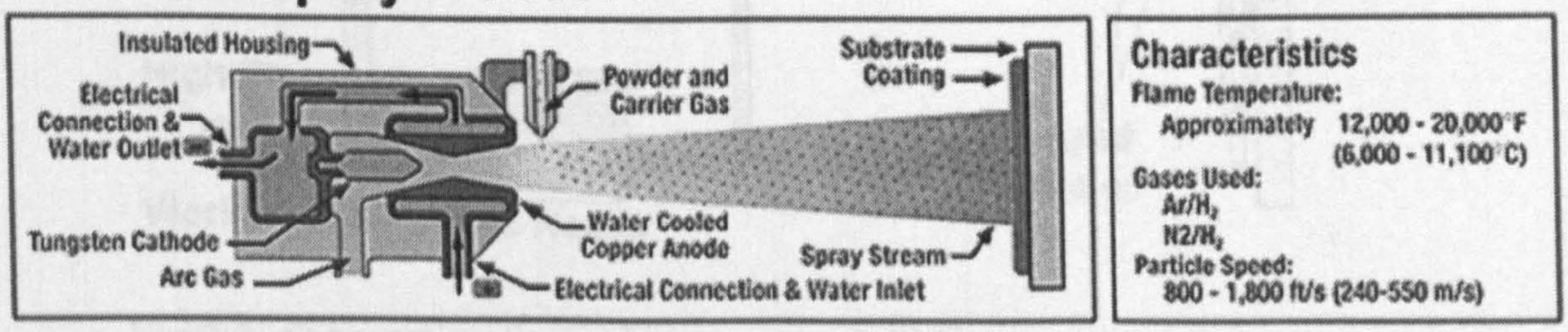

Fig. 2.1: Schematic diagram of thermal spray processes; a), Flame spray; b), Wire flame spray; c), HVOF; d), Air Plasma spray [9].

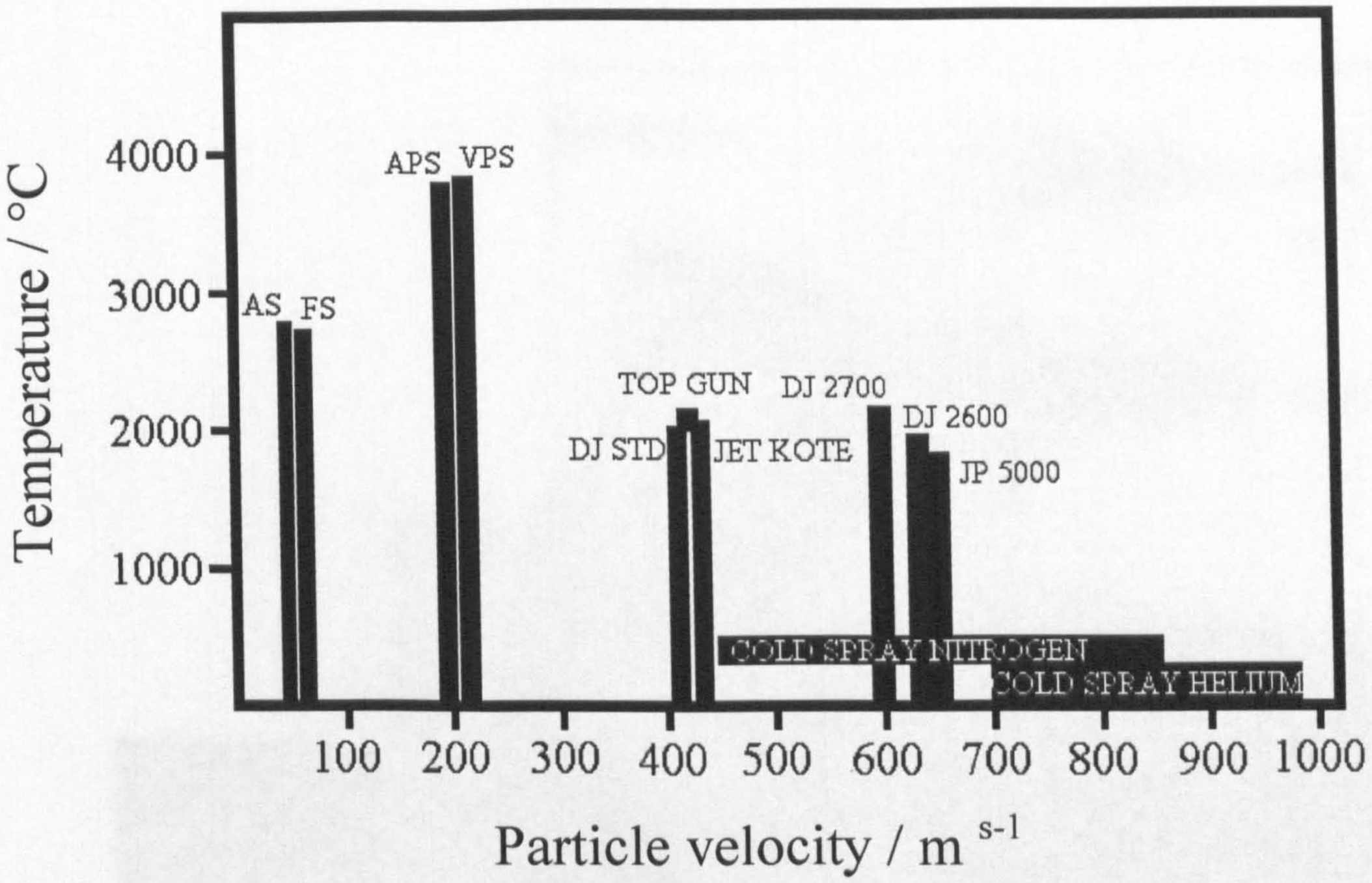

Fig 2.2: Plot showing particle velocity and gas temperature in various thermal spray processes. Adapted from Gaertner *et al.* [10].

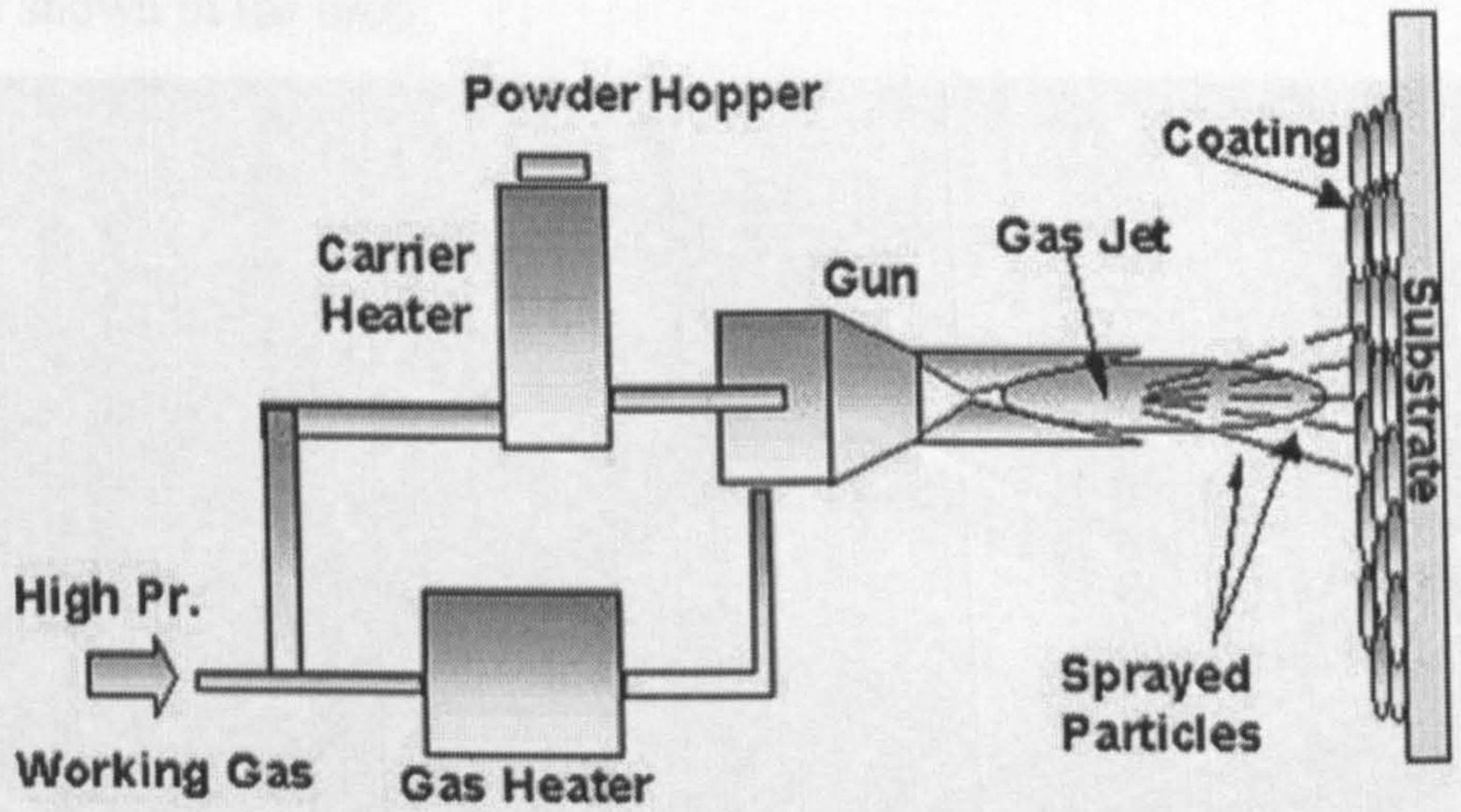

Fig 2.3: Schematic of a cold spray system [30].

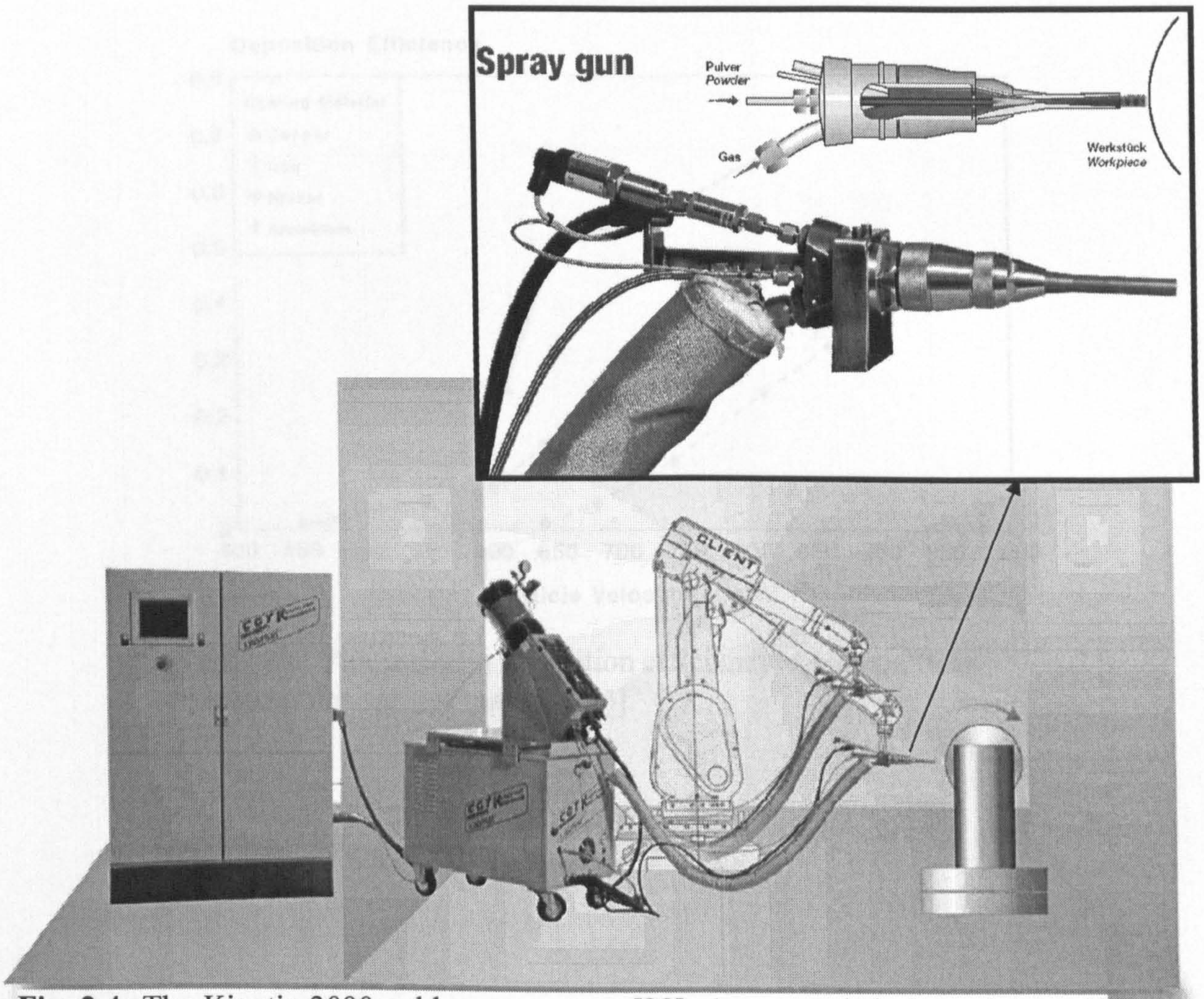

Fig. 2.4: The Kinetic 3000 cold spray system [28]. An expanded view of the cold spray gun is shown in the inset.

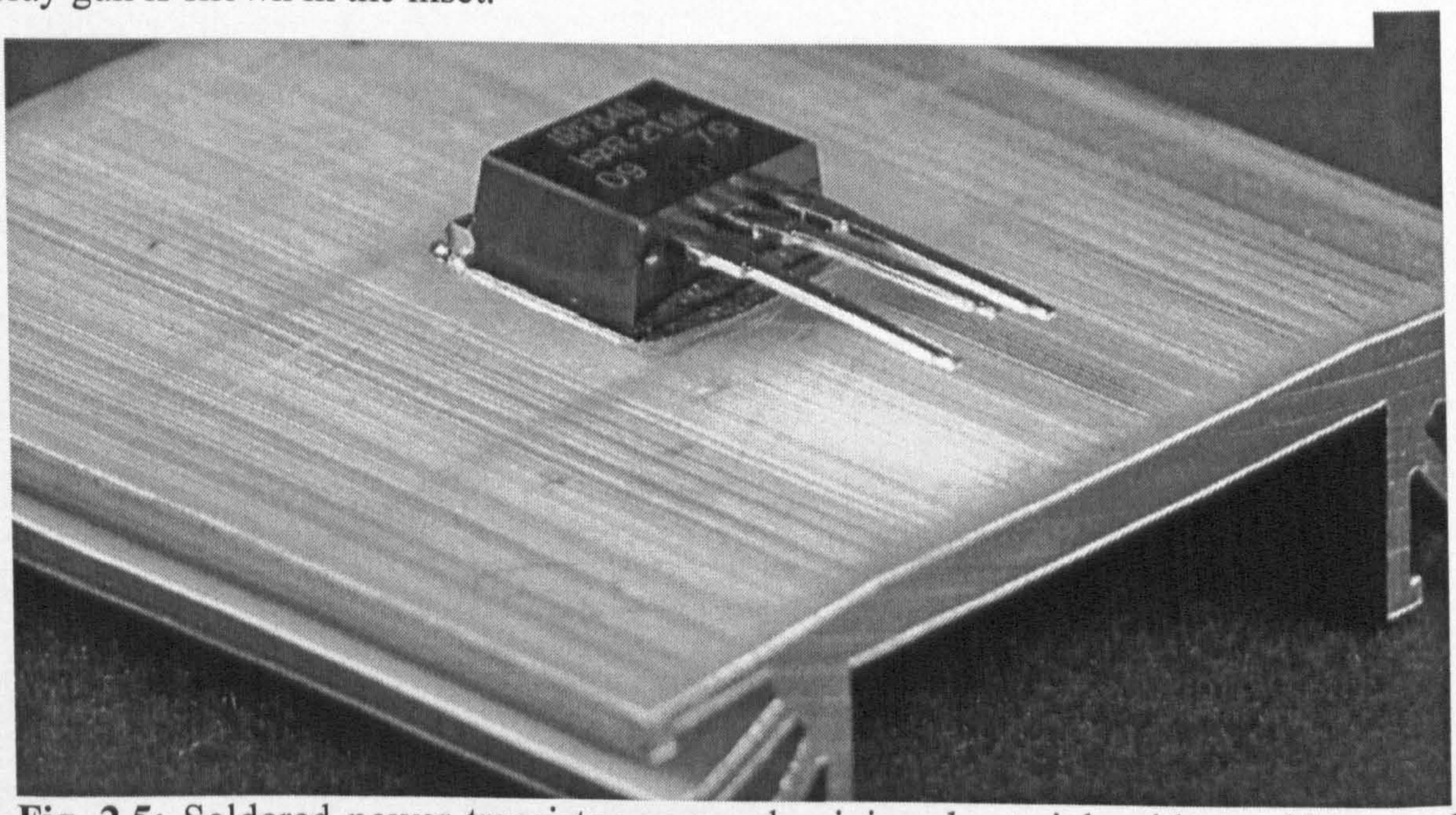

Fig. 2.5: Soldered power transistor on an aluminium heat sink with a cold sprayed copper layer [32].

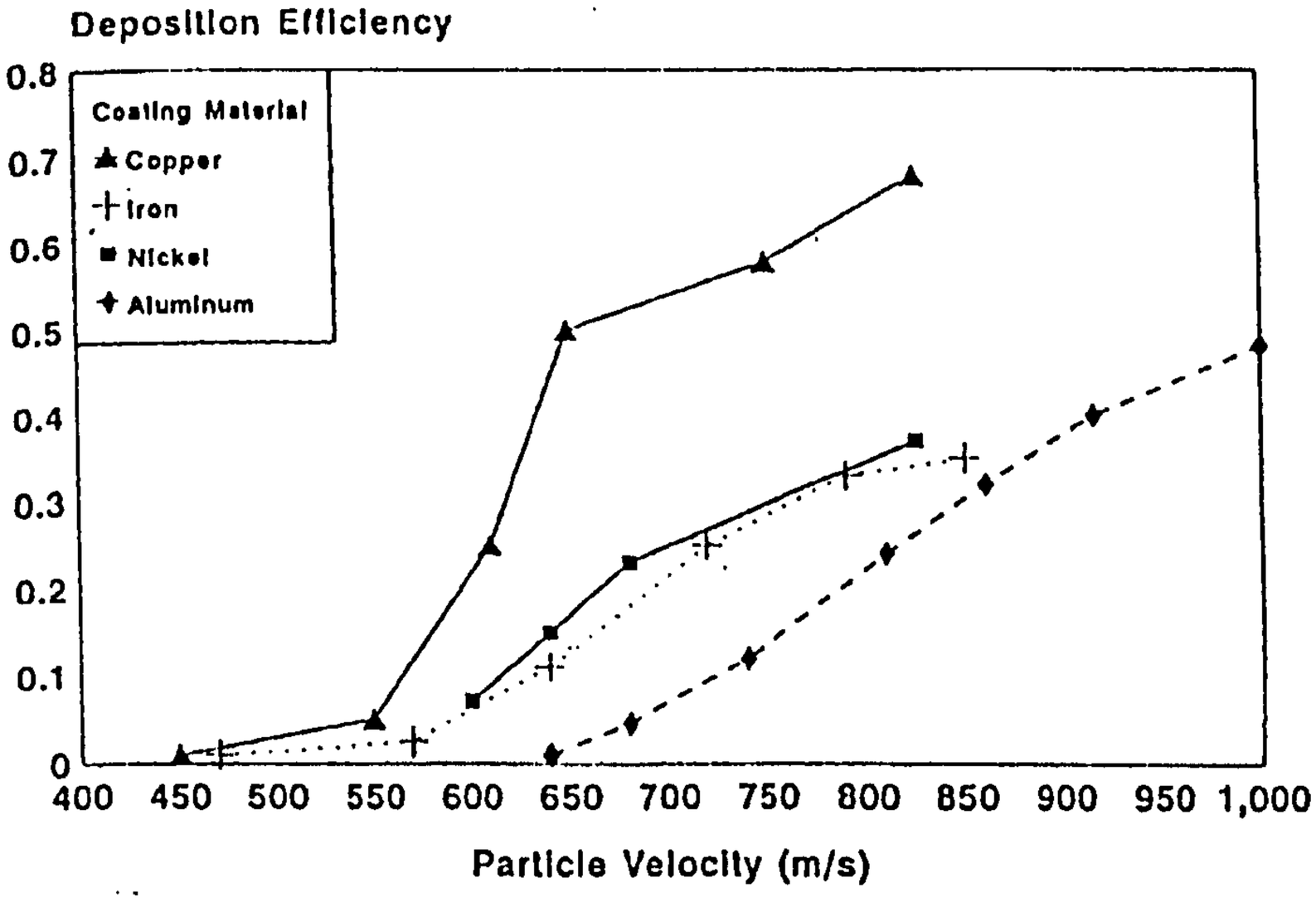

Fig. 2.6: Plot showing deposition efficiency versus particle velocity for various materials [4].

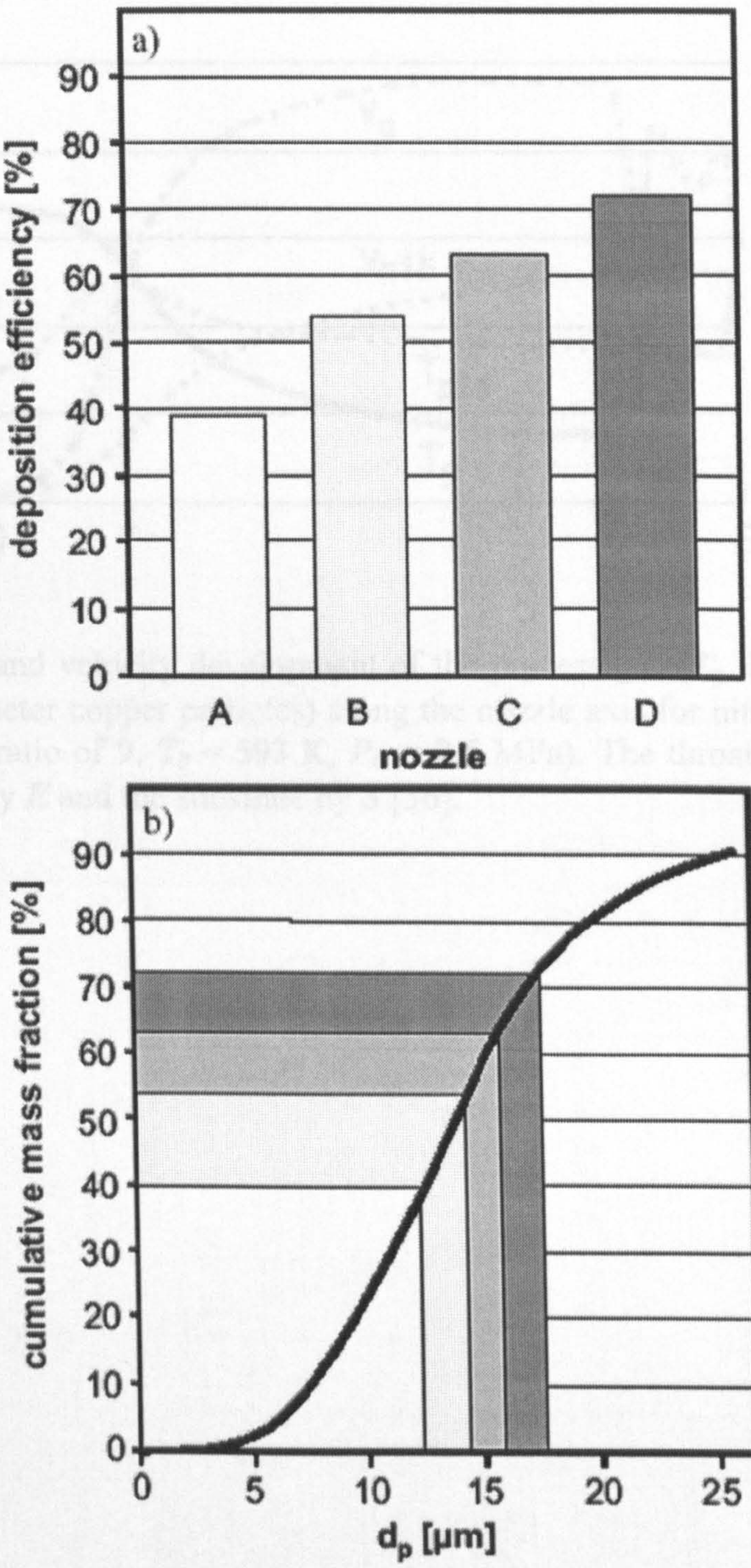

Fig. 2.7: Deposition efficiency (a) and size distribution of particles (b) for spray tests with 4 different nozzle geometries [36].

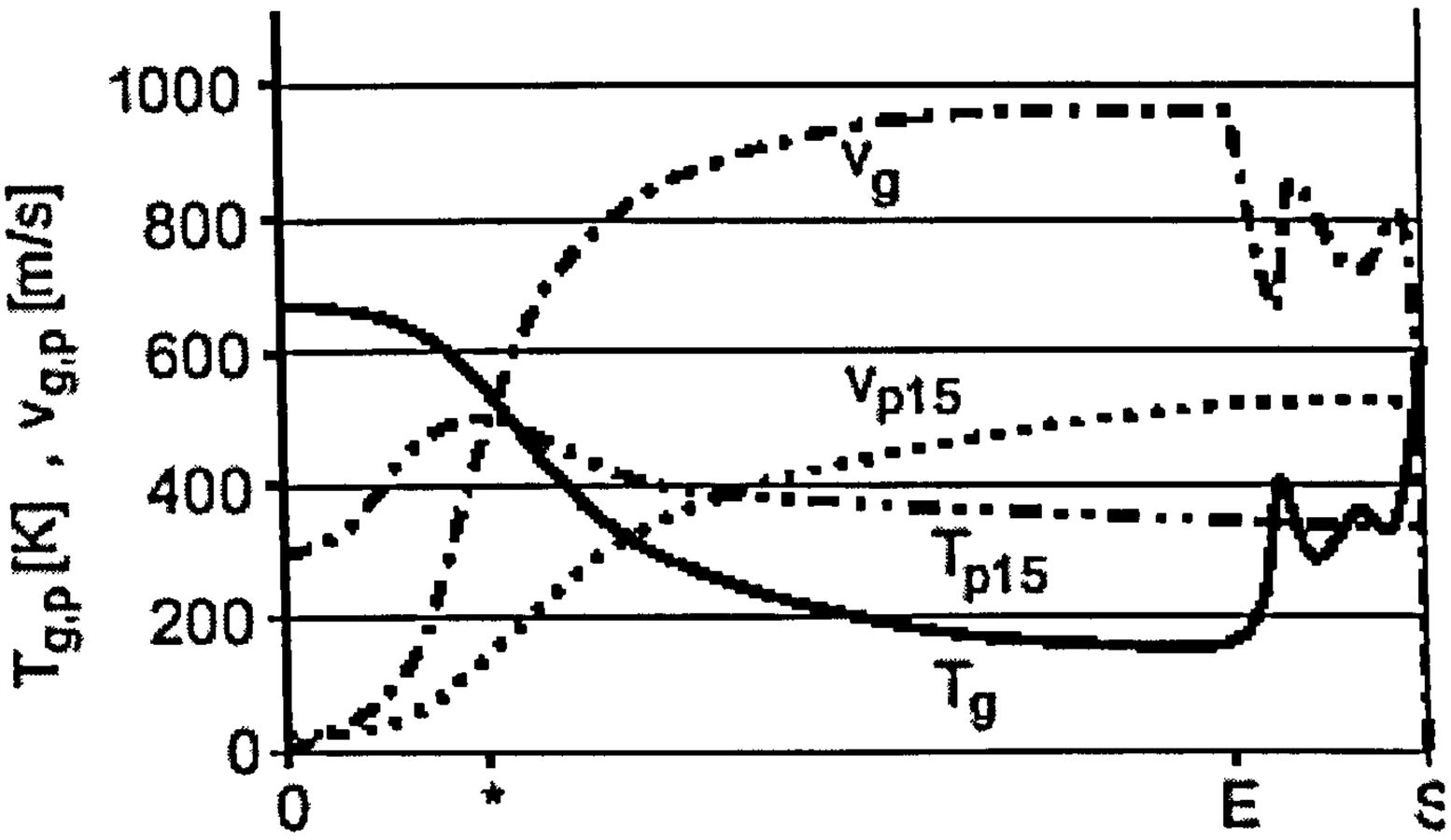

Fig. 2.8: Temperature and velocity development of the process gas (T_g, V_g) and particles (T_p, V_p for 15 µm diameter copper particles) along the nozzle axis for nitrogen as process gas (nozzle expansion ratio of 9, T_0 = 593 K, P_0 = 2.5 MPa). The throat of the nozzle is denoted by *, the exit by E and the substrate by S [36].

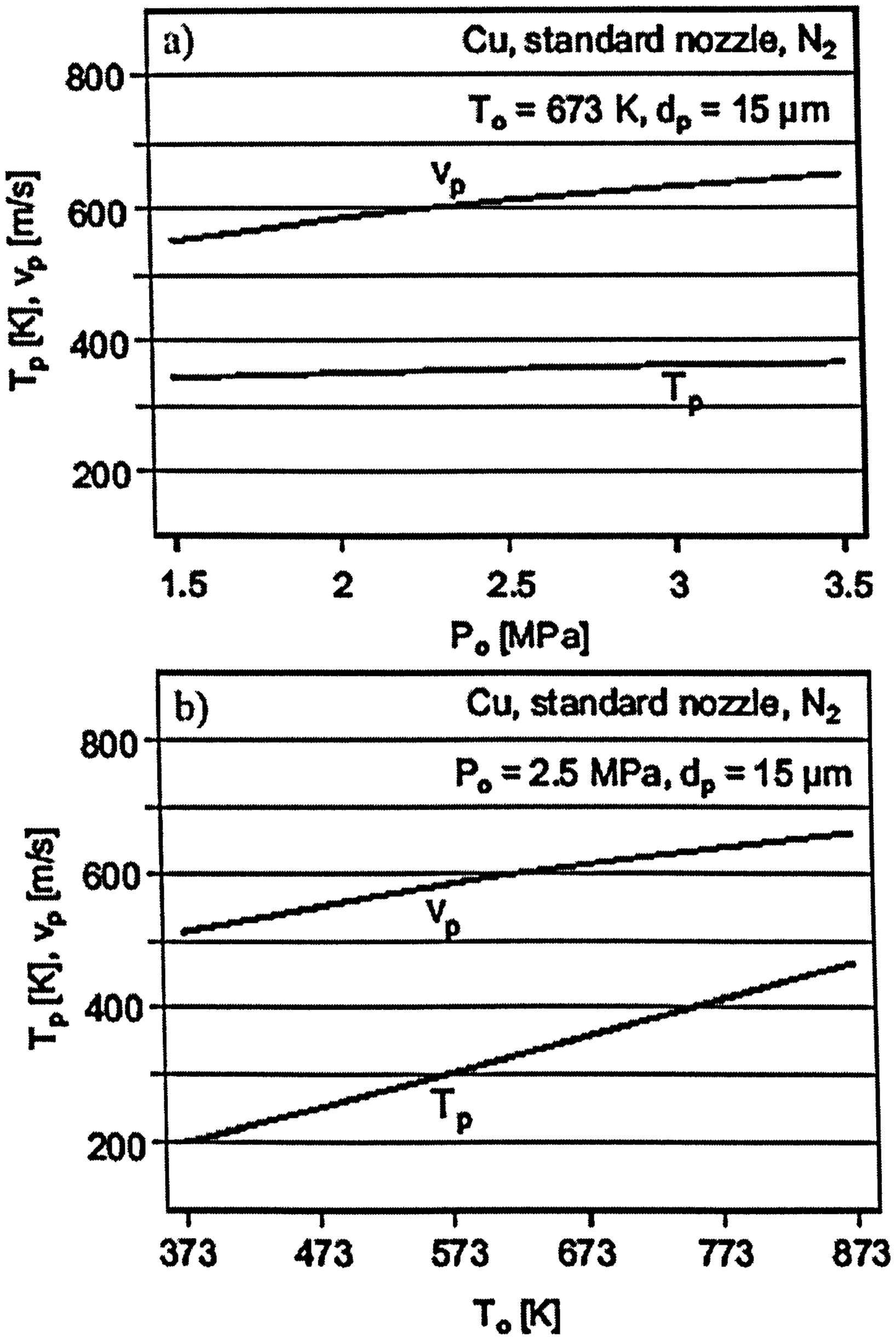

Fig.2.9: Temperature and velocity of 15 µm diameter Cu particles at the nozzle exit using N_2 as process gas. As a function of a) process gas inlet pressure (nozzle having expansion ratio of 9, T_0 = 673 K and b) process gas inlet temperature (nozzle having expansion ratio of 9, P_0 = 2.5 MPa) [36].

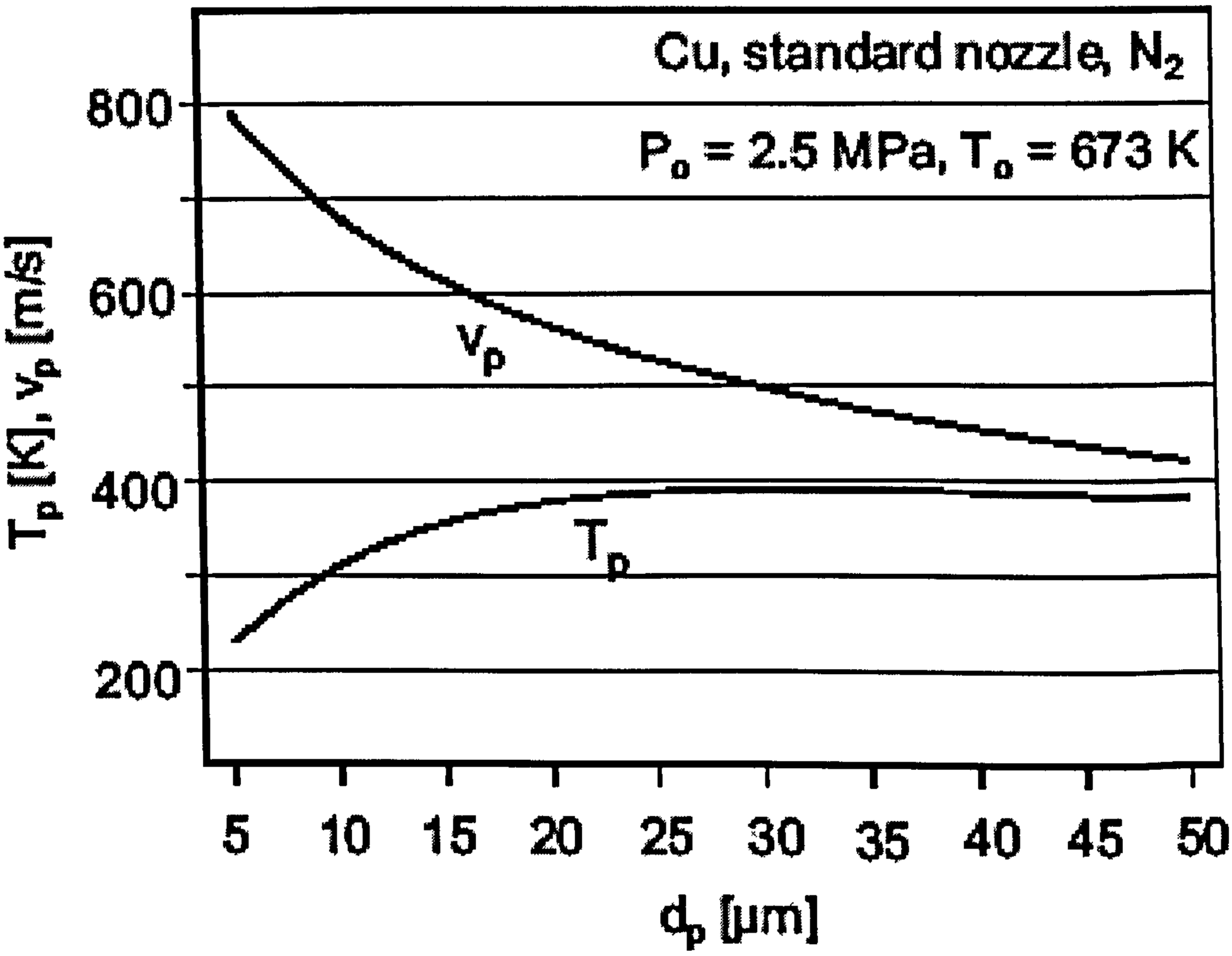

Fig. 2.10: Effect of the particles diameter on the temperature and velocity of Cu particles at the nozzle exit using N_2 as process gas (nozzle having expansion ratio of 9, $T_0 = 673$ K, $P_0 = 2.5$ MPa) [36].

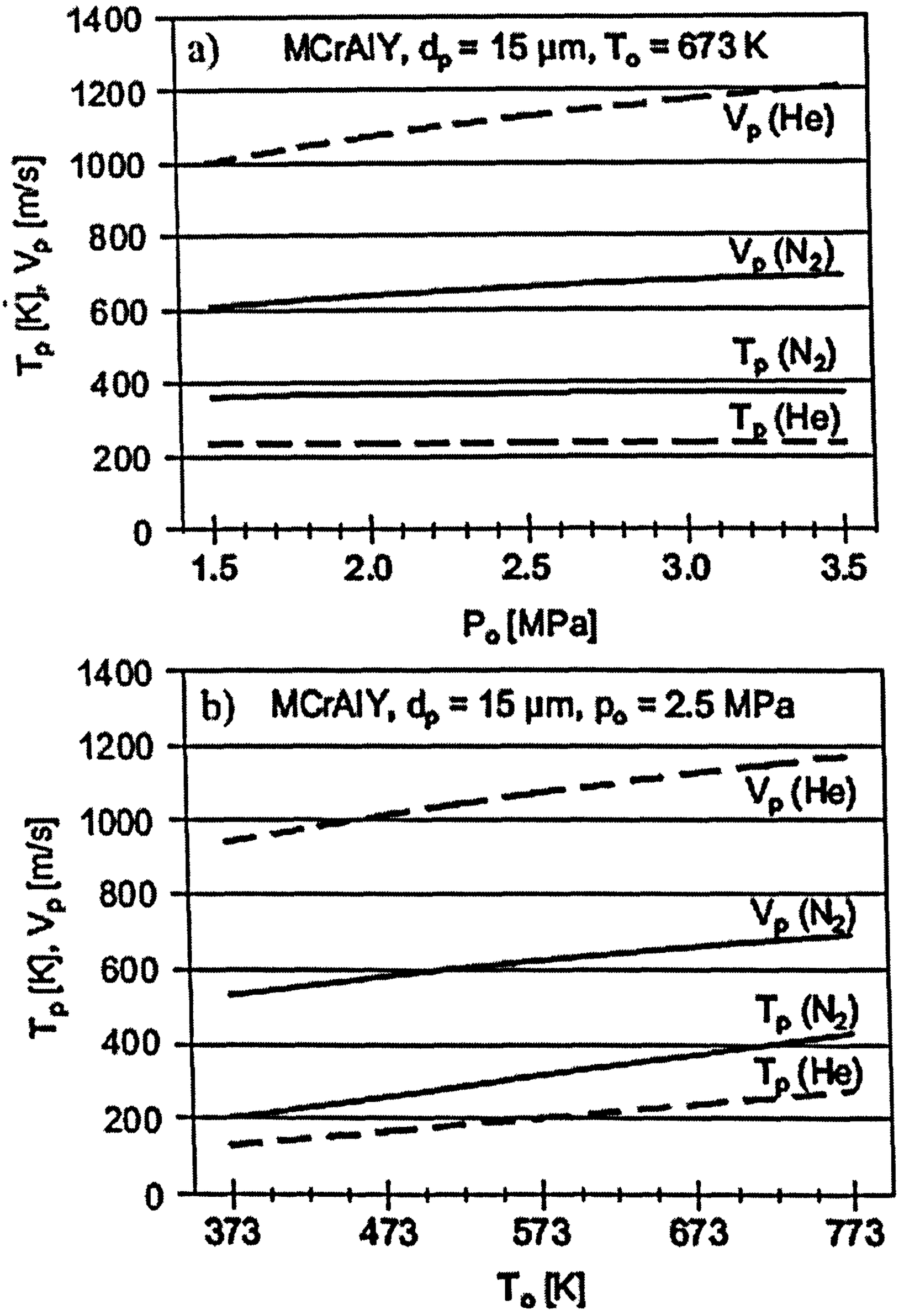

Fig. 2.11: Effect of the process gas nature (N_2 or He) on the temperature and velocity of 15 mm diameter MCrAlY particles at the nozzle exit, a) for different process gas pressure (nozzle expansion ratio of 9, T_0 = 673 K) and b) for different process gas temperature (nozzle expansion ratio of 9, P_0 = 2.5 MPa) [36].

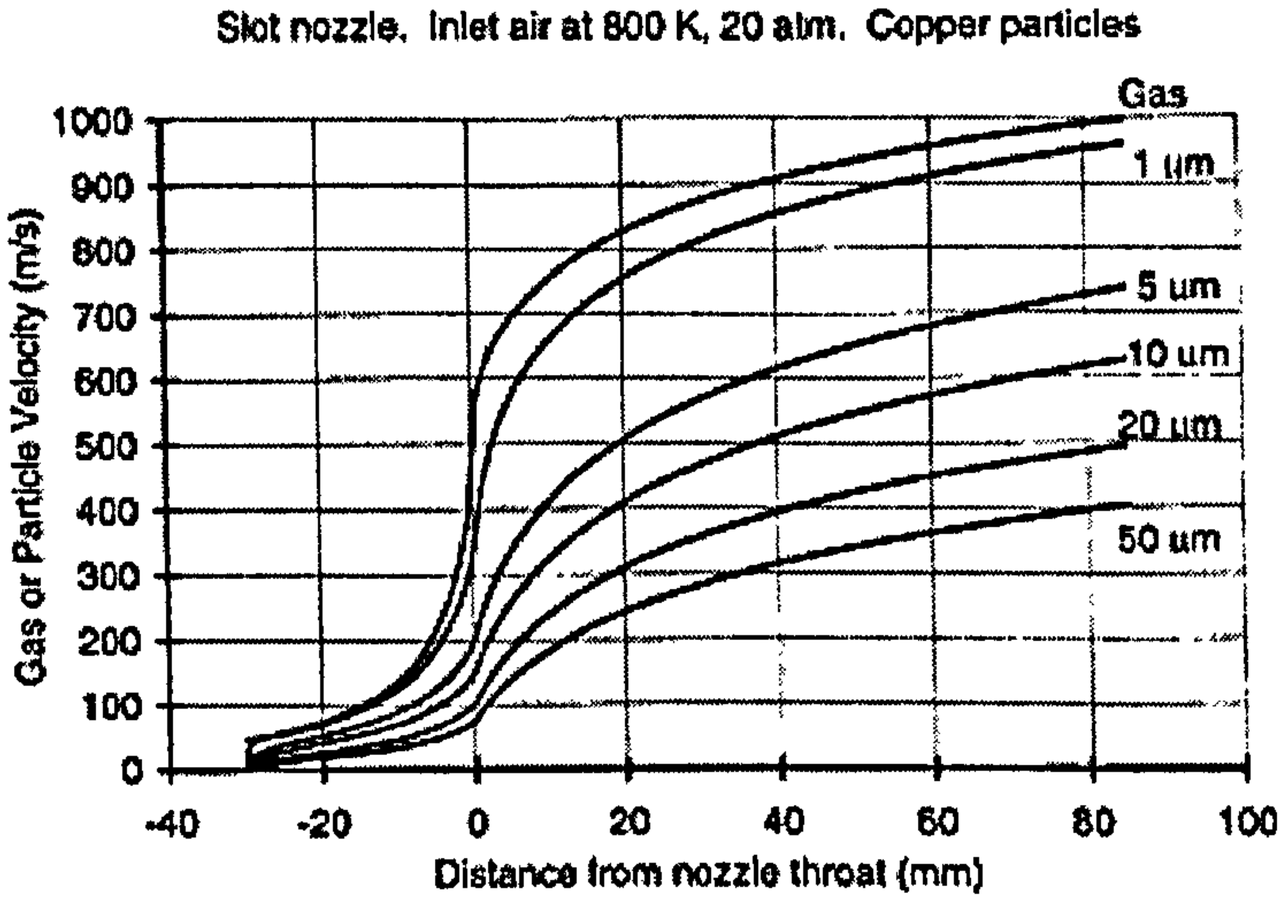

Fig. 2.12: Computed air and particle velocities versus distance along the nozzle for Cu particles using air at 800 K and 20 atmosphere as process gas. For particle velocity curves, particle diameters are denoted in μm [24].

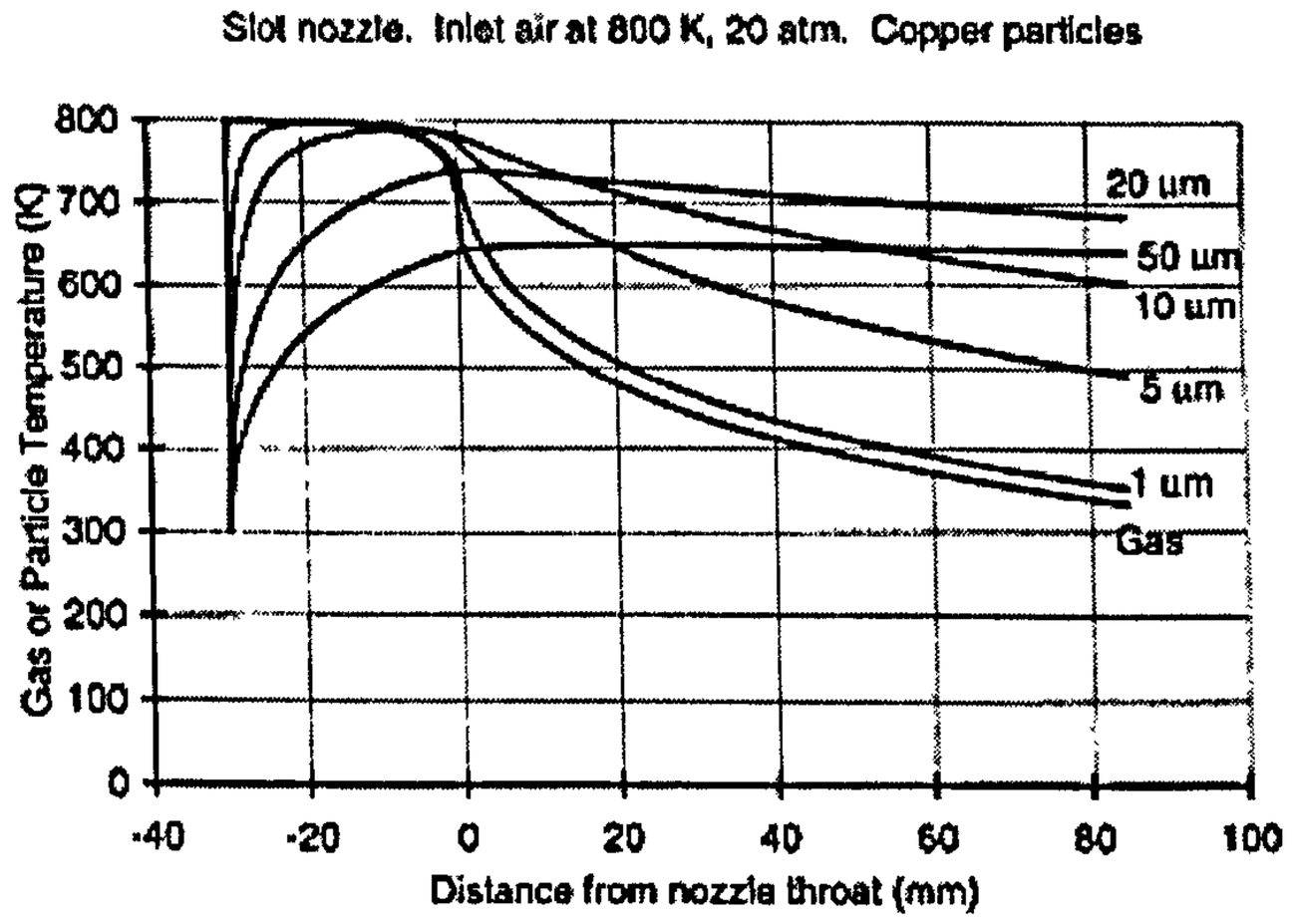

Fig. 2.13: Computed air and particle temperatures versus distance along the nozzle for Cu particles using air at 800 K and 20 atmosphere as process gas. For particle velocity curves, particle diameters are denoted in μm [24].

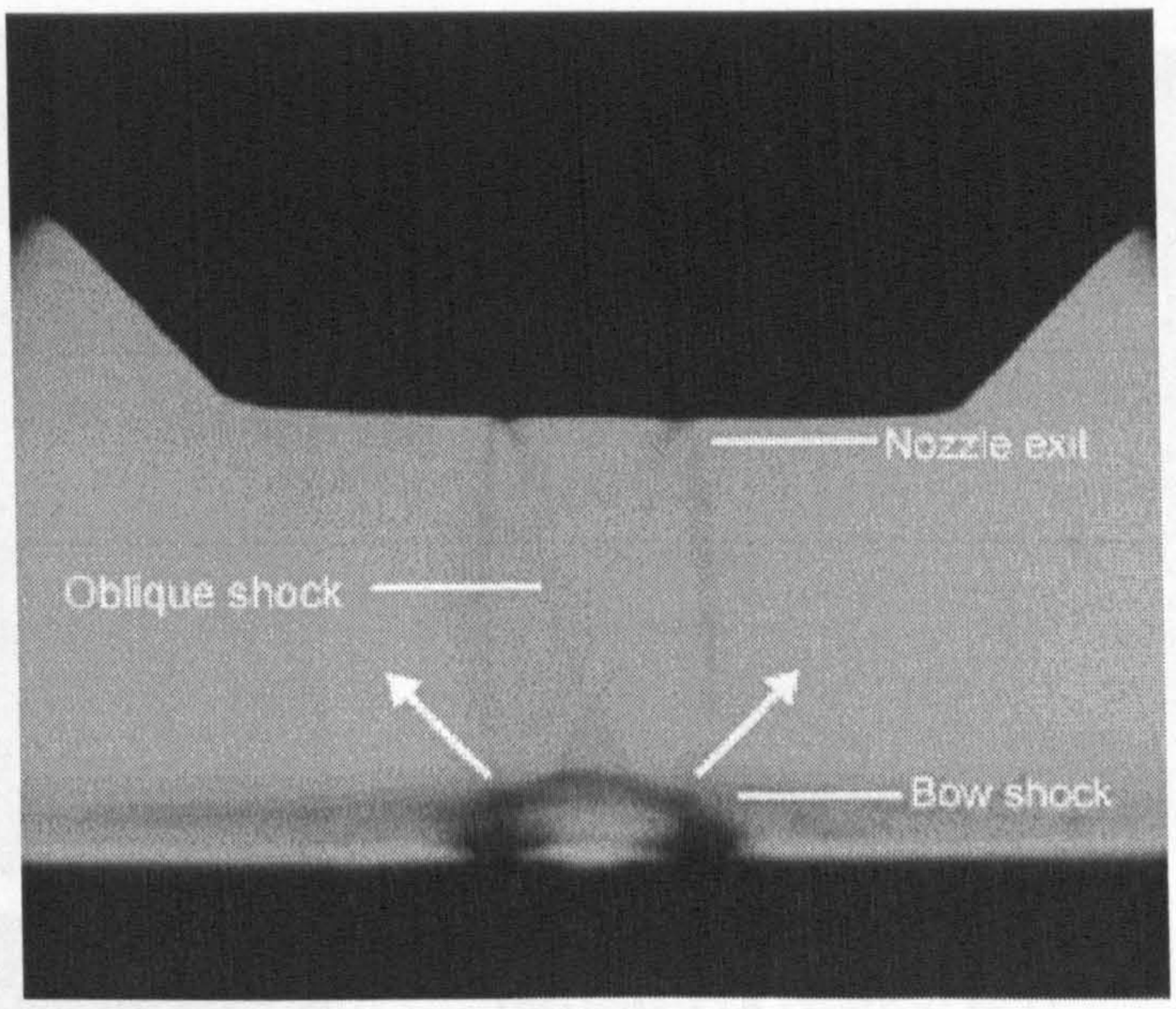

Fig. 2.14: As gas jet impinges on surface, a high-pressure region immediately above the substrate forms a bow shock opposing the gas jet, causing deceleration of particles before impact [41].

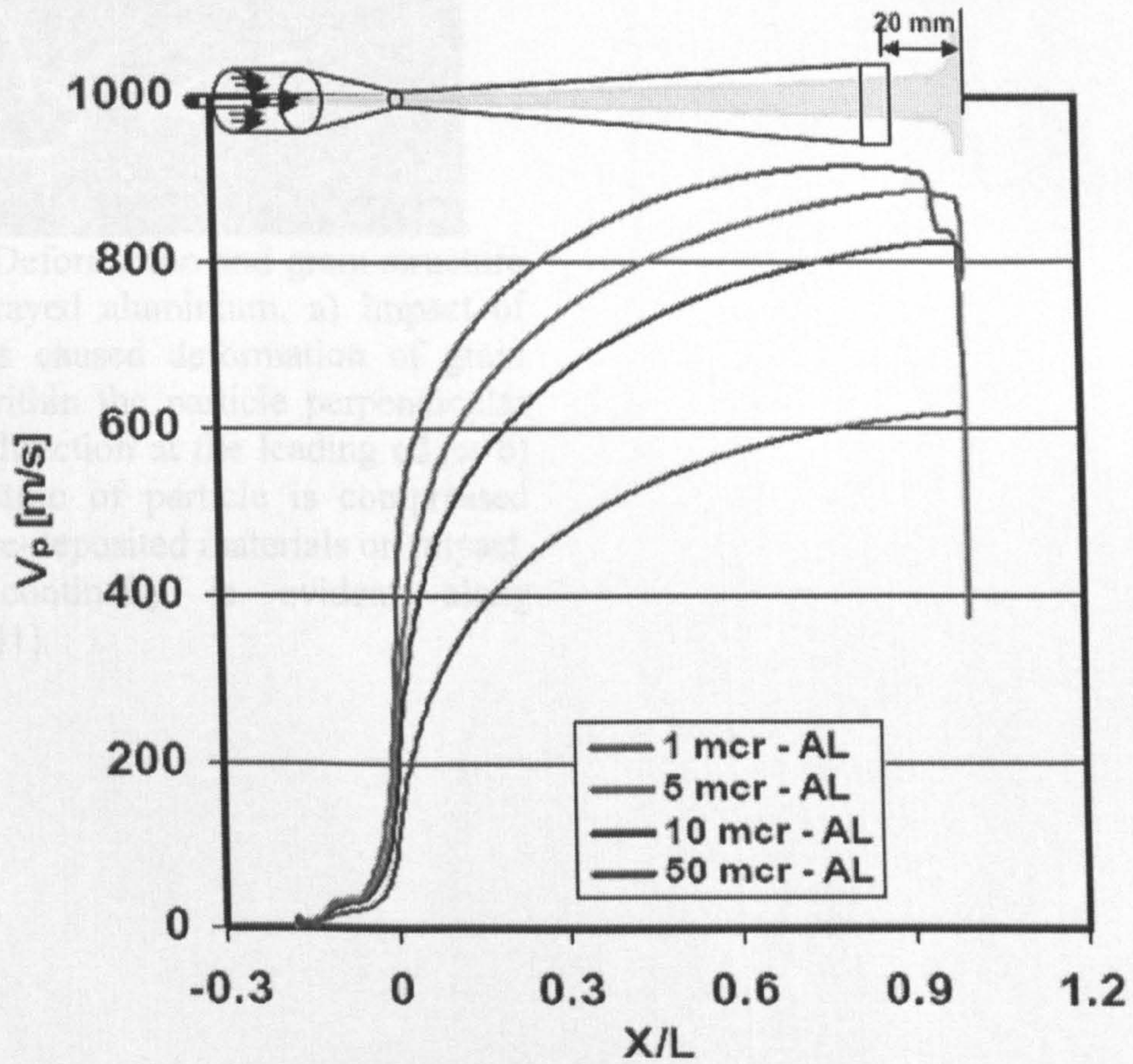

Fig. 2.15: Effect of bow shock on particle velocity of aluminium having different particle sizes [40].

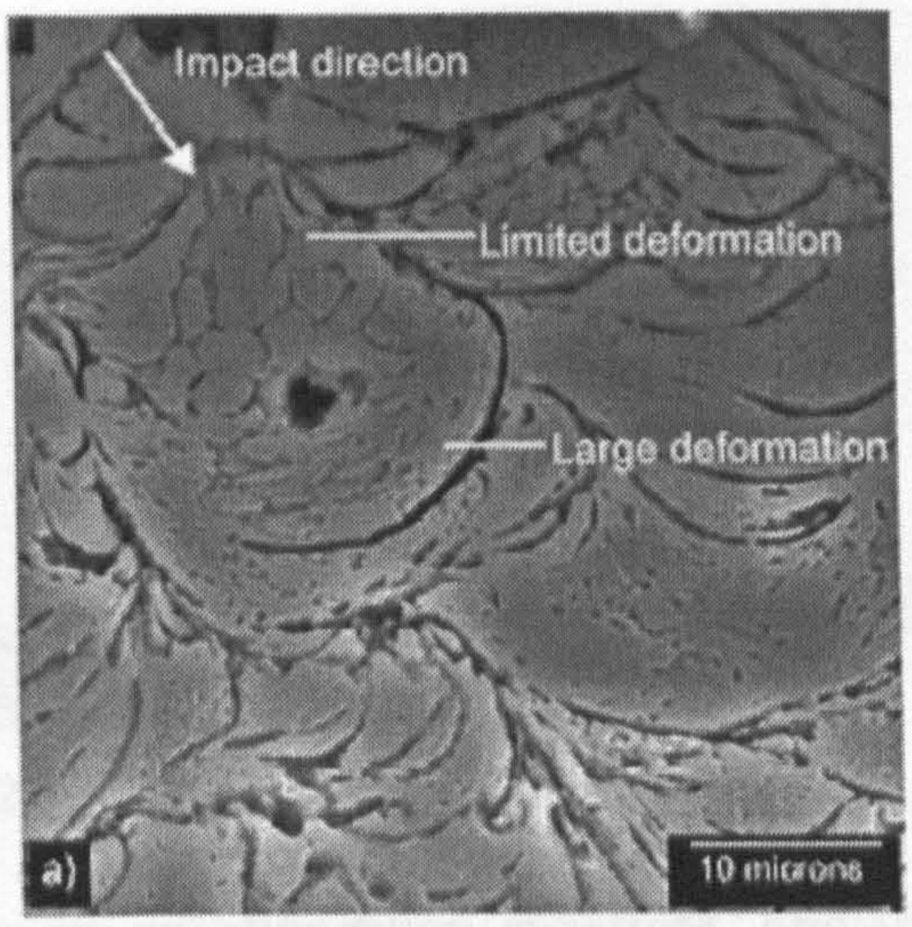

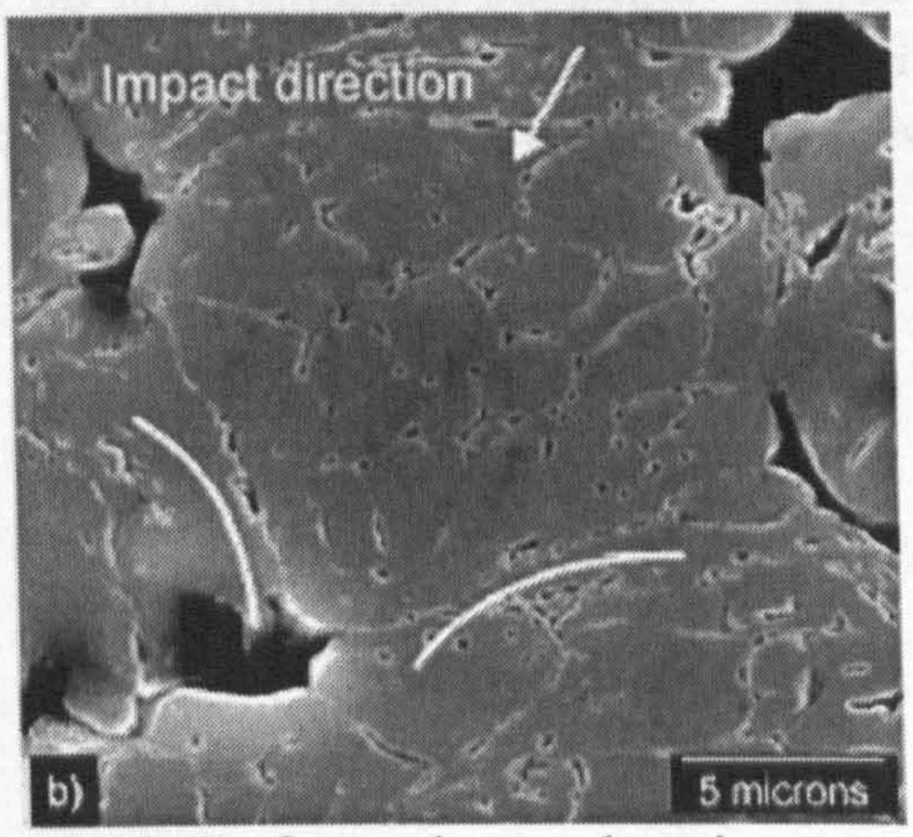

Fig. 2.16: Deformation and grain structure in cold sprayed aluminium. a) Impact of particle has caused deformation of grain structure within the particle perpendicular to impact direction at the leading edge; b) grain structure of particle is compressed between pre-deposited materials on impact. Material continuity is evident along interface [41].

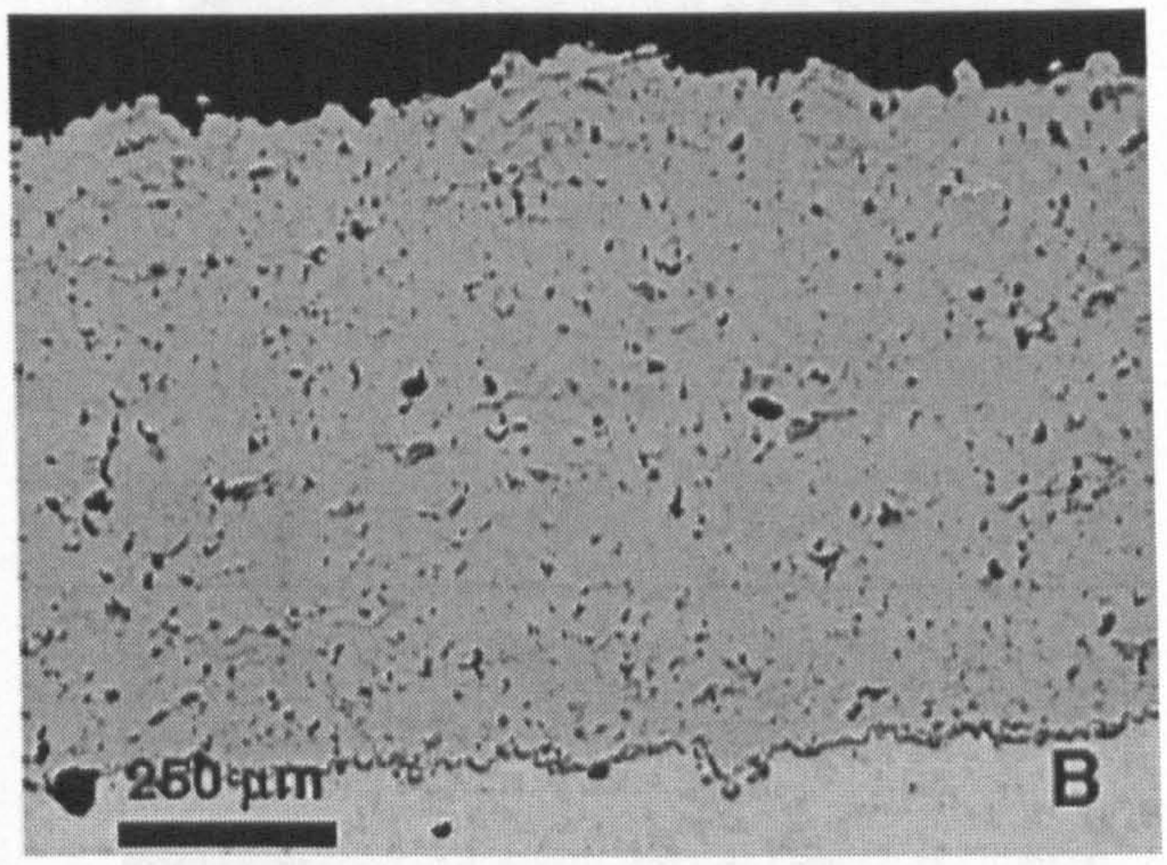

Fig. 2.17: Microstructure of cold sprayed Inconel 718 coating [47].

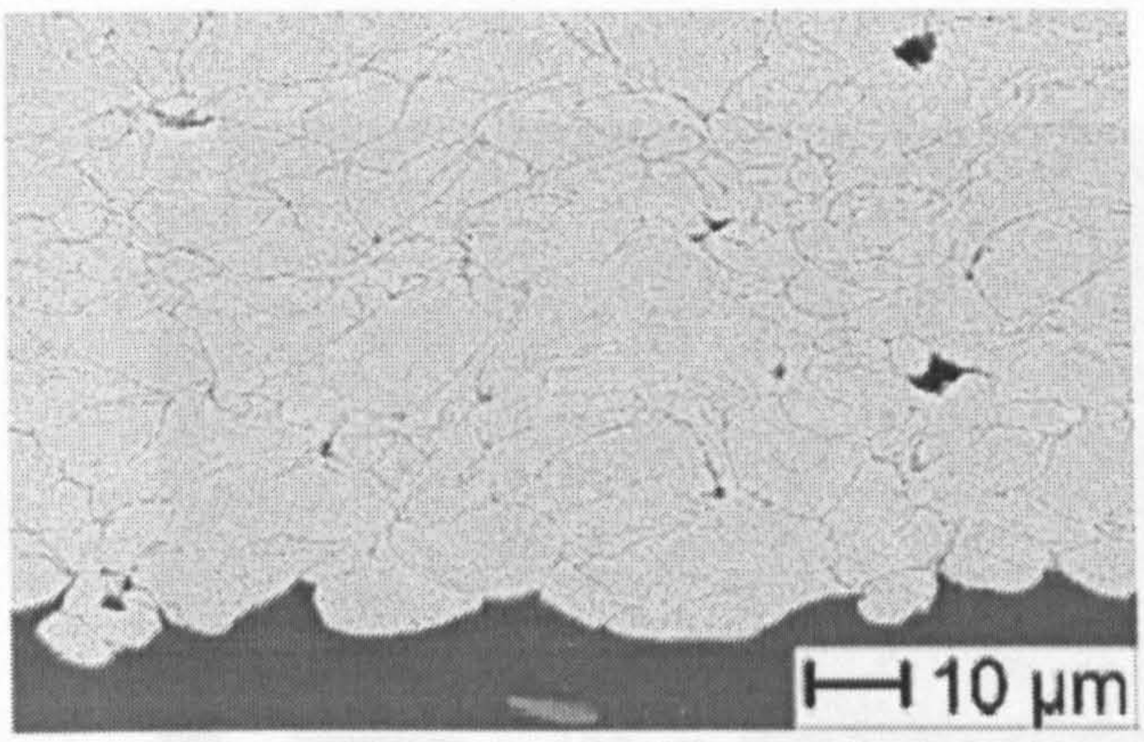

Fig. 2.18: Scanning electron micrographs (BSE) of a cross-section of a cold sprayed Cu coating on an aluminium substrate. Etched to reveal the particle/particle boundaries. The particles appear well bonded, and there is very little porosity [45].

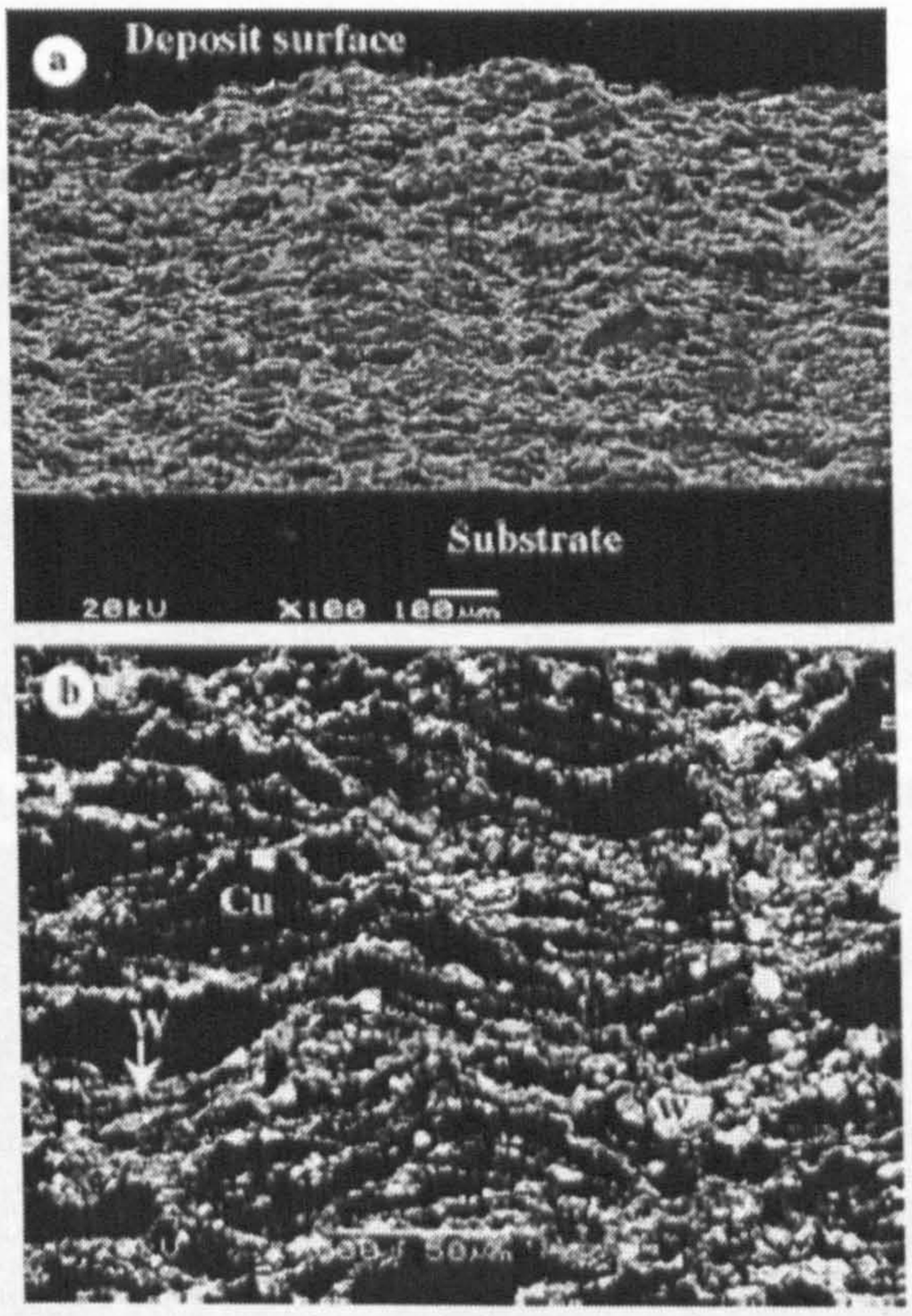

Fig. 2.19 (a-b): SEM images of cross-sections of cold sprayed agglomerated Cu-W powder. The Cu-W powder was mixed in the ratio 75Cu-25W, wt % and ball milled for 20 h [46].

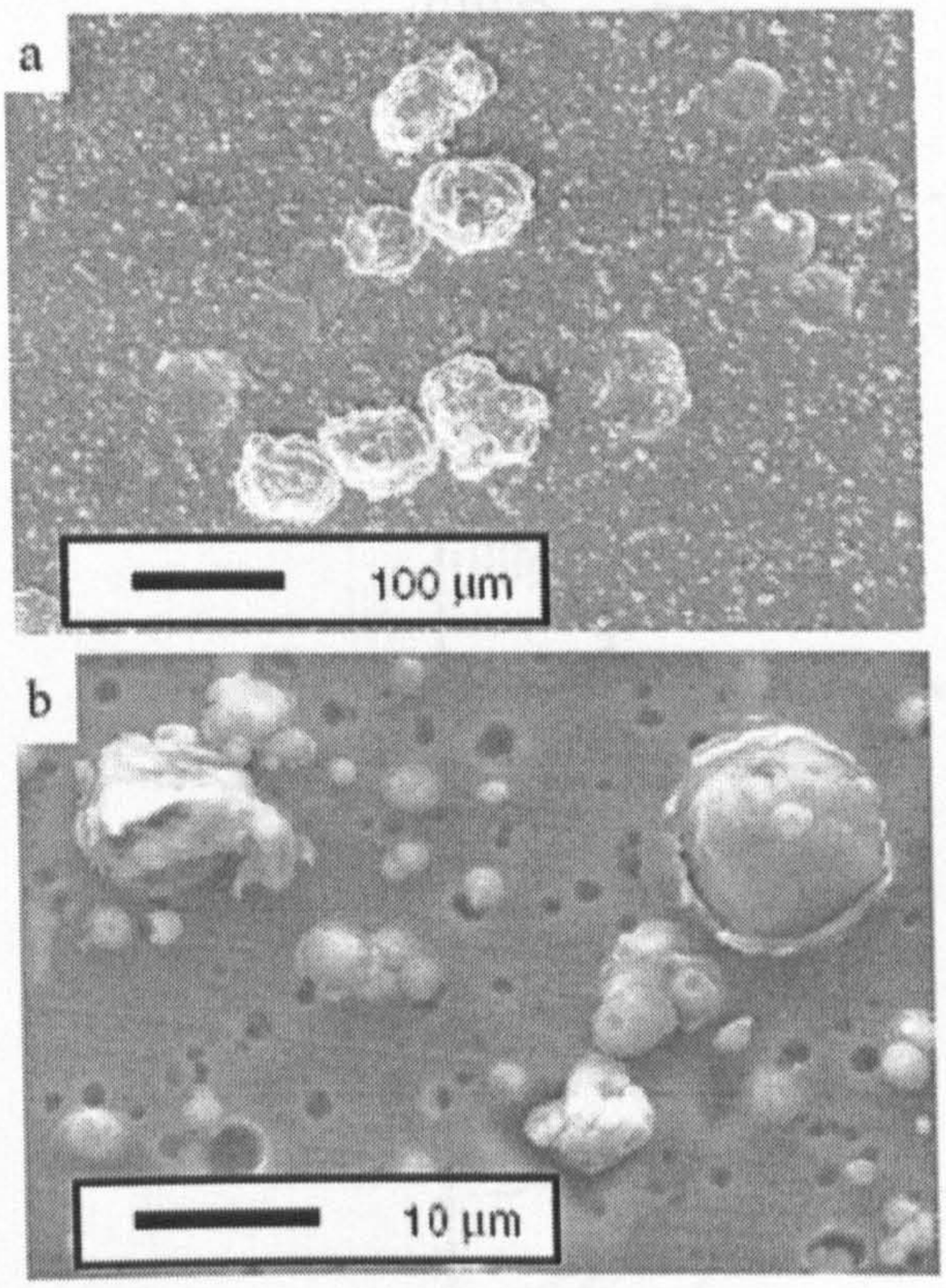

Fig. 2.20: Surface of aluminium alloy substrate following cold spraying with aluminium particles. A) Low magnification image showing bonding of both large and small particles; b) high magnification image showing deposition of very fine particles along with micro-cratering [44].

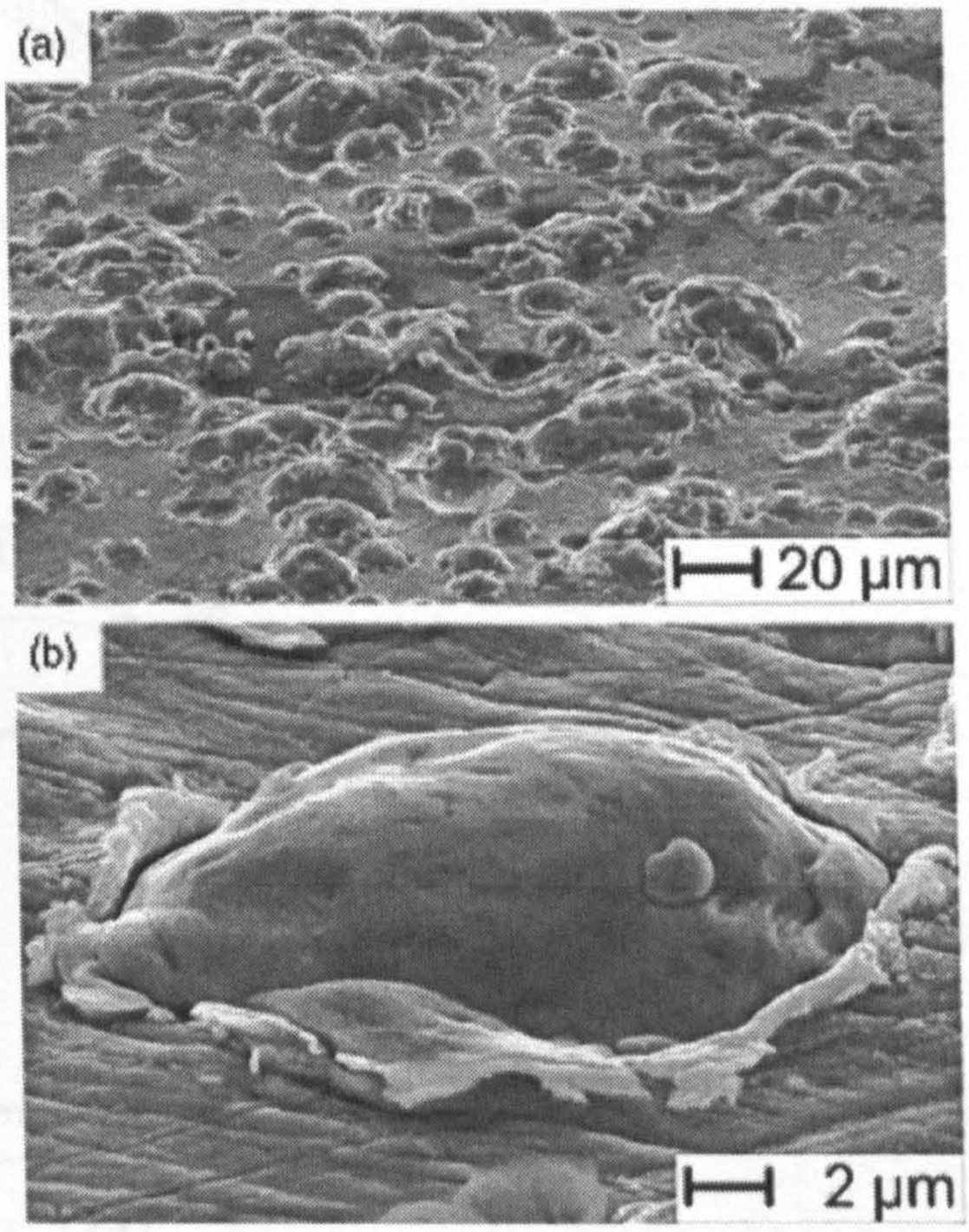

Fig. 2.21: Scanning electron micrographs (secondary electron mode) of wipe test samples of copper particles on a copper substrate, showing a) an overview and b) a close-up image [45]. Metal jetting is seen in (b).

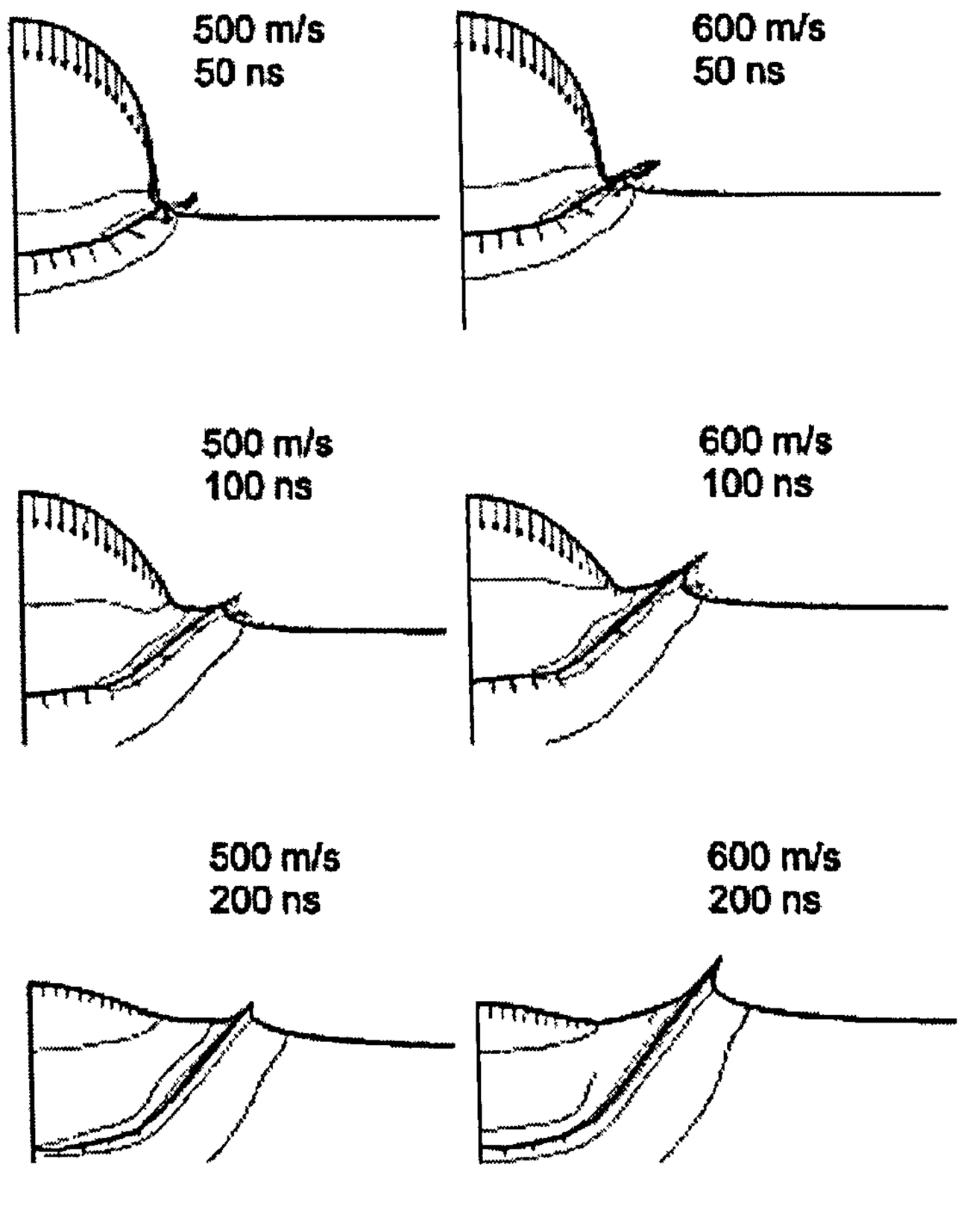

Fig. 2.22: Simulated impact of a copper particle on a copper substrate, for the initial particle velocities of 500 and 600 m s^{-1}. The arrows represent the velocities of nodes at the respective surfaces of particle and substrate, and the contours indicate temperature distribution [45].

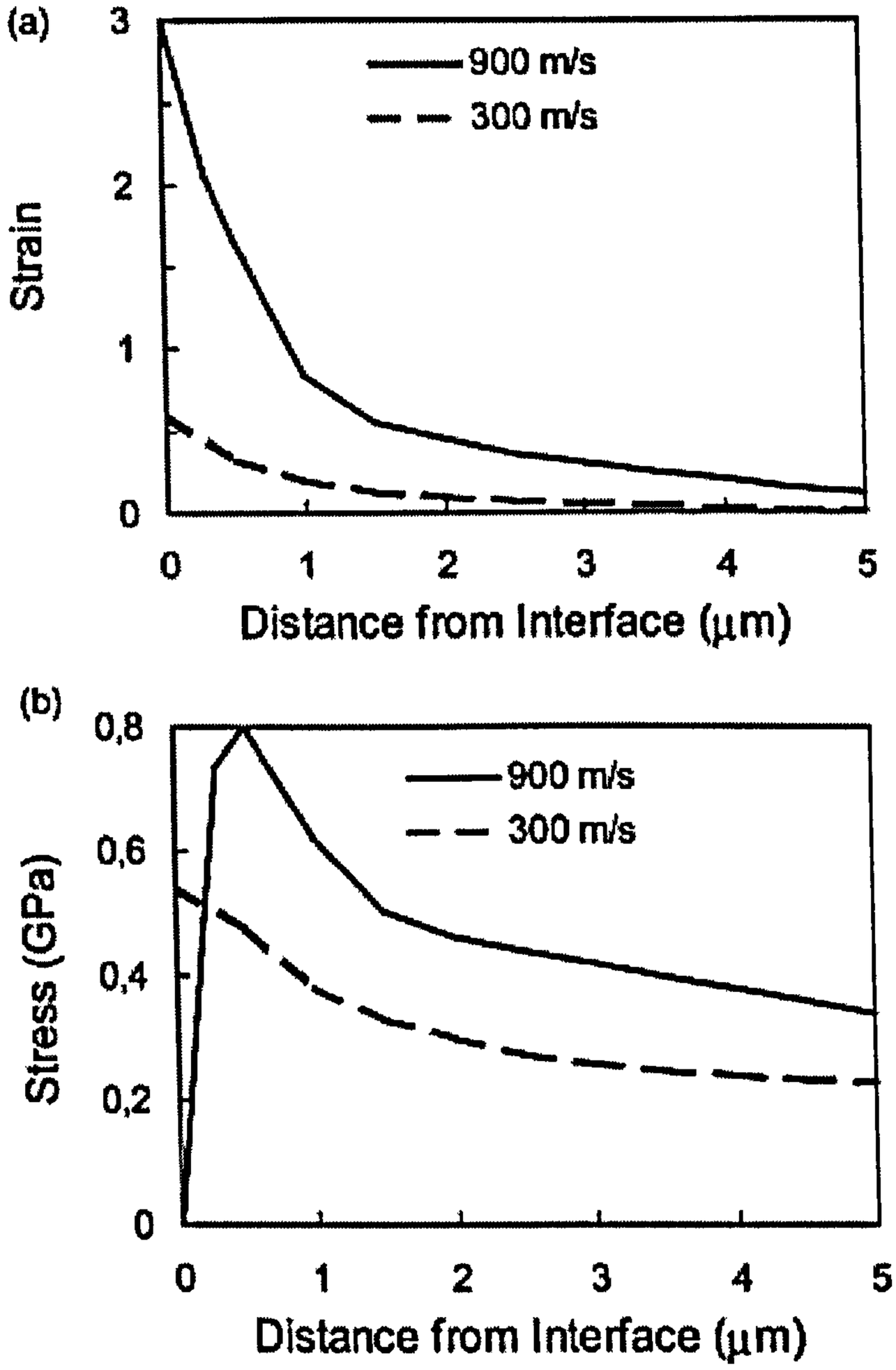

Fig. 2.23: Calculated profiles of a) plastic strain and b) flow stress for impact velocities of 300 and 900 m s^{-1}. Both, strain and stress increase monotonically by approaching the interface for the impact velocity. For the higher velocity, however, the shear stress falls to zero at the interface, indicating adiabatic shear instability [45].

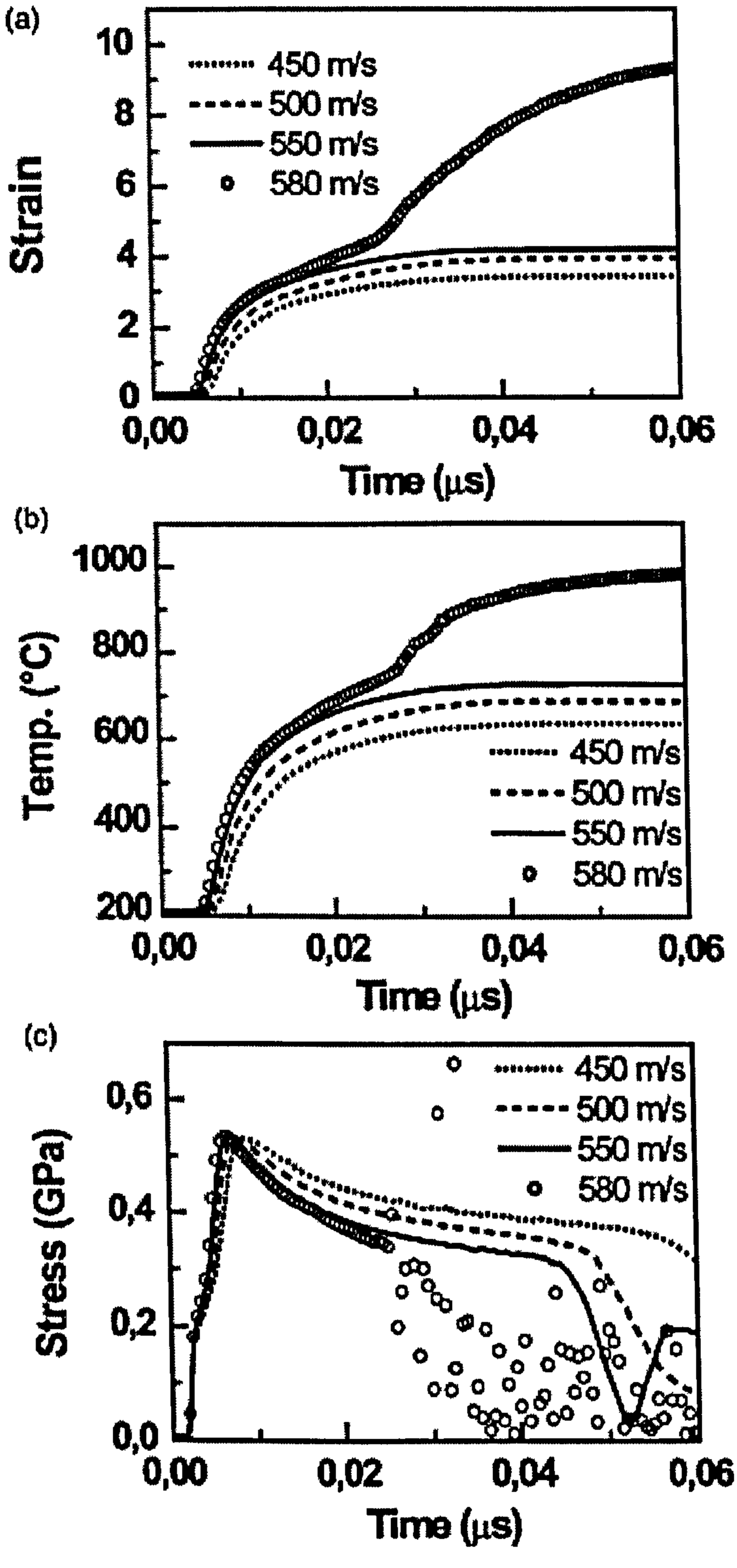

Fig. 2.24: Calculated temporal development of (a) plastic strain (b) temperature and (c) flow stress at the nodes of highest deformation in a sprayed particle for various impact velocities. There is a change in trend of variation of these variables with time, as the initial particle velocity is increased from 550 to 580 m/s, indicating a shear instability. From Assadi *et al* [45].

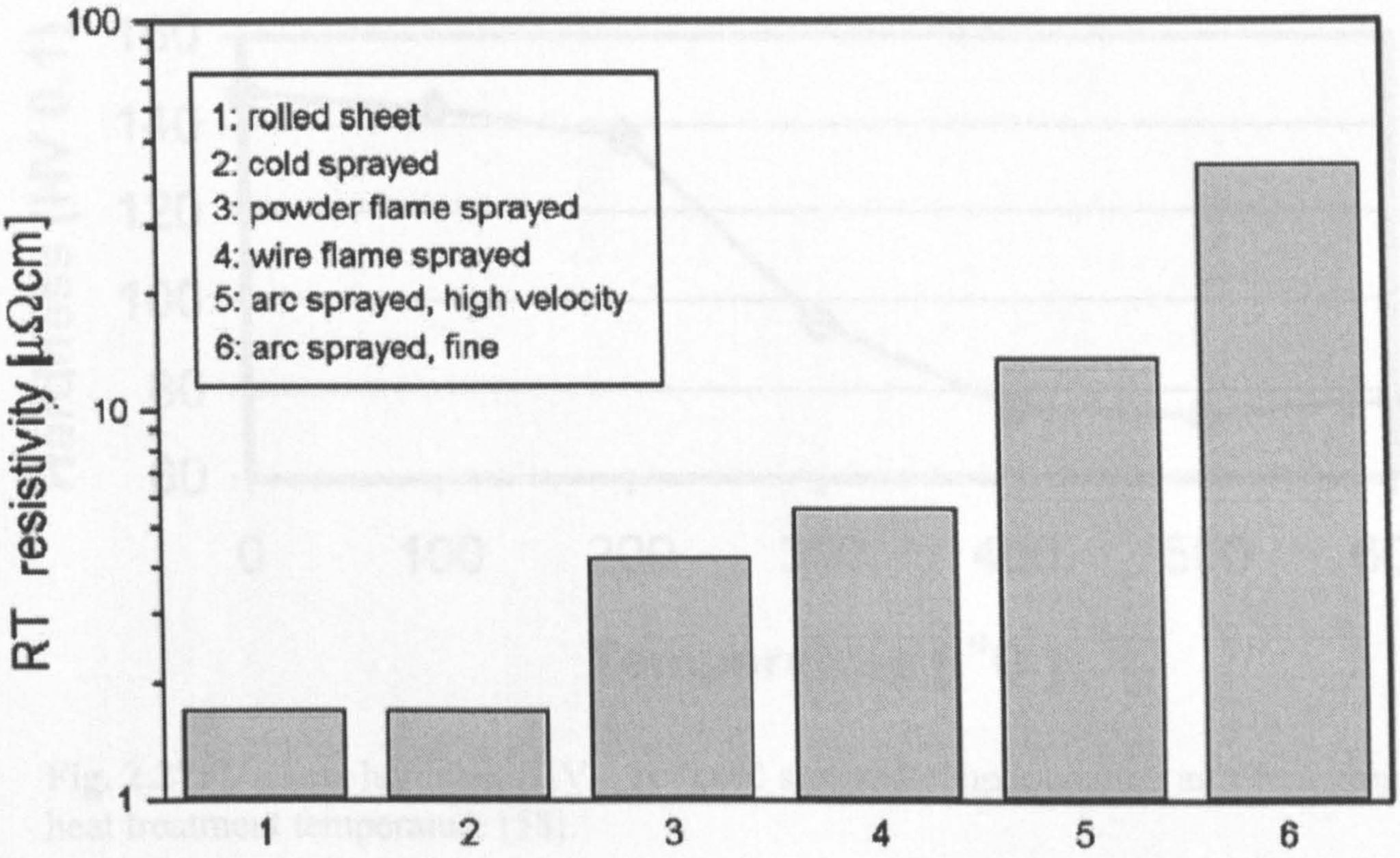

Fig. 2.25: Room temperature resistivity of a rolled Cu sheet, a cold sprayed Cu coating, a powder flame sprayed Cu coating, a wire flame sprayed Cu coating, a high velocity arc sprayed Cu coating, and a fine arc sprayed Cu coating [54].

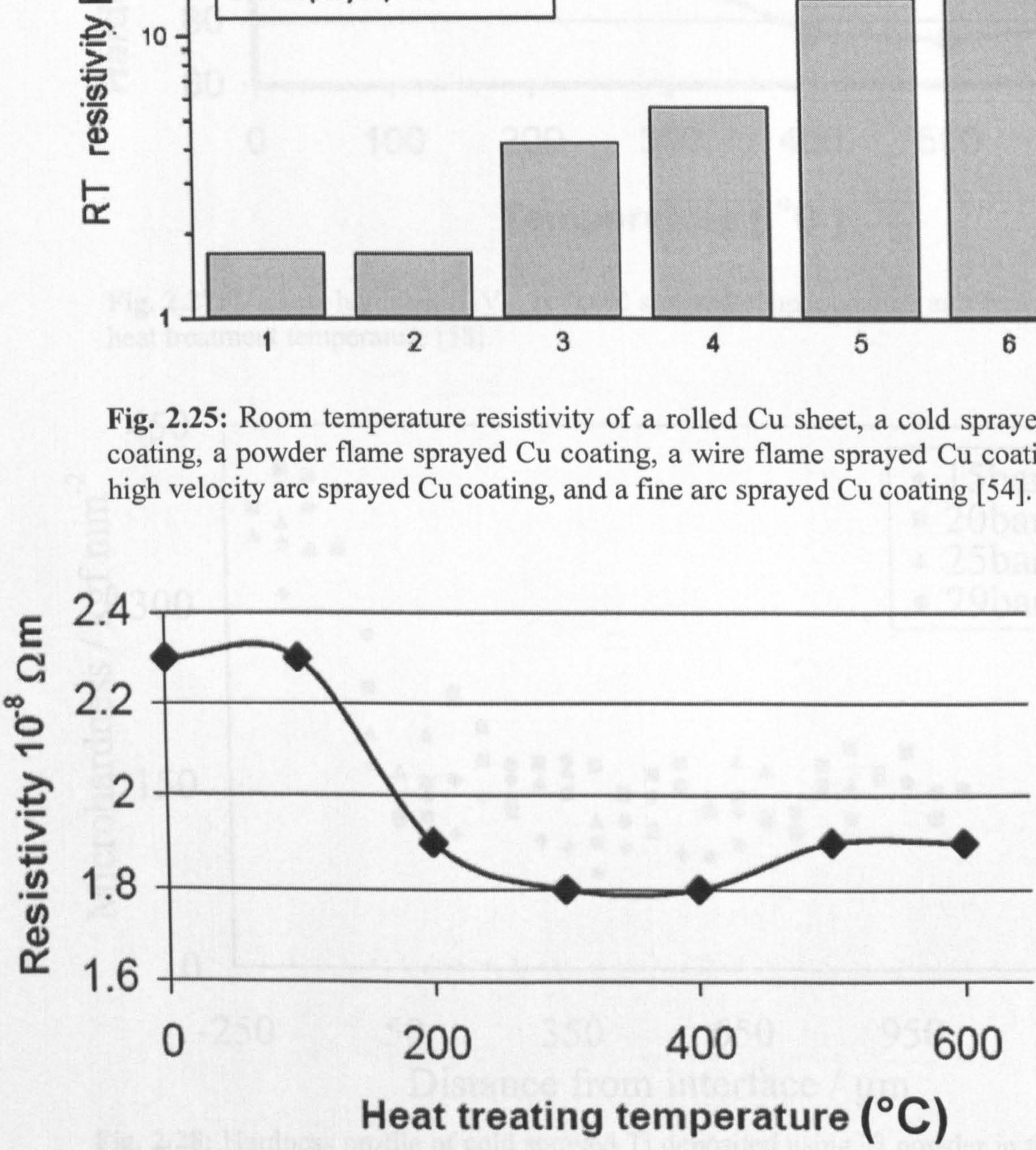

Fig. 2.26: Resistivity of cold sprayed Cu as a function of heat-treating temperature [58].

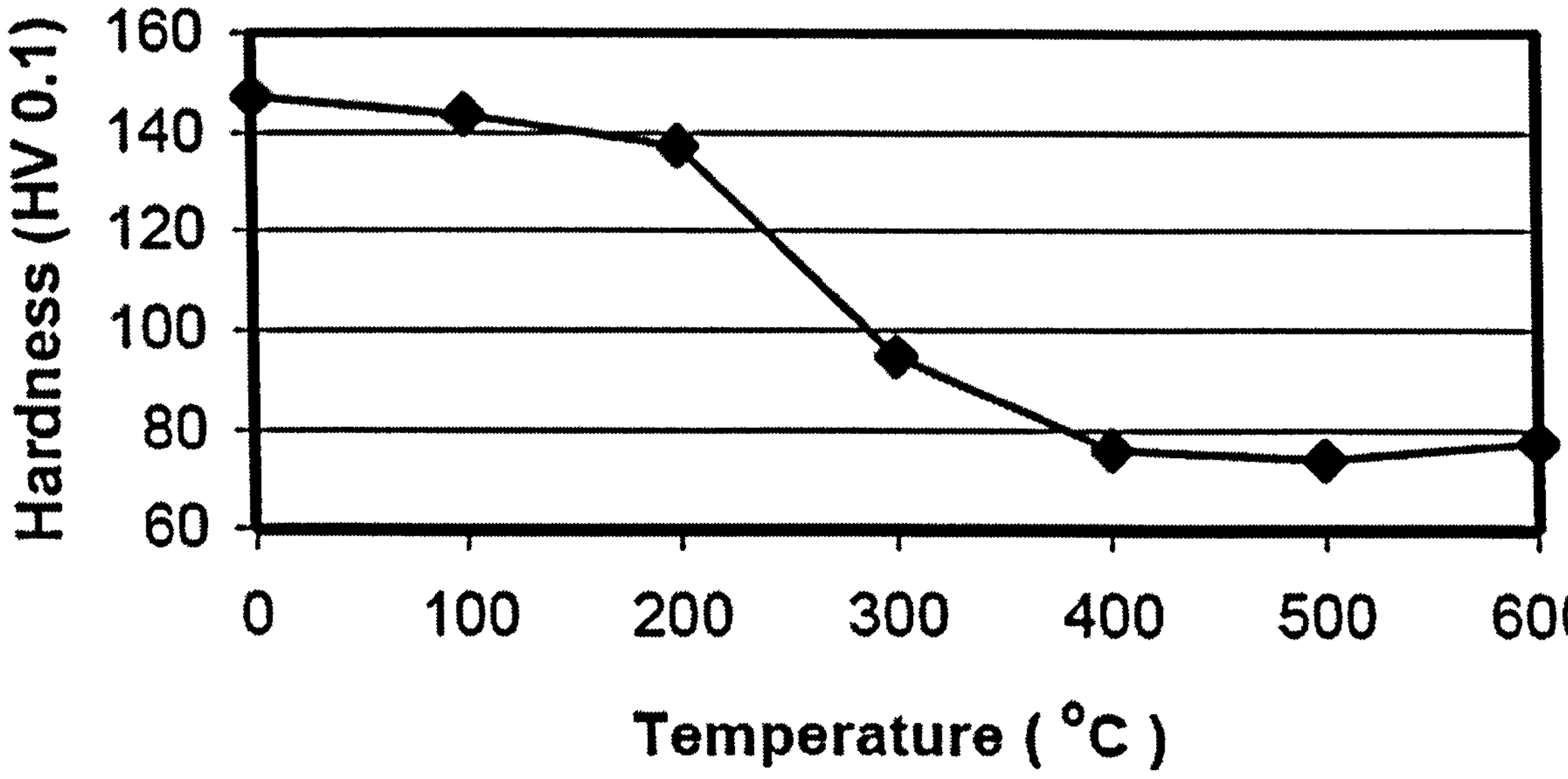

Fig. 2.27: Vickers hardness ($HV_{0.1}$) of cold sprayed copper coating as a function of heat treatment temperature [58].

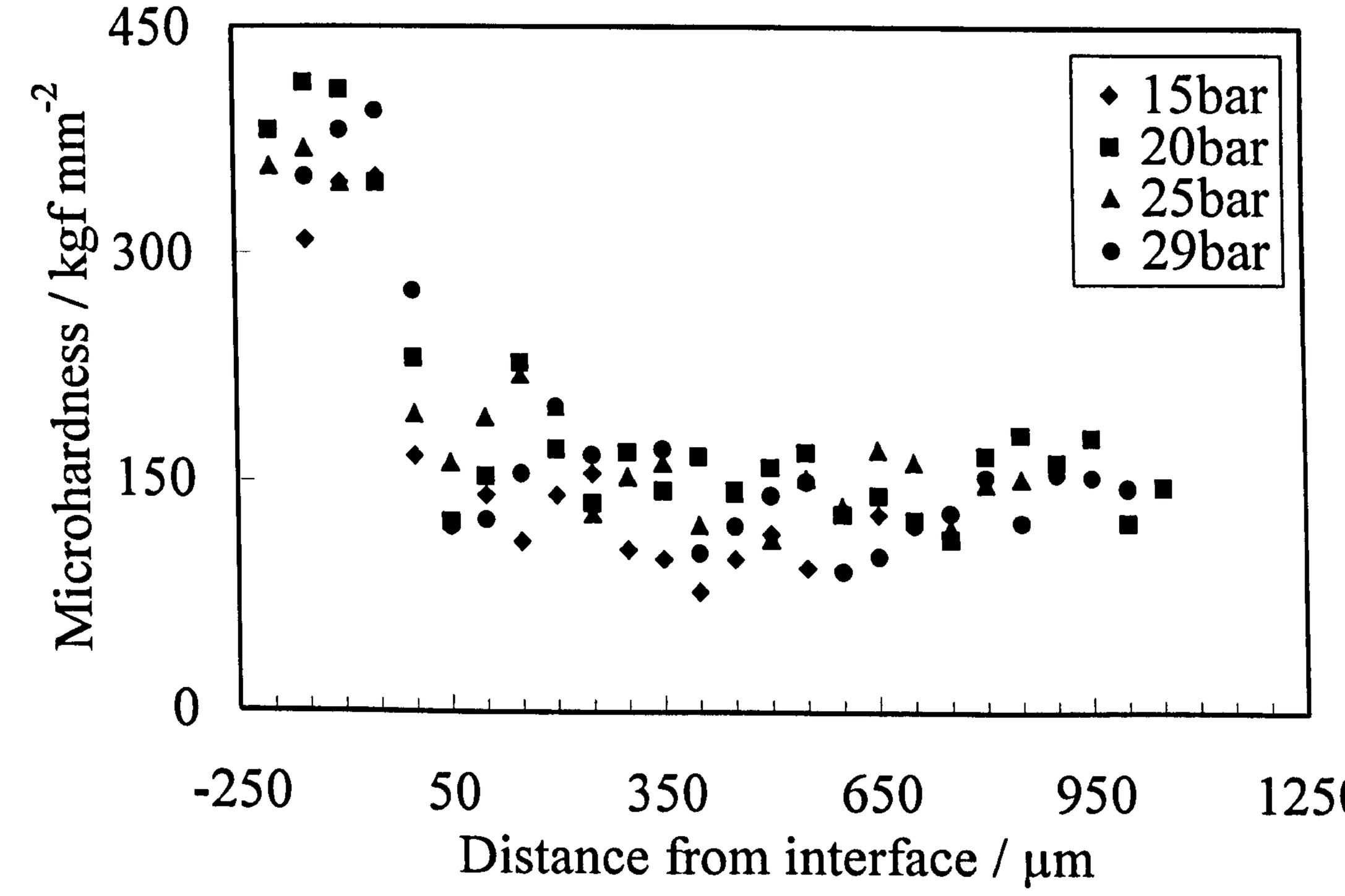

Fig. 2.28: Hardness profile of cold sprayed Ti deposited using Ti powder in the size range of -25 +5 μm and gas at 298 K and different gas pressures [59].

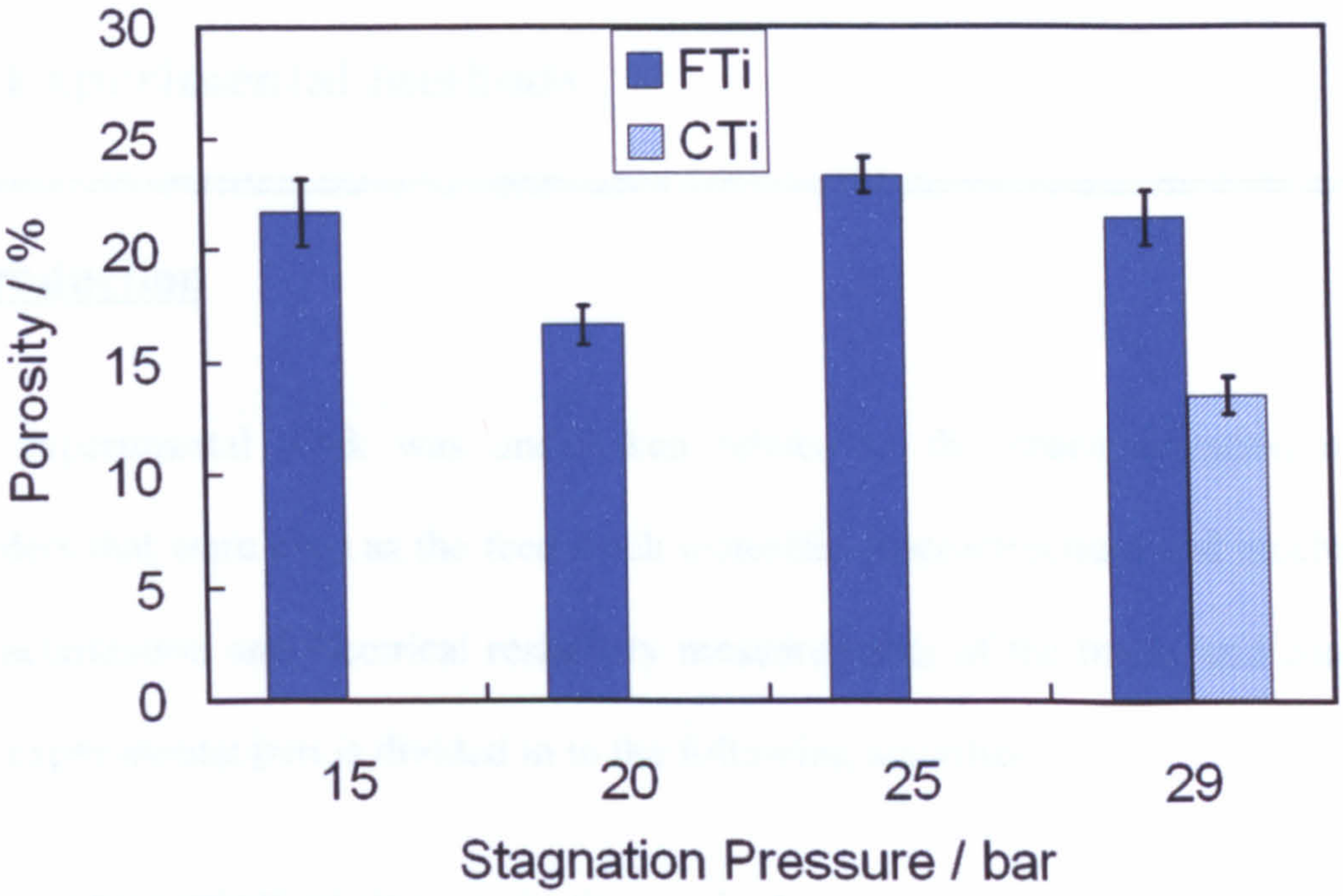

Fig. 2.29: Porosity in cold sprayed Ti versus gas pressure using gas at 298 K. FTi and CTi represent Ti powder in size range of -25 +5 μm and -45 +5 μm respectively [56].

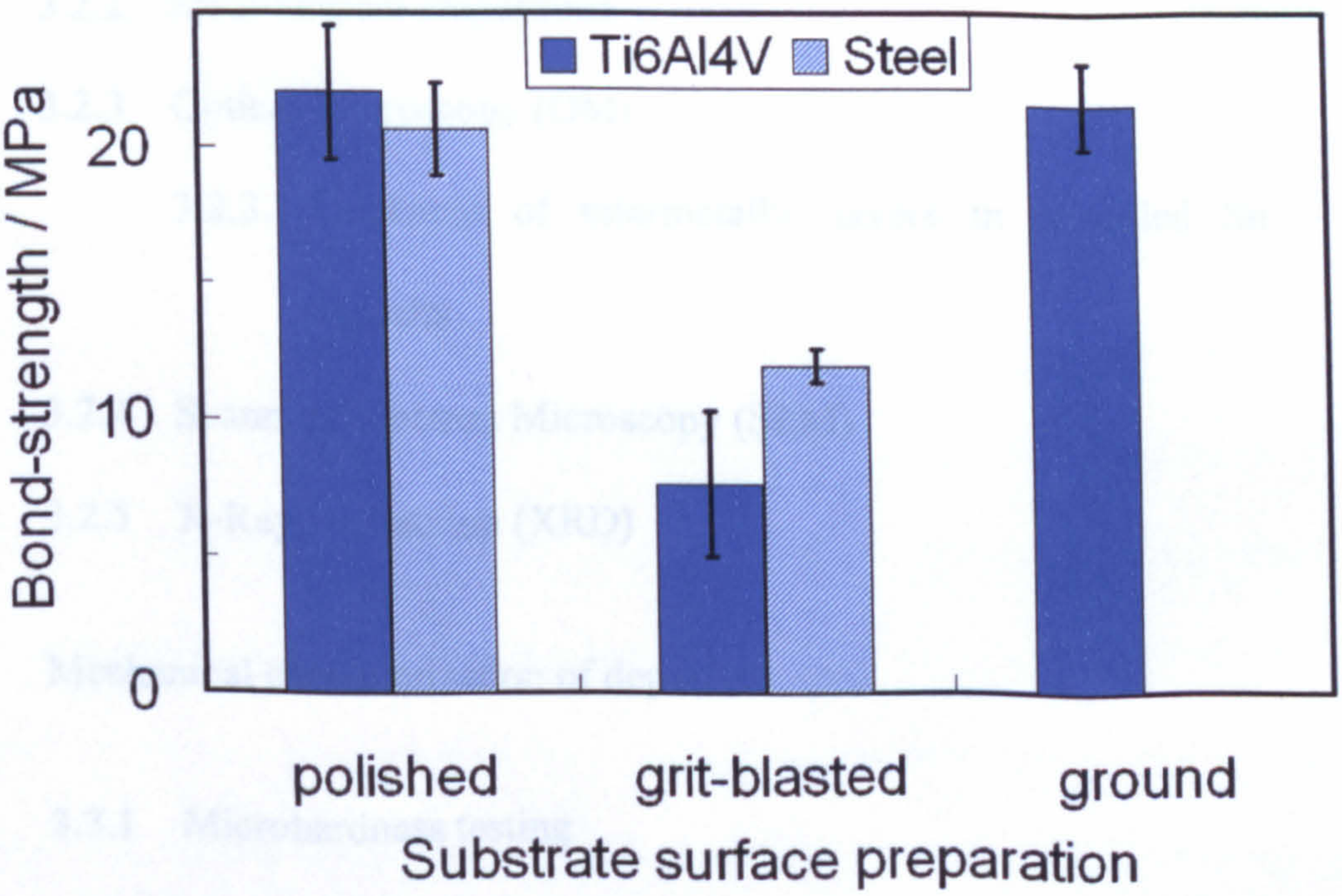

Fig. 2.30: Adhesion of cold sprayed Ti on Ti6Al4V and steel substrates. Ti deposited using gas at 298 K and 29 bar pressure [56]. -45 +5 μm size Ti powder used.

Chapter 3

General Experimental methods

3.1 Introduction

The experimental work was undertaken related to the characterization of the powders that were used as the feed stock materials, microstructural and mechanical characterization and electrical resistivity measurements of the tracks and coatings. The experimental part is divided in to the following activities:

3.2 Microstructural characterization methods

3.2.1 Powder particle size analysis

3.2.2 Metallurgical preparation

3.2.3 Optical Microscopy (OM)

3.2.3.1 Thickness of intermetallic layers in annealed Sn – Cu deposits

3.2.4 Scanning Electron Microscopy (SEM)

3.2.5 X-Ray Diffraction (XRD)

3.3 Mechanical characterization of deposits

3.3.1 Microhardness testing

3.2 Microstructural characterization methods

3.2.1 Powder particle size analysis

Copper and tin powders were used for deposition of tracks by cold spraying. A Malvern Instruments Laser Mastersizer was used to measure the powder size distribution. The powders were stored in vacuum desiccators to minimize oxidation.

3.2.2 Metallurgical preparation

The microstructure of powder particles was examined in the optical microscope and scanning electron microscope (SEM). Tin powder was observed under the SEM by sprinkling the powder on to an adhesive carbon tape to obtain a uniform layer of powder on the tape. The tape was then stuck on a holder for observation under an SEM. Copper powder was viewed under the optical microscope in the unetched and etched condition. The procedure of sample preparation for optical microscopy of copper powder and deposits was similar. The tin – copper and copper deposits were cut using a diamond saw to obtain specimens for metallographic observation. It was observed that the deposits exhibited change in its microstructure and microhardness when subjected to temperatures prevalent during hot mounting (423 K) hence it was decided to process the metallographic samples using the cold setting resin. The powder and deposit specimens were embedded in cold setting mounting resin before grinding and polishing. The grinding and polishing was done on emery

papers starting with size 400 grit and progressively polishing with finer size grit up to 2400. Water was used for sample cooling and lubrication. Thereafter polishing was done using diamond paste of 6 μm and 1 μm. Final polishing was carried out using 0.01 μm water based colloidal silica solution. The copper powder and deposits were observed in the unetched and etched condition. Etching of copper was performed using a solution of 5g $FeCl_3$ and 5ml HCl in 100ml ethanol.

3.2.3 Optical microscopy

Optical microscopy was carried out using a Zeiss microscope fitted with a digital camera to record images. The copper powder and deposits were observed under the microscope and images taken at various magnifications of 100, 200, 400 and 1000.

3.2.3.1 Thickness measurement of intermetallic layers in annealed Sn - Cu deposits

Optical microscope images of tin – copper deposits were used to obtain the thickness of the intermetallic compound formed after annealing of deposits. In order to measure the thickness of intermetallic layers optical micrographs of the interface region were recorded using a 100 X objective lens. Five locations were chosen at random and interface positions identified. The thickness of the individual Cu_3Sn (ε) and Cu_6Sn_5 (η) layers were then measured at each location and the mean thickness and standard error computed. The tin – copper deposits were stored in refrigerator

prior to metallographic preparation and observation. The sample preparation and measurements were completed within one day of removal from the refrigerator.

3.2.4 Scanning electron microscopy

Two different instruments were employed in the course of the work namely a FEI – XL 30 and a JEOL 6400. Images were obtained using the back scattered (BSE) and secondary electron (SE) signals. On selected samples energy dispersive X – ray analysis (EDXA) was performed to determine chemical composition of diffusion layers. Quantitative elemental analysis was performed with a standards-based ZAF correction program utilizing an Oxford instruments (series 300) EDX system comprising a Pentafet Plus Series Si (Li) detector (crystal cross-sectional area 10 mm^2) and an ultra-thin entrance window. The beam current during analysis was normalized to that of the reference standards by performing a gain calibration at regular intervals using a cobalt standard.

3.2.5 X-Ray diffraction

X – Ray diffraction (XRD) analysis of as-sprayed and heat treated deposits of copper was undertaken using a Siemens D 500 powder diffractometer with Cu Kα radiation. The deposits were naturally de-bonded from the substrate and thus free standing deposits were used for XRD analysis. The conditions employed were a

step size of 0.01°, a counting time of 6 seconds per step in the 2θ range 40 – 140°. Annealed copper powder was also analysed in this way in order to provide reference data [61, 62].

The X – ray data were collected from the surface of deposits. The purpose of the XRD analysis was to determine coherent crystallite size and internal microstrain by measuring the widths of the XRD peaks after correction for instrumental broadening using the annealed copper powder sample as the reference. After recording an XRD spectrum and removing the $K\alpha_2$ diffraction component, all peaks were carefully measured to determine the full width at half-maximum (FWHM) (in radians). In order to obtain the pure broadening, B, of any peak it is necessary to first remove the instrumental broadening, B_I, from the measured broadening, B_M, according to the equation [61, 63],

$$B^2 = B_M^2 - B_I^2 \quad \text{---------- Equation 3.1}$$

The pure broadening, B, is assumed to be due to a combination of small coherent crystallite size and the presence of internal microstrain such that,

$$B = B_s + B_c \quad \text{---------- Equation 3.2}$$

Where B_s is strain broadening and B_c crystal size broadening. Hall and Williamson [61, 63] showed that,

$$B_s = C \tan\theta \quad \text{---------- Equation 3.3}$$

And

$$B_c = \frac{\varsigma\lambda}{d_c \cos\theta} \quad \text{---------- Equation 3.4}$$

Where, $C = 2\frac{\Delta d}{d}$ ---------- **Equation 3.5**

d is interplanar spacing and Δd is change in interplanar spacing, thus $\Delta d/d$ is the microstrain measurement, $\varsigma = 0.9$, d_c = crystallite size, λ = wavelength of the X-ray radiation used and θ the Bragg angle.

So,

$$B\cos\theta = C\sin\theta + \frac{\varsigma\lambda}{d_c} \quad \text{---------- Equation 3.6}$$

Hence, the independent components of broadening were obtained in this work by plotting $B\cos\theta$ versus $\sin\theta$; termed the Hall – Williamson plot [61].

Sample of as received powder were also analysed by XRD for phase identification and in particular presence of oxides in the powder. The conditions employed were a 2θ range of 10° to 100°, step size of 0.02° and step time 4 s.

3.3 Mechanical characterization of deposits

3.3.1 Microhardness testing

Microhardness measurements of as-sprayed and annealed deposits were carried out on deposit cross-sections using a 200 gf load with a Leco 400M microhardness tester. At least five measurements were made on the specimens and the mean value of measurements was reported.

3.3.2 Tensile testing

Copper deposits on an aluminium substrate having a nominal thickness of ~ 5 mm were machined using electrical discharge machining for removal from the substrate and then further machined to form tensile test samples. The deposition of copper was carried out as described in chapter 6, section 6.2.2. The tensile test specimens had a parallel (gauge) length of 30 mm and width of 6 mm in the gauge length, and thickness of 2 mm. The schematic diagram of the tensile sample is shown in **Fig. 3.1**. A rolled copper sheet of dimensions 3 mm x 300 mm x 300 mm was used to prepare tensile test samples, as per the dimensions described above, to provide tensile test comparison with bulk copper. A number of samples were machined, both from sprayed copper as well as rolled copper. Some were tested in the as machined condition while some were annealed as per procedure described in 3.6.1, before testing. The tensile tests were performed using a JJ Lloyd tensile testing machine fitted with a 30 kN load cell with a cross head speed of 2 mm min^{-1}. Scribe

marks were put on the samples in their gauge lengths 25 mm apart, before carrying out the tensile testing to enable determination of % elongation after the tensile test.

3.3.3 Pull – off adhesion testing

Adhesion testing was performed on deposits formed on 100 mm x 100 mm x 3 mm substrates. The adhesion of the deposits to the substrates was tested using the Precision Adhesion Testing equipment (PAT, DFD instruments, Norway). Mild steel dollies having a diameter of ~ 15 mm were glued to the deposits using a two part epoxy resin (Hysol 9466, Henkel Loctite Ireland). A picture of the PAT tester and the dollies along with representative sprayed sample is shown in **Fig. 3.2**. The epoxy was cured at room temperature for 24 hours to attain its full strength. After curing the dollies were pulled apart using the PAT and the breakage of the deposits from the substrate was observed and the stress required for breakage from the substrate recorded. The epoxy had a tensile pull – off strength of ~ 20 MPa thus deposits having a pull – off strength ≤ 20 MPa could be measured with this method. The deposits whose adhesion was higher then 20 MPa, the failure occurred in the epoxy while the deposits remained intact on the substrate. In this case the deposit adhesion could only be reported as being higher then 20 MPa.

3.4 Electrical resistivity testing

The resistivity of pure copper and Sn – Cu tracks was measured at room temperature using the four-point probe method. First, the resistance of a 0.02 m length of the track was measured accurately from current and voltage determination. The method for resistance measurement is shown schematically in **Fig. 3.3**. The material whose resistance is to be measured is termed as R_x. During this test R_x was connected in series to a resistance whose value was known, this resistance is termed as R_{std}. A fixed amount of current was passed through these resistances and the voltage drop

across R_x and R_{std} i.e. V_x and V_{std} was measured. R_x is then calculated using,

$$R = \frac{V}{I}$$

therefore;

$$I = \frac{V_{std}}{I_{std}} = \frac{V_x}{R_x}$$

and;

$$R_x = \frac{R_{std}}{V_{std}} \times V_x$$

In the rig, the current is first measured by connecting the leads to the ends of the track and then another measurement is made by reversing the polarity of the current passing through the rig. This is done to eliminate any error coming in the measured values due to thermal effects. The resistivity of the unknown sample is calculated as

$$\rho = AR/L$$

Where, ρ is the resistivity of the unknown sample, A is the cross section area of the track, R is the measured resistance of the track and L is the length over which the resistance was measured.

The cross section area of the track was determined by using a profilometer to determine track profiles at five different locations. The profile data were integrated to obtain values of cross section area. The mean value from those five measurements was utilized to calculate the resistivity. There is an error in the area measurement using the profilometer as the deposited track tends to de-bond from the substrate. The nature of this de-bond is shown in **Fig. 3.4**, where it is seen that the tin-copper track has de-bonded from the nylon substrate. Such de-bonding is observed to a lesser or greater degree in many deposited tracks. The de-bonding of the track thus leads to over estimation of the track area as the de-bonded area is also measured as part of the track profile and this, results in over estimation of the calculated resistivity.

A standard copper specimen (Cu 99.995% pure) was obtained from Advent research Materials LTD, and electrical resistance measurements were carried out on this sample of known dimensions (0.25 mm x 15 mm x 100 mm). The resistance of this sample was periodically measured along with other resistance measurements to ascertain any drift in the values measured. The resistivity of the standard copper sample was 17.50 nΩ m. The resistivity of annealed copper reported in data books is 16.73 nΩ m [64].

3.5 Profilometry of substrates and deposits

The surface roughness and the deposit profiles were investigated by a profilometer (Surfcom, Advanced Metrology systems Ltd Leicester, England) equipped with a diamond stylus. The traverse speed of the stylus was maintained at 0.3 mm s^{-1}. The surface roughness data was read from the profilometer display and the profile data was logged onto a PC. The profile data was then plotted in excel for further analysis.

3.6 Annealing of deposits

3.6.1 Copper deposits for recrystallization and tensile testing studies

Copper deposits deposited on aluminium substrate were removed from the aluminium substrate by machining off the aluminium substrate. The machining was carried out using electrical discharge machining (EDM) to minimize stress to the deposits during machining. The machined deposits were cut using a diamond saw in to pieces of size 10 to 15 mm square and 1 mm thick. The copper deposits were subsequently annealed in air using a fan assisted furnace at temperatures of 373 K, 423 K, 473 K, 523 K, 573 K and 773 K for 3600 s. The samples were placed on a ceramic holder for annealing.

Annealing of the tensile test samples was performed in a tube furnace in an atmosphere of $H_2$75% - $N_2$25% at temperatures of 773 K and 873 K. The samples were heated at the rate of 10 K per min to a temperature of 473 K and thereafter the temperature was raised at a rate of 1 K per min to the required temperature to minimize thermal shock in the specimens.

3.6.2 Interdiffusion in tin – copper deposits

Sn-Cu deposits were de-bonded from the substrates and the free standing deposits were heat treated at two different temperatures namely 343 K and 443 K using a fan assisted oven. Samples temperatures were monitored directly using a chromel / alumel thermocouple and were found to be within ± 1 K of the set furnace temperature. At specific time intervals a sample was removed from the oven and air cooled to room temperature. The resistance was measured as described in section 4.4 and a small length (5 – 10 mm) cut from the end for subsequent microstructural examination. This small sample was immediately stored in a refrigerator at 271 K and the remaining length was then put back in the oven for further heat treatment.

3.7 Characterization of materials

3.7.1 Characterization of powders

Commercially available pure tin and copper powders were employed. The commercially pure tin powder was supplied by Flame Spray Technologies b. v., Netherlands. It had a nominal size range 10 - 38 μm and had a near spherical morphology. The copper powder was supplied by BSA Metal Powders Plc (Formerly MBC Metal Powders), Birmingham UK. It had a nominal size range of 5 - 22 μm also with a spherical morphology.

The XRD pattern of the copper powder is shown in **Fig. 3.5**. The various peaks on the pattern are labelled. All the peaks correspond to copper and there is no evidence for oxide peaks. Thus, the oxide level is below the detection limit by XRD. The storage of the powder was under vacuum, hence the possibility of powder oxidation or contamination during storage is minimized. The size distribution of the copper powder used for CGDS trials is shown in **Fig. 3.6.** The size analysis was carried out by Malvern mastersizer as per the procedure described in section 3.2.1. It is seen that 80 vol. % of the particles are in the size range of -22 +5 μm; approximately 5 vol. % < 5 μm and 15 vol. % > 20 μm. The d_{50} value was 15 μm; i.e. 50 % particles had particle size ≤ 15 μm. The SEM image of the copper powder is shown in **Fig. 3.7**. The powder is largely spherical and some particles have satellites attached to them. The satellites are artefacts of the gas atomization process. An image of the etched cross-sections of powder particles is shown in **Fig. 3.8**. The etched microstructure shows that the grain size within the powder particles is between 5 - 10 μm.

The size analysis of tin powder is shown in **Fig. 3.9** and SEM image is shown in **Fig. 3.10**. It is seen that the tin powder is largely spherical with 90 vol % of the particles being in the size range of -38 +10 μm; approximately 3 vol % of powder is > 30 μm and 7 vol % is < 5 μm. The d_{50} value was ~ 13 μm; i.e. 50 % particles had particle size ≤ 13 μm. The satellites attached to some particles are artefacts of the gas atomization process.

3.7.2 Details of substrates

The substrates used for deposition trials were; various types of polymers, plasma sprayed alumina on mild steel, mild steel and aluminium. The thickness, hardness and surface roughness of the substrates used for deposition trials is shown in **Table 3.1** [65-68]. The properties of polymer substrates are shown in **Table 3.2**. The properties of polymers important for deposition in cold spraying are the glass transition temperature (T_g), ultimate tensile strength (UTS) and % elongation to failure. Air plasma spraying was used to deposit the alumina coating on mild steel. Yazaki provided the alumina coated mild steel substrates. All the substrates were wiped clean with acetone or industrial methylated spirit and blown dry with compressed air just before depositing copper or tin.

Table 3.1: Properties of metallic and ceramic substrates used for deposition trials.

Property/Substrate	Aluminium	Mild steel	Alumina coated mild steel
Hardness / kgf mm^{-2}	40 ± 0.9	120 ± 4	625 ± 15
Roughness / μm	0.34 ± 0.05	0.59 ± 0.08	3 ± 0.2

Table 3.2: List of polymers used as substrate to deposit copper with their relevant properties, from [65-68]. Rockwell R scale uses 12.7 mm steel ball indentor, a minor load of 10 kgf and a major load of 50 kgf [69].

Polymer	Glass transition temperature (T_g) / K	Melting temperature / K	Density kgm^{-3}	Ultimate tensile strength / Mpa	Elongation at break / %	Hardness / Rockwell R
Nylon 6/6 (PA66)	323 (50 °C)	488 (215 °C)	1140	82	83	121
Nylon 6/6 with 30 % glass fibre (PA6T)	368 (95 °C)	599 (326 °C)	1450	180	5	120
Poly (butylene terepthalate) (PBT)	339 (66 °C)	500 (227 °C)	1311	52	120	117
Polypropylene (PP)	263 (-10 °C)	449 (176 °C)	~ 900	36	120	96
Polyethylene (PE)	253 (-20 °C)	410 (137 °C)	~ 940	20	380	63
Poly phenylene sulfide (PPS)	358 (85 °C)	558 (285 °C)	1670	138	4	123
Noryl	427 (154 °C)	483 (210 °C)	1270	54	40 - 60	119

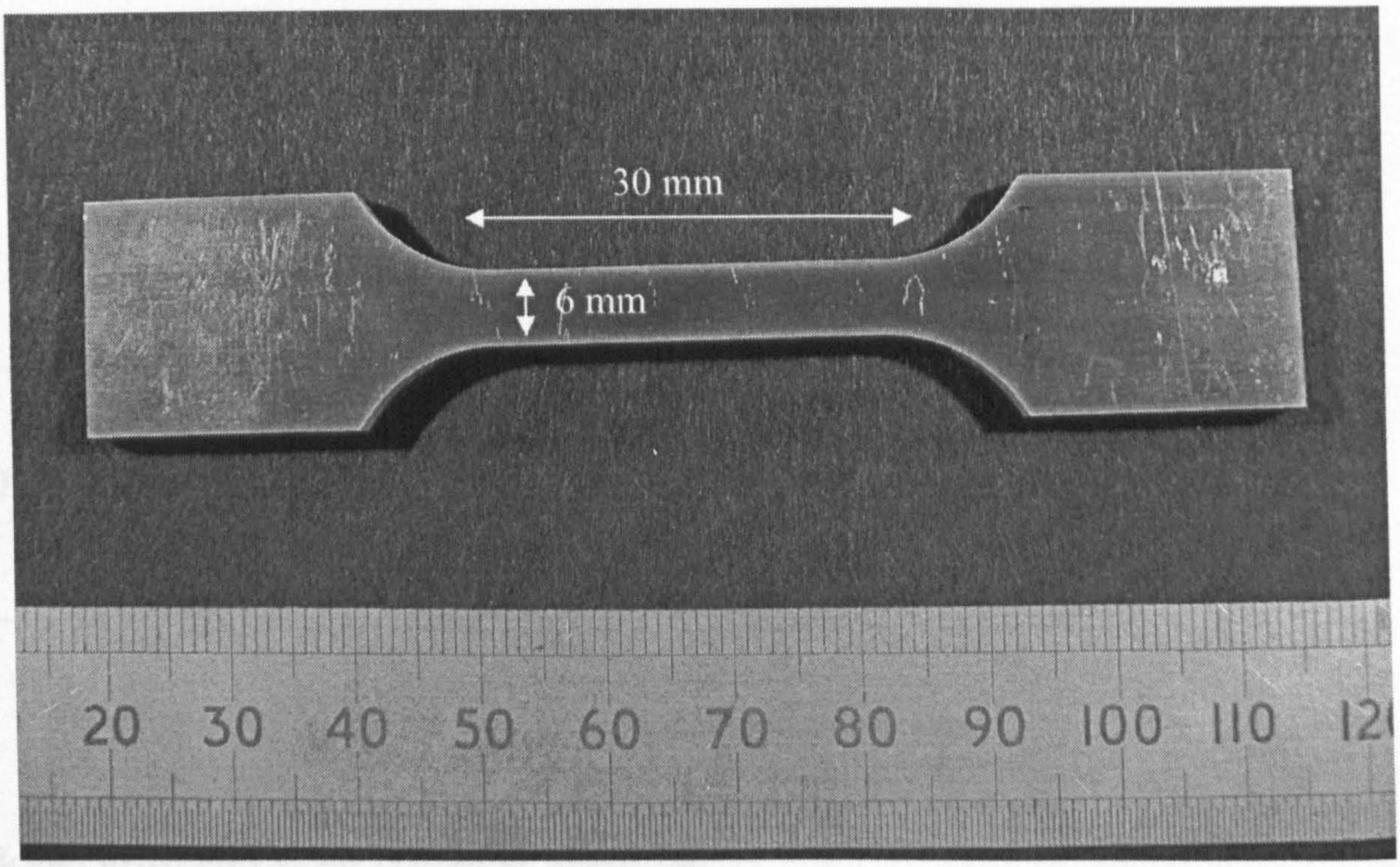

Fig. 3.1: Image of tensile test specimen, showing the gauge length (30 mm) and width in gauge length (6 mm).

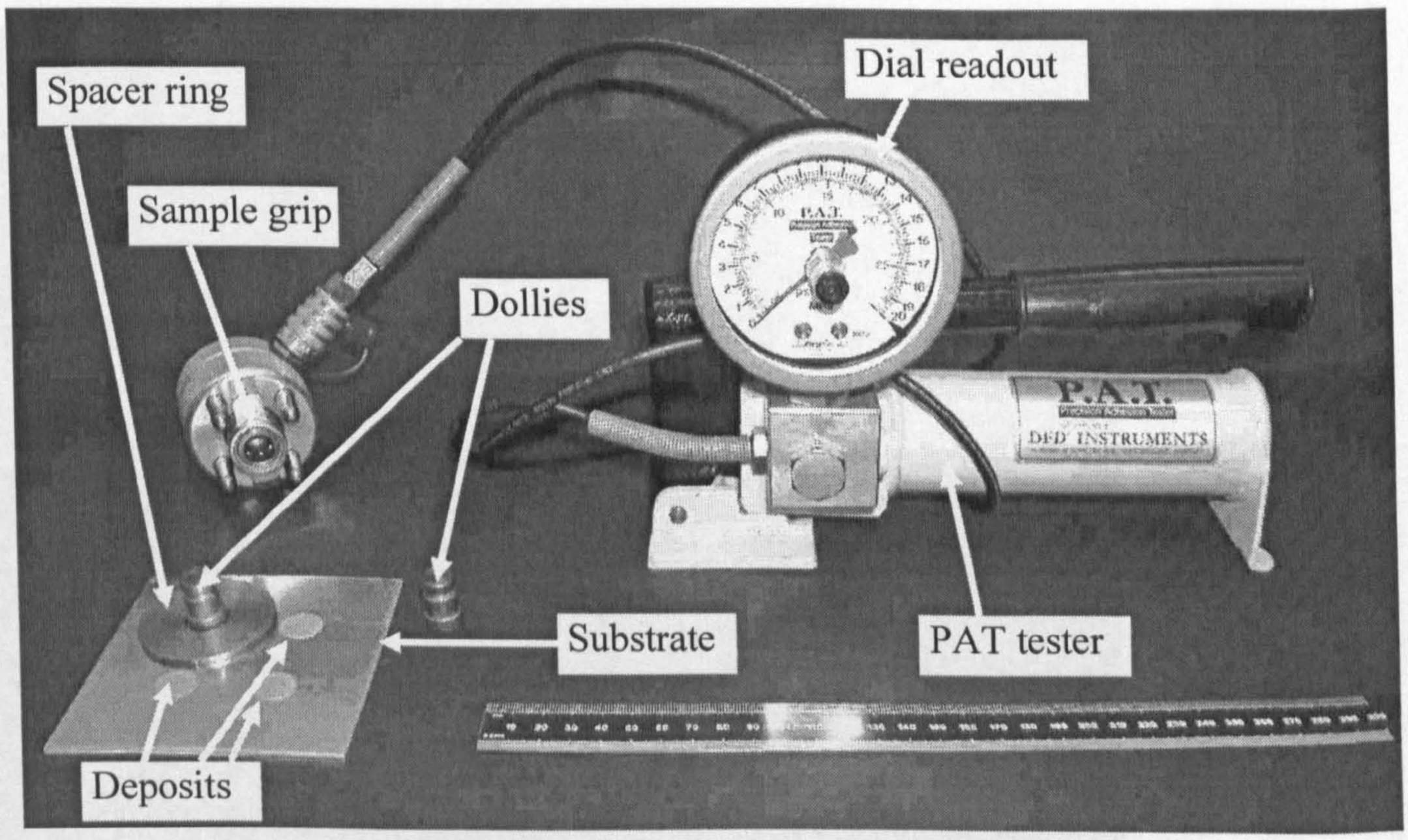

Fig. 3.2: Image showing PAT adhesion tester, adhesion test sample with Cu deposits, dollies used for adhesion testing and spacer ring used to provide an even surface for adhesion testing.

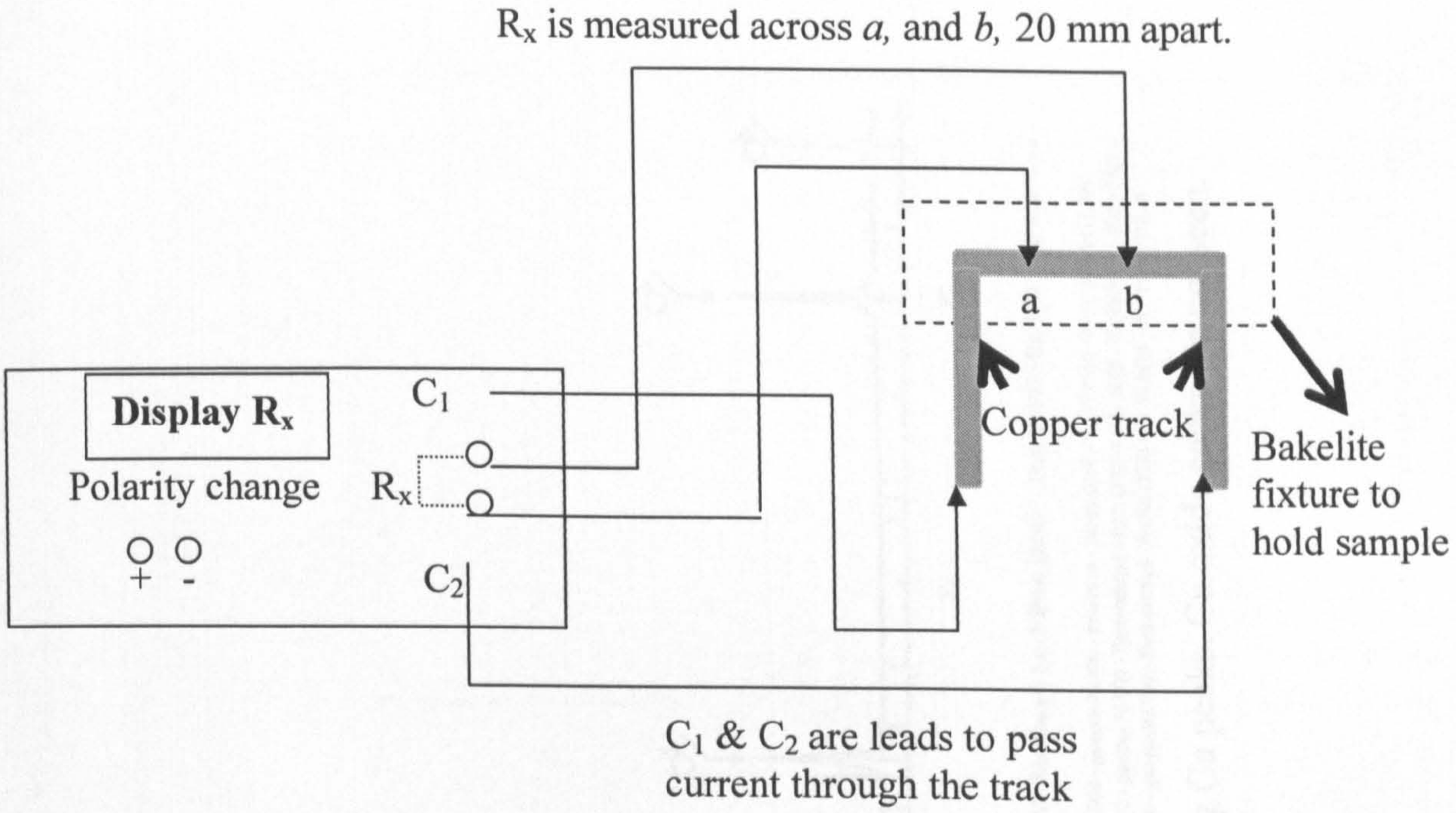

Fig. 3.3: Schematic of the resistance testing rig.

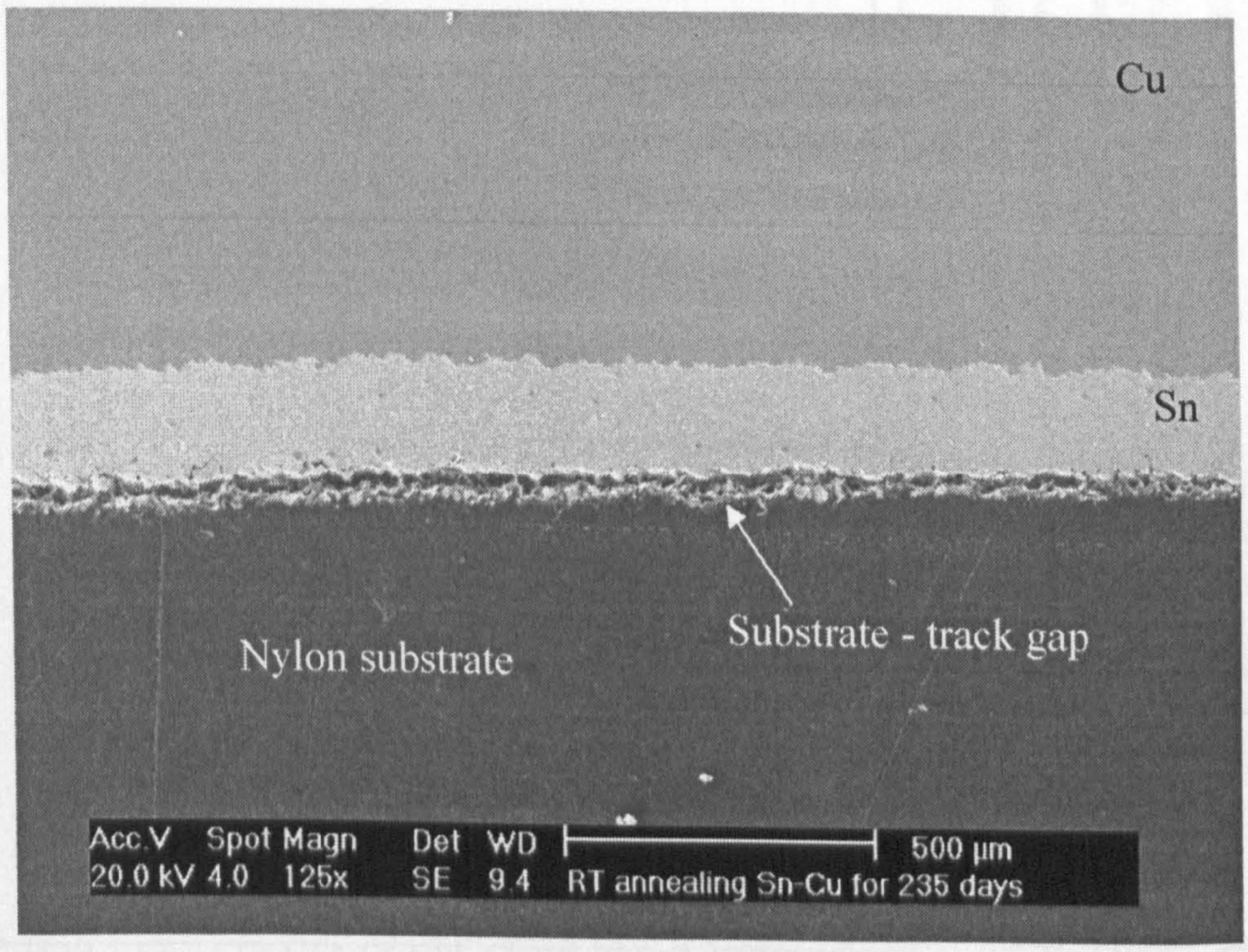

Fig. 3.4: SEM image of Sn-Cu track deposited on nylon. The track has naturally de-bonded from the nylon substrate thus leaving a gap between the Sn-Cu track and nylon substrate.

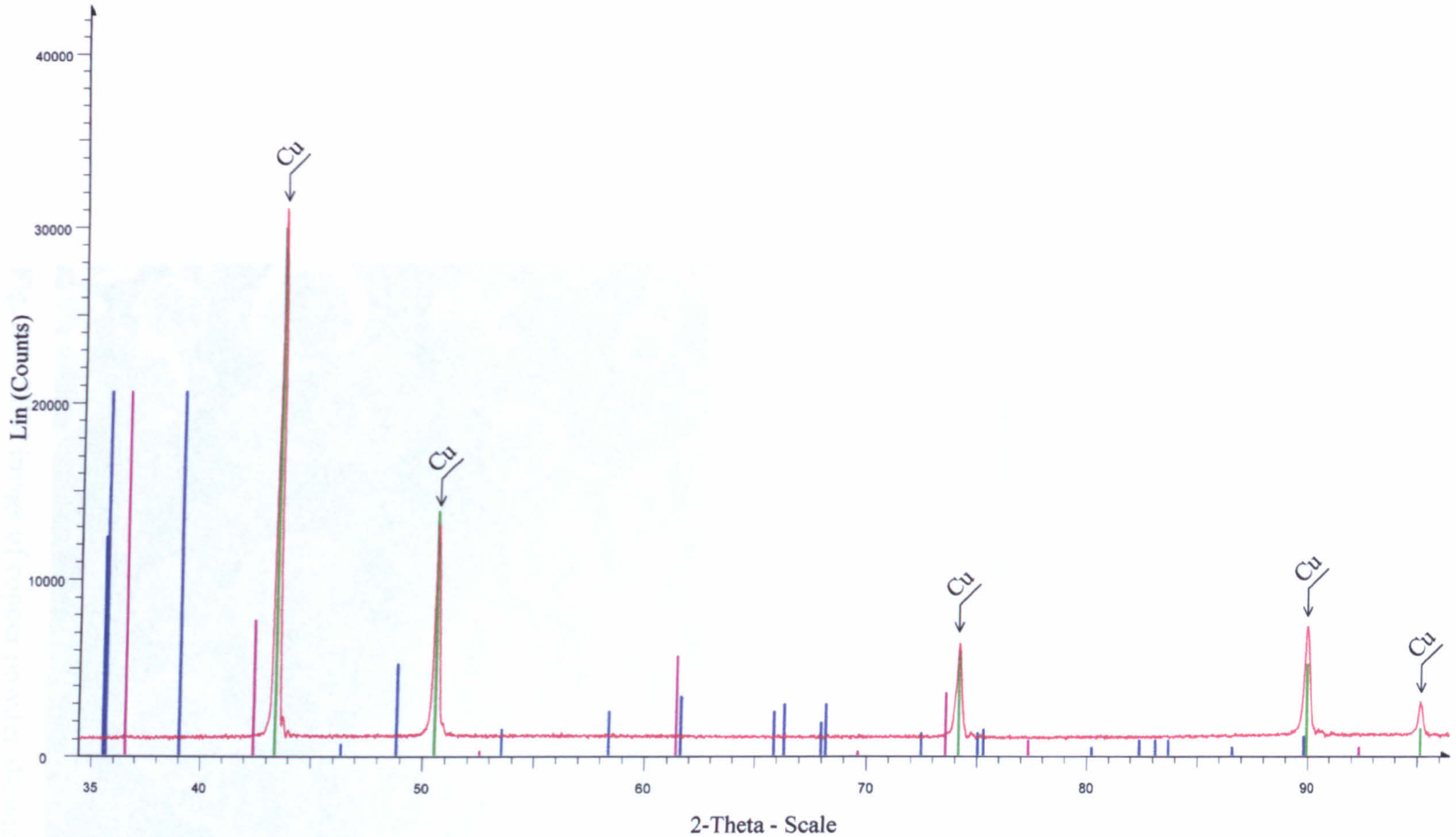

Fig. 3.5: X – Ray diffraction pattern of gas atomised Cu powder showing Cu peaks. Cu oxide peaks are not seen.

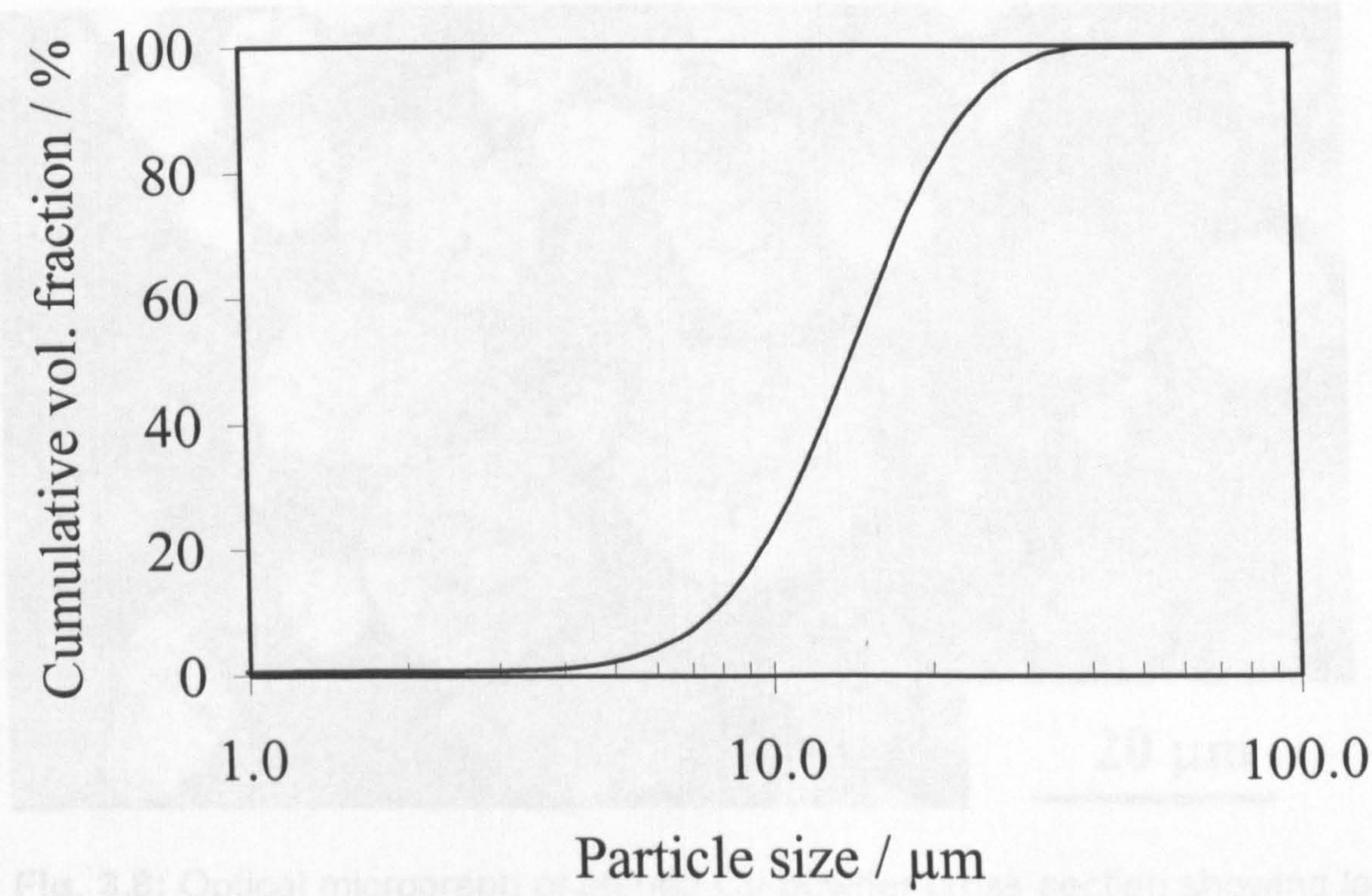

Fig. 3.6: Size distribution of copper powder.

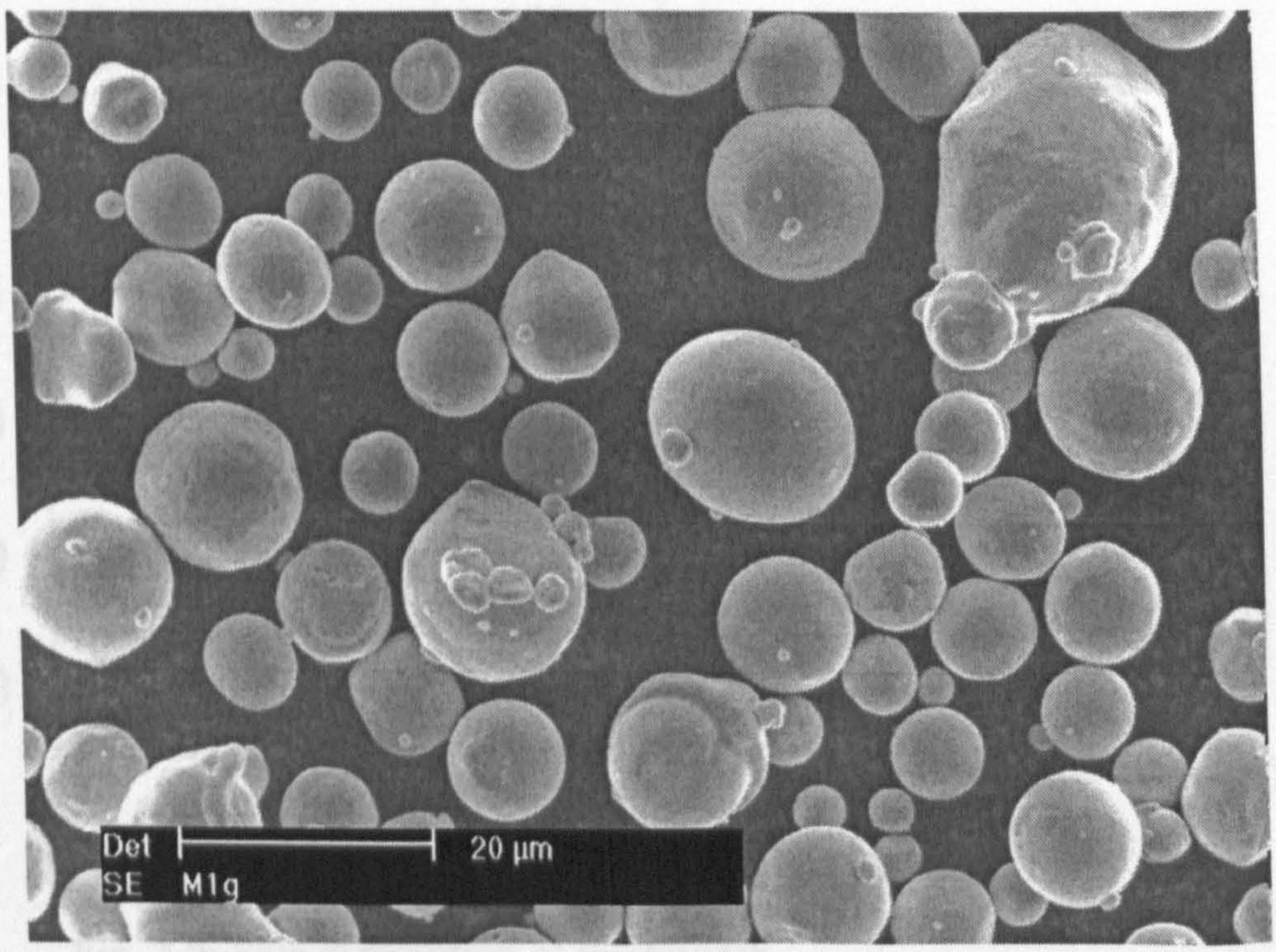

Fig. 3.7: SEM image of copper powder showing spherical particles and some particles with satellites attached to them.

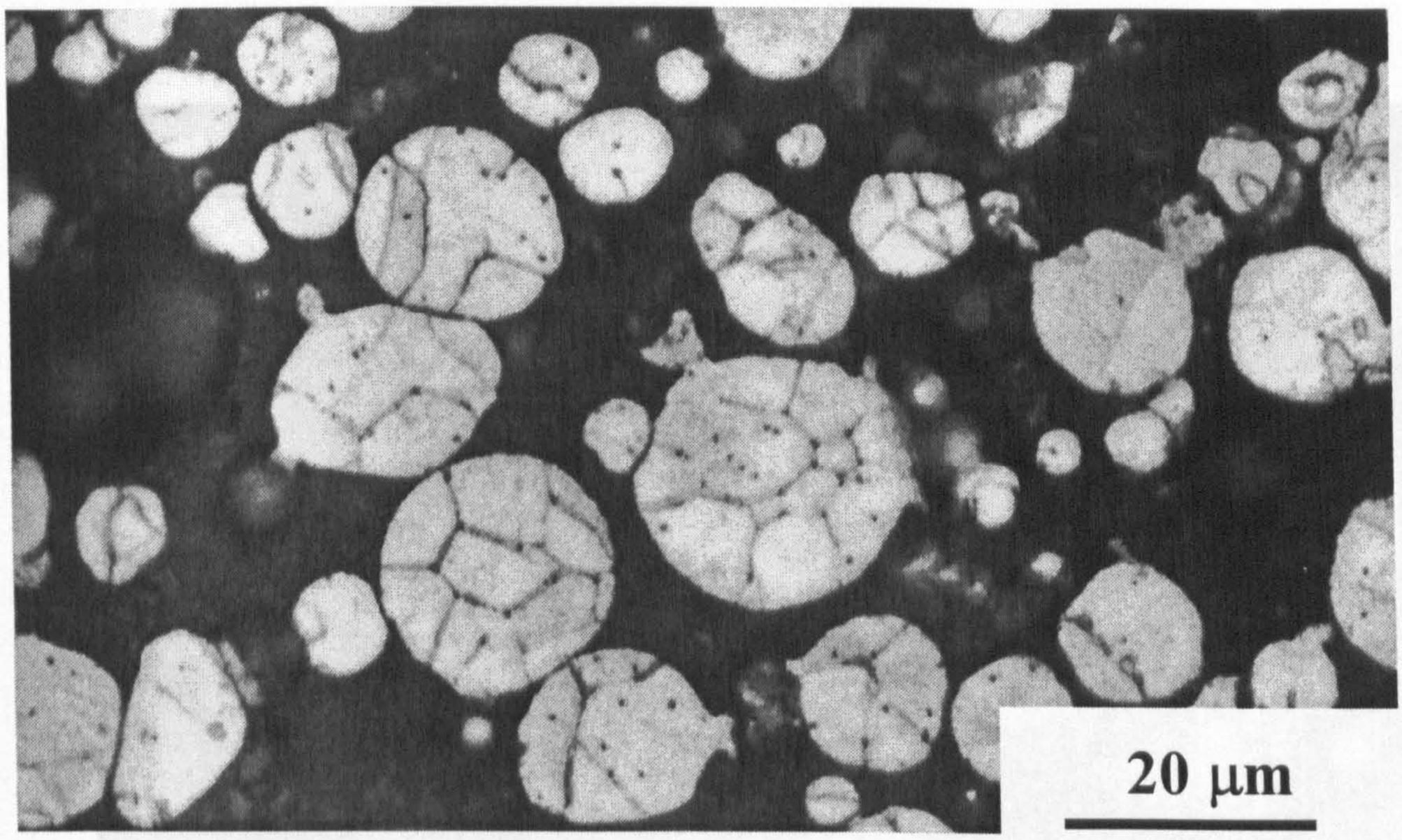

Fig. 3.8: Optical micrograph of etched Cu powder cross-section showing large individual grains within the powder particles

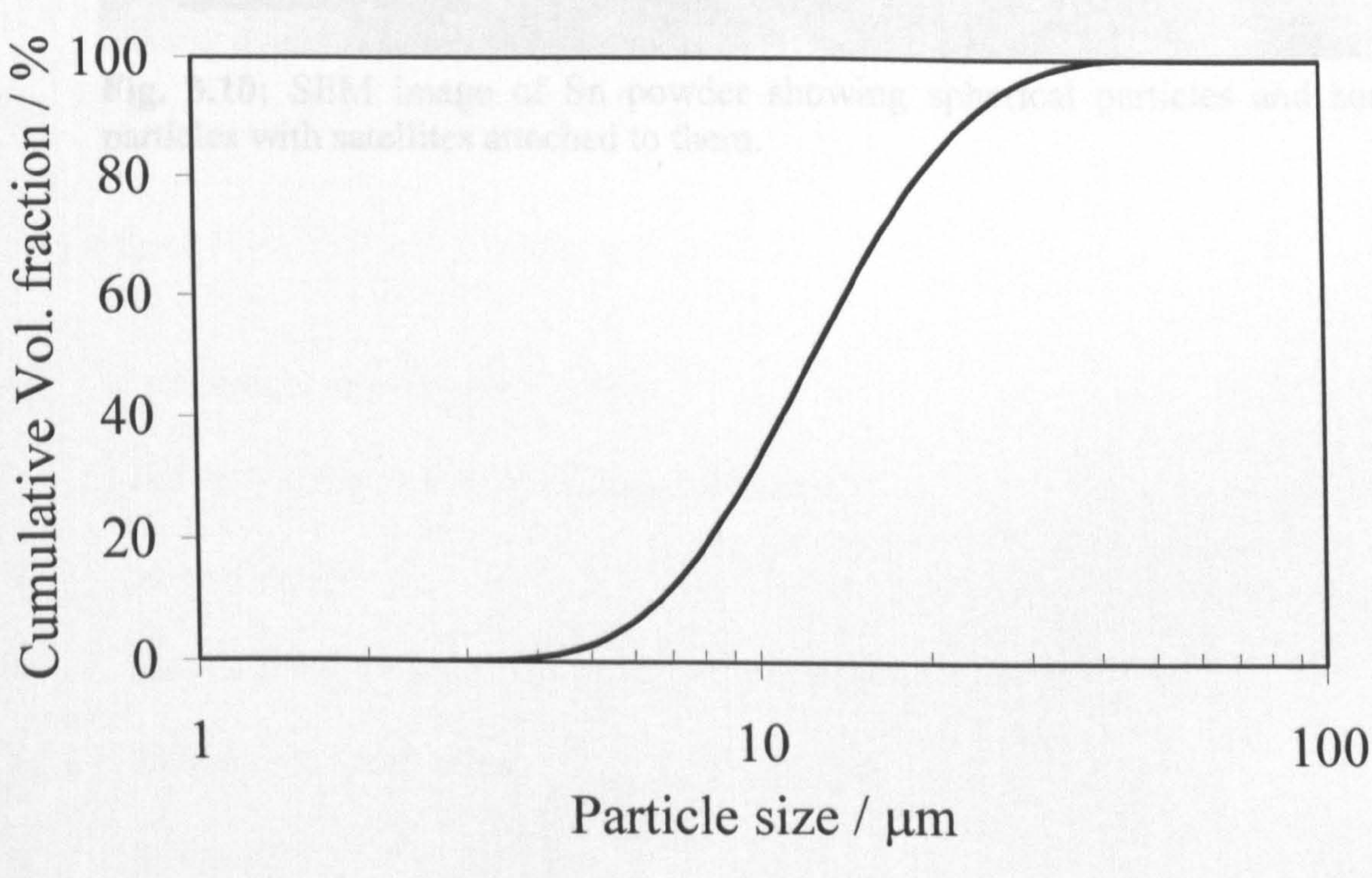

Fig. 3.9: Size distribution of tin powder.

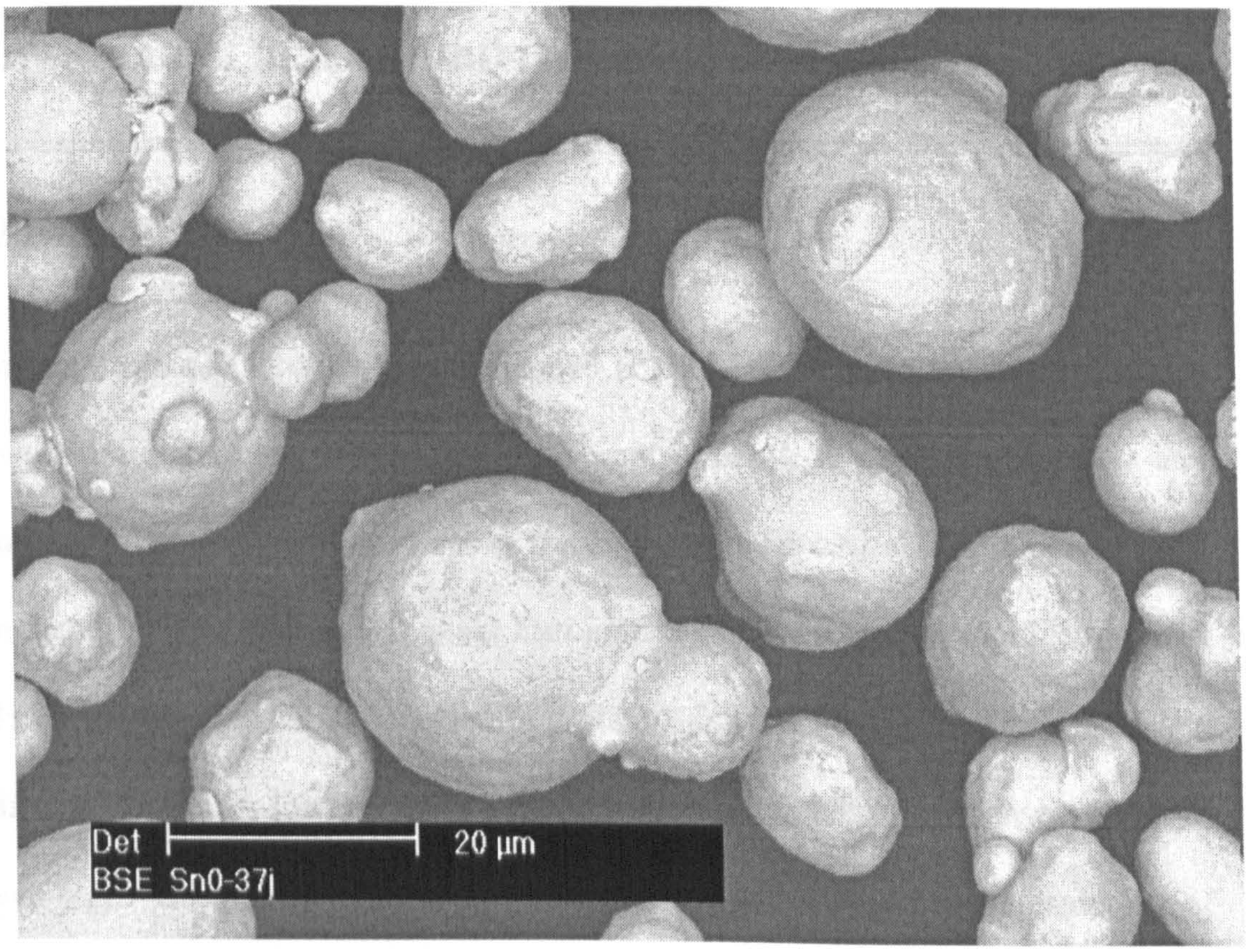

Fig. 3.10: SEM image of Sn powder showing spherical particles and some particles with satellites attached to them.

Chapter 4

System development and preliminary experiments

4.1 Introduction

The primary aim of the work was to deposit copper tracks on to various substrates with well defined characteristics such as bond strength, electrical resistivity and mechanical properties. The cold spray tracks were produced at The University of Nottingham (NU) as well as at Yazaki Europe Ltd (YEL-HH) in Hemel Hempstead, UK. Helium was used as the accelerating gas to deposit all the tracks. The reason for using helium is its lower atomic weight compared to other inert gases and high value of γ ($\gamma = 1.66$ for helium as compared to 1.4 for nitrogen. Further details of gas dynamic behaviour are given in **Appendix 1**).

This chapter is divided into sections as follows;

4.2 Description of cold spray system

4.3 Gas flow controls at Nottingham and Yazaki

4.4 Nozzle design

4.5 Measurement of powder feeding to the cold spray nozzle

4.6 Preliminary spray trials

4.7 Discussion

4.8 Conclusions

The details of the cold spray system and their constituent components are described in section 4.2. Although the cold spray systems at Nottingham and Yazaki are similar in principle, there are certain important differences with respect to gas flow control and design of the nozzle. These are discussed in sections 4.2 - 4.4. The experiments to measure the powder feed rate and its stability are described in section 4.5. A description of the preliminary trials carried out with the cold spray systems is presented in section 4.6. This is followed by a discussion of the results and conclusions in sections 4.7 and 4.8 respectively.

The information generated in these initial experiments and trials was used to design a matrix of cold spray trials to deposit copper on a variety of substrates and optimize the cold spray conditions to deposit well adhering deposits of copper. This work is described in chapter 5.

4.2 Description of the cold spray system

Schematic diagrams of the cold spray systems installed at Yazaki and Nottingham are given in **Figs. 4.1** and **4.2** respectively. The cold spray systems at Nottingham and Yazaki are housed in a spray chamber. In outline a cold spray system consists of a gas supply system, high pressure powder feeder to feed powder to the nozzle, cold spray nozzle and an exhaust system for gas and powder. The cold spray system

at Yazaki has a heater to raise the temperature of the main driving gas if required. The process gas is supplied from multiple cylinders. The gas pressures in the system are limited to a maximum of 30 bar and the system is provided with safety interlocks to prevent the gas pressures increasing beyond 30 bar. The oxygen level in the spray chamber is monitored by oxygen sensors. The oxygen sensors are interlocked with the gas supply system such that the system will shut down if oxygen level in the spray chamber reduces below 18 %.

In the cold spray system at University of Nottingham the relative movement between the nozzle and substrates is achieved by placing the substrates on a X-Y table equipped with servo motors and computer software to program the spray path or raster. The cold spray system at Yazaki is equipped with a six axis industrial robot to manipulate the cold spray nozzle with substrates remaining stationary to deposit the required patterns.

4.3 Gas flow controls

4.3.1 Gas flow controls at University of Nottingham

The schematic diagram of the cold spray system installed at the University of Nottingham (NU) is shown in **Fig. 4.2**.The cold spray rig at NU is configured to work using a bank of four helium cylinders to supply helium gas for the cold spray process. A separate single helium cylinder provides the carrier gas to feed the

powder to the nozzle. The carrier gas (i.e. that which passes through the powder feeder) and the process gas (i.e. that which is delivered directly to the nozzle) mix in a chamber located just before the cold spray nozzle. This is shown in **Fig. 4.2** and also in **Fig. 4.3**, which shows the design of the standard nozzle used at Nottingham. The carrier gas flow is controlled through a needle valve on the carrier gas line and it has the capacity to control gas flows up to a maximum of ~ 250 slpm (7.60×10^{-4} kg s^{-1}). **The carrier gas pressure and the process gas pressure can be independently controlled as the cylinders supplying carrier gas and process gas have separate control valves.** The maximum limit for any pressure to be set on the carrier gas supply is 30 bar and the process gas is usually set at one bar below the carrier gas pressure to prevent the flow of powder and gas back through the carrier gas line. The cylinder regulator reading when no process gas is flowing is taken as the stagnation pressure of the system and the cylinder regulator pressure recorded when the process gas is flowing is taken as the run time pressure of the system.

4.3.2 Cold spraying at Yazaki

A schematic of the Yazaki cold spray rig is shown in **Fig. 4.1**. The cold spray rig at Yazaki is configured to run using a bank of fifteen helium cylinders. **Mass flow controllers are used to control the gas flows.** The mass flows of the carrier gas and process gas along with the pressures are displayed on the console of the cold spray system. The supply gas line is divided in the mass flow controller cabinet into

separate lines for carrier gas and process gas. The sensors to measure the gas pressure and temperature are located in the chamber formed before the converging-diverging section of the spray nozzle. This is shown schematically in **Fig. 4.4**, which shows the design of the standard nozzle used for trials at Yazaki. Pressure and temperature recorded at this location is, as an approximation, taken to be the stagnation pressure and temperature of the gas.

In the YZK spray rig, carrier gas flows can be achieved as per the process requirements and carrier gas mass flows > 3.04×10^{-4} kg s^{-1} are possible. However, it is observed that repeatable powder feeding is only obtained when the carrier gas flow is between mass flows of $1.27 - 2.43 \times 10^{-4}$ kg s^{-1} (60 to 80 slpm). The YZK rig also has a gas heater in the process gas line and the process gas can nominally be heated up to a maximum temperature of 748 K. The gas mass flow measured at gas temperature of 298 K and various pressures is shown in **Table 4.1**.

4.4 Nozzle design

In this section the design aspects of the nozzle used for cold spray deposition are discussed.

Nozzles used in cold spray can have either circular or rectangular cross-sections of throat and exit. The nozzles used for all trials at Nottingham and Yazaki had circular cross-sections of throat and exit. The exit velocity of gas depends upon the

area ratio of the nozzle, A_{ex}/A_{th} where A_{ex} is the cross-section area of nozzle exit and A_{th} is the cross-section area of nozzle throat measured just before the start of the diverging part for a nozzle of conical shape.

The spray trials at University of Nottingham have been primarily conducted using a nozzle design that will hereafter be termed the standard nozzle. The design of standard nozzle is shown in **Fig. 4.3**. The powder injector fits in the chamber upstream of the throat (i.e. in to the high pressure region). The powder injector fed powder at a distance of 5 mm upstream of the converging part of the nozzle. The detailed dimensions of the standard nozzle are given in **Table 4.2**.

The spray trials at Yazaki were carried out using a nozzle similar to standard nozzle of Nottingham. However, there were important differences, which are summarized in **Table 4.2**. The nozzle used at Yazaki has a diffuser at the beginning of the convergent portion and, the gas and powder inlets are located at the diffuser plate. The exit mach number of Nottingham nozzle was 4.5 and for the Yazaki nozzle it was 4.9. These values were calculated assuming isentropic behavior as explained in chapter 2, section 2.4. The exit velocity of gas and particle for the Yazaki nozzle were also calculated using the one-dimensional model and particle acceleration model (chapter 2, section 2.4.6) and are presented in **Appendix 1**.

4.5 Measurement of powder feeding to the nozzle

In this section the experiments conducted to measure and control the powder feed rate (PFR) of copper to the cold spray nozzle are described. A comparison is made between the powder feed rate calculated using the volume of the powder wheel used in the feeder and, the measured powder feed rate.

4.5.1 Operation of the powder feeder

The powder is fed to the cold spray nozzle using a Praxair model 1264, high pressure powder feeder. The powder feeder shown in **Fig. 4.5** has a pressurized canister on the top which is filled with the powder to be sprayed. A schematic diagram of the powder feeder mechanism is shown in **Fig 4.6**. The powder feeder consists of a canister to hold the powder and a heating jacket is provided to heat the canister up to a maximum of 338 K. In the powder canister, the powder rests above the gland plate, which is offset from a slotted wheel, **Fig. 4.6**. The slotted wheel is rotated and the slots (or holes) are exposed to the powder whereupon these holes are filled with powder. The holes carry the powder to the carrier gas tube which forces the powder out of the holes and thereafter it is carried by the carrier gas through a high pressure hose to the cold spray nozzle. During cold spray spraying, the canister is maintained at a positive pressure with respect to the process gas pressure to prevent back flow of gas and powder in the powder and carrier gas lines.

4.5.2 Controlling and estimating the powder feed rate to the nozzle

The powder feed rate is controlled by:

(1) Slot (or hole) volume

A larger slot volume will carry more powder thus increase powder feed rate.

(2) Rotational speed of the slotted wheel.

Larger quantities of powder will be delivered to the carrier gas line at higher rotational speeds of slotted wheel.

In the present study a powder wheel with 120 holes along the circumference was used to feed the powder. The amount of powder fed to the spray device was controlled by the rate of rotation of the powder wheel i.e. a higher rotation speed fed more powder.

A weighing system attached to the powder feeder was used to measure the weight of the powder and feeder, **Fig. 4.5**. The weighing system consists of a load cell assembly mounted below the base plate which also supports the powder hopper and a PC controlled data logger for acquiring and displaying the data from the load cell. The weight of the hopper was recorded before and after spraying for a fixed time. The powder feed rate (PFR) was obtained by dividing the powder sprayed by the total time of spray. Calibration of the powder feeder was carried out by operating the cold spray system at different powder wheel speeds (PWS) and measuring the

weight of powder sprayed. The accuracy of the weighing system was verified by measuring 0.1 N dead weights on the weighing system. The error in the measurement of the dead weights was found to be less than 5%. The measured powder feed rate of copper is shown in **Fig. 4.7**. The measured powder feed rate is given by,

$$P_f^m = mP_s \quad \text{---------- Equation 4.1}$$

Where;

P_f^m, is the powder feed rate; m, is the slope of the trend line and P_s is the powder wheel speed. From **Fig. 4.7**, m was found to be; 0.24 g s^{-1} rpm^{-1}.

P_f^t can also be calculated from the wheel volume (volume of the slots) and P_S using the formula given below;

$$P_f^t = \frac{\rho_{powder} V_w P_s}{60} \quad \text{---------- Equation 4.2}$$

Where; P_f^t is the theoretical powder feed rate in g s^{-1}, ρ_{powder} is the density of powder, V_w is the volume of the slots in the powder wheel in and P_s is the powder wheel rotational speed. The 120 hole wheel has a slot volume of 3.28×10^{-6} m^3 (data provided by Praxair). The loose density of copper powder was determined by weighing a known volume of powder (10^{-4} m^3) and then dividing the measured

weight of this powder by the volume. The loose density of copper powder was calculated to be 5190 kg m^{-3}. The relationship between P_f^t and P_s from **Equation 4.2** is also plotted in **Fig. 4.7**. The slope of the equation in this case is 0.28 g^{-1} s^{-1} rpm^{-1}. It is seen that there is good agreement between the measured and calculated powder feed rates. The measured feed rate is slightly lower then the calculated value, this may arise due to error in estimating the powder density during actual powder feeding. During powder feeding the carrier gas keeps the powder in the canister in a fluidized condition. The powder in the fluidized condition will have lower density than that measured in the static condition.

4.6 Preliminary trials

This section describes the preliminary trials carried out to identify the key cold spray parameters in terms of their influence on the deposition process and properties of the deposits. In these trials, copper was deposited on mild steel and alumina coated mild steel substrates. The deposits were analyzed qualitatively as well as quantitatively to understand the influence of cold spray parameters. In this section the formation and buildup of deposits is described. The deposit profiles were measured for single and multiple passes of the nozzle over the substrate. A single traverse of the nozzle over the substrates is known as one pass.

4.6.1 Cold spray conditions to deposit copper

Preliminary trials to deposit copper were carried out using room temperature process gas (298 K) at the University of Nottingham and using heated process gas at Yazaki. The gas flow and temperature were varied in the cold spray process to determine the range of conditions for depositing copper. Cold spray conditions to deposit copper at Nottingham are shown in **Table 4.3 (a)**. The cold spray conditions to deposit copper at Yazaki are shown in **Table 4.3 (b)**. The gas pressure in the Yazaki rig was maintained at 22 bar by decreasing the gas flow rate when the gas temperature was increased. The gas flow rate at various temperatures to maintain a gas pressure of ~ 22 bar, is given in **Table 4.4**. The deposits were formed by depositing single and multiple passes of the nozzle over the substrates. The stand off distance had been previously optimized to 0.02 m for depositing copper and the same was used for these trials. The powder feed rate was maintained at 0.5 g s^{-1}.

4.6.2 Deposit profile in single and multiple passes without off-set

The profile of the deposits was measured by profilometry as described in section 3.5. Profilometer traces across tracks (perpendicular to the direction of travel) are shown in **Fig. 4.8 (a-d)**; the profile seen in **Fig. 4.8 (a)** represents deposit formed by a single traverse of the nozzle over the substrate, while **Fig 4.8 (b-d)** represent 2, 3 and 4 passes respectively. Each track is thicker in the centre region than at its periphery. Such a profile develops due to lower gas velocity near the nozzle wall where the gas flow is not strictly one-dimensional and isentropic due to the presence

of a boundary layer near the wall. This results in lower particle velocity near the nozzle wall and results in lower deposition efficiency in that region. Additionally it is also possible that the bulk of powder flow is in the centre of the nozzle with very little powder flow near the nozzle walls.

The maximum thickness i.e. peak height is seen to increase approximately linearly with number of passes. De-lamination of tracks was observed in the centre of the tracks for thicker tracks.

The effect of traverse speed on maximum track thickness was also examined using the same conditions but a range of gas temperatures. **Fig. 4.9** shows a graph of thickness plotted against $1/v$ where v is the traverse speed. For all temperatures thickness increased linearly with $1/v$ up to a speed of 0.025 m s^{-1} (i.e. $1/v = 40$ s m^{-1}). The thickness of deposits decreases with increase in traverse speed because the same mass of material in unit time is being spread over a greater surface area when using higher traverse speeds. At lower speeds (i.e. 0.012 m s^{-1}) the increase in thickness deviated from this linear trend. The deposit formed at 298 K gas temperature had de-bonded from the centre of the track and hence the thickness was overestimated during measurement. This is seen in the positive deviation from linear behavior of the curve for this data point in **Fig. 4.9**. In the case of deposits formed using heated gas, where de-bonding was not significant a negative deviation from linear behavior was observed. At lower speeds thicker tracks are deposited and the track buildup is at increasingly off-normal angles. The angle of spraying can be

estimated as the $tan^{-1}\frac{w}{2h}$; where w is the width of the track and h is the height of the profile. **Fig. 4.8** shows that the width of the track is ~ 5 mm. The spray angles calculated for 5 mm wide deposits of various thicknesses is shown in **Table 4.5**. It is seen that the spray angle decreases from ~ 85.4 ° for a deposit thickness of 0.2 mm to ~ 68 ° when the thickness of deposit increases to 1 mm. Li *et al.* studied the effect of spray angle on deposition efficiency for copper powder (-45 μm + 5 μm) [70]. They observed that for normal impacts of particles the deposition efficiency was ~ 98 %, when the impact angle was 80 °, the deposition efficiency was 92 % and for impacts at 70 ° the deposition efficiency was 85 %. This they attributed to the decrease in the normal component of particle velocity for off-normal impacts.

4.6.3 Qualitative assessment of deposits

The qualitative analysis of the deposits was based on two criteria; a) relative DE, and, b) adhesion. The relative track DE was estimated from the deposited track thickness and traverse speed. Differences in track thickness due to change in deposition conditions provide a relative estimate of DE (assuming constant PFR). Higher track thickness implies higher DE and lower track thickness implies lower DE. Adhesion was estimated by visual inspection of the deposited track; existence of a gap between the track and the substrate provided a means of estimating the adhesion qualitatively. Thus, initial assessment of the substrates and spraying

conditions for suitability in cold spray process was based on the above mentioned criteria of DE and adhesion.

Copper deposited on mild steel using single pass with gas at 298 K detached from the substrates and only very weakly adhering deposits were formed on alumina coated mild steel. When the gas was heated to 673 K adhering copper deposits were formed on mild steel. Deposits on alumina coated mild steel spalled when gas was heated above 473 K, but the bond failure was between the alumina coating and the mild steel while the copper remained adhered to the alumina coating. When copper was deposited in overlapping multiple passes on mild steel, adhering deposits were formed for gas heated to 473 K and above.

4.6.4 Deposit Characteristics

When sprayed using room temperature gas (298 K) the bonding of the deposit is poor with both mild steel and alumina substrates. The microstructure of copper deposited using conditions described in **Table 4.3 (a)** on alumina coated mild steel, is shown in **Fig. 4.10**. It shows partial de-bonding of the copper deposit from alumina substrate. **Fig. 4.11** shows the etched microstructure of copper de-bonded from an alumina coated mild steel substrate, deposited using gas at 298 K and conditions described in **Table 4.3 (b)**. The deposit has very low porosity and

etching delineates the particle boundaries. The particles are highly flattened due to deformation upon impact.

Heating the process gas improved the adhesion of copper on mild steel as well as on alumina. At gas temperatures above 473 K, adhering deposits were formed on mild steel as well as alumina coated mild steel. The alumina layer had the tendency to de-bond from the mild steel substrate when deposition was carried out using gas above 473 K. The etched microstructure of copper deposited on alumina coated mild steel using gas heated to 673 K and conditions described in **Table 4.3 (b)** is shown in **Fig. 4.12**. Copper is well adhered to alumina, however the alumina layer had detached from the mild steel substrate. Etching has revealed the particle boundaries and some very fine sub-grains are also seen.

The etched microstructure of copper deposited on mild steel using gas at 673 K and conditions described in **Table 4.3 (b)** is shown in **Fig. 4.13**. Copper is seen to be well adhered to mild steel. The dark features seen at the copper-mild steel interface belong to a narrow region of considerable plastic deformation in the mild steel and copper.

Fig. 4.14 shows the microhardness of the coatings as a function of gas temperature, for, coatings sprayed with two different nozzle-substrate traverse speeds. A significant drop in microhardness of the coatings is observed as the gas temperature was increased.

4.7 Discussion

The deviation from linear increase in thickness at lower traverse speed is due to the lower DE for deposition while using lower traverse speeds. The deposit buildup at lower traverse speeds progresses at increasingly off-normal spray angles as the thickness of deposit increases (**Table 4.5**). The off-normal spray angles result in decrease of deposition efficiency.

The tendency for deposits to de-bond was seen in deposits formed at Nottingham as well as Yazaki while using process gas at 298 K. Heating the process gas above 473 K decreased the tendency for deposits to de-bond from mild steel substrates. The tendency of deposits to de-bond seems to be related to the residual stress developed in the coatings during the spraying process. Even if the residual stress itself is independent of thickness, the strain energy release (associated with the relaxation of the residual stress) for coating de-bonding increases linearly with deposit thickness, and thus once coatings exceed a critical thickness de-bonding occurs.

Heating the process gas provides a mechanism for stress relieving and also might be associated with better bonding of the sprayed particles to the substrate due to the higher velocity of particles achieved with heated gas. The overall effect is increase in deposit thickness that can be achieved before de-bonding occurs.

The effect of heating the process gas has the effect of heating the substrate by impingement of the hot gas jet and does not significantly heat the particles during flight. This is seen from the hardness of deposits formed at two traverse speeds (**Fig. 4.14**) where it is seen that deposit hardness decreased more rapidly for traverse speed of 12 mm s^{-1} as compared to traverse speed of 50 mm s^{-1}. With this change in traverse speed, the temperature and velocity of particles upon impact will not be altered; however, the coating itself will reach a higher temperature due to the increased time of impingement of the heated gas and thus it is proposed that it is this latter effect that controls the heating of the deposit.

The improvement in adhesion of copper deposits on mild steel while using heated process gas (**Fig. 4.13**) is probably related to the higher velocities generated and reduction in residual stress at higher temperatures. There appears to be a narrow region in mild steel near the interface where significant deformation seems to have taken place. The bonding of copper to alumina is probably due to interlocking of splats during spraying as formation of a metallurgical bond between alumina and copper during cold spraying is not likely. The lower adhesion of copper deposits on alumina when sprayed using gas at 298 K seems to be the reason for de-bonding seen in **Fig. 4.10**. The deposits formed on alumina coated mild steel appear well bonded to alumina when sprayed using gas heated to 673 K (**Fig. 4.12**). The improvement in the bonding of copper is probably related to the greater degree of flattening of copper particles at higher temperatures due to which greater interlocking of copper and alumina is attained. However, the impingement of the

hot gas on the plasma sprayed alumina produces tensile stress in the alumina layer as there is a mis-match in the co-efficient of thermal expansion of alumina and mild steel. The co-efficient of thermal expansion of alumina (7.4 μm m^{-1} °C) is lower than that of mild steel (12.6 μm m^{-1} °C); hence, mild steel expands more than alumina layer. The greater expansion of mild steel with respect to alumina generates tensile stress in alumina resulting in de-lamination at higher spraying gas temperatures.

The project requirement was to spray copper onto an insulating substrate. Due to difficulties in depositing copper on alumina coated mild steel, it was decided to try and deposit copper on various polymer substrates. It was decided to undertake detailed spray trials to investigate and then optimize the spray parameters for depositing copper on metallic, ceramic and polymer substrates. The initial step was to spray on a wide variety of substrates and then shortlist from these substrates for inclusion in further trials to optimize cold spray conditions. The first trials were termed as spray matrix of cold spray trials. These trials are presented in the next chapter.

4.8 Conclusions

The following conclusions are drawn from the preliminary trials;

1) Cold spray parameters influence the deposition process as well as the properties of the sprayed deposits. The deposits are highly cold worked due to the high velocity impact of the particles.
2) At lower traverse speeds the DE decreases as the impact is at increasingly off-normal angles.
3) Cold sprayed coatings exhibit compressive residual stresses and the residual stress is an important factor in the observed adhesion of cold sprayed copper. Using higher gas temperatures seems to reduce the residual stresses in the copper deposits.
4) Copper cannot be deposited on mild steel substrate for process gas temperature below 473 K. Heating the process gas increases the adhesion of deposits on mild steel but does not seem to influence the deposit efficiency.
5) The major effect of process gas heating is in heating already deposited material and it does not seem to significantly heat the spray particles in flight.
6) Copper deposits on alumina coated mild steel result in de-bonding of the copper layer at gas temperatures below 473 K and in de-bonding of the alumina layer from the mild steel substrate at process gas temperatures above 473 K.

Table 4.1: Gas pressures attained at different gas mass flows for He gas at 298 K in the Yazaki system using standard nozzle.

Pressure / bar	11	15	22	26	29
Mass flow / 10^{-3} kg s^{-1}	1.522	1.96	2.906	3.53	4.126

Table 4.2: Design features of nozzle used at Nottingham (NU) and Yazaki (YZK).

Feature	Nottingham	Yazaki
Convergent region length (l_1) / mm	10	34
Convergent region initial diameter (D_1) / mm	13	18
Divergent region length (l_2) / mm	100	96
Total length ($l_1 + l_2$) / mm	110	126
Diameter of throat (D_{th}) / mm	1.45	1.3
Diameter of exit (D_{ex}) / mm	4	4
Area ratio (A_{ex}/A_{th})	7.62	9.46
Calculated exit Mach number of nozzle	4.5	4.9
Distance of powder injector from start of convergent region / mm	5	0
Diameter of powder injector exit / mm	1	3

Table 4.3 (a): Deposition conditions used at Nottingham for preliminary experiments to deposit copper on mild steel and alumina coated mild steel substrates.

Process gas pressure / bar	Carrier gas flow / 10^{-4} kg s^{-1}	Powder feed rate / g s^{-1}	Process gas temperature / K	Stand off distance / m
22	3.78	0.5	298	0.02

Table 4.3 (b): Deposition conditions used at Yazaki for preliminary experiments to deposit copper on mild steel and alumina coated mild steel substrates. The gas mass flows to attain 22 bar pressure in the Yazaki system is given in **Table 4.4**

Process gas pressure / bar	Carrier gas flow / 10^{-4} kg s^{-1}	Powder feed rate / g s^{-1}	Process gas temperature / K	Stand off distance / m
22	1.82	0.5	298 - 673	0.02

Table 4.4: Gas mass flow in YZK system at different process gas temperatures to maintain a constant pressure of 22 bar.

Temperature / K	298	373	423	473	523	573	623	673
Mass flow / 10^{-3} kg s^{-1}	2.90	2.34	2.23	2.11	2.00	1.91	1.84	1.78

Table 4.5: Estimated spray angles for various thicknesses of deposits formed using gas heated to 423 K and conditions as specified in **Table 4.3 (b)**.

Measured track thickness / mm	1.00	0.75	0.35	0.20
Estimated spray angle / °	68	73	82	85

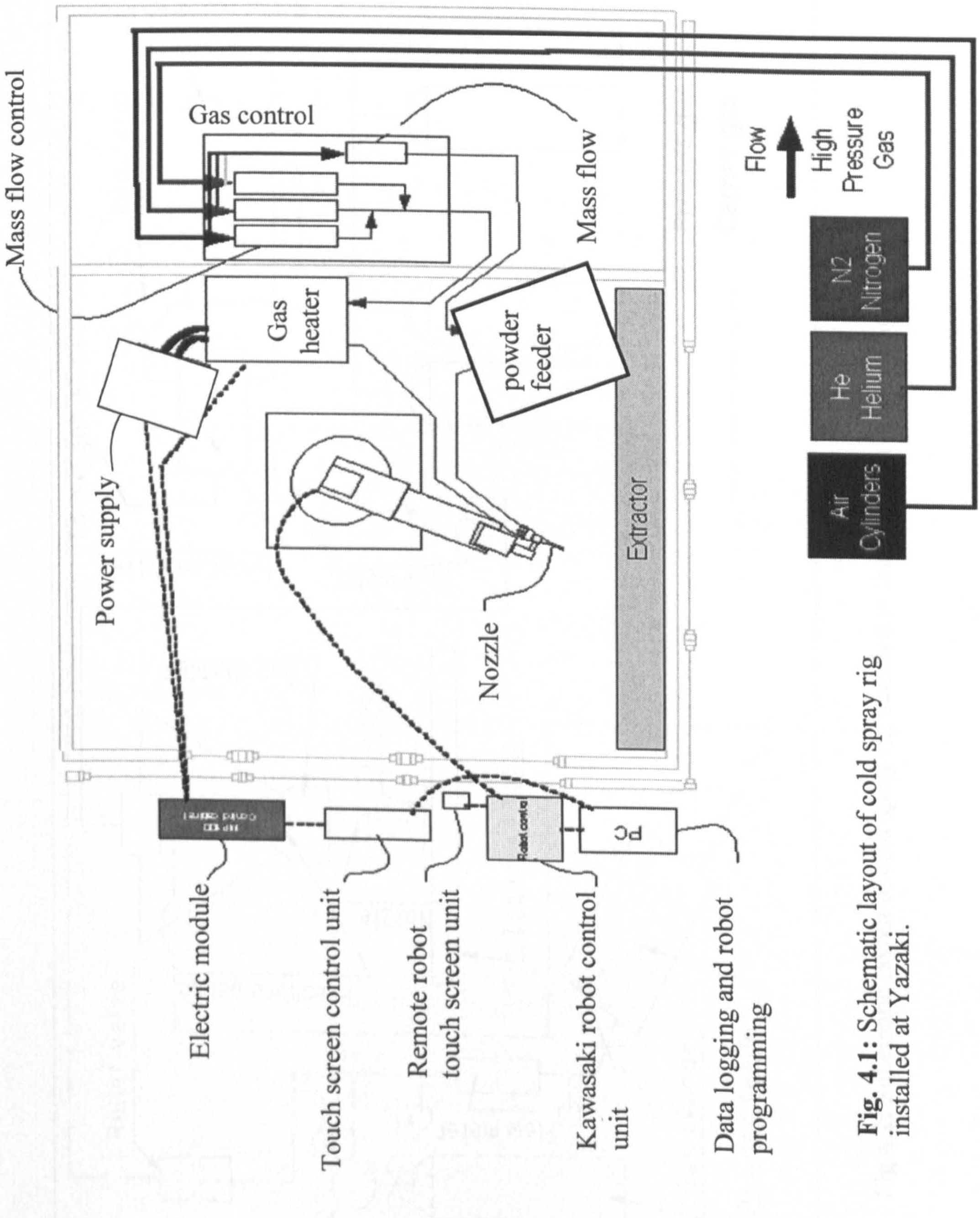

Fig. 4.1: Schematic layout of cold spray rig installed at Yazaki.

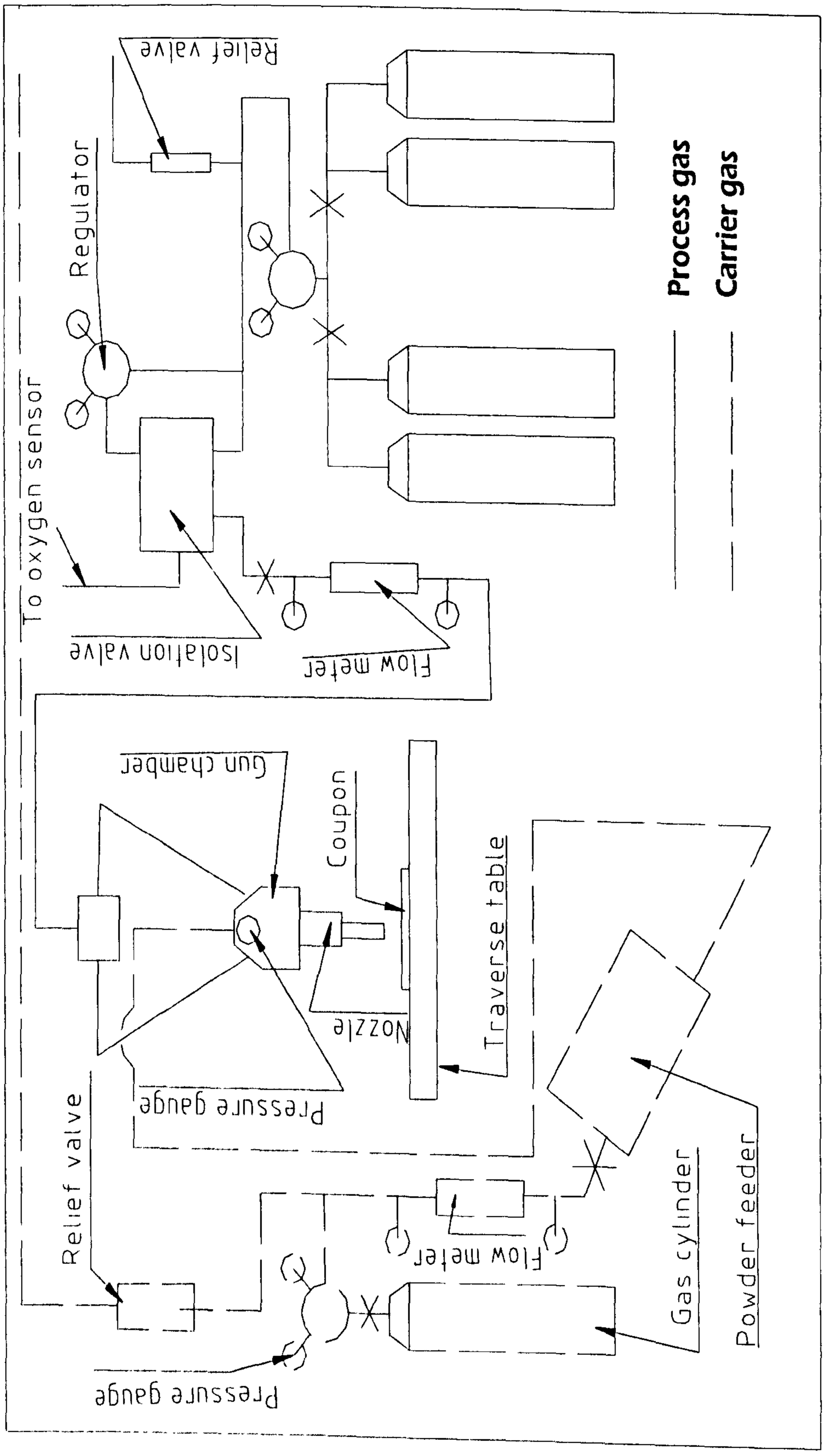

Fig 4.2: Schematic layout of cold spray rig installed at the University of Nottingham

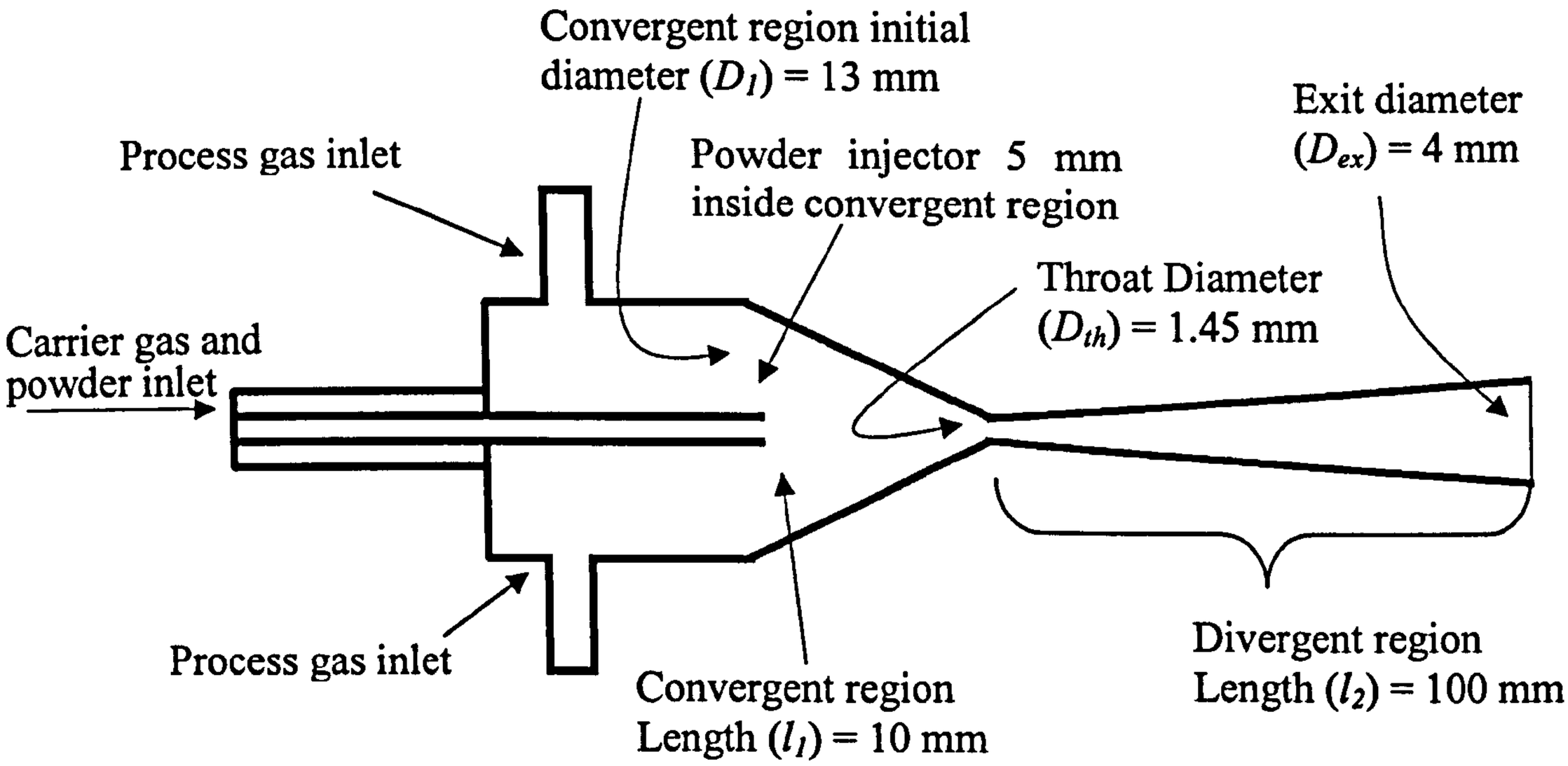

Fig. 4.3: Design of standard nozzle used at University of Nottingham.

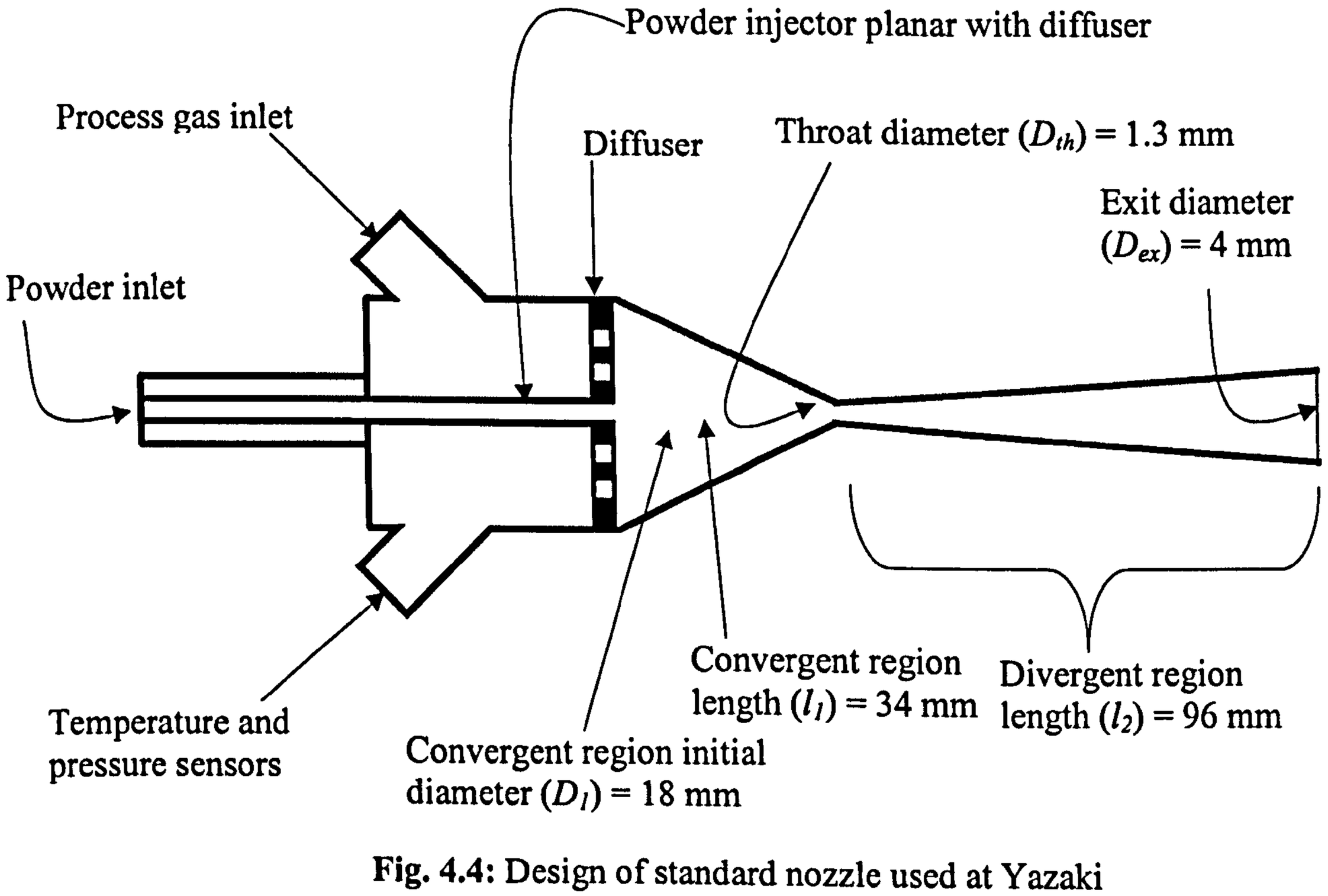

Fig. 4.4: Design of standard nozzle used at Yazaki

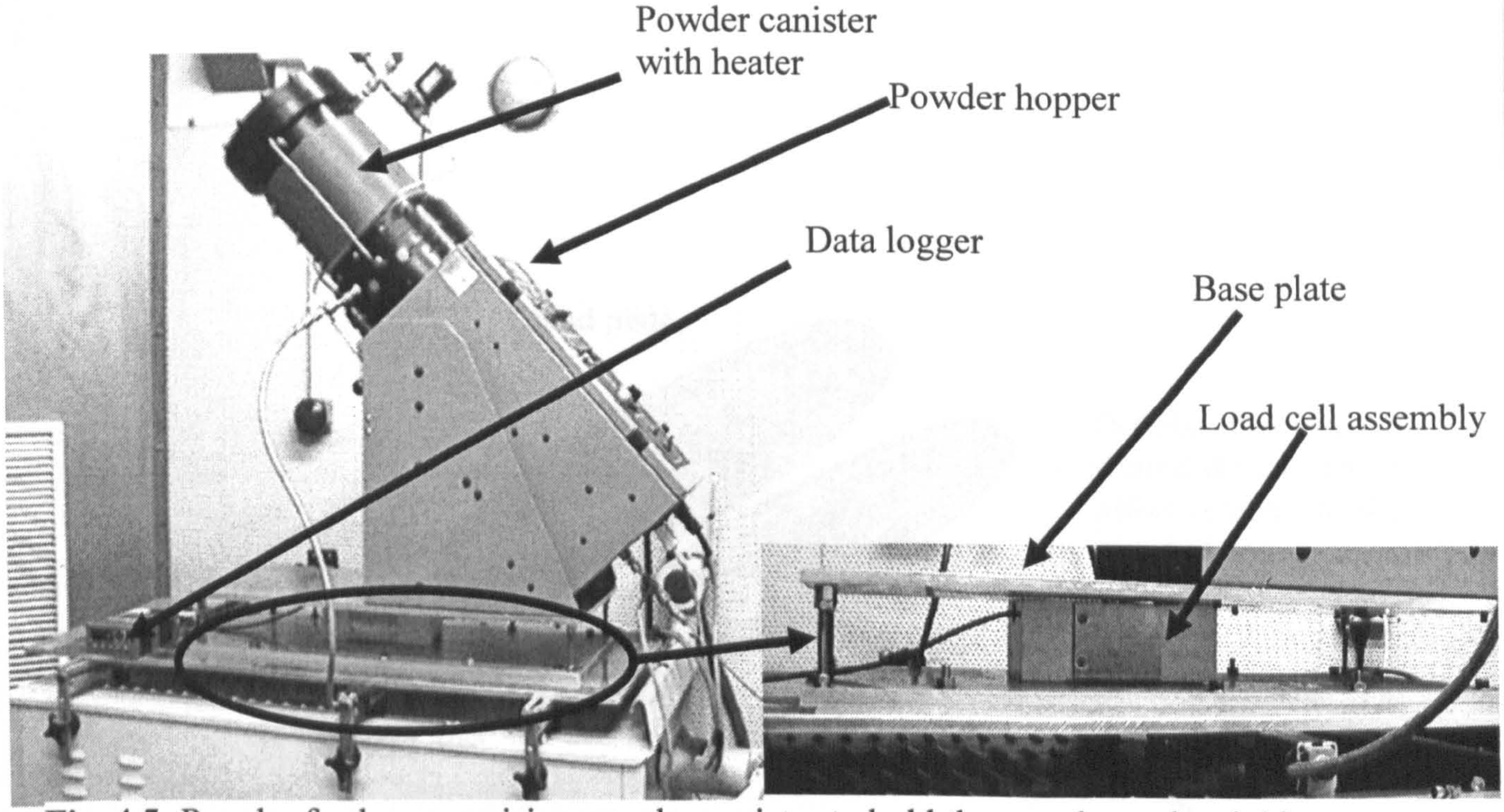

Fig. 4.5: Powder feeder comprising powder canister to hold the powder and weighing system mounted on the base plate comprising of load cell assembly and data logger.

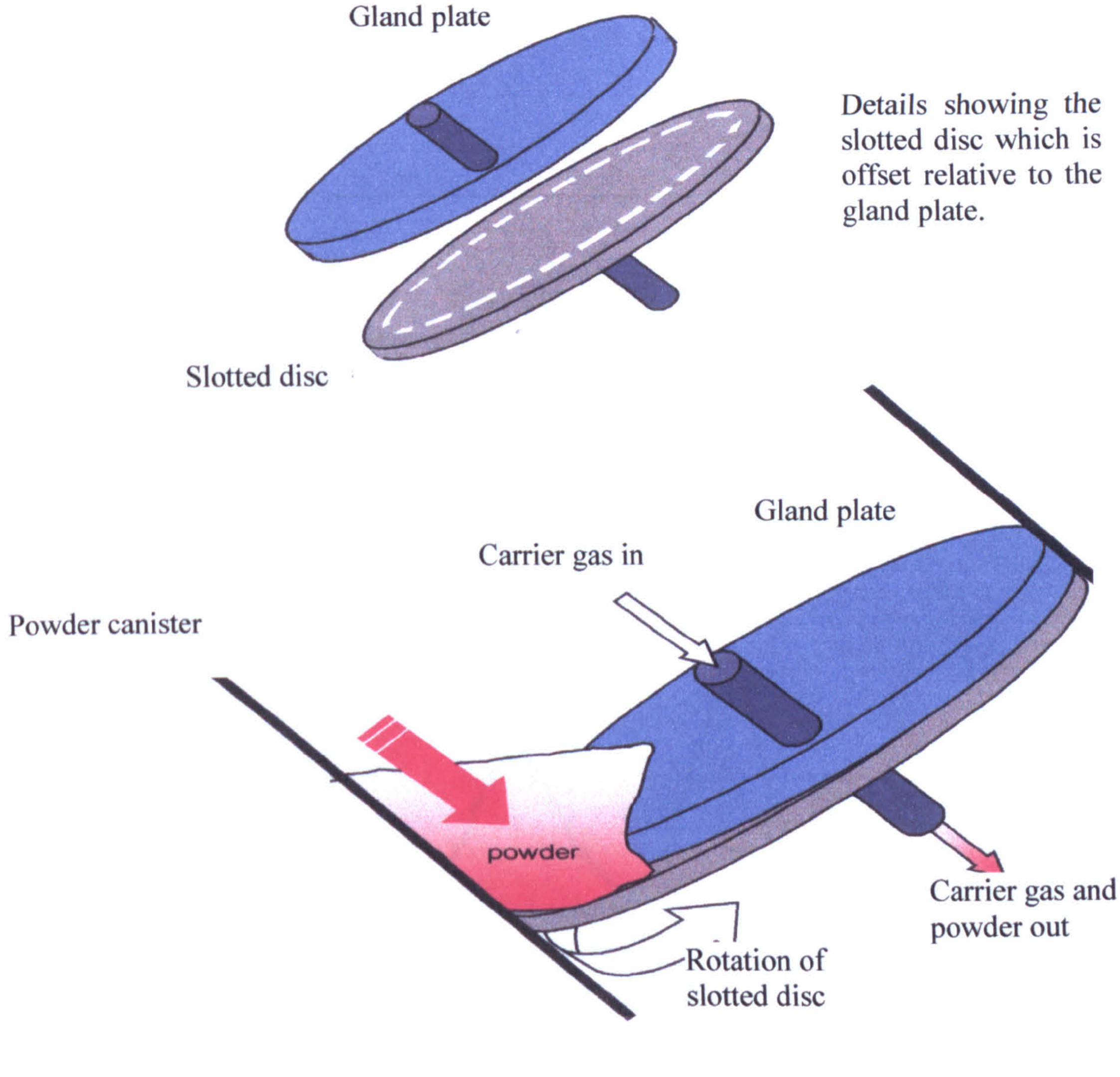

Fig. 4.6: Schematic diagram showing the principle of operation of the powder feeder

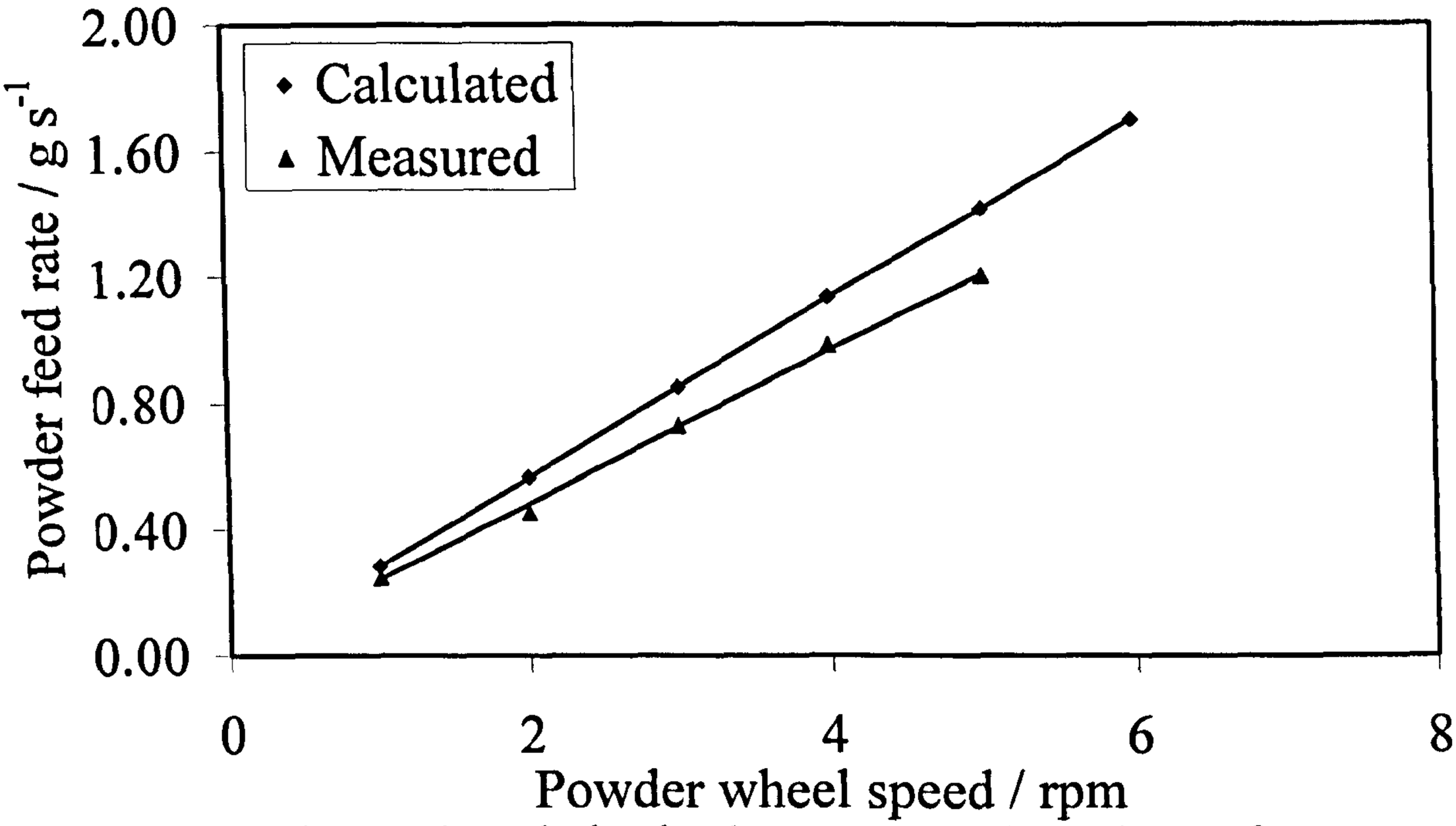

Fig. 4.7: Plot showing calculated and measured powder feed rates of copper at different powder wheel speeds using 120 hole powder feed wheel. The slope of the trend line for calculated and measured powder feed rate are 0.28 and 0.24 g s^{-1} rpm^{-1} respectively.

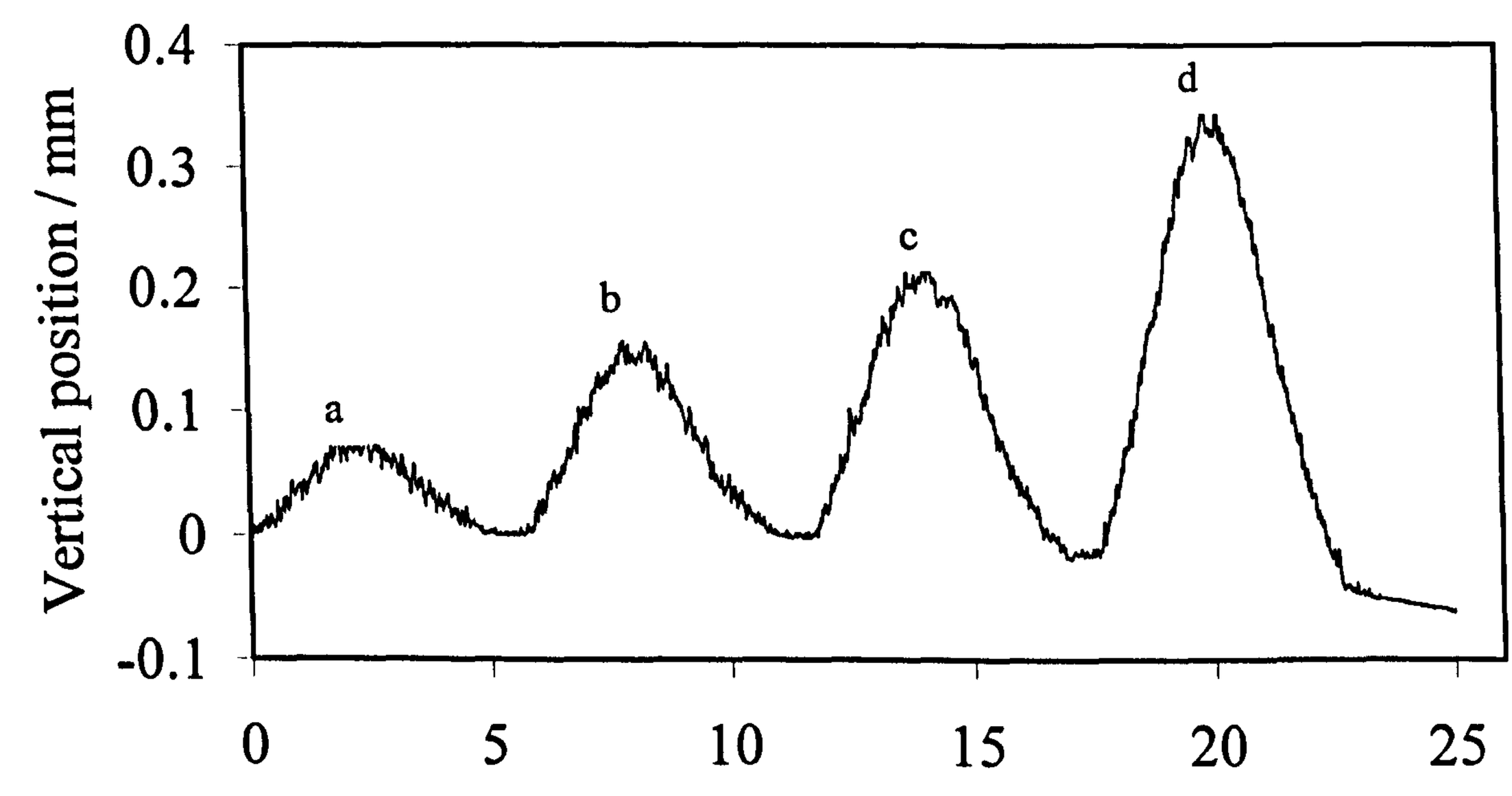

Fig. 4.8: Profiles of copper sprayed at Nottingham using traverse speed of 100 mm s^{-1}, but different number of passes of the nozzle over substrate (alumina coated mild steel); a = 1 pass, b = 2 passes, c = 3 passes and d = 4 passes. Deposition conditions as described in **Table 4.3 (a)**.

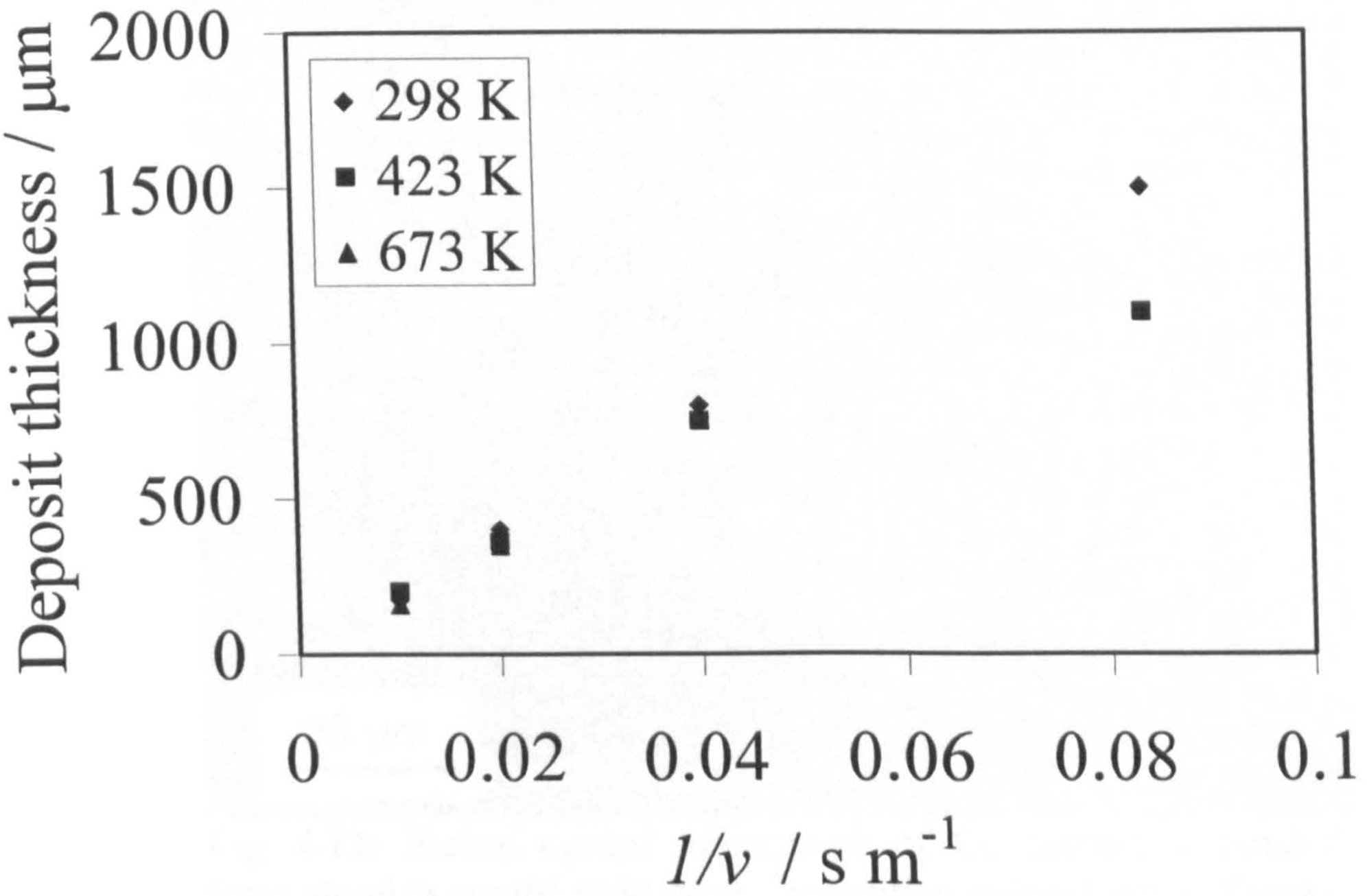

Fig. 4.9: Plot of deposit thickness versus 1/traverse speed at different gas temperatures. Deposition conditions as described in **Table 4.3 (b)**.

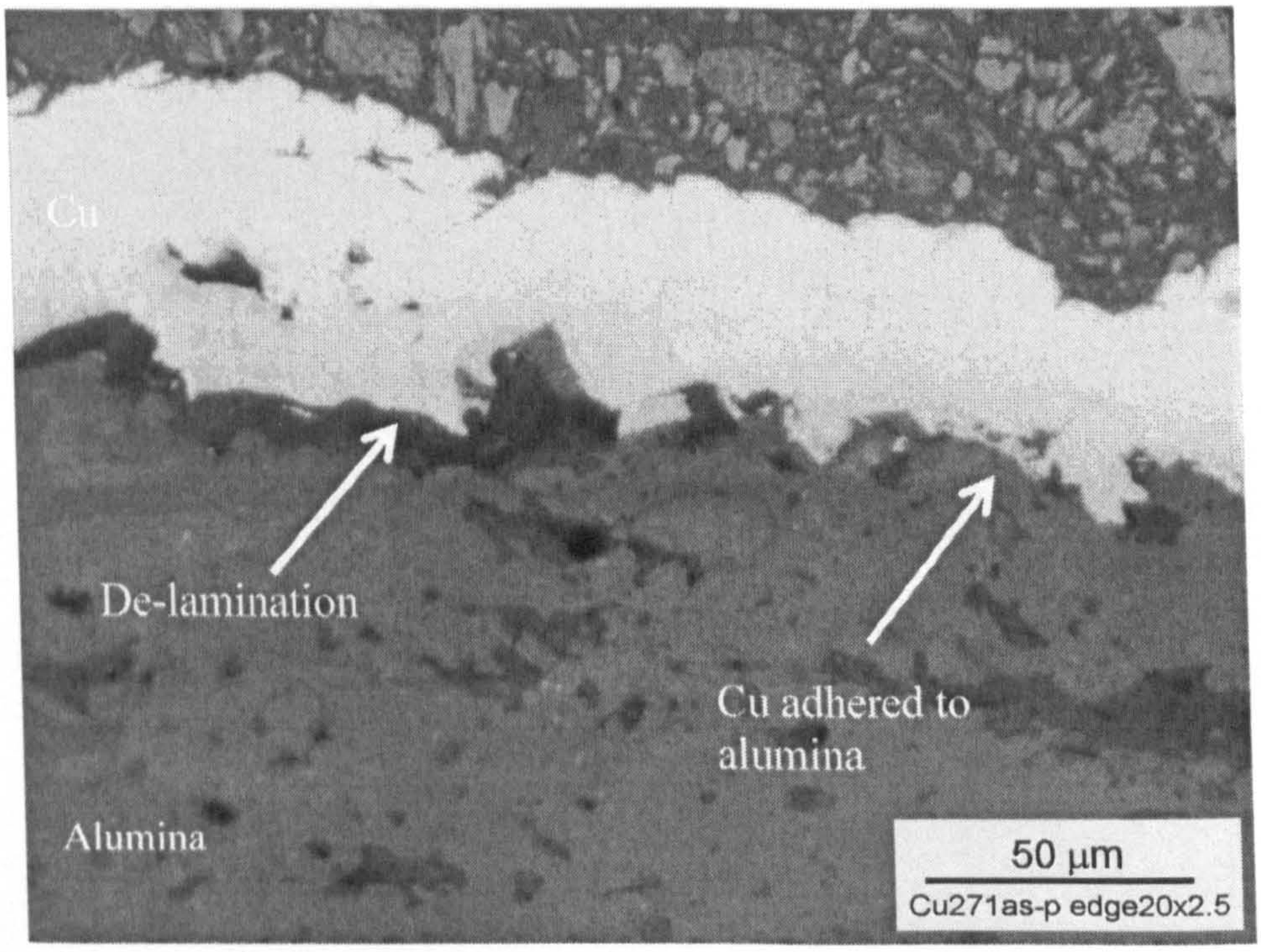

Fig. 4.10: Optical micrograph of Cu deposited on alumina coated mild steel at Nottingham using traverse speed of 12 mm s^{-1} and conditions described in **Table 4.3 (a)**, showing partial de-lamination of the Cu layer from the alumina.

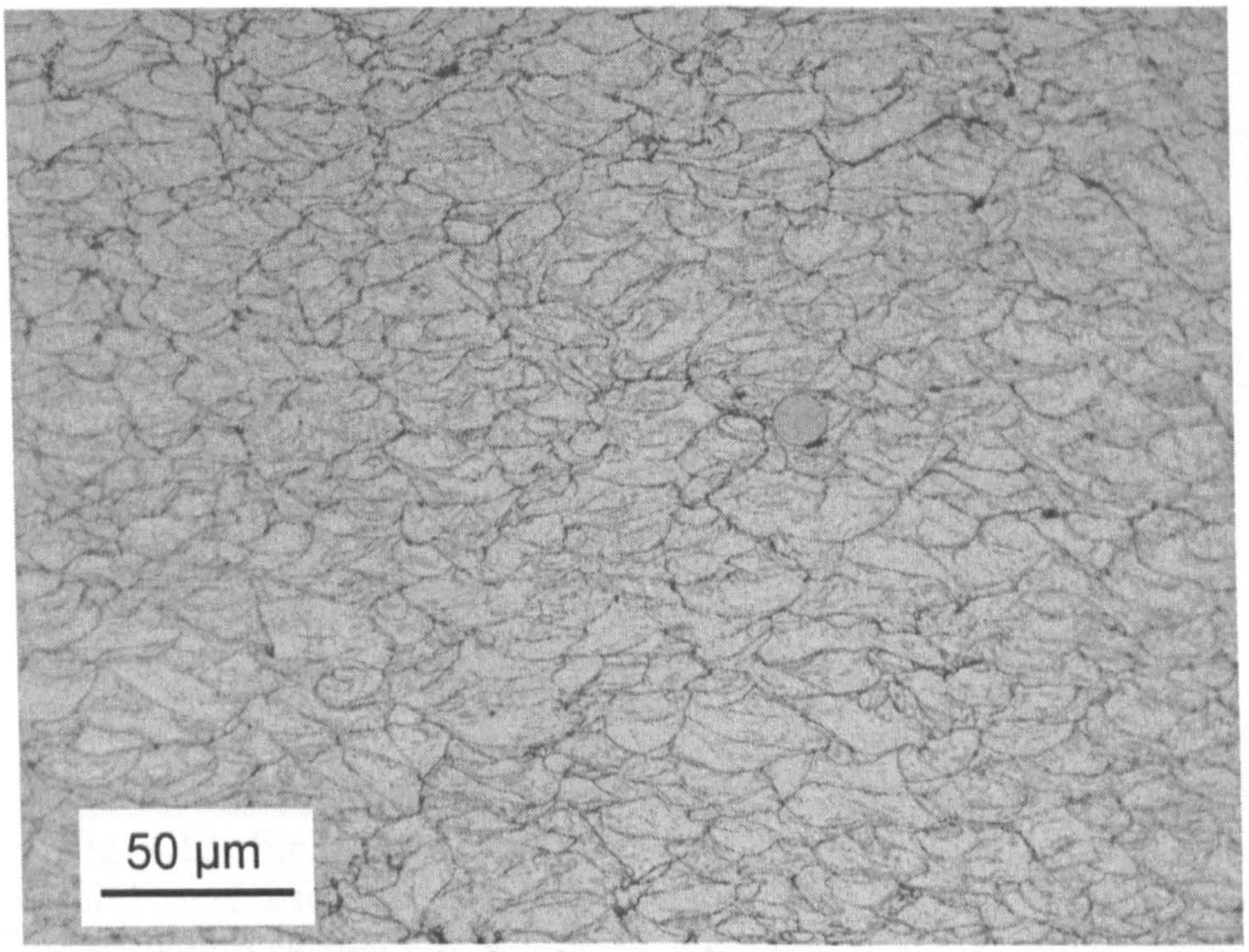

Fig. 4.11: Etched optical micrograph of Cu deposit de-bonded from alumina coated mild steel. Deposition carried out at Yazaki, using traverse speed of 100 mm s^{-1}, gas at 298 K and conditions described in **Table 4.3 (b)**.

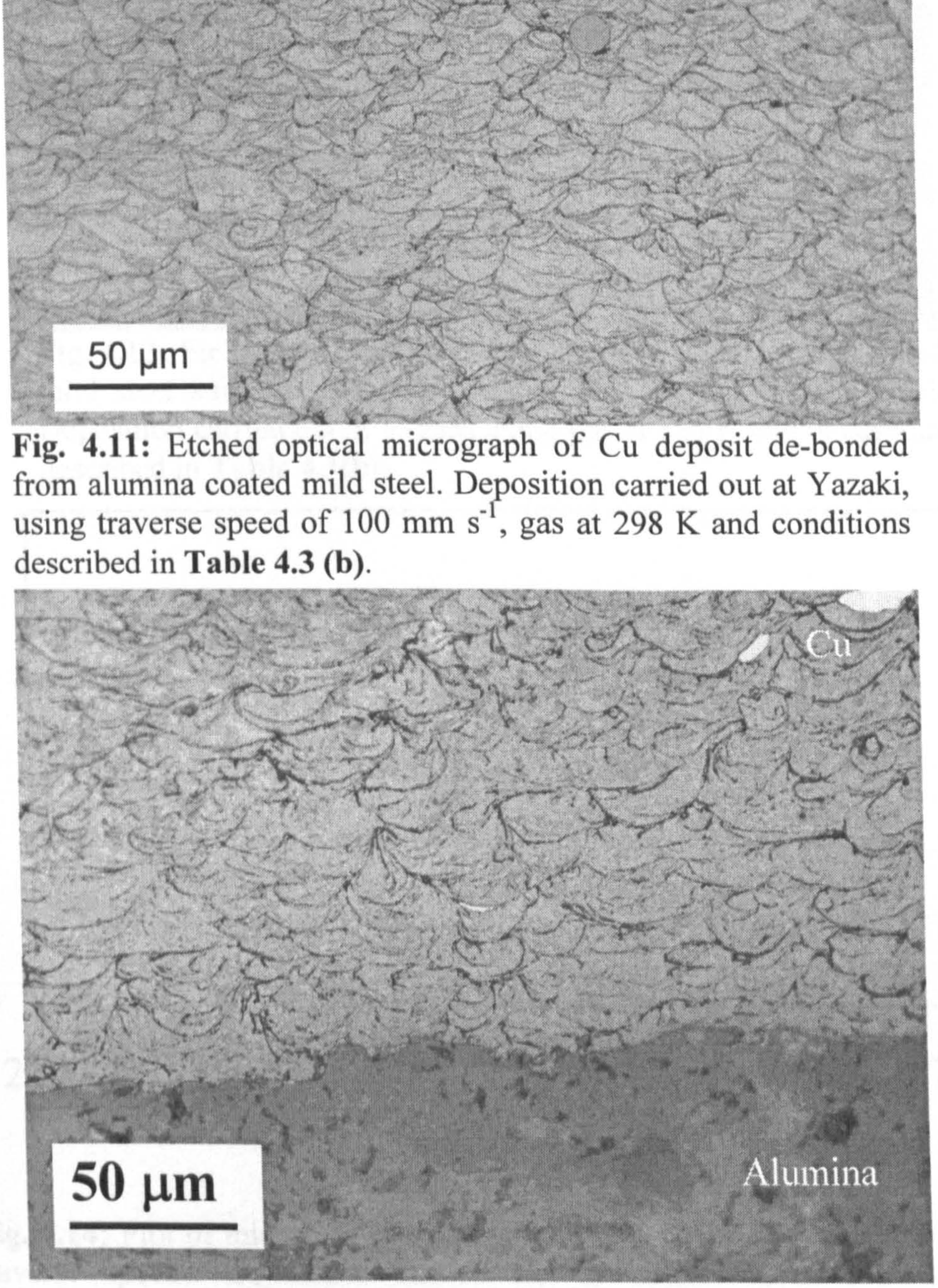

Fig. 4.12: Etched optical micrograph of Cu deposited on alumina coated mild steel showing Cu well bonded to alumina. Deposition carried out at Yazaki, using a traverse speed of 100 mm s^{-1}, gas at 673 K and conditions described in **Table 4.3 (b)**.

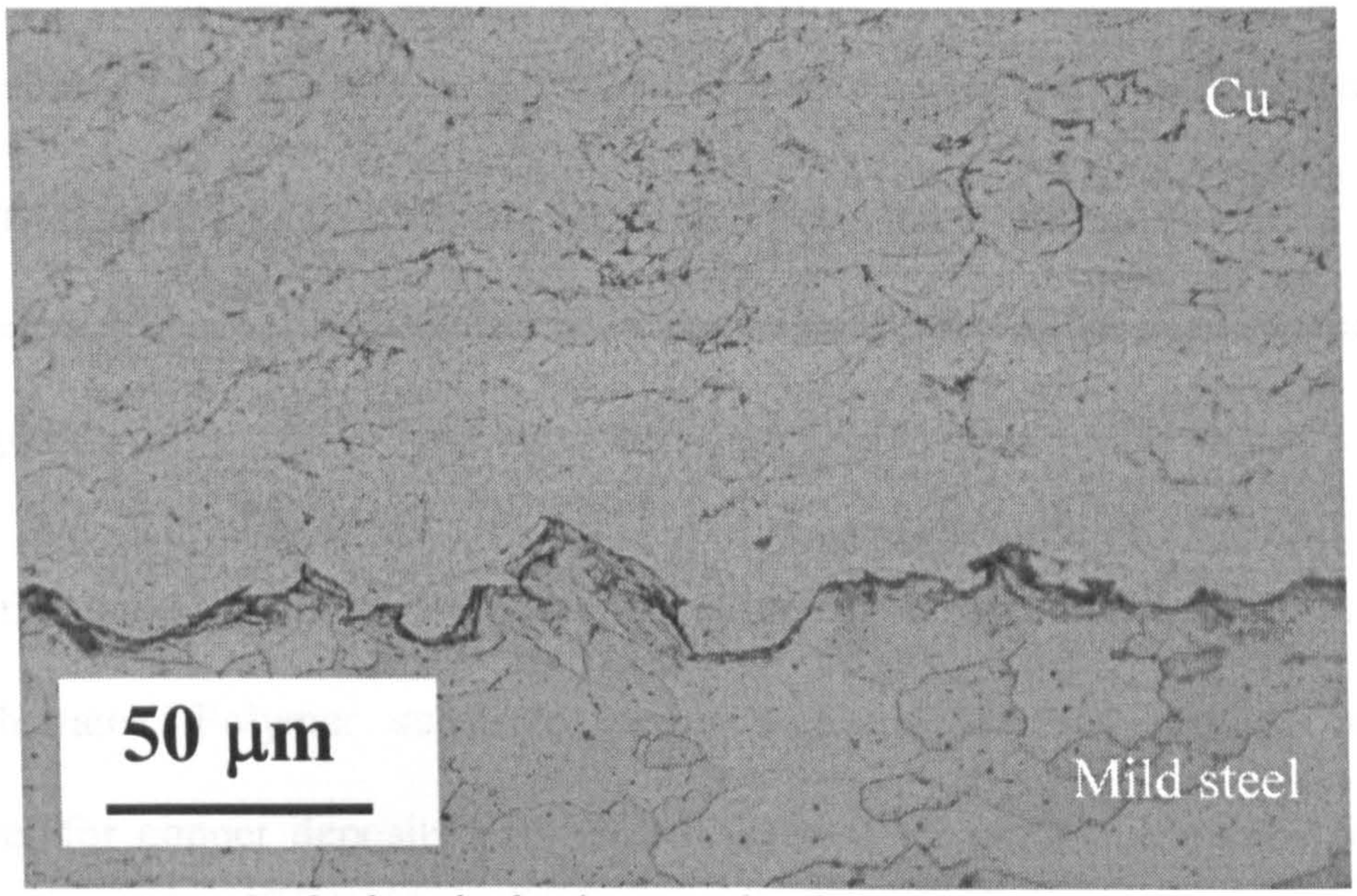

Fig. 4.13: Etched optical micrograph of copper deposited on rolled mild steel substrate, showing copper well bonded to mild steel. Deposition carried out at Yazaki using gas at 673 K and conditions described in **Table 4.3(b)**.

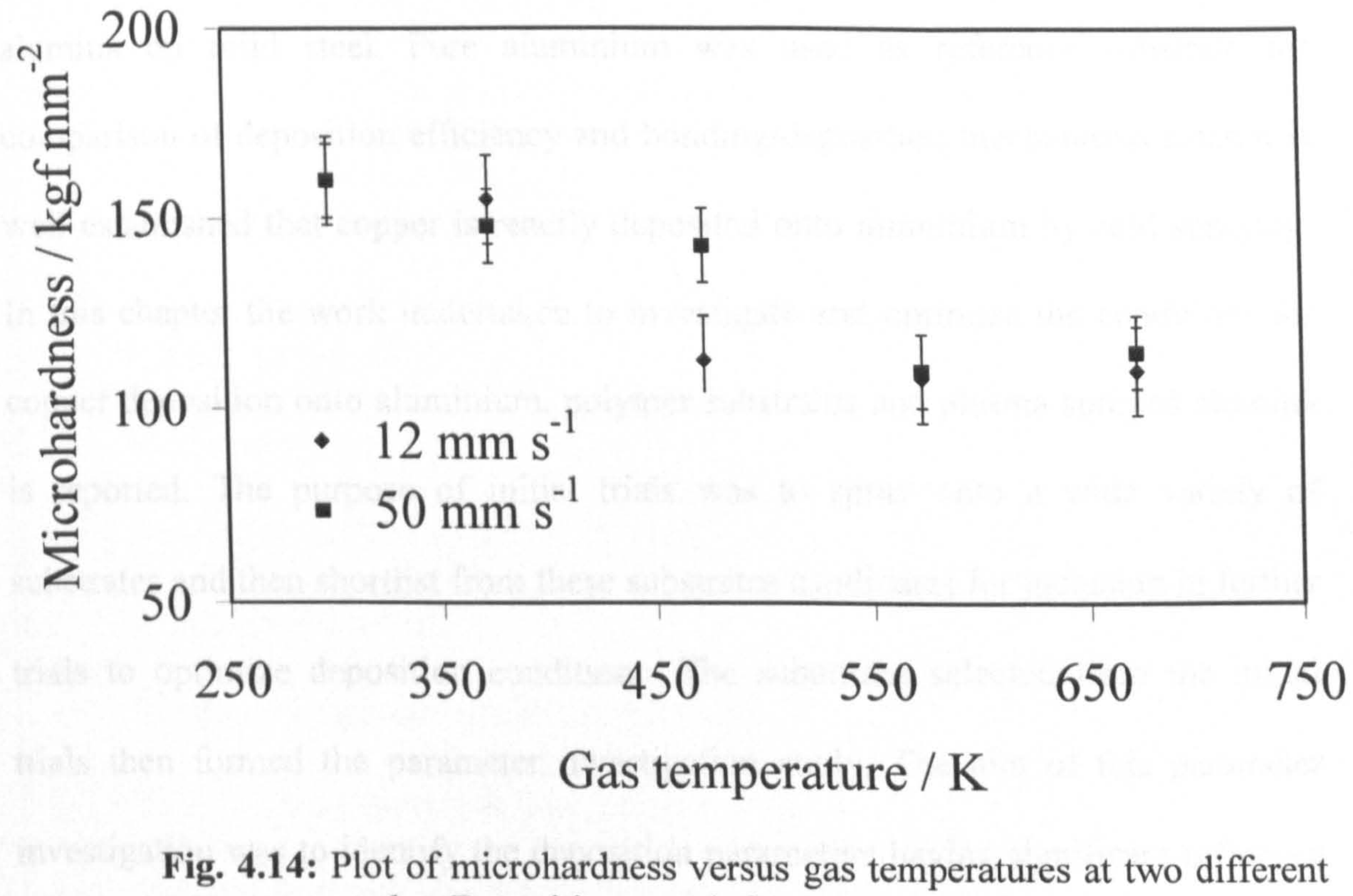

Fig. 4.14: Plot of microhardness versus gas temperatures at two different traverse speeds. Deposition carried out at Yazaki using conditions described in **Table 4.3 (b)**.

Chapter 5

Deposition of conducting tracks on insulating substrates

5.1 Introduction

The aim of this study is to investigate deposition of conducting tracks onto insulating substrates. Polymer substrates were included as they provide an insulating layer for copper deposits and help in the overall process economy by avoiding the plasma spraying of alumina as an insulator onto metallic substrates. Hence, a range of polymer substrates were selected along with plasma sprayed alumina on mild steel. Pure aluminium was used as reference substrate for comparison of deposition efficiency and bonding/deposition mechanisms since it is well established that copper is readily deposited onto aluminium by cold spraying. In this chapter the work undertaken to investigate and optimize the conditions for copper deposition onto aluminium, polymer substrates and plasma sprayed alumina is reported. The purpose of initial trials was to spray onto a wide variety of substrates and then shortlist from these substrates candidates for inclusion in further trials to optimize deposition conditions. The substrates selected from the initial trials then formed the parameter investigation study. The aim of this parameter investigation was to identify the deposition parameters having significant influence on the deposition process and optimize the

parameters for depositing copper on to the selected substrates. This also involved trials using tin as an interlayer between the substrate and copper deposit.

The deposits were qualitatively assessed for adhesion and deposition efficiency (DE). Adhesion testing was carried out as per the procedure described in Chapter 3 (section 3.3.3).

Cross-sections and plan view of the deposits were examined using optical microscopy and SEM to provide understanding of the interaction between the substrate and the sprayed particles. Microhardness testing of deposits was also undertaken. The procedures for optical microscopy, SEM and micro-hardness testing are described in chapter 3 (sections 3.2.3, 3.2.4 and 3.3.1 respectively).

This chapter is organized as follows:

5.2 Initial experiments

This section describes the initial trials to deposit copper on polymer, metallic and ceramic coated substrates. The procedure for spraying copper is described and the substrates are assessed qualitatively for suitability.

5.2.1 Spray deposition for initial experiments

The initial trials focused on identifying substrates for more detailed experiments to investigate influence of spray conditions on deposition. The polymer substrates used were: PA6T, PBT, PP, PE, PPS and Noryl. **Table 3.2** lists the relevant properties of the various substrates used. In addition to the polymer substrates aluminium and alumina coated mild steel substrates were included. The trials consisted of depositing single copper tracks on the substrates laid out on an XY table. The arrangement of the substrates is shown in **Fig. 5.1**. The substrates were each 50 mm x 25 mm x 3 mm in size. Deposition was carried out across the 25 mm width of the substrates. The substrates were traversed relative to the nozzle and deposition on all the substrates was accomplished in the same run. The surface roughness and

microhardness of the aluminium and alumina substrates is given in **Table 3.1.** The surface preparation for the substrates is described in chapter 3, section 3.7.2. The cold spray conditions used to deposit copper in initial trials are shown in **Table 5.1**.

5.2.2 Results of initial experiments

Table 5.2 shows the thickness of single pass copper deposits on various substrates and qualitative assessment of adhesion. Adhering copper tracks were deposited on aluminium. Copper tracks de-bonded from the alumina-coated mild steel. Copper deposits on PA6T and PBT were well adhered, whereas on NORYL substrate the deposits de-bonded. The deposits formed on PPS were weakly adhering. Erosion of the PE and PP substrates was observed due to impact of the copper particles. The PE substrate was eroded to a greater extent and copper deposits could not be formed on PE. PP did not erode to the same extent and weakly adhering copper deposits were formed on PP.

Fig. 5.2 (a-g) shows macro photographs of typical deposits on PA6T, PBT, PP, PPS, Noryl, PE and alumina coated mild steel. Well-adhered tracks are seen on PA6T and PBT (**Fig. 5.2 (a-b)**). On PP, despite erosion of substrate, 70 μm thick copper deposits could be formed and on PPS the deposits, although formed have very low adhesion (**Fig. 5.2 (c-d)**). The deposits on NORYL de-bonded from the substrate (**Fig. 5.2 (e)**). On PE no copper deposits could be formed due to erosion of

the substrate during deposition (**Fig. 5.2 (f)**). **Fig. 5.2 (g)** shows copper deposits de-bonded from the alumina coated mild steel substrate.

Substrates identified from these initial trials for more detailed study were, PA6T, PA66, PP, PBT, alumina coated mild steel and aluminium. PA6T and PBT exhibited a good adhesion rating in the initial trials. Copper could be deposited on PA6T and PBT; hence they were included in future trials. PP was included in further trials to ascertain if copper could be deposited on PP under different set of deposition parameters. Substrates excluded from further trials were PE, PPS and NORYL as copper deposits did not adhere well to them, or substrates were eroded while spraying.

5.2.3 Polymer substrate suitability to deposit copper

The properties of various polymers included in these trials are shown in **Table 3.2**. It is seen that the glass transition temperature (T_g) is a key fundamental property of polymer to be considered for a polymer to be suitable for depositing copper. The glass transition temperature (T_g) is the temperature at which the noncrystalline portions of the polymer change from a glassy state (at low temperature) to rubbery state (at higher temperatures). It represents the temperature above which the polymer stiffness decreases significantly.

It is seen that copper was deposited only on substrates which had a $T_g > \sim 323$ K; for lower T_g erosion of the substrates occurred. Copper deposits were formed on polymers having ultimate tensile strength of at least 50 MPa. Thus, wear is seen in polymers like PP and PE which have low T_g and tensile strength and Copper is deposited on polymers like PA6T and PBT whose T_g and tensile strength is higher than 323 K and 50 MPa respectively. The presence of nylon in PA6T which has an elongation of 83 % prevents the erosion of PA6T substrate during the deposition process. Copper deposits de-bonded from PPS although it had high T_g (358 K) and tensile strength (138 MPa); the reason for this seems to be its low elongation to break (4 %). In the case of Noryl, a combination of low tensile strength and low melting point seems to result in poor adhesion of copper deposits.

5.3 Spray parameter study

Five substrates namely PA6T, PBT, PP, alumina coated mild steel and aluminium were identified from the initial experiments for detailed parameter investigation. The spray deposition experiments were conducted at both University of Nottingham and Yazaki, and results of qualitative assessment of deposits are described in this section. At Nottingham all trials were conducted using helium at 298 K whereas at Yazaki, heating of the helium driving gas was investigated. Samples for adhesion testing were sprayed at Yazaki. The surface preparation of the substrates is described in chapter 3, section 3.7.2.

5.3.1 Deposition trials at University of Nottingham

The parameters used for trials at Nottingham are shown in **Table 5.3 (a) & (b)**. 25 mm wide and 100 mm long substrates were lined up on the XY table and deposition was carried out in the same run

The carrier gas flow was set in the carrier gas flow meter at ~ 0.01 $m^3 s^{-1}$ (600 litres per minute) for all the runs. The actual carrier gas flow rate depended upon the gas pressure. **Table 5.3 (b)** shows the actual carrier gas mass flow rate for different process gas pressures for a flow meter reading of 600 litres per minute in the carrier gas line.

5.3.2 Results of deposition trials at Nottingham

Figs. 5.3 (a-f) show macro photographs of typical deposits on PA6T and aluminium, using different process gas pressures. The deposits are seen to be well adhered to the substrate. The width of the deposits is ~ 5.0 mm, which is similar to the width seen in the deposit profiles in chapter 4, **Fig. 4.8**.

The deposits were qualitatively assessed by measuring the thickness of deposits and visual inspection of the adhesion between substrate and deposits. **Tables 5.4-5.8** show the results of the trials. The increase in deposit thickness, on aluminium, with

the number of passes and increasing powder feed rate is approximately linear. Such an observation cannot be made for other substrates as the deposits de-bonded for various spray conditions. However, even on aluminium, some deviation from linear increase in thickness, particularly when copper is deposited in single passes is seen. Fluctuation in the powder feed rate as well as differences in deposition efficiency during spraying, may be responsible for the deviation from linear behaviour observed.

There appears to be a thickness threshold, which is different for each substrate, after which the deposits start to de-bond. This threshold of thickness depends upon the spraying conditions used. **Table 5.4** shows that copper can be deposited on aluminium for almost all the spray conditions employed. Some de-bonding is seen in deposits formed at powder feed rate of 1.0 g s^{-1}, using pressures of 18 bar and 22 bar. However, copper deposits up to ~ 0.8 mm thick could be deposited on aluminium without de-bonding. **Tables 5.5** & **5.6** show that copper could be deposited on PA6T and PBT for a wide range of parameters. Using higher stagnation pressures seems to decrease the tendency of copper to de-bond from PA6T and PBT. 0.5 mm thick tracks were deposited on PA6T and 0.31 mm thick tracks were deposited on PBT without de-bonding. For deposition of copper on PA6T using gas at room temperature, gas pressure of 26 bar and powder feed rate of ~ 0.75 g s^{-1} seems to be the most suitable. For deposition on PBT gas pressure of 22 bar and powder feed rate of 0.5 g s^{-1} seems to be most suitable.

It is seen that for deposition at 11 bar pressure, the thickness of deposits is much less than for deposition at higher pressures. For copper on aluminium (**Table 5.4**) at 11 bar pressure, the maximum thickness was 0.33 mm deposited in 4 passes at powder feed rate of 1 g s^{-1}, but when pressure was increased to 15 bar, while maintaining a powder feed rate of 1 g s^{-1} and using 4 passes, the deposit thickness increased to 0.81 mm. The lower thickness of deposits formed while spraying at 11 bar gas pressure, as compared to spraying at higher pressures indicates a lower DE for deposition at 11 bar. Such a trend is not seen for PA6T (**Table 5.5**), where the thickness of deposits formed using gas pressures of 11 bar - 26 bar is largely similar while using the same powder feed rate and number of passes. At 29 bar pressure there seems to be a slight decrease in the deposit thickness on PA6T.

Thin deposits were formed on alumina coated mild steel and the deposits were found to de-bond when the thickness was increased above 0.17 mm in most cases (**Table 5.7**). Increasing the gas pressure had a detrimental effect on adhesion of copper on alumina coated mild steel as at higher pressures deposits de-bonded. Low powder feed rates (~ 0.25 g s^{-1}) and a single pass at lower gas pressures seemed to favour deposition on alumina coated mild steel. Deposits on PP were only weakly adhering; those thicker than 0.2 mm de-bonded from the substrate (**Table 5.8**).

5.3.3 Deposition trials at Yazaki

The parameters used for heated gas deposition at Yazaki are shown in **Table 5.10 (a)**. During the spray trials at Yazaki the layout of the substrates was similar to that at Nottingham (**Fig. 5.1**). A set of tracks were also deposited using room temperature He to compare with those produced at Nottingham. The major differences between spraying at Nottingham and Yazaki are outlined below.

1 Only a single pass was employed but the traverse speed was varied between 0.012 m s^{-1} to 0.4 m s^{-1}.

2 The gas mass flow rate was fixed at 2.9 x 10^{-3} kg s^{-1}; this corresponded to a gas pressure of 22 bar for a stagnation temperature of 298 K. The measured gas pressure at various gas temperatures for gas mass flow of 2.9 x 10^{-3} kg s^{-1} is given in **Table 5.10 (b)** The measured gas mass flow and pressure at 298 K is given in **Table 5.10 (c)**.

The samples for adhesion testing were prepared at Yazaki by spraying overlapping tracks off-set from each other by 1 mm using parameters described in **Table 5.11**. The parameters were adjusted to obtain a deposit thickness of ~ 0.5 mm. For example, at higher powder feed rates, higher traverse speed was used and number of passes were adjusted between 2-3 passes to obtain deposit thickness of ~ 0.5 mm. A mild steel plate with 15 mm diameter holes was used as a mask on a substrate to obtain circular deposits. The adhesion testing was carried out as per the procedure described in chapter 3, section 3.3.3.

5.3.4 Results of deposition trials at Yazaki

Tables 5.12 – 5.15 show the deposit thickness and qualitative assessment of adhesion. A comparison of the deposit thickness data in **Tables 5.12 – 5.15** with the data for Nottingham trials in **Tables 5.4 – 5.8** shows that the thickness of the deposits formed at Yazaki (using gas at 298 K), is higher than those formed at Nottingham. Thus, the process deposition efficiency (DE) is higher for the Yazaki system as compared to the Nottingham system. This is probably due to the differences in the Yazaki and Nottingham system outlined in chapter 4, and may be related to the higher expansion ratio of the Yazaki nozzle.

The threshold of deposit thickness before spontaneous de-bonding takes place seems to be similar for the two systems. When using gas at 298 K the threshold of deposit thickness is seen to be ~ 0.7 mm for aluminium and ~ 0.4 mm for PA6T **(Tables 5.4 – 5.5 & 5.12 – 5.13)**.

Copper deposited on aluminium using heated gas had very good adhesion and did not show de-bonding anywhere on the track for all the spray conditions employed **(Table 5.12)**. The maximum thickness of single pass deposits, without any de-bonding was ~ 1.35 mm on aluminium. However, increasing the gas temperature did not result in an increase in the deposit thickness when other parameters were unchanged. For example, deposition of copper on aluminium using traverse speed of 0.025 m s^{-1}, powder feed rate of 0.32 g s^{-1} and gas temperatures between 298 K – 523 K gave deposit thickness of ~ 0.6 mm **(Table 5.12)**. Using heated gas for

deposition on polymer substrates resulted in erosion of substrates above a temperature of 348 K for PA6T and above 298 K for PBT (**Table 5.13 – 5.14**). On PA6T, the threshold of deposit thickness for de-bonding was ~ 0.38 mm when the gas was at 298 K and this threshold increased to ~ 0.49 mm when the gas was heated to 323 K. CGDS trials with heated gas resulted in increased tendency for the deposits to de-bond from alumina coated mild steel substrates (**Table 5.15**). PP substrate eroded while spraying copper using gas at 298 K as well as when using heated gas; heated gas increased the erosion rate.

5.3.5 Deposition trials on PA66

In view of the relative success in depositing copper on glass filled nylon (PA6T) a limited study on deposition on unfilled nylon (PA66) was conducted. The aim was to provide a baseline for evaluation of the influence of the reinforcing glass fibres.

Copper deposition using conditions described in **Table 5.17**, was carried out on nylon 6/6 (PA66) substrates. The macro photographs of copper deposited on PA66 are shown in **Fig. 5.4**. Thickness of copper deposits and qualitative assessment of adhesion is reported in **Table 5.18**. Tracks deposited using process gas at 298 K and pressure between 11 bar and 22 bar are seen to be well adhered to PA66 substrate; increasing the pressure to 26 bar and above results in erosion of the substrate. copper could not be deposited on PA66 using process gas heated to 340 K; heating

the process gas resulted in erosion of substrates for process gas pressures as low as 11 bar, and at higher pressures the erosion of PA66 resulted in no measurable copper deposits being produced.

5.4 Deposition efficiency of copper on aluminium and polymer substrates

In this section, the deposition efficiency (DE) of copper on aluminium and PA6T substrates is reported.

The DE was calculated using the measured powder feed rates. For the measurement of DE, substrates were weighed before and after depositing the coating. The time duration for spraying was noted using a stopwatch. The DE was calculated using the formula;

$$DE\% = 100\frac{(W_2 - W_1)}{P_f t} \quad \text{---------- Equation 5.1}$$

Where, W_2 is the mass of substrate after spraying, W_1 is the mass of substrate before spraying, P_f is the measured powder feed rate in and t is time of spraying.

5.4.1 Deposition efficiency of copper on aluminium

The DE of copper on aluminium versus stagnation pressure is shown in **Fig. 5.5,** and, versus powder feed rates is shown in **Fig. 5.6**. The measurements of DE show that for the spray conditions used in these experiments, it was always above 75 % (**Figs. 5.5 & 5.6**). **Fig. 5.5** shows that the lowest value of ~ 78 % is observed when stagnation pressure of ~ 15 bar was used. The DE for stagnation pressure ≥ 22 bar was 90 ± 1 %. Thus higher DE was obtained for higher stagnation pressures. **Fig. 5.6** shows that DE was 90 ± 1 % for powder feed rate up to 0.75 g s^{-1} but it is seen to drop to ~ 85 % as the powder feed rate was increased further to 1.25 g s^{-1}. The powder feed rate of 0.75 g s^{-1} is equivalent to 21 wt % of the gas mass flow, while a powder feed rate of 1.25 g s^{-1} is equivalent to 36 wt % of the gas mass flow.

5.4.2 Deposition efficiency for copper on PA6T

The DE of copper on PA6T is shown in **Fig. 5.7**. The DE is reported for a gas mass flow of 2.9 x 10^{-3} kg s^{-1} and for gas at 298 K and 333 K. The gas mass flow of 2.9 x 10^{-3} kg s^{-1} at 298 K corresponds to a pressure of 22 bar and at 333 K corresponds to a pressure of 25 bar. It is seen that heating the gas to 333 K increased the DE from ~ 80 % to ~ 95 %. It is also seen that increasing the powder feed rate from 0.5 g s^{-1} to 0.75 g s^{-1} decreased the DE marginally from ~ 95 % to ~ 93 %. It should be noted that DE of ~ 95 % was observed for deposition on PA6T whereas from **Fig. 5.6** it is seen that for deposition on aluminium, DE ~ 90 % was observed. However it is also seen from **Tables 5.4 & 5.5** that the threshold for de-bonding is lower on PA6T.

Thus, DE on PA6T is better than aluminium but deposits de-bond at lower thickness.

5.5 Adhesion test results

Fig. 5.8 shows the adhesion of copper on aluminium for different gas pressures between 11 bar and 29 bar, and temperature of 298 K and 523 K. The powder feed rate to deposit these coatings was ~ 0.5 g s^{-1}. **Fig. 5.8** shows that increasing gas pressure from 11 bar to 29 bar while using gas at 298 K increased the adhesion from 6.8 MPa to 16 MPa. The adhesion test carried out on copper deposits produced by heating the gas to 523 K did not result in failure between copper and aluminium, instead failure within the epoxy used in the tests was observed at ~ 20 MPa. Thus, it can be concluded that the adhesion of copper deposited using heated gas is above 20 MPa.

The measured values of adhesion for depositing copper on PA6T using gas mass flow of 2.9 x 10^{-3} kg s^{-1} different gas temperatures and powder feed rates are plotted in **Fig. 5.9**. Increasing the gas temperature above 298 K improves the adhesion of the deposits up to gas temperatures of 348 K. The highest adhesion of 2.75 MPa is seen for deposition using 348 K and powder feed rates of 0.25 and 0.37 g s^{-1}. Increasing the gas temperature to 373 K decreases the adhesion to 1.75 MPa. Increasing the powder feed rate up to 0.75 g s^{-1} did not have a significant effect on

the adhesion of copper on PA6T. It must be noted that depositing single tracks using gas heated above 348 K resulted in de-bonding of the copper tracks on PA6T (section 5.3.4). The deposits for pull-off tests were formed by depositing successive tracks off-set to each other. This seemed to improve adhesion as adhering deposits were formed for gas heated to 373 K. The lower residual stresses associated with deposits formed by successive tracks off-set to each other may have been responsible for this.

5.6 Summary of results in section 5.2 to 5.5

The results of the initial trials and the parameter study are summarized below;

1. Thicker deposits were formed using the Yazaki cold spray rig as compared to the University of Nottingham rig while using the same cold spray conditions. This indicates higher DE for Yazaki rig. It is probably related to the higher expansion ratio of the Yazaki cold spray nozzle.
2. Copper deposits adhered well to aluminium and polymers PA6T and PBT **(Table 5.2)**.
3. The impact of copper particles erodes PE and PP, whereas weakly adhering deposits are formed on PPS. Copper deposits on Noryl and alumina coated mild steel de-bonded from the substrate **(Table 5.2** and **Fig. 5.2)**.

4. High deposition efficiency (~ 90 %) can be achieved for deposition of copper. Powder loading of the gas stream, ≥ 36 wt % of total gas flow, reduces the DE from ~ 90 % to ~ 85 %. Heating the process gas to 333 K increased the DE for copper deposition on PA6T from ~ 80 % to ~ 95 % **(Fig. 5.7)**.

5. Adhesion strength of copper deposits on aluminium increases as the process gas pressure is increased **(Fig. 5.8)**. Copper deposits formed using process gas pressure of 11 bar have adhesion of ~ 7 MPa but increasing the process gas pressure to 29 bar increases the adhesion strength to ~ 15 MPa.

6. Heating the process gas improves the adhesion of copper deposits on aluminium; when the process gas is heated to 523 K, the adhesion strength is above 20 MPa **(Fig. 5.8)**.

7. Copper deposited on PA6T, using process gas at room temperature has adhesion strength of < 2 MPa. Heating the process gas to 345 K increases the adhesion strength on PA6T to ~ 2.8 MPa **(Fig. 5.9)**. Heating the process gas above 373 K results in erosion of PA6T substrate.

5.7 Tin bond coat for depositing copper tracks on polymers

In an effort to widen the range of polymers onto which copper could be deposited and to improve the adhesion, investigations were performed using cold sprayed tin as a bond coat for the copper. The selection of tin was based on the observations

that copper tends to erode polymers during cold spraying. Thus a material with lower yield strength is more likely to adhere and also form a layer onto which copper could bond. The yield strength of tin is 9 MPa compared with 48 MPa (0.2 % proof stress) for annealed oxygen free copper. There is also the requirement that the two materials should not react chemically during deposition and this criterion is met by tin and copper combination. The results of these trials are reported in the following sections 5.7.1 and 5.7.2.

5.7.1 Deposition of tin and Sn + Cu tracks

The characterization of the tin powder used to deposit tin tracks on polymers is described in chapter 3, section 3.7.1. The conditions used to deposit tin on polymer substrates are shown in **Table 5.19**; copper was deposited using the spray conditions described in **Table 5.1**. The results of deposition of tin are shown in **Table 5.20**. Well adhering tin deposits were formed on all the polymer substrates including Noryl, PP, PE and PPS which previously were eroded by spraying of copper powder. Subsequently, copper could also be deposited on the tin layer. A thickness of ~ 80 - 100 μm of tin was required for forming successful bond coat. Lower thickness (< 50 μm) of tin resulted in either erosion of the substrate + tin or de-bonding of the tracks following copper deposition. Macro photographs of Sn + Cu deposits on PA6T and PA66 substrates are shown in **Fig. 5.10**. Well-adhered Sn + Cu deposits are seen. The top copper layer is clearly visible; there is no sign of

any apparent de-bonding of either the tin or the copper layer. The thickness of copper deposits formed on tin coated PA6T and PA66 is lower than the thickness of copper deposits formed without any tin bond coat (**Tables 5.5 and 5.18**). This indicates lower DE for depositing copper on tin coated PA66 and PA6T. A macro photograph of Sn + Cu deposit on PP (using a powder feed rate of 0.5 g s^{-1} instead of 0.25 g s^{-1}), is shown in **Fig. 5.11**. Copper was deposited using six sets of overlapping passes to a total thickness of ~ 600 μm. The Sn + Cu deposits are well adhered to PP. A sample was cut from one edge for cross-section observation. The microstructures of deposits on tin coated substrates are described in section 5.9.2.

5.7.2 Adhesion test results (Sn + Cu)

The adhesion of copper deposits sprayed using four different powder feed rates between 0.37 g s^{-1} to 0.75 g s^{-1} and gas at 298 K, on tin coated PA6T substrates, is reported in **Fig. 5.12**. The failure during adhesion testing occurred between the tin deposit and the substrate and gave a value of ~ 6 MPa. This is more than twice the adhesion strength of copper deposits on PA6T without a tin bond coat (**Fig. 5.9**). Thus, using a tin bond coat improved the overall adhesion of the deposits. Heating the process gas above 298 K for depositing copper resulted in erosion of tin layer.

The adhesion of copper and Sn + Cu on PA66, deposited at different process gas pressures, is shown in **Fig. 5.13**. Without any tin bond coat, copper had adhesion

below 1 MPa. Copper deposited using process gas pressure of 11 bar and 29 bar debonded from the substrate during pull-off tests with dial showing a zero reading, indicating poor adhesion strength. The adhesion of tin + Cu deposits is ≤ 2 MPa. This is lower than the adhesion of copper and Sn + Cu on PA6T (**Figs 5.9 & 5.12**). The use of a tin bond coat improves the adhesion of Sn + Cu deposits on PA6T as well as PA66 substrates.

5.7.3 Summary of sections 5.7.1 and 5.7.2

1 Copper could be deposited directly on aluminium, PA66, PA6T and PBT. Copper could be deposited on PA66, PA6T, PBT, PP, PE, PPS and NORYL substrates when a bond coat of tin was used.

2 Well adhered tin deposits can be formed on all types of polymer substrates and subsequently copper could be deposited on the tin layer.

3 A minimum thickness of ~ 80 μm of tin was required for it to work as bond coat. Lower thickness of tin resulted in erosion of the tin layer during copper deposition.

4 Using a tin bond coat increases the overall adhesion of tracks on PA6T to ~ 6 MPa; more than twice the adhesion of copper deposited directly on PA6T.

5 Thicker deposits are formed when copper is deposited directly on PA66 and PA6T as compared to when a tin bond coat is used.

6 Copper deposited using gas heated above 298 K resulted in erosion of the tin bond coat.

5.8 Fundamental studies on deposition mechanisms

In this section the results of SEM observation of the impact of tin and copper particles on aluminium and nylon (PA66) and glass filled nylon (PA6T) substrates taken from the centre of the spray pattern are described. The impact of copper particles was studied at two different gas stagnation (process gas) pressures, 11 bar and 29 bar, at a single gas temperature of 298 K. The impact of tin particles was studied at a pressure of 11 bar and 298 K. The deposits were formed by traversing the nozzle over the substrates at 0.5 m s^{-1} using a powder feed rate of 0.25 g s^{-1} for copper and 0.12 g s^{-1} for tin.

5.8.1 Impact of copper particles on aluminium substrate

The impact on aluminium at 11 bar is shown in **Figs. 5.14** and **5.15**. Craters are formed in aluminium due to impact of copper particles. Copper particles are largely spherical although some flattened disks are also seen. The flattened disks have a diameter of ~ 25 μm **(Fig 5.15)**. The spherical particles also have a diameter of around 25 μm. Thus, it is likely that the larger particles (~ϕ 25 μm) upon impact do

not deform significantly while finer particles are deformed and form disk like structures.

The impact on aluminium at 29 bar pressure is shown in **Figs. 5.16** and **5.17**. The density of copper particles in this image is higher then the density of copper particles in **Fig. 5.14** from the 11 bar deposit. Very few craters are seen in **Fig. 5.16** suggesting that more particles adhere during spraying at 29 bar than at 11 bar. Some spherical particles were also seen for impact at 29 bar pressure. The spherical particles seen were usually above 30 μm in diameter. Copper seems to be deeply embedded in aluminium and at least one instance of the metal jetting phenomenon is seen in **Fig. 5.17** (shown by arrow).

5.8.2 Impact of copper particles on nylon (PA66 and PA6T)

The impact of copper particles on PA66 substrate at 11 bar pressure is shown in **Figs. 5.18** and **5.19**. Angular craters are formed in PA66 due to impact of copper particles, which is related to the erosion of the substrate. These craters are distinctly different from the more regular ones, circular in appearance seen in aluminium. **Fig. 5.18** shows copper particles, usually < 10 μm in diameter deeply embedded in PA66 (shown by arrows). Larger particles seem to be loosely adhering to PA66.

The impact of copper on PA66 at 29 bar gas pressure is shown in **Figs. 5.20** and **5.21**. Metal jetting is seen in **Fig. 5.20** during impact of copper onto previously

embedded copper particles. During spraying at 11 bar finer copper particles are embedded in PA66 and while spraying at 29 bar coarser copper particles are embedded in PA66 (**Figs. 5.18 & 5.20**). Impacts at 29 bar pressure also result in increased deformation of the copper particles and erosion of PA66; this is shown in **Fig. 5.21** where a crater is seen along with a deformed copper particle. A comparison of this crater with that shown in **Fig. 5.19** (for impact at 11 bar pressure) reveals that the extent of fracture of the substrate in impact at 29 bar pressure is much higher than at 11 bar.

The impact of copper on PA6T at 11 bar pressure is shown in **Figs. 5.22** and **5.23**. The impact at 11 bar pressure exposes the glass fibres in PA6T by erosion of the nylon matrix. The glass fibres seem to be largely undamaged. The copper particles embedded in PA6T are around 10 μm or smaller. The copper particles are not significantly deformed.

The impact of copper on PA6T at 29 bar pressure is shown in **Figs. 5.24** and **5.25**. The glass fibres are fractured and PA6T is eroded. In **Fig. 5.25** the copper particles are seen to be deeply embedded in PA6T and at some places metal jetting is seen at the site of copper-copper impacts. A notable feature of impacts on PA66 and PA6T is the presence of deformed and un-deformed particles. The un-deformed particles are embedded in the polymer. The deformation of the copper particles is largely seen to be due to the impact of copper particles over previously embedded copper particles.

5.8.3 Impact of tin particles on nylon (PA66 and PA6T)

Figs. 5.26 and **5.27** show the plan view of tin deposits on PA66. The impact of tin does not result in any significant erosion of PA66 (**Fig. 5.26**) unlike the effect of impact of copper particles. The tin particles are embedded in PA66 and they appear to be highly deformed (**Fig. 5.27**). PA66 is also plastically deformed in the region surrounding the embedded tin particle. The fine particles of tin are probably formed during impact (no particles of this size were in the feedstock) and could be associated with the metal jetting phenomenon in tin during impact.

The plan view of tin deposits on PA6T is shown in **Figs. 5.28** and **5.29**. **Fig. 5.28** shows tin particles embedded in PA6T. PA6T is plastically deformed in places where tin is embedded. This is different from fracture of the PA6T substrate due to impact of copper particles (**Figs. 5.23 & 5.24**). **Fig. 5.29** shows a high density of tin particles most of which are well deformed. Fine particles of tin are again clearly visible in the plan views.

5.8.4 Impact of copper particles on tin coated nylon (PA66 and PA6T)

The plan view of copper deposits on PA66 + Sn, sprayed at 11 bar pressure is shown in **Figs. 5.30** and **5.31**. In **Fig. 5.30**, the copper particles are not deformed to

any appreciable extent and they are deeply embedded in tin. The tin particle seen in **Fig. 5.31** has a highly deformed structure and fine tin particles are seen scattered around the tin particle. The plan view of copper deposits on PA66 + Sn sprayed at 29 bar pressure is shown in **Fig. 5.32**. **Fig. 5.32** shows considerable flattening of the copper particles. Metal jetting of copper is seen in some places in **Fig. 5.32**.

The plan view of copper deposits on PA6T + Sn sprayed at 11 bar pressure is shown in **Fig. 5.33** and for spraying at 29 bar pressure is shown in **Fig. 5.34**. The copper particle is seen embedded in tin in **Fig. 5.33**. Metal jetting is seen in tin due to impact of copper particle in **Fig. 5.33**. Droplets of tin are seen and thin sheets of tin are formed due to deformation of tin by impact of copper particles. CGDS of copper at 29 bar resulted in deformation of the copper particles and metal jetting in copper **(Fig. 5.34)**. Copper deposited using 29 bar process gas pressure on tin coated PA66 and PA6T substrates covered the tin layer almost completely and it was not possible to observe tin in these samples.

5.9 Studies on the interface and deposit microstructures

It was seen in the preceding section that there is significant deformation of the substrate and sprayed particle during CGDS. This section reports the investigation of the deposit – substrate interface. The coating microstructures were studied to qualitatively analyze the deposits for porosity and adhesion. Microhardness of

deposits was measured to investigate work hardening in the deposits and co-relate them to the CGDS conditions used.

5.9.1 Microstructures of copper deposited on aluminium

Fig. 5.35 shows cross-sectional images of the copper coating on the aluminium substrate following deposition using gas at 298 K, powder feed rate of 0.5 g s^{-1}, traverse speed of 0.05 m s^{-1} and three pressures ranging from 11 bar to 29 bar. The substrates were originally in the as rolled condition, H_v = 40 kgf mm^{-2} with a roughness of 0.34 ± 0.05 μm. The undulations observed in the interface between the substrate and coating result from the impacts of the copper particles during spraying. It is noticeable that the degree of disruption of the original interface has increased significantly on increase of the pressure from 11 bar to 29 bar. The coatings shown in **Fig. 5.35** appear to have good bonding to the aluminium substrate. **Fig. 5.36** shows a copper coating naturally de-bonded from its aluminium substrate. It is notable that some copper remains bonded to the substrate whilst some aluminium has also fractured from the substrate and remains well bonded to the detached copper coating. The fracture in the aluminium substrate could result from a loss in ductility in this layer due to the high levels of cold work associated with impact of the copper particles. Whilst a variation in the morphology of the interface is evident as the gas pressure is increased, no change in the level of porosity in the coatings themselves was observed over the range of pressures

examined (**Fig. 5.35**). No porosity was observed using optical microscopy. **Fig. 5.37** shows the hardness of the coatings as a function of gas pressure where an increase in hardness is observed as the pressure was increased up to 22 bar; further increase produced no further increases in coating hardness.

5.9.2 Characterization of cold sprayed copper deposited using heated gas

Figs. 5.38 (a - c) show the etched microstructures of deposits using a pressure of 22 bar, powder feed rate of 0.5 g s^{-1}, traverse speed of 0.05 m s^{-1} and gas at 298 K, 473 K and 673 K respectively. When sprayed at 298 K, the original powder particle boundaries are delineated; significant deformation of the particles during spraying has occurred to produce a dense coherent coating. The coatings sprayed at elevated temperatures show fine scale structure within the particles themselves; which could well be sub-micron grains. The microhardness of the deposits shown in **Fig. 5.38 (a-c)** is shown in **Fig. 5.39**. The hardness of copper sprayed at 298 K is 166 kgf mm^{-2}, which reduces with gas heating and when gas is heated to 673 K the hardness is 110 kgf mm^{-2}. The fine sub-micron grains seen in **Fig. 5.38 (b)** coincide with the decrease in hardness of deposits seen in **Fig. 5.39**, for deposition at 473 K. The recrystallization of copper deposits and microstructural and mechanical properties of copper deposits after annealing at various temperatures are described in further detail in chapter 6.

5.9.3 Microstructures of copper deposited on PA66, PA6T and PP

Cross-section images from optical microscopy of copper deposits on PA66, PA6T and PP are shown in **Fig. 5.40**, **Fig. 5.41** and **Fig. 5.42** respectively. Copper was deposited using the conditions described in **Table 5.17** on PA66 and **Table 5.3** on PA6T and PP respectively. Deposition on PA66, PA6T and PP employed gas at 11 bar, 22 bar and 29 bar.

An impact-affected zone is seen at the substrate–deposit interface consisting of fractured surface of the substrate and embedded copper particles. PA66 suffers a much greater amount of fracture due to the impact of copper particles as compared to PA6T. The impact-affected zone in PA66 is larger due to the greater degree of fracture in PA66 as compared to PA6T. The impact-affected zone progressively increases with increasing gas pressure in both PA66 and PA6T (**Fig. 5.40 (a-c)** & **Fig. 5.41 (a-c)**). **Fig. 5.41** shows that the glass fibres in PA6T are surrounded by copper particles and the fracture of substrate is reduced where the copper particles encounter the glass fibres. It is also seen that the particles embedded in PA66 and PA6T are largely spherical, whereas the particles impacted upon previously embedded particles are flattened. The PP substrate is eroded due to impact of copper particles. This is demonstrated clearly in **Fig. 5.42 (c)**, where it is seen that a curvature is formed at the interface of PP – copper due to the erosion of PP by impact of copper particles at the centre of the track where particle flux was greatest.

5.9.4 Microstructures of copper deposited on tin coated PA66, PA6T and PP

Fig. 5.43 & **5.44** shows the Sn + Cu deposits on PA66 and PA6T respectively; copper was deposited using process gas at 298 K, powder feed rate of 0.5 g s^{-1} and CGDS conditions described in **Table 5.3** (PA6T) and **Table 5.17** (PA66). Process gas pressure of 11 bar, 22 bar and 29 bar was used. Tin was deposited using conditions described in **Table 5.19**. The tin bond coat and the copper layer on top of tin are adhered well to the PA66 and PA6T substrate. The gaps seen in the PA66/PA6T – copper interface (**Fig. 5.40** & **5.41**) are not seen in the deposits formed using tin bond coat. Thus, qualitatively the tin bond coat improves the adhesion of copper deposits on polymers. The measurements of pull – off tests reported in section 5.5 and 5.7.2 indicate that the adhesion of Sn + Cu deposits is higher by a factor of ~ 2 as compared to copper deposits, on PA66 and PA6T substrates (**Fig. 5.8, Fig. 5.12** & **Fig. 5.13**).

Fig. 5.45 shows the Sn + Cu deposit on PP substrate deposited using six passes of the spray gun over the substrate. The thickness of tin and copper is ~ 200 μm and 600 μm respectively. No gaps are seen at the interface of either PP – Sn or Sn – Cu. Hence, well adhering deposits of Sn + Cu are formed on PP.

5.10 Summary of results

1. Metal jetting is seen in plan views of copper deposits formed using gas at 29 bar. Fine particles of tin are seen in the plan view of tin deposits.
2. The thickness of copper deposited directly on PA66 and PA6T is approximately independent for deposition pressures of 11 bar to 29 bar, whereas on aluminium and tin coated polymer substrate the thickness of copper deposits is lower when gas pressure of 11 bar is used.
3. The interface in copper deposits on aluminium is heavily deformed. The deformation increases when higher gas pressures are used.
4. The impact-affected zone at the copper-PA66/PA6T interface is formed due to; a) embedding of copper particles and; b) due to fracture of PA66/PA6T. Tin and copper deposits on PA66 and PA6T substrate are formed due to the embedding of the tin and copper particles in the substrate.
5. Glass fibers in PA6T are surrounded by copper; the strengthening effect of glass fibers improves the adhesion of copper deposits. Thus, in PA6T a larger proportion of particles are embedded in the impact affected zone as compared to PA66.

5.11 Discussion

The suitability of the polymer substrates for depositing copper was discussed in section 5.2.3. In this section the results of parameter study, DE, adhesion, microstructure and microhardness are discussed.

5.11.1 Deposition of copper on aluminium, PA66 & PA6T and tin coated PA66 & PA6T

The thickness of copper deposits on tin coated PA66 and PA6T for single pass, is, ~ 60 μm when deposited using process gas pressure of 11 bar. The thickness increases to ~ 100 μm when deposited using process gas pressure of 22 and 29 bar (**Fig. 5.43** & **5.44**). This indicates lower deposition efficiency for deposition of copper tracks on tin coated substrate at 11 bar pressure. **Figs. 5.40** & **5.41** indicate that such a decrease in deposition efficiency is not observed for depositing copper directly on PA66 and PA6T. In section 5.3.2 it has been reported that when similar conditions of powder feed rate and No. of passes was used, the thickness of copper deposits on aluminium was lower for 11 bar process gas pressure as compared to 15 bar – 29 bar whereas, the thickness of copper deposits on PA6T was not influenced significantly by the process gas pressure (**Tables 5.4** and **5.5**). The lower deposition efficiency for depositing copper on metallic surfaces (aluminium or tin) while using 11 bar process gas pressure is probably related to the different mechanisms by which copper adheres to polymers and metals. This difference seems to be related to the difference in behavior of polymers and metals when subjected to deformation and cold work. The tendency of polymers to erode due to impact of copper particles was observed whereas in aluminium, particularly when 29 bar gas pressure was used; the craters formed due to impact are associated with metal jetting

phenomenon (**Table 5.2 & Fig. 5.17**). The sprayed copper particles have sufficient kinetic energy when sprayed using process gas pressures between 11 bar to 29 bar, to embed in PA66 and PA6T; however adhesion of copper particles on aluminium is related to metal jetting phenomenon which takes place only if the particles are traveling over the critical velocity. The above discussion for deposition on PA66, PA6T and aluminium substrate is related to single pass deposited at a relatively fast traverse speed of 0.1 m s^{-1}. If multiple passes are used to deposit the tracks or if slower traverse speeds are used it is possible that the track thickness and thus, the overall deposition efficiency may show behavior similar to that seen for deposition on metals (i.e. lower deposition efficiency at 11 bar process gas pressure). This is because after an initial layer of copper is formed the tracks build-up continues by further impacts on previously deposited copper and not on the polymer substrate.

5.11.2 Mechanism of copper deposition onto aluminium

It is generally accepted that metal jetting and related phenomenon promote a metallurgical bond at the deposit substrate interface in cold spraying [45]. If the velocity exceeds the critical velocity then metal jetting and bonding is expected to take place; however, if the impact velocity is below the critical velocity, then impacts of the particles will lead to craters being formed in the substrate. Deposition of copper at 11 bar pressure results in more craters being formed and the deposition efficiency remains low as compared to deposition at 29 bar gas pressure.

Plan view images of copper impacts at 29 bar gas pressure on aluminium show metal jetting (**Fig. 5.17**), whereas no metal jetting is seen for impacts at 11 bar gas pressure (**Fig. 5.14** and **5.15**). Impacts of copper on aluminium at 11 bar pressure result in embedding and flattening of smaller particles while larger particles ~ > ϕ 25 μm do not deform and maintain their spherical shape. Impacts of copper at 29 bar resulted in flattening of larger particles also. It is likely that deposition at 11 bar pressure resulted in acceleration of finer particles to above the critical velocity, but not the coarser particles. Thus, only the finer fraction of the powder was deposited, while the coarser size fraction rebounded after impact (leaving behind craters). Impact at 29 bar pressure resulted in deposition of the finer as well as the coarser size fraction of the powder due to the acceleration of all powder sizes to above the critical velocity. Hence, thicker deposits are formed at 29 bar as compared to 11 bar.

The metal jetting phenomenon at 29 bar gas pressure increases the adhesion of copper deposits on aluminium (~ 16 MPa) as compared to 11 bar gas pressure (~ 7 MPa), where metal jetting was not observed (**Fig. 5.8**). Heating the process gas results in higher particle velocity and raises the substrate temperature due to impingement of hot gas. Metal jetting raises the local temperature at impact to near the melting point of sprayed material [45]. A combination of high particle velocity and higher local temperature promote adhesion on metal substrates at higher gas temperatures. This is seen in the pull-off test results on aluminium; deposits formed using gas at 298 K had lower adhesion than those formed at 523 K (**Fig. 5.8**).

5.11.3 Mechanism of metal deposition on polymers

a) Copper

Erosion of polymer substrates was observed in the case of polymers that had low T_g and tensile strength. The impact of copper particles onto PA66 and PA6T does not result in metal jetting. The metal jetting seen in **Figs 5.17** and **5.25** is due to the impact of copper particle on the previously deposited copper particle. **Figs 5.40 & 5.41** shows that single particles of copper embedded in the polymer are largely spherical whereas copper particles that have suffered impacts of other copper particles are deformed. The impact of the relatively hard copper particles onto polymers will result in deformation in the polymer and thus a temperature rise in the near-surface regions by conversion of the kinetic energy of impact in to heat [2]. Weston *et al.* [71] measured the temperature rise in a polymer during impact of solid CO_2 pellets (10 mm diameter) at a velocity of 225 and 241 m s^{-1} on polypropylene. They observed that the temperature recorded by thermocouples embedded in the PP rose to 363 K immediately after impact. They proposed that the impacts where the temperature does not rise above T_g results in brittle erosion of PP and where the temperature rises over T_g plastic deformation of the polymer takes place. During impact of copper particles on PA66 and PA6T sufficient heat is generated to raise the temperature above T_g. Polymers loose their rigidity when heated to temperatures above T_g and impacts of copper particles in this situation results in erosion. The amount of erosion depends upon the strength of polymer;

thus, PA6T (tensile strength = 180 MPa) which is a glass reinforced polymer erodes much less than PA66 (tensile strength = 82 MPa) which does not have any glass reinforcement. Another phenomenon seen during impact of copper particles is the embedding of copper particles in PA66 and PA6T. Polymers like PA66, PA6T and PBT have sufficient strength to allow copper particles to embed. PA66, PA6T and PBT provide enough support to the powder particle embedded to allow subsequent impacts to build. This phenomenon is responsible for the formation of adhering deposits on PA66, PA6T and PBT. The impact-affected zone is formed in PA66 and PA6T due to a combination of the phenomenon of erosion of substrate and embedding of copper particles. In PA66 the impact affected zone is wider due to greater erosion of the substrate whereas in PA6T more copper particles are seen embedded in the substrate hence copper has higher adhesion on glass-reinforced nylon (PA6T) than on PA66 (**Fig. 5.9** & **Fig. 5.13**). This higher adhesion results from the higher tensile strength of PA6T as compared to PA66 (**Table 3.2**), due to which the erosion of substrate due to impact of copper particles is minimized. The higher strength of PA6T is obtained by adding glass fibres to PA66. The glass fibres seem to withstand the impact of copper particles better than nylon matrix. This is seen in **Fig. 5.22** and **Fig. 5.23**, where the glass fibre does not seem to have been damaged during spray deposition but the surrounding nylon matrix is fractured. At higher gas pressures (**Fig. 5.24**) very few glass fibers are seen; however, the adhesion of copper on PA6T is increased at this pressure. It is likely that, at this gas pressure, the glass fibres are eroded but copper is deeply embedded in PA6T. The

contrast between erosion rate of nylon matrix and glass fibre may have a role to play in this by providing anchors for deformed copper particle to adhere. The nylon matrix is eroded more while erosion is minimized in locations where the glass reinforcement is present, thus providing an anchor for copper particle to adhere. Such anchoring is seen in **Fig. 5.41** where it is seen that copper particles have surrounded the glass fibres. Polymers like PP and PE have low T_g and tensile strength and they cannot withstand the impact of copper particles and the erosion of substrate is the primary mechanism operating on such polymers.

b) Tin

It is hypothesized that tin particles (observed in **Figs. 5.26-5.29, 5.31 & 5.33**) droplet melts upon impact and forms a splat. The particles of tin are formed due to the break up of the splat. Mostaghimi *et al.* modeled the splat formation in plasma sprayed coatings [72, 73]. They predicted the splat shape formed during plasma spraying of Ni on substrates maintained at temperatures of 563 K and 673 K (**Fig. 5.46**). They showed that break-up of the splat on a flat surface is primarily due to solidification. When solidification was artificially suppressed in their model, no break-up was predicted. The prediction from their model has been experimentally verified [72]. Zhang *et al.* [43, 44]studied the impact of aluminium particles on tin substrate in cold praying. The observed melting of tin substrate due to impact of aluminium particles. Melting of tin upon impact or due to impact of other particles (copper or tin) on previously deposited tin results in significant flattening of the tin.

The fine particles of tin seen in **Fig. 5.27 – 5.29 & 5.31** are formed due to the melting of tin. The particles seen in cold sprayed tin are formed due to break-up of the tin splat during solidification and/or due to the radial forces acting on the splat during the impact. The presence of tin particles is evidence that melting on impact has taken place. The layer of tin thus formed provides a matrix of tin in which copper particles are deposited.

Tin could be deposited on most of the polymers as it is a much softer material than copper (Yield strength of tin is 9 MPa and 0.2 % proof stress for copper is ~ 50 MPa). Upon impact, both the tin and polymer will exhibit deformation and thus heating. The plastic deformation of PA66 and PA6T due to impact of tin particles **(Figs. 5.26 & 5.29)**, and melting of the tin particles result in tin particle embedding in the substrate. Subsequent impacts of tin particles lead to growth of deposits on the previously embedded tin layer. The significantly less erosion of substrate by tin as compared to copper improves the adhesion of Sn + Cu tracks on PA66 and PA6T. A comparison of the adhesion of copper to; PA6T **(Fig. 5.9)** and tin coated PA6T **(Fig. 5.12)**, reveals that copper deposited on tin coated PA6T has higher bond strengths (~ 6 MPa) than copper deposited on PA6T without any tin bond coat (~ 1.75 MPa). On PA66 the adhesion increased from < 1 MPa to ~ 2 MPa when tin bond coat was used.

The adhesion test samples failed at the PA6T/PA66 - tin interface. Metal jetting was observed in copper **(Figs. 5.32 & 5.34)** and tin **(Fig. 5.33)** due to impact of copper

particles. Metal jetting results in the formation of metallurgical bonds in the deposits and improves adhesion of copper on tin.

From the above discussion, the following mechanism can be proposed for adhesion of copper and tin on polymers;

1 Initial impacts result in erosion of polymer substrate, the extent of erosion depends upon the polymer and particle properties. The stronger polymers like PA66, PA6T and PBT do not suffer massive erosion; instead the kinetic energy of impacting particle is sufficient to result in copper particle embedding in these polymers.

2 The extent of bonding depends upon degree of erosion versus embedding of particles, materials which do not erode the substrate substantially are more likely to embed in the polymer; tin due to its low yield point could be deposited on all the polymers.

3 Impact of subsequent copper particles is on previously embedded copper and further deposit growth takes place by the interaction between embedded copper and incoming copper particle. Further growth of the deposit is similar to growth of deposit on metallic substrates. The metal jetting seen in **Fig. 5.25** supports this hypothesis.

4 Polymers like PP and PE suffer significant erosion during impact of copper particles due to their low strength. PPS is a very glassy polymer and

although it has high strength, but its glassy nature results in brittle erosion of substrate during impact.

The bond strength of copper on PA6T increases with increase in process gas temperature. The range of temperatures used to deposit copper for bond strength (pull-off) tests was up to a maximum of 373 K, the effect of heating the gas is to increase the particle velocity and heating the substrate due to impingement of hot gas, and not so much on heating the particle; thus it seems likely that higher particle velocities obtained by heating the process gas produces better adhesion on PA6T substrate. The wearing effect of heated gas on PA6T substrate is not substantial, probably due to high tensile strength and T_g of PA6T. The qualitative assessment of adhesion on PA66 shows that heating the process gas results in erosion of PA66 (**Table 5.18**). Thus for PA66 the impingement of hot gas results in softening, leading to erosion during impact of copper particles. The difference in the tensile strength and T_g of PA6T (180 MPa, 368 K) and PA66 (82 MPa, 323 K) may be responsible for this.

5.11.4 Deposition efficiency

The DE is an important criterion for process optimization in CGDS. Higher DE indicates that a greater proportion of the particles have accelerated above the critical velocity. The gas density in the nozzle increases with increasing pressure resulting

in higher drag forces on the particles and thus to higher acceleration. For aluminium substrate, **Fig.5.4** indicates that as the pressure is dropped below 22 bar, the DE decreases, indicating that a lower proportion of particles have reached the critical velocity for deposition upon impact. The thickness measurements shown in **Table 5.4** reveal that the thickness of deposits achieved for spraying at 11 bar pressure is lower than that for higher pressures. As discussed in section 5.11.1, for deposition at 11 bar pressure, the larger size fraction of particles is excluded from the deposition process due to their lower velocity; and consequently the % of particles exceeding the critical velocity is lower.

The velocity achieved by the particles depends not only on the gas conditions, but also upon the particle loading within the gas stream (**Fig. 5.5**) where a loading of greater than 21 wt % has resulted in a significant decrease in DE. The loading of the gas stream may result in lower velocities of particles because the gas stream may not be able to accelerate greater number of particles above the critical velocity.

The DE for depositing copper on PA6T is shown in **Fig. 5.6**. The higher particle velocities and heating of substrate during spraying using gas at 333 K as compared to 298 K may be responsible for the higher DE seen for copper deposition at 333 K in **Fig. 5.6**. The softening of PA6T due to heating by impingement of heated gas would improve the embedding of copper particles in to PA6T. Thus it seems that more copper particles are embedding in to PA6T when gas is heated to 333 K.

5.11.5 Microstructures and microhardness

The increase in particle velocity with increasing gas pressure results in higher levels of cold work in the coating leading to higher levels of microhardness (**Fig. 5.37**). The higher velocities also result in a larger degree of impact deformation observed on aluminium substrate at the substrate-deposit interface (**Fig. 5.35**).

The effect of heating of the gas is not limited to changes in flow conditions and thus to particle impact velocity. **Fig. 5.38** shows that deposition using heated gas results in recrystallization of the deposit as seen from microstructural observations and from the decrease in microhardness (**Fig. 5.39**). It is also observed that the tendency for coatings to debond from aluminium substrate is greatly reduced (or eliminated) when spraying at elevated temperatures indicating that the recrystallization also results in stress relief. It is of note that significant effects are observed (both microstructurally and in terms of microhardness) at temperatures as low as 473 K. The recrystallization occurs in a short time period (the jet is moving at its slowest at 50 mm s^{-1} over the substrate); such rapid recrystallization at these low temperatures is driven by the very high levels of work hardening that the particles have suffered upon their own impact and from subsequently impacting particles.

5.12 Summary and conclusions

1. The higher expansion ratio of nozzle used at Yazaki results in thicker deposits thus, implying higher deposition efficiency.
2. Copper can be deposited directly on polymers, which have high T_g and tensile strength. Such polymers are PA66, PA6T and PBT. Other polymers are eroded due to impact of copper.
3. Tin can be deposited on all the polymers and subsequently copper can be deposited on tin coated polymers. Pull-off tests reveal that the adhesion of Sn + Cu deposits is higher than copper deposits on PA66 and PA6T substrates. The use of tin bond coat raises issues relating to the stability of the Sn + Cu tracks and the influence of tin bond coat on the electrical resistivity of tracks. These issues are addressed in chapter 6.
4. Using higher process gas pressures and heating the process gas improves the adhesion of copper deposits on aluminium.
5. The process deposition efficiency for depositing copper is high for the spray conditions examined in this study. Thus, it is likely that the spraying conditions used in our study accelerate most of the particles above the critical velocity required for deposition.
6. The grain size in as-sprayed copper deposits is very fine. The grains are not resolvable in the optical microscope. Copper deposited using heated gas results in formation of very fine grains at gas temperatures of 473 K, where fine crystals are seen in the etched microstructure **(Fig. 5.38 (b))**. Annealing at 673

K promotes nucleation of more grains and also grain growth in previously nucleated grains.

Table 5.1: Deposition parameters used at Nottingham to deposit copper for initial experiments.

Stagnation pressure / bar	Powder feed rate / g s^{-1}	Carrier gas flow rate / kg s^{-1} 10^{-4}	Traverse speed / m s^{-1}	No. of passes	Stand-off distance / m
22	0.25	3.8	0.05	1	0.02

Table 5.2: Thickness of copper deposits on polymer, metallic and ceramic substrates; and qualitative assessment of their adhesion. Deposition conditions as described in **Table 5.1**.

Substrate thickness / mm		Thickness of copper / μm	Qualitative assessment of adhesion	Remarks
Aluminium	2.97	120	1	Good adhesion.
APS alumina	1.05	Nil	3	Deposits de-bonded
PA6T	3.04	100	1	Good adhesion
PBT	2.92	90	1	Good adhesion
NORYL	2.98	Nil	3	Deposits de-bonded
PP	3.04	70	2	Erosion of substrate
PE	4.89	Nil	3	Erosion of substrate
PPS	2.93	130	2	Poor adhesion

Table 5.3 (a): Deposition conditions to deposit copper at University of Nottingham during parameter study experiments. Deposition carried out using gas at 298 K.

Stagnation pressure / bar	Powder feed rate / g s^{-1}	No. of passes	Traverse speed / m s^{-1}	Carrier gas flow rate / m^3 s^{-1}	Stand-off distance / m
11 to 29	0.25 to 1	1 to 4	0.1	0.01	0.02

Table 5.3 (b): Carrier gas mass flow at different gas pressures corresponding to flow meter reading of 0.01 m^3 s^{-1} in the University of Nottingham cold spray rig.

Gas pressure / bar	10	15	20	22	25	30
Gas mass flow / kg s^{-1} 10^{-4}	2.6	3.1	3.6	3.8	4.1	4.4

Table 5.4: Deposit thickness on aluminium for spraying copper at different pressures, powder feed rates and No. of passes using traverse speed of 0.1 m s^{-1} and stagnation temperature of 298 K. Thickness in mm. Key to colour coding of cells described in **Table 5.9**. Deposition trials carried out at Nottingham.

Gas pressure / bar	Powder feed rate / g s^{-1}															
	0.25				0.50				0.75				1.00			
	No. of passes															
	1	2	3	4	1	2	3	4	1	2	3	4	1	2	3	4
11	0.07	0.10	0.16	0.16	0.07	0.13	0.20	0.26	0.08	0.15	0.24	0.31	0.08	0.16	0.25	0.33
15	0.08	0.13	0.19	0.21	0.12	0.22	0.31	0.37	0.18	0.31	0.42	0.62	0.19	0.38	0.58	0.81
18	0.06	0.15	0.17	0.24	0.12	0.20	0.29	0.41	0.17	0.29	0.45	0.57	0.17	0.34	0.56	0.74
22	0.07	0.12	0.14	0.22	0.06	0.13	0.19	0.30	0.13	0.21	0.33	0.48	0.16	0.30	0.43	0.72
26	0.06	0.12	0.14	0.21	0.06	0.12	0.21	0.30	0.10	0.21	0.31	0.47	0.16	0.27	0.43	0.67
29	0.08	0.11	0.19	0.25	0.07	0.15	0.23	0.34	0.11	0.21	0.34	0.53	0.14	0.34	0.58	0.81

Table 5.5: Thickness of copper deposit on PA6T sprayed at different pressures, powder feed rates and No. of passes using traverse speed of 0.1 m s^{-1} and stagnation temperature of 298 K. Thickness in mm. Key to colour coding of cells described in **Table 5.9**. Deposition trials carried out at Nottingham.

Gas pressure / bar	Powder feed rate / g s^{-1}															
	0.25				0.50				0.75				1.00			
	No. of passes															
	1	2	3	4	1	2	3	4	1	2	3	4	1	2	3	4
11	0.19	0.23	0.28	0.32	0.21	0.28	0.38	0.1	0.27	0.3	0.12	0.12	0.23	0.31	0.13	0.13
15	0.07	0.13	0.19	0.22	0.09	0.24	0.34	0.43	0.2	0.37	0.54	0.69	0.29	0.45	0.64	0.08
18	0.26	0.28	0.36	0.36	0.24	0.32	0.41	0.48	0.24	0.35	0.44	0.55	0.23	0.32	0.52	0.8
22	0.08	0.15	0.22	0.26	0.11	0.16	0.24	0.35	0.21	0.27	0.36	0.5	0.25	0.32	0.51	0.82
26	0.22	0.26	0.28	0.31	0.17	0.23	0.31	0.37	0.2	0.29	0.38	0.43	0.23	0.33	0.46	0.59
29	0.06	0.12	0.19	0.29	0.1	0.22	0.31	0.42	0.24	0.27	0.47	0.59	0.24	0.48	0.65	0.87

Table 5.6: Thickness of copper deposit on PBT sprayed at different pressures, powder feed rates and No. of passes using traverse speed of 0.1 m s^{-1} and stagnation temperature of 298 K. Thickness in mm. Key to colour coding of cells described in **Table 5.9**. Deposition trials carried out at Nottingham.

Gas pressure / bar	Powder feed rate / g s^{-1}															
	0.25				0.50				0.75				1.00			
	No. of passes															
	1	2	3	4	1	2	3	4	1	2	3	4	1	2	3	4
11	0.08	0.09	0.15	0.19	0.15	No deposits										
15	0.05	0.14	0.19	0.23	0.10	0.24	0.30	0.45	0.15	0.29	0.41	0.58	0.25	0.43	0.52	0.10
18	0.06	0.08	0.19	0.21	0.12	0.19	0.30	0.35	0.15	0.33	0.45	0.48	0.13	0.26	0.44	0.04
22	0.07	0.10	0.16	0.23	0.08	0.11	0.19	0.31	0.07	0.13	0.26	0.35	0.06	0.18	0.25	0.05
26	0.12	0.16	0.19	0.25	0.11	0.15	0.22	0.35	0.13	0.23	0.30	0.36	0.13	0.27	0.45	0.51
29	-	0.15	0.20	0.22	0.05	0.10	0.21	0.28	0.04	0.08	0.21	0.34	0.04	0.13	0.38	0.60

Table 5.7: Thickness of copper deposit on alumina coated mild steel sprayed at different pressures, powder feed rates and No. of passes using traverse speed of 0.1 m s^{-1} and stagnation temperature of 298 K. Thickness in mm. Key to colour coding of cells described in **Table 5.9**. Deposition trials carried out at Nottingham.

Gas pressure / bar	Powder feed rate / g s^{-1}															
	0.25				0.50				0.75				1.00			
	No. of passes															
	1	2	3	4	1	2	3	4	1	2	3	4	1	2	3	4
11	0.03	0.09	0.10	0.17	0.06	0.12	0.16	0.21	0.07	0.13	0.19	0.27	0.06	0.15	0.20	0.26
15	0.07	0.09	0.16	0.22	0.11	0.20	0.27	0.38	0.14	0.33	0.48	0.53	0.16	0.37	0.51	0.72
18	0.06	0.13	0.16	0.25	0.12	0.18	0.26	0.32	0.12	0.28	0.46	0.60	0.16	0.28	0.45	0.67
22	0.01	0.05	0.11	0.13	0.04	0.07	0.13	0.22	0.03	0.15	0.22	0.38	0.11	0.15	0.40	0.58
26	0.04	0.08	0.10	0.15	0.05	0.07	0.17	0.00	0.11	0.23	0.34	0.43	0.11	0.27	0.39	0.50
29	0.02	0.08	0.13	0.20	0.03	0.10	0.19	0.28	0.07	0.00	0.36	0.50	0.12	0.32	0.00	0.00

Table 5.8: Thickness of copper deposit on PP sprayed at different pressures, powder feed rates and No. of passes using traverse speed of 0.1 m s^{-1} and stagnation temperature of 298 K. Thickness in mm. Key to colour coding of cells described in **Table 5.9**. Deposition trials carried out at Nottingham.

Gas pressure / bar	Powder feed rate / g s-1															
	0.25				0.50				0.75				1.00			
	No. of passes															
	1	2	3	4	1	2	3	4	1	2	3	4	1	2	3	4
11	No deposits formed, PP substrate wears															
15	0.05	0.13	0.17	No deposits formed, PP substrate wears												
18	0.05	0.07	0.12	0.12	No deposits formed, PP substrate wears											
22	0.06	0.07	0.10	0.18	0.07	0.07	0.12	0.20	0.05	0.11	0.14	0.23	0.05	0.09	0.14	0.07
26	-	-	0.16	0.18	-	-	0.16	-	PP Substrate wears							
29	-	-	-	0.15	PP substrate wears											

Table 5.9: Key to colour coding of cells in **Tables 5.4-5.8**.

	No apparent damage to track
	Minimum damage to track. Track slightly lifted at some edges
	Medium damage to track. Track lifted up from centre of cross-section and edges
	Maximum damage to track. Track totally de-bonded from substrate

Table 5.10 (a): Cold spray parameters to deposit copper on various substrates. Trials carried out at Yazaki using heated process gas. Process gas pressure at different gas temperatures is given in **Table 5.10 (b)**.

Total gas mass flow (process + carrier) / 10^{-3} kg s^{-1}	Stagnation temperature / K	Powder feed rate / g s^{-1}	Traverse speed / m s^{-1}	No. of passes	Stand-off distance / m
2.9	298 - 523	0.25 – 1.5	0.012 – 0.4	1	0.02

Table 5.10 (b): Measured process gas pressure at different process gas stagnation temperatures for fixed mass flow rate of 2.9 x 10^{-3} kg s^{-1}.

Process gas temperature / K	298	323	340	348	373	423	473	523
Process gas pressure / bar	21	23	24	24	25	26	28	30

Table 5.10 (c): Measured process gas pressure at different gas mass flow rate and 298 K process gas temperature in Yazaki system.

Process gas mass flow rate / 10^{-3} kg s^{-1}	1.5	2.1	2.5	2.9	3.5	4.1
Process gas pressure / bar	11	15	18	22	26	29

Table 5.11: Cold spray parameters used at Yazaki to deposit copper for adhesion testing samples. The parameters of traverse speed and number of passes were adjusted to obtain ~ 0.5 mm thick deposits.

Total gas mass flow (process + carrier) / kg s^{-1}	Stagnation temperature / K	Powder feed rate / g s^{-1}	Traverse speed / m s^{-1}	No. of passes	Stand-off distance / m
0.0029	298 - 523	0.25 – 0.75	0.2 – 0.5	2-3	0.02

Table 5.12: Thickness of copper on aluminium sprayed at different process gas temperatures, powder feed rates and traverse speeds. Deposition carried out at Yazaki using gas mass flow rate of 2.9 x 10^{-3} kg s^{-1}. Thickness is reported in mm. Key to colour coding of cells described in **Table 5.16**.

Traverse speed / m s^{-1}	Process gas temperature / K													
	298		323		348		373		423		473		523	
	Powder feed rate / g s^{-1}													
	0.25	0.32	0.25	0.32	0.25	0.32	0.25	0.32	0.25	0.32	0.25	0.32	0.25	0.32
0.4	0.03	0.1	0.03	0.05	0.03	0.05	0.03	0.09	0.03	0.06	0.03	0.06	0.08	0.07
0.2	0.06	0.12	0.06	0.09	0.06	0.11	0.06	0.12	0.05	0.11	0.07	0.13	0.03	0.11
0.1	0.12	0.21	0.12	0.17	0.13	0.17	0.14	0.18	0.11	0.17	0.1	0.18	0.21	0.19
0.05	0.21	0.37	0.19	0.32	0.19	0.29	0.2	0.32	0.2	0.33	0.2	0.24	0.33	0.38
0.025	0.42	0.6	0.39	0.65	0.44	0.66	0.37	0.7	0.4	0.63	0.46	0.68	0.48	0.62
0.012	0.9	1.61	0.82	1.35	0.88	1.38	0.83	1.46	0.81	1.34	0.83	1.27	1.07	1.36

Table 5.13: Thickness of copper on PA6T sprayed at different process gas temperatures, powder feed rates and traverse speeds. Deposition carried out at Yazaki using gas mass flow rate of 2.9 x 10^{-3} kg s^{-1}. Thickness is reported in mm. Key to colour coding of cells described in **Table 5.16**.

Traverse speed / m s^{-1}	Process gas temperature / K													
	298		323		348		373		423		473		523	
	Powder feed rate / g s^{-1}													
	0.25	0.32	0.25	0.32	0.25	0.32	0.25	0.32	0.25	0.32	0.25	0.32	0.25	0.32
0.4	0.03	0.13	0.04	0.08	0.03		0.08	0.09	No deposits formed. Substrate erosion occurs during spraying					
0.2	0.06	0.17	0.06	0.15	0.08		0.23	0.11						
0.1	0.15	0.26	0.09	0.27	0.17	0.38	0.44	0.35						
0.05	0.21		0.23	0.49	0.38	0.67	0.81	0.62						
0.025	0.38		0.38	0.1	0.49									
0.012														

Table 5.14: Thickness of copper on PBT GF 30 sprayed at different process gas temperatures, powder feed rates and traverse speeds. Deposition carried out at Yazaki using gas mass flow rate of 2.9 x 10^{-3} kg s^{-1}. Thickness is reported in mm. Key to colour coding of cells described in **Table 5.16**.

Traverse speed / m s^{-1}	Process gas temperature / K													
	298		323		348		373		423		473		523	
	Powder feed rate / g s^{-1}													
	0.25	0.32	0.25	0.32	0.25	0.32	0.25	0.32	0.25	0.32	0.25	0.32	0.25	0.32
0.4	0.03	0.08												
0.2	0.05	0.14												
0.1	0.18	0.22	No deposits formed. Substrate erosion occurs during spraying											
0.05	0.44	0.44												
0.025														
0.012														

Table 5.15: Thickness of copper on alumina coated mild steel sprayed at different process gas temperatures, powder feed rates and traverse speeds. Deposition carried out at Yazaki using gas mass flow rate of 2.9×10^{-3} kg s^{-1}. Thickness is reported in mm. Key to colour coding of cells described in **Table 5.16**.

Traverse speed / m s^{-1}	Process gas temperature / K													
	298		323		348		373		423		473		523	
	Powder feed rate / g s^{-1}													
	0.25	0.32	0.25	0.32	0.25	0.32	0.25	0.32	0.25	0.32	0.25	0.32	0.25	0.32
0.4	0.02	0.08	0.01	0.05	0.03	0.06	0.02		0.1	0.6				
0.2	0.08	0.15	0.07	0.19	0.16	0.15								
0.1					0.23									
0.05													0.15	
0.025													0.15	
0.012														

Table 5.16: Key to colour coding of cells in **Tables 5.12-5.15**.

	No apparent damage to track
	Minimum damage to track. Track slightly lifted at some edges
	Medium damage to track. Track lifted up from centre of cross-section and edges
	Maximum damage to track. Track totally de-bonded from substrate

Table 5.17: Cold spray conditions used at Yazaki to deposit copper on PA66.

Process gas pressure / bar	Powder feed rate / g s^{-1}	Carrier gas flow / 10^{-4} kg s^{-1}	Process gas temperature / K	Traverse speed / m s^{-1}	Stand – off distance / m
11 - 29	0.5	1.8	298 & 340	0.1	0.02

Table 5.18: Thickness and qualitative assessment of adhesion of copper deposits on PA66. Deposition carried out as per conditions described in **Table 5.17**.

Process gas pressure / bar	Process gas temperature / K			
	298		340	
	Thickness / mm	Adhesion	Thickness / mm	Adhesion
11	0.02	1	0.09	2
15	0.1	1	No deposits formed as substrate eroded during spraying.	3
18	0.12	1		3
22	0.12	1		3
26	0.13	2		3
29	0.12	2		3

The adhesion of deposits is assessed qualitatively as follows, 1 = well adhered with no signs of de-lamination at any place, 2 = de-lamination seen in some places, 3 = totally delaminated.

Table 5.19: Cold spray conditions used at Nottingham to deposit tin on polymers.

Process gas pressure / bar	Carrier gas flow / 10^{-4} kg s^{-1}	Powder feed rate / g s^{-1}	Process gas temperature / K	Traverse speed / m s^{-1}	Stand – off distance / m
11	2.4	0.12	298	0.05	0.02

Table 5.20: Thickness and qualitative assessment of adhesion of tin and tin + copper deposits on polymers. Tin and copper were deposited at Nottingham using conditions described in **Table 5.19** & **Table 5.1** respectively.

Substrate thickness / mm		Thickness of tin / μm	Thickness of copper on tin / μm	Qualitative assessment of adhesion		Remarks
				Tin	Tin + copper	
PA6T	3.04	~ 80	120	1	1	Good adhesion of tin and copper.
PA66	3.03	~ 80	120	1	1	Good adhesion of tin and copper.
PBT	2.92	~ 80	100	1	1	Good adhesion of copper on PBT.
NORYL	2.98	~ 80	120	1	1	Good adhesion of tin and copper.
PP	3.04	~ 80	100	1	1	Good adhesion of tin and copper.
PE	4.89	~ 80	100	1	1	Good adhesion of tin and copper.
PPS	2.93	~ 80	70	1	1	Good adhesion of tin and copper.

The adhesion of deposits is assessed qualitatively as follows, 1 = well adhered with no signs of de-lamination at any place, 2 = de-lamination seen in some places, 3 = totally delaminated.

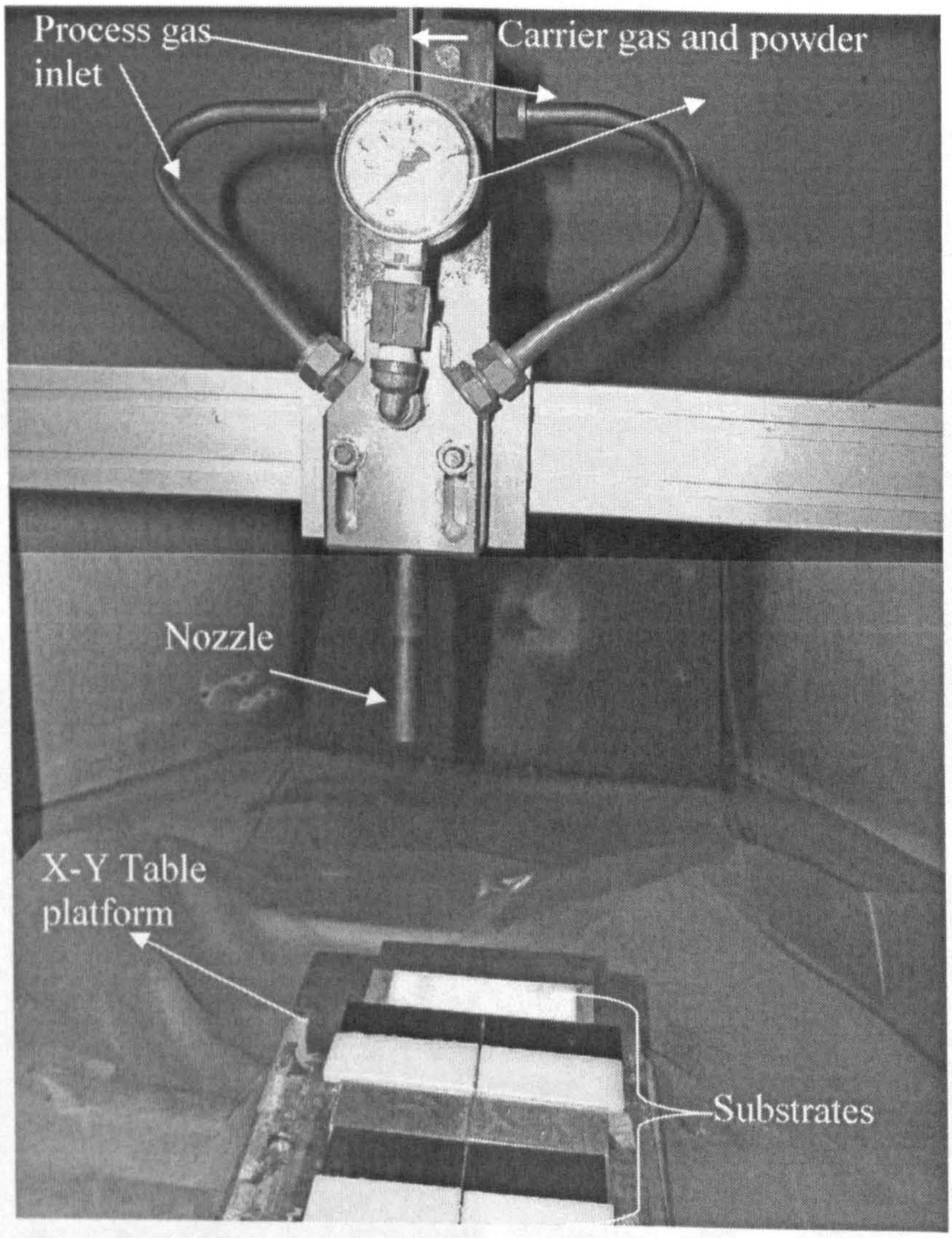

Fig. 5.1: Photograph of cold spray system at Nottingham showing the cold spray nozzle, gas & powder inlet and arrangement of substrates for deposition trials.

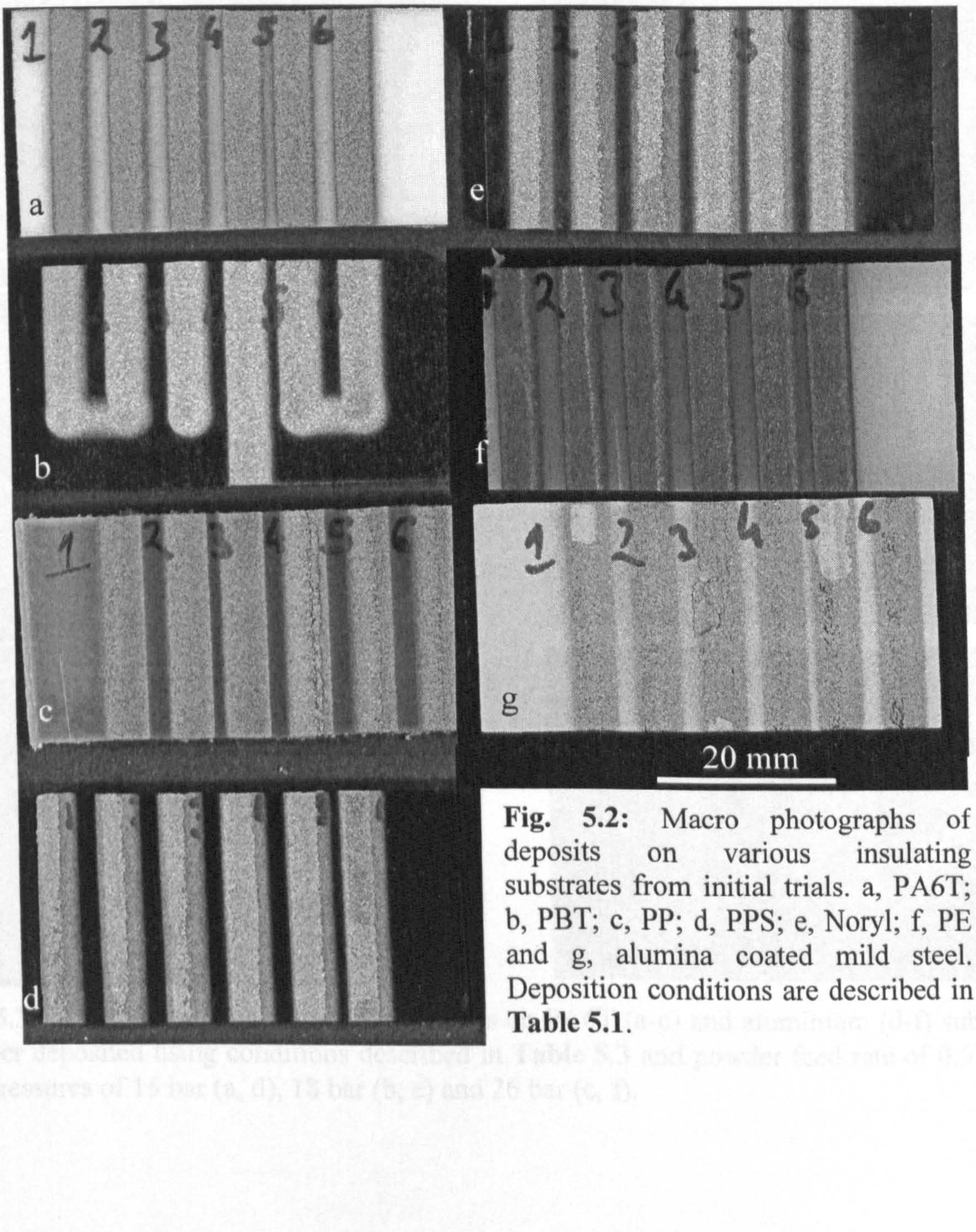

Fig. 5.2: Macro photographs of deposits on various insulating substrates from initial trials. a, PA6T; b, PBT; c, PP; d, PPS; e, Noryl; f, PE and g, alumina coated mild steel. Deposition conditions are described in **Table 5.1**.

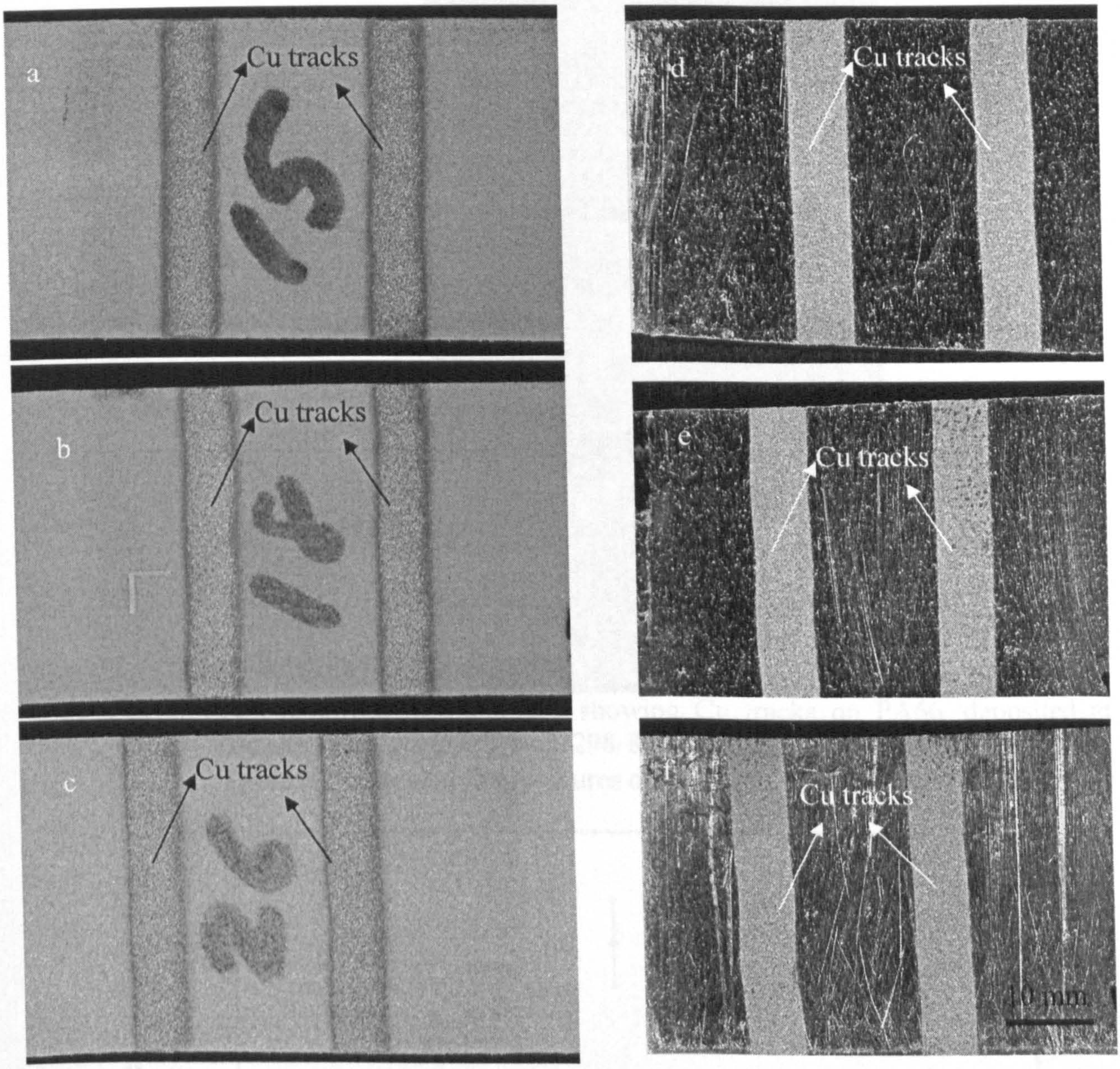

Fig. 5.3: Macrophotographs of copper deposits on PA6T (a-c) and aluminium (d-f) substrates. Copper deposited using conditions described in **Table 5.3** and powder feed rate of 0.5 g s^{-1} at gas pressures of 15 bar (a, d), 18 bar (b, e) and 26 bar (c, f).

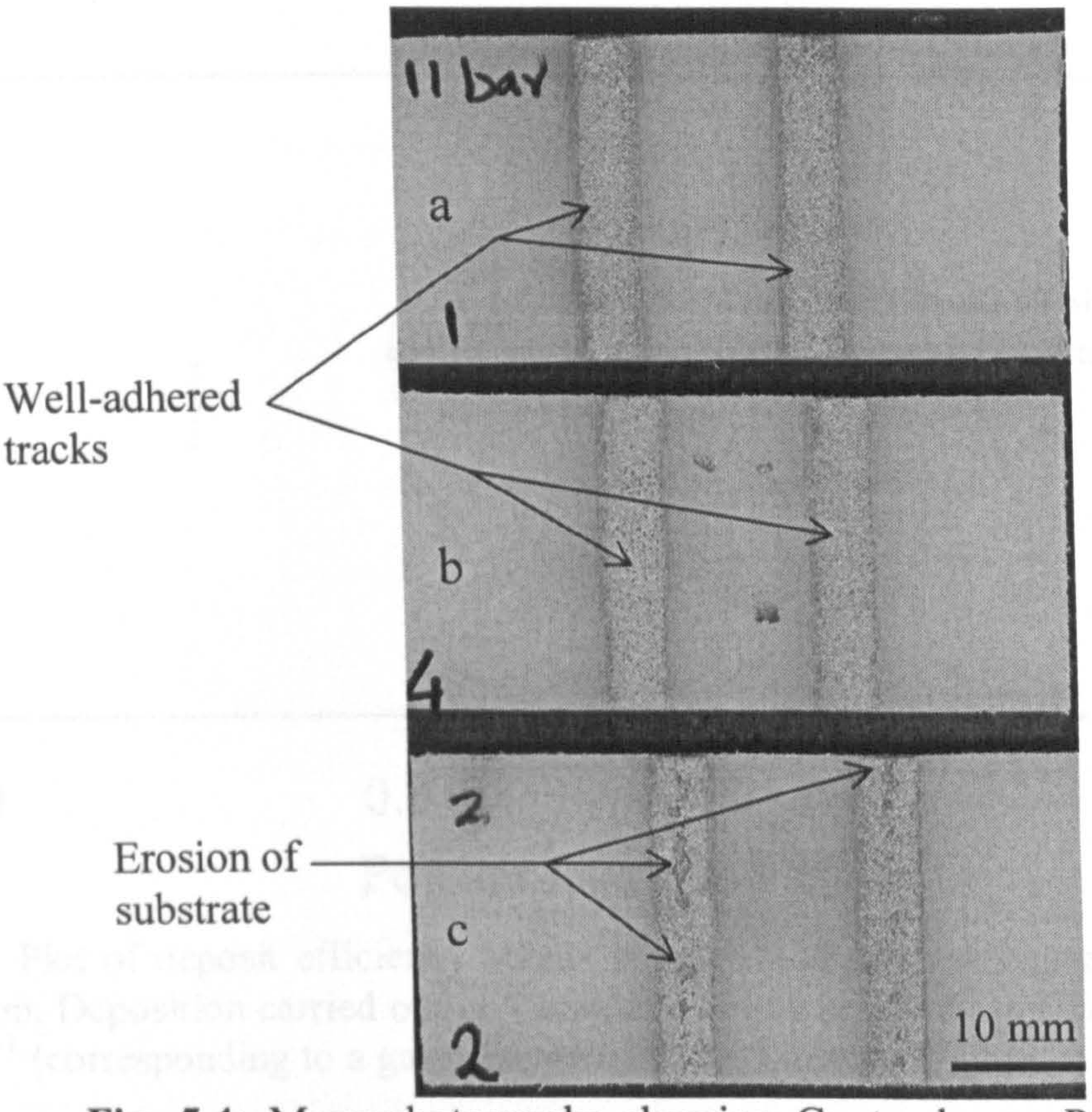

Fig. 5.4: Macrophotographs showing Cu tracks on PA66, deposited at Yazaki using process gas at 298 K and spraying conditions described in **Table 5.17**. Process gas pressures of a, 11 bar; b, 18 bar and c, 26 bar.

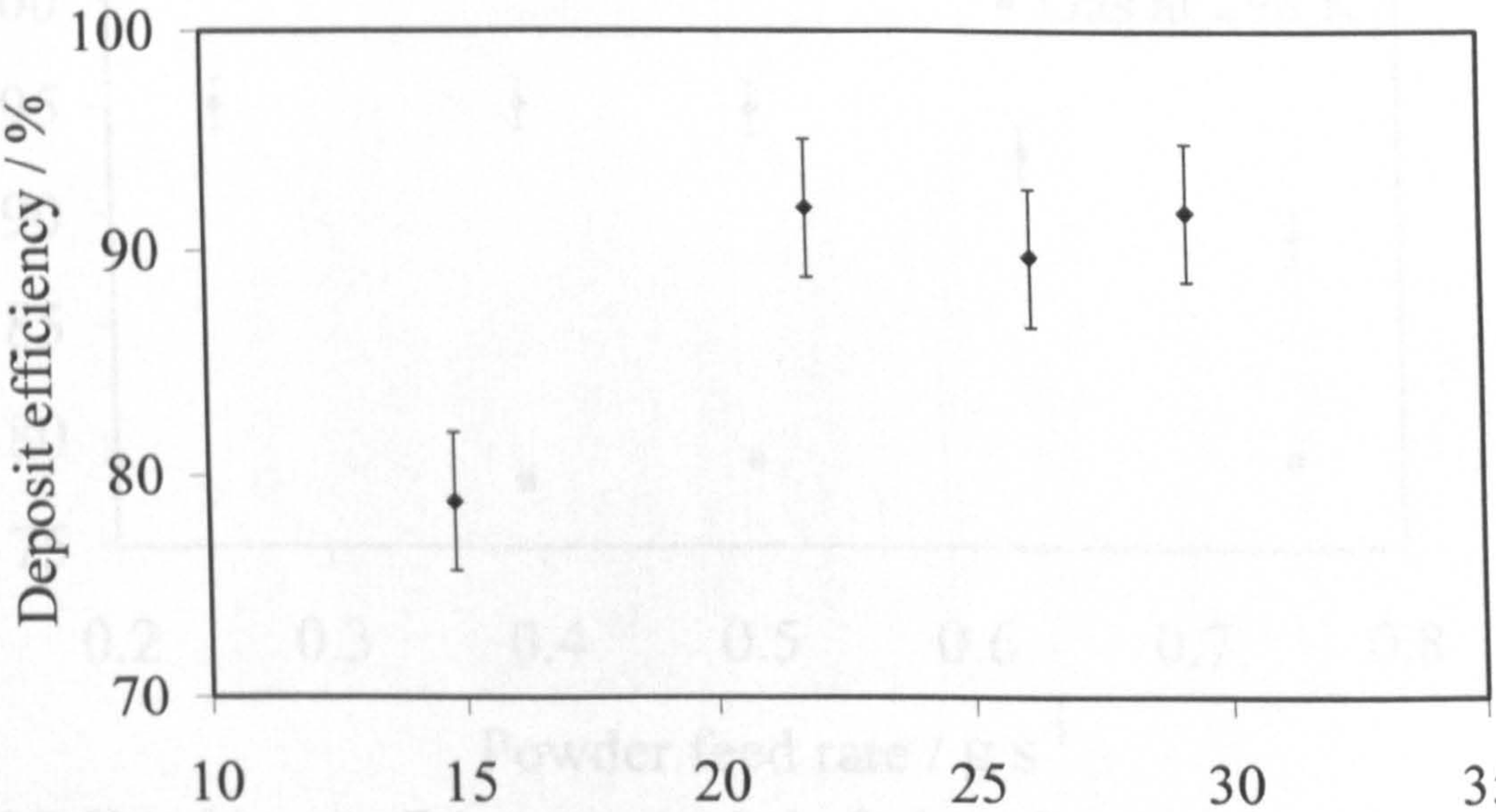

Fig. 5.5: Plot of deposition efficiency versus stagnation pressure for copper deposition on aluminium. Powder feed rate = 0.25 g s^{-1}, gas temperature = 298 K and traverse speed of 0.2 m s^{-1}. Deposition conditions described in **Table 5.10 (c)**.

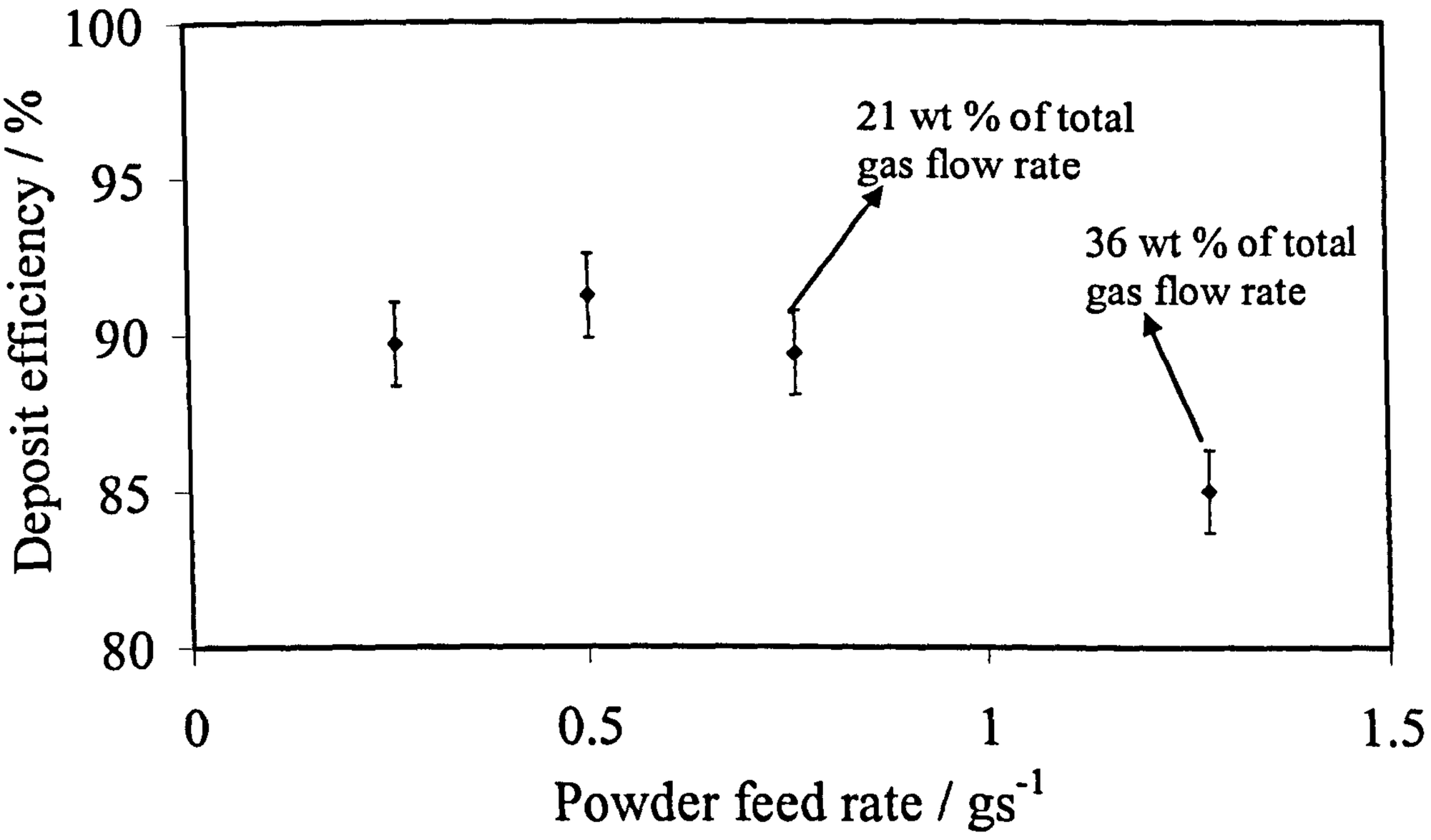

Fig. 5.6: Plot of deposit efficiency versus powder feed rate for copper deposition on aluminium. Deposition carried out at Yazaki using gas at 298 K, gas flow rate of 3.5 x 10^{-3} kg s^{-1} (corresponding to a gas pressure of 26 bar), traverse speed of 0.2 m s^{-1}.

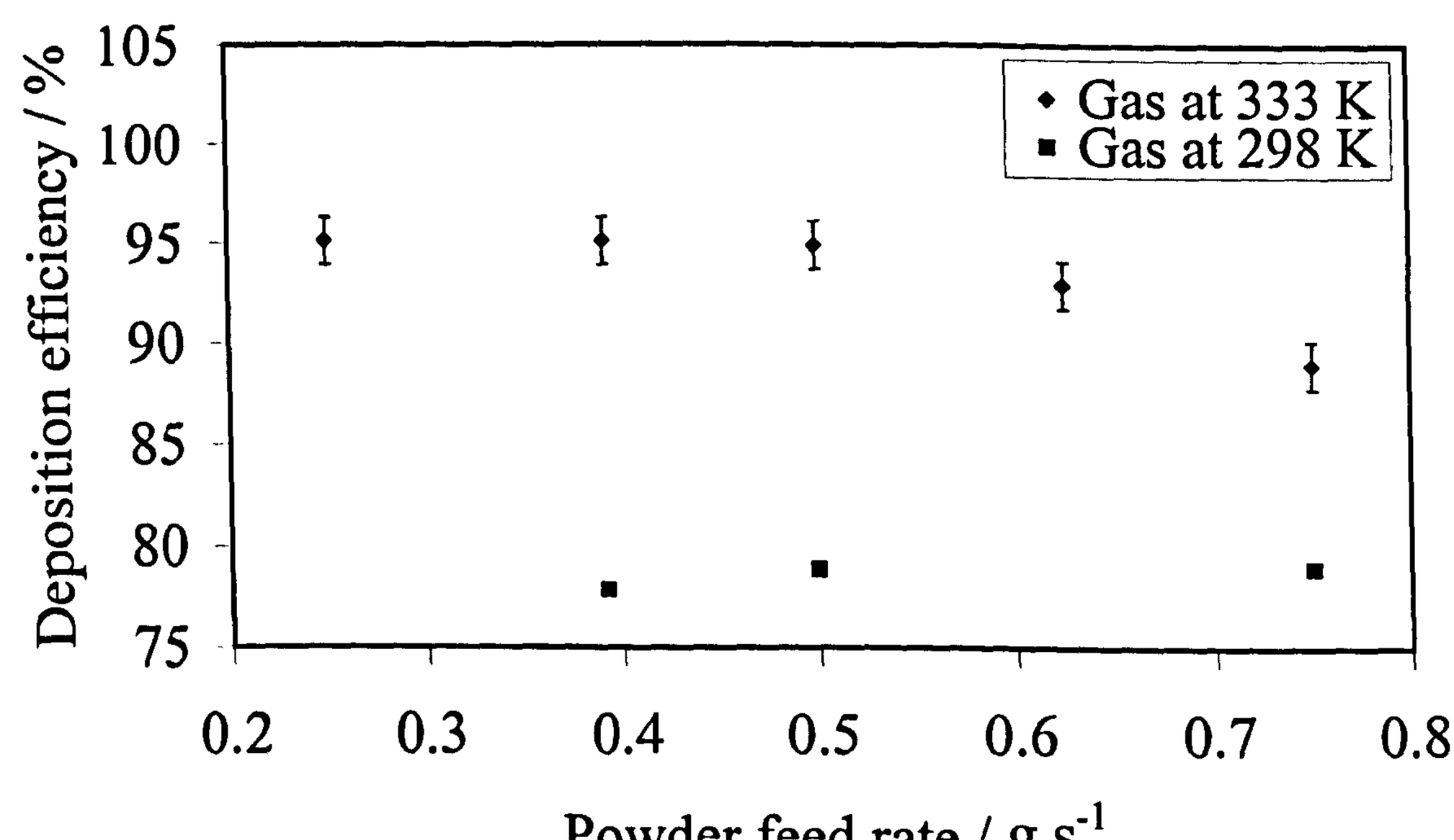

Fig. 5.7: Plot of deposit efficiency versus powder feed rate for copper deposition on PA6T using a gas flow rate of 2.9 x 10^{-3} kg s^{-1} (corresponding to a gas pressure of 22 bar) and traverse speed of 0.2 m s^{-1}. Deposition carried out at Yazaki.

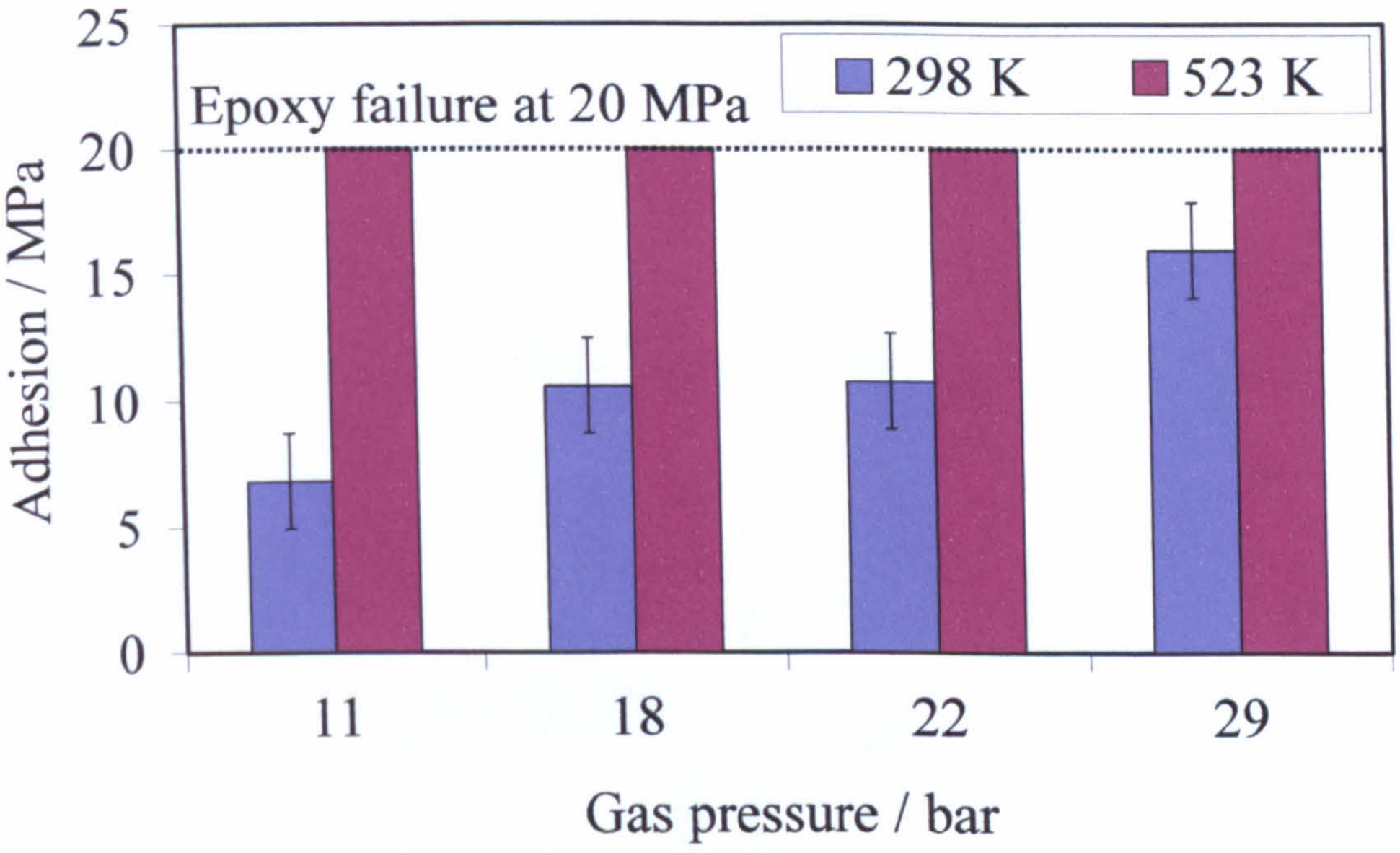

Fig. 5.8: Bar chart of adhesion test data of Cu deposited on Al versus gas pressure. Deposition carried out at Yazaki using gas flow of 2.9 x 10^{-3} kg s^{-1}, two different gas temperatures; 298 K and 523 K, powder feed rate of 0.5 g s^{-1}, traverse speed of 0.3 m s^{-1} and in 2 passes. 523 K samples exhibited failure in epoxy resin.

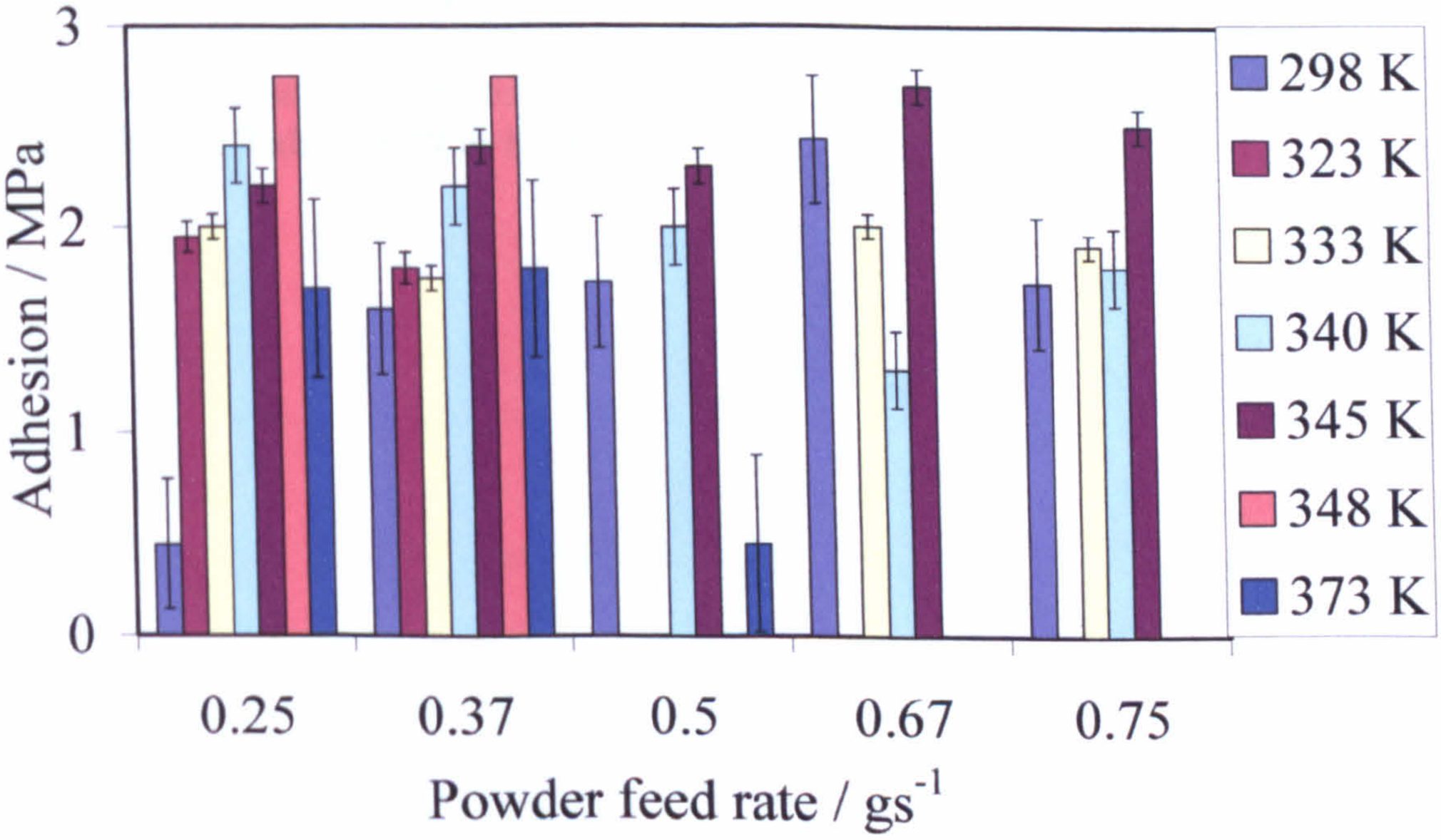

Fig. 5.9: Bar chart showing adhesion test data of Cu on PA6T versus powder feed rate for different gas temperature. Deposition carried out at Yazaki using conditions described in **Table 5.11**.

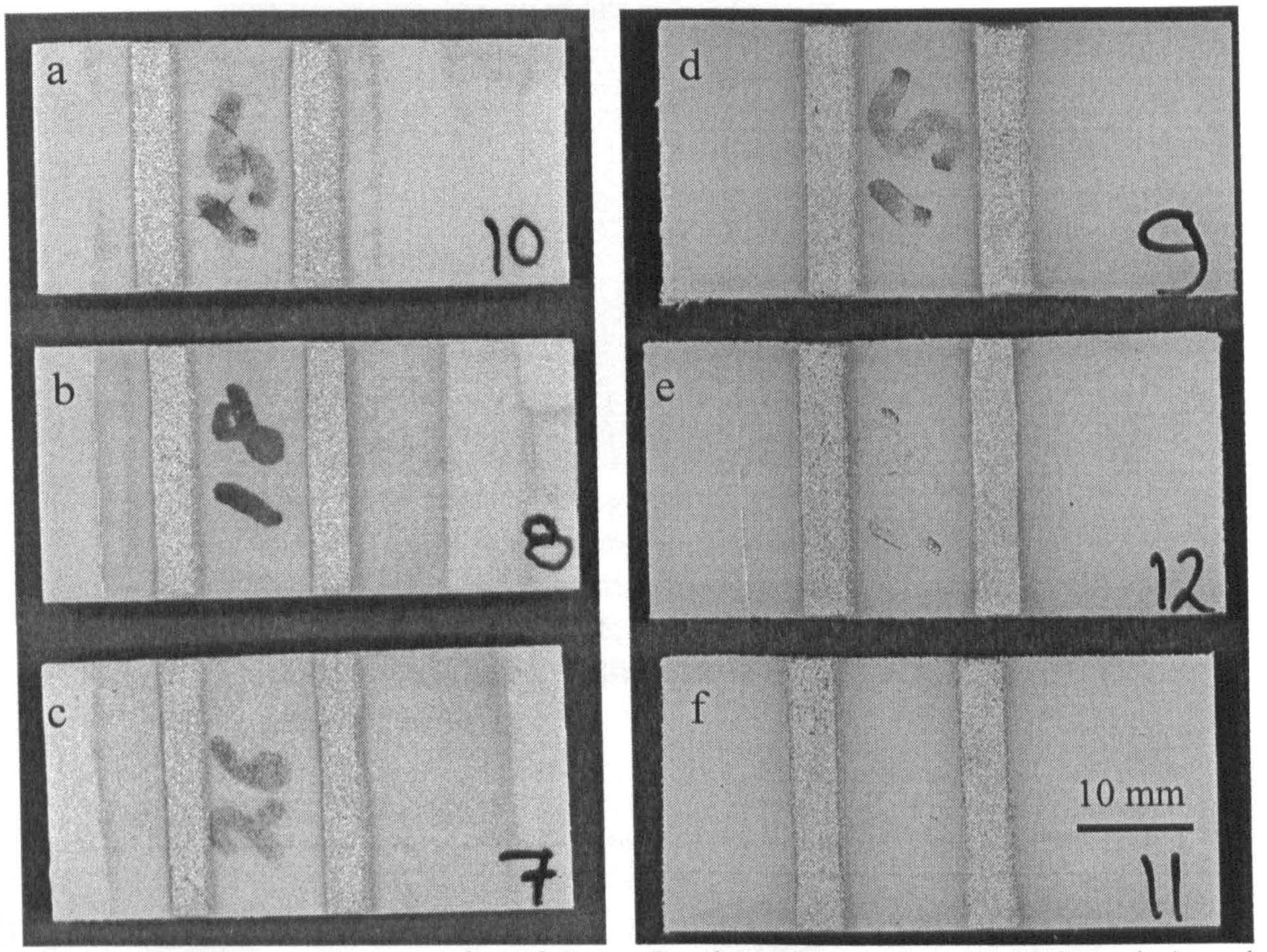

Fig. 5.10: Macro photographs of Sn + Cu deposits on PA6T (a, b and c) and PA66 (d, e and f). Cu deposited using process gas pressure of 15 bar (a, d); 18 bar (b, e) and 26 bar (c, f). Cu is seen to be well adhered to the tin coated substrate. Sn and Cu deposition carried out at Nottingham using conditions described in **Tables 5.19** & **5.1** respectively.

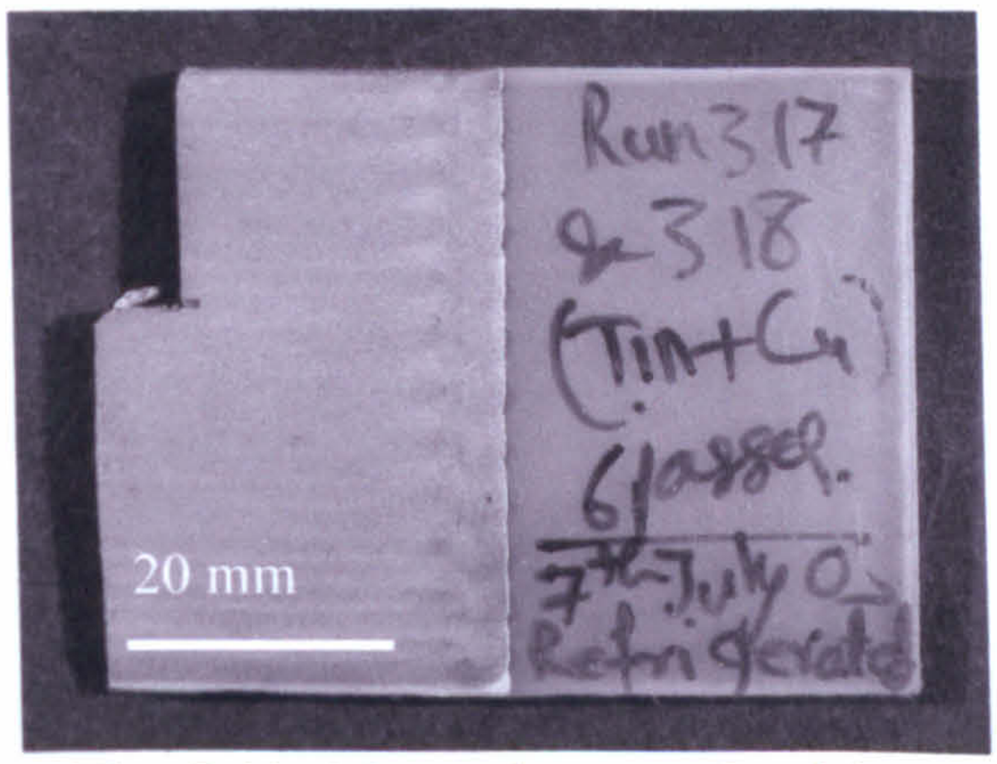

Fig. 5.11: Macrophotograph of 0.6 mm thick Cu deposit on Sn coated PP. CGDS parameters used are described in **Table 5.1**; except, six passes were used with a powder feed rate of 0.5 g s^{-1}

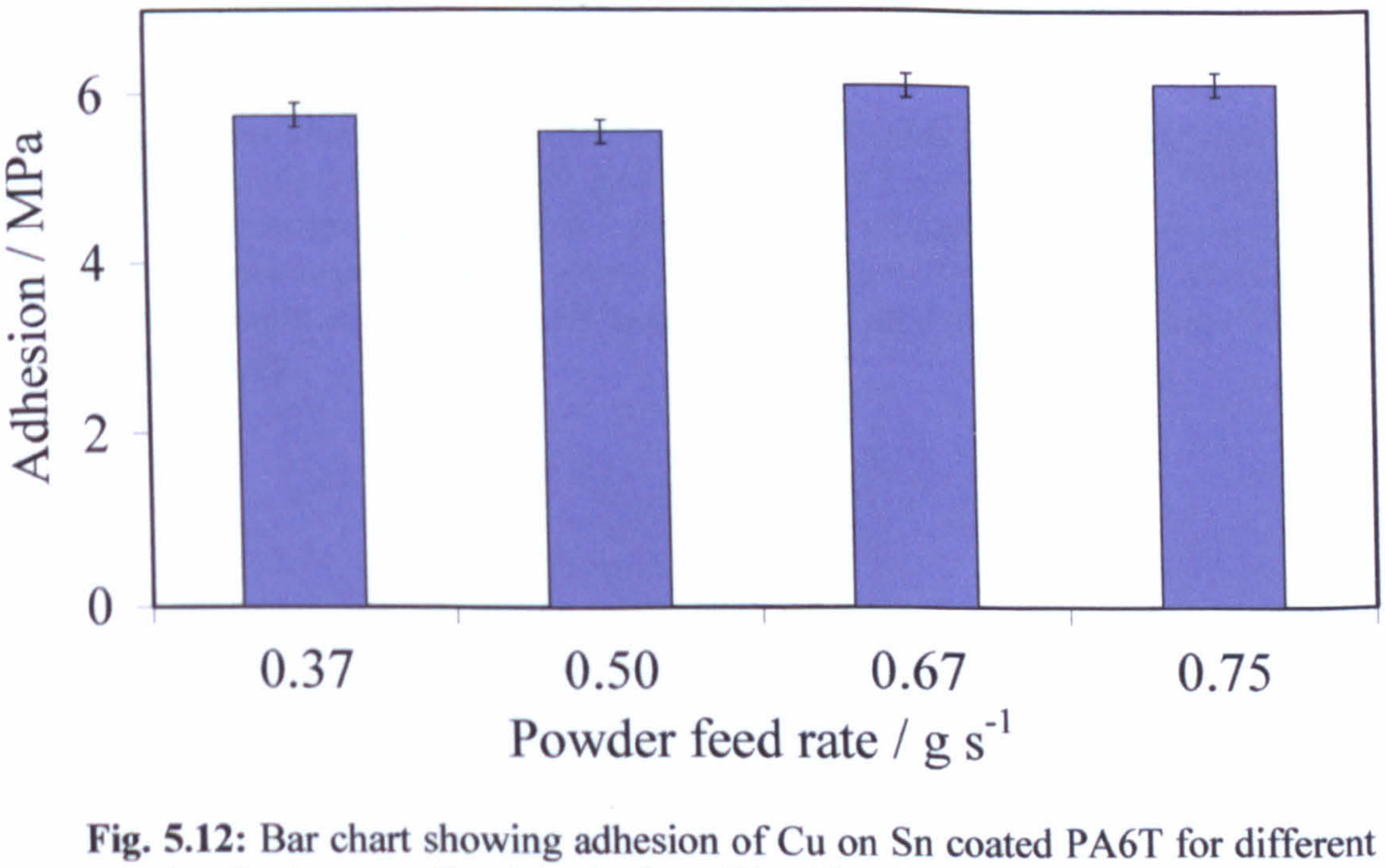

Fig. 5.12: Bar chart showing adhesion of Cu on Sn coated PA6T for different powder feed rates; Cu deposited at Yazaki using conditions described in **Table 5.11** and gas at 298 K. Tin deposited using conditions described in **Table 5.19**. De-bonding occurred between the tin layer and the substrate.

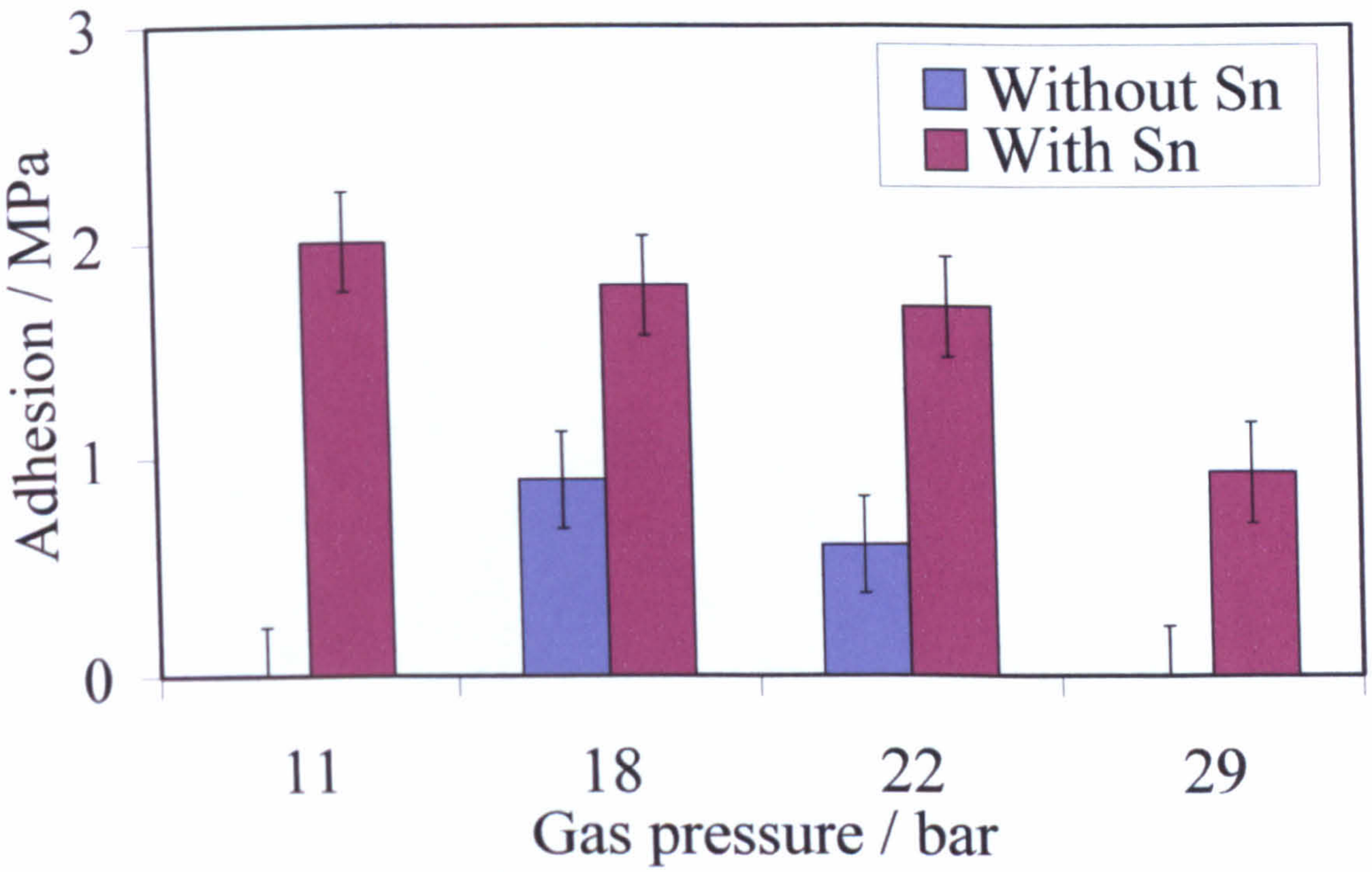

Fig. 5.13: Bar chart showing adhesion test data for different gas pressures used in copper deposition on PA66 with and without a tin bond coat Sprayed using gas at 298 K and powder feed rate of 0.5 g s^{-1}. 2 passes of the gun at a traverse speed of 0.3 m s^{-1} were used. Deposits formed at 11 bar and 29 bar pressure on PA66 de-bonded at loads of ~ 0 in pull-off tests. Tin deposited as per conditions described in **Tables 5.19**.

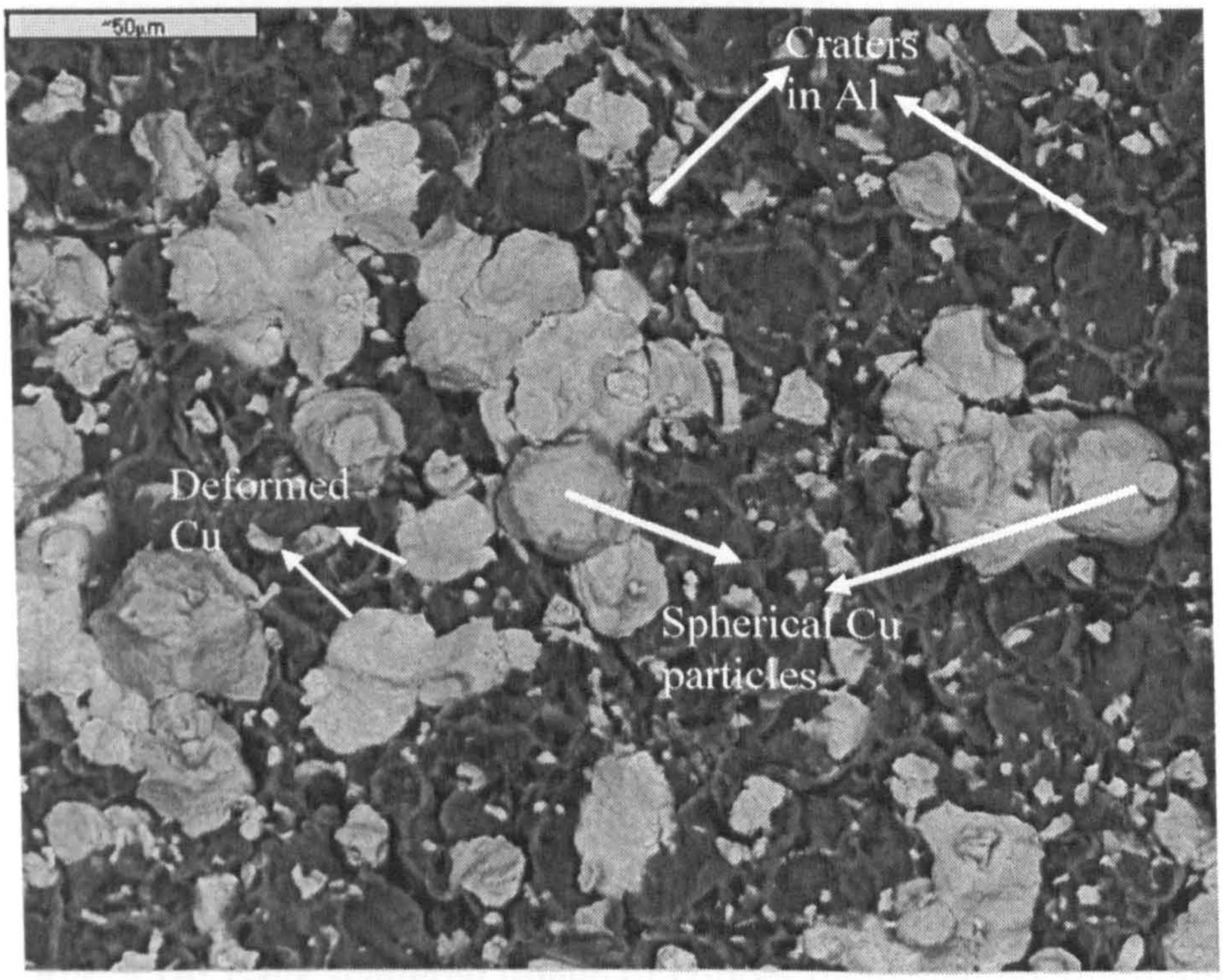

Fig. 5.14: Back scattered image of copper deposited on aluminium at 11 bar and 298 K showing both deformed and un-deformed particles. Deposition using traverse speed of 0.5 m s^{-1} and powder feed rate of 0.25 g s^{-1}.

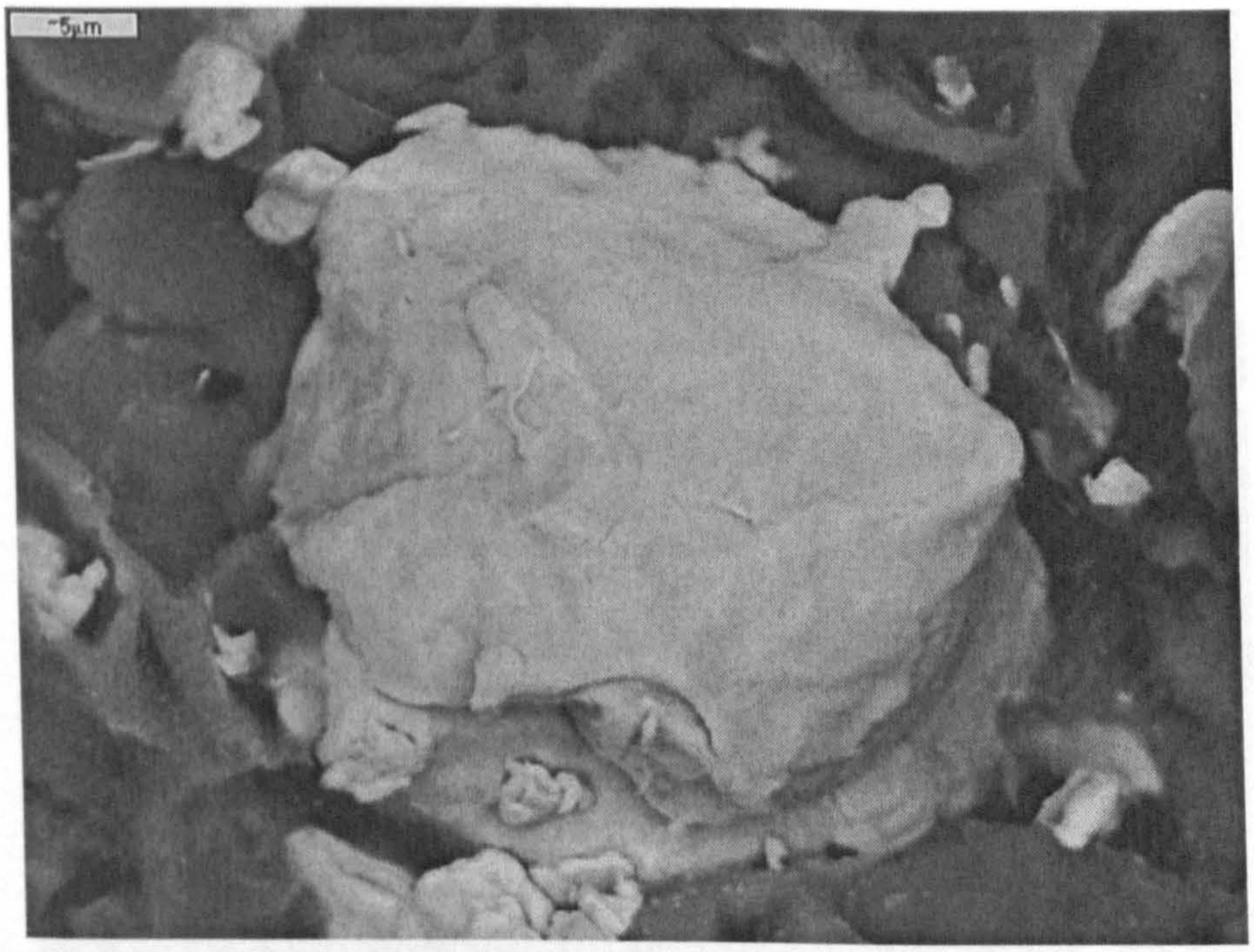

Fig. 5.15: BSE image of copper deposited on aluminium at 11 bar and 298 K showing deformation of copper particle due to impact of another copper particle. Deposition using traverse speed of 0.5 m s^{-1} and powder feed rate of 0.25 g s^{-1}.

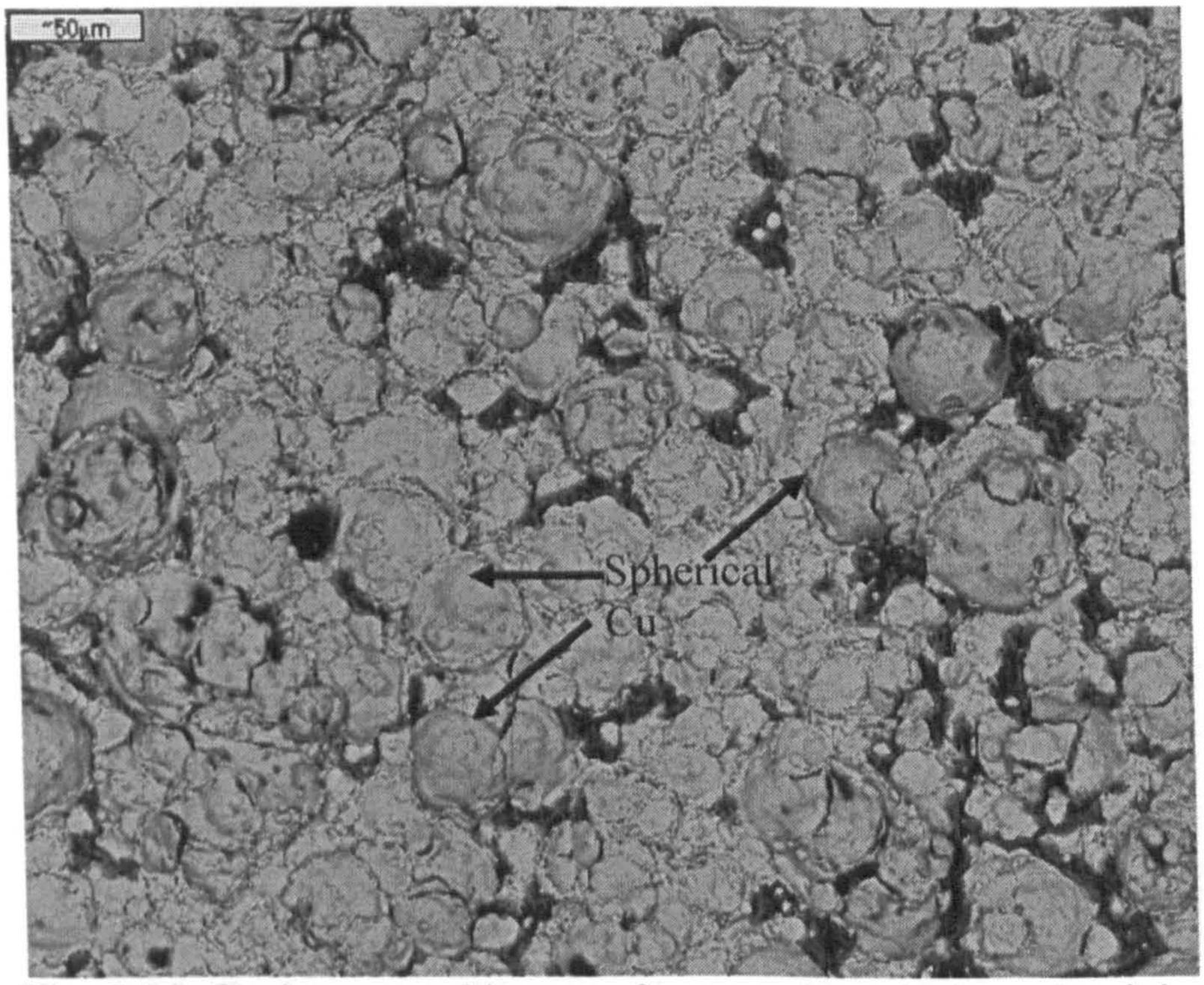

Fig. 5.16: Back scattered image of copper deposited on aluminium at 29 bar and 298 K showing largely deformed copper particles. A few spherical copper particles are also seen. Deposition using traverse speed of 0.5 m s^{-1} and powder feed rate of 0.25 g s^{-1}.

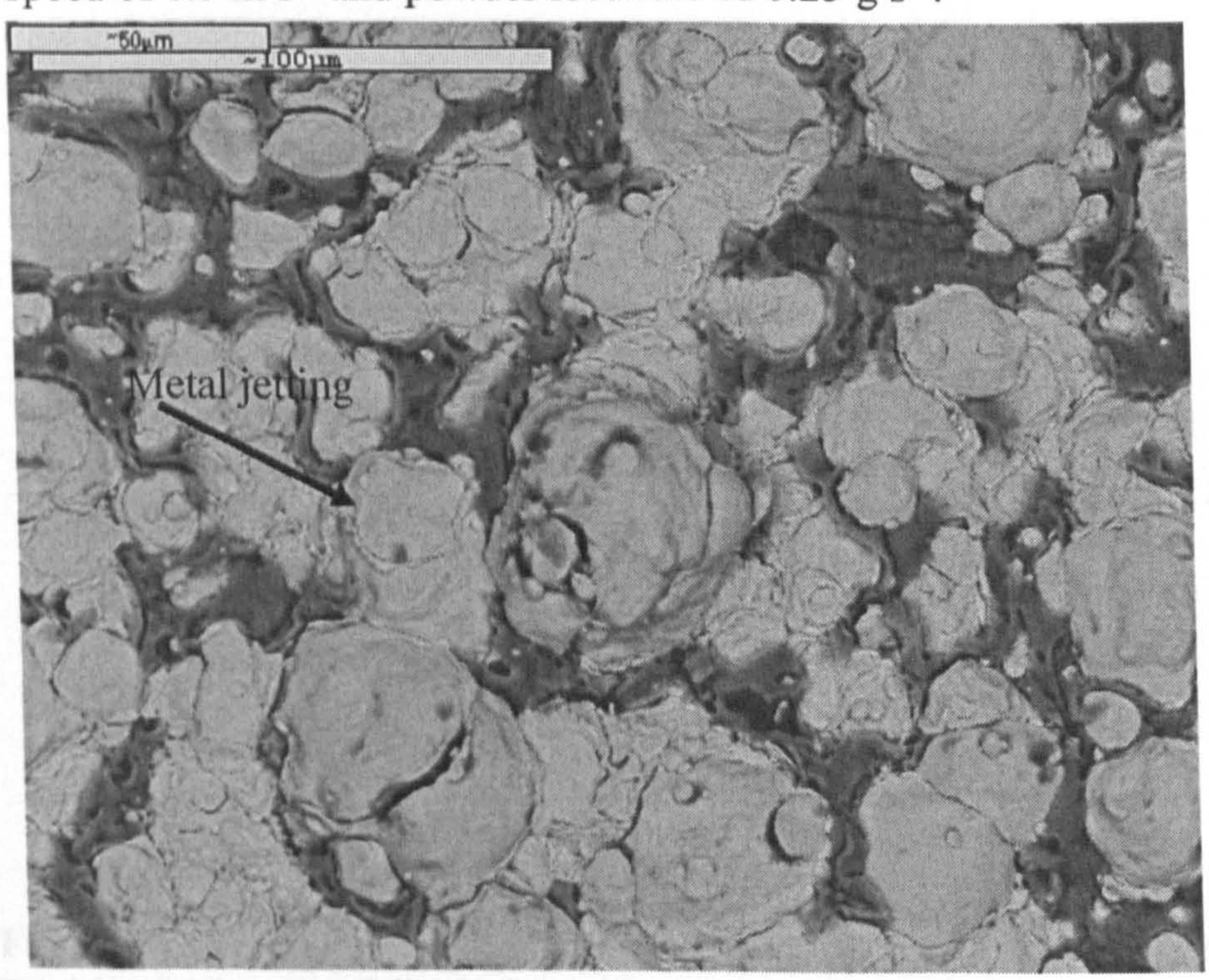

Fig. 5.17: Back scattered image of copper deposited on aluminium at 29 bar and 298 K showing deformation and metal jetting in copper. Deposition using traverse speed of 0.5 m s^{-1} and powder feed rate of 0.25 g s^{-1}.

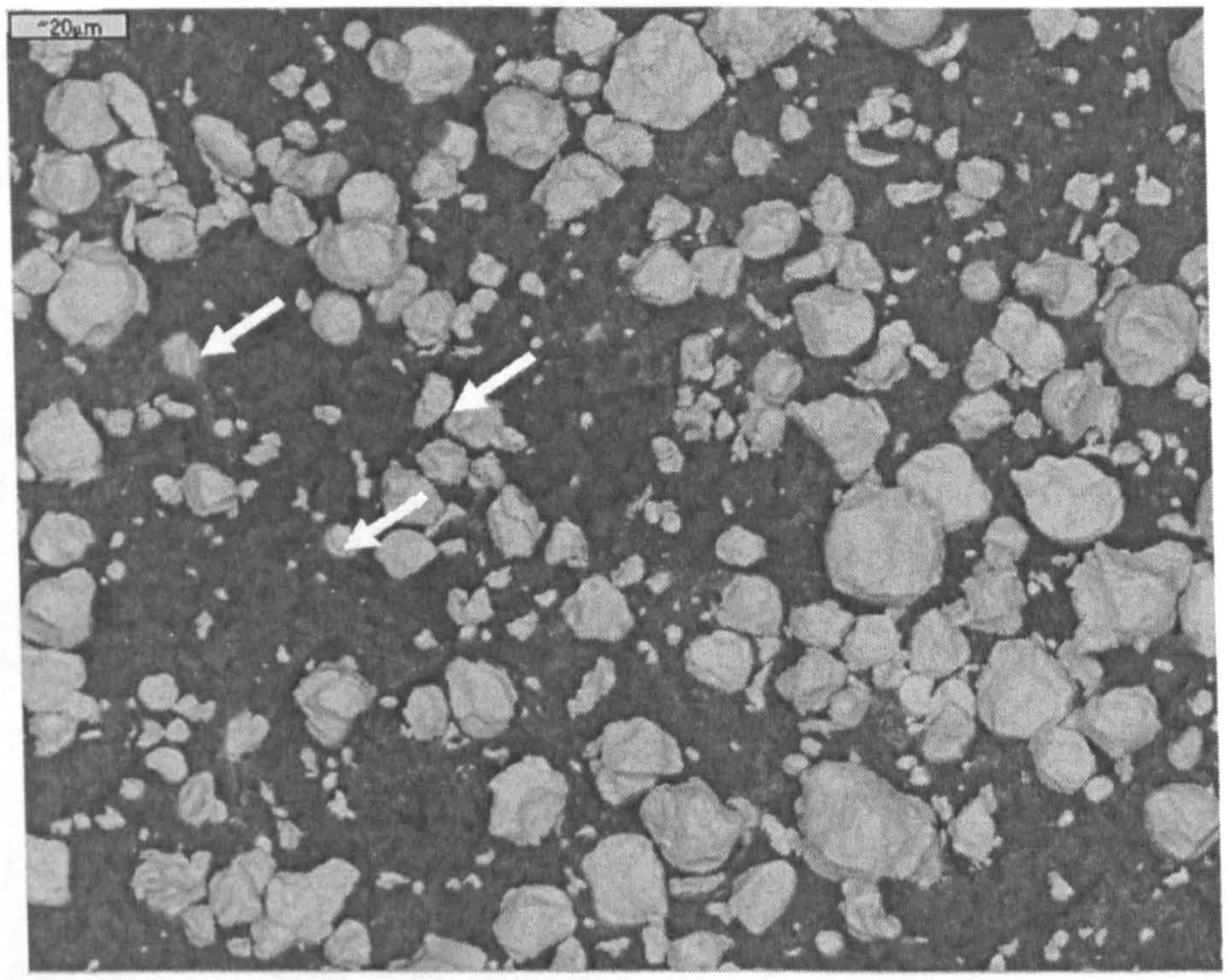

Fig. 5.18: Back scattered image of copper deposited on PA66 at 11 bar and 298 K. Largely un-deformed copper particles are seen embedded (shown by arrows) in PA66. Deposition using traverse speed of 0.5 m s^{-1} and powder feed rate of 0.25 g s^{-1}.

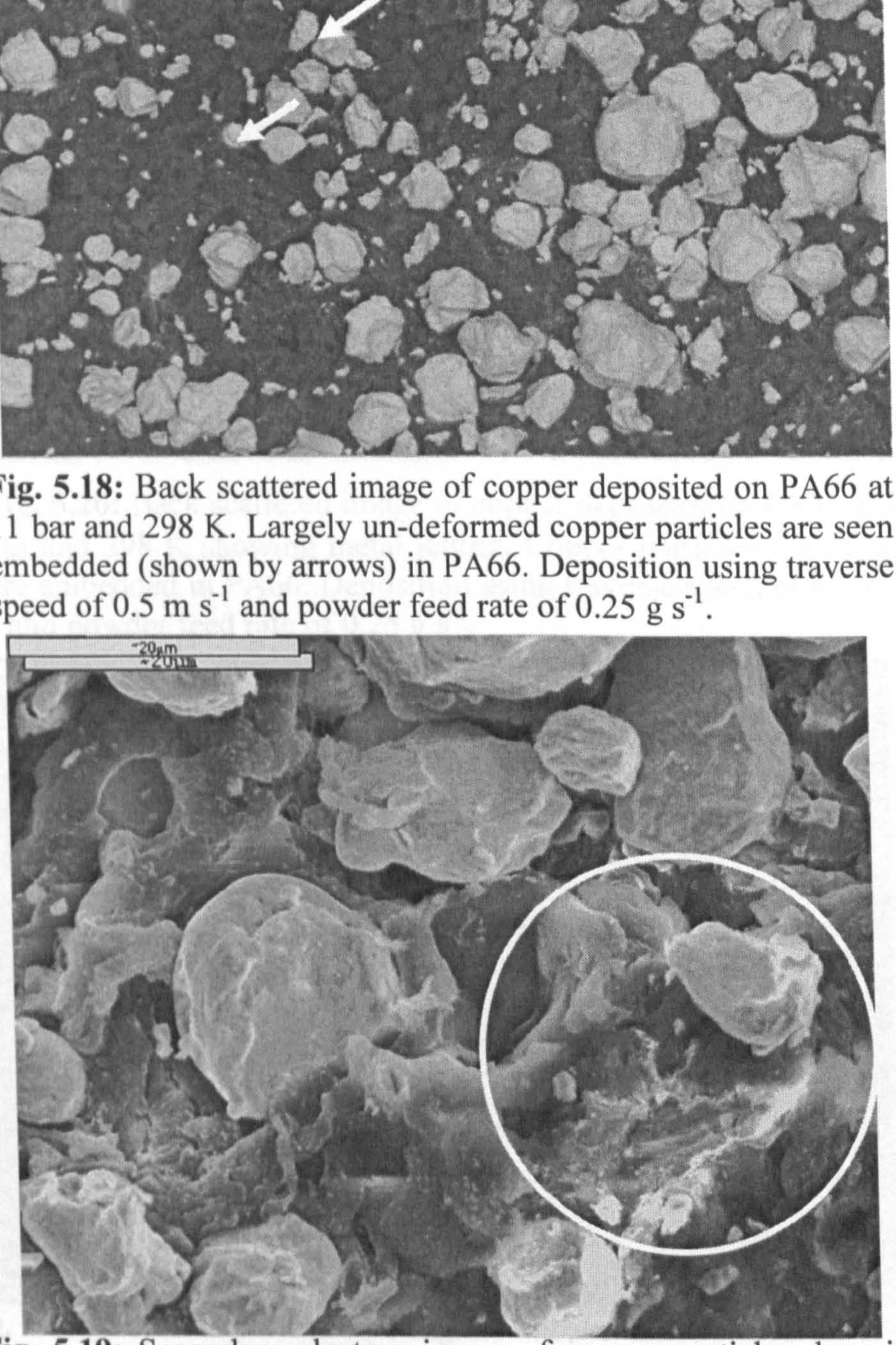

Fig. 5.19: Secondary electron image of copper particles deposited on PA66 at 11 bar and 298 K. Craters are formed in PA66 due to impact of copper particles (circled area). Deposition using traverse speed of 0.5 m s^{-1} and powder feed rate of 0.25 g s^{-1}.

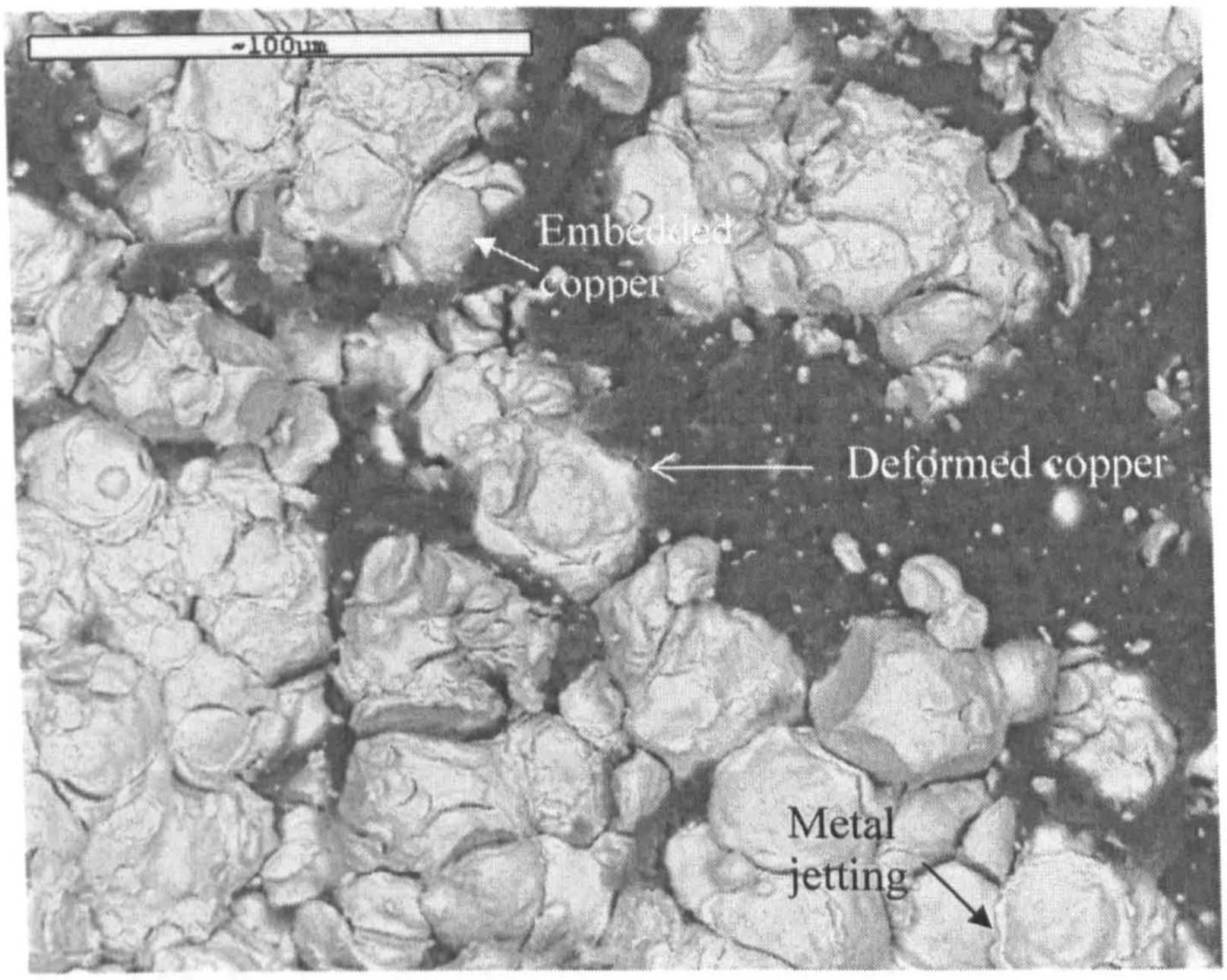

Fig. 5.20: Back scattered image of copper deposited on PA66 at 29 bar and 298 K showing metal jetting. Copper particles ~ ϕ 25 μm are embedded in PA66. Deposition using traverse speed of 0.5 m s^{-1} and powder feed rate of 0.25 g s^{-1}.

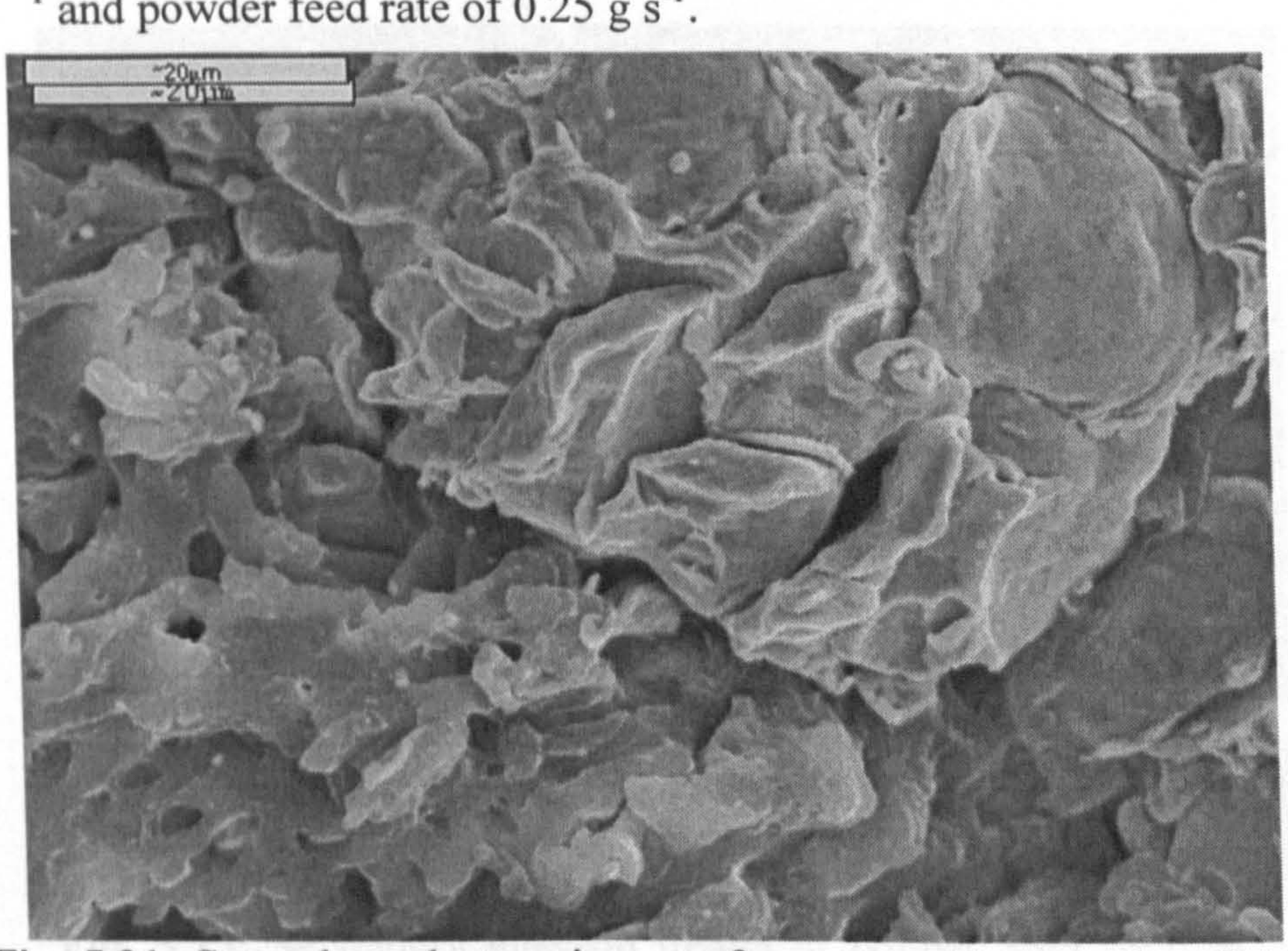

Fig. 5.21: Secondary electron image of copper cold sprayed on PA66 at 29 bar and 298 K showing the erosion of PA66 substrate due to impact of copper (lower left hand corner). Deformed copper particle is seen in the upper right hand corner. Deposition using traverse speed of 0.5 m s^{-1} and powder feed rate of 0.25 g s^{-1}.

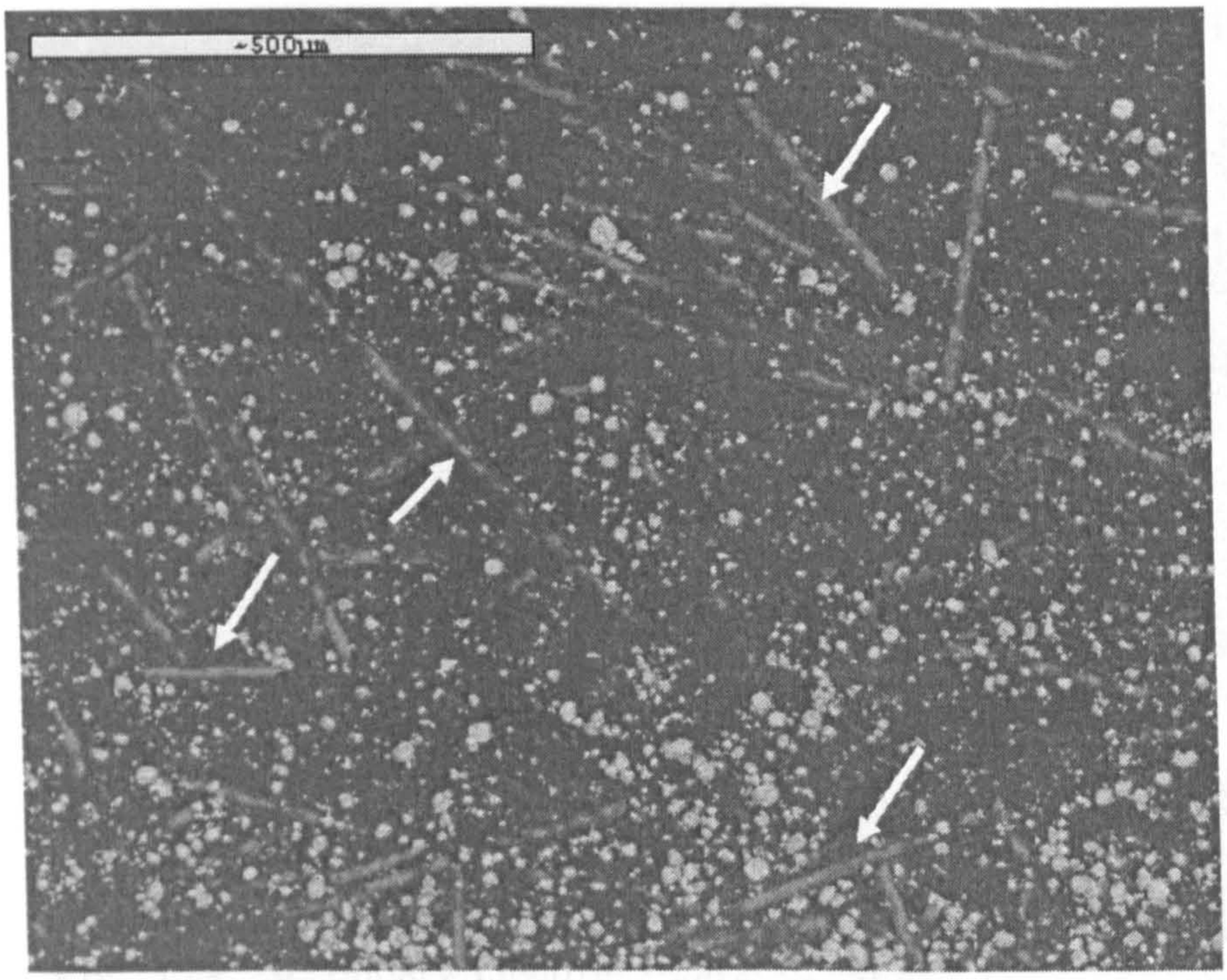

Fig. 5.22: Back scattered image of copper cold sprayed on PA6T at 11 bar and 298 K. The glass fibres are exposed by the impact (shown by arrows). Copper particles are seen embedded in the nylon. Deposition using traverse speed of 0.5 m s^{-1} and powder feed rate of 0.25 g s^{-1}.

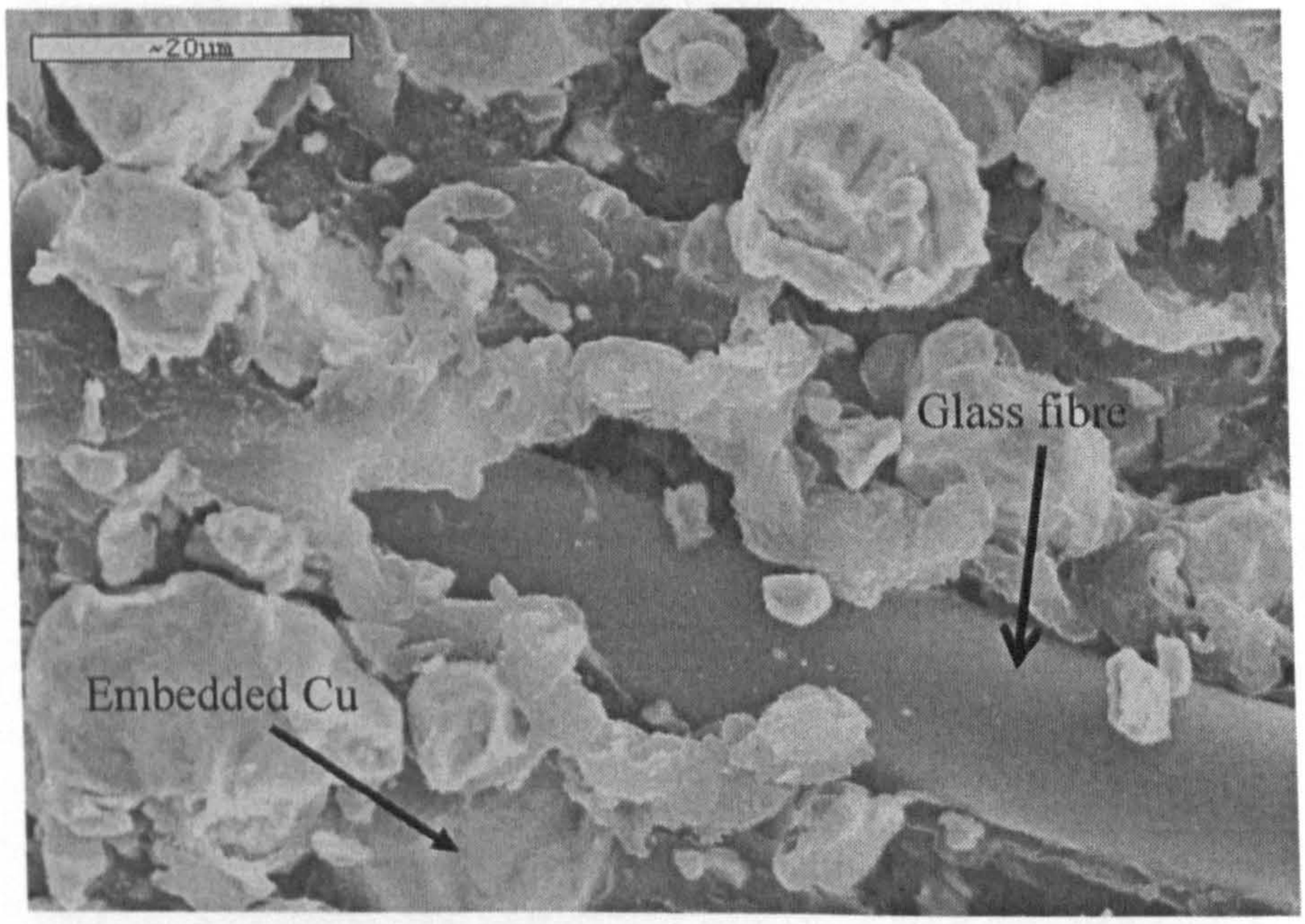

Fig. 5.23: Secondary electron image of copper cold sprayed on PA6T at 11 bar and 298 K. The glass fibre is relatively undamaged but the surrounding nylon matrix is fractured. Copper particles are seen embedded in nylon. Deposition using traverse speed of 0.5 m s^{-1} and powder feed rate of 0.25 g s^{-1}.

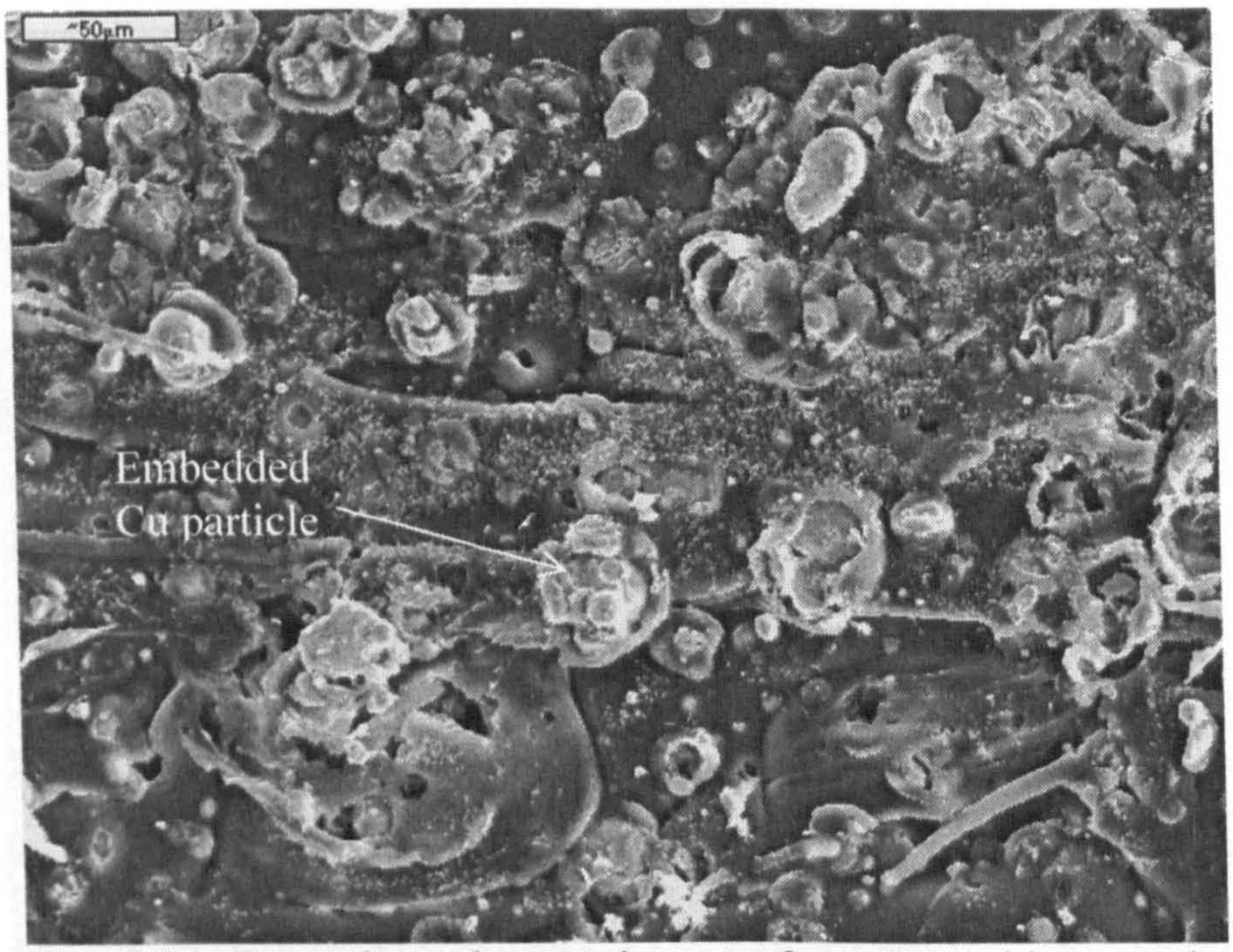

Fig. 5.24: Secondary electron image of copper cold sprayed on PA6T at 29 bar and 298 K respectively. Very few glass fibres are seen and the substrate is heavily fractured. Deposition using traverse speed of 0.5 m s^{-1} and powder feed rate of 0.25 g s^{-1}.

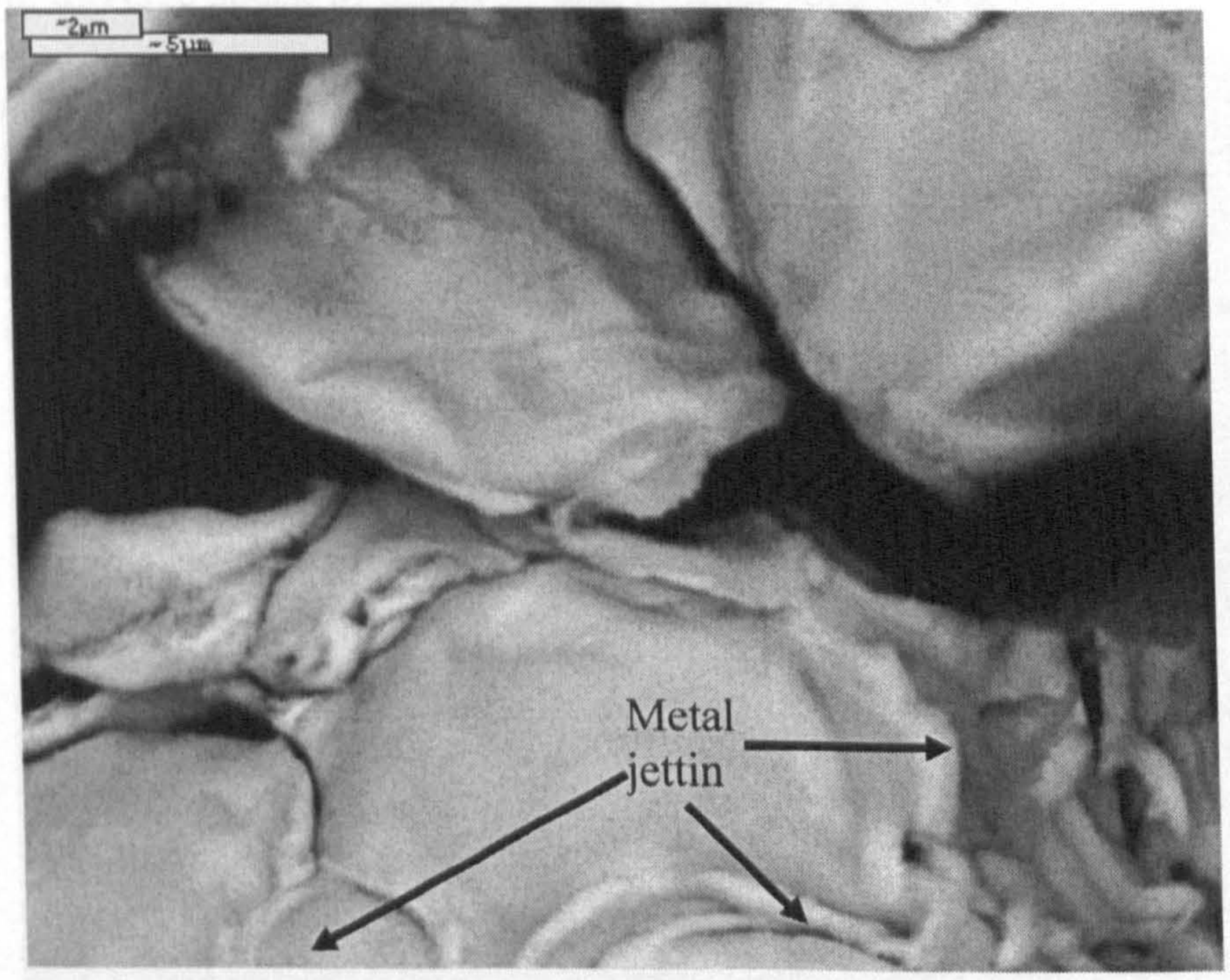

Fig. 5.25: Back scattered image of copper cold sprayed on PA6T at 29 bar and 298 K showing deformation and metal jetting in copper (shown by arrows). Copper is deeply embedded in PA6T. Deposition using traverse speed of 0.5 m s^{-1} and powder feed rate of 0.25 g s^{-1}.

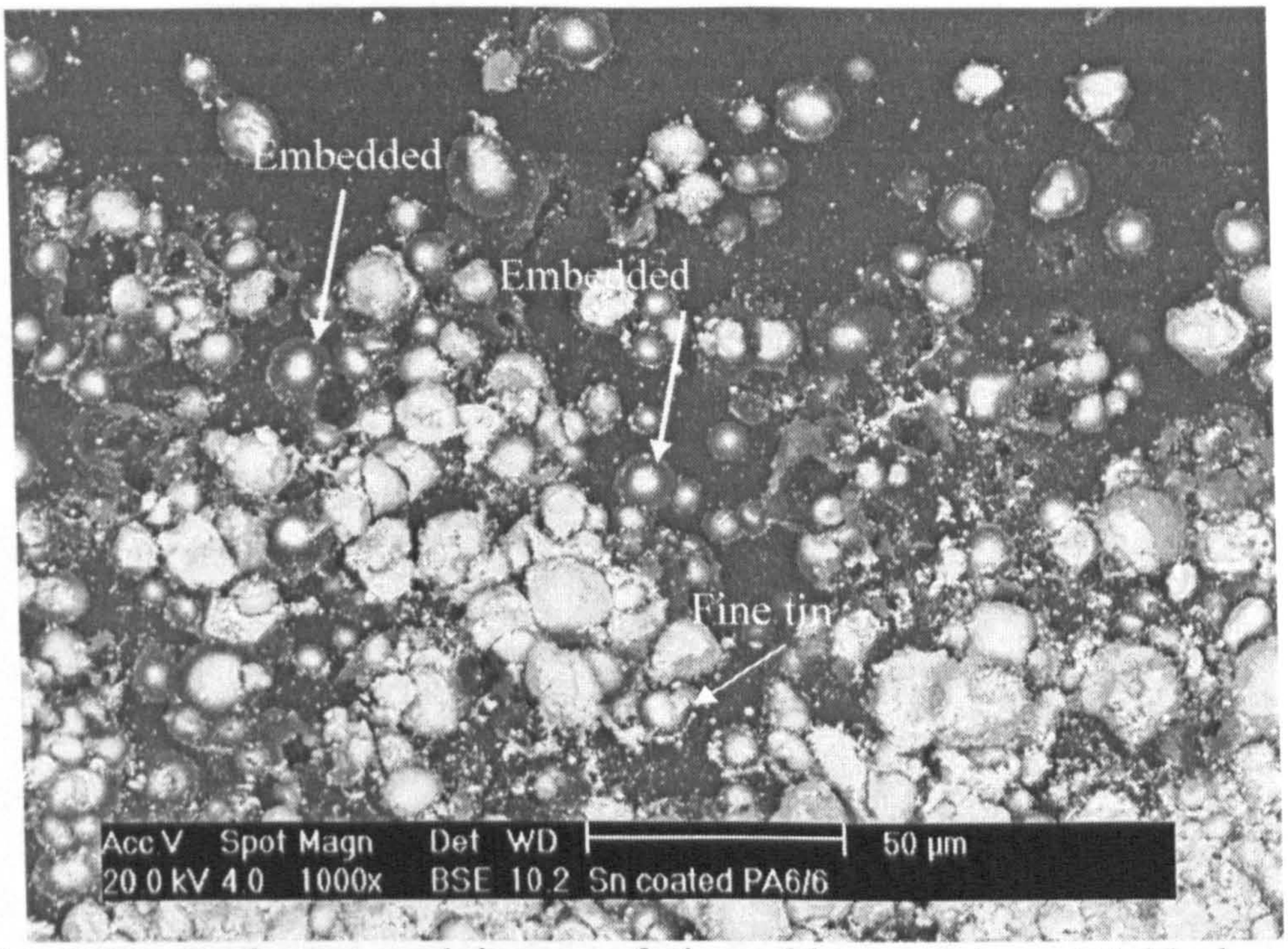

Fig. 5.26: Back scattered image of tin cold sprayed on PA66 showing plastic deformation of PA66 where tin is embedded. Deposition using conditions described in **Table 5.19** but using a traverse speed of 0.5 m s^{-1}.

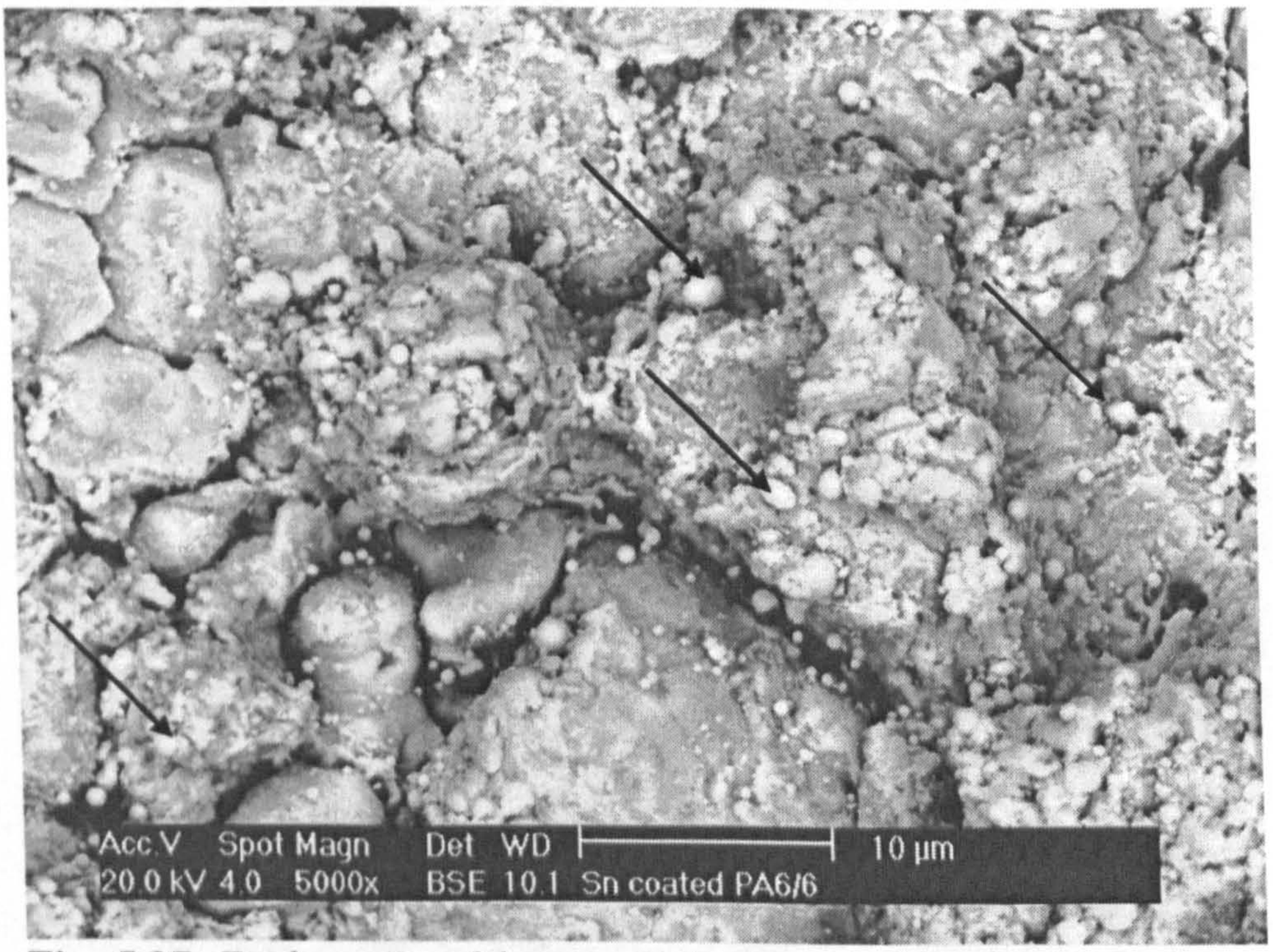

Fig. 5.27: Back scattered image of Sn deposited on PA66. Deformed tin particles form a matrix of tin where other tin particles are embedded. Fine particles of tin are shown by arrows. Deposition using conditions described in **Table 5.19** but using a traverse speed of 0.5 m s^{-1}.

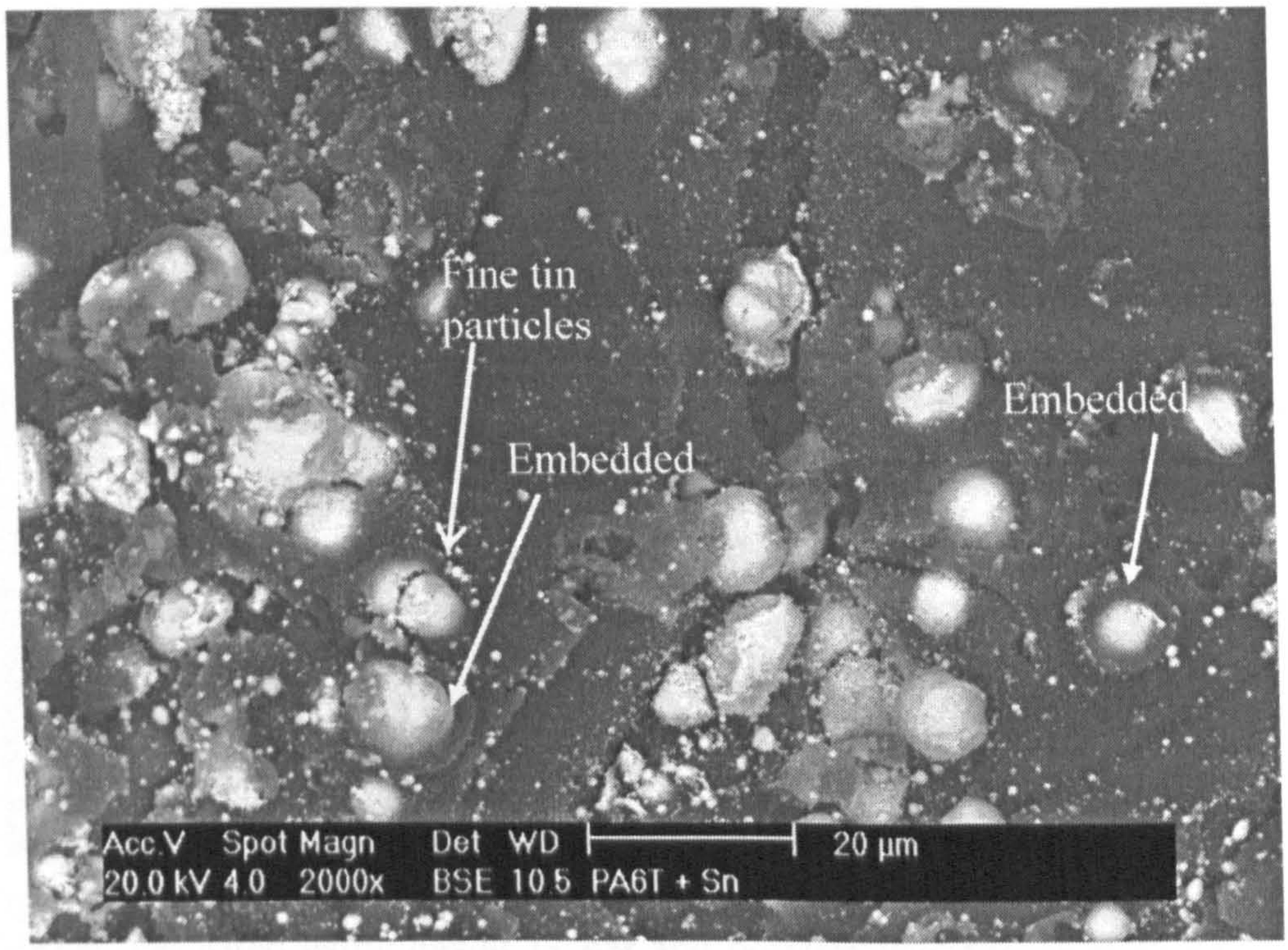

Fig. 5.28: BSE image of tin deposited on PA6T. PA6T is plastically deformed in places where tin is embedded. Deposition using conditions described in **Table 5.19** but using a traverse speed of 0.5 m s^{-1}.

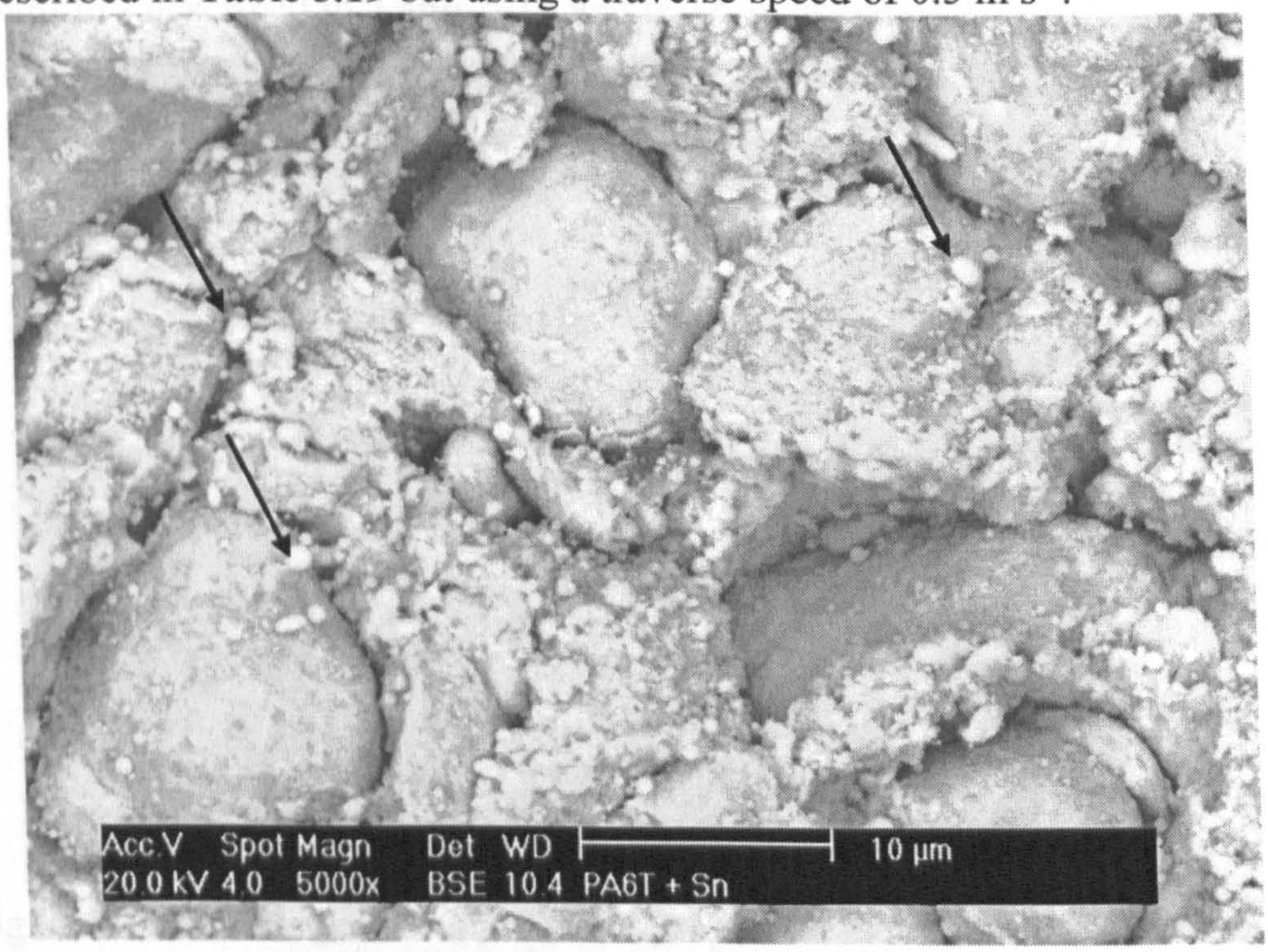

Fig. 5.29: Back scattered image of tin deposited on PA6T showing tin particles embedded in the previously deposited tin particles. Fine tin particles are seen (shown by arrows). Deposition using conditions described in **Table 5.19** but using a traverse speed of 0.5 m s^{-1}.

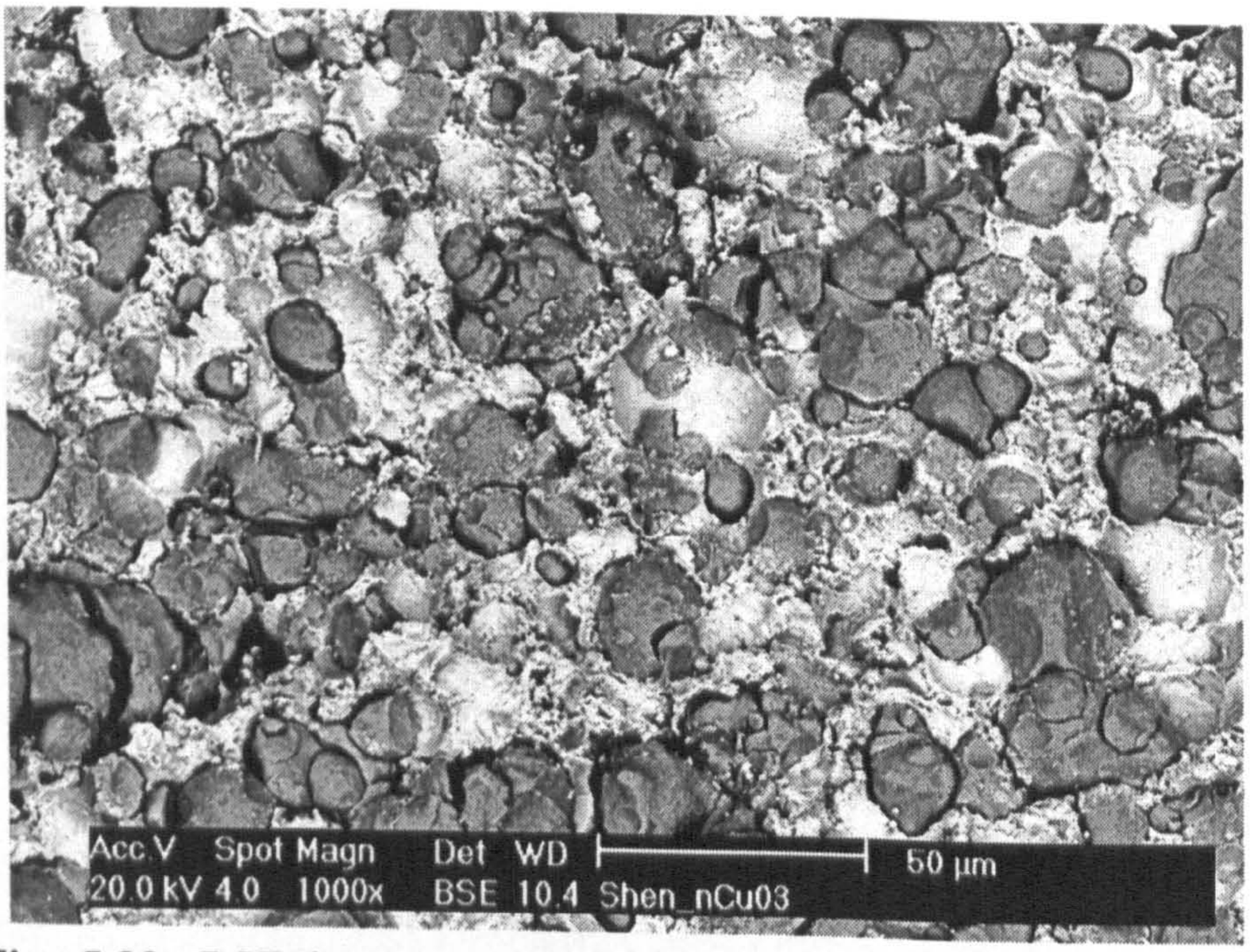

Fig. 5.30: BSE image of impact of copper particles on PA66 + Sn. Copper deposited using gas at 11 bar and powder feed rate of 0.25 g s^{-1}. Copper particles (darker phase) are embedded in tin (brighter phase). Copper particle maintains its spherical shape. Tin deposited using conditions described in **Table 5.19** and traverse speed of 0.5 m s^{-1}.

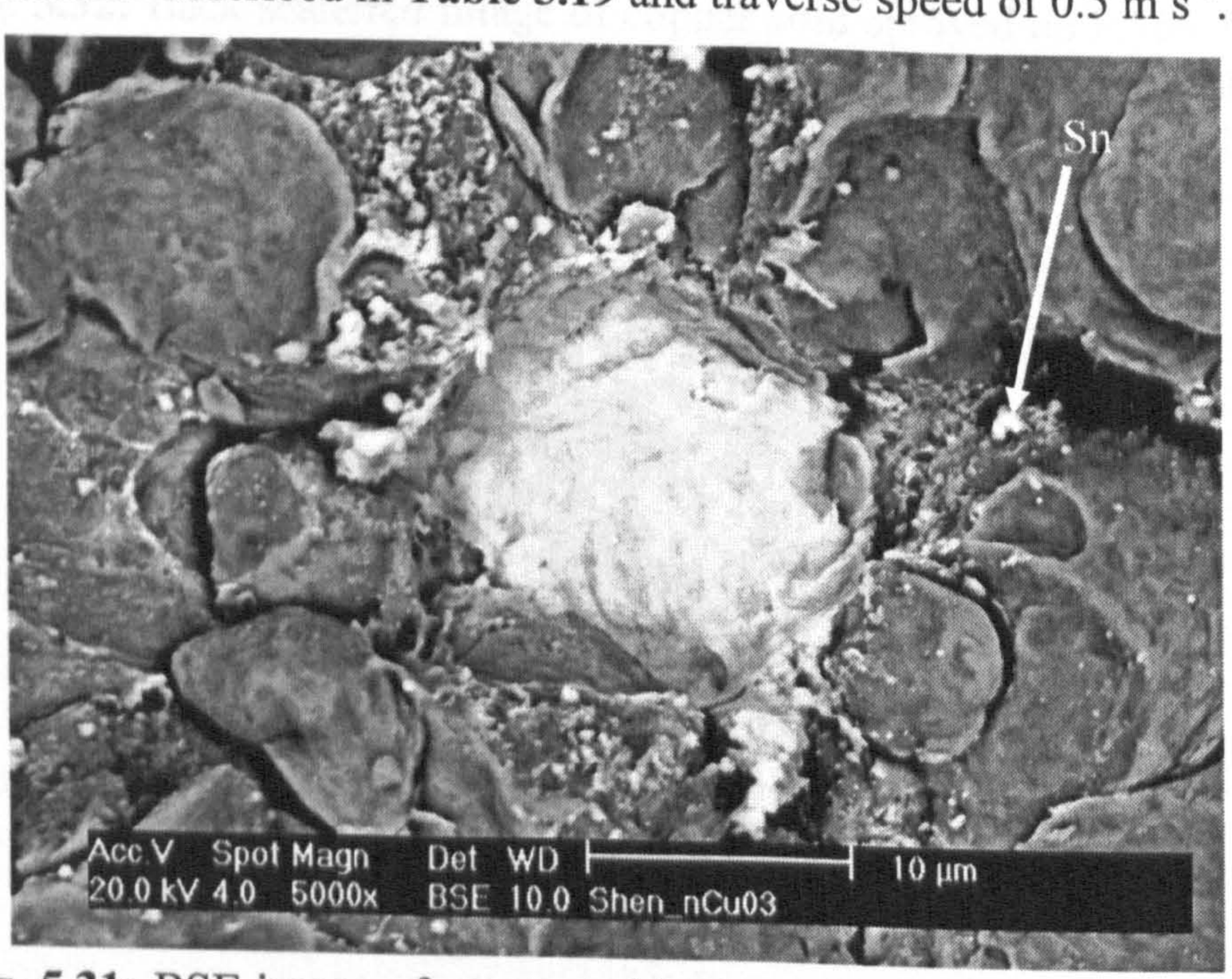

Fig. 5.31: BSE image of copper cold sprayed on PA66 + Sn at 11 bar and powder feed rate of 0.25 g s^{-1}, showing splashing in the form of fine particles of tin. The darker phase is identified as copper and the brighter phase is tin. Tin deposited using conditions described in **Table 5.19** and traverse speed of 0.5 m s^{-1}.

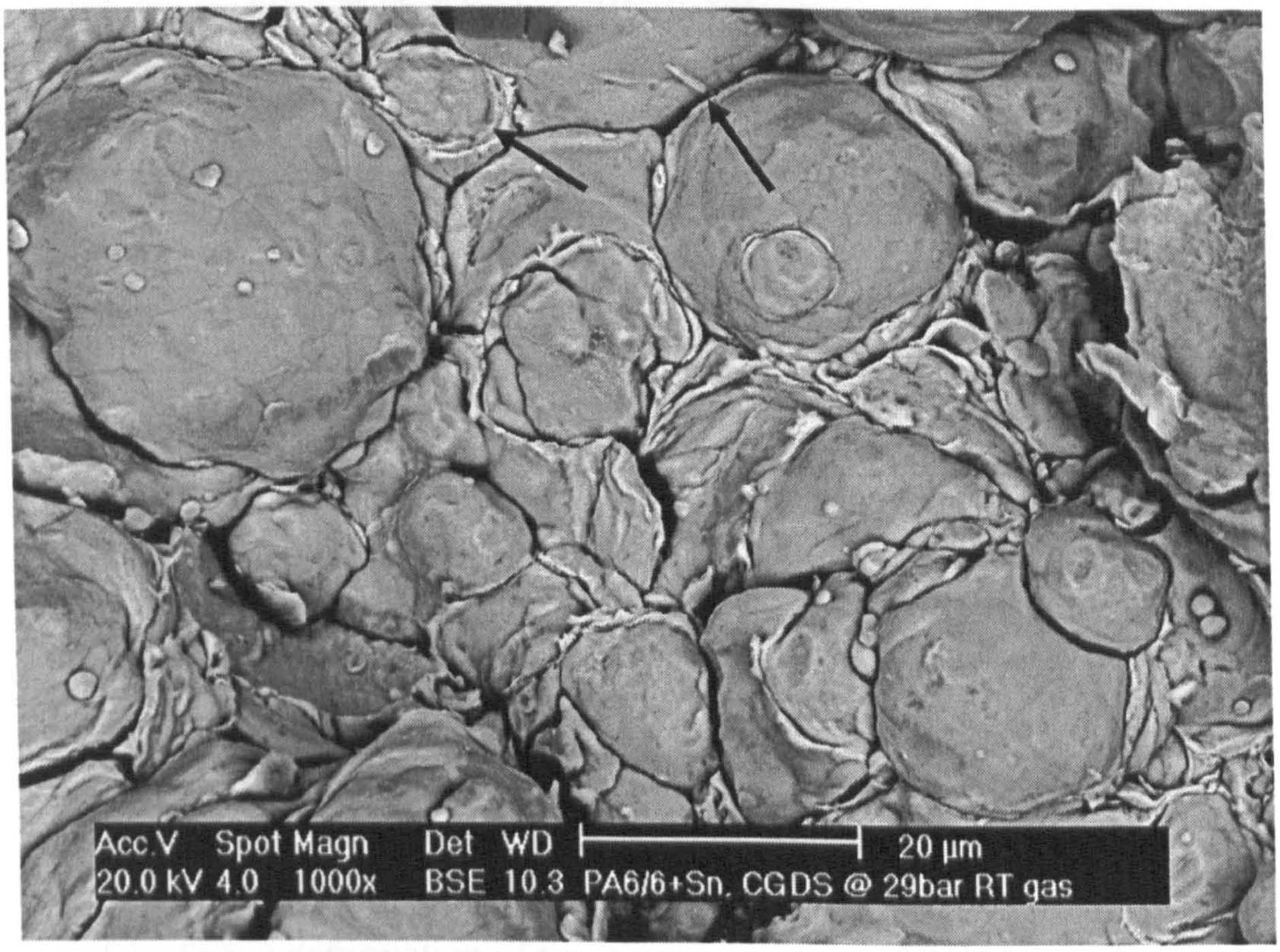

Fig. 5.32: Back scattered image of copper cold sprayed on PA66 + Sn at 29 bar using powder feed rate of 0.25 g s^{-1} showing deformation and metal jetting in copper (shown by arrows). Tin deposited using conditions described in **Table 5.19** and traverse speed of 0.5 m s^{-1}.

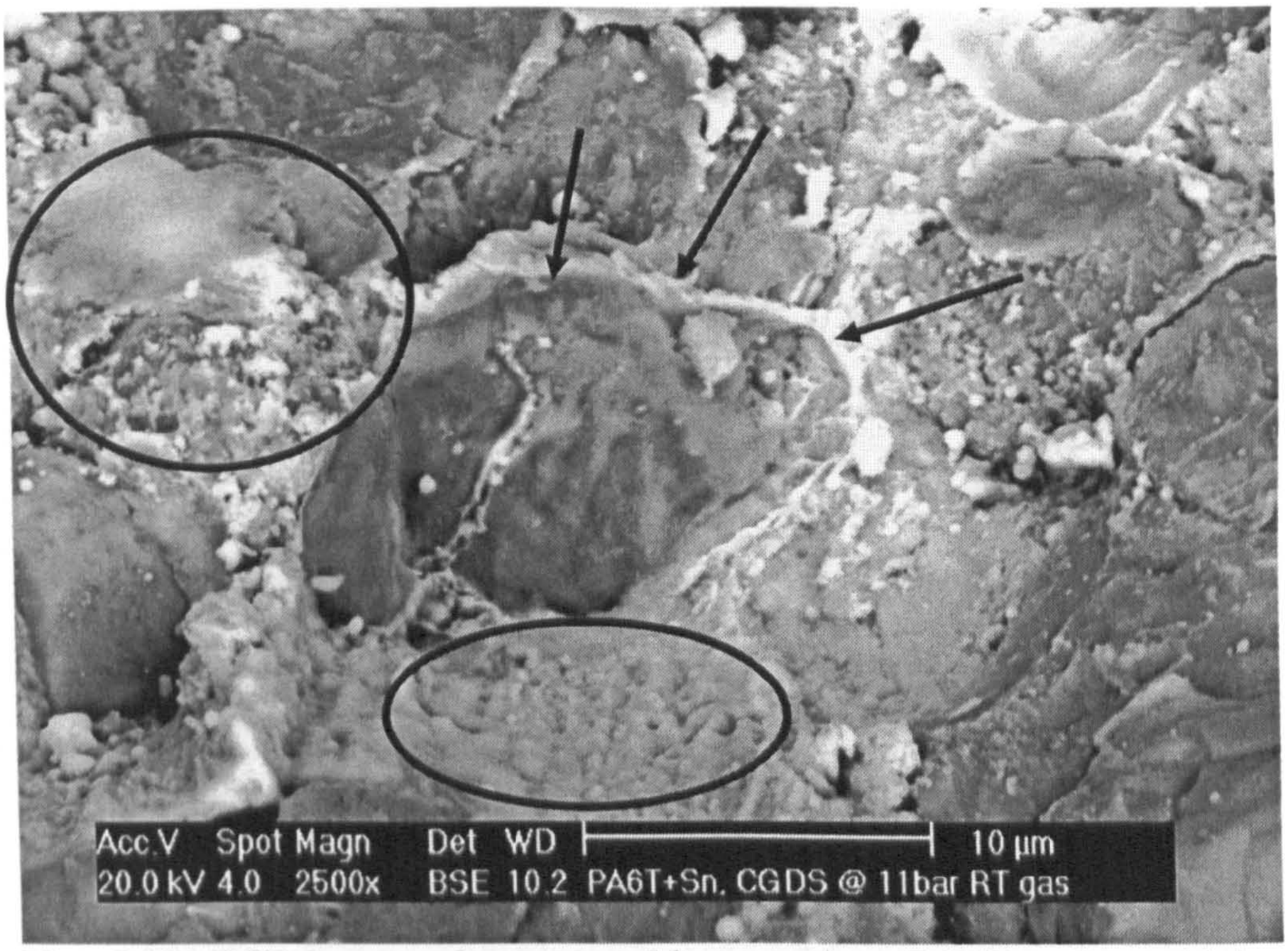

Fig. 5.33: BSE image of copper cold sprayed on PA6T + Sn at 11 bar using powder feed rate of 0.25 g s^{-1}, showing fine particles formed in tin and extensive deformation of tin (shown inside circle). Metal jetting in tin due to impact of copper is also seen (shown by arrows). Tin deposited using conditions described in **Table 5.19** and traverse speed of 0.5 m s^{-1}.

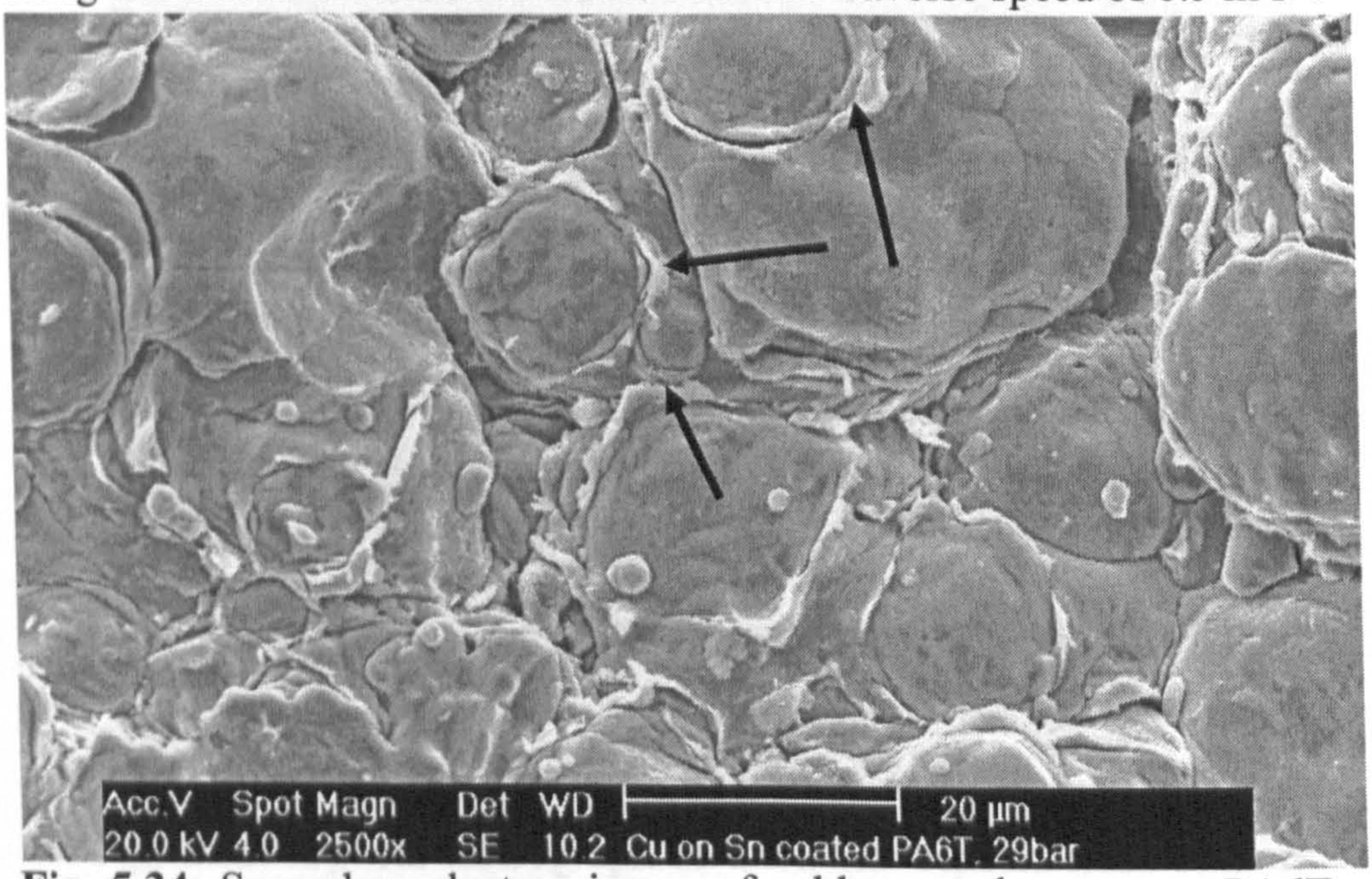

Fig. 5.34: Secondary electron image of cold sprayed copper on PA6T + Sn at 29 bar using powder feed rate of 0.25 g s^{-1}, showing deformation and metal jetting (shown by arrows). Tin deposited using conditions described in **Table 5.19** and traverse speed of 0.5 m s^{-1}.

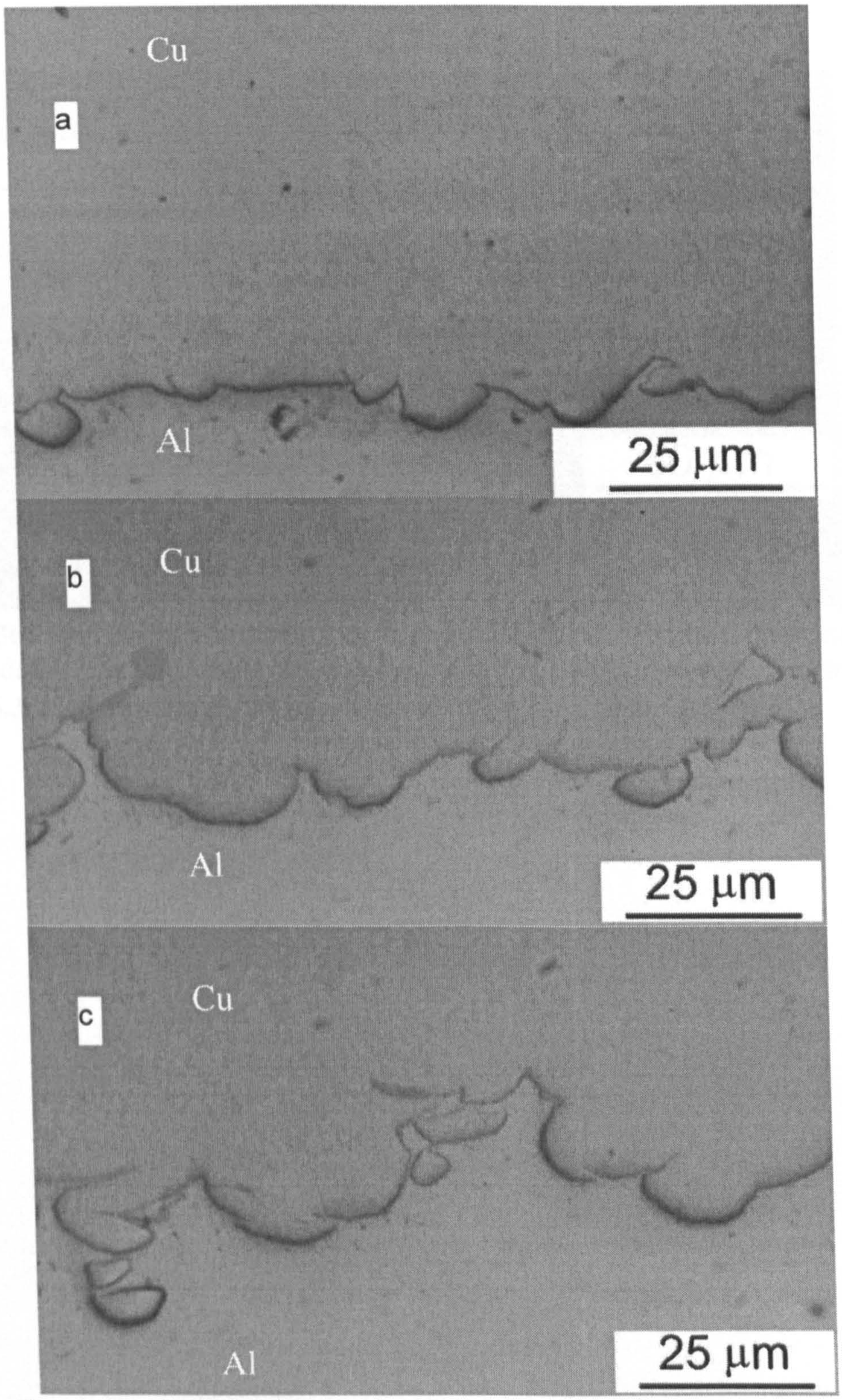

Fig. 5.35: Optical micrograph of unetched deposit cross sections showing the morphology of the interface, (a) 11 bar pressure; (b) 22 bar pressure; (c) 29 bar pressure. Deposition using conditions described in **Table 5.3**, powder feed rate of 0.5 g s^{-1} and 2 passes.

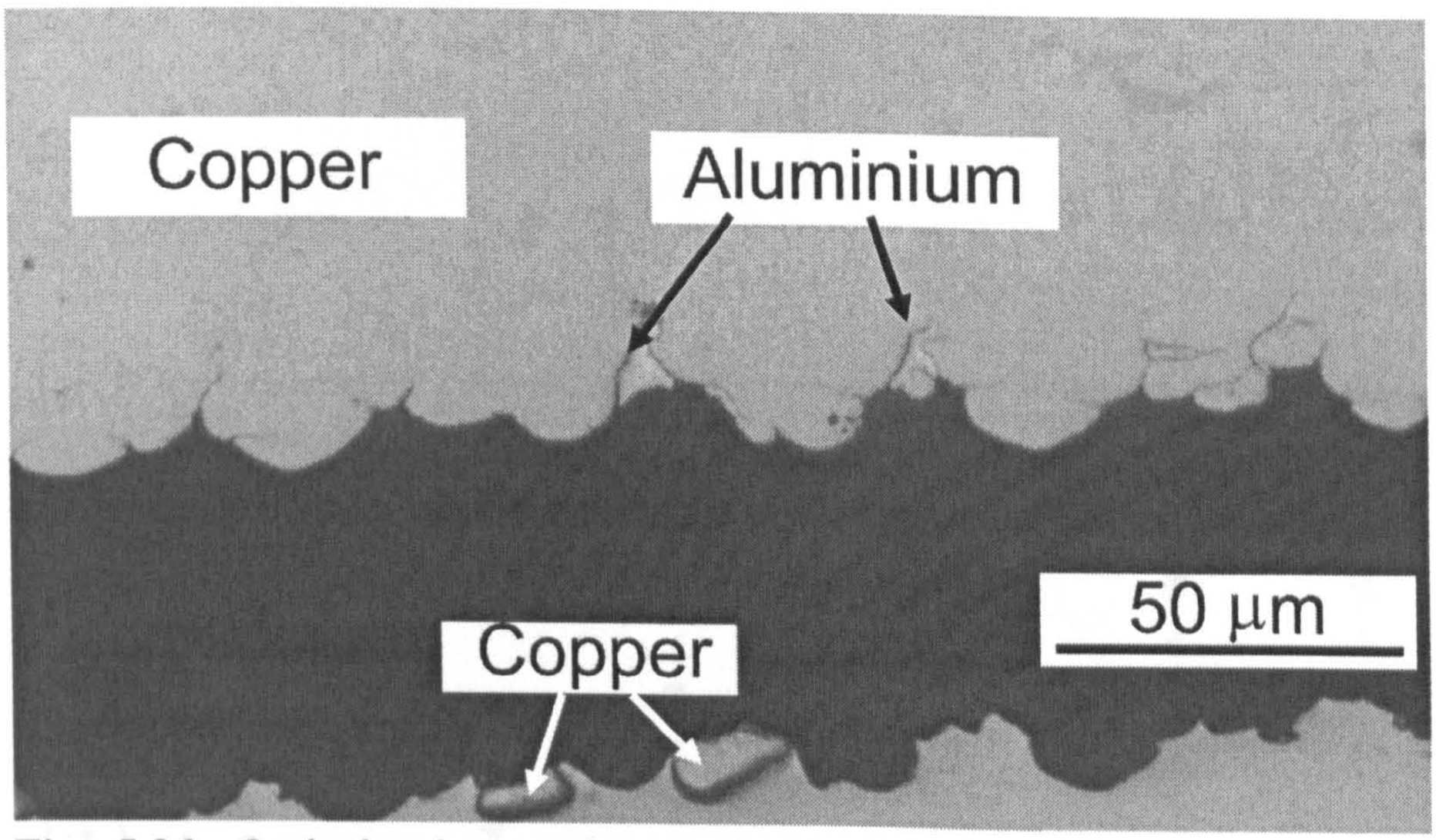

Fig. 5.36: Optical micrograph showing a de-bonded interface between copper deposit and Al substrate. Deposition using conditions described in **Table 5.3**, 29 bar pressure, powder feed rate of 1.0 g s^{-1} and 3 passes.

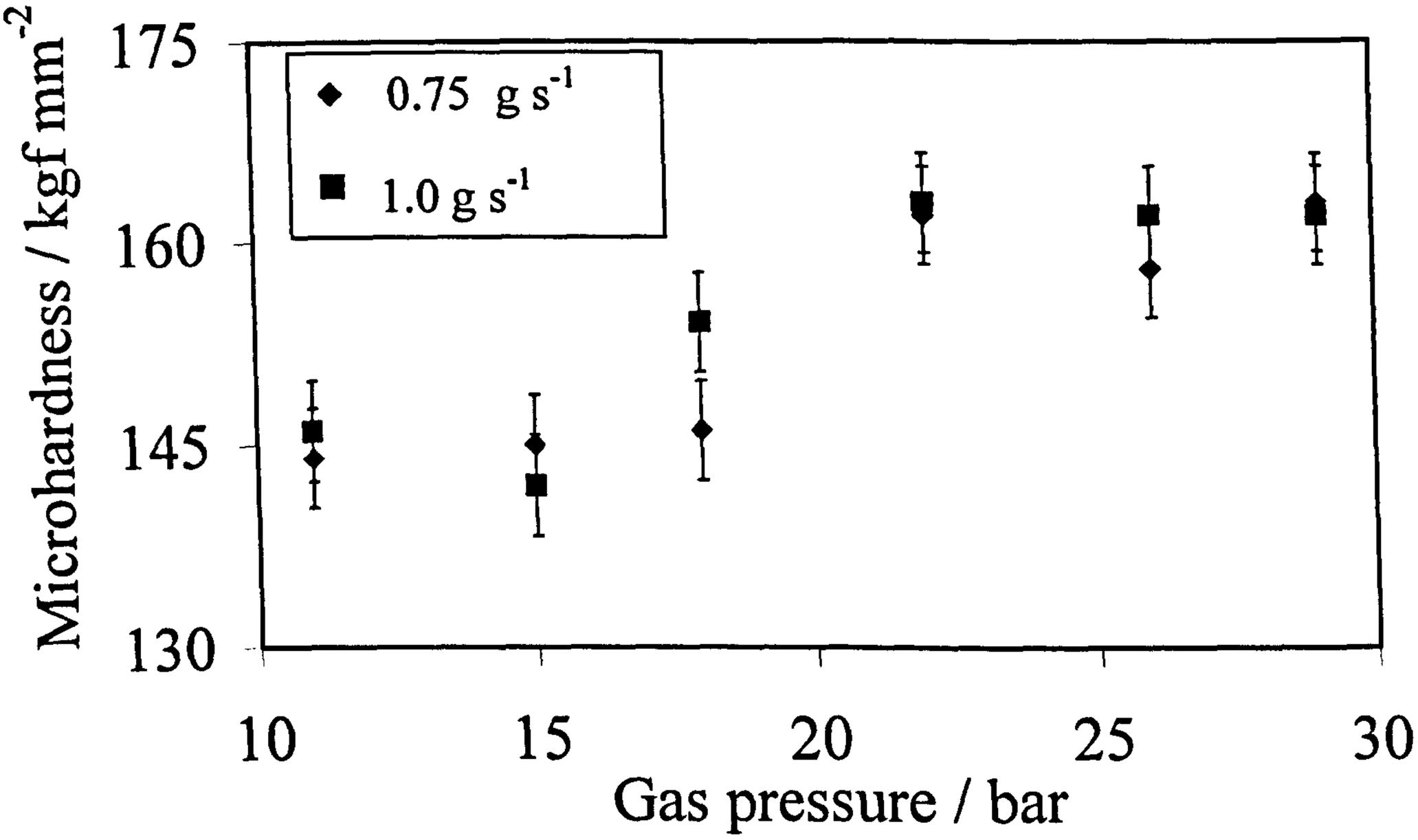

Fig. 5.37: Plot of microhardness of copper deposited using single pass on aluminium at different stagnation pressures for two different powder feed rates. Deposition using conditions described in **Table 5.3**.

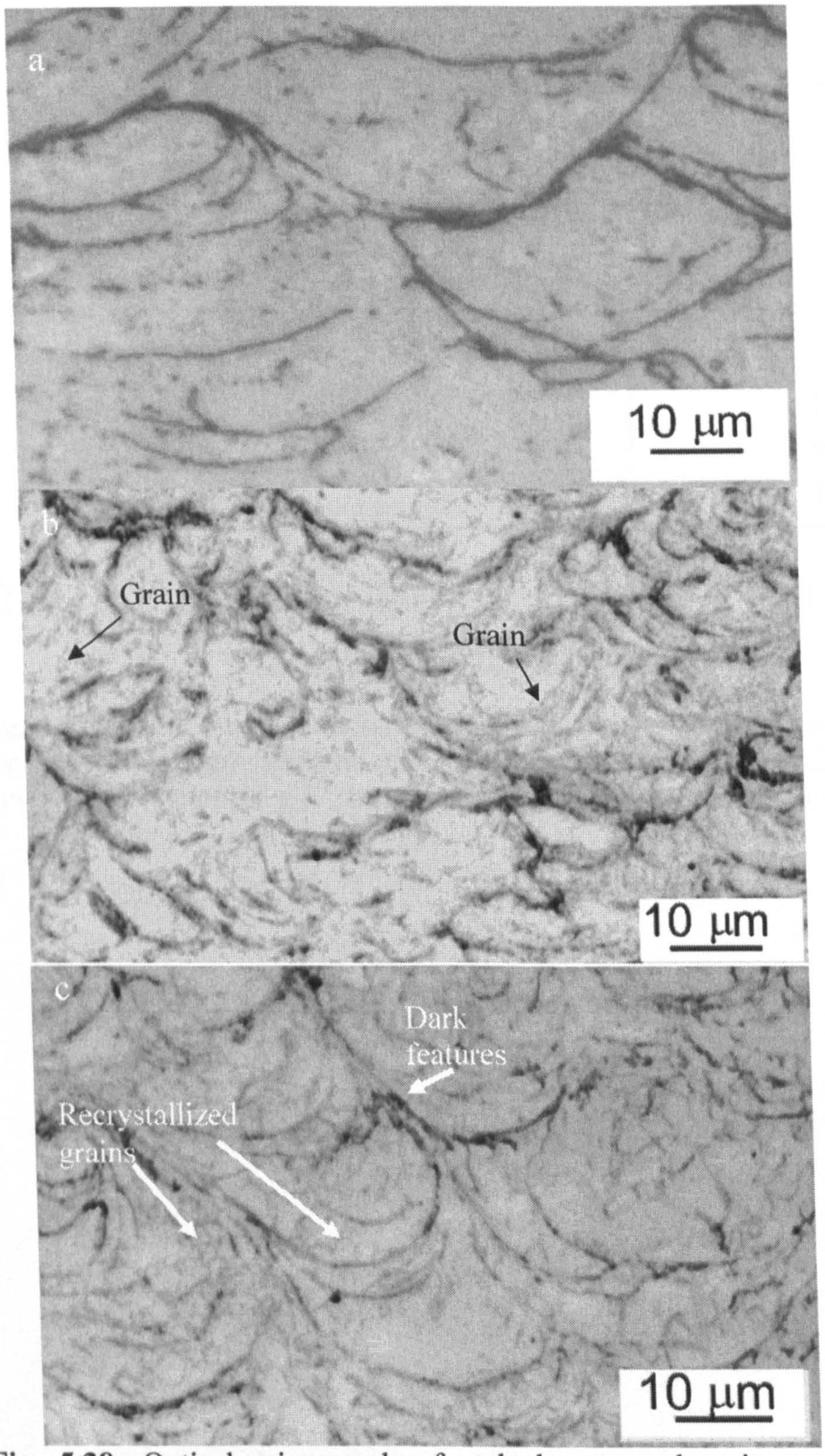

Fig. 5.38: Optical micrograph of etched copper deposit cross section, deposited at Yazaki using gas at 22 bar showing the particles and grains; (a), 298 K gas temperature; (b), 473 K gas temperature; (c), 673 K. Deposition using powder feed rate of 0.5 g s^{-1} and traverse speed of 0.05 m s^{-1} and two passes.

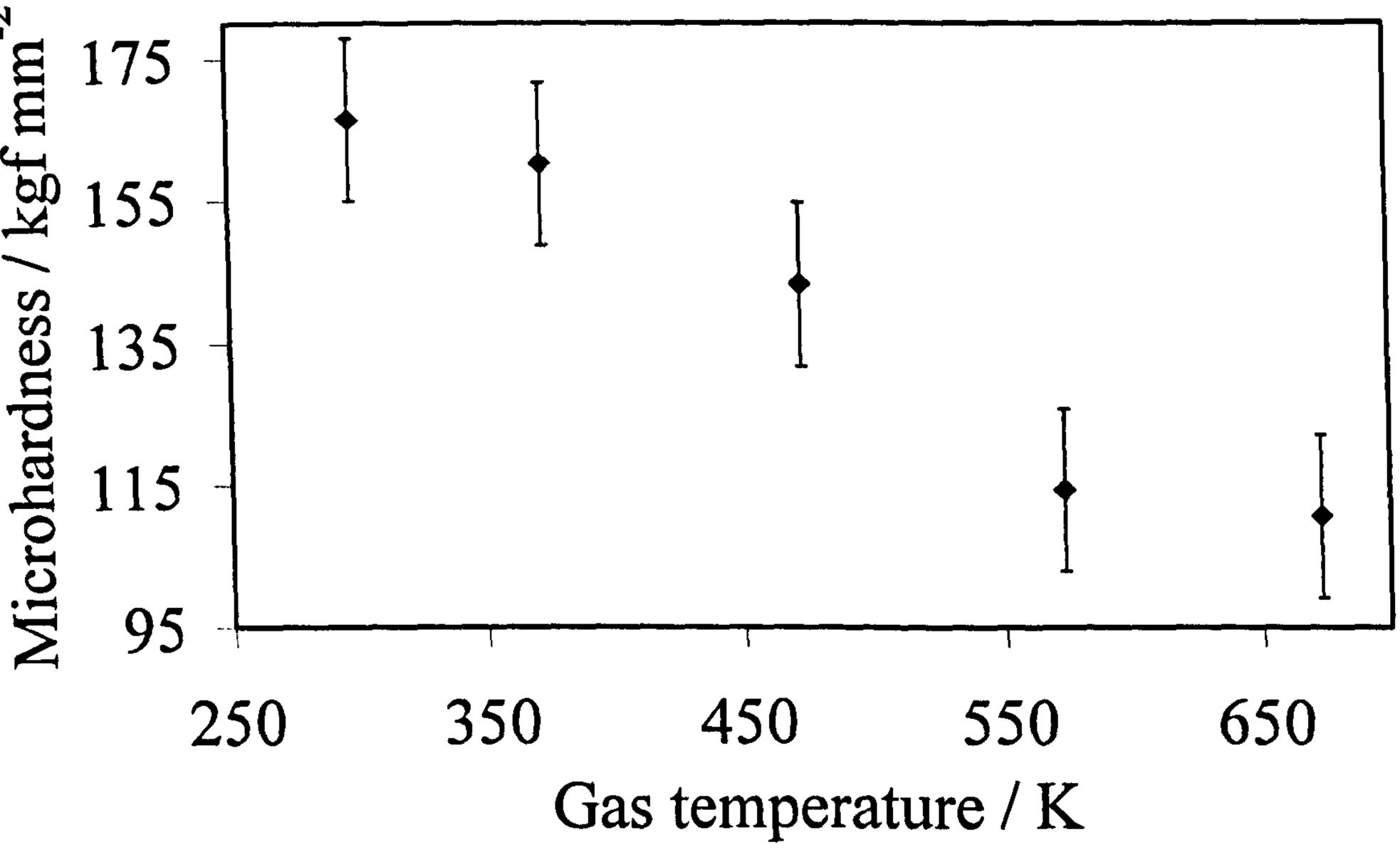

Fig. 5.39: Plot of microhardness versus gas temperature of cold sprayed copper on aluminium. Deposition at Yazaki using gas pressure of 22 bar, powder feed rate of 0.5 g s^{-1}, traverse speed of 0.05 m s^{-1} and 2 passes.

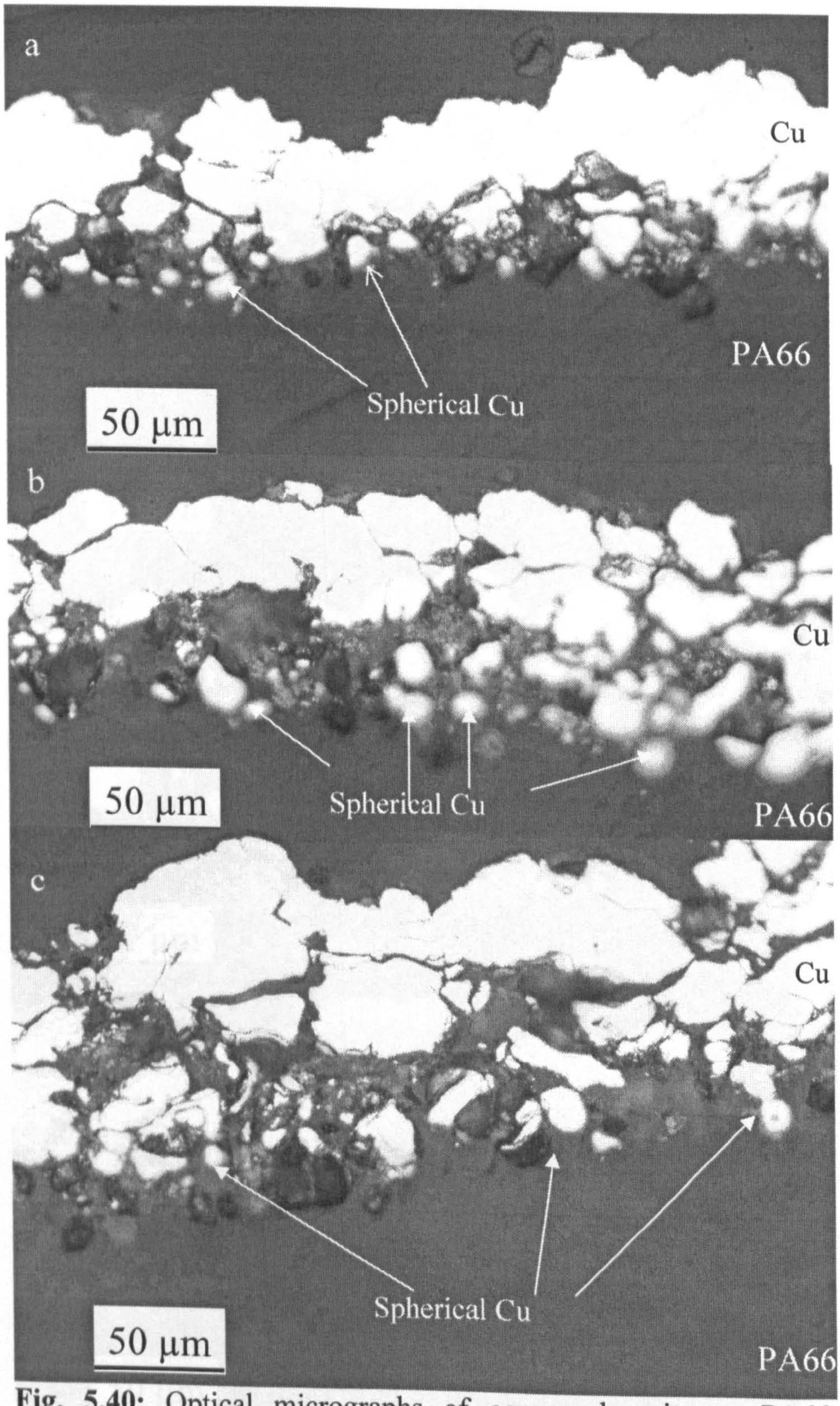

Fig. 5.40: Optical micrographs of copper deposits on PA66; deposited using gas at 298 K and conditions described in **Table 5.17** and process gas pressure of; a, 11 bar; b, 22 bar; c, 29 bar. Powder feed rate of 0.5 g s^{-1} and single pass.

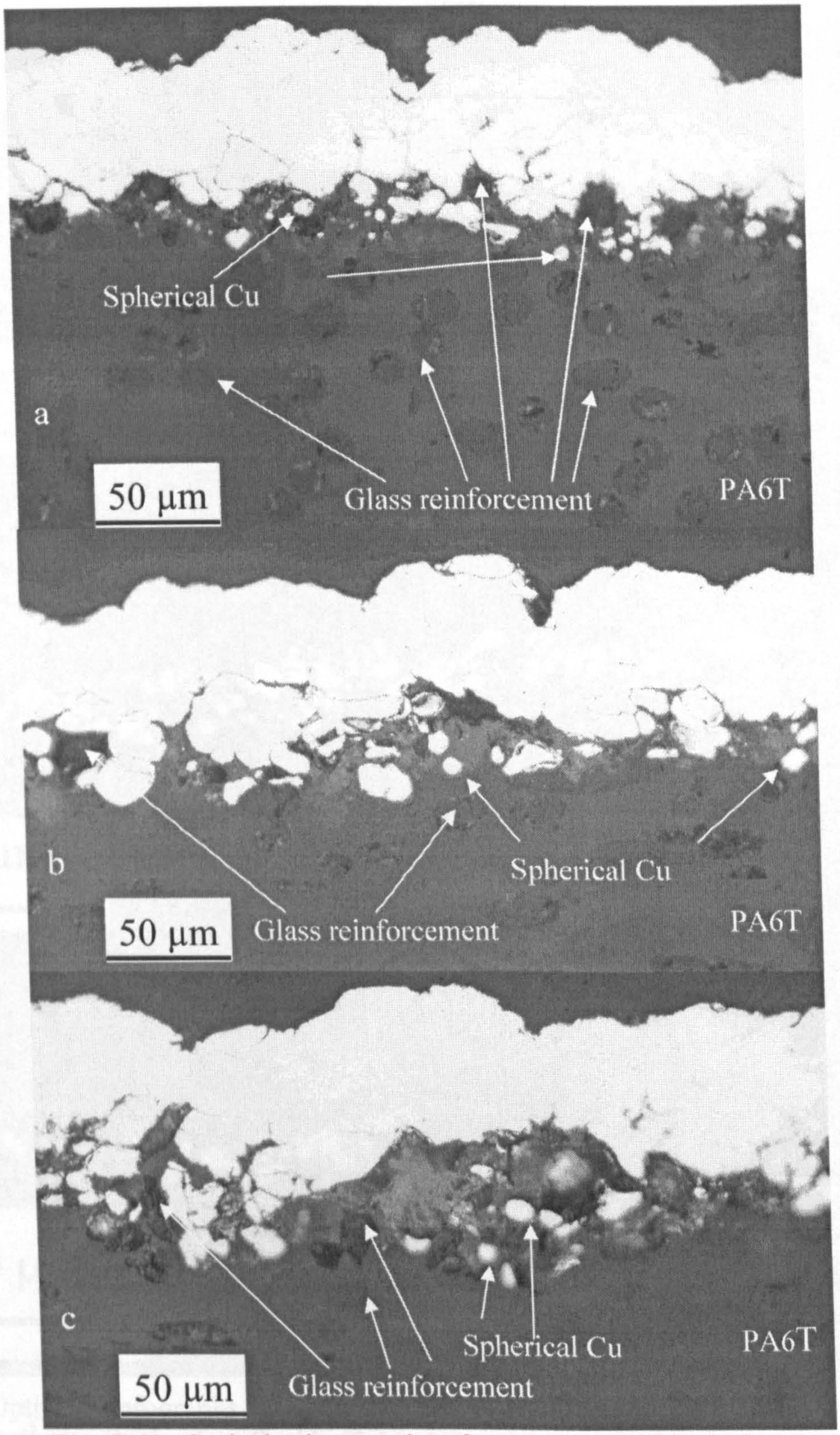

Fig. 5.41: Optical micrographs of copper on PA6T; deposition conditions described in **Table 5.3**, gas pressure of; a, 11 bar; b, 22 bar; c, 29 bar. Powder feed rate of 0.5 g s^{-1} and 1 pass.

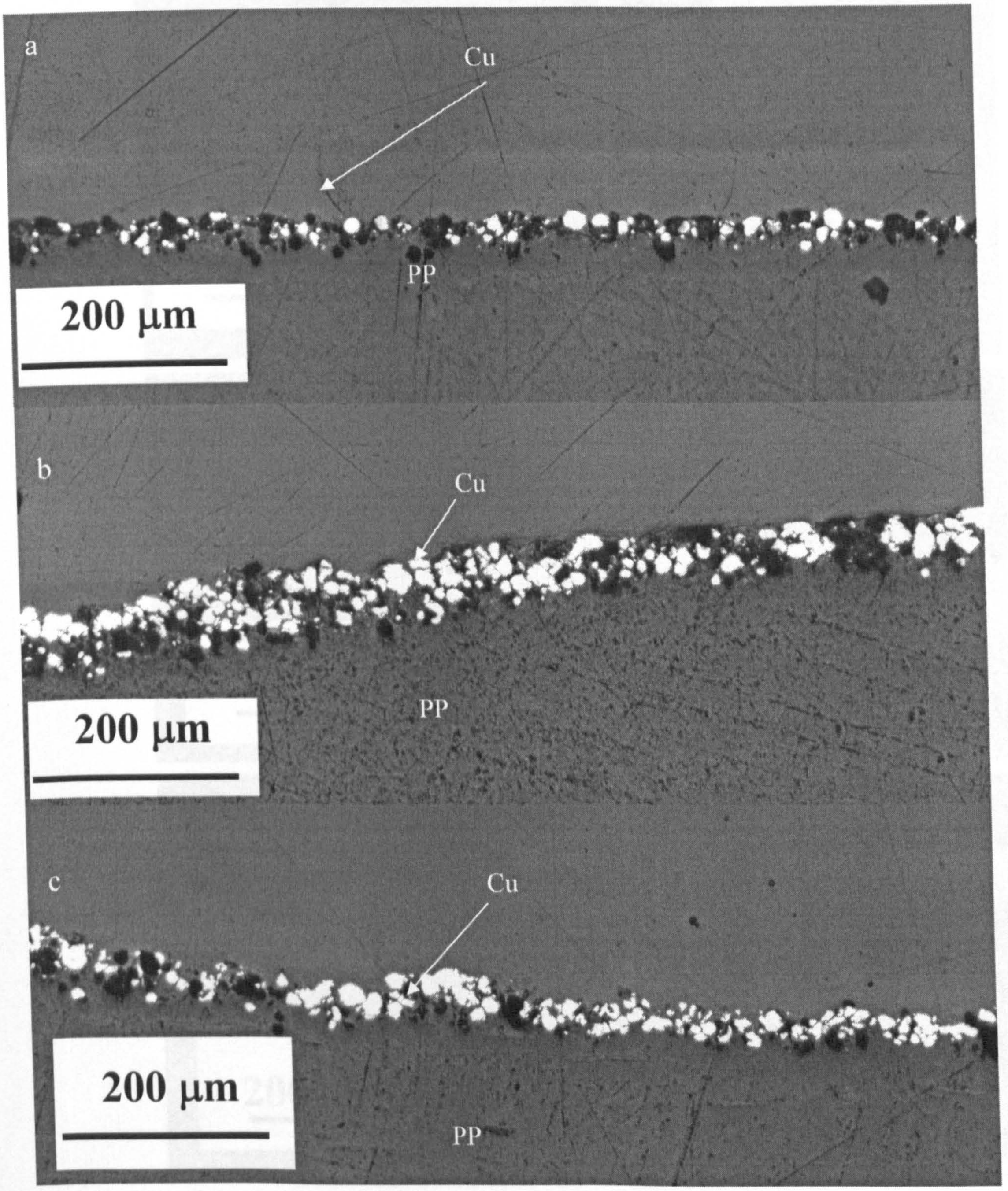

Fig. 5.42: Optical micrographs of copper deposited on PP in 1 pass using powder feed rate of 0.5 g s^{-1}, conditions described in **Table 5.3** and pressure of; a, 11 bar; b, 22 bar; c, 29 bar. In "c"; the substrate is curved at the interface of Cu – PP due to erosion of PP.

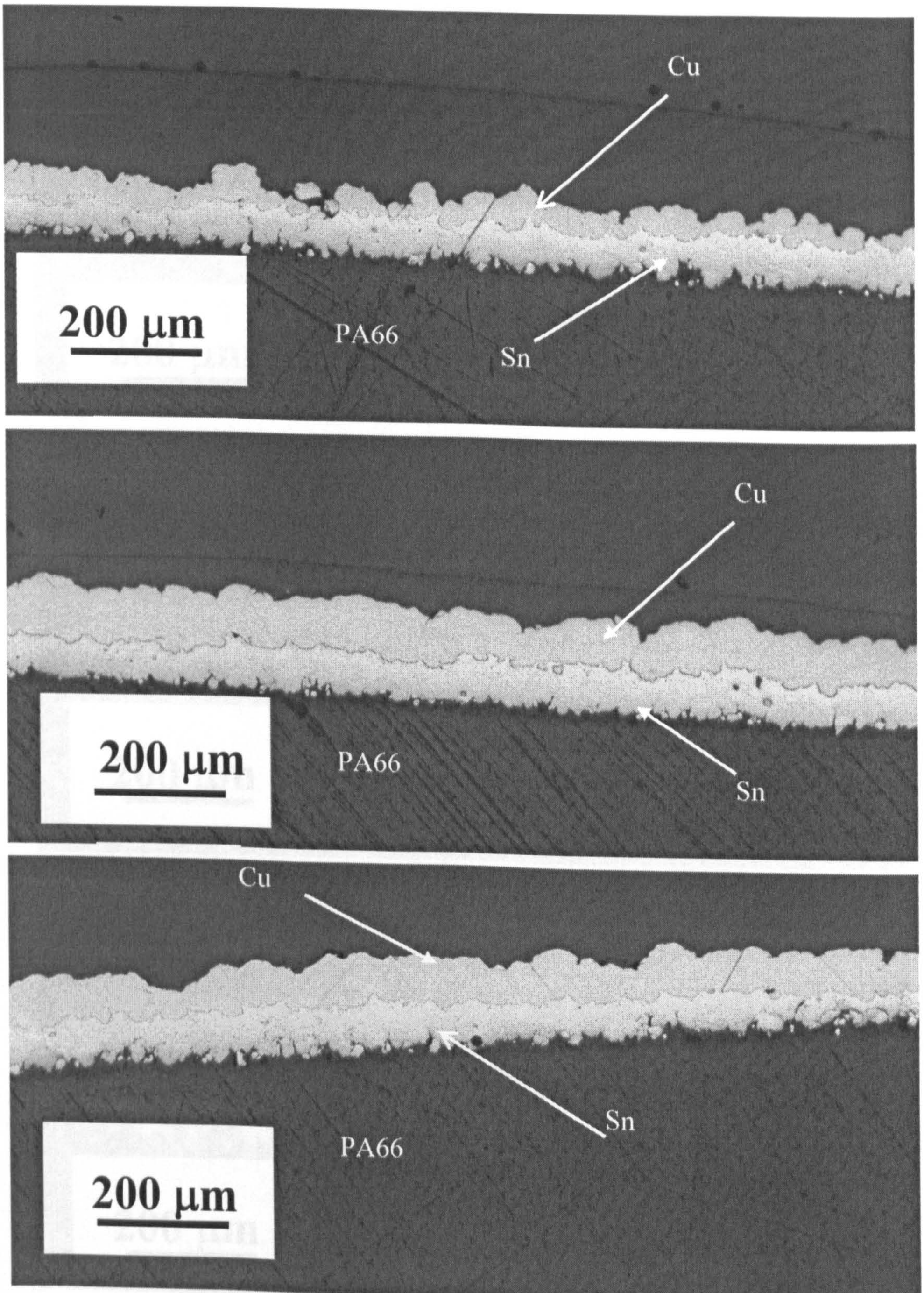

Fig. 5.43: Optical micrographs of Sn + Cu deposits on PA66; Cu deposited in single pass using process gas at 298 K and conditions described in **Table 5.17** and process gas pressure of; a, 11 bar; b, 22 bar; c, 29 bar. Sn deposited using conditions described in **Table 5.19**.

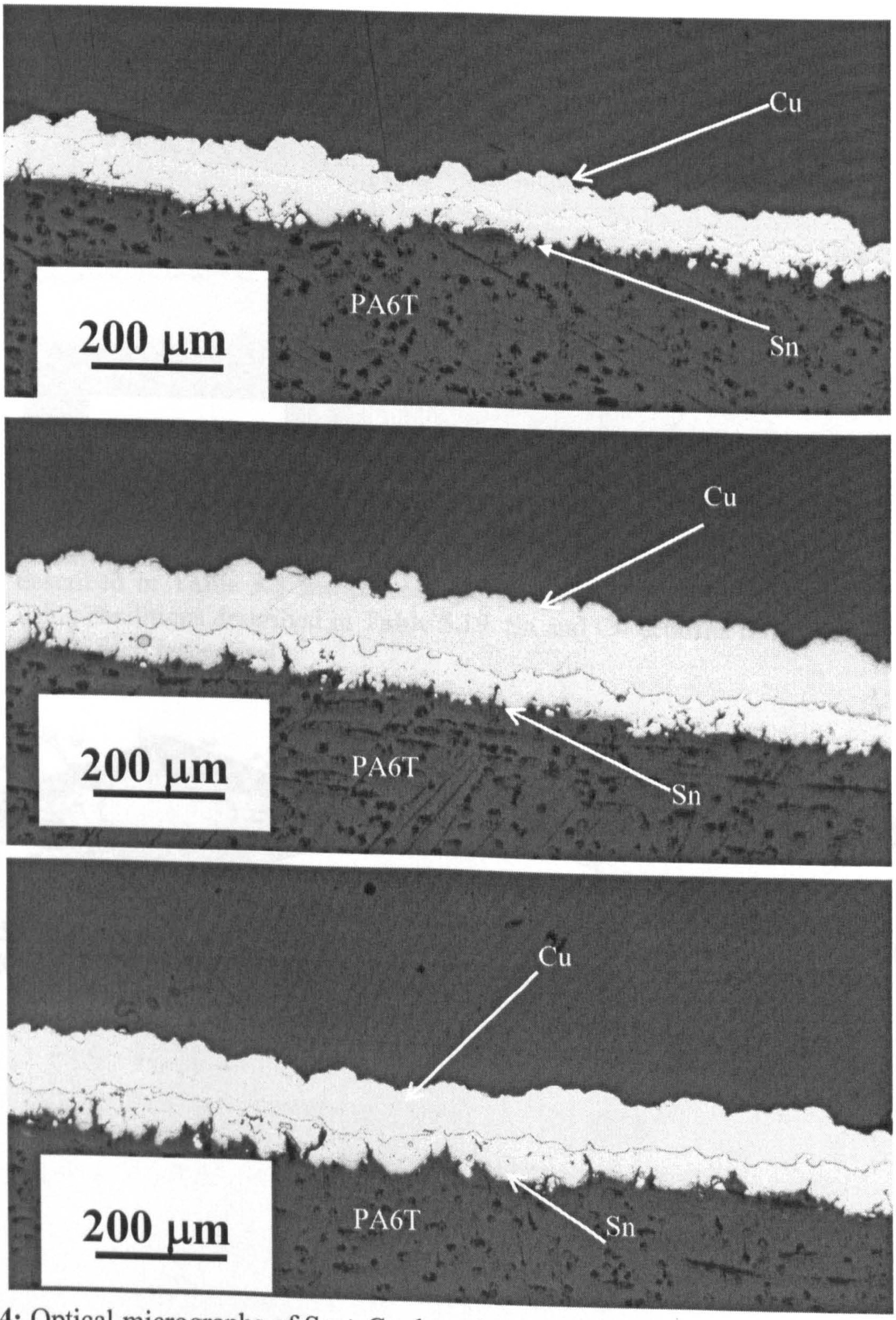

Fig. 5.44: Optical micrographs of Sn + Cu deposits on PA6T; copper deposited in single pass using gas at 298 K, powder feed rate of 0.5 m s^{-1} and conditions described in **Table 5.3** (PA6T) and gas pressure of; a, 11 bar; b, 22 bar; c, 29 bar. Sn deposited using conditions described in **Table 5.19**. Copper and tin deposited in single pass.

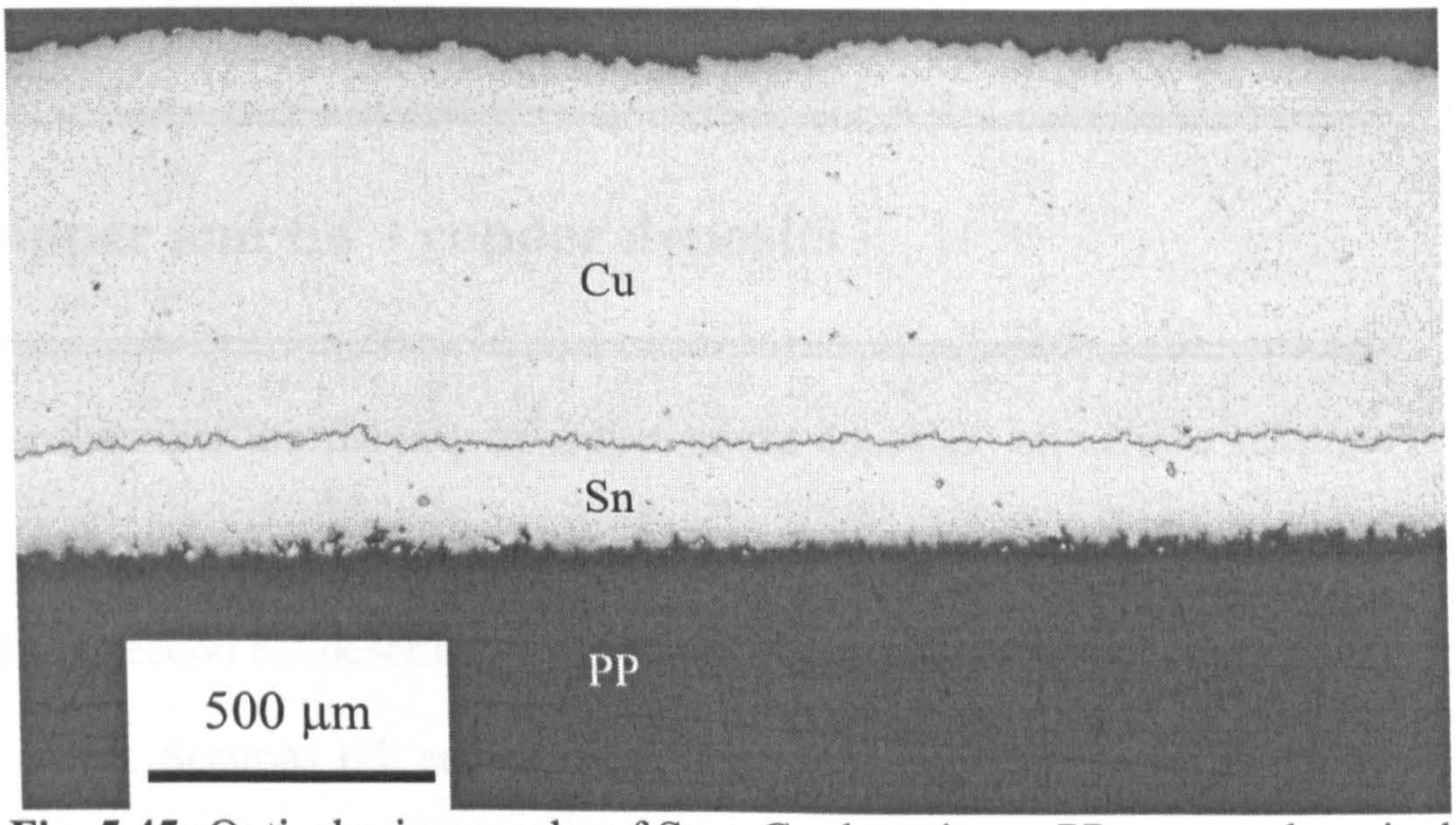

Fig. 5.45: Optical micrographs of Sn + Cu deposits on PP; copper deposited using process gas at 298 K, powder feed rate of 0.5 g s^{-1} and conditions described in **Table 5.3** and process gas pressure of; 22 bar. Sn deposited using conditions described in **Table 5.19**. Sn and Cu deposits formed in six passes each respectively.

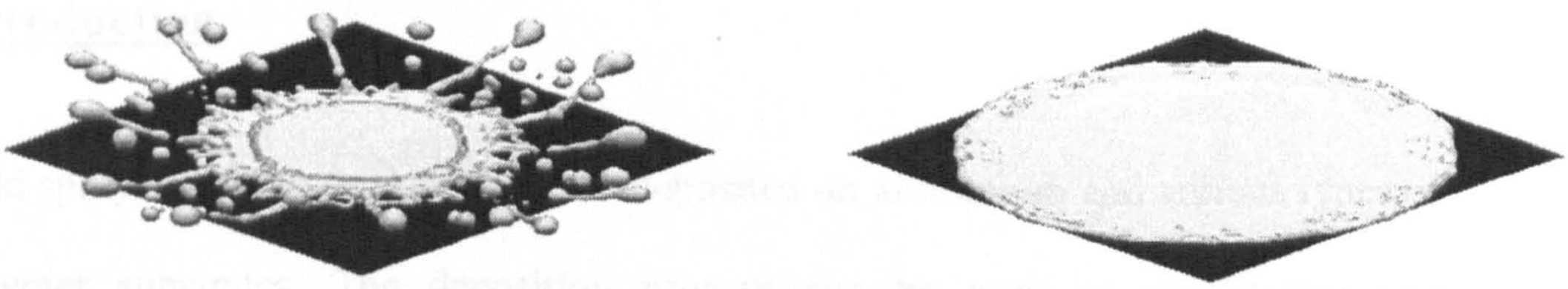

Fig. 5.46: Predicted nickel splat shapes at two different substrate temperatures. Left: 563 K; right: 673 K from Mostaghimi *et al* [72, 73].

Chapter 6

Stability of copper and tin – copper deposits

This chapter describes the stability of copper tracks deposited on various substrate materials. An investigation in the stability of cold sprayed copper is described in the section 6.2 and section 6.3 describes the investigation in to stability of copper tracks deposited on tin. Sections 6.2 and 6.3 both have their separate literature review sections.

6.1 Introduction

Cold sprayed copper tracks have been deposited on aluminium and various types of polymer substrates. The deposition process can be seen as constituting two components, i.e. interaction between substrate and impacting copper particle and interaction between previously deposited copper particle and the impacting copper particle. The overall adhesion and development of the track microstructure is governed by the phenomena happening during impact, at the substrate and between the deposited particles. The generation of heat during the deposition process also influences the process. The adhesive and cohesive strength of the deposits are determined by the phenomena occurring during these impacts. This chapter describes the metallurgical phenomena at impact in copper deposits in terms of Cu-

Cu interactions within the deposits. Tin was used as bond coat to deposit copper on nylon substrates. Sn-Cu interaction at the interface has been studied by annealing the deposits at higher temperatures.

6.1.1 Stability of copper tracks – microstructure and properties

The mechanical and electrical properties of copper deposits depend upon the deposit microstructure. The electrical and mechanical properties are influenced by the cold work and dislocation density in the tracks. Thus, understanding the microstructure of the deposits would increase the understanding of the deposition process and the influence of deposition conditions on the properties of the deposited coatings.

Investigations to understand the microstructure and mechanical behavior were carried out according to procedures outlined in sections 3.2 and 3.3, on as sprayed deposits as well as annealed deposits. The tracks were annealed as per the procedure outlined in section 3.6.1. The results of these investigations are reported in section 6.2.

6.1.2 Diffusion in tin – copper tracks

It was observed that copper tracks can be more readily deposited on to tin coated polymers, whereas in the absence of tin coating substrate erosion takes place for most polymer substrates. It was seen that using a tin bond layer with nylon substrates increases the adhesion of tin – copper tracks for all the spraying conditions tested (chapter 5, sections 5.5 & 5.7). Growth of intermetallic compounds at room temperature during storage has been widely reported for tin – copper couples in soldered copper joints. This intermetallic is expected to influence the over all stability of the deposited tin – copper tracks. Hence, understanding the nature and behavior of the tin bond coat is important from the point of view of overall tin – copper track stability and reliability.

The behavior and nature of the cold sprayed tin – copper was investigated by annealing tin – copper tracks as per the procedure described in section 3.6.3. The annealed tracks were then studied using optical microscopy and SEM as per procedure described in section 3.2. Resistivity measurements were carried out as per procedure described in section 3.4. The results of these experiments are reported in section 6.3.

6.2 Stability of copper tracks – microstructure and properties

In this section, the work undertaken to investigate the stability of the cold sprayed copper deposits during annealing and their resultant mechanical and electrical

properties is described. Background literature relevant to this study is reviewed in sections 6.2.1 to 6.2.4. The general features of spray deposition were described in chapters 4 and 5 and so the procedures used to deposit copper for this study are only briefly detailed in section 6.2.5. Similarly, characterization procedures are briefly detailed in 6.2.6, with the main body of results reported in 6.2.7.

6.2.1 Literature review

6.2.1.1 Deformation structures in copper

Cold gas dynamic spraying (CGDS) is a relatively new spray deposition technique wherein the deposits form due to the high velocity impacts leading to significant plastic deformation and adiabatic shear phenomenon at the deposit-substrate and the internal interface of the particles [13, 19, 27, 45, 54, 74, 75]. Assadi *et al.* modelled the strain in cold spraying of copper by using finite element method for a 10 μm size copper particle travelling at a velocity of 550 m s^{-1} [45]. They found that cold spraying can produce plastic strain of ~ 4 and strain rate of 0.5 x 10^9 s^{-1} at nodes of highest deformation in the particle. Adiabatic shear occurred when the particle velocity was increased to 580 m s^{-1} and the strain during adiabatic shear was seen to be ~ 10. The localized temperature at the nodes with highest deformation increased to ~ 1250 K due to adiabatic heating. The results from their study are shown in **Fig. 2.24**. The adiabatic shear results in a rise in local temperature (at point of impact

where adiabatic shear takes place) and high strains accompanied by a lowering of the stress to attain that strain. These high velocity impacts lead to significant cold working and in some cases recrystallization and/or dynamic recrystallization in the deposited material [75, 76]. The technique of cold spraying can be considered as a high strain and high strain rate process. The evolution of a material's microstructure and properties in cold spraying shows many similarities to high strain rate and/or high strain processing with explosive deformation, severe plastic deformation induced by torsion straining under high pressure and equi-channel-angular-pressing (ECAP) [45, 77-83]. A recent study by Borchers *et al.* [76] has focussed on studying the microscopic changes in the internal interface between the particles of FCC metals during cold spraying; they describe the copper deposit as being non-homogenous due to the presence of equiaxed nanosized grains, elongated nanosized grains, large grains with extremely high dislocation density, and micron sized grains with recrystallization twins in the absence of dislocations. The TEM image from Borchers *et al.* [76] is shown in **Fig. 6.1**. Similar non-homogenous microstructures have been reported for ECAP copper, wherein the copper had non-homogenous microstructures even after strains of ~10 [82, 84, 85]. It was also seen that recrystallization in fine grained copper did not occur until a certain minimum annealing temperature was provided, although the high dislocation density provided sufficient stored energy for grain nucleation and grain growth. For example Islamgaliev *et al.* [83] have reported an annealing temperature of 473 K, for copper following severe strain by torsion, before grain growth takes place from an initial

grain size of 107 nm. The stacking fault energy of copper is 60 mJ mm^{-2} and for aluminium it is 200 mJ mm^{-2} [76, 86]. The non homogenous microstructure of copper is attributed to the low stacking fault energy of copper leading to dislocations which are arranged in a dissociated manner which hinders cross slip and makes recovery difficult [76, 80, 82, 86]. The absence of recovery in copper leads to high dislocation density, and consequently significant strain energy is available for recrystallization.

6.2.1.2 Dynamic recrystallization in cold worked copper

The possibility of dynamic recrystallization in such deformed copper is very high due to high dislocation density and absence of recovery process in copper [87-90]. In cold spraying, high velocity impacts lead to adiabatic shear and metal jetting, leading to adiabatic heating and a localised rise in temperature. Similar features have been observed in the impact of shaped charges. **Fig. 6.2** shows the principle and schematic features of shaped charge [91]. A shaped charge consists in its simplest form, of an explosive with a conical cavity, lined with metal. When the detonation wave generated by an explosion reaches the conical metal liner, the intense pressure forces the tip of the cone to collapse. A jet emerges at a high velocity. The emerging jet when it impacts a target surface results in high strain rate and high strain deformation of target and produces metal jetting [92, 93]. It has been shown by Meyers *et al.* [94] in their study of high strain and high strain rate deformation of shaped charges of copper, that a strain of 3 at high strain rate (~ 10^5

s^{-1}) is sufficient to raise the localised temperature above 0.4 T_M, the temperature above which dynamic recrystallization in copper is expected to take place. Murr *et al.* observed that dynamic recrystallization was a common microstructural feature which appears to be central to, and facilitating of, extreme plastic flow in the solid state in their experiments on hypervelocity impact crater formation in copper targets and copper shaped charges [93]. The localized strain, strain rate and temperature in cold spraying is much higher than the values employed by Meyers *et al.* [94] for dynamic recrystallization to occur in copper. It is thus reasonable to suggest that dynamic recrystallization could occur during cold spray deposition of copper. Microstructures in dynamically recrystallized copper are characterized by grain size which is relatively independent of strain [87, 94]. The recrystallized grain size after dynamic recrystallization depends upon the strain rate; higher strain rates lead to finer grain sizes. The presence of dislocations inside the recrystallized grains is also taken to indicate dynamic recrystallization [94]. The strain rate influences the grain size and at higher strain rates the recrystallized grain size is smaller [87].

Meyers *et al.* showed that copper shaped charges had strains of >5 and strain rate of ~ 10^5 s^{-1}, while strains of ~ 3 at these strain rates are sufficient to result in localised temperature rise above 0.4 T_M. In ECAP, copper was strained to ~ 10 at strain rates of 10^{-3} s^{-1}. Dynamic recrystallization was observed in shaped charges of copper but not in ECAP [80, 82]. The reason for the absence of dynamic recrystallization is the absence of local temperature rise in absence of high strain rates during ECAP. The

high strain rates induce adiabatic heating along with adiabatic shear and lead to rise in the local temperature.

6.2.1.3 Grain refinement and microstrain after cold working

The effect of cold working is to produce grain refinement, and it is also responsible for introducing non uniform microstrain in the heavily cold worked material. The grain size and microstrain are often measured using the peak broadening in X-ray diffraction spectra [61-63, 79, 81, 83, 85, 95-99]. The peak broadening in an X-ray peak profile can be measured as the full width at half maxima (FWHM). The peak broadening is due to grain refinement and due to the microstrain associated with dislocations present inside the grains. A technique to relate the peak broadening data to the grain size and microstrain was first enunciated by Hall and Williamson and thereafter it has been used by many workers to separate the peak broadening data into components of grain size and microstrain [61, 63, 83]. The technique is explained in chapter 3, section 3.2.5.

The grain size of copper measured by various workers from peak broadening and TEM studies is shown in **Table 6.1**. The microstrain in nano crystalline copper prepared either by severe plastic deformation [83] or electrodeposition [81] was shown to be ≤ 0.06 %. The electrodeposited copper was cold rolled to obtain strains of 2300 %. After cold rolling the microstrain showed a significant increase to about 0.15 % although the grain size remained around 30 nm. Annealing rolled electro deposited copper at 373 K resulted in decrease of microstrain to 0.1 % but the grain

size remained unchanged. Annealing at 473 K increased the grain size to 80 nm and reduced the microstrain to 0. The ECAP material had relatively coarser grain size of about 300 nm and grain coarsening was not observed for annealing at 373 K, but when annealing temperature was increased to 423 K the grain size increased to 3 μm.

6.2.1.4 Properties of nano crystalline copper

The properties of nano crystalline copper produced by different cold working methods is shown in **Table 6.2**. Islamgaliev *et al.* [83] measured the electrical resistivity of copper deformed by severe plastic deformation and having a grain size of ~ 50 nm after deformation. They report a decrease in electrical resistivity of around 7 % for annealing at 448 K, and annealing at 523 K reduced the resistivity by more than 50 % (They do not report the actual values of resistivity measured). The grain size after annealing at 448 K was 110 nm and after annealing at 523 K it was ~ 600 nm. Annealing at temperatures below 448 K did not have significant effect on the resistivity. The hardness of copper without any annealing was 160 kgf mm^{-2} which reduced to 110 kgf mm^{-2} following annealing at 473 K. The hardness remained relatively unchanged for annealing below 423 K.

The hardness of ECAP copper was reported by Neishi *et al.* to be ~ 150 kgf mm^{-2}; annealing ECAP copper at 373 K did not decrease the hardness, but annealing at

423 K decreased the hardness to 100 kgf mm^{-2} and annealing at 473 K decreased the hardness to 80 kgf mm^{-2} [80]. The hardness decrease in ECAP coincides with the grain growth after annealing, as reported in **Table 6.1**.

The properties of electrodeposited nano crystalline copper were studied by Lu *et al* [81, 100-103]. They report the hardness of as deposited nano crystalline copper to be ~ 110 kg mm^{-2} [101]. The hardness increases to its maximum value of 120 kg mm^{-2} when electro deposited copper is strained to ~ 1000 %. For strains above 1000 %, the hardness does not increase further. This they attribute to increase in microstrain in the deposits due to rolling. The grain size and microstrain from their studies is given in **Table 6.1**. The room temperature electrical resistivity of electro deposited copper measured by them is 28.8 nΩ m [81].

There have been some reports on the tensile properties of nano crystalline copper. Wang *et al.* [84] studied the behaviour of nano crystalline copper fabricated by the ECAP route. ECAP copper had a grain size of ~ 300 nm. The as-fabricated copper had a tensile strength of ~ 375 MPa and strain to failure of 15 %. ECAP copper was rolled to 1180 % after cooling in liquid nitrogen. Rolling refined the grain size to ~ 200 nm. The tensile strength increased to ~ 460 MPa and strain to failure was 20 % after this rolling treatment. Sanders *et al.* [77, 78] carried out tensile testing of nano crystalline copper produced by compaction of nano crystalline copper powder which was produced by inert gas condensation. The compaction was carried out in vacuum for 10 min at 423 K under 1.4 GPa of pressure. The stress strain plots

obtained by them for nano crystalline copper of different grain sizes are shown in **Fig. 6.3**. Copper with grain size of 26 nm and 49 nm had tensile strength > 400 MPa but low strain to failure of ~ 1 %. When grain size was increased to 110 nm strain of 3 % was observed with a tensile stress of ~ 400 MPa after which the test was stopped because the displacement range was exceeded. The failure of samples with smaller grain size seemed to be flaw dominated, with little deformation before failure. In fact, the presence of flaws and artefacts like voids, residual stress and microstrain is seen to be the cause of brittle failure in many nano crystalline materials [77, 84, 103]. Thus it is seen that nano crystalline copper is characterized by high tensile strength > 350 MPa but low strain to failure of ~ 1 %.

Ostwaldt *et al.* [79] studied behaviour of polycrystalline copper under compressive stress at strain rates between 1×10^{-4} s^{-1} and 1×10^{3} s^{-1} at room temperature, 673 K and 883 K. At room temperature, they observed a monotonic increase in stress with strain. The stress strain curves determined at 883 K show a local maximum for all strain rates and for 673 K such a local maximum is seen in tests carried out at high strain rates. This is followed by a fall in stress. They interpreted this behaviour as being evidence of dynamic recrystallization where the local maximum is the strain at which dynamic recrystallization is initiated which results in grain coarsening and a decrease in stress. The studies on high strain rate phenomenon in copper indicate that dynamic recrystallization is an important recovery mechanism at higher strain rates and more so when the straining process is accompanied by a temperature increase [54, 76, 79, 94].

6.2.1.5 Deformation mechanisms during tensile testing of nano crystalline copper

A material is generally considered to be nano crystalline if its average grain size is < 100 nm and ultra fine grained if its grain size is 100 – 300 nm [77, 84]. An enhancement in both the strength and ductility has been predicted for nano crystalline and ultra fine grain material based on the Hall-Petch relationship [86, 104-106];

$$\sigma_y = \sigma_i + k\sqrt{d}$$ ---------- **Equation 6.1**

Where, d is the grain size and k is a constant. σ_Y is the yield stress and σ_0 is the friction stress needed to move individual dislocations. The reported data show three different regions: (1) a region from single crystal to a grain size about 1 μm where the classical Hall-Petch description can be used; (2) a region for grain sizes ranging from about 1 mm to 30 nm where the Hall-Petch relation roughly holds, but deviates from the classical 0.5 exponent to a value near zero; and (3) a region beyond a very small critical grain size where the Hall-Petch slope is essentially zero, with no increase in strength on decreasing grain size or where strength actually decreases with decreasing grain size.

Nano crystalline materials possess higher tensile strength than coarse grained materials; however most of the nano crystalline materials exhibit a room temperature tensile elongation to failure of no more than a few %. It has been postulated that small grain sizes lead to reduced flaw sizes and increased difficulties

for the imposed stress concentration at the flaw to exceed the critical toughness of the material, thus suppressing the crack nucleation/propagation instability [84]. The tensile strength of ECAP copper and nano crystalline copper reported in the preceding section [84] indicates that the above mentioned mechanism seems to be valid for ultra fine grain copper but not for nano crystalline copper. The increase in the strength and ductility of ECAP copper is consistent with an extrapolation of the Hall-Petch relationship for coarse grain material to the fine grain size [84].

Lu *et al.* fabricated defect free nano crystalline copper by electro deposition [100-103]. The copper with a grain size of 30 nm was rolled at room temperature using strain rates between 1×10^{-3} to 1×10^{-2}. They reported strains of 5100 % without breakage of the copper. The conventional coarse grained polycrystalline copper usually breaks after an extension of 800 %. They attribute the deformation process of the nano crystalline copper to grain boundary activities rather than lattice dislocations and propose a two stage mechanism for deformation in a nano crystalline copper [102];

1. Stage 1: $\varepsilon < 1000$ %. In this case, the deformation process seems to be dominated by dislocation activities (probably in the larger grains or at the grain boundaries). Generation and motion of dislocations may result in a substantial increase in the density of defects (i.e., microstrain) and in the misorientation between neighbouring grains due to pile up of dislocations at grain boundaries. Hence the grain boundary energy increases in this stage. This tendency can also

be verified by the results of hardness measurements, which show a slight hardening effect during this stage [101].

2. Stage II: $\varepsilon \geq 1000$ %. The microstrain, grain boundary enthalpy and grain boundary structure, as well as the grain size remain unchanged in this deformation stage. Also, the hardness of the nano crystalline copper becomes constant when $\varepsilon \geq 1000$ % [101]. This implies that lattice dislocation activity is no longer a dominating mechanism in the deformation. Instead grain boundary activities (grain boundary sliding or grain boundary diffusional creep) may be activated and become more dominant in the deformation as the grain boundary structure is evolved to be of higher energy (with a higher density of defects). When the deformation is controlled by grain boundary activities, the strain hardening effect disappears [101], and grain boundary structure as well as the dislocation density tends to be saturated. Such a two stage behaviour in the nano crystalline copper during cold rolling has also been verified in the variation of the electrical resistance with the degree of deformation [81].

Due to the low strain rates and temperatures involved, dynamic recrystallization may not be an important phenomenon in their experiments.

6.2.2 CGDS deposition of copper

Deposition was performed with the Yazaki system, the general features of which are described in chapter 4, section 4.3.2; using the nozzle No. 1 (described in chapter 4, section 4.4). One set of deposits was produced at constant gas mass flow rate of 2.9 x 10^{-3} kg s^{-1} using helium gas at 298 K and the other set using the same gas mass flow rate but a gas temperature of 523 K. The powder feed rate was 0.38 g s^{-1} in both cases. The aluminium substrates were placed in a holder for spraying and the gun was traversed at a speed of 0.2 m s^{-1}, relative to the substrates. Using a gas temperature of 523 K twenty-five passes of the gun over an area of 25 mm x 100 mm were used to give a deposit thickness of ~ 5 mm. Deposition using room temperature gas was performed under similar conditions except that only six passes were used to obtain a deposit thickness of ~ 0.6 mm. Thicker deposits could not be produced because de-bonding occurred. Samples for tensile testing were machined from the 5 mm thick deposits deposited using gas heated to 523 K.

The substrate temperature was measured during spraying using heat sensitive tapes and its temperature was ≤ 373 K.

6.2.3 Characterization of deposits

Annealing of the deposits is described in chapter 3, section 3.6.1. The grain size and microstrain were measured using X-ray diffraction peak broadening and calculated

using the Hall - Williamson method described in chapter 3, section 3.2.5. Tensile testing and electrical resistivity measurement of the deposits was done on samples machined from thick deposits deposited using process gas heated to 523 K. Microhardness testing was done on deposits prepared using gas at 298 K and 523 K. The method to carry out hardness testing and tensile testing is described in chapter 3, section 3.3.1 and 3.3.2 respectively. Tensile testing was carried out only on deposits formed using gas at 523 K as, thick deposits (~ 5 mm) suitable for machining of tensile samples, could only be produced at this temperature. Tensile testing was also carried out on rolled copper sheet in the rolled condition and after annealing at 773 K for 1 hr to obtain reference data for comparison with cold sprayed copper. Electrical resistivity of the copper was measured by the 4 point probe method as described in chapter 3, section 3.4 and section 3.4.1 using 75 mm long samples of various cross-sectional areas, cut from the material deposited at 523 K.

6.2.4 Results

6.2.4.1 XRD analysis

Typical XRD spectra for the annealed reference powder, as-sprayed deposit (using gas at 523 K) and deposit annealed at 573 K for 1 hr are shown in **Figs. 6.4 & 6.5**. **Fig. 6.4** shows the major peaks obtained from copper in the 2θ range of 40° to 100°

and the peak at 2θ of ~ 90° is shown in detail in **Fig. 6.5** which clearly reveals the peak broadening in the as-sprayed deposit. The sharpest peak is observed for the copper reference powder annealed at 773 K whilst there is very little broadening of the peak from the deposit annealed at 573 K in comparison with this reference.

The Hall – Williamson plot according to **Equation 3.6** for as-sprayed copper, sprayed using gas at 523 K is shown in **Fig. 6.6** where B is the experimental broadening and 2θ the diffraction angle. The slope and intercept values determined from this plot and similar plots obtained from annealed deposits are summarized in **Table 6.3**. The presence of measurable intercepts and slopes in the Hall-Williamson plots is taken to indicate the presence of fine grain size (nanometre size grains) and microstrain within the grains respectively. The slope did not significantly differ from zero for the samples deposited at 298 K indicating absence of microstrain. The XRD data from deposits using gas at 523 K had slopes significantly > 0; and intercepts, thus these deposits had nanometre sized grains as well as microstrain. The crystallite size and microstrain values calculated from these slope and intercept values in **Table 6.3**, using **Equations 3.4 & 3.5**, are given in **Table 6.4**. It should be noted that when deposits sprayed at 298 K were annealed at temperatures of 473 K and above there was negligible peak broadening due to either crystallite size or microstrain effects. This corresponds to a grain size in excess of ~ 300 nm and a microstrain ~ 0. A Similar effect was observed for deposits sprayed using gas heated to 523 K when annealed above 573 K.

Copper deposited using gas at 298 K does not show any microstrain and has a finer grain size (40 nm) in the as – sprayed condition as compared to copper deposited using gas at 523 K (60 nm). However, in copper sprayed using room temperature gas, annealing at temperatures as low as 373 K results in grain sizes becoming larger than the grain size of copper sprayed using gas at 523 K when annealed above 423 K. The grain size of deposits sprayed using gas heated to 523 K does not change significantly for annealing up to 423 K. Grain sizes increase in these deposits is observed only when annealed above 423 K. The microstrain in copper sprayed using 523 K gas remains relatively constant for annealing up to 423 K and for annealing above 473 K no microstrain was detectable.

6.2.4.2 Optical microscopy

Figs. 6.7 (a–c) and **Figs. 6.8 (a–c)** show the etched optical micrographs of as-sprayed copper, and following annealing at 473 K and 773 K for 1 hr, respectively. **Fig. 6.7** shows the microstructures for deposits sprayed using gas at 523 K and **Fig. 6.8** shows microstructures for deposits sprayed using gas at 298 K. In **Fig. 6.7 (a)** and **6.8 (a)** etching has clearly delineated the boundaries between the heavily deformed powder particles. The severe deformation is due to the high strain rate imposed by the impact during cold spraying. Individual grains are not revealed within the particles, in contrast to those clearly seen in the as-received powder, **Fig. 3.8**. In **Fig. 6.7 (b)** the boundaries between individual particles are still evident with

features at particle boundaries, which are possibly porosity or oxide and some very fine recrystallized grains. However, in **Fig. 6.7 (c)** recrystallization grains are clearly seen and the recrystallized grain size is 1 – 5 μm. Again, dark features at particle boundaries are evident, typically about 1 – 5 μm in size. In **Fig 6.8 (b)** small recrystallized grains are seen; this is different from **Fig. 6.7 (b)** where only a very few much finer grains are seen. The grains visible in **Fig. 6.8 (c)** are largely in the size range 1 – 5 μm, however a few larger grains of the order of 5 -10 μm are also seen. The features at particle boundaries are visibly larger and more in number with a more spherical nature. **Fig. 6.9** shows the etched BSE image of copper sprayed at 298 K gas temperature and annealed at 773 K for 1 hr. Recrystallized grains are seen and dark features are also evident. EDX analysis of the dark features revealed that the dark features were composed entirely of copper (~ 100 %) and no oxygen was detected. Thus it is most likely that the dark features are porosity and not oxides.

6.2.4.3 Electrical resistivity measurements

The results of the resistivity measurements along with the resistivity of a 99.998 % pure copper foil are shown in **Fig. 6.10** & **Table 6.5**. **Table 6.5** shows that the standard deviation in the measurement of resistance is lower then the measured value by approximately a factor of 10. A copper foil was used as a reference to compare the resistivity of cold sprayed copper and calibrate the equipment. It is

seen that the resistivity of as sprayed copper using gas at 523 K is ~ 27.1 nΩ m and annealing at temperatures up to 473 K did not decrease the resistivity significantly. However, annealing at 573 K decreased the resistivity to ~ 23.9 nΩ m and annealing at 773 K reduced the resistivity further to ~ 21.1 nΩ m. The resistivity of the reference copper foil was 17.5 nΩ m, which decreased to 16.7 nΩ m after annealing at 773 K for 1 hr. The resistivity of annealed copper is reported to be 16.73 nΩ m in data books [107].

6.2.4.4 Mechanical testing of deposits

The microhardness of the as-sprayed deposits and after annealing at various temperatures for 1 hr is shown in **Fig. 6.11.** The microhardness of deposits decreases after annealing; however, the temperature at which the hardness decreases is different in deposits sprayed using gas at 298 K and 523 K.

The deposits formed using gas heated to 523 K had a microhardness of ~ 180 kg mm^{-2}. The hardness of the deposits remained relatively unchanged for annealing temperatures up to 523 K. However, the microhardness of the deposits decreased when annealed at 573 K and above. The deposits attained a value ~ 90 kgf mm^{-2} for annealing at 673 K and annealing at higher temperature of 873 K decreased the deposit hardness further to about 65 kgf mm^{-2}.

The as sprayed deposits sprayed using gas at 298 K had a lower hardness as compared to the deposits formed using gas at 523 K. Annealing at temperatures as low as 373 K reduced the deposits hardness and they attained a value ~ 90 kgfmm^{-2} for annealing at 573 K. Annealing at 873 K reduced the hardness to ~ 70 kgfmm^{-2}.

The stress – strain curves obtained from tensile testing of as sprayed copper and after annealing at 873 K are shown in **Fig. 6.12 (a–b)**. The results obtained from mechanical testing of as-deposited copper and following annealing at 873 K for 1 hr are shown in **Table 6.6** and SEM images of the fracture surfaces of the cold sprayed copper tensile test samples are shown in **Fig. 6.13 (a–b)**. The as-sprayed deposit had a high tensile strength of 375 MPa and microhardness of 180 kgf mm^{-2} but had a negligible elongation to fracture (< 1 %). The fracture surface does not show any evidence of ductile fracture and it seems that fracture has taken place along copper particle boundaries, **Fig. 6.13 (a)**. After annealing the deposits at 873 K, the tensile strength and microhardness values decreased to 230 MPa and 65 kgf mm^{-2} respectively and elongation to failure increased to 26 %. The fracture surface shows characteristic ductile features, **Fig. 6.13 (b)** but some defects (denoted by arrows) are also evident and these might be responsible for the reduced elongation. These defects are probably the pores seen in **Figs. 6.7 (c)**, **6.8 (c)** and **6.9**.

The stress-strain plots of rolled copper sheet both in as-received condition and following annealing at 773 K for 1 hr are shown in **Fig. 6.14 (a-b)** and the results obtained from mechanical testing are shown in **Table 6.6**. The rolled copper sheet

had a tensile strength of 260 MPa, microhardness of 89 kgf mm^{-2} and % elongation to failure of 42 %. After annealing, the tensile strength of rolled copper sheet decreased to 208 MPa, microhardness decreased to 48 kgf mm^{-2} and % elongation to failure increased to 60 %.

6.2.5 Discussion

6.2.5.1 As-sprayed microstructure

Dynamic recrystallization as a mechanism to achieve a steady state recrystallized grain size in high strain high strain rate deformation of copper has been suggested by many researchers [90, 91, 93-95, 108]. Meyers *et al.* suggest that dynamic recrystallization is a thermally activated process which is important for ~ 0.4 T_m (T_m = melting temperature in Kelvin) [90, 94]. In the case of copper 0.4 T_m is 542 K. The high plastic deformation of particles during cold spraying is similar to explosive welding [33, 43, 44, 109] and the related phenomena of metal jetting and adiabatic shear are also known to occur in cold spraying [90]. During spraying, a gas temperature of 523 K was employed along with multiple gun passes to build up a deposit thickness of ~ 5 mm. It has been previously shown that the heated gas heats the substrate and indeed in this study the substrate was found to reach ~ 373 K. The particle temperature versus gas temperature while using helium as process gas is shown in **Fig. 2.11 (b)** [36]. It is seen that the particle temperature is < 200 K

when gas is heated to 523 K. Dynamic recrystallization might take place during spray deposition due to the combined effect of high dislocation density and localized elevated temperature during spraying due to adiabatic shear and influence of substrate heating by heated process gas. Moreover, the presence of internal dislocations (microstrain) in the as sprayed deposits also indicates dynamic recrystallization in the deposits [94]. The microstructure of as-sprayed coatings for deposition using gas at 523 K is one of dynamically recrystallized grains ~ 60 nm in size and dislocations associated with microstrain within the grains.

In the case of copper deposited using gas at 298 K the microstructure seems to consist of very fine grains, which are essentially free of internal dislocations. The fine grain size of 37 nm and the absence of microstrain suggest that the dislocations are associated with the grain boundaries. Grain growth in these fine grains is achieved by annealing at 373 K. The absence of dislocations within the grains and the finer as-sprayed grain size suggests that dynamic recrystallization may not be an important feature of deposits formed using gas at 298 K. The as-sprayed microstructure seems to be characterized by very fine grain size due to cold working. The mechanism for heat generation during cold spraying is due to the impact of particles, by conversion of kinetic energy in to heat (friction heating), and by adiabatic shear. These mechanisms are more localized in nature as compared to heating of substrate or previously deposited coating by impingement of hot gas. The heating associated with adiabatic shear and friction heating, during spraying at 298 K might result in some dynamic recrystallization, generating very fine grains.

Deposition at 523 K leads to much higher particle velocities, but the particle is not heated significantly by the gas during flight (see **Appendix 1** for particle velocity and temperature calculations). The heating effect of the gas is more important for the previously deposited coating due to the impingement of the hot gas. Thus, it might be easier to deform the previously deposited coating when heated gas is used in the deposition process. Moreover dynamic recrystallization could be an important factor during cold spraying using gas at 523 K. The dislocations associated with microstrain seen in the deposits formed using gas at 523 K are due to the combination of continued deformation and dynamic recrystallization during cold spraying. The lower particle velocity and absence of hot gas impingement in copper sprayed at 298 K results in lower levels of cold working as compared to spraying at 523 K. Moreover it is likely that due to lower temperatures and lower levels of cold working, dynamic recrystallization is also not a major factor in these deposits. Thus dislocations within sub-grains are apparently absent in deposits formed using gas at 298 K.

The present results for spraying at 298 K largely support the transmission electron microscopy study of Borchers *et al.* [27, 76] (**Fig. 6.1**). They found high dislocation densities in cell walls but few dislocations within the cells and cell sizes of 50 – 200 nm. Our study has confirmed the existence of coherent crystallite sizes around 100 nm. In the case of spraying at 523 K, dislocations within the cell (microstrain) were also observed. The differences in their work and the present study (for deposition at 523 K) might be related to the differences in spraying conditions used to deposit

copper. They have used nitrogen gas heated to 623 K and a nozzle with expansion ratio of 9 for deposition of copper whereas in our experiments we used a nozzle with expansion ratio of 9.46 and He gas heated to 523 K for deposition. The differences in the type of gas used, the temperature of gas during spraying and the different expansion ratio of nozzle are likely to produce different grain sizes and dislocation arrangement in deposits. The heating of the particles is significantly larger when nitrogen is used as the process gas (**Fig. 2.11** [36]).

6.2.5.2 Recrystallization and grain growth during annealing

Recrystallization – grain growth in cold sprayed copper seems to proceed differently for deposits formed using room temperature gas (298 K) and deposits formed using gas heated to 523 K. The first point to note is that recovery is largely absent in copper because of its low stacking fault energy. Recrystallization involves nucleation of new grains and their subsequent growth. Nuclei are formed in regions where dislocation concentrations are highest. A certain local concentration of elastic energy is needed. Hence in material deposited with gas at 298 K, there is considerable stored energy in sub-grain walls where nuclei will readily form even at low temperatures. In material deposited using gas at 523 K, the presence of a more diffuse sub-grain (cell) structure means that more thermal energy is required to produce a nucleus as the regions of highly concentrated stored elastic energy are not present.

In the first scenario (process gas at room temperature, 298 K), the fine grains do not need high activation energy for grain growth to proceed as the grains are free of dislocations and hence there is no need to nucleate new grains. It is possible that some very fine grains are formed due to dynamic recrystallization and annealing of these deposits simply results in growth of these grains. However, in deposits formed using gas at 523 K, the grains have many internal dislocations, which require activation energy for re – arrangement of these dislocations to nucleate new grains. The microstructures in **Fig. 6.8 (a-c)** show that for copper deposited using room temperature gas a fine grained structure is visible for annealing at 473 K (**Fig. 6.8 b**), and annealing at 773 K (**Fig. 6.8 c**) increases the grain size to the range of 5 – 10 μm.

In the second case (gas heated to 523 K), new grains are nucleated from the dislocations and then grain growth occurs. It is seen that the grain size after annealing at 773 K remains in the range of 1 – 5 μm (**Fig. 6.7 c**). The microstructure of the deposit sprayed at 523 K seems to be more stable during annealing due to the formation of dynamically recrystallized grains during the deposition process with a more diffuse cell structure.

The absence of recovery in copper due to its low stacking fault energy also results in the dislocations being available for nucleation of new grains, the consequence of which is a large number of smaller sized grains after recrystallization. Thus, higher dislocation density in copper deposited using gas at 523 K produces a finer grain

size after annealing at 773 K (1 – 5 μm) as compared to copper deposited using gas at 298 K (5 – 10 μm) and is due to difference in dislocation arrangements in the as-deposited material..

6.2.5.3 Microstructure and hardness of deposits

The very fine grain size (~60 nm) in the as-sprayed deposit is the reason for the high hardness of the as-sprayed deposit (~180 kgf mm^{-2} for copper sprayed using gas at 523 K and ~ 155 kgf mm^{-2} for copper sprayed using gas at 298 K, **Fig.6.11**). Copper deposited using gas heated to 523 K is harder than Copper sprayed using gas heated to 298 K because of the microstrain present in copper deposited using gas heated to 523 K (**Table 6.3**).

In the case of copper sprayed using gas at 523 K; the grain size increases from ~ 60 nm to 120 nm with increasing annealing temperature from 298 K to 473 K, while the microstrain remains relatively unchanged at a value of about 1.8 x 10^{-3} (**Table 6.4**). Despite this increase in grain size, the microhardness of copper deposits remains approximately constant for annealing at temperatures up to 523 K (**Fig. 6.11**). However, when the annealing temperature was increased to 573 K and above, the dislocations associated with microstrain re-arrange to nucleate new grains and subsequently recrystallization proceeds with further grain growth. The re-arrangement of dislocations and nucleation of new grains cause a fall in deposit

hardness. These results are consistent with the observations made earlier for nano crystalline materials [106]. The low stacking fault energy of copper may be contributing to this phenomenon, as recovery is not usually observed in metals with low stacking fault energy. In absence of recovery the mechanical properties of copper are not regained until recrystallization begins [86]. The activation energy for nucleation of recrystallization to proceed is provided by annealing at temperatures equal to or above 573 K. At temperatures below 573 K, although some grain coarsening could take place in the pre-existing grains, the grain interiors still have high dislocation density as evidenced by the microstrain in the deposits.

In the copper deposited using gas at 298 K there is no activation barrier to be crossed for recrystallization as internal dislocations are not present. The hardness decreases upon annealing at 373 K due to rapid grain growth of the fine grain structure in the as-sprayed material.

Neishi *et al.* have reported microhardness for equi channel angular pressing (ECAP) of copper with a strain of 6, after annealing for 1 hr at temperatures between 298 K and 673 K [80, 82]. They report a reduction in microhardness from ~150 kgf mm^{-2} to ~75 kgf mm^{-2} when the annealing temperature is increased from 298 K to 573 K. In their paper they also report that the hardness of copper remains unchanged for annealing at temperatures up to 373 K. These results differ from the present results on cold sprayed copper deposits. In copper sprayed using gas at 298 K the hardness decreases for annealing temperatures as low as 373 K. The hardness of copper

deposited using gas heated to 523 K decreases only for annealing temperatures of 573 K and above. This suggests that the deformation process in cold spraying using gas at 298 K and 523 K produces different internal dislocation arrangements than ECAP. The lower hardness of ECAP copper after annealing at 573 K is most likely due to the coarser starting grain size (300 nm) of ECAP copper as compared to cold sprayed copper, **Table 6.4**.

6.2.5.4 Tensile behaviour of deposits

The tensile testing of deposits shows a largely ductile failure for deposits annealed at 873 K. This indicates that there already exists a clean well adhered interface between particles in the as-sprayed state and during annealing the microstructure develops by the mechanism outlined above. In the as-sprayed coating a near brittle fracture is observed. However, the tensile strength is very high this again supports the hypothesis of well adhered particles. The high tensile strength of cold sprayed copper could be due to the nano-crystalline structure of copper and the low ductility due to the presence of defects in the material [77, 84, 103, 110]. Annealing the copper deposits at 873 K is likely to result in some sintering of the deposited copper particles. There is intimate and largely oxide free contact between copper particles in cold sprayed copper. Moreover, the copper is nano crystalline. Thus, annealing at 873 K could lead to sintering in the copper deposits enhanced by the rapid diffusion through the nano crystalline grain structure of copper. The sintering of annealed

copper deposits results in better ductility and lower tensile strength than as sprayed copper. However, the % elongation of annealed copper deposits is lower than that of annealed copper sheet; this is probably due to the fine grain size of sprayed copper (1 – 5 μm) after annealing and also due to the presence of pores.

It is likely that the two stage mechanism proposed by Lu *et al.* [102] for deformation in nano crystalline copper (described here in section 6.2.4) operates for cold sprayed copper, however the presence of defects dominates the tensile behaviour of as sprayed copper and they show low elongation to failure.

6.2.5.5 Resistivity of deposits

The resistivity of as sprayed copper is higher then resistivity of the reference copper foil. The defects in metal such as vacancies, dislocation and grain boundaries are known to scatter electrons and increase resistivity [86], thus cold sprayed copper is expected to have higher resistivity than rolled copper sheet due to its higher grain boundary area. When sprayed copper is annealed, the resistivity does not decrease markedly until after recrystallization. The temperature for onset of decrease in resistivity and recrystallization for cold sprayed copper deposited using gas at 523 K is 573 K; at lower annealing temperatures the resistivity remains relatively unchanged. The resistivity after annealing at 773 K is 21.1 nΩ m, which is higher than the resistivity of annealed copper reported in data books (16.73 nΩ m) and

measured on annealed copper foil (17.50 nΩ m) at University of Nottingham (**Fig. 6.10**). This is probably due to the fine grained structure (~ 5 μm) after annealing in cold sprayed copper as well as the presence of pores which reduce the effective cross-sectional area.

6.2.6 Conclusions

Cold spraying of copper results in considerable grain refinement as compared to the original powder. Deposition conditions employed influence the microstructure and mechanical properties of the deposits. Higher particle impact velocity in copper deposited using gas at 523 K introduces dislocations (microstrain) in the deposits. Copper deposited using gas at 523 K did not show any recovery when annealed below 573 K whereas annealing at or above 573 K, recrystallization occurs and results in decrease of hardness.

The onset of recrystallization is accompanied by a decrease in electrical resistivity. The resistivity of as sprayed copper decreases from 27.1 nΩ m to 21.1 nΩ m after annealing at 773 K for 1 hr.

The deposits sprayed using gas at room temperature (298 K) show grain growth for low temperatures of annealing and there does not seem to be any activation barrier for grain growth to occur in absence of internal dislocations in grains. Thus,

deposition conditions are important factors in determining the microstructure and properties of cold sprayed copper.

In the as-sprayed condition tensile failure occurs at a high stress but with virtually no plastic deformation. Following recrystallization the tensile behaviour is not dissimilar to that of bulk material indicating atomic bondings across interparticle boundaries have developed. The differences in grain sizes and distribution of dislocations in this work, as compared to previous work on copper deposition [76] could be related to the differences in spraying conditions employed.

6.3 Interdiffusion of copper and tin

In a previous chapter the use of tin as a bond coat to improve the bonding of cold sprayed copper to certain polymers was described and promising results, in terms of pull-off bond strength, were obtained. However, there is the possibility of Sn - Cu interdiffusion occurring in bimetallic layers produced in this way and the purpose of the work reported in this chapter was to investigate such behavior by annealing bimetallic layers at temperatures above room temperature but below the melting point of tin (505 K). As significant interdiffusion between tin and copper has been reported previously and since cold sprayed copper, and probably also tin, possess a submicron grain size there is clearly the potential for such an effect to be accelerated in cold sprayed layers.

In the present chapter the literature pertaining to copper – tin interdiffusion is first reviewed, relevant experimental details are presented, experimental findings are reported and finally these are discussed in the light of previous work and conclusions drawn.

6.3.1 Literature review

6.3.1.1 Cu – Sn interdiffusion

The diffusion characteristics of tin-copper diffusion couples have been studied by a number of workers for both high and low temperature regimes. The low temperature regime is usually taken to mean up to a maximum of 453 K [111-115]. The high temperature regime is usually up to 1123 K and in this temperature regime the diffusion occurs partly in the presence of liquid tin [116] which melts at 505 K (232 °C).

One or more intermetallic compounds are generally formed in tin-copper couples after annealing, in the low as well as high temperature regimes. It is seen from the copper – tin alloy phase diagram (shown in **Fig. 6.15**) and from the diffusion studies carried out by various researchers at temperatures below 493 K that the intermetallic compounds formed in this temperature range are the ε phase (Cu_3Sn) and the η′ phase (Cu_6Sn_5) [111-126]. Tu confirmed the existence of η′ by XRD studies of Sn – Cu thin films [126]. The Cu_6Sn_5 phase found in the Cu – Sn thin films is η′. The transformation from η′ to η occurs at ~ 459 K. η′ is a long period superlattice i.e. the ordered form of η phase. This is confirmed by the appearance of extra superlattice lines in the X-ray patterns. However, this transformation reportedly has no effect on tin – copper inter-diffusivity [119, 126] and in the majority of literature the η′ phase is not separately identified and is generally referred to as the η phase. When a copper – tin couple is aged at relatively low temperature (293 K to 343 K), η grows without developing an obvious ε layer.

However, when the system is aged at higher temperature (408 K to 493 K), both η and ε layers appear [112-115, 119, 121-123, 126, 127].

6.3.1.2 Nature of intermetallic phase formation

The methods used to produce tin – copper couples for interdiffusion studies are reported as follows:

1. Electroplating tin over copper [113-115];
2. Dipping copper plates in to liquid tin or liquid lead – tin solutions having compositions similar to commonly used solders to form an initial layer of intermetallic compound + tin, further annealing leads to growth of the intermetallic layer [113-115, 118, 120, 123, 125, 127];
3. Clamping together cylinders of tin, copper and tin – copper intermetallic compounds with stainless steel clamps and annealing in argon atmosphere in the temperature range of 463 K – 493 K for one hour. After annealing for one hour the clamps were removed and annealing was continued without the clamps [116];
4. Using copper – tin soldered joints [124].

The diffusion of copper into tin and a variety of metals has been studied and it is seen that the copper diffuses rapidly into metals like gold, silver and tin at temperatures below the melting point, i.e. in the solid state. The rapid diffusion rate

of copper into these metals at low temperatures is attributed to a grain boundary mechanism by some researchers [111, 112, 114, 126] and to interstitial diffusion of copper by others [121, 126, 128]. Transition from lattice (bulk) diffusion to grain boundary diffusion usually occurs anywhere between 463 K and 353 K, depending on the nature of tin – copper couples. This transition from bulk diffusion to grain boundary diffusion has been identified by an apparent decrease in the activation energy seen in the plots for $\log D$ versus $\frac{1}{T}$ where, D is the diffusion coefficient and T is the absolute temperature. Generally, the smaller the grain size, the higher the temperature of transition [112, 114, 129] i.e. in material with finer grain size the grain boundary diffusion mechanism persists until higher temperatures. Kay *et al.* [113]] studied the effect of work hardening of the copper substrate on the diffusion of plated tin. They observed that at 343 K the work hardened copper had a thicker intermetallic compound layer as compared to the annealed copper. However, at 443 K the intermetallic compound thickness was the same for work hardened and annealed copper. This they attributed to annealing of the copper during diffusion at 443 K. Haimovich [112], in his study of hot air levelled tin (HALT), attributed the lower growth rate of intermetallics in HALT, as compared to electroplated Sn – Cu, for diffusion at 373 K, to the extremely large grain size of tin generated in HALT. The large grain size leads to the relative contribution of grain boundary diffusion being insignificant down to very low temperatures (The grain size of tin is not mentioned in their work).

The relative rates of diffusion of tin and copper have been studied using inert markers during diffusion [121, 122, 130]. It is reported that inert markers in a copper – tin diffusion couple are displaced toward the copper side during growth at low temperature (293 K to 343 K) but toward the tin side at higher temperatures (> 443 K). These observations have been interpreted to mean that copper diffusion dominates at low temperatures, while tin diffusion is dominant at higher temperatures.

The thickness (W) of the intermetallic has been represented by an equation of the usual form

$$W = W_o + kt^n$$ ---------- **Equation 6.2**

The exponent n is 0.5 for ordinary diffusional growth and has been found to have this value for intermetallic growth in a semi-infinite copper – tin couple [112, 121, 123, 129]. K is the growth rate constant and W_0 is the initial thickness of the intermetallic layer. The thicknesses of intermetallic compounds formed during annealing of tin – copper couples are shown in **Table 6.7**. It is seen from **Table 6.7** that the thickness of the intermetallic compound is not the same for Sn – Cu couples produced by different techniques. Annealing of electrodeposited tin on copper produces an intermetallic compound of much lower thickness as compared to Sn – Cu couples formed by dipping copper in liquid tin, or soldered Sn – Cu. This is probably due to the initial reaction taking place in the presence of liquid tin when diffusion couples are formed by dipping. The reaction of liquid tin with copper

generates a thin initial layer of intermetallic compound and further annealing results in the growth of this layer. In diffusion couples where a third element, usually lead, is present, this does not apparently have a significant influence on the thickness of intermetallic layer. The exception is where a high ratio of lead (> 80 %) limits the amount of tin available for the formation of the intermetallic compound [124].

There have not apparently been any studies related to interdiffusion in cold sprayed materials. The grain size in as sprayed copper determined in other studies and also in the present work is ~ 50 – 100 nm [33, 76]. However, the influence of such fine grain deposits on diffusion behavior during annealing has not been studied.

6.3.1.3 Kinetics of intermetallic growth – analytical model

Mei *et al.* [121] proposed an analytical model for diffusion in Cu – Sn couples, the same is outlined here.

They considered a binary diffusion couple of semi-infinite copper and tin plates brought into contact at $t = 0$. The two intermetallic phase's ε and η form as layers and grow as planar plates, so that the net diffusion is one-dimensional. A schematic illustration of the analytical model is shown in **Fig. 6.16.**

The model given above is a good representation of the processes in tin - copper diffusion, where the interfaces given by ξ_{ij} are moving with respect to annealing

time. The rate of growth of the intermetallics can be computed from the movement of the interfaces which depend upon the interdiffusion coefficients in the ε and η phases.

The solution of the diffusion equation obtained from Fick's second law, to calculate the layer thickness of ε and η, ιs given by Mei *et al.* [121]. The layer thickness depends upon the position of the interface position parameters, ξ_{ij}. ξ_{ij} is the instantaneous position between phase *i* and *j* (*i*, *j* = 1, copper solid solution; = 2, ε; = 3, η; = 4, tin solid solution). E.g., the thickness of η phase is given by $\xi_{23} - \xi_{12}$ where ξ_{23} is the instantaneous position of ε and η interface at time *t* and ξ_{12} is the instantaneous position of copper solid solution and ε interface, at time *t*. The interface position parameters obtained from the solution of the diffusion equation were plotted against annealing temperature. The plot obtained by Mei *et al.* [121] is shown in **Fig. 6.17**. The boundary position between the copper solid solution and the ε phase, ξ_{12}, is negative, which shows that the Cu-ε boundary migrates toward the copper side. Similarly, the ε–η boundary moves toward copper. The boundary between the η and tin moves into the tin solution but by only about half the distance that ξ_{12} moves into copper. Therefore the centre of the intermetallic layer (including both ε and η phases) migrates into copper. Unless there is a significant Kirkendall effect, the original Cu - Sn interface is located near the centre of the η-phase region and shifts towards the copper side as the temperature decreases. Diffusion studies

using diffusion markers placed at Sn - Cu interface also report the movement of diffusion markers towards the centre of η phase after ageing [122].

The model discussed above is valid under certain conditions; namely [121]:

1. Bulk diffusion is assumed to occur

2. Kirkendall effect is neglected

3. The interfaces are planar and the tin and copper layers are semi – infinite.

6.3.2 Cold spray deposition

Commercially available pure tin and copper powders were employed for deposition by cold spraying as reported in chapter 3 section 3.7.1. The powders were deposited onto commercial grade nylon-66 substrates of dimensions $100\ mm \times 100\ mm \times 3\ mm$. Spray deposition was carried out using the Yazaki system, described in chapter 4, section 4.3.

The spray gun was attached to a five axis robot arm which allowed accurate and repeatable positioning of the deposits. Tracks of tin were deposited onto the nylon substrate whilst copper was overlaid directly on to the tin.

First, five separate tracks of tin were deposited, each in two passes and each approximately 100 mm long. Then the copper was sprayed directly onto the initial

tin deposits, again in two passes. Helium gas at room temperature was used to deposit the tracks. The parameters employed for spray deposition are given in **Table 6.8**. The tin layer was approximately 100 μm thick and the copper layer approximately 600 μm thick following 2 passes.

6.3.3 Sample heat treatment

Tin – copper tracks were heat treated at two different temperatures namely 343 K and 443 K in a fan assisted oven. Sample temperatures were monitored directly using a chromel / alumel thermocouple and were found to be within ± 1 K of the set furnace temperature. At specific time intervals a sample was removed from the oven and air cooled to room temperature. The resistance was measured as described in section 2.5 and a small length (5 – 10 mm) cut from the end for subsequent microstructural examination. This sample was immediately stored in a refrigerator at 271 K and the remaining length was then put back in the oven for further heat treatment. The samples de-bonded from the nylon substrates during heat treatment, hence after the first cycle of annealing the nylon substrate was discarded and only the free standing tracks were annealed further. For comparative purposes cold sprayed copper tracks were also annealed.

6.3.4 Microstructural examination

Samples for microstructural study were removed from the refrigerator and prepared immediately for examination by optical and scanning electron microscopy. The procedure for optical microscopy is described in chapter 3 section 3.2.3, scanning electron microscopy is described in section 3.2.4 and the procedure for thickness measurement of the intermetallic layer is described in section 3.2.3.1.

6.3.5 Resistance measurements

The tin - copper couples and for comparison cold sprayed copper tracks were removed from the furnace at different time intervals to measure the resistance. Thus, resistance data were obtained for the tracks for different annealing treatments.

The resistance of cold sprayed Sn - Cu couples and copper tracks were measured using the four-point probe method. The procedure for measuring the resistance is described in chapter 3, section 3.4.

The results were converted to % change in resistance. Since repeated measurements were made on the same length of track, and assuming no change in cross-sectional area during annealing, the % change in resistance equals % change in overall track resistivity.

6.3.6 Results

6.3.6.1 Identification of the intermetallic phases

Fig. 6.18 shows a SEM BSE image of a tin-copper couple annealed at 443 K for 1.261×10^7 s (146 days); the position of a line scan is seen in the image and signals from the line scan itself is shown in **Fig. 6.19**. It is clear that layers of different composition formed in this tin – copper couple which are most probably, copper solid solution, ε phase, η phase and a tin solid solution phase. The composition change between the phases occurs over a very short distance and within the phase remains relatively constant. The two intermetallic layers along with the copper and a highly porous tin layer are also clearly seen in the BSE image (**Fig. 6.18**) where the different mean atomic numbers of the constituent phases create the contrast. It is evident that what is believed to be the η phase is significantly thicker than the ε phase. A second SEM image of a sample heat treated at 443 K for 1.261×10^7 s (146 days) showing the various intermetallic compound layers formed is shown in **Fig. 6.20**. This is taken from the same sample as that used for **Fig. 6.18** but from a different region. The porous tin layer in this sample fractured during preparation. The chemical composition determined by quantitative EDX spot analysis in various regions identified in **Fig. 6.20** is shown in **Table 6.10** along with calculated composition of η and ε. The EDX spot analysis confirmed the presence of tin rich and copper rich solid solution layers. The phase present adjoining the copper layer was identified as ε (Cu_3Sn) and the phase adjoining the tin layer was identified as η (Cu_6Sn_5). This η layer is possibly η′ (an ordered form of η phase [16, 21]) but, this layer is referred to as the η in the present work. The SEM image of a sample heat

treated at 343 K for 1.16 x 10^7 s (135 days) is shown in **Fig. 6.21**. A single layer of intermetallic is seen, with a contrast intermediate between that of copper and tin. The EDX results of the phases identified in **Fig. 6.21** are shown in **Table 6.10**. Quantitative EDX analysis gave a composition of 36 at% tin. However, since the layer is 3 – 5 mm thick beam spreading will have occurred into the surrounding phases so it is not possible to be certain whether this is η or ε phase. On the basis of previous reports it is most probably η [114, 115].

6.3.6.2 Characterization of intermetallic compound layer growth

The SEM image of an as - deposited tin-copper track is shown in **Fig. 6.22**. The layer thickness of tin and copper are clearly visible on the nylon-66 substrate. The tin and copper layers are well bonded to each other without any apparent porosity between the two layers. It is seen that the maximum thickness of the tin layer is approximately 100 μm and the approximate thickness of the copper layer is 600 μm.

The SEM image of tin copper couple maintained at room temperature (298 K) for 2.03 x 10^7 s (235 days) is shown in **Fig. 6.23**. A thin discontinuous intermetallic layer is seen, which is presumably η phase [115], showing interdiffusion occurred even at this temperature.

The SEM images of the samples heat treated at 343 K and 443 K, for different heat treatment times are shown in **Fig. 6.24 (a–f)** and **Fig. 6.25 (a–f)** respectively. Intermetallic phases are seen after heat treatment for only one day at 343 K and 443 K. The sample heat treated at 443 K shows two distinct phases, ε and η which are identified in the BSE image of the microstructure by their different grey level contrast whereas in sample annealed at 343 K only a single phase is seen. The dual layer is difficult to discern in **Fig. 6.25 (a)** but the higher magnification image in **Fig. 6.25 (d)** shows the dual layer. In **Fig. 6.25 (c)** (heat treatment for 1.08×10^7 s (125 days)), the dual layer is clearly evident. In the sample heat treated at 443 K porosity is seen in the tin layer at an early stage in the annealing cycle and the porosity increases as the annealing time increases (as seen in **Figs. 6.20 & 6.25**). The porosity is negligible for annealing up to 2.16×10^6 s (25 days, **Fig. 6.25 (b)**).

Fig. 6.26 shows the BSE image after annealing for 4.23×10^6 s (49 days). It is seen that significant porosity has developed after annealing for 49 days and annealing further up to 125 days results in a more porous tin layer. After annealing for 1.26×10^7 s (146 days), it was observed that the tin layer had largely been converted into a dense intermetallic layer. Another significant feature observed during annealing at 443 K is the formation and development of transverse cracks in the η layer. After 49 days small cracks are seen (**Fig. 6.26 (b)**) and further annealing increases the size and number of cracks (**Fig. 6.25 (c)** and **(f)**) The samples held at 343 K appeared to form only a single intermetallic phase, believed to be η, even after annealing for up to 1.16×10^7 s (135 days). Furthermore there was no evidence for

porosity in the tin phase. The BSE image of tin layer (without any copper layer over it) annealed at 443 K for 2.67 x 10^6 s (31 days) is shown in **Fig. 6.27**. Porosity is not observed in the tin layer. Therefore, the formation of porosity appears to depend upon Cu – Sn interdiffusion and intermetallic phase formation and not on evaporation of tin in the furnace.

An etched optical microscope image of cold sprayed copper annealed at 443 K for 1.26 x 10^7 s (146 days) is shown in **Fig. 6.28**. **Fig. 6.28** shows a few very fine recrystallized grains of the order of (1-3 μm). The microhardness of cold sprayed copper after annealing at 443 K for 1.26 x 10^7 s (146 days) was measured to be ~ 90 kg mm^{-2} and after annealing at 343 K for 8.64 x 10^6 s (100 days) it is ~ 111 kgf mm^{-2}. The microhardness of the as-deposited copper was ~ 166 kgf mm^{-2}.

6.3.6.3 Thickness of intermetallic layers

The mean values of measured thickness of total, η phase, ε phase and η + ε phase for 343 K and 443 K heat treatments for 1.16 x 10^7 s and 1.26 x 10^7 s (135 and 146 days) respectively is shown in **Table 6.11**. The ratio $\eta/(\eta+\varepsilon)$, for heat treatment at 443 K, shows that the intermetallic layer is dominated by η phase as nearly 90% of the intermetallic compound is composed of η phase after annealing for 1.26 x 10^7 s (146 days).

A plot of intermetallic compound layer thickness versus time is shown in **Fig. 6.29**. The thickness of intermetallic compound increases with annealing time. The thickness of intermetallic compound after 135 days is ~ 5 μm. The SEM image of Sn - Cu couple annealed at 343 K for 3.11 x 10^6 s (36 days) is shown in **Fig. 6.30**. The image shows a single layer of intermetallic compound at the interface. The intermetallic compound thickness is not uniform throughout the interface and it ranges between 2 – 5 μm.

Examination of the samples annealed at 443 K showed dense, uncracked η and negligible porosity up to 16 days. At 25 days porosity began to become significant but no cracking of η was observed. After 49 days significant porosity and some cracking was beginning to appear, whereas after 49 days sever cracking and significant porosity was seen. The intermetallic layer growth data for annealing at 443 K is plotted in **Fig. 6.31 (a-b)**. Two distinct regions of growth of intermetallic layers are seen; the first region is for annealing up to 2.16 x 10^6 s (25 days) and the second region is for annealing from 2.16 x 10^6 s (25 days) to 1.26 x 10^7 (146 days). **Figs. 6.31 (a)** and **(b)** shows the plot of thickness versus annealing time up to 2.16 x 10^6 s (25 days) and 1.26 x 10^7 (146 days) respectively. The η and ε layers grow at a steady rate in the annealing period up to 25 days. After 25 days the thickness of η and ε is ~ 13 μm and ~ 6 μm respectively. Annealing for more than 25 days leads to rapid growth of η but ε thickness decreases; after 146 days the thickness of η and ε is ~ 45 μm and ~ 5 μm respectively.

6.3.6.4 Measurements of resistance

The % change in resistance of the tracks after heat treatment was calculated by the following equation,

$$\delta R_i = 100\frac{(R_t - R_0)}{R_0} \quad \text{---------- Equation 6.3}$$

Where, R_t is the measured resistance after heat treatment for time t and R_0 is the resistance of the as sprayed tracks i.e. without any heat treatment.

Figs. 6.32 and **Fig. 6.33** show the change in resistance of the tin-copper couples and pure copper tracks, after annealing at 343 K and 443 K respectively. The resistance for t = 0 is the value of resistance before the annealing cycle was started. In the case of the 343 K anneal the resistance decreased continuously with time and after annealing for 1.166 x 10^7 s (135 days) was approximately 8% lower than the t = 0 value. In the case of 443 K anneal the resistance decreased after annealing for 8.64 x 10^4 s (one day) by more than 10% but thereafter the annealing is seen to increase the resistance and after 1.261 x 10^7 s (146 days) the resistance was only approximately 5% below the resistance value for t = 0. In the case of copper, resistance decreased continuously at both annealing temperatures. At 343 K for 1.1 x 10^7 s (127 days) the decrease was more than 11 %. After annealing at 443 K for 8.64 x 10^7 s (one day) it was ~ 16 % and after annealing for 1.1 x 10^7 s (127 days) was ~ 20 %.

6.3.7 Discussion

6.3.7.1 General aspects of phase formation

The Cu – Sn phase diagram is shown in **Fig. 6.15** [131]. The phase diagram suggests that at 343 K and 443 K the equilibrium phases are copper rich solid solution, ε, η′ (or η) and tin rich solid solution. Annealing at 443 K resulted in the formation of ε, η and the two solid solution phases in agreement with the phase diagram. This is also in agreement with observations reported in references [111-126]. From the 343 K annealing experiments it was not possible to conclusively identify the phase which formed. On the basis of previous experiments conducted in this temperature range [112-115, 123] it is most likely to be η.

Overall, the phases which nucleate and grow at the Cu – Sn interface in cold sprayed deposits are consistent with those found in layers formed by other routes e. g. annealing electroplated layers, layers formed by hot dipping, layers formed by vapour deposition.

The formation of transverse cracks in the η phase seems to be due to the tensile stresses in the layer resulting from the volume changes to produce ε and η phase.

6.3.7.2 Porosity formation in tin layer

An important feature seen in the present study was the high volume fraction of porosity in the tin layer of Sn – Cu couples. This does not seem to have been

reported previously for Sn – Cu couples. Although in previous works the thickness of η was < 30 μm (**Table 6.7**) whereas in our study the thickness of η was 44 ± 6 μm. The formation of pores in the tin was observed in the higher temperature diffusion couple but not in the lower temperature one. Also such significant porosity was not noted in the single layer tin track annealed at 443 K. This strongly suggests that the interdiffusion of copper and tin and intermetallic phase formation are directly influencing porosity formation and that it was not due to evaporation of tin in the furnace.

The tin layer starts becoming porous after annealing beyond a period of 2.16×10^6 s (25 days) at 443 K. The development of porosity in tin could be a result of faster diffusion of tin into η phase as compared to the diffusion of copper from η phase into tin. This will result in a net vacancy flux into tin. These vacancies could, under condition of tensile stress in tin or the presence of a non-reactive gas form pores. This is the well known Kirkendall effect [129]. Another possible explanation could be creep damage in the tin at the relatively high homologous annealing temperature (T/T_m=443/505). At such a high homologous temperature relatively low stresses could give high creep rate and significant creep strain. The stresses might arise from the volume changes associated with phase changes. The tin could be experiencing a tensile strain rate as a result of phase growth. Alternately residual stresses from the spray deposition could be such as to put the tin in tension.

The rapid diffusion of tin might be due to the fine sub – grain size and high level of dislocation density expected in the tin and copper phases. **Fig. 6.28** shows that the grain size of copper after annealing is ~ 1 – 3 μm. Diffusion through grain boundaries occurs when very fine grains are present, which is the case for cold sprayed copper. The fine grain size provides larger grain boundary areas for grain boundary diffusion. Thus it is likely that diffusion through grain boundaries is responsible for the rapid diffusion of tin.

The porosity development coincides with formation of cracks in the η phase. The role played by the porosity and the cracks in the subsequent diffusion phenomenon is quite complex and it is not possible to provide suitable explanations of their role in the diffusion phenomenon at this stage.

6.3.7.3 Rate of growth of intermetallic phases

From the literature; layer thickness is expected to increase as $\sqrt{t}$ if growth is bulk diffusion controlled [112-115, 123, 130]. Hence, plots of intermetallic compound layer thickness versus square root of heat treatment time ($\sqrt{t}$) for heat treatment temperature of 343 K and 443 K are shown in **Fig. 6.34** and **Fig. 6.35** respectively along with best fit linear regression lines. Intercepts and slopes for the various phases in the tin-copper couple in different annealing periods are shown in **Table 6.12**.

Clearly at 343 K the intermetallic layer growth is linear with respect to $\sqrt{t}$ and the thickness of the intermetallic layer after 1.16 x 10^7 s (135 days) annealing is ~ 5 μm. However, the regression line shows a negative intercept with the y-axis. The negative intercept suggests a time delay in the formation of the intermetallic compound. This probably represents the incubation period to nucleate the phase at this low annealing temperature. In the present study ε phase was not observed for diffusion at 343 K. Mei *et al.* [121] estimated that for diffusion at 343 K the ε layer would comprise 33 % of the intermetallic layer, however as the total intermetallic layer thickness at this temperature is only ~ 5 μm after annealing for 135 days, it is possible that;

1. The high surface volume ratio of equilibrium ε phase may prevent its formation [121].
2. The thickness of ε layer is below the level detectable by optical microscopy and SEM.

The intermetallic growth for annealing at 443 K (**Fig. 6.35**) is more complex. It shows a linear relation to $\sqrt{t}$ in the annealing periods 1- 25 days and 49 – 146 days, but the slopes and intercepts in these regions for the intermetallic growth are different. The regression line for ε and η phases in the annealing period for 1 – 25 days has a positive slope and intercept with the y-axis. The positive intercept suggests growth of the intermetallic compound more rapid than bulk diffusion. The growth of intermetallic compounds in the annealing period of 49 – 146 days is not

expected to follow the $\sqrt{t}$ relation ship due to the transverse cracking and the formation of porosity.

The ratio of ε/η shown in **Fig. 6.36** has a value of ~ 0.45 after 2.16 x 10^6 s (25 days) of annealing at 443 K. Mei *et al.* [121] have reported this ratio to be equal to 0.55 in their study and Prakash *et al.* [123] have reported value of 0.44 in their study. Mei *et al.* solved Fick's diffusion equation and determined the interdiffusion coefficients in ε and η phases ($\overline{D}_\varepsilon$ and $\overline{D}_\eta$). The values of $\overline{D}_\varepsilon$ and $\overline{D}_\eta$ obtained by them are given below [121],

$$\overline{D_\varepsilon}(m^2/s) = 5.48x10^{-9}\exp\left[\frac{-61.86}{RT}\right]$$
$$\overline{D_\eta}(m^2/s) = 1.84x10^{-9}\exp\left[\frac{-53.92}{RT}\right] \quad \text{---------- Equation 6.4}$$

Where the activation energies are given in kJ / mole, R is the universal gas constant and T is the absolute temperature. **Equation 6.4** suggests that η has lower activation energy for interdiffusion than ε phase thus at lower temperatures the higher ratio of η phase is expected. It might be possible that in cold sprayed Sn – Cu couples this behavior persists up to 443 K.

Mei *et al.* [121] plotted the $\frac{\xi_{ij}}{\sqrt{t}}$ (ξ_{ij} is the interface position parameter and t is the time of annealing) versus the annealing temperature, for the model shown in **Fig. 6.16**. The plot obtained from their data is shown in **Fig. 6.17**. The data from their

study was extrapolated to 443 K and the plot with the extrapolated data is shown in **Fig. 6.37**. The thickness of the intermetallic compound can be obtained from the interface positions, for e.g. the thickness of ε phase can be calculated as (ξ_{23} - ξ_{12})$x\sqrt{t}$. The thickness of the ε, η and ε + η calculated from **Fig. 6.37** and the measured values obtained in this study, for annealing time of 2.16 x 10^6 s (25 days), are shown in **Table 6.13**. It is seen that the thickness of the intermetallic compound developed in our study was higher than the values predicted by the model of Mei *et al.* [121]. The large grain boundary area associated with the fine grain size of cold sprayed copper could be responsible for this. Diffusion through grain boundaries is a much rapid process as compared to bulk diffusion [112, 114, 115, 121, 122]. It seems likely that in the cold sprayed Sn - Cu diffusion couples, for annealing temperature of 443 K, diffusion through grain boundaries is an important mechanism.

6.3.7.4 Resistance of cold sprayed Sn - Cu

The resistance of the tin – copper tracks after annealing depends upon [132]:

1) The reduction in dislocation density in the copper due to annealing. This is expected to decrease the resistance.
2) The formation of intermetallic compound after annealing. This is expected to increase the resistance.

3) Porosity in tin layer.

The overall decrease in resistance observed for tin – copper tracks after annealing at 343 K and 443 K for 1.16 x 10^7 s (135) days and 1.26 x 10^7 s (146 days) respectively, shows that, the reduction in dislocation density in copper has greater influence on the resistance of the tracks. However, this effect is greater for tracks annealed at 343 K as compared to tracks annealed at 443 K as the resistance of tracks annealed at 343 K has decreased by 8 % and the tracks annealed at 443 K show a 5 % decrease in resistance. The track annealed at 343 K show a gradual decrease in resistance to a lowest value approximately 15 % below the starting value, after 4.23 x 10^6 s (49 days) annealing, and thereafter the resistance gradually increases and attains a value about 8 % below the starting value, after 1.16 x 10^7 s (135 days) annealing. This may be due to the gradual decrease in dislocation density at such low annealing temperature which attains is lowest value after annealing for 4.23 x 10^6 s (49 days) and thereafter the growth of the intermetallic compound results in increase of the resistance. The track annealed at 443 K shows a decrease in the resistance of about 10 % after annealing for 8.64 x 10^4 s (1 day) and the resistance than increases to a value about 5 % below the starting value after further annealing. This behavior may be due to the decrease in dislocation density with in one day to a low value and with further annealing the growth of the intermetallic compound will result in increase in resistance. The microstructure in **Fig. 6.28** shows that annealing at 443 K for 146 days results in recrystallization in copper. The decrease in resistance of Sn – Cu tracks is due to recrystallization and

grain growth in copper. The copper track without any tin undercoating shows that for annealing at 343 K the decrease in resistance follows trend similar to Sn – Cu tracks. Thus at annealing temperature of 343 K, it is likely that the decrease in resistance of copper and tin – copper tracks is due to decrease in dislocations due to annealing at 343 K and the formation of intermetallic compound in tin – copper tracks does not significantly influence the resistance of the tracks. The decrease in dislocation density in copper tracks annealed at 443 K results in decrease of resistance after one day of annealing to ~ 16 % below $t = 0$ (t is the time of starting the annealing treatment) and then it gradually decreases to a value of ~ 20 % below $t = 0$ after annealing for 3.19 x 10^6 s (37 days) and thereafter the resistance stays at around this value for the entire duration of annealing. There is no increase in resistance after longer annealing times observed in the case of pure copper tracks as in the case of Sn – Cu tracks, where the increase in resistance is due to formation of the intermetallic compound and development of porosity in tin layer.

6.3.8 Conclusions

The intermetallic compounds are formed during annealing of the cold sprayed Sn - Cu couples at 343 K and 443 K for annealing period as low as one day. Intermetallic layer was also formed in Sn - Cu sample maintained at room temperature for 2.03 x 10^7 s (235 days).

Only a single phase of the intermetallic compound is seen in samples annealed at 343 K, which is estimated to be most probably η. At 443 K ε and η phases were observed. These results are in agreement with the work of other researchers.

The formation of transverse cracks in η and the formation of porosity in tin are important features observed in samples annealed at 443 K. These features influence the formation of intermetallic compound as the onset of porosity and cracking after 49 days of annealing coincides with a different region in the plot of intermetallic thickness versus $\sqrt{t}$ **(Fig. 6.35)**.

The intermetallic layer grows with longer annealing times. The growth rate of the η phase during annealing at 443 K was found to be much higher as compared to the growth rate of this phase reported by other workers. This higher growth rate could be due to diffusion through grain boundaries in the cold sprayed Sn – Cu couples.

The electrical resistance of the Sn - Cu deposits decreases after annealing, at 343 K and 443 K. Thus, reduction of the resistance due to decrease in dislocation density seems to be the dominant mechanism while increase in resistance due to the formation of intermetallic layer and porosity does not have a major effect on the resistance of the annealed Sn - Cu deposits.

Table 6.1: Grain size and microstrain of copper after cold work and, annealing at various temperatures (shown in bold italics) for 1 hr. Data for electro deposited copper are for annealing for ~ 2 hr.

Cold work method		Grain size / nm			Microstrain / %			Method used to determine grain size and microstrain	Ref.
ECAP		< 300 ***298*** K	< 300 ***373*** K	~ 3000 ***423*** K	-	-	-	Measurement from TEM image	[82, 84]
Severe plastic deformation		50 ***273*** K	90 ***398*** K	110 ***448*** K	0.06 ***273*** K	0.05 ***398*** K	0 ***448*** K	XRD peak broadening	[83]
Compaction of inert gas condensed Cu powder, ~ 99 % dense		26 - 110 (Compaction temperature of 423 K)			-	-	-	XRD peak broadening	[77]
Ball milled Cu powder after milling		46 hrs		96 hrs	46 hrs		96 hrs	XRD peak broadening	[133]
		31		15	0.03		0.02		
Electro deposited	As deposited	~ 30 ***298*** K	~ 40 ***373*** K	~ 80 ***473*** K	~ 0.03 ***298*** K	0.03 ***373*** K	0 ***473*** K	XRD peak broadening	[81]
	Rolled (ε = 2300 %)	~ 30 ***298*** K	~ 40 ***373*** K	~ 80 ***473*** K	~ 0.15 ***298*** K	0.1 ***373*** K	0 ***473*** K		

Table 6.2: Properties of cold worked Cu prepared by different cold working methods. The annealing temperatures for ECAP and SPD, and the grain size of compacted powder are given in bold italics.

Cold work or fabrication method	Hardness / kgf mm^{-2}				Resistivity / nΩ m	Room temperature tensile strength / MPa				Ref.
ECAP	150 ***298*** K	150 ***373*** K	100 ***423*** K	70 ***573*** K	-	375				[83, 84]
Severe plastic deformation (SPD)	160 ***298*** K	160 ***423*** K	110 ***473*** K	70 ***673*** K	-	-				[83]
Compacted inert gas condensed Cu powder, ~ 99 % dense	90 ***16*** nm	75 ***26*** nm	65 ***49*** nm	50 ***110*** nm	-	340 ***16*** nm	425 ***26*** nm	460 ***49*** nm	415 ***110*** nm	[77]
Electro deposited	110				28.8	-				[81, 101]

Table 6.3. Slopes and intercepts of Hall-Williamson plots obtained from full width at half maximum of XRD peak profiles of cold sprayed copper.

Process gas temperature / K	Annealing temperature / K	298	373	423	473	573
298	Intercept / 10^{-3} radians	3.73	2.26	1.63	~ 0	~ 0
	Slope / 10^{-3}	~ 0	~ 0	~ 0	~ 0	~ 0
523	Intercept / 10^{-3} radians	2.33	1.89	1.97	1.20	~ 0
	Slope / 10^{-3}	3.66	3.59	3.22	3.55	~ 0

Table 6.4: Grain size and microstrain calculated from slopes and intercepts in **Table 6.3**.

Process gas temperature / K	Annealing temperature / K	298	373	423	473	573
298	Grain size / nm	40	60	85	> 300	> 300
	Strain / x 10^{-3}	~ 0	~ 0	~ 0	~ 0	~ 0
523	Grain size / nm	60	75	70	115	> 300
	Strain / x 10^{-3}	1.83	1.80	1.6	1.78	~0

Table 6.5: Measured value of resistance and the resistivity calculated from these values for cold sprayed Cu deposited using gas heated to 523 K and annealed at various temperatures. Resistance and resistivity values of 99.998 % Cu sheet are also shown. Resistance was measured over a length of 20 mm.

Annealing temperature / K	Mean resistance (from six measurements) / 10^4 nΩ	Standard deviation / 10^3 nΩ	Cross-section area of track or sheet / 10^{-6} m^2	Resistivity / nΩ m
298	6.14	1.91	8.8209	27.09
373	6.13	1.21	8.8209	27.05
473	3.37	3.98	15.83	26.70
573	2.97	4.33	16.1	23.91
773	4.78	1.21	8.8209	21.16
298 (Cu sheet)	9.11	1.02	3.84	17.50
773 (Cu sheet)	7.89	2.20	4.25	16.76

Table 6.6: Microhardness and tensile strength of cold sprayed and bulk Cu. Scribe marks were made on the samples before tensile testing. Elongation was measured on the samples as the increase in the length between scribe marks after breakage.

Material	Microhardness / kg mm^{-2}	Tensile strength / MPa	Elongation to fracture / %
Cold sprayed	180	375	<1
Cold sprayed and annealed (873 K / 1 hr)	65	230	26
Cu sheet rolled	89	260	42
Cu sheet rolled and annealed (773 K / 1 hr)	48	208	60

Table 6.7: Intermetallic layer thickness after annealing Sn–Cu and Sn + Pb – Cu couples at different temperatures and times.

Diffusion couples		Annealing temperature / K	Duration of annealing / days	Intermetallic layer thickness / μm			Reference
				η	ε	ε + η	
Electro deposited tin on Cu		343	~ 310	-	-	~5	[113, 115]
		443		-	-	~30	
Fused Sn - Pb on copper		293	2209	-	-	3	[114]
		353	70	2	0.9	2.9	
		393	28	3.3	1.5	4.8	
		433	28	6.3	3.7	10	
Hot dipped tin on phosphor bronze		323	625	-	-	~0.3	[112]
		348	625	-	-	~1.5	
		373	144	-	-	~2.3	
Hot dipped Sn and Sn-Pb solder on Cu	Pure Sn	448	29	~9	~5	~14	[123]
	82Sn18Pb		29	~9	~5	~14	
	63Sn37Pb		29	~9	~5	~14	
	27Sn73Pb		29	~6	~4	~10	
Solder on Cu	63Sn37Pb	443	30	~13	~5	~18	[124]

Table 6.8: Spray parameters to deposit tin and copper.

Material	Gas flow rate / kg s^{-1} (x 10^{-3})	Gas pressure / bar	Powder feed rate / g s^{-1}	No. of passes	Stand-off distance / mm	Traverse speed / mms^{-1}
Tin	1.52	10	0.2	2	5	100
Copper	2.9	22	0.9	2	15	100

Table 6.9: Measured and calculated compositions of phases shown in **Fig. 6.19**. Sample annealed at 443 K for 146 days.

Region	Contrast	Measured composition (at. % Sn)	Calculated composition (at% Sn)
Tin	Bright	99.6	-
η	Light grey	47.9	46
ε	Dark grey	28.1	25
Copper	Dark	0	-

Table 6.10: Composition of various regions in tin – copper sample annealed for 1.16 x 10^7 s (135 days) at 343 K, shown in **Fig. 6.20**.

Region	Composition (at. % Sn)
Bright	99
Grey	36
Dark	0

Table 6.11: Thickness of intermetallic phases after annealing at 343 K and 443 K

Heat treatment temperature	Layer thickness / μm			Thickness ratio, $\frac{\eta}{\varepsilon+\eta}$
	ε phase	η phase	$(\varepsilon+\eta)$ phase	
343 K for 1.16 x 10^7 s (135 days)	-	4 ± 2 (Cu rich phase)	4 ± 2	-
443 K for 1.26 x 10^7 s (146 days)	5 ± 1.5	44 ± 6	49 ± 7.5	0.9

Table 6.12: Slopes and intercepts obtained following linear regression analysis of graphical data plotted in **Figs. 6.27 & 6.29** for different annealing times.

Annealing temperature / K	Time / s	Phase	Slope / 10^{-4} $\mu m\ s^{-1/2}$	Intercept / μm -0.502 3.15	R^2 value
343	1.16×10^7 s (up to 135 days)	η	14.51	-0.502	0.972
443	2.16×10^6 s (up to 25 days)	η	53.4	3.15	0.7492
		ε	34.3	0.33	0.9321
	4.23×10^6 s to 1.26×10^7 s (49 to 146 days)	η	159.3	-12.4	0.9941
		ε	-4.2	6.51	0.3365

Table 6.13: η and ε phase thickness calculated from interphase position parameters from Mei *et al.* [2] and measured values from this study, for annealing at 443 K.

Time / s	Thickness / μm	η	ε
2.16×10^6 (25 days)	Calculated (**Fig. 21**)	9	4
	Measured (**Fig. 16**)	13	6

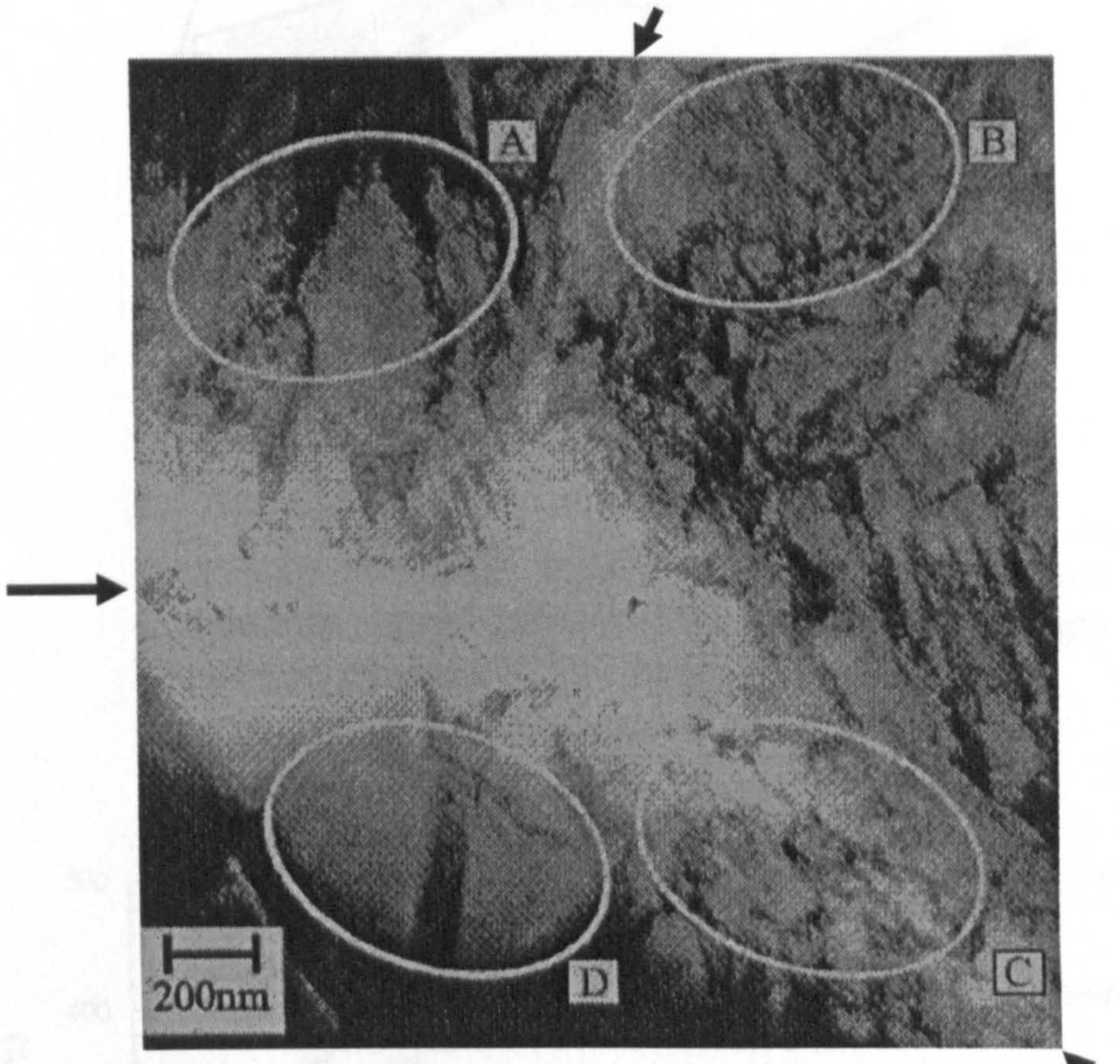

Fig. 6.1: TEM micrograph of an interparticle triple point in a cold spray copper coating showing typical microstructural features. Particle-particle boundaries are marked with arrows. A, high dislocation density with dislocations arranged in walls, grain size above 1 μm; B, aligned elongated grains sized about (50 x 150) nm^2 in projection, featuring nonequilibrium grain boundaries characterized by ultra high dislocation densities adjacent to the grain boundaries; C, equiaxed ultrafine grains about 100 nm in diameter. They exhibit heavily deformed zones around the grain boundaries with extremely high dislocation densities, while the inner part of the grains are rather free of dislocations; D, dislocation free region exhibiting twins, grain size above 1 μm. From Borchers *et al*. [76].

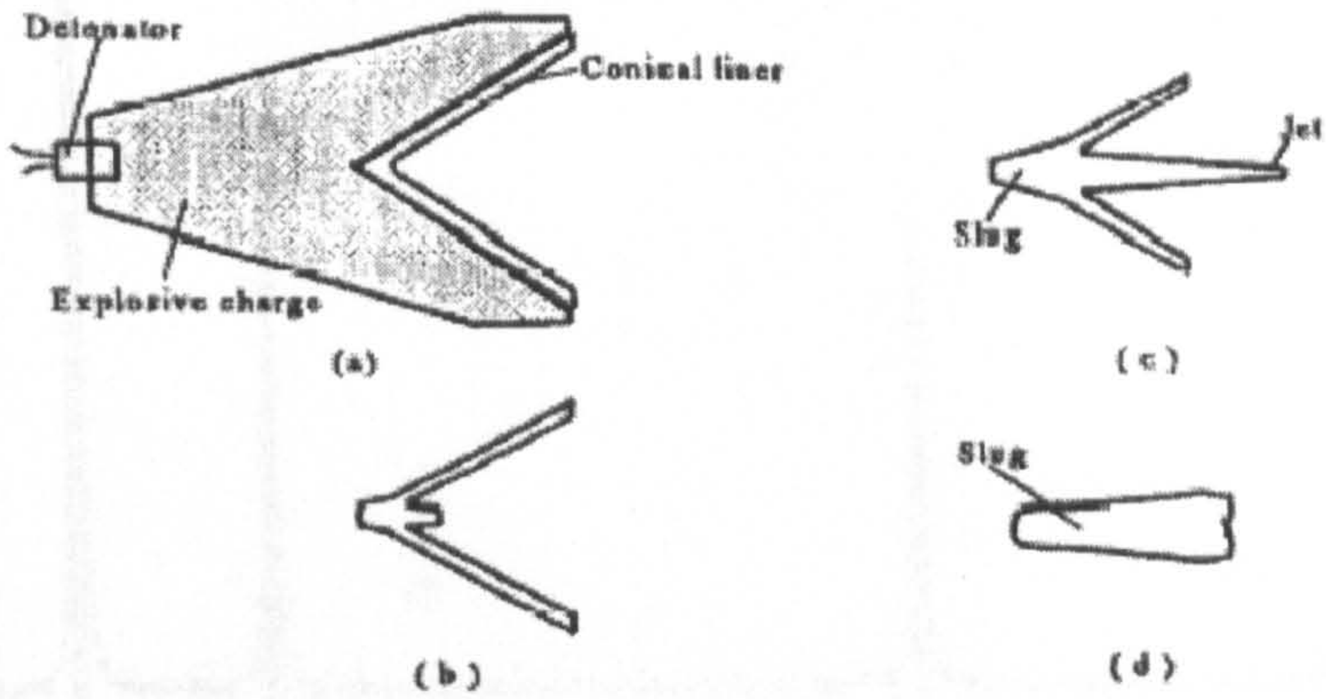

Fig. 6.2: Development of a shocked metal flow at explosion: a) initial stage, b) & c) after partial compressive collapse, d) slug collected from target-length L = 18 mm, diameter D_{max} = 7 mm, D_{min} = 3 mm [91].

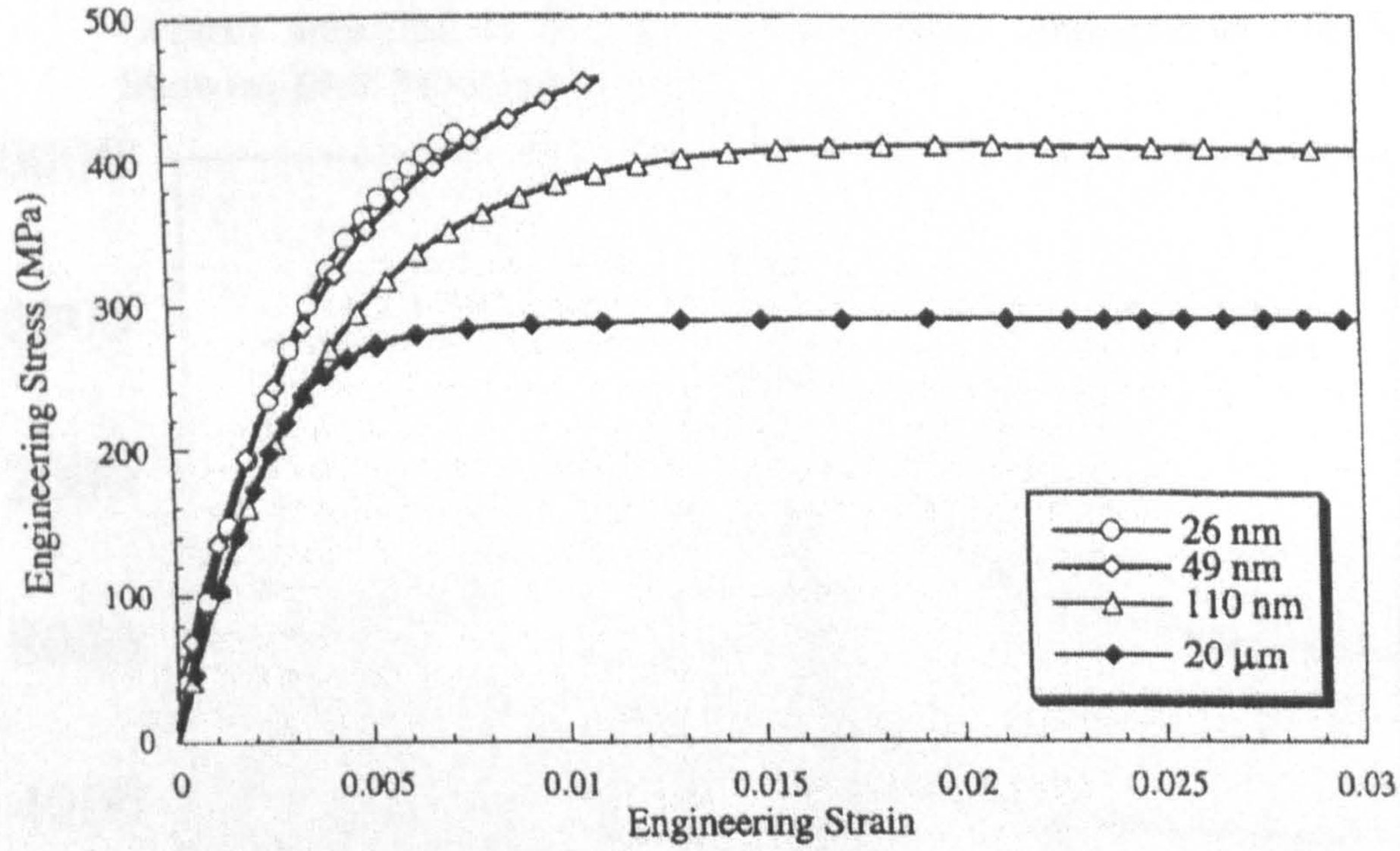

Fig. 6.3: Stress-strain plots for Cu fabricated by compaction of nano crystalline Cu powder prepared by inert gas condensation method. From Sanders *et al*. [77, 78]. The test for grain size of 110 nm and 20 μm was stopped because the displacement range was exceeded.

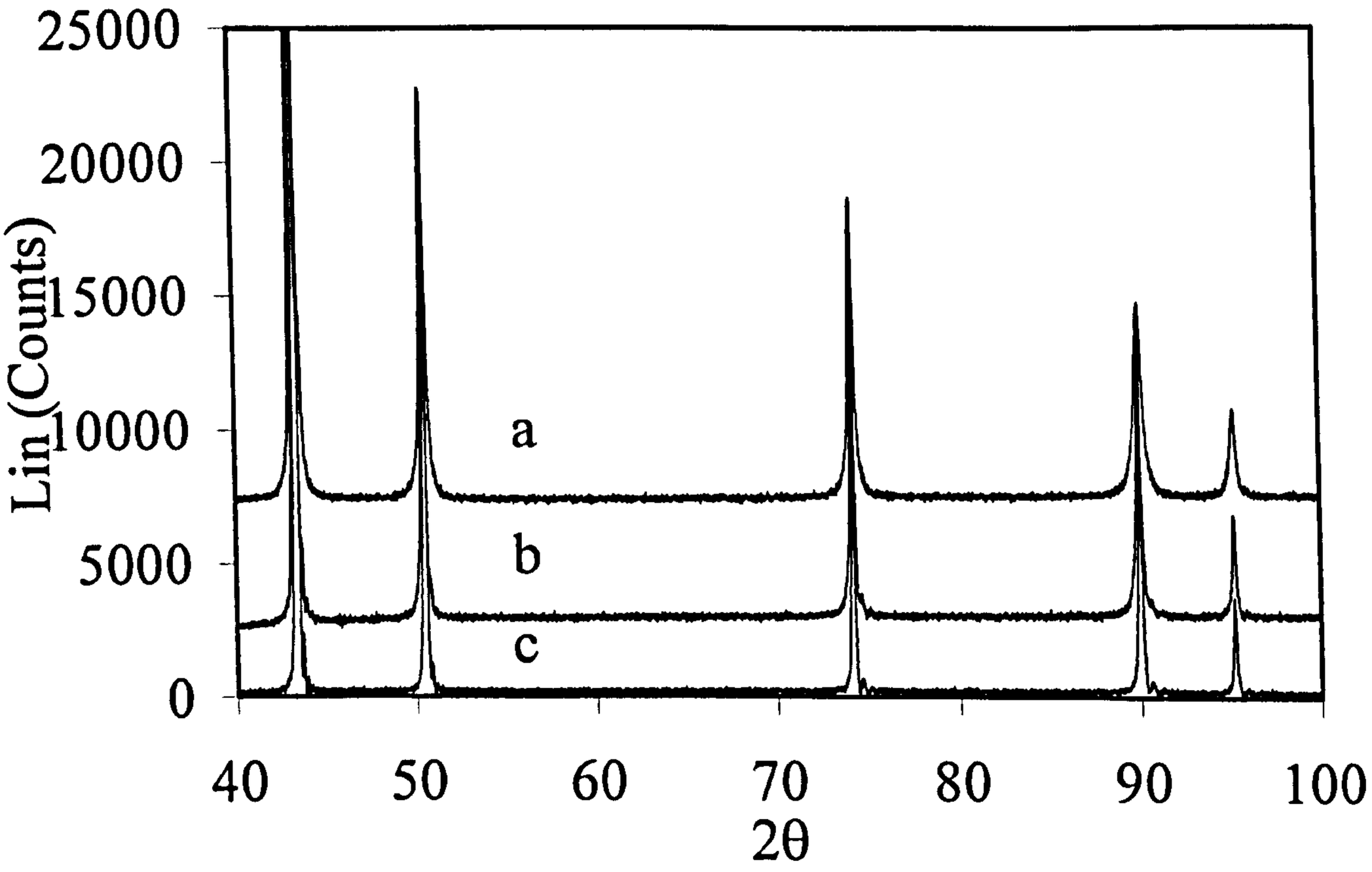

Fig. 6.4: X-Ray diffraction pattern for; a) As-sprayed deposit, b) Deposit annealed at 573 K, c) Cu powder annealed at 773 K. Showing peak broadening in (a).

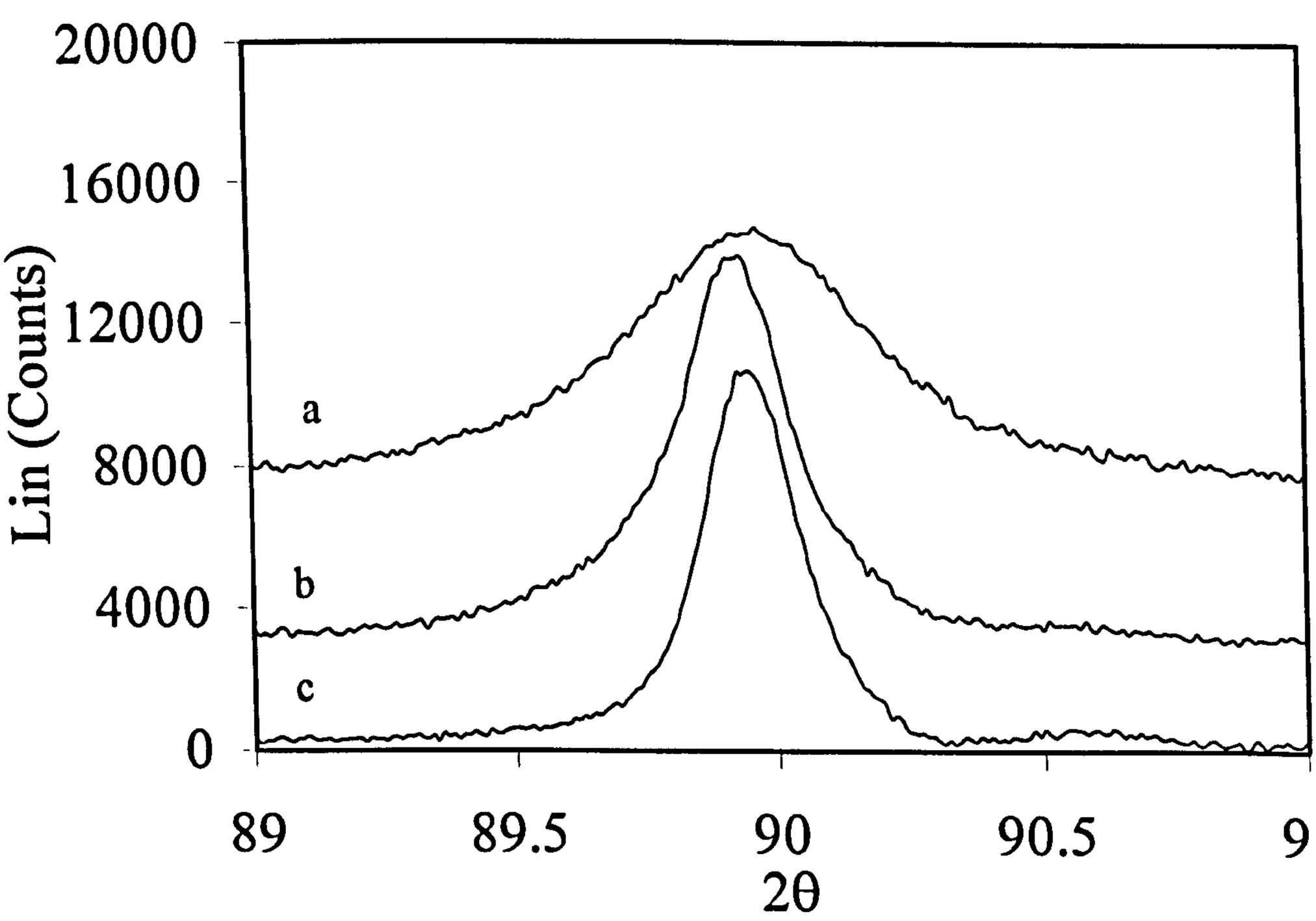

Fig. 6.5: Detail of XRD peak at 89.9° showing peak profiles; a) As-sprayed deposit, b) Deposit annealed at 573 K, c) Cu powder annealed at 773 K.

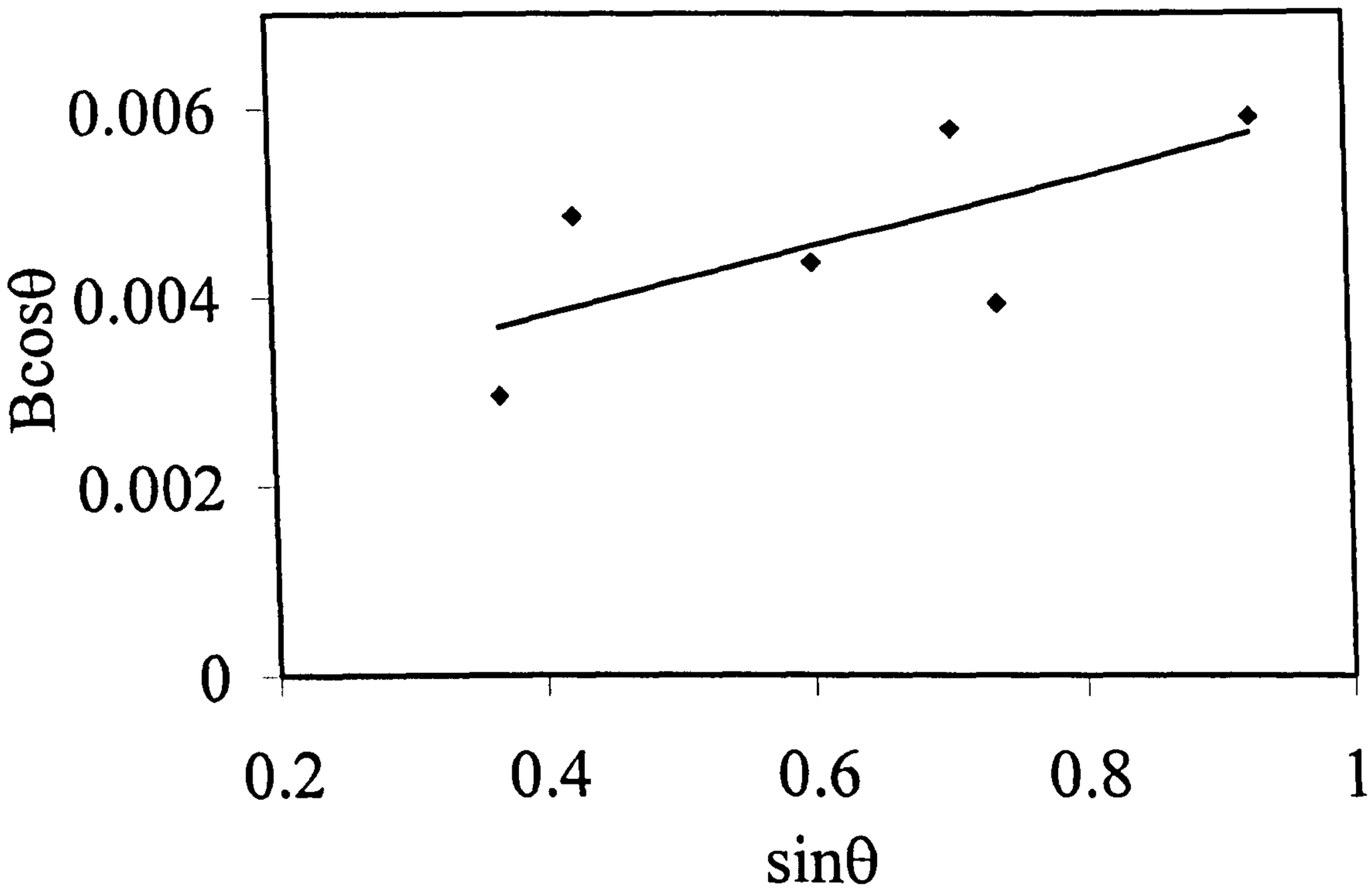

Fig. 6.6: Hall – Williamson plot for as sprayed Cu deposited using gas at 523 K showing experimental data points and linear regression line with a slope of 3.66×10^{-3}, intercept of 2.31×10^{-3} and correlation coefficient of 0.4549.

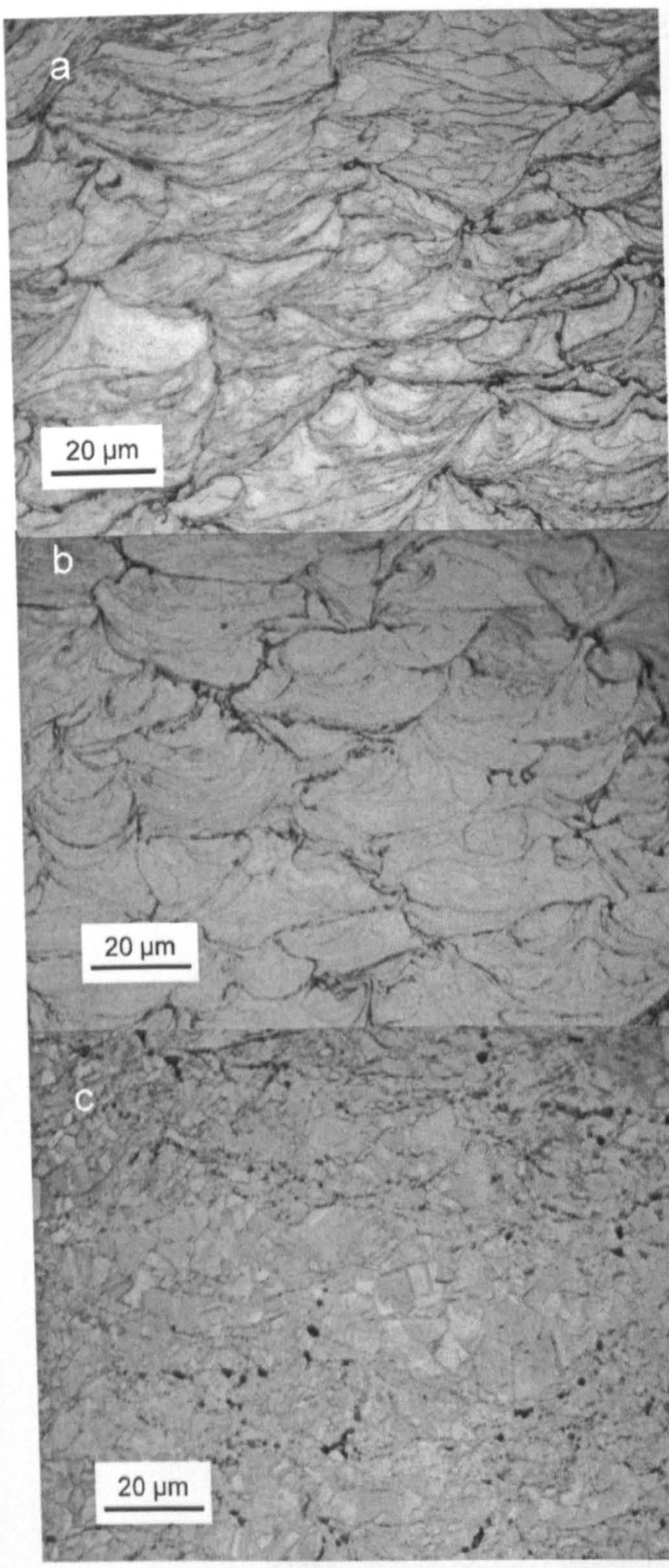

Fig. 6.7: Optical microscope image of Cu deposited using gas at 523 K. a) as sprayed, b) annealed at 473 K, c) annealed at 773 K. In (c) fine recrystallized grains can be seen.

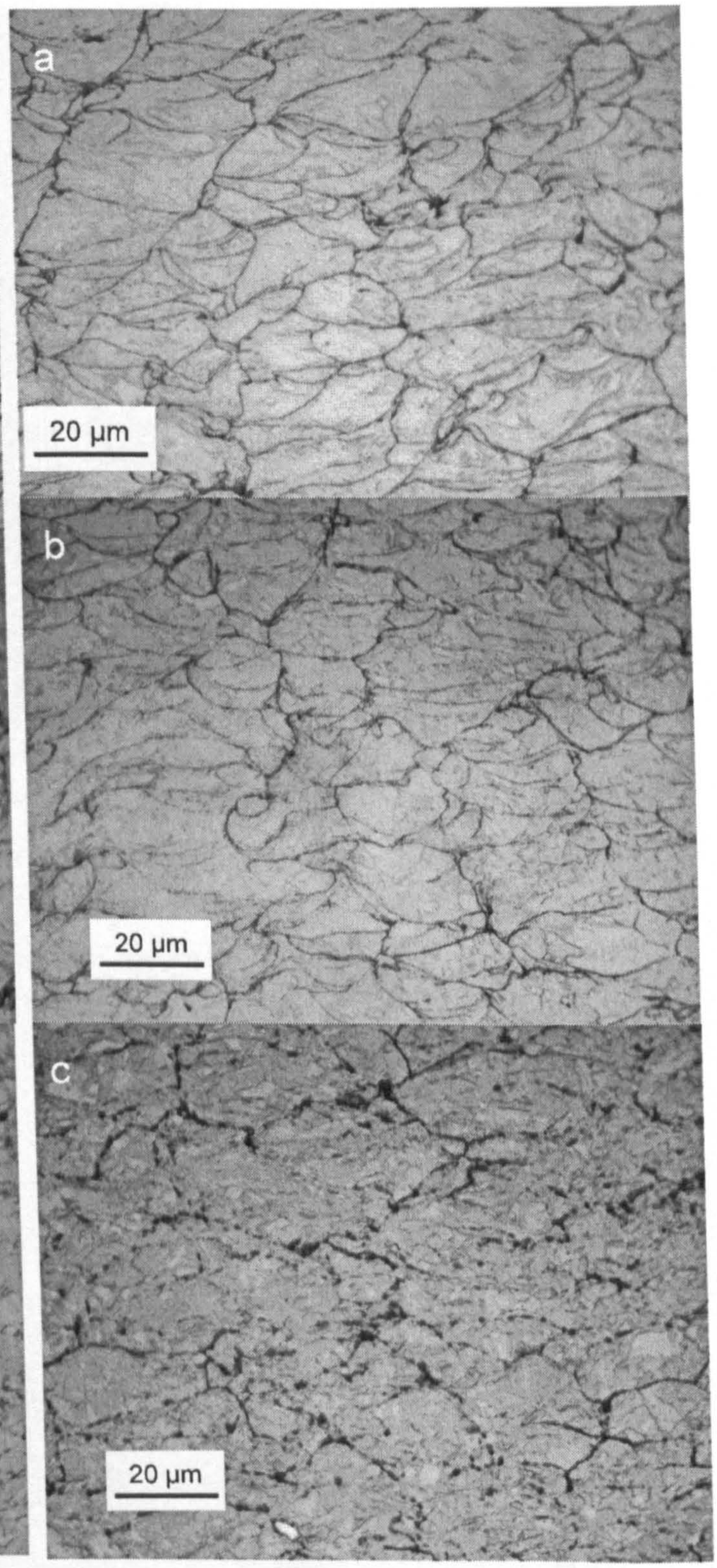

Fig. 6.8: Optical microscope image of Cu deposited using gas at 298 K. a) as sprayed, b) annealed at 473 K, c) annealed at 773 K. In (b) a few fine recrystallized grains can be seen and in (c) larger recrystallized grains can be seen.

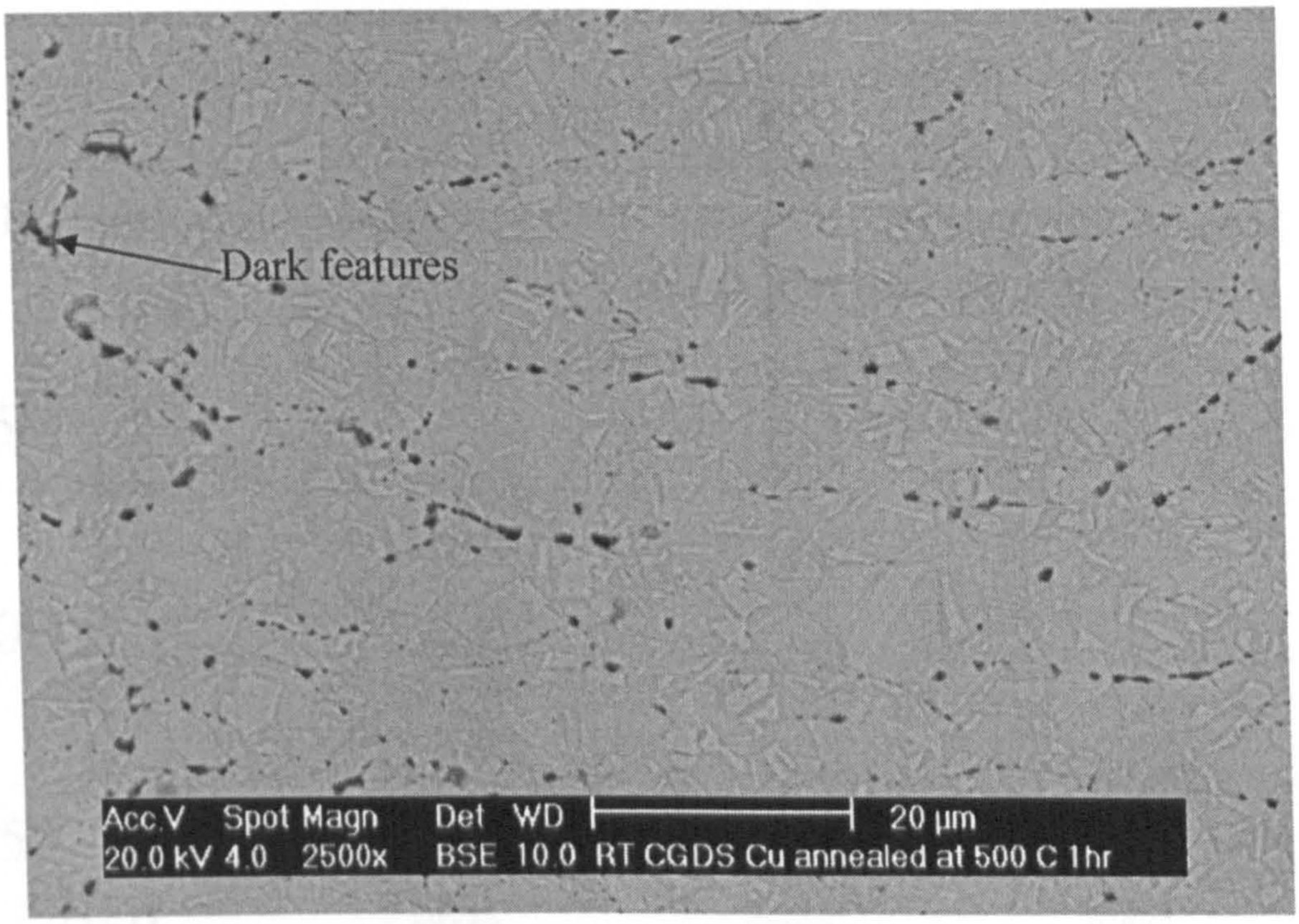

Fig. 6.9: BSE image of Cu cold sprayed at 298 K and annealed for 1 hr at 773 K, showing recrystallized grains and dark features.

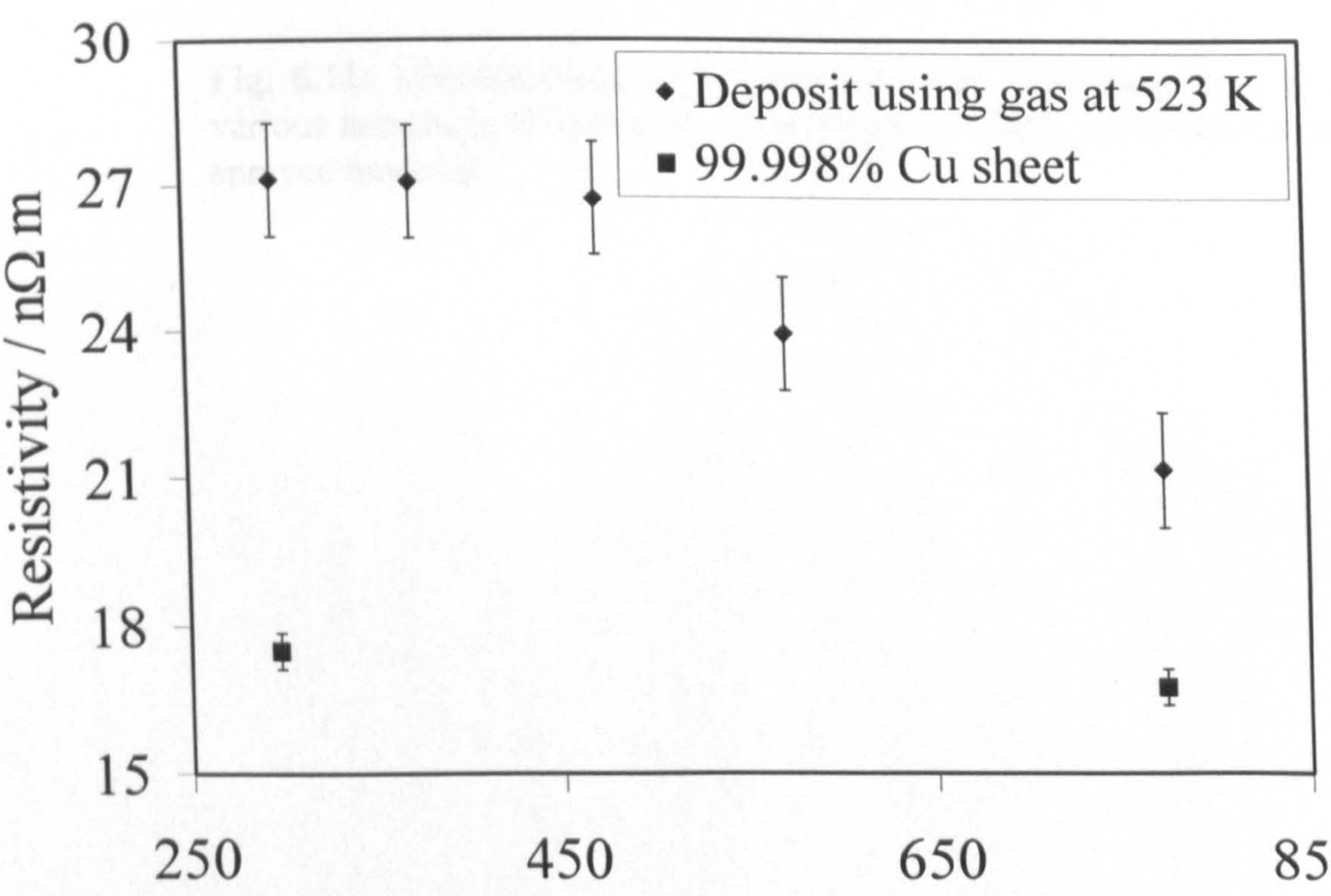

Fig. 6.10: Plot showing resistivity of cold sprayed and bulk copper after annealing for 1 hr at different temperatures.

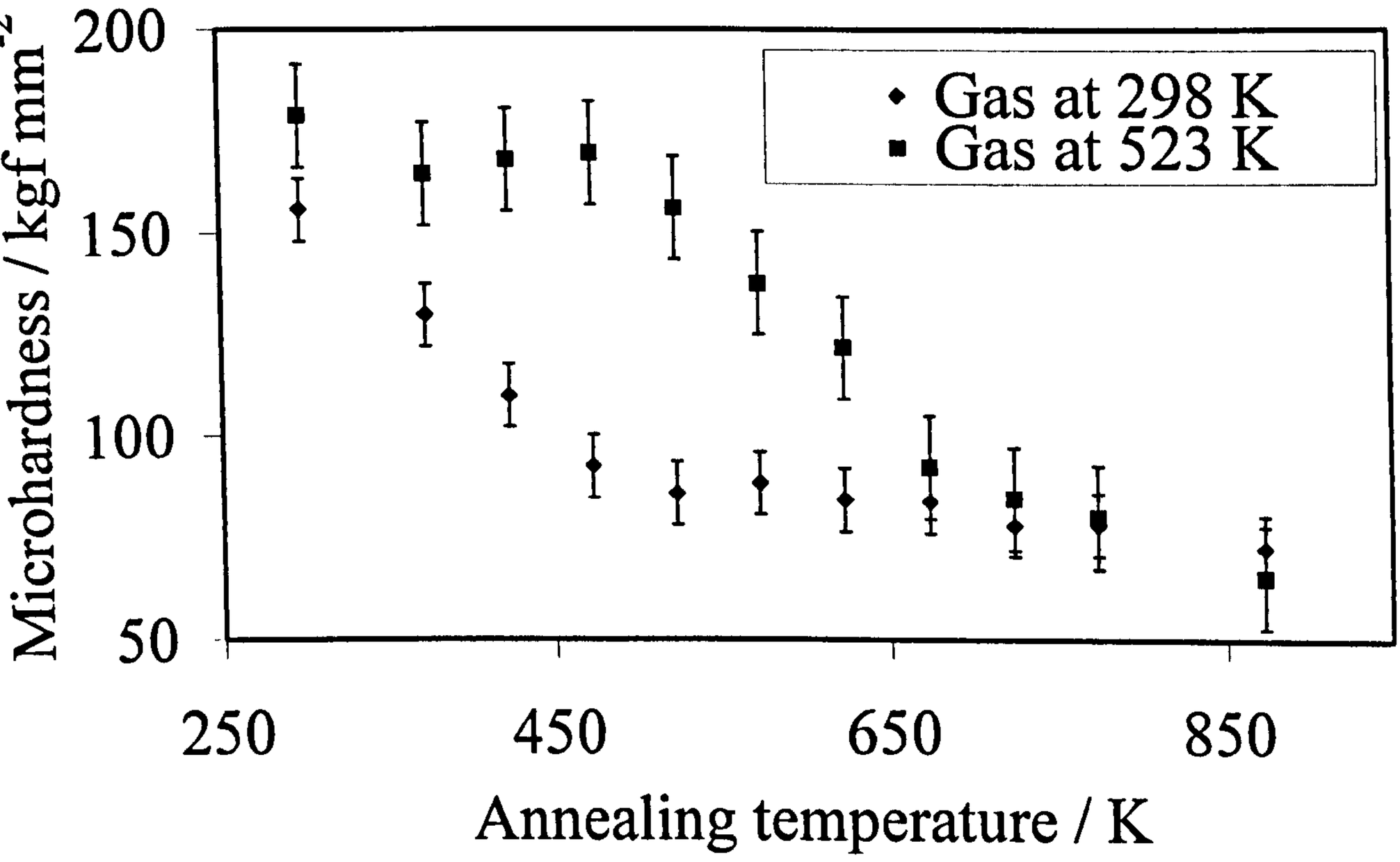

Fig. 6.11: Microhardness of Cu deposits after annealing for 1 hr at various annealing temperatures. The points at 298 K correspond to as-sprayed material.

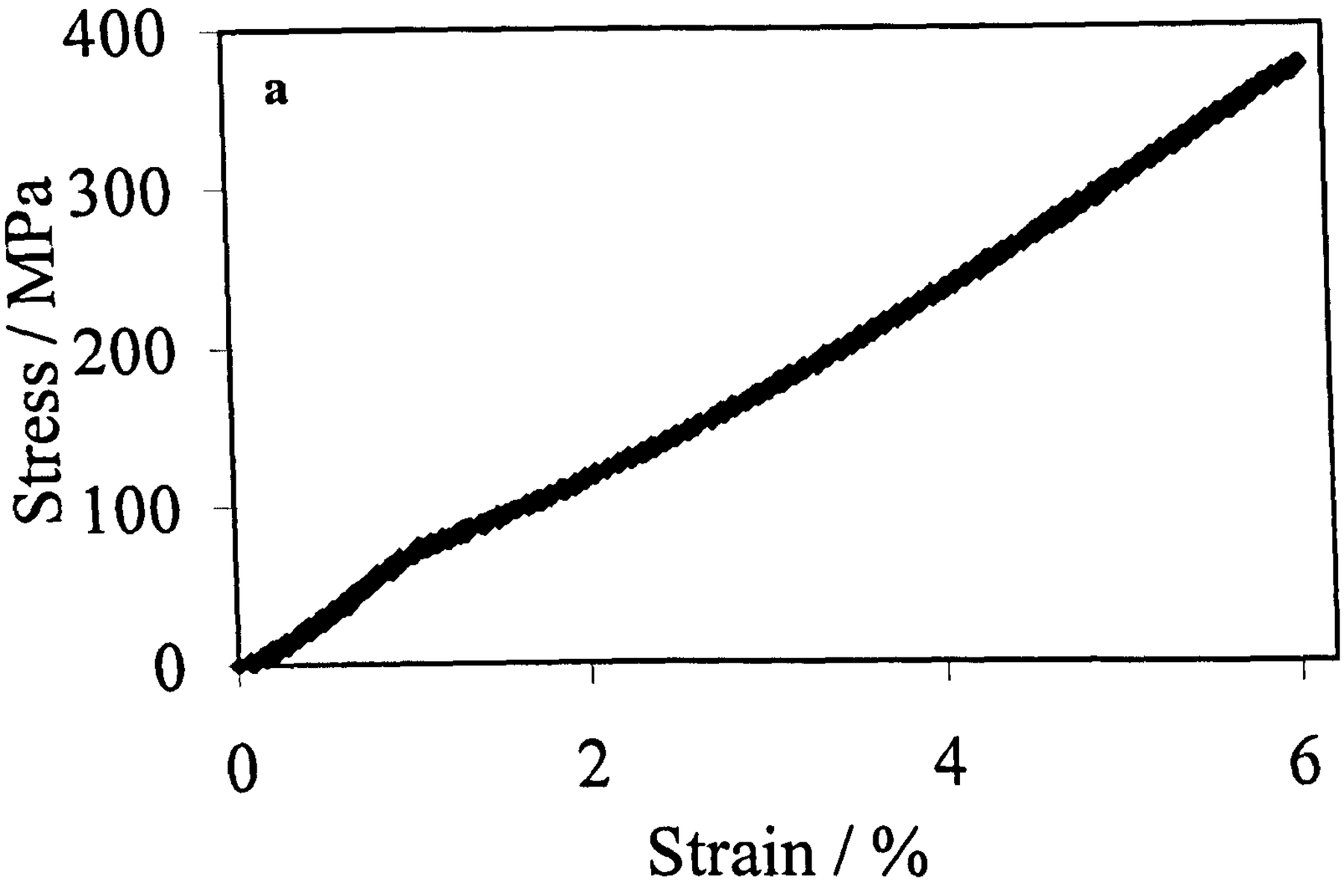

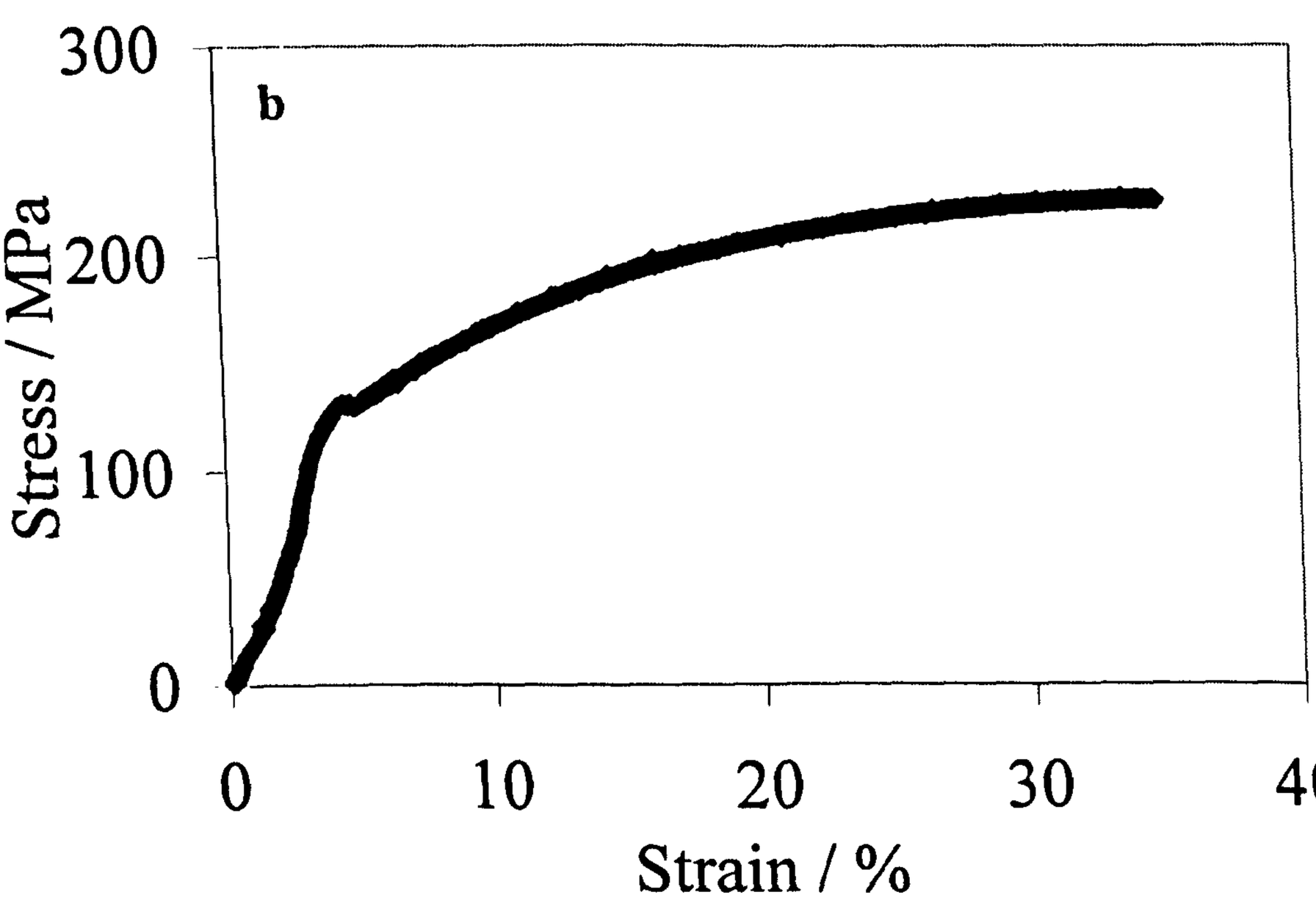

Fig. 6.12 (a–b): Engineering stress – strain plot of cold sprayed Cu deposited using gas heated to 523 K and gas mass flow of 2.9 x 10^{-3} kg s^{-1}; (a) as sprayed copper, (b) after annealing at 873 K for 1 Hr. Strain values derived from cross head movement.

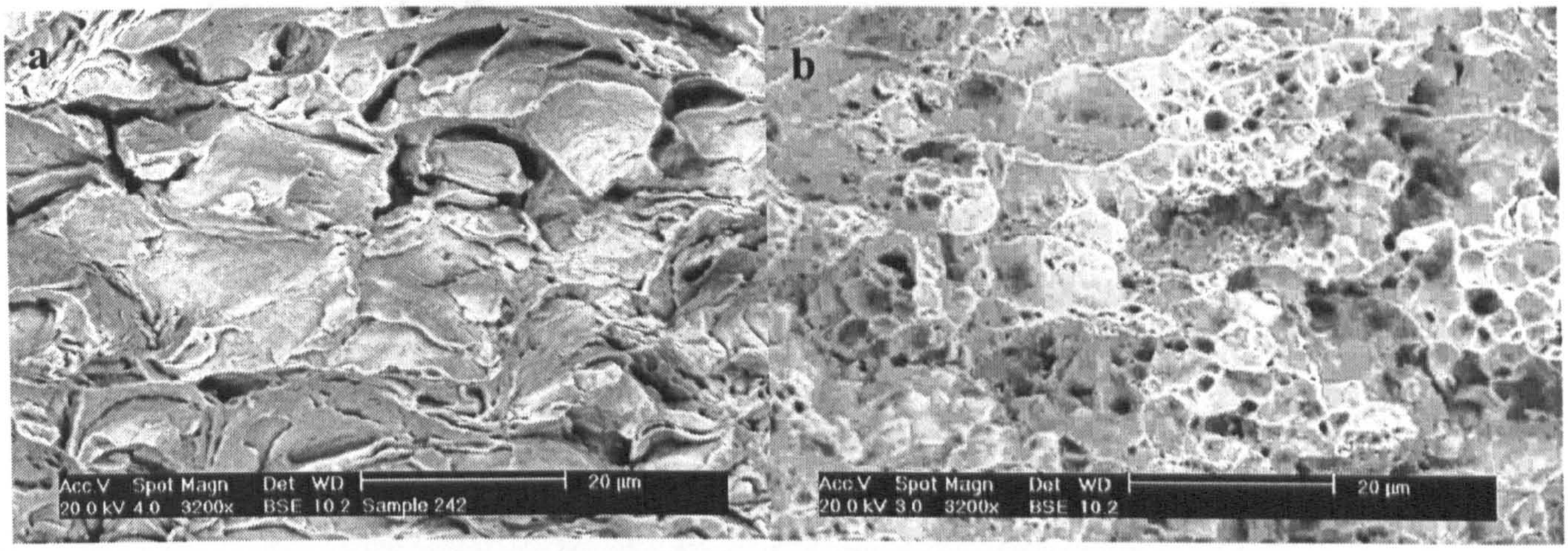

Fig. 6.13 (a - b): SEM images of fracture surfaces following tensile testing; (a) As-sprayed deposit showing fracture largely at particle – particle interface, (b) deposit annealed at 873 K, showing a typical ductile dimple fracture surface. The arrow indicates secondary phase particles on the fracture surface.

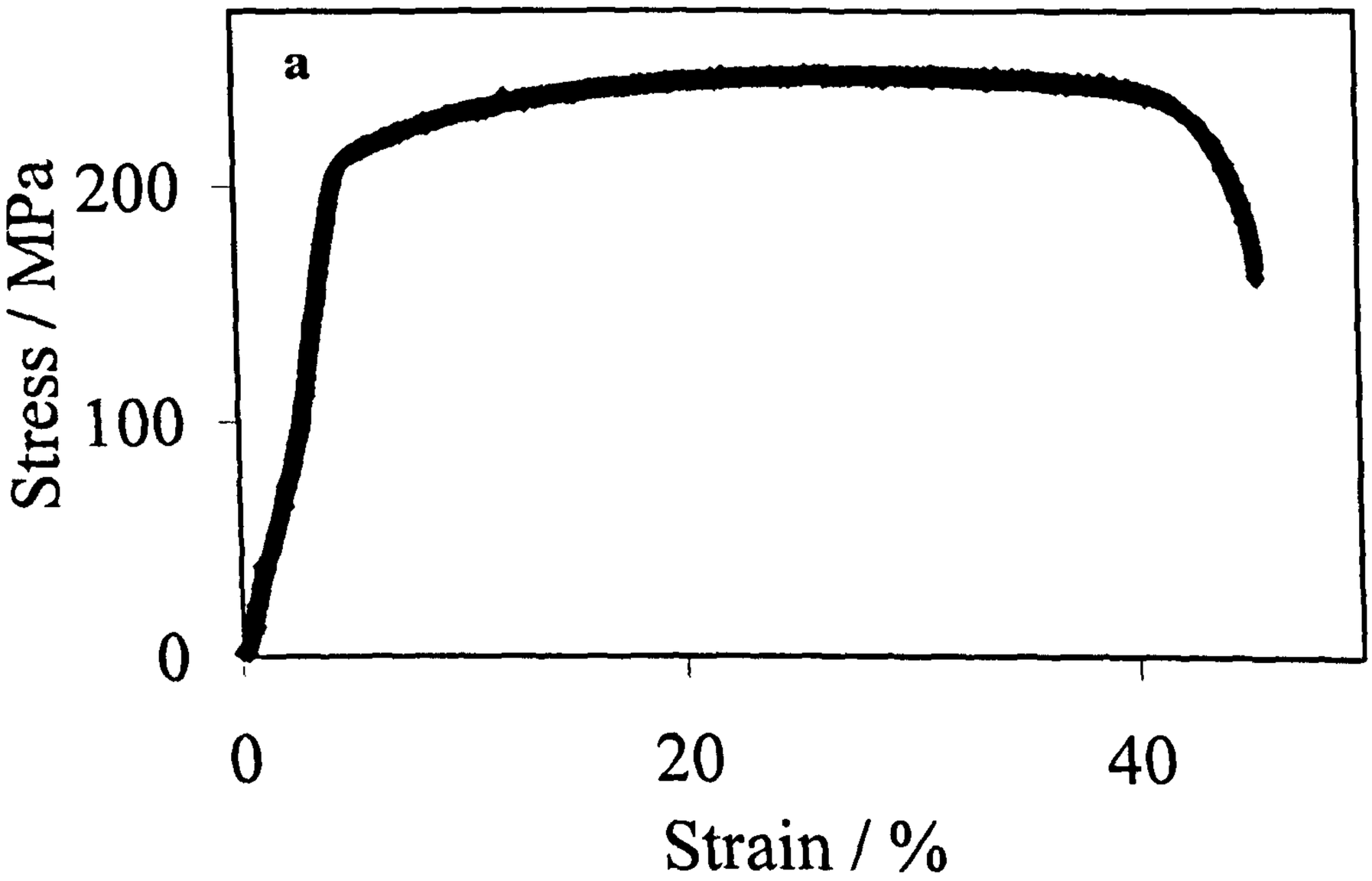

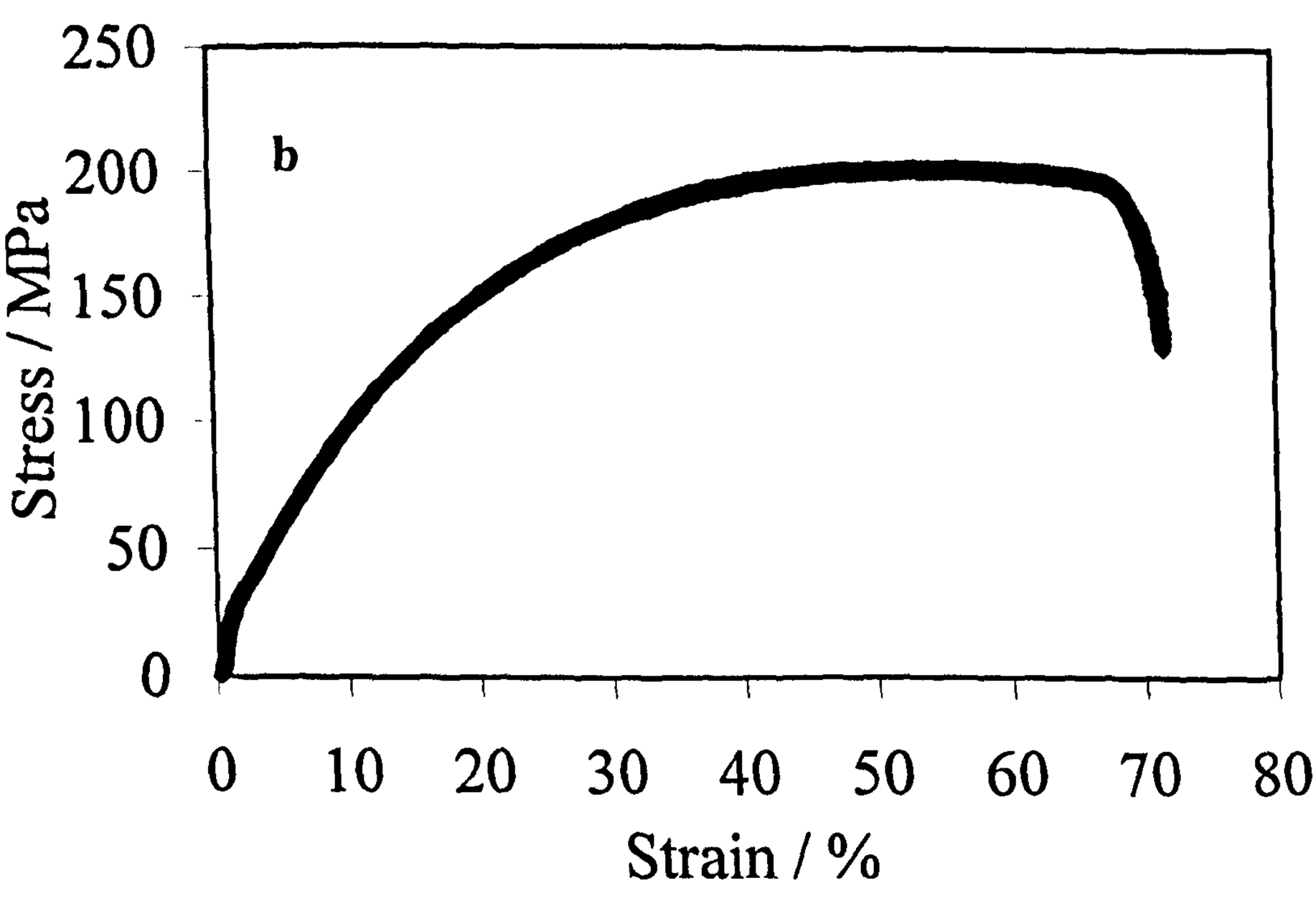

Fig. 6.14 (a–b): Stress – strain plot of cold rolled Cu. (a) as rolled, (b) after annealing at 773 K for 1 hr.

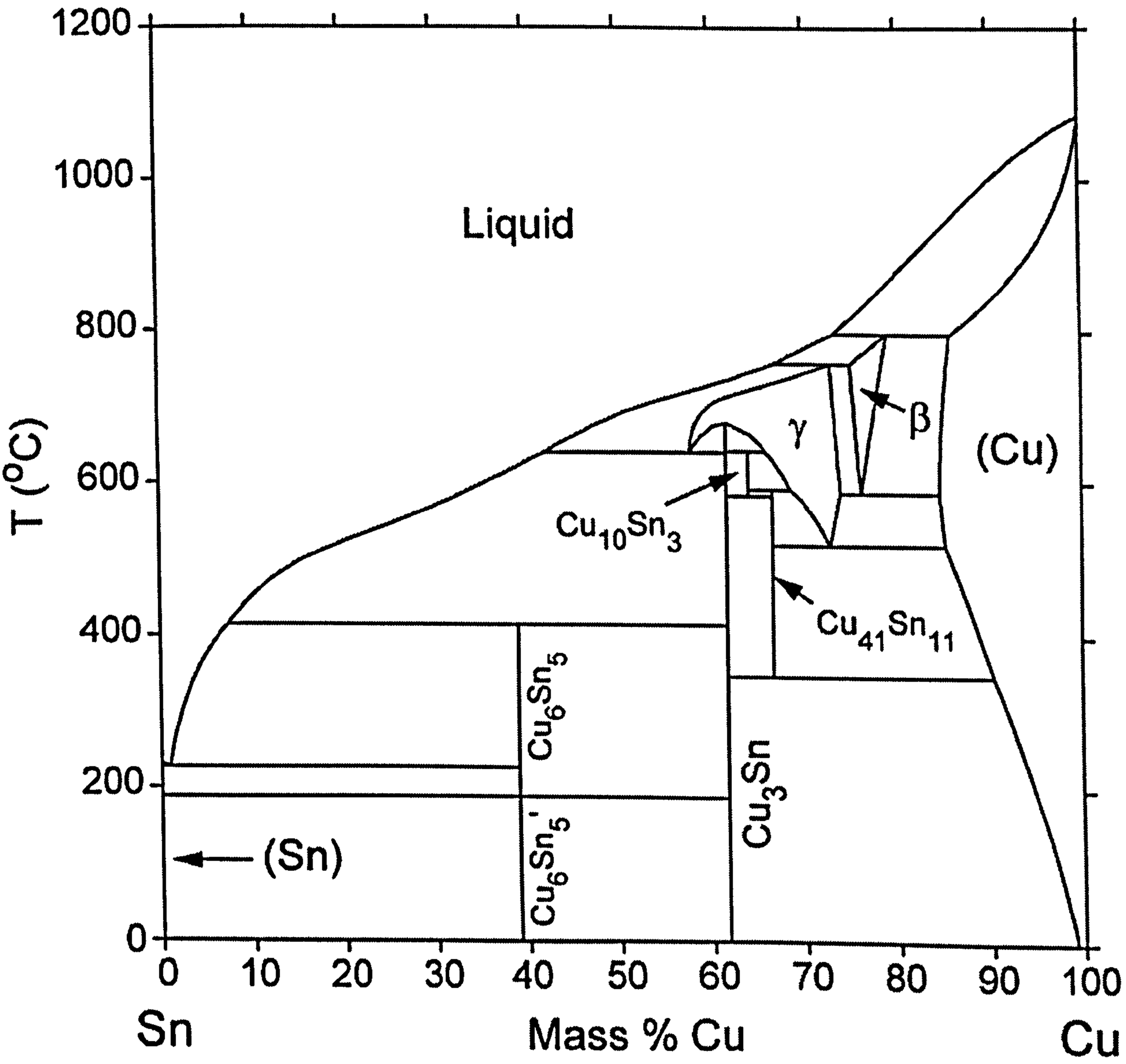

Fig. 6.15: Tin – copper phase diagram [131].

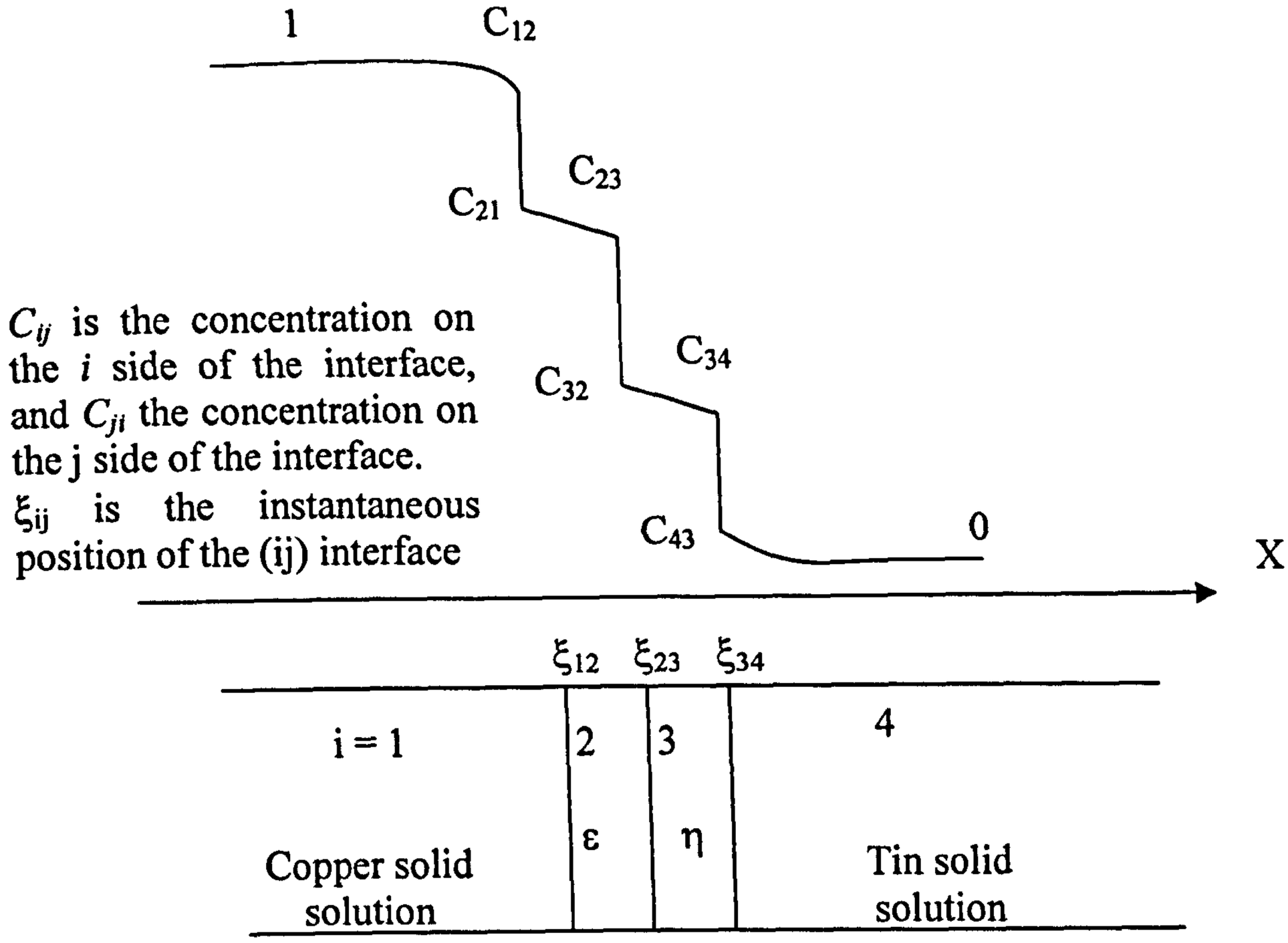

Fig. 6.16: Schematic drawing of the analytical model [121].

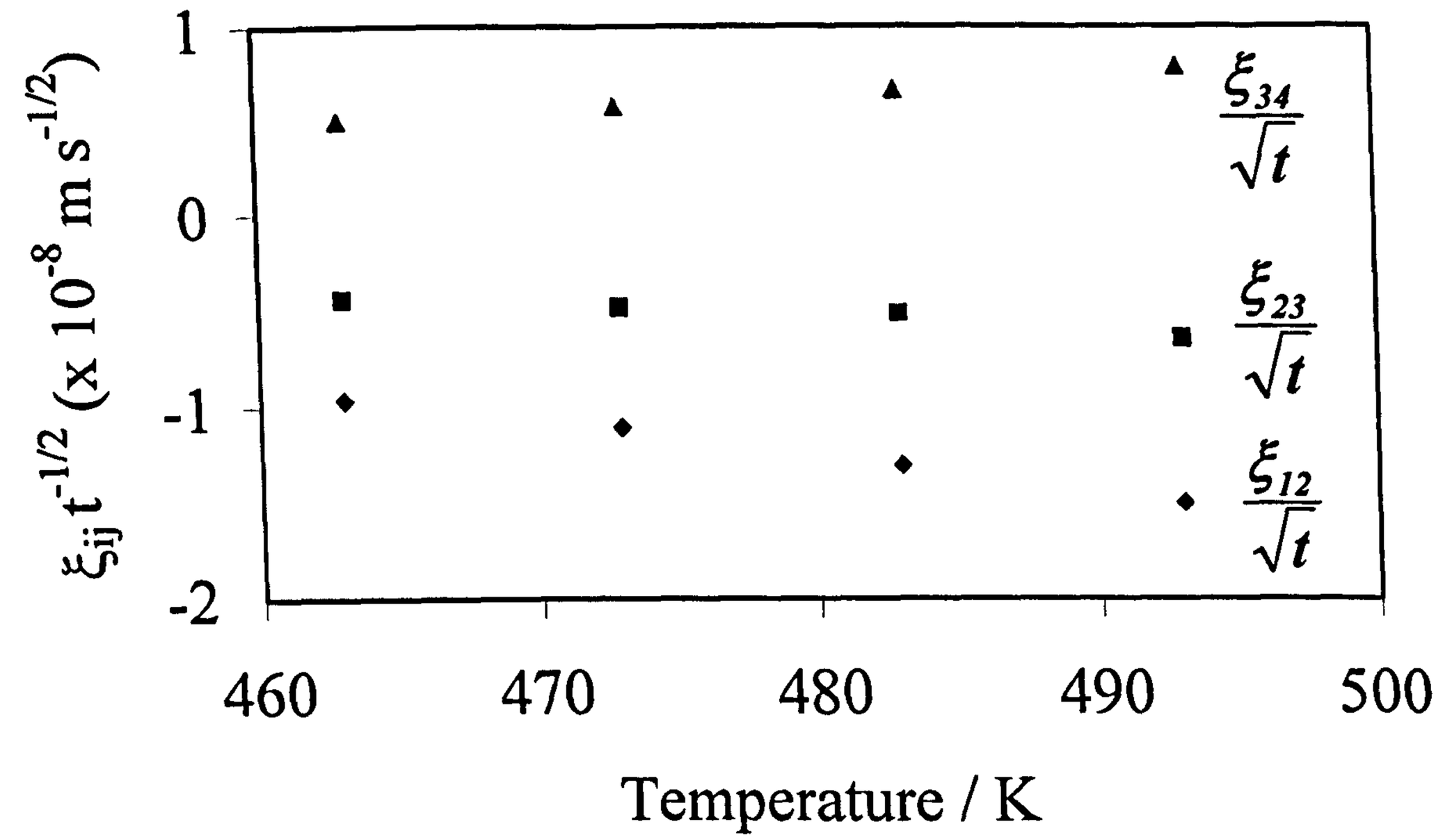

Fig. 6.17: Calculated interphase position parameters *vs* temperature. ξ_{ij} is the instantaneous position between phase i and j (i, j = 1, Cu solid solution; = 2, ε; = 3, η; = 4, Sn solid solution) [121].

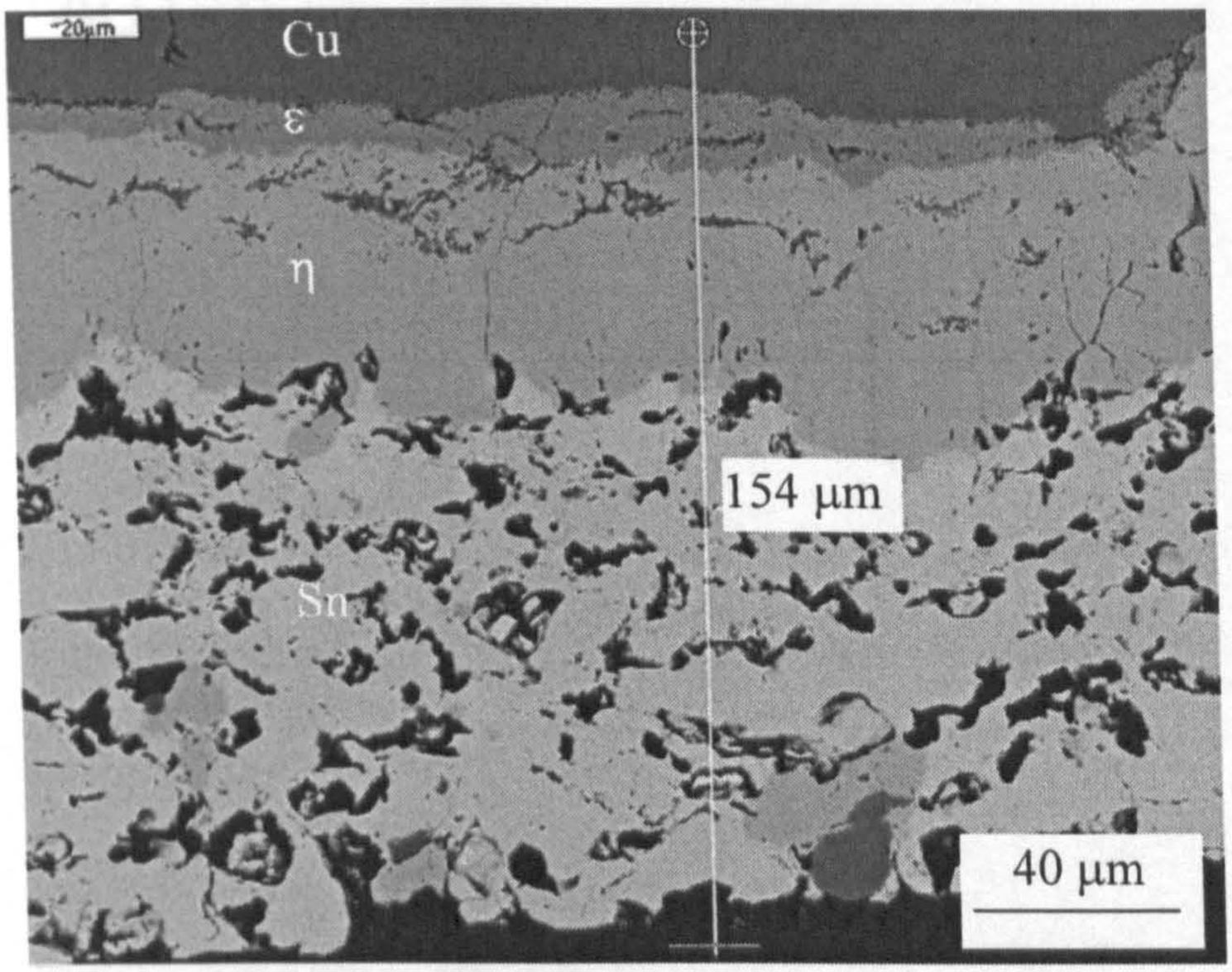

Fig. 6.18: BSE image of Sn - Cu couple annealed at 443 K for 1.26 x 10^7 s (146 days), showing Cu, porous Sn, two intermetallic phases and the position of the line scan.

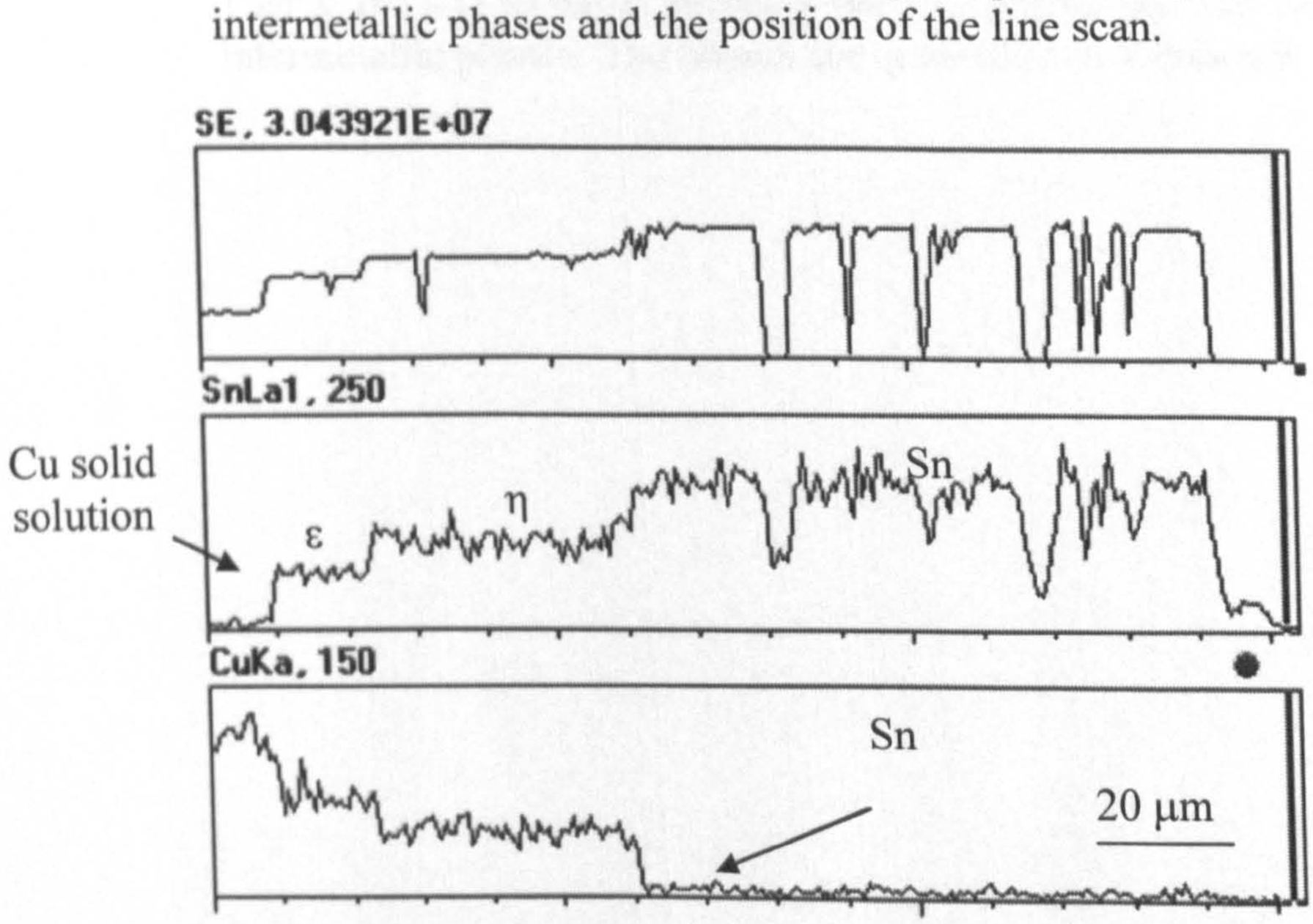

Fig. 6.19: Line scan of the Sn-Cu diffusion couple annealed at 443 K for 1.26 x 10^7 s (146 days), showing the composition with respect to the line shown in **Fig. 6.18**. Cu, Sn, ε and η phases are labeled.

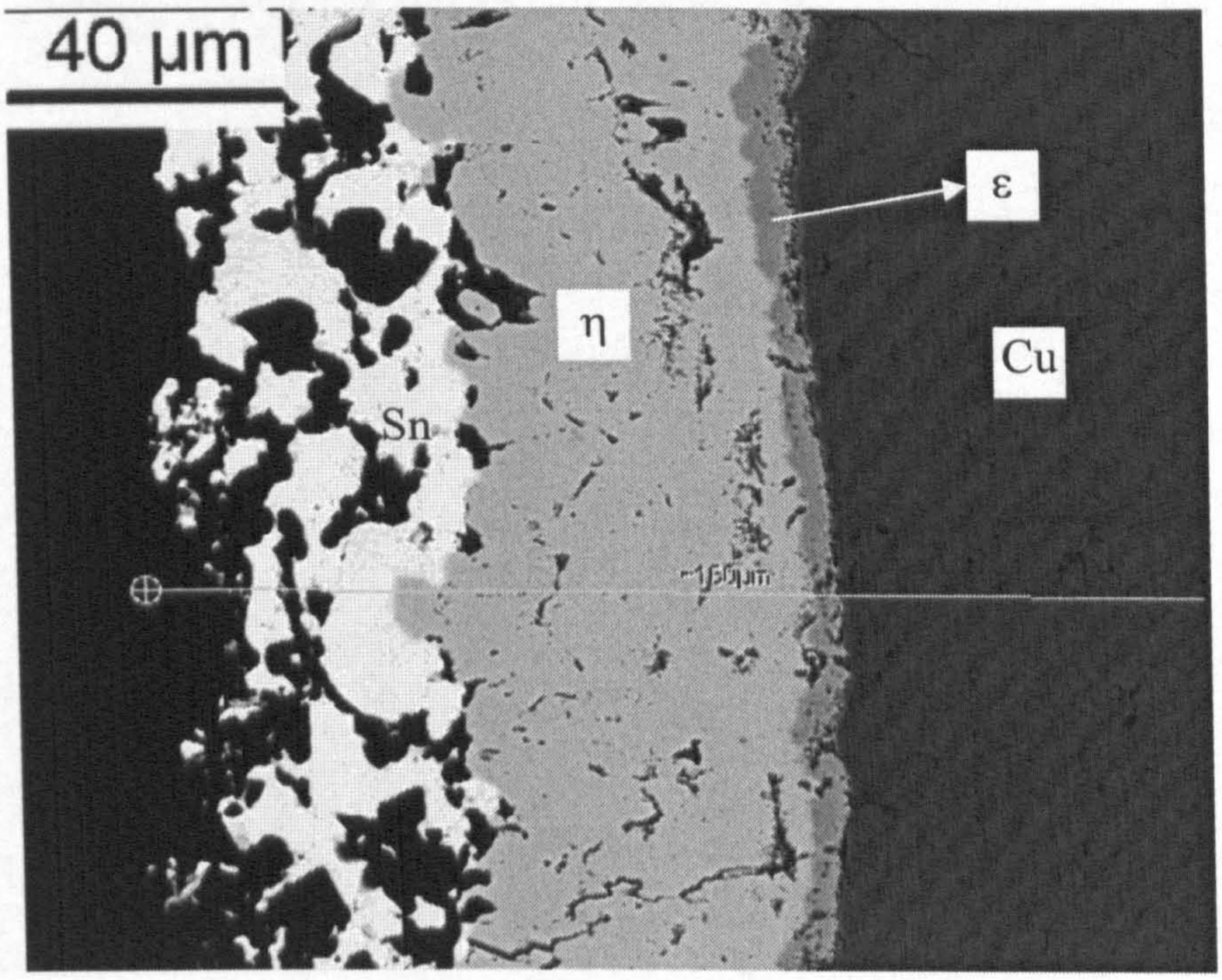

Fig. 6.20: BSE image of Sn - Cu couple annealed at 443 K for 1.26×10^7 s (146 days) showing the Cu, porous Sn, and two intermetallic phases. The phases are quantified in **Table 6.9**.

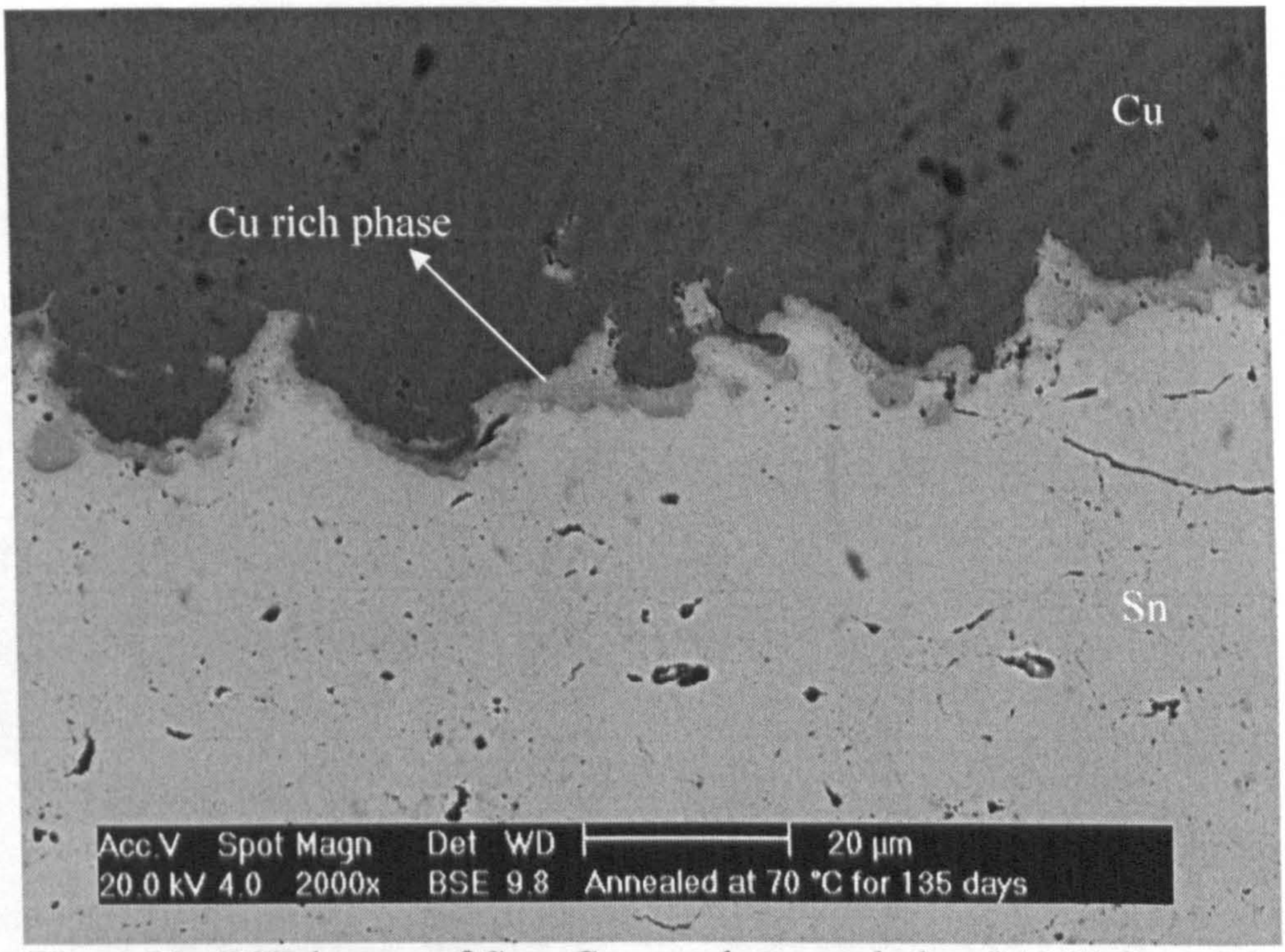

Fig. 6.21: BSE image of Sn - Cu couple annealed at 343 K for 1.16 x 10^7 (135 days) showing the Cu rich layer. The phases are quantified in **Table 6.10**.

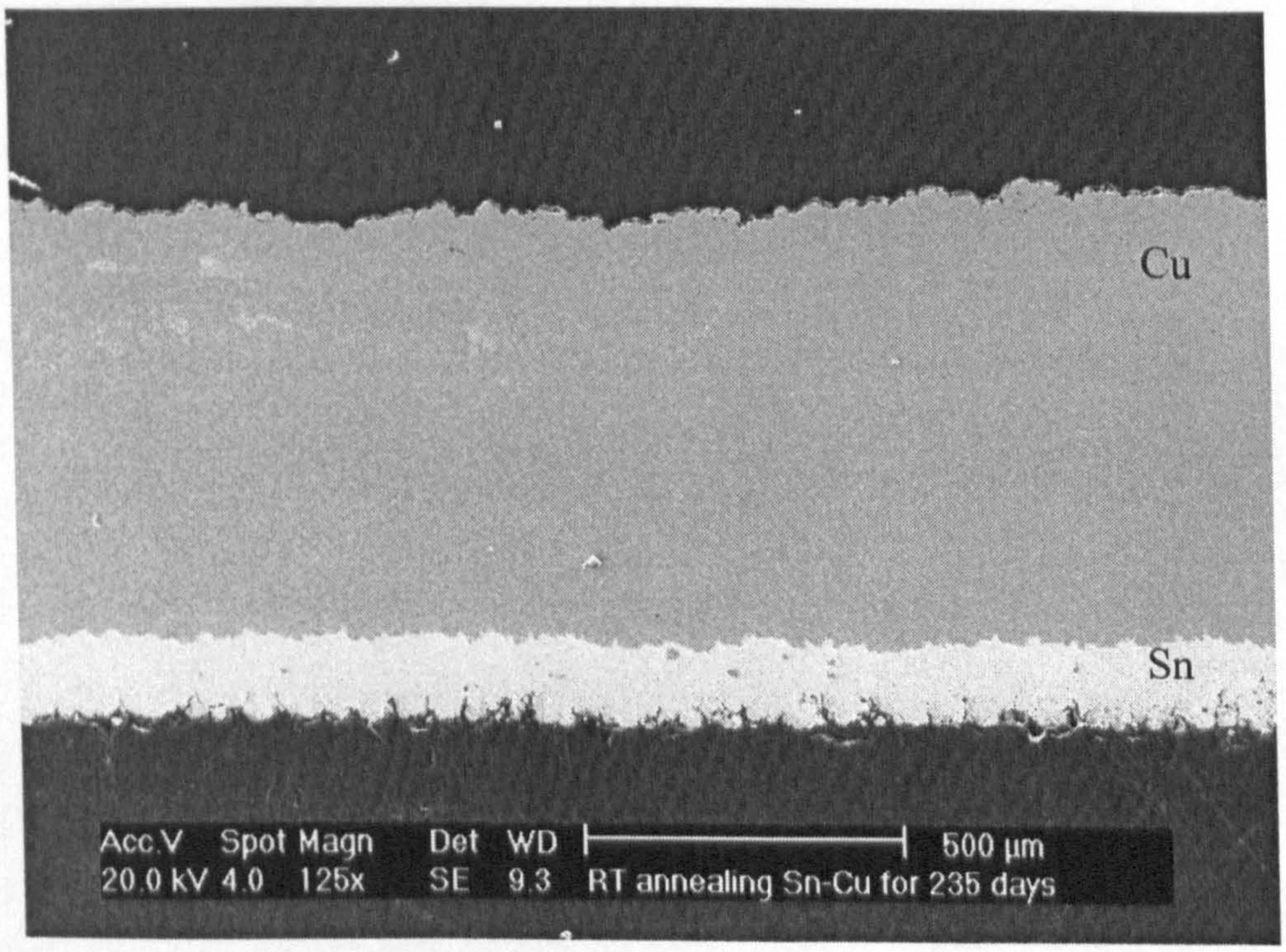

Fig. 6.22: BSE image of Sn-Cu track showing the profile and thickness of tin and copper layers.

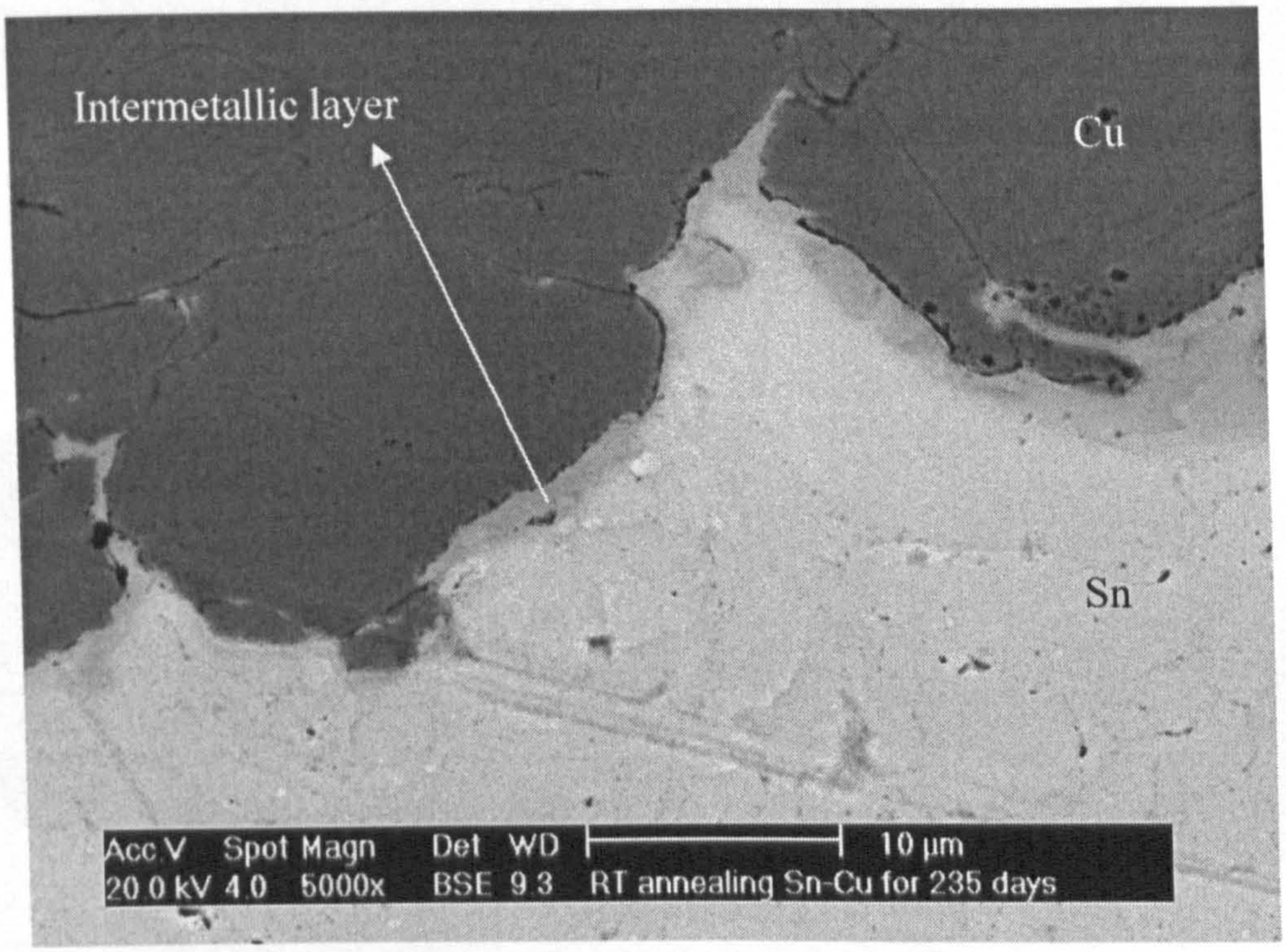

Fig. 6.23: BSE image of Sn-Cu couple after holding at room temperature (298 K) for 2.03×10^7 s (235 days). A discontinuous and thin layer of intermetallic compound is seen.

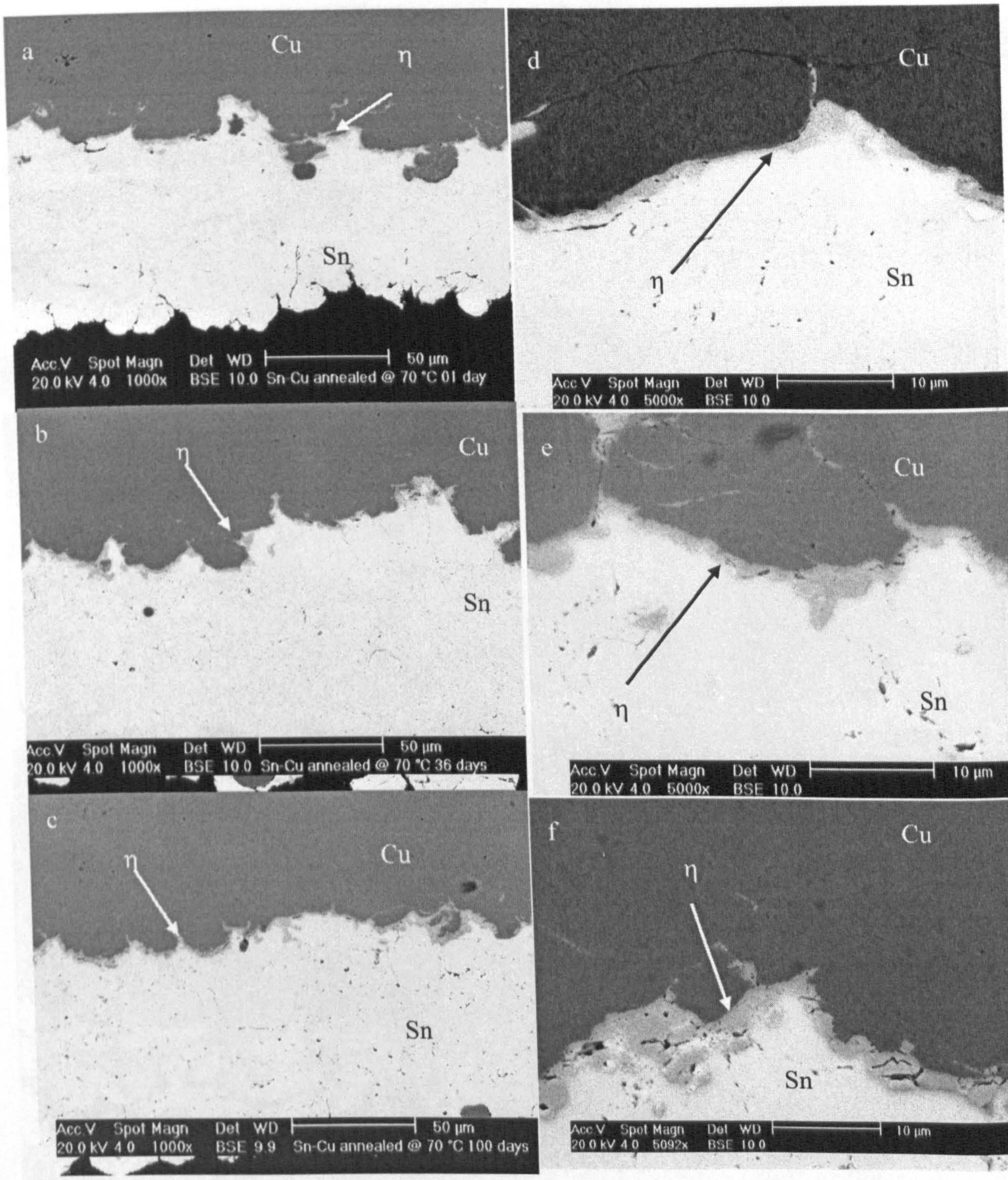

Fig. 6.24: BSE image of Sn-Cu samples annealed at 343 K for; 'a' and 'd', 8.64×10^4 s (1 day); 'b' and 'e', 3.11×10^6 s (36 days) and 'c' and 'f', 8.64×10^6 s (100 days); showing the formation of a single layer of intermetallic compound.

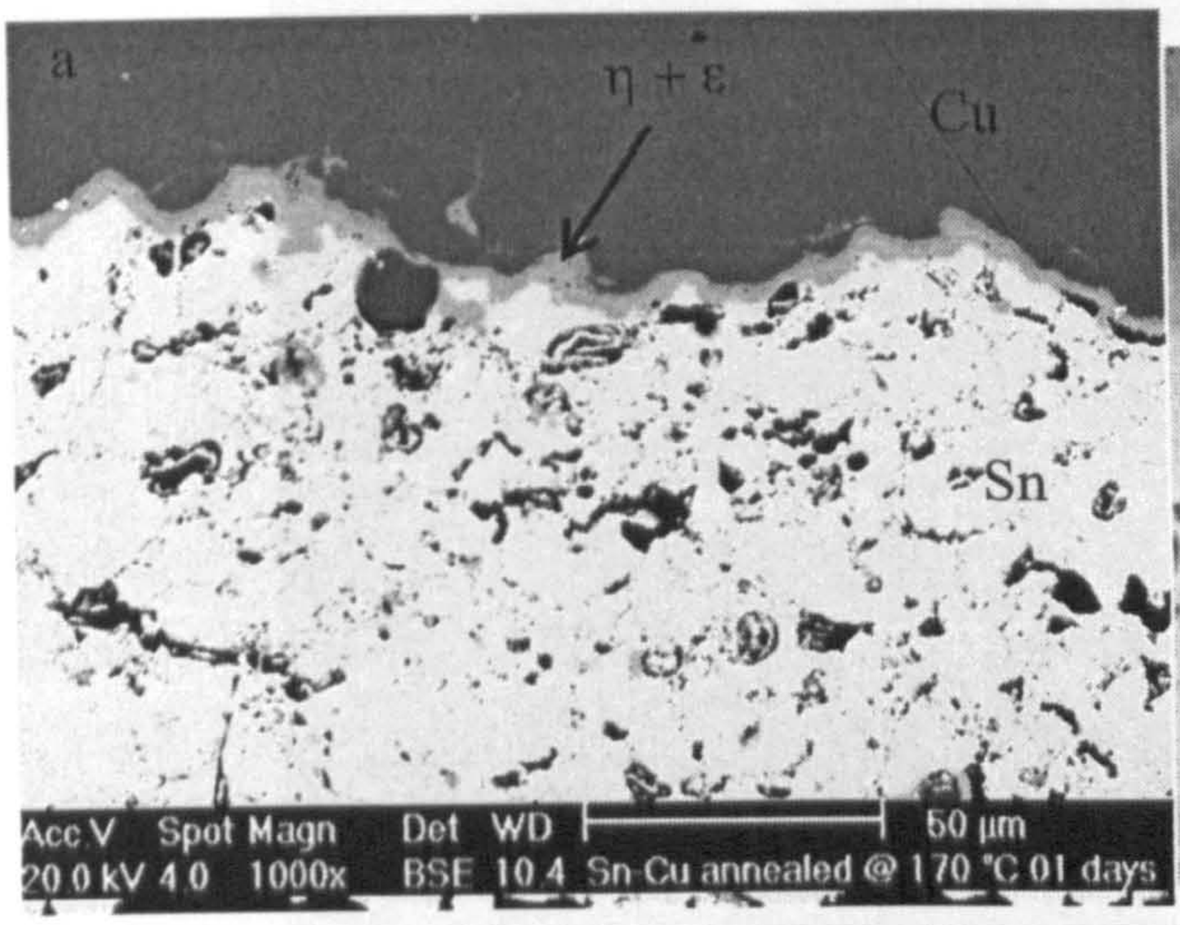

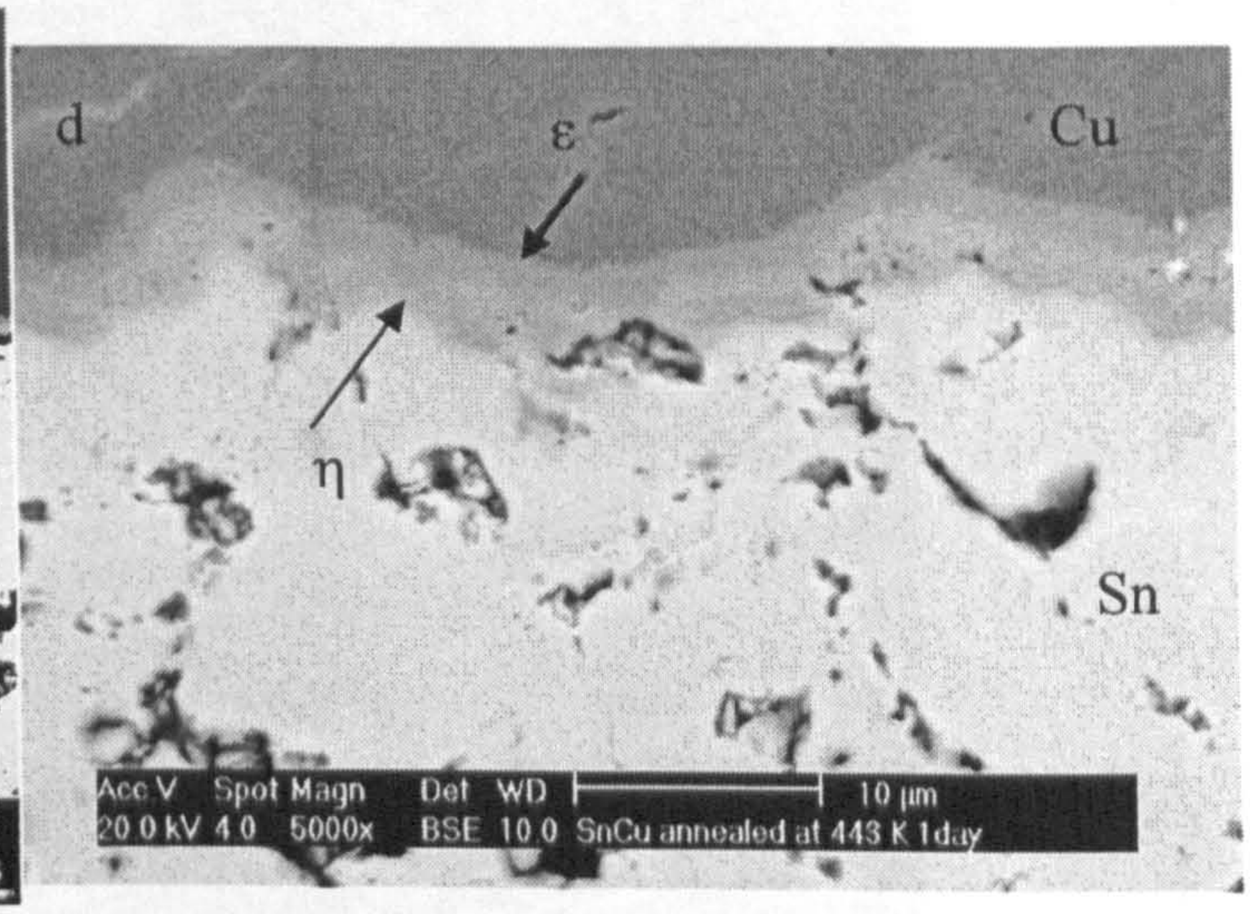

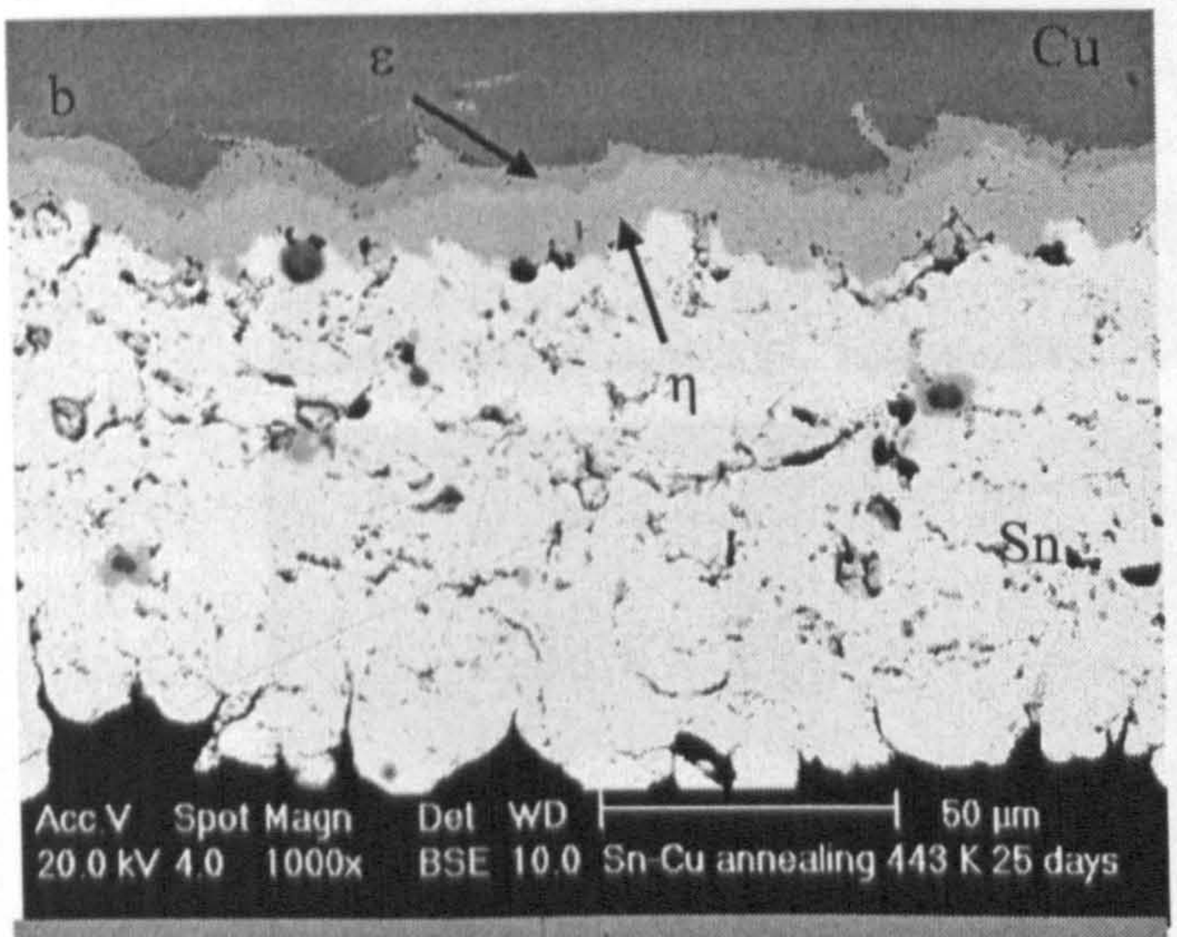

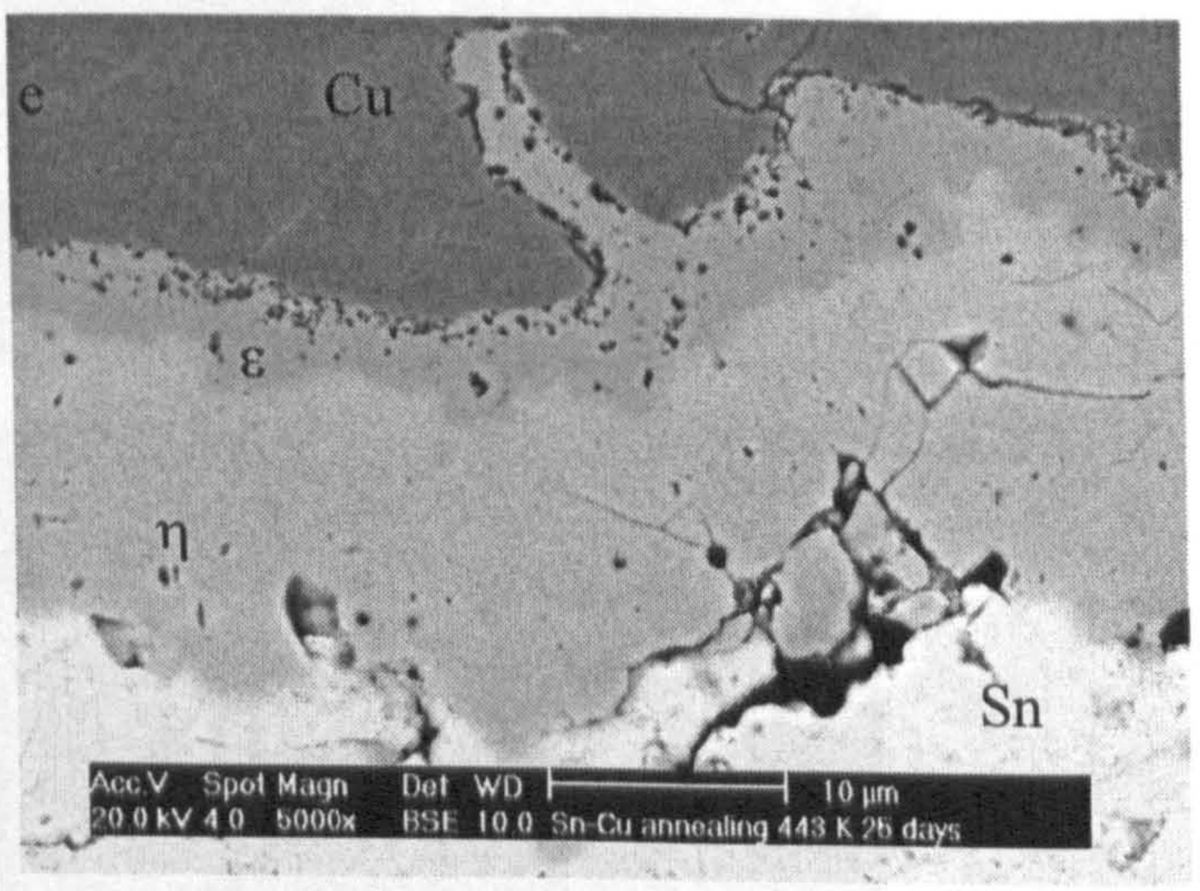

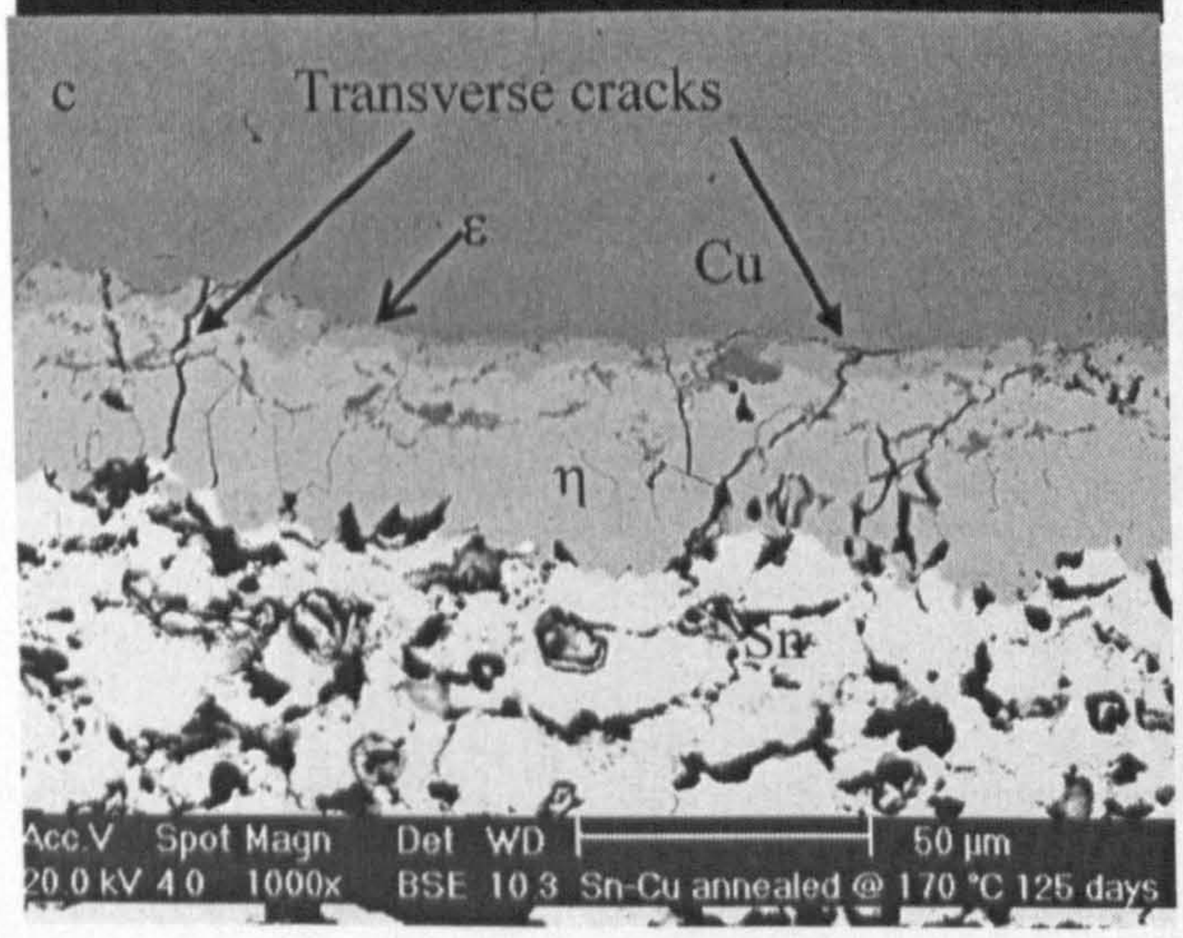

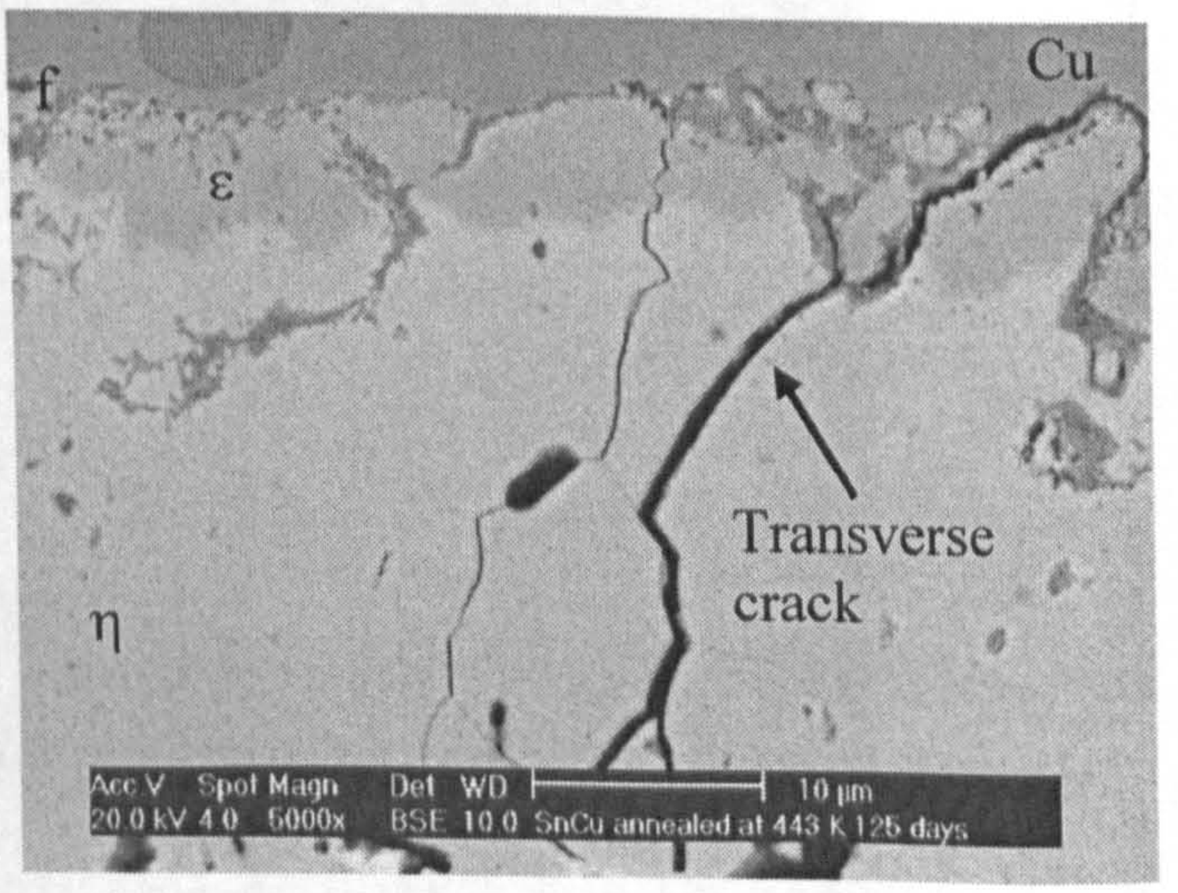

Fig. 6.25: BSE image of Sn-Cu samples annealed at 443 K for; 'a' and 'd', 8.64 x 10^6 s (1 day); 'b' and 'e', 2.16 x 10^6 s (25 days) and 'c' and 'f', 1.08 x 10^7 s (125 days); showing the formation of intermetallic compound and transverse cracks in η after annealing for 125 days.

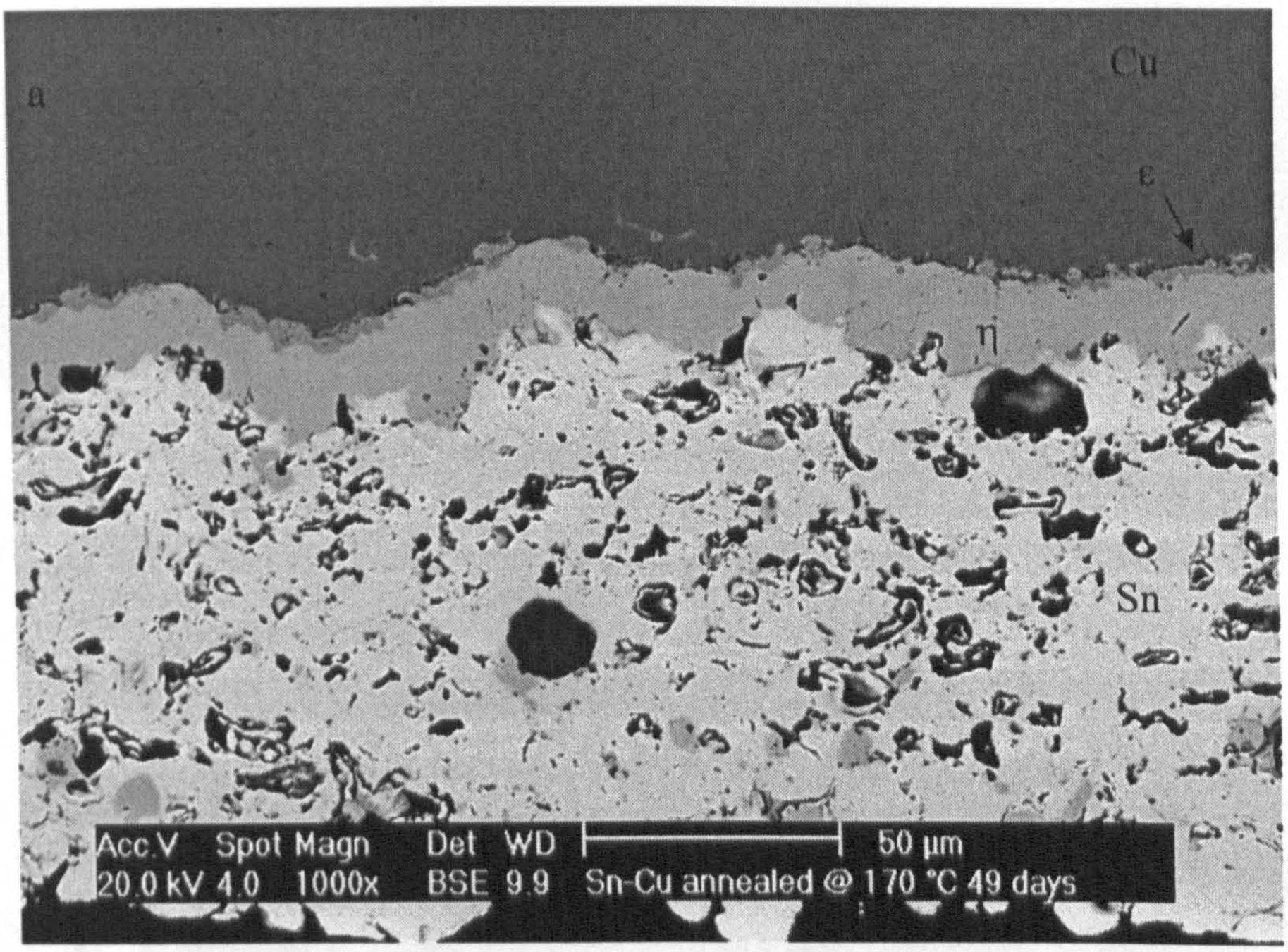

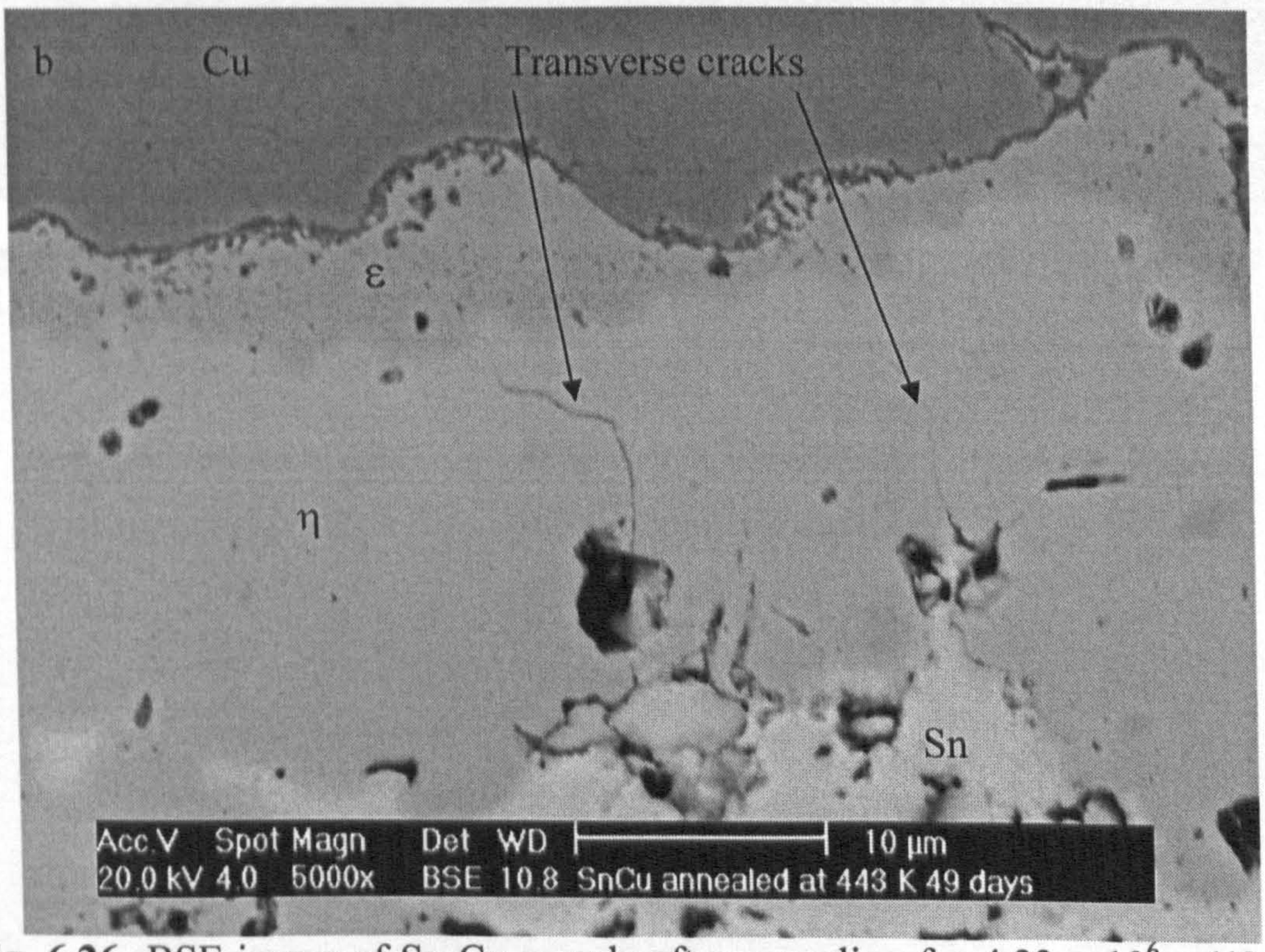

Fig. 6.26: BSE image of Sn-Cu sample after annealing for 4.23×10^6 s (49 days) showing; a), the η and ε phases and porosity in the tin layer; b), the formation of small transverse cracks in the η layer is seen (shown by arrows).

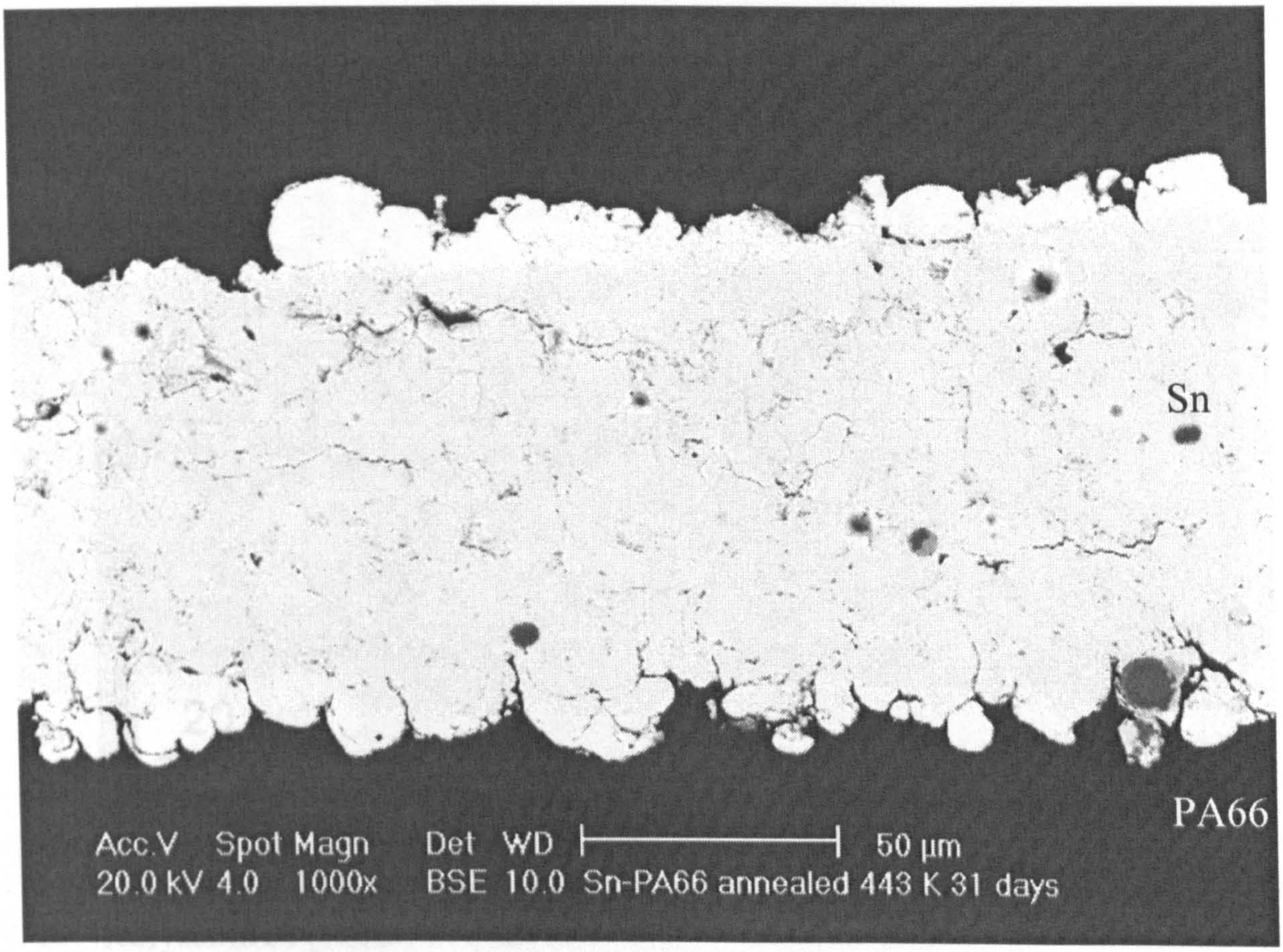

Fig. 6.27: BSE image of single layer Sn deposit on PA66, annealed for 2.67 x 10^6 s (31 days) at 443 K showing a largely dense layer of tin.

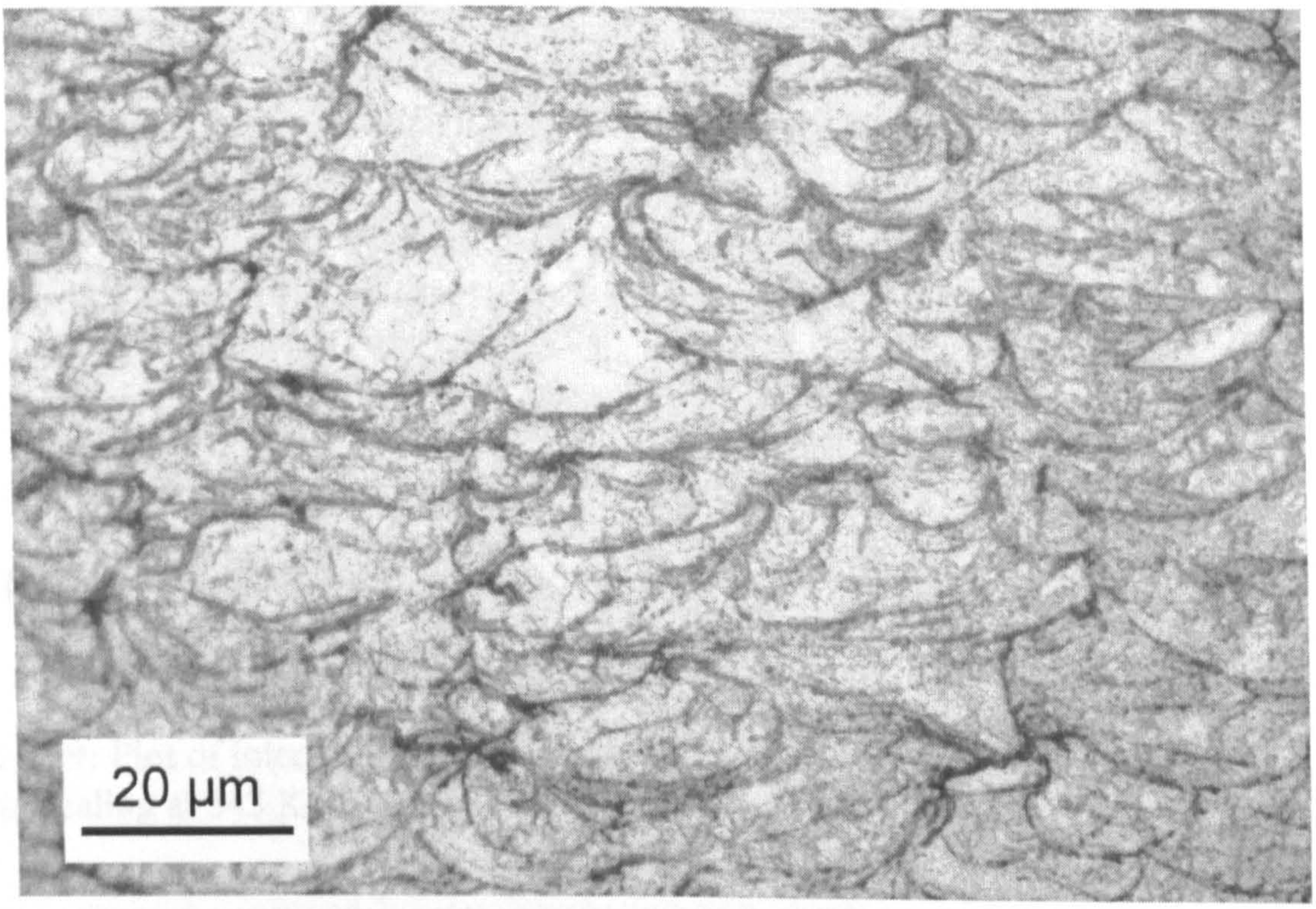

Fig. 6.28: Etched optical micrograph of Cu deposited using driving gas at room temperature and annealed at 443 K for 146 days showing few very fine recrystallized grains (1 – 3 µm).

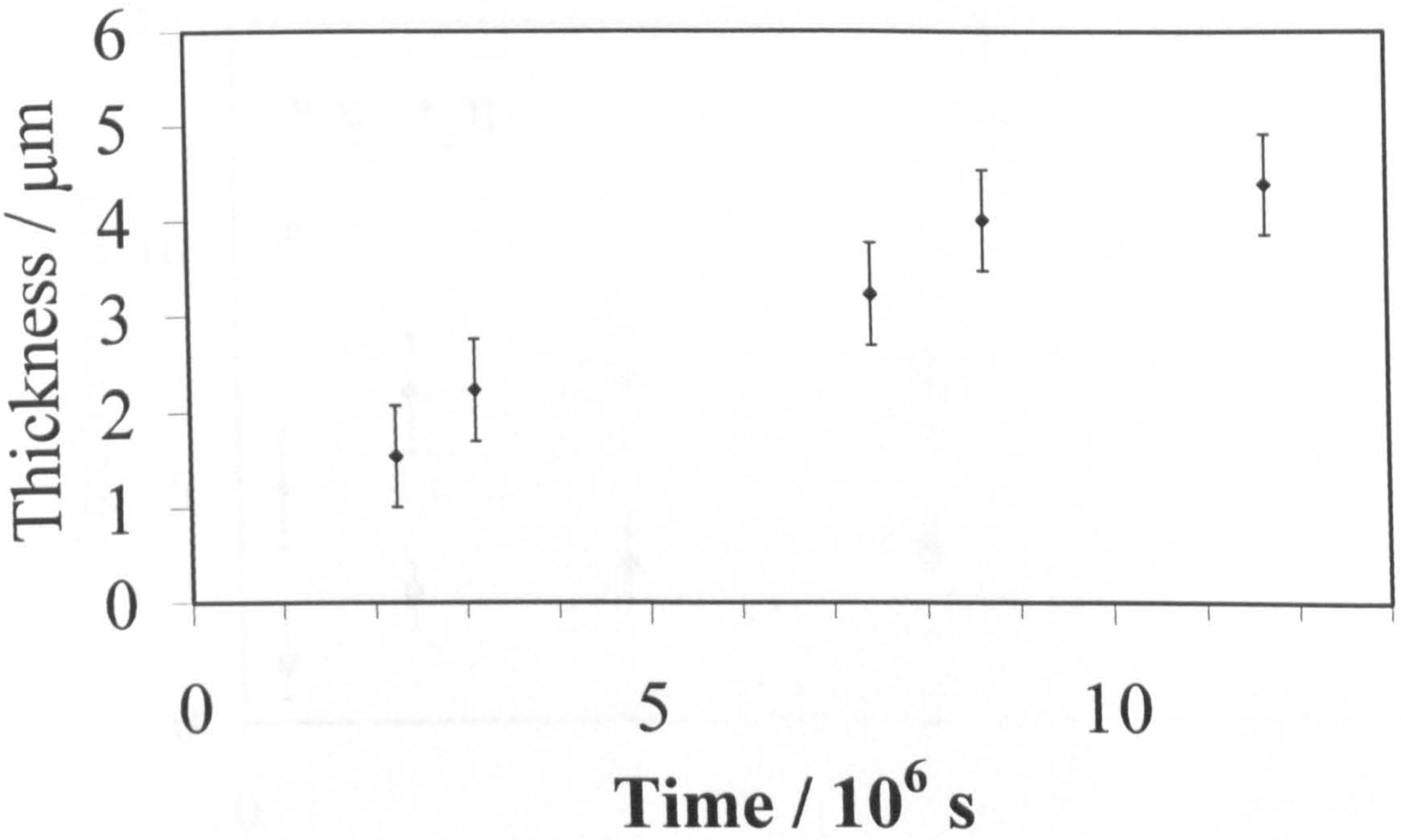

Fig. 6.29: Plot of intermetallic compound thickness versus annealing time for annealing at 343 K, slope and intercept are given in **Table 6.12**.

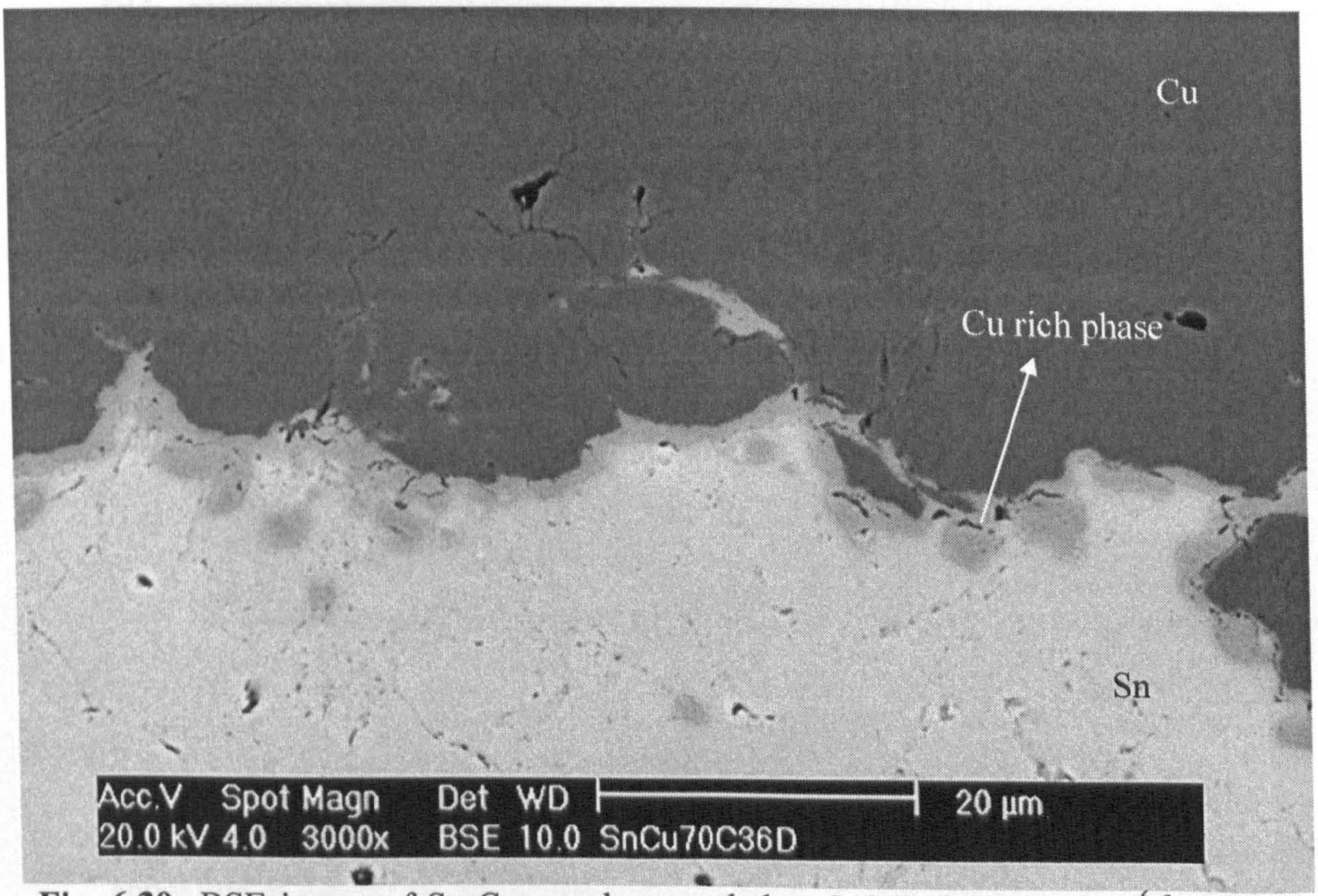

Fig. 6.30: BSE image of Sn-Cu couple annealed at 343 K for 3.11 x 10^{6} ^{s} (36 days) showing the intermetallic layer which is approximately 2 µm thick.

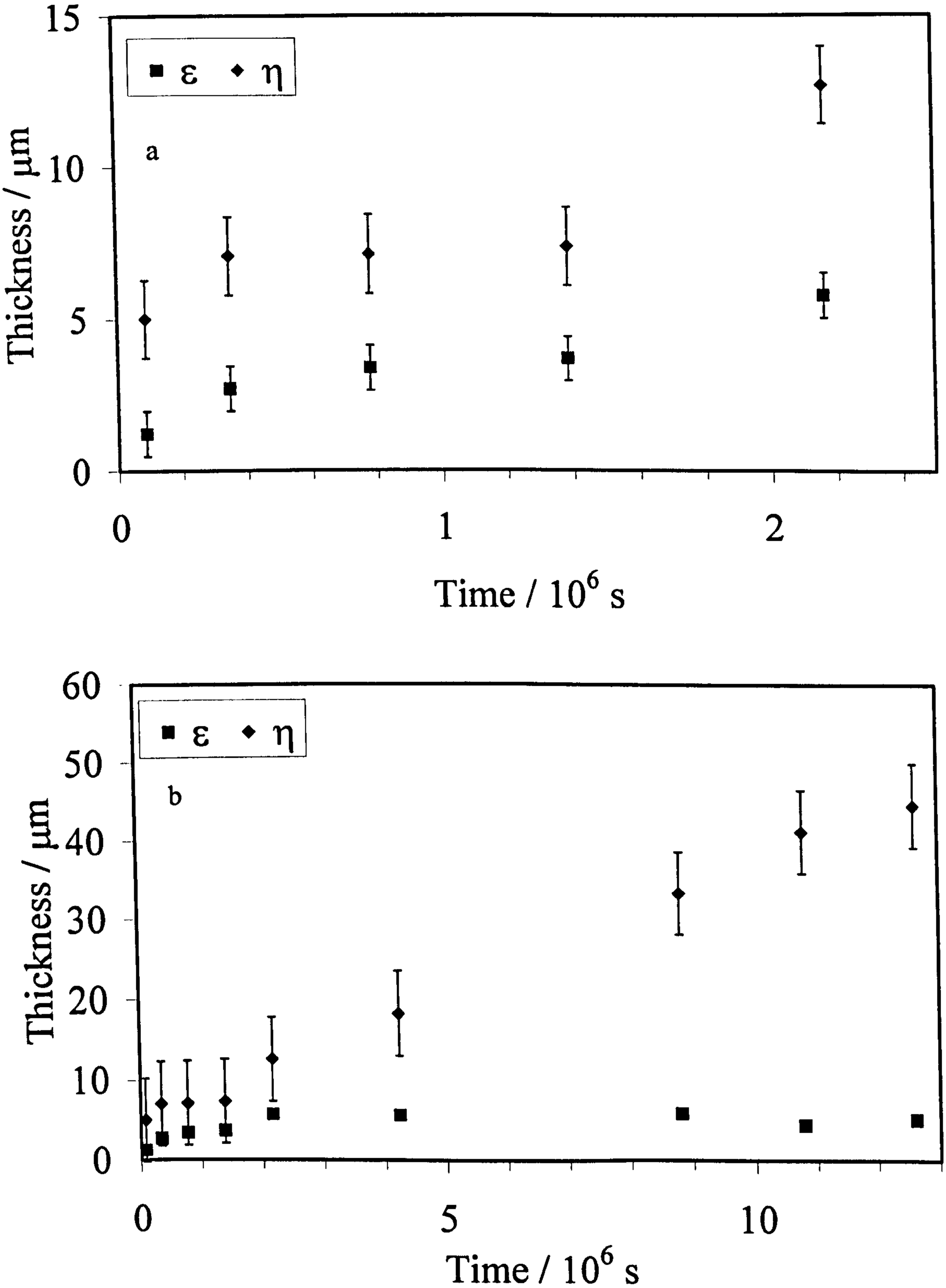

Fig. 6.31: Plot of intermetallic compound thickness versus annealing time for annealing at 443 K; a), for annealing time up to 25 days and b), for annealing time up to 146 days.

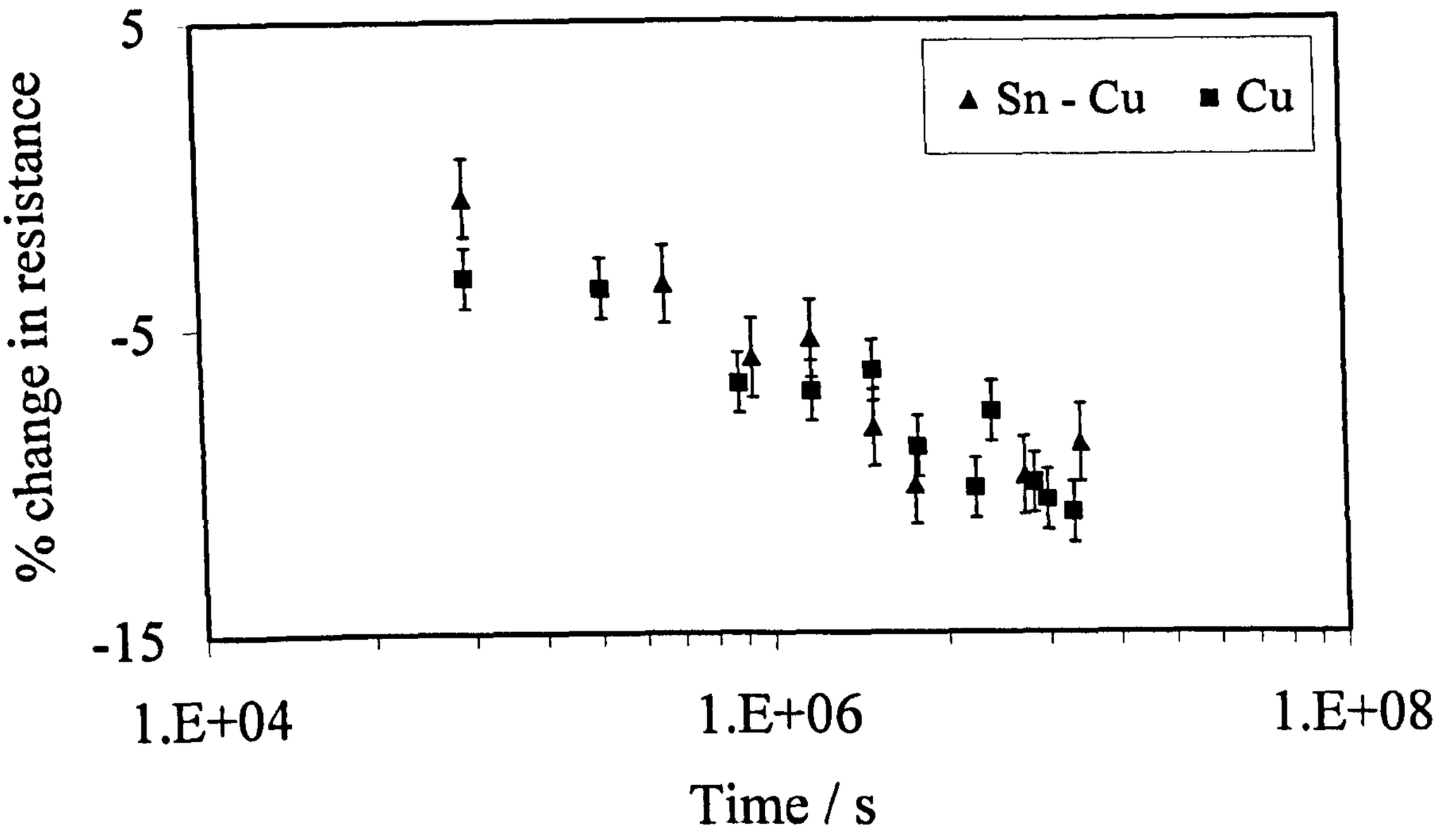

Fig. 6.32: Plot showing percentage change in resistance of copper and Cu - Sn samples versus annealing time for an annealing temperature of 343 K.

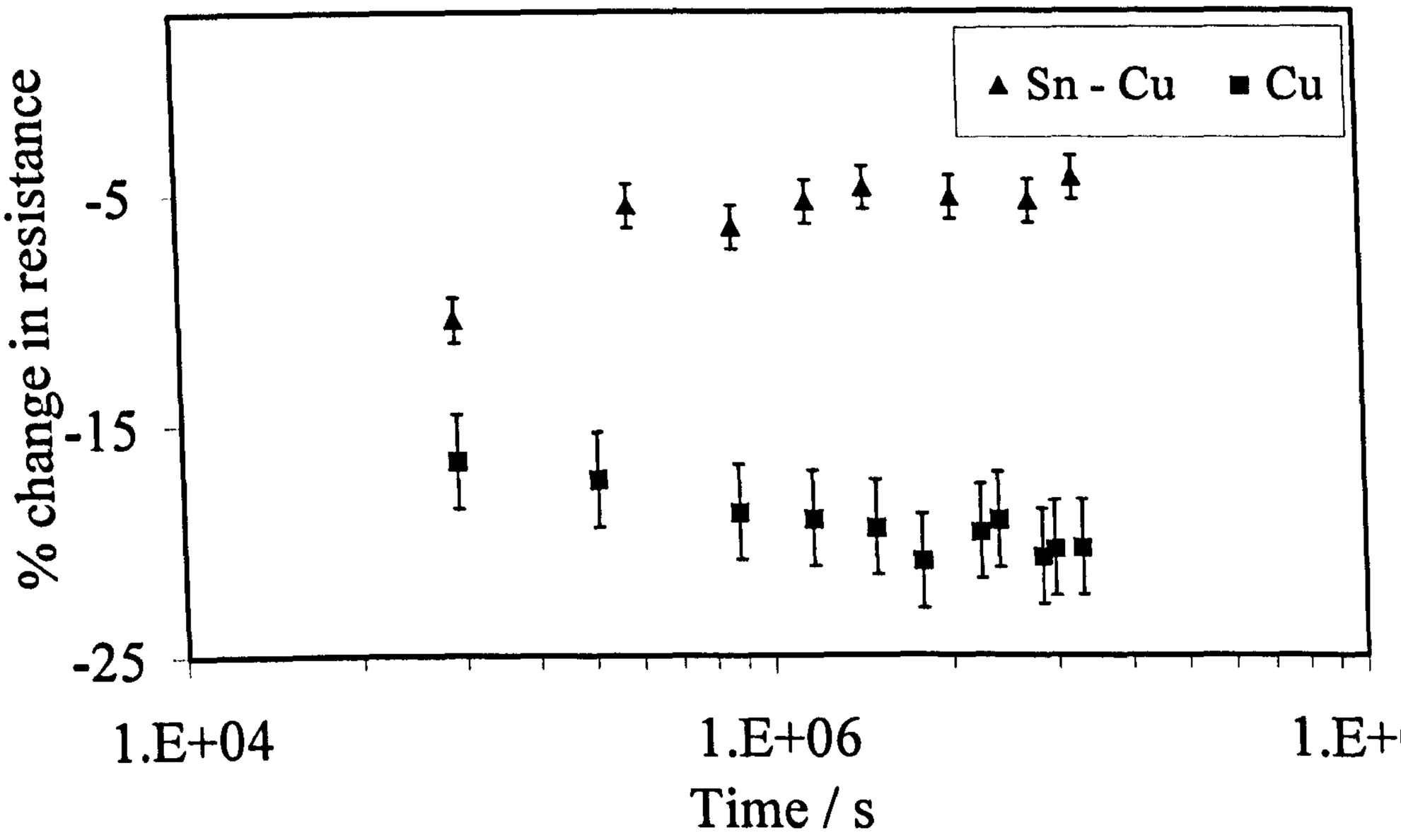

Fig. 6.33: Plot showing percentage change in resistance of copper and Cu - Sn samples versus annealing time for an annealing temperature of 443 K.

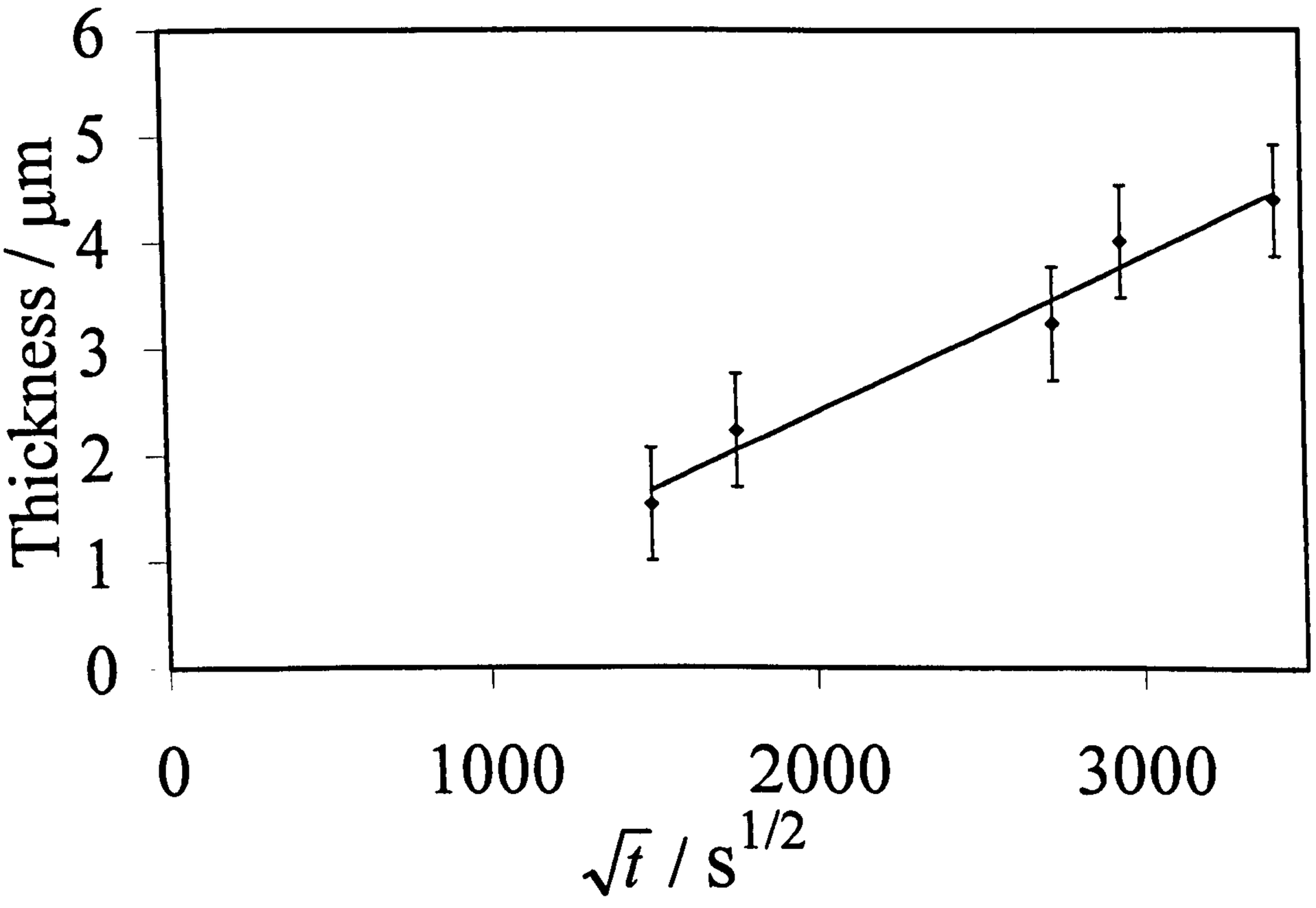

Fig. 6.34: Plot showing thickness of intermetallic layers versus $\sqrt{t}$ for an annealing temperature of 343 K.

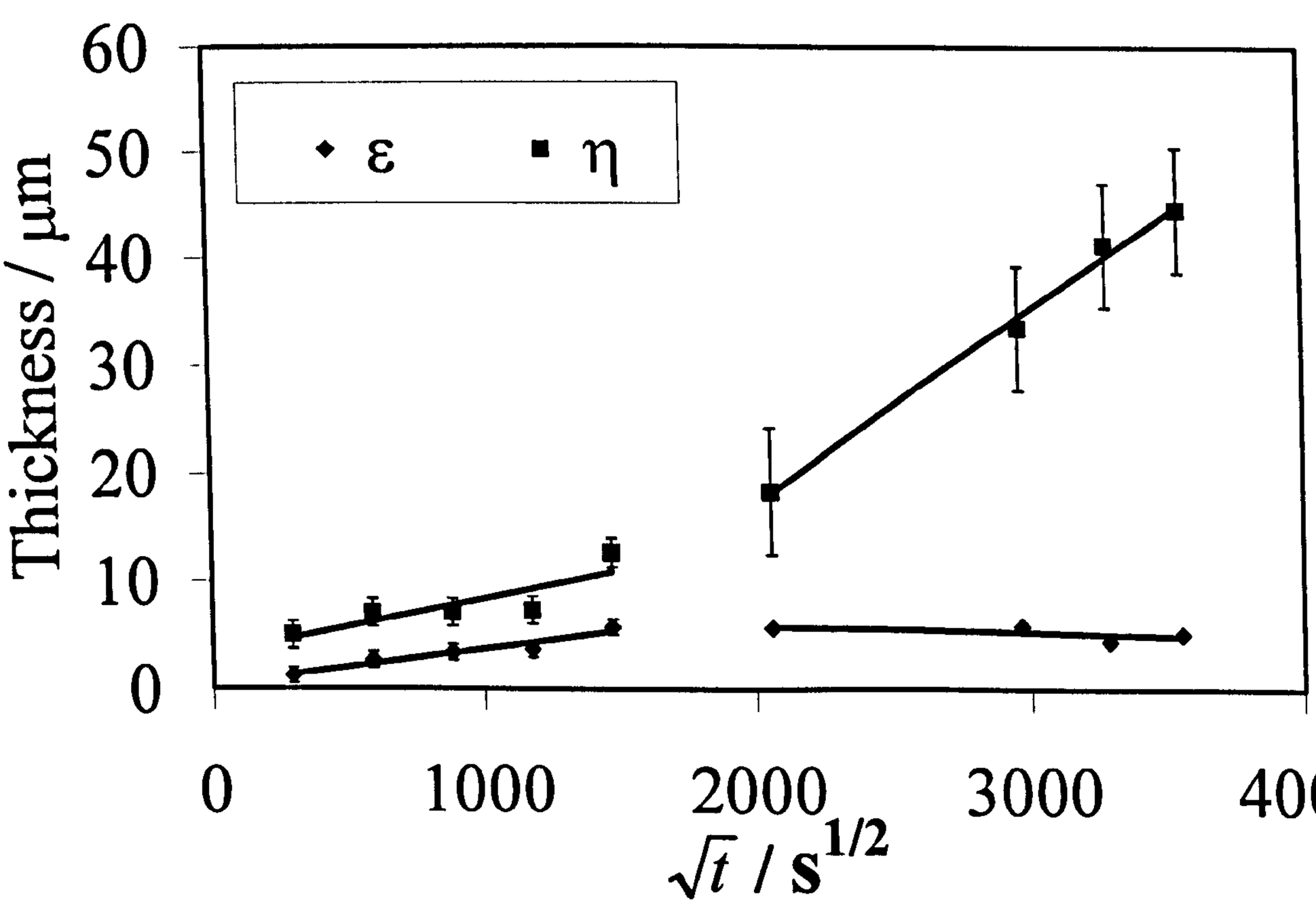

Fig. 6.35: Plot showing growth of intermetallic layer versus $\sqrt{t}$ for an annealing temperature of 443 K. The slopes and intercepts obtained following linear regression analysis are shown in **Table 6.12**.

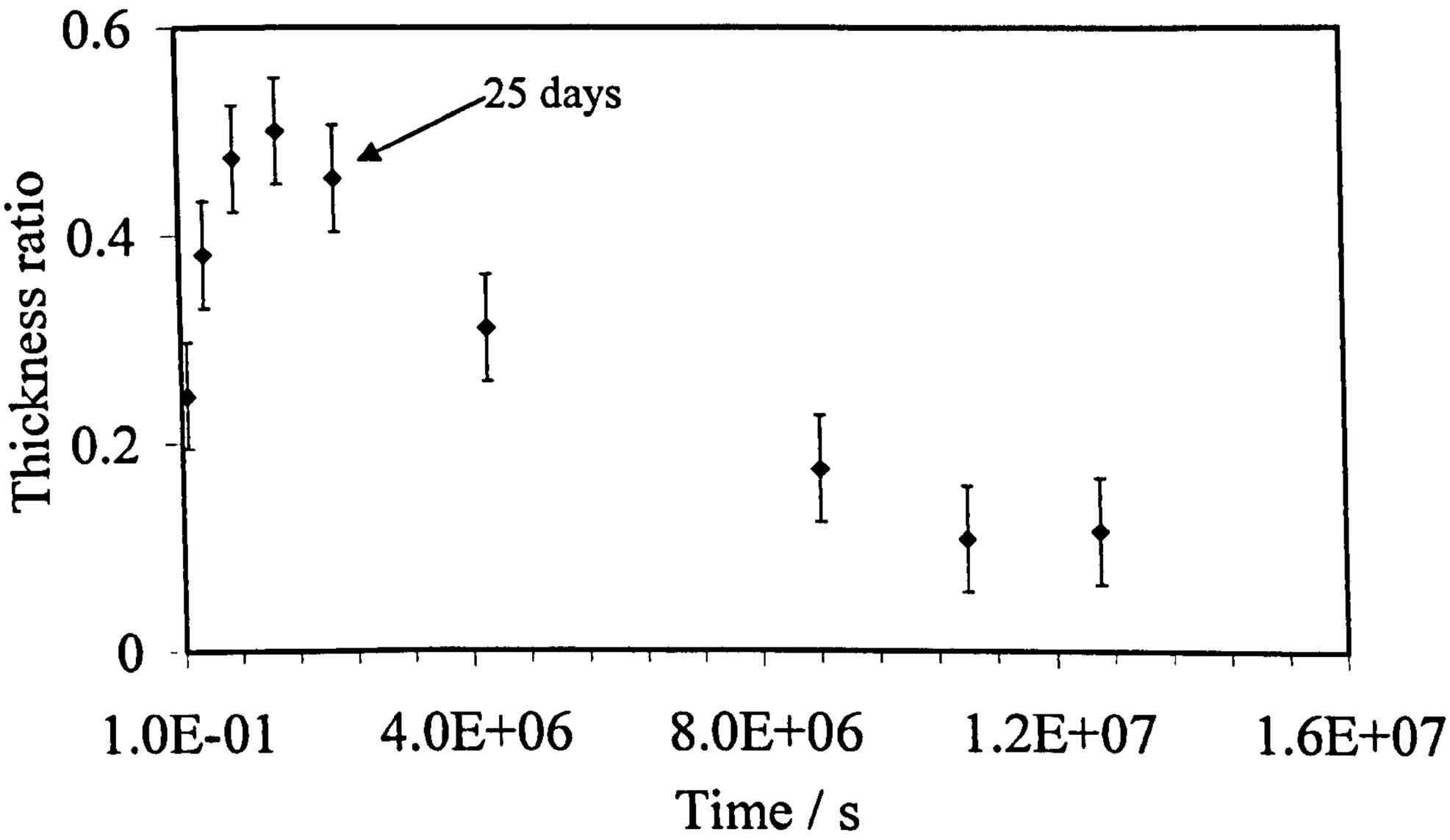

Fig. 6.36: Plot showing thickness ratio ε / η phase versus time in tin – copper track for annealing at 443 K.

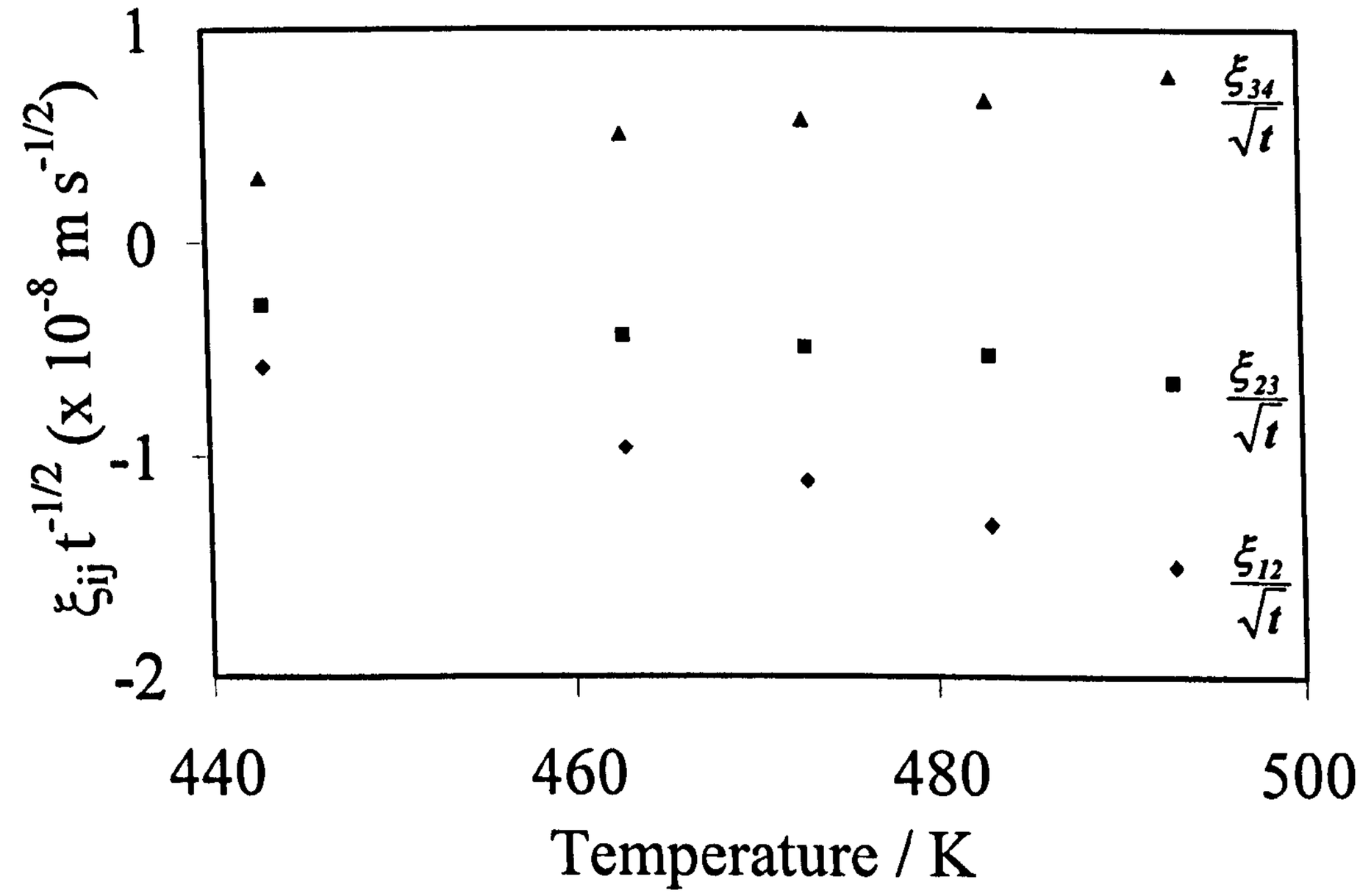

Fig. 6.37: Plot showing the calculated interphase position parameters versus temperature. ξ_{ij} is the instantaneous position between phase i and j. ξ_{12} = interphase position between Cu solid solution and ε phase, ξ_{23} = interphase position between ε phase and η phase, ξ_{34} = interphase position between η phase and tin solid solution [121].

Chapter 7

Conclusions

Copper and tin tracks were produced by cold spraying using gas atomized powders having spherical morphology. Cold spraying was carried out using a wide range of cold spraying conditions. The cold spraying conditions had significant influence on the properties of the deposited tracks. The process gas pressure and temperature, powder feed rate and traverse speeds were identified as important parameters affecting the deposit formation and properties. The grain size and microstrain in the deposit was measured using XRD and it was related to the deposition conditions used. Annealing tin – copper samples resulted in the formation of intermetallic compound; the nature and properties of this intermetallic compound formation were investigated. Following conclusions can be drawn from this work

7.1 Process characteristics

The cold spray process can be used to deposit well adhering deposit of copper and tin – copper on a variety of substrates. The deposition of copper on aluminium as well as polymer substrates is characterized by deposition efficiencies > 90 % in

most cases. Well adhering deposits of copper were formed on aluminium using gas at 298 K. Gas heating above 473 K was required to deposit copper on mild steel and alumina coated mild steel. The absence of significant heating or no heating at all during the deposition process results in deposition of coatings which are not oxidized or altered due to chemical reactions during flight. The width of the track formed for the nozzle design used in our experiments is ~ 5 mm and it was seen that the deposit thickness increased more or less linearly with number of passes and decrease in traverse speed, except where thick deposits were formed (~ 1 mm). In case of thick deposits the increase in thickness showed a negative deviation from linear behavior.

7.2 Deposit formation and growth

7.2.1 Metallic substrates

The mechanism of deposit adhesion on metallic and non – metallic substrates seems to be different. On metallic substrates adhesion takes place due to excessive deformation of sprayed particle and/or substrate leading to adiabatic shear and metal jetting. This provides clean interfaces between particle – substrate or particle – particle and promotes the formation of metallurgical bonds. Metal jetting is observed in aluminium substrate and well adhered deposits were formed on aluminium for a wide range of spraying conditions. Heating the process gas seems

to improve the adhesion on aluminium as the bond strength measured in pull – off tests increased from ~ 12 MPa > 20 MPa when using gas heated to 523 K to deposit copper. The copper deposits had the tendency to de-bond beyond a certain thickness. Heating the process gas increased the thickness at which the deposits de-bonded and led to recrystallization in as-sprayed copper when gas is heated to 673 K.

7.2.2 Polymer substrates

The impact of copper particles on polymers resulted in the wear of substrate and also some embedding of particles in the polymer. Polymers with low strength were unable to withstand the impacts of copper particles and excessive wear is observed in them and consequently copper can not be deposited on them. Polymers that had high strength, signified by T_g above 323 K and tensile strength above 50 MPa, suffered less wear during spraying and copper particles could be embedded into them. Subsequent growth of the deposits involved metal jetting as the impacts were on previously embedded copper particles.

Tin can be deposited on all the polymers investigated in this work. The impact of tin particles did not result in any apparent wear of polymer. The use of tin bond coat improves the overall adhesion of tin + copper deposits.

7.2.3 Ceramic substrates

Copper sprayed using gas at 298 K de-bonded from alumina coated substrate. The adhesion of copper on alumina was improved when gas was heated to > 473 K, however, the alumina layer itself de-bonded from the mild steel substrate, possibly due to mis-match of thermal expansion coefficient. The mechanism of adhesion on alumina seems to be mechanical interlocking of copper particles with the plasma sprayed alumina splats. Heated gas increases the flattening of copper particles which promotes better interlocking between copper and alumina.

7.3 Stability of copper and tin – copper deposits

Cold sprayed copper have nanometre sized grained structure which is the result of excessive deformation of copper particles upon impact on the substrate or previously deposited particles. Copper deposits formed using gas heated to 523 K also has dislocations associated with microstrain within the grains. Dynamic recrystallization seems to be an important mechanism by which cold sprayed copper recovers their properties. Dynamic recrystallization is seen to be an important mechanism in copper sprayed at 523 K and as a result the microstructure is more stable. Upon annealing at temperatures ≥ 573 K recrystallization and grain growth seemed to proceed by nucleation of new grains from the dislocations associated with microstrain. In copper sprayed at 298 K dynamic recrystallization did not appear to be an important mechanism and grain growth is observed for annealing at temperatures as low as 373 K. Cold sprayed copper has high hardness due to

significant cold working during spraying. The recrystallization and grain growth resulted in decrease of hardness in copper sprayed at 298 K and 523 K, albeit at two different temperatures; at 373 K for copper sprayed at 298 K and at 573 K for copper sprayed at 523 K.

The formation of intermetallic compound was confirmed for annealing at 343 K and 443 K. At 343 K a single layer of intermetallic compound formed which is most probably η. At 443 K two intermetallic compound layers are formed; these are identified as η and ε. The growth of intermetallic compound at 443 K is very complex and it is characterized by the formation of porosity in the tin and transverse cracks in the η layer after 25 days of annealing. The role played by the porosity and transverse cracks in the growth of intermetallic layer is not clear yet, however it was seen that the rate of growth η phase increased and the thickness of ε phase decreased when annealed beyond 25 days. The rate of growth of intermetallic compound in cold sprayed tin - copper couples is seen to be larger than that reported for tin – copper couples prepared by other methods. This could be due to diffusion through grain boundaries in copper as copper has nanometer size grains and diffusion through grain boundaries is much faster as compared to bulk diffusion.

7.4 Deposit properties

7.4.1 Mechanical properties of cold sprayed copper

The as-sprayed copper had high hardness and tensile strength of ~ 375 MPa, but negligible elongation to failure. The low ductility of cold sprayed copper is probably due to the presence of defects which are artifacts of the cold spray deposition process. The hardness and tensile behavior of cold sprayed copper following annealing at 873 K is similar to bulk copper as a result of recrystallization and grain growth, indicating that atomic bonding has formed across interparticle boundaries. The fracture surface of as-sprayed copper did not show any evidence of ductile fracture, rather the fracture was along interparticle boundaries. The fracture surface of deposit annealed at 873 K showed characteristic dimpled structure, evidence of a ductile fracture.

7.4.2 Resistivity of copper and tin – copper tracks

In cold sprayed copper the onset of recrystallization is accompanied by a decrease in electrical resistivity. The resistivity of as-sprayed copper decreases from 27.1 nΩ m to 21.1 nΩ m after annealing at 773 K for 1 hr. In tin – copper samples there was a decrease in resistance after annealing at 343 K and 443 K, however growth of intermetallic layer in samples annealed at 443 K resulted in an increase in resistance however, it was seen that the overall resistance was still less that that measured in as-sprayed samples. The resistivity of tin – copper tracks decreased by about 5 % following annealing at 443 K for 146 days and by 8 % following annealing at 343 K for 135 days.

Chapter 8

Future work

There is a generic need to improve process understanding. The effect of particle velocity and temperature on the deposition process and properties of deposits is not fully understood. This investigation could be carried out using in-flight diagnostics like particle velocity measurement (DPV 2000) and mathematical modeling (i.e. CFD) to understand the influence of particle velocity and heating. Such work would allow the stability of the process to be monitored and a process window (essential for putting into production) identified.

There is a need to further improve the bonding between copper and polymers. In pursuit of this, a number of avenues can be investigated such as, Surface treatment of polymers including cleaning and surface texturing to improve mechanical keying of the cold sprayed material, use of interlayer other than tin; for e.g. zinc. Optimum thickness of interlayer could be studied. The role of substrate temperature can be explored in more detail along with effect of heated gas and its effect on particle velocity and substrate temperature. More detailed study of impact of copper and tin with polymers needs to be undertaken.

This study could be better qualified if simultaneous particle velocity is measured and varied in a systematic way.

A systematic study of the mechanical properties of cold sprayed material would yield further information about the mechanisms involved in failure of cold sprayed material and also help to optimize the cold spray process to produce deposits with low defects. Post spray processing of cold spray material should be investigated to improve their properties. This will lead to better understanding of the electrical and mechanical properties of cold sprayed material. The microstructure of sprayed copper can be characterized by TEM studies along with XRD to look at grain structure and dislocation behaviour.

The nature of interfaces in the as-sprayed condition and after annealing could also be investigated to see if oxide is present.

Acknowledgements

I would like to express my gratitude to my supervisors, Professor D. G. McCartney and Dr. Philip Shipway for their advice and support throughout the course of this PhD. I would like to thank Yazaki Europe limited for sponsoring the PhD project.

I would like to thank Dr. Deen Zhang for his valuable inputs regarding operation of the cold spray equipment at Nottingham, Mr. Keith Dinsdale, Mr. Martin Roe and Ms. Julie Thornhill for training me on the XRD and SEM and all the staff in the Wolfson building for technical assistance.

I would like to thank my friends for making my stay in UK most enjoyable and memorable. Most importantly, I would like to express my deepest gratitude to my family and my wife Alka for their support, love and encouragement.

Eklavya Calla

August 2005

Appendix 1

Gas and particle velocities calculated using the one dimensional isentropic gas flow model and the particle acceleration model described in chapter 2, section 2.4 for nozzle having area expansion ratio of 9.46 and designed exit Mach No. of 4.9.

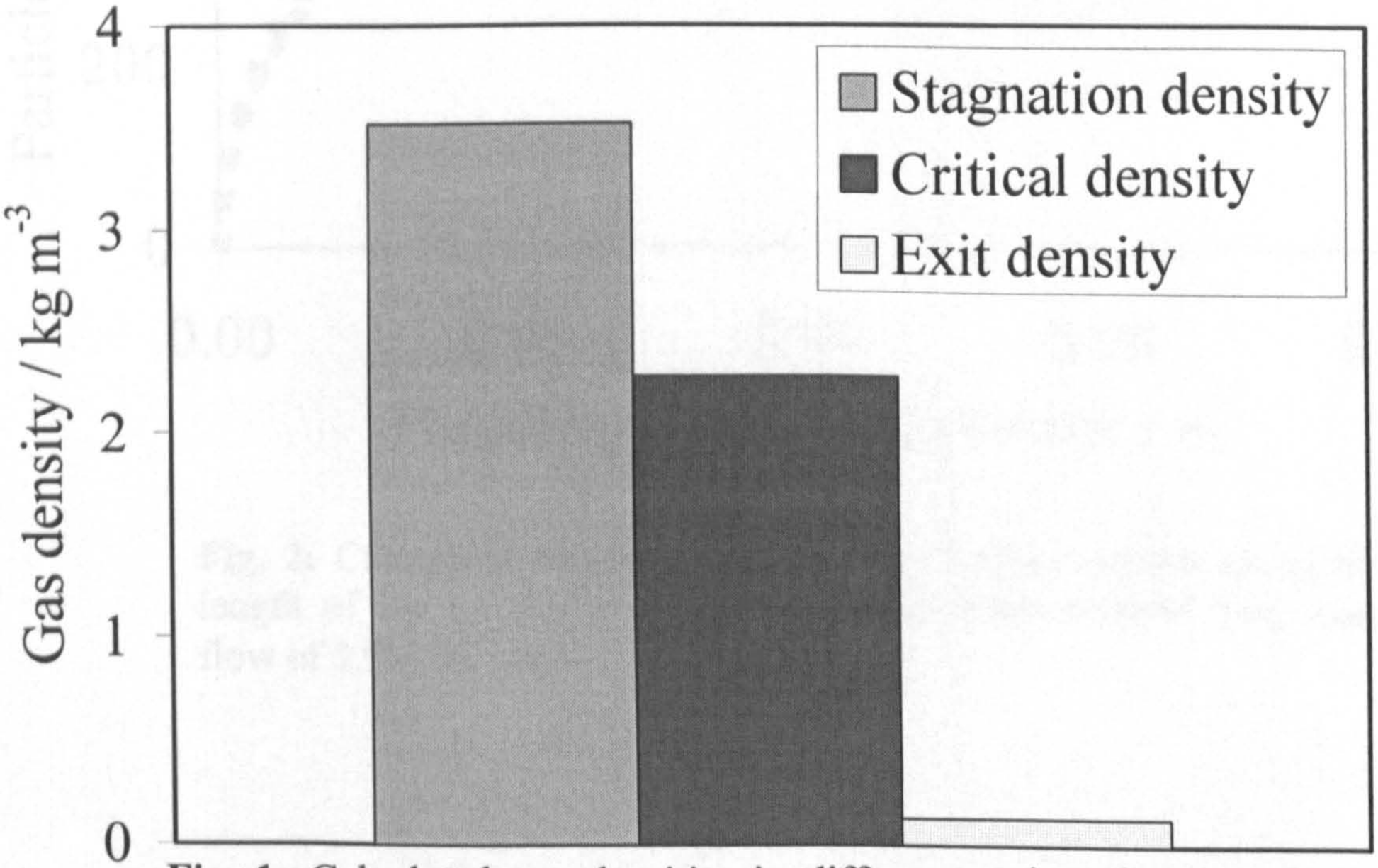

Fig. 1: Calculated gas densities in different regions in the nozzle using helium as driving gas at a gas mass flow of 2.9×10^{-3} kg s^{-1}.

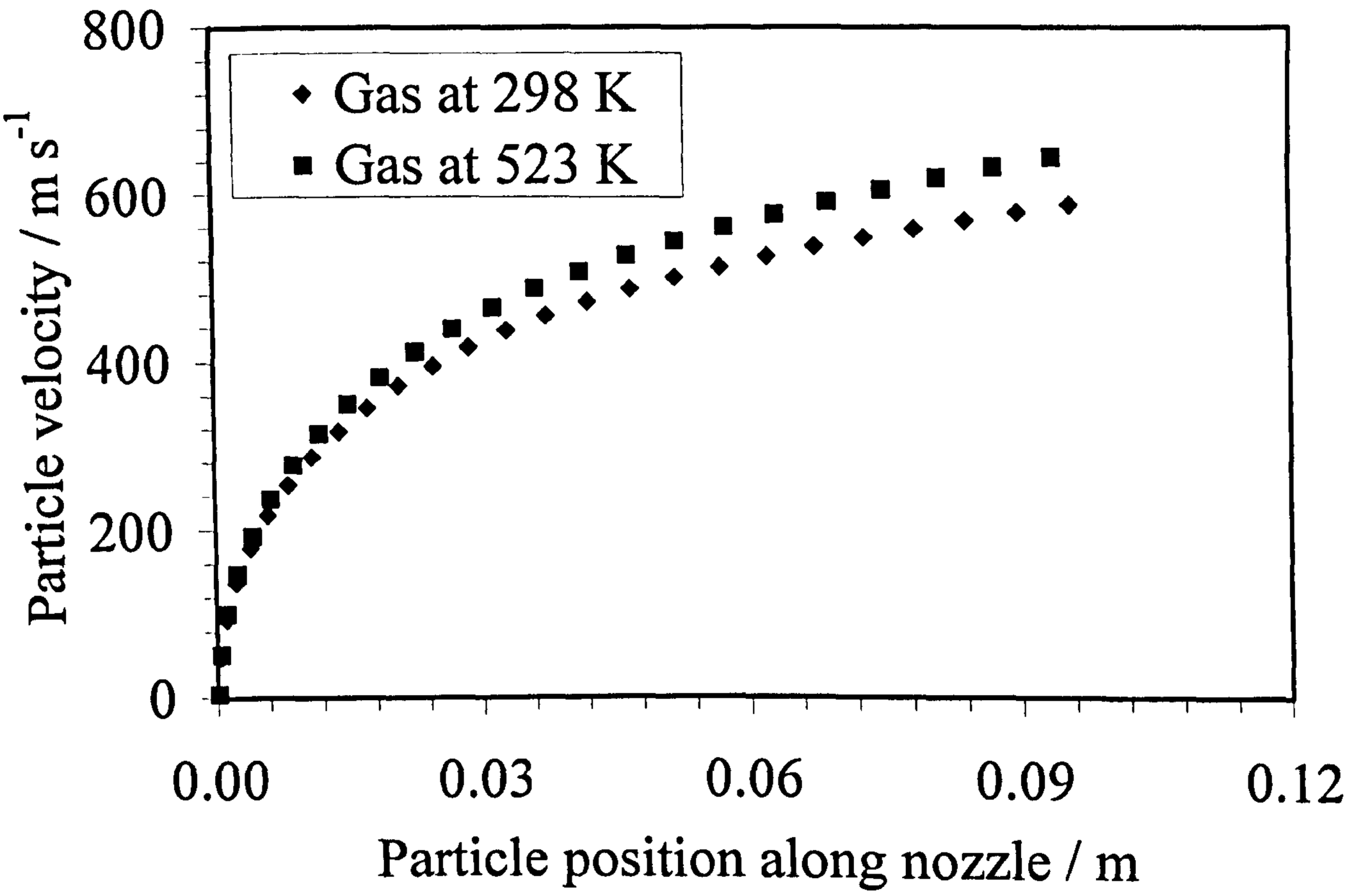

Fig. 2: Calculated velocity of 15 μm size copper particle along the length of the nozzle for two different gas temperatures. Gas mass flow of 2.9×10^{-3} kg s^{-1}.

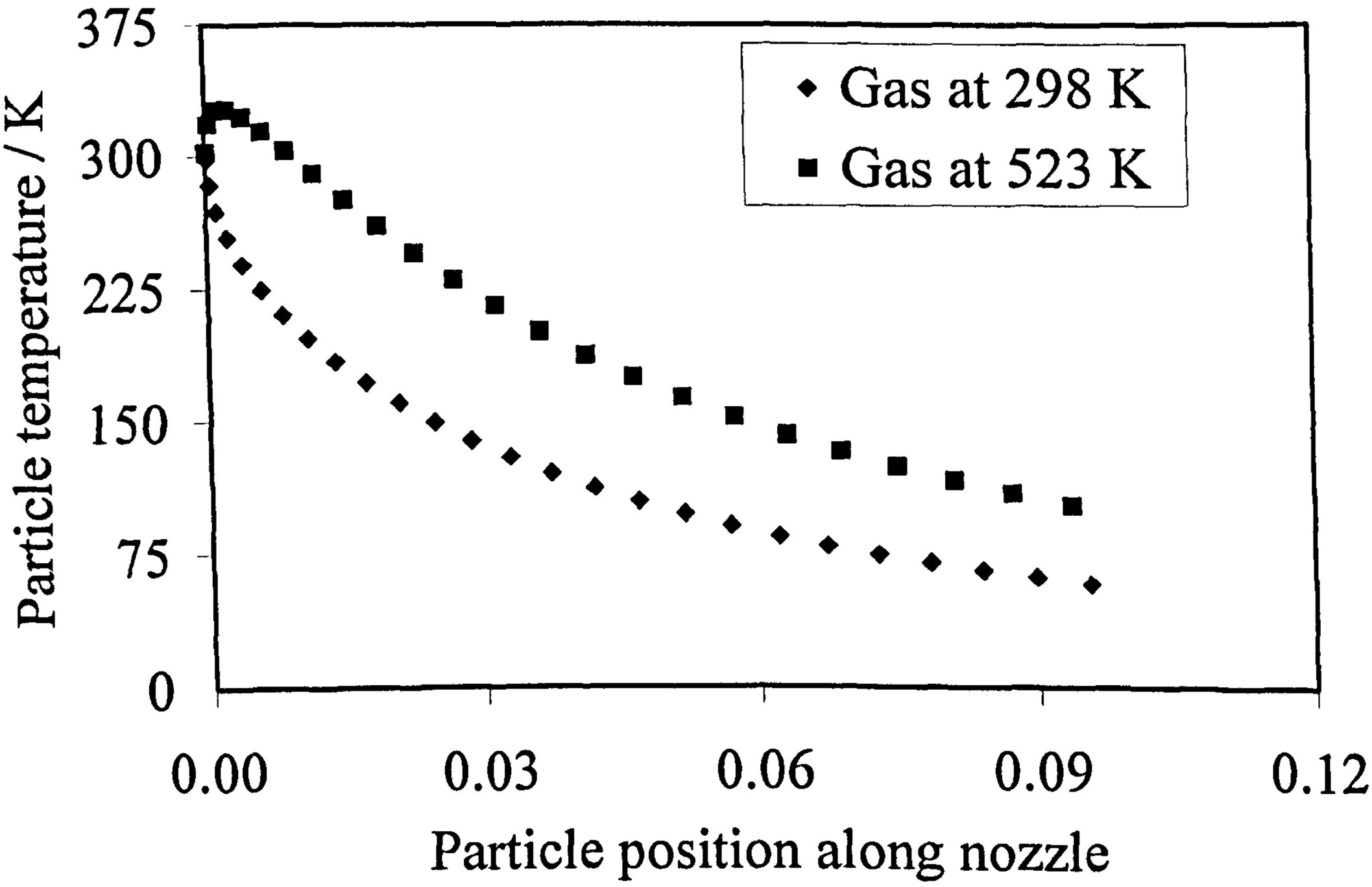

Fig. 3: Calculated temperature of 15 μm size copper particle along the length of the nozzle for two different gas temperatures. Gas mass flow of 2.9×10^{-3} kg s^{-1}.

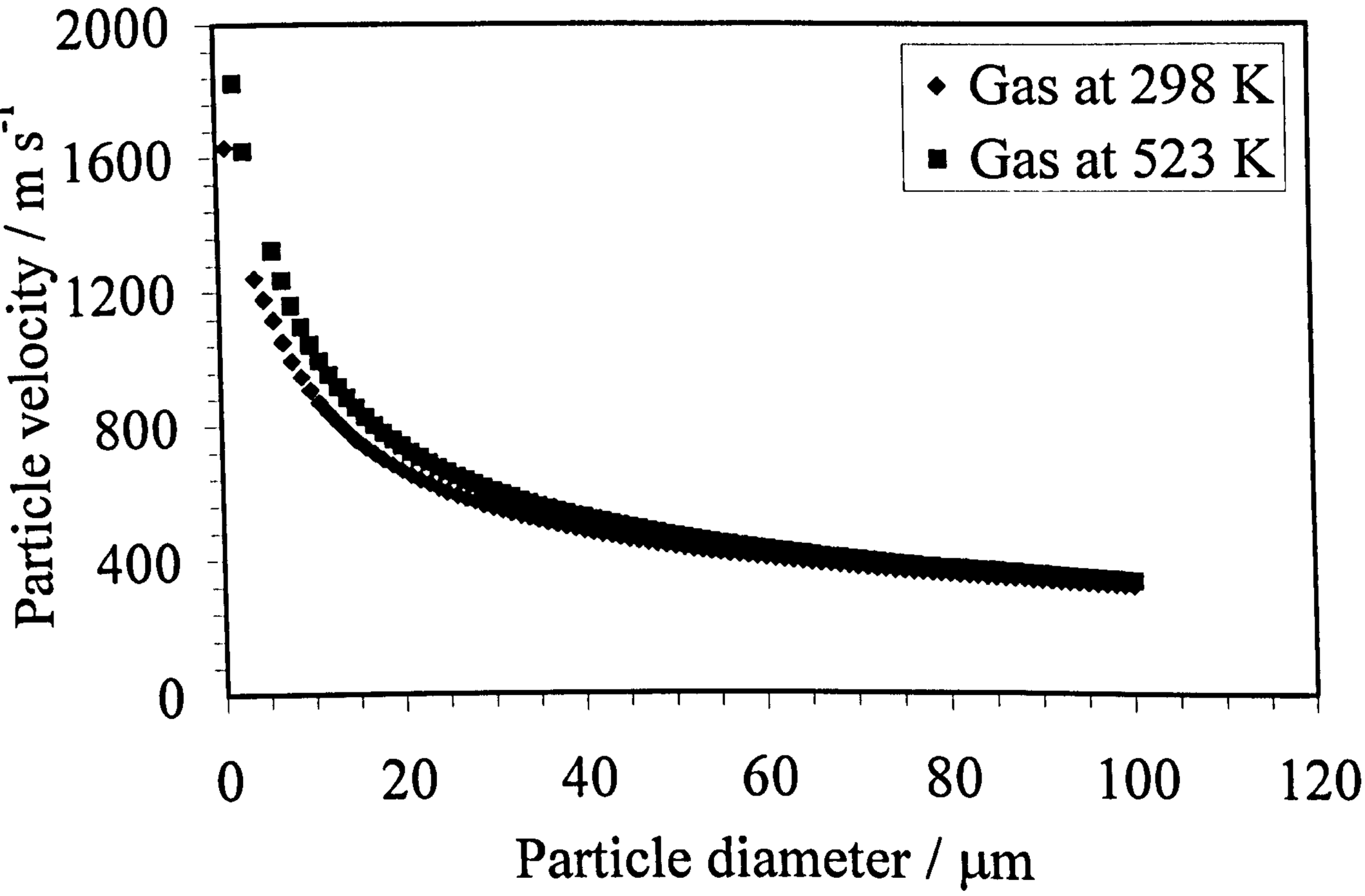

Fig. 4: Plot showing calculated velocities of copper particles versus particle diameter for gas at 298 K and 523 K.

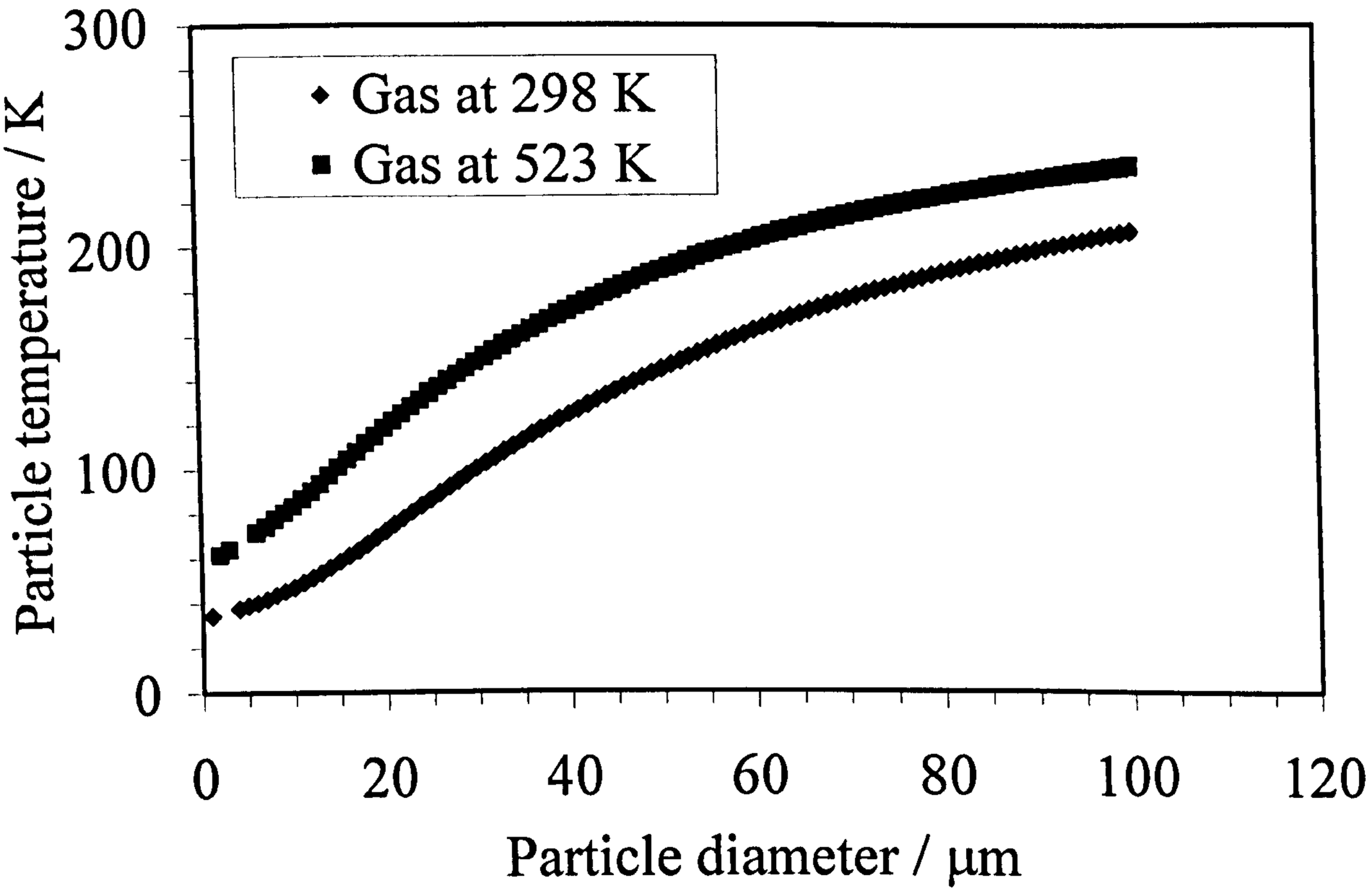

Fig. 5: Plot showing calculated temperature of copper particles versus particle diameter for gas at 298 K and 523 K.

References

1. Rickerby, D.S. and A. Matthews, *Advanced surface coatings*, ed. D.S. Rickerby and A. Matthews. 1991, Glasgow: Blackie.

2. Pawlowski, L., *Science and Engineering of thermal spray coatings*. 1995, Chichester: John Wiley & Sons.

3. Schoop, M.U., *A new process (spray process) for the production of metallic coatings*. Metallurgical and Chemical Engineering, 1910. VIII(7): p. 404-406.

4. McCune, R.C., A.N. Papyrin, J.N. Hall, and W.L. Riggs II. *An exploration of the Cold-Gas-Dynamic spray method for several materials systems*. in *Advances in Thermal Spray Science and Technology*. 1995. Houston: ASM International: p. 1-5.

5. Smith, R.W. and R. Knight, *Thermal Spraying.1. Powder consolidation - From coating to forming*. JOM-Journal of The Minerals Metals & Materials Society, 1995. 47(8): p. 32-39.

6. Karthikeyan, J., C.M. Kay, J. Lindeman, R.S. Lima, and C.C. Berndt. *Cold spray processing of titanium powder*. in *Thermal Spray via Applied Research*. 2000. Montreal: ASM International: p. 255-262.

7. Sakaki, K., K. Huruhashi, Tamaki, Y. Shimizu, and J. Nagano. *Effect of nozzle geometry on cold spray process*. in *International Thermal Spray Conference*. 2002. Essen, Germany: ASM International: p. 385-389.

8. Alkhimov, A.P., A.N. Papyrin, N.I. Nesterovich, and M.M. Shuspanov, *Gas dynamic spraying method for applying a coating*, U.S. patent 5302414, Editor. 1994, Papyrin, A. N.: United States. p. 1-17.

9. Hermanek, F.J., *Thermal spraying: What it was and what it has become*. 2005, International Thermal Spray Association.

10. Gartner, F., T. Stoltenhoff, T. Schmidt, and H. Kreye. *The cold spray process and its potential for industrial applications*. in *Thermal Spray Connects: Explore its Surfacing Potential*. 2005. Basel, Switzerland: ASM International: p. 158-163.

11. Browning, J.A., *Viewing the future of high-velocity oxyfuel (HVOF) and high-velocity air fuel (HVAF) thermal spraying*. Journal of Thermal Spray Technology, 1999. 8(3): p. 351-356.

12. Shukla, V., G.S. Elliott, B.H. Kear, and L.E. McCandlish, *Hyperkinetic deposition of nanopowders by supersonic rectangular jet impingement*. Scripta Materialia, 2001. 44(8-9): p. 2179-2182.

13. Dykhuizen, R.C. and M.F. Smith, *Gas dynamic principles of cold spray*. Journal of Thermal Spray Technology, 1998. 7(2): p. 205-212.

14. Oosthuizen, P.H. and E. Carscallen, *Compressible fluid flow*. 1997, New York: McGraw Hill.

15. Jodoin, B., *Cold spray nozzle Mach number limitation*. Journal of Thermal Spray Technology, 2002. 11(4): p. 496-507.

16. Gu, S., D.G. McCartney, C.N. Eastwick, and K. Simmons, *Numerical modeling of in-flight characteristics of inconel 625 particles during high-velocity oxy-fuel thermal spraying*. Journal of Thermal Spray Technology, 2004. 13(2): p. 200-213.

17. Thei, J. *Modelling of Cold Gas Dynamic Spraying (CGDS)*. MEng project. University of Nottingham, UK. 2004. p. 1-79

18. Alkhimov, A.P., V.F. Kosarev, and S.V. Klinkov, *The features of cold spray nozzle design*. Journal of Thermal Spray Technology, 2001. 10(2): p. 375-381.

19. McCune R. C., W.T.D., E. L. Cartwright, A. N. Papyrin, E. F. Rybicki and J. R. Shadley. *Characterization of copper and steel coatings made by the cold gas dynamic spray method*. in *Practical Solutions for Engineering Problems*. 1996: ASM-International: p. 397-403.

20. McCune, R.C., W.T. Donlon, O.O. Popoola, and E.L. Cartwright, *Characterization of copper layers produced by cold gas dynamic spraying.* Journal of Thermal Spray Technology, 2000. 9(1): p. 73-82.

21. Shukla, V., G.S. Elliot, and B.H. Kear, *Nanopowder deposition by supersonic rectangular jet impingement.* Journal of Thermal Spray Technology, 2000. 9(3): p. 394-398.

22. Dykhuizen, R.C., M.F. Smith, D.L. Gilmore, R.A. Neiser, X. Jiang, and S. Sampath, *Impact of high velocity cold spray particles.* Journal of Thermal Spray Technology, 1999. 8(4): p. 559-564.

23. Gilmore, D.L., R.C. Dykhuizen, R.A. Neiser, T.J. Roemer, and M.F. Smith, *Particle velocity and deposition efficiency in the cold spray process.* Journal of Thermal Spray Technology, 1999. 8(4): p. 576-582.

24. Van Steenkiste, T.H., J.R. Smith, R.E. Teets, J.J. Moleski, D.W. Gorkiewicz, R.P. Tison, D.R. Marantz, K.A. Kowalsky, W.L. Riggs Ii, and P.H. Zajchowski, *Kinetic spray coatings.* Surface and Coatings Technology, 1999. 111(1): p. 62-71.

25. Richter, P., W. Krommer, and P. Heinrich. *Equipment Engineering and process control for cold spraying.* in *International Thermal Spray Conference.* 2002: ASM International: p. 375-379.

26. Sakaki, K. and Y. Shimizu, *Effect of the increase in the entrance convergent section length of the gun nozzle on the high-velocity oxygen fuel and cold spray process.* Journal of Thermal Spray Technology, 2001. 10(3): p. 487-496.

27. Stoltenhoff, T., J. Voyer, and H. Kreye. *Cold Spraying: State of the Art and Applicability.* in *International Thermal Spray Conference.* 2002: ASM International, Ohio, USA: p. 366-374.

28. Cheng, O. *Equipment engineering and process control for cold spraying.* in *Thermal spray solutions: Advances in Technology and Solutions.* 2004. Osaka, Japan: ASM International: p. 309-314.

29. Karthikeyan, J., *Cold spray technology: International Status and USA Efforts.* 2004, ASB Industries Inc.: Barberton. p. 1-14.

30. Karthikeyan, J., *Cold spray technology*, in *Advanced Materials and Processes*. March 2005. p. 33-35.

31. Grasme, D. *First serial application of cold spraying for coating heat sinks*. in *Conference proceedings of HVOF Colloquium*. 2003. Erding, Germany: 800 Exemplare: p. 119-122.

32. Marx, A., A. Paul, Kohler, and G. Hutti. *Cold spraying - innovative layers for new applications*. in *Thermal Spray Connects: Explore its Surfacing Potential*. 2005. Basel, Switzerland: ASM International: p. 209-215.

33. Gartner, F., C. Borchers, T. Stoltenhoff, and H. Kreye. *Numerical and microstructural investigations of the bonding mechanisms in cold spraying*. in *Thermal Spray 2003: Advancing the Science and Applying the Technology*. 2003: ASM International: p. 1-8.

34. Papyrin, A.N., S.V. Klinkov, and V.F. Kosarev. *Effect of the substrate surface activation on the process of cold spray coating formation*. in *Thermal Spray Connects: Exploring its Surfacing Potential*. 2005. Basel, Switzerland: ASM-International: p. 145-150.

35. Van Steenkiste, T.H., J.R. Smith, and R.E. Teets, *Aluminum coatings via kinetic spray with relatively large powder particles*. Surface and Coatings Technology, 2002. 154(2-3): p. 237-252.

36. Voyer, J., T. Stoltenhoff, and H. Kreye. *Development of cold gas sprayed coatings*. in *Advancing the Science and Applying the Technology*. 2003: ASM International: p. 71-78.

37. Stoltenhoff, T., H. Kreye, W. Krommer, and H.J. Richter. *Cold spraying - From thermal spraying to high kinetic energy spraying*. in *HVOF Colloquium 2000*. 2000: Gemeinschaft thermisches spritzen: p. 29-38.

38. Stoltenhoff, T., H. Kreye, H.J. Richter, and H. Assadi. *Optimization of the cold spray process*. in *Thermal spray 2001: New surfaces for a New Millenium*. 2001. Singapore: ASM International: p. 409-416.

39. Smith, M.F., T.J. O'Hearn, J.E. Brockmann, and R.A. Neiser. *A comparision of two laser-based diagnostics for analysis of particles in thermal spray streams*. in

Proceedings of the 8th National Thermal Spray Conference. 1995. Houston, Texas USA: ASM International: p. 105-110.

40. Taeyoung, H., Z. Zhibo, A.G. Bryan, and J.R. Smith. *A fundamental study of the kinetic spray process*. in *International Thermal spray conference 2004 Thermal Spray Solutions Advances in Technology and Applications*. 2004. Osaka, Japan: ASM International: p. 363-370.

41. Morgan, R., P. Fox, J. Pattison, C. Sutcliffe, and W. O'Neill, *Analysis of cold gas dynamically sprayed aluminium deposits*. Materials Letters, 2004. 58(7-8): p. 1317-1320.

42. Papyrin, A.N., V.F. Kosarev, S.V. Klinkov, and A.P. Alkhimov. *On the interaction of high speed particles with a substrate under cold spraying*. in *International Thermal Spray Conference*. 2002. Essen Germany: ASM International: p. 380-384.

43. Zhang, D., P.H. Shipway, and D.G. McCartney. *Particle-substrate interactions in cold gas dynamic spraying*. in *Thermal Spray 2003: Advancing the Science and Applying the Technology*. 2003: ASM International, Ohio, USA: p. 45-52.

44. Zhang, D., P.H. Shipway, and D.G. McCartney, *Cold gas dynamic spraying of aluminum: The role of substrate characteristics in deposit formation*. Journal of Thermal Spray Technology, 2005. 14(1): p. 109-116.

45. Assadi, H., F. Gartner, T. Stoltenhoff, and H. Kreye, *Bonding mechanism in cold gas spraying*. Acta Materialia, 2003. 51(15): p. 4379-4394.

46. Kang, H.-K. and S.B. Kang, *Tungsten/copper composite deposits produced by a cold spray*. Scripta Materialia, 2003. 49(12): p. 1169-1174.

47. Karthikeyan, J. and C.M. Kay. *Cold spray technology: An industrial perspective*. in *Thermal Spray 2003: An Industrial Perspective*. 2003: ASM International: p. 117-121.

48. Li, C.-J. and W.-Y. Li, *Deposition characteristics of titanium coating in cold spraying*. Surface and Coatings Technology, 2003. 167(2-3): p. 278-283.

49. Novoselova, T., P. Fox, R. Morgan, and W. O'Neill, *Experimental study of titanium/aluminium deposits produced by cold gas dynamic spray.* Surface and Coatings Technology. In Press, Corrected Proof.

50. Van Steenkiste, T. and D.W. Gorkiewicz, *Analysis of tantalum coatings produced by the kinetic spray process.* Journal of Thermal Spray Technology, 2004. 13(2): p. 265-273.

51. Zhao, Z.B., B.A. Gillispie, and J.R. Smith, *Coating deposition by the kinetic spray process.* Surface and Coatings Technology. In Press, Corrected Proof.

52. Grujicic, M., J.R. Saylor, D.E. Beasley, W.S. DeRosset, and D. Helfritch, *Computational analysis of the interfacial bonding between feed-powder particles and the substrate in the cold-gas dynamic-spray process.* Applied Surface Science, 2003. 219(3-4): p. 211-227.

53. Grujicic, M., C.L. Zhao, W.S. DeRosset, and D. Helfritch, *Adiabatic shear instability based mechanism for particle/substrate bonding in the cold-gas dynamic-spray process.* Materials and Design, 2004. 25: p. 681-688.

54. Borchers, C., F. Gartner, T. Stoltenhoff, H. Assadi, and H. Kreye, *Microstructural and macroscopic properties of cold sprayed copper coatings.* Journal of Applied Physics, 2003. 93(12): p. 10064-10070.

55. Choi, H., S. Yoon, S. Uhm, and C. Lee, *Characterization of the spraying beads deposited by the kinetic spraying process.* Surface and Coatings Technology, 2005. 192(2-3): p. 374-381.

56. Marrocco, T., D.G. McCartney, and P. Shipway. *Production of titanium deposits by cold gas dynamic spray.* in *Thermal Spray Connects: Explore its Surfacing Potential.* 2005. Basel, Switzerland: ASM International: p. 224-231.

57. Raletz, F., G. Ezo'o, M. Vardelle, and M. Ducos. *Characterization of cold-sprayed nickel-base coatings.* in *Thermal spray solutions Advances in Technology and Applications.* 2004. Osaka, Japan: ASM International: p. 323-328.

58. Lagerborn, J., H. Makinen, and P. Vuoristo. *Effect of heat treatment on properties of cold sprayed coatings.* in *Thermal spray connects: Explore its Surfacing Potential.* 2005. Basel, Switzerland: ASM International: p. 241-244.

59. Marrocco, T., *Hardness profile of cold sprayed titanium coatings.* Personal communication

60. Grainger, S., *Engineering Coatings*. 1989: Abington publishing.

61. Lu, L. and M.O. Lai, *Mechanical alloying*. 1998: Kluwer Academic Publishers. 165-169.

62. Pradhan, S.K., T. Chakraborty, S.P. Sengupta, C. Suryanarayana, A. Frefer, and F.H. Froes, *X-Ray-Powder Profile Analyses On Nanostructured Niobium Metal Powders.* Nanostructured Materials, 1995. 5(1): p. 53-61.

63. Sastry, K.Y., L. Froyen, J. Vleugels, O. Van der Biest, R. Schattevoy, and J. Hennicke, *Mechanical milling and field assisted sintering consolidation of nanocrystalline Al-Si-Fe-X alloy powder.* Reviews on Advanced Materials Science, 2004. 8(1): p. 27-32.

64. Robinson, P., *Properties of wrought copper and copper alloys*, in *Metals Handbook tenth edition. Volume2 Properties & selection: Nonferrous alloys and special-purpose materials*, S.R. Lampman and T.B. Zorc, Editors. 1990, ASM International: Ohio, USA. p. 265-345.

65. Clements, L.L., *Polymer science for engineers*, in *Engineered materials handbook. Volume 2: Engineering plastics*, C.A. Dostal, Editor, ASM International: Ohio. p. 48-62.

66. Kohan, M.I., *Polyamides (PA)*, in *Engineered materials handbook. Volume2: Engineering plastics*, C.A. Dostal, Editor, ASM International: Ohio. p. 124-127.

67. Maccani, R.R., *Characteristics crucial to the application of engineering plastics*, in *Engineered materials handbook. Volume2: Engineering plastics*, C.A. Dostal, Editor, ASM International: Ohio. p. 68-73.

68. Seymour, R.B., *Overview of polymer chemistry*, in *Engineered materials handbook. Volume2: Engineering plastics*, C.A. Dostal, Editor, ASM International: Ohio. p. 63-67.

69. *Hardness testing*, in *ASM Handbook Volume 08: Mechanical Testing and Evaluation*, H. Kuhn and D. Medlin, Editors, ASM International: Ohio. p. 69-113.

70. Li, C.-J., W.-Y. Li, Y.-Y. Wang, G.-J. Yang, and H. Fukanuma, *A theoretical model for prediction of deposition efficiency in cold spraying.* Thin Solid Films. In Press, Corrected Proof.

71. Weston, D.P., P.H. Shipway, and S.J. Harris, *Coating removal from an industrial polypropylene blend by cryogenic blasting: the development of substrate damage.* Wear, 2005. 258: p. 392-401.

72. Mostaghimi, J., M. Pasandideh-Fard, and S. Chandra, *Dynamics of splat formation in plasma spray coating process.* Plasma Chemistry and Plasma Processing, 2002. 22(1): p. 59-84.

73. Mostaghimi, J. and S. Chandra, *Splat formation in plasma-spray coating process.* Pure Applied Chemistry, 2002. 74(3): p. 441-445.

74. Stoltenhoff, T., H. Kreye, and H.J. Richter, *An analysis of the cold spray process and its coatings.* Journal of Thermal Spray Technology, 2002. 11(4): p. 542-550.

75. Dykhuzien, R.C. and R.A. Neiser. *Optimizing the cold spray process.* in *Thermal Spray 2003: Advancing the Science and Applying the Technology.* 2003: ASM International, Ohio, USA: p. 19-26.

76. Borchers, C., F. Gartner, T. Stoltenhoff, and H. Kreye, *Microstructural bonding features of cold sprayed face centered cubic metals.* Journal of Applied Physics, 2004. 96(8): p. 4288-4292.

77. Sanders, P.G., J.A. Eastman, and J.R. Weertman, *Elastic and tensile behavior of nanocrystalline copper and palladium.* Acta Materialia, 1997. 45(10): p. 4019-4025.

78. Sanders, P.G., J.A. Eastman, and J.R. Weertman. *Tensile behaviour of nanocrystalline copper.* in *Processing and properties of nanocrystalline materials.* 1996: The Minerals, Metals & Materials Society: p. 381-386.

79. Ostwaldt, D. and P. Klimanek, *The influence of temperature and strain rate on microstructural evolution of polycrystalline copper.* Materials Science and Engineering A-Structural Materials Properties Microstructure and Processing, 1997. 234: p. 810-813.

80. Neishi, K., Z. Horita, and T.G. Langdon, *Grain refinement of pure nickel using equal-channel angular pressing.* Materials Science and Engineering A-Structural Materials Properties Microstructure and Processing, 2002. 325(1-2): p. 54-58.

81. Lu, L., N.R. Tao, L.B. Wang, B.Z. Ding, and K. Lu, *Grain growth and strain release in nanocrystalline copper.* Journal of Applied Physics, 2001. 89(11): p. 6408-6414.

82. Komura, S., Z. Horita, M. Nemoto, and T.G. Langdon, *Influence of stacking fault energy on microstructural development in equal-channel angular pressing.* Journal of Materials Research, 1999. 14(10): p. 4044-4050.

83. Islamgaliev, R.K., F. Chmelik, and R. Kuzel, *Thermal structure changes in copper and nickel processed by severe plastic deformation.* Materials Science and Engineering A-Structural Materials Properties Microstructure and Processing, 1997. 234: p. 335-338.

84. Wang, Y.M., E. Ma, and M.W. Chen, *Enhanced tensile ductility and toughness in nanostructured Cu.* Applied Physics Letters, 2002. 80(13): p. 2395-2397.

85. Shih, M.H., C.Y. Yu, P.W. Kao, and C.P. Chang, *Microstructure and flow stress of copper deformed to large plastic strains.* Scripta Materialia, 2001. 45(7): p. 793-799.

86. Cotteril, P. and P.R. Mould, *Recrystallization and grain growth in metals*, Surrey University Press. p. 18-19 and 52-53.

87. Derby, B. and M.F. Ashby, *On dynamic recrystallization.* Scripta Metallurgica, 1987. 21(6): p. 879-884.

88. Chokshi, A.H. and M.A. Meyers, *The prospects for superplasticity at high-strain rates - preliminary considerations and an example.* Scripta Metallurgica Et Materialia, 1990. 24(4): p. 605-610.

89. Blaz, L., T. Sakai, and J.J. Jonas, *Effect of initial grain-size on dynamic recrystallization of copper.* Metal Science, 1983. 17(12): p. 609-616.

90. Andrade, U., M.A. Meyers, K.S. Vecchio, and A.H. Chokshi, *Dynamic recrystallization in high-strain, high-strain-rate plastic-deformation of copper.* Acta Metallurgica Et Materialia, 1994. 42(9): p. 3183-3195.

91. Yu, Q., M. He, and Y. Zhou, *Grain refinement in a copper alloy by shaped charge explosion.* Scripta Materialia, 1997. 37(1): p. 37-44.

92. Molinari, J.F., *Finite element simulation of shaped charges.* Finite Elements in Analysis and Design, 2002. 38(10): p. 921-936.

93. Murr, L.E., C.S. Niou, E.P. Garcia, E. Ferreyra, T.J.M. Rivas, and J.C. Sanchez, *Comparison of jetting-related microstructures associated with hypervelocity impact crater formation in copper targets and copper shaped charges.* Materials Science and Engineering A, 1997. 222(2): p. 118-132.

94. Meyers, M.A., L.W. Meyers, J. Beatty, U. Andrade, K.S. Vacchio, and A.H. Choksi. *High strain, high strain rate deformation of copper.* in *Shock-Wave and High Strain Rate Phenomenon in Materials*. 1992: Marcel Dekker, New York: p. 529-542.

95. Fecht, H.J., E. Hellstern, Z. Fu, and W.L. Johnson, *Nanocrystalline metals prepared by high-energy ball milling.* Metallurgical Transactions A-Physical Metallurgy and Materials Science, 1990. 21(9): p. 2333-2337.

96. Kirin, A. and Bonefaci.A, *X-Ray Line Broadening Study Of Splat Cooled Aluminum And Aluminum Tin And Aluminum-Nickel Solid-Solutions.* Journal of Physics F-Metal Physics, 1974. 4(10): p. 1608-1617.

97. Lu, L., L.B. Wang, B.Z. Ding, and K. Lu, *Comparison of the thermal stability between electro-deposited and cold-rolled nanocrystalline copper samples.* Materials Science and Engineering A-Structural Materials Properties Microstructure and Processing, 2000. 286(1): p. 125-129.

98. Sanders, P.G., A.B. Witney, J.R. Weertman, R.Z. Valiev, and R.W. Siegel, *Residual stress, strain and faults in nanocrystalline palladium and copper.* Materials Science

and Engineering A-Structural Materials Properties Microstructure and Processing, 1995. 204(1-2): p. 7-11.

99. Sen, P., J. Ghosh, A. Abdullah, P. Kumar, and Vandana, *Preparation of Cu, Ag, Fe and Al nanoparticles by the exploding wire technique.* Proceedings of The Indian Academy of Sciences-Chemical Sciences, 2003. 115(5-6): p. 499-508.

100. Lu, L., S.X. Li, and K. Lu, *An abnormal strain rate effect on tensile behavior in nanocrystalline copper.* Scripta Materialia, 2001. 45(10): p. 1163-1169.

101. Lu, L., M.L. Sui, and K. Lu, *Superplastic extensibility of nanocrystalline copper at room temperature.* Science, 2000. 287(5457): p. 1463-1466.

102. Lu, L., M.L. Sui, and K. Lu, *Cold rolling of bulk nanocrystalline copper.* Acta Materialia, 2001. 49(19): p. 4127-4134.

103. Lu, L., L.B. Wang, B.Z. Ding, and K. Lu, *High-tensile ductility in nanocrystalline copper.* Journal of Materials Research, 2000. 15(2): p. 270-273.

104. Masumura, R.A., P.M. Hazzledine, and C.S. Pande, *Yield stress of fine grained materials.* Acta Materialia, 1998. 46(13): p. 45274534.

105. Meyers, M.A., U. Andrade, and A.H. Chokshi, *The effect of grain-size on the high-strain, high-strain rate behaviour of copper.* Metallurgical Transactions A-Physical Metallurgy and Materials Science, 1995. 26(11): p. 2881-2893.

106. Pande, C.S. and R.A. Masumura. *A model for flow stress dependence on grain size for nanocrystalline solids.* in *Processing and properties of nanocrystalline materials*. 1996: The Minerals, Metals & Materials society: p. 387-396.

107. Davis, J.R., editor., *ASM desk editions online*. 1998, ASM International.

108. Tian, W.H., A.L. Fan, H.Y. Gao, J. Luo, and Z. Wang, *Comparison of microstructures in electroformed copper liners of shaped charges before and after plastic deformation at different strain rates.* Materials Science and Engineering A, 2003. 350(1-2): p. 160-168.

109. Schmidt, T., F. Gaertner, and H. Kreye. *High strain rate deformation phenomenon in explosive powder compaction and cold gas spraying.* in *Thermal Spray 2003: Advancing the Science and Advancing the Technology.* 2003: ASM International, Ohio, USA: p. 9-8.

110. Koch, C.C., *Optimization of strength and ductility in nanocrystalline and ultrafine grained metals.* Scripta Materialia, 2003. 49(7): p. 657-662.

111. Bandyopadhyay, A.K. and S.K. Sen, *A study of intermetallic compound formation in a copper-tin bimetallic couple.* Journal of Applied Physics, 1990. 67(8): p. 3681-3688.

112. Haimovich, J., *Cu-Sn intermetallic compound growth in hot-air-leveled tin at and below 100 °C.* AMP Journal of Technology, 1993. 3: p. 46-54.

113. Kay, P.J. and C.A. Mackay, *The growth of inter-metallic compounds on common basis materials coated with tinand tin-lead alloys.* Transactions of Institute of Metal Finishing, 1976. 54: p. 68-74.

114. Revay, L., *Interdiffusion and formation of intermetallic compounds in tin - copper alloy surface - coatings.* Surface Technology, 1977. 5(1): p. 57-63.

115. Unsworth, D.A. and C.A. Mackay, *A preliminary report on growth of compound layers on various metal bases plated with tin and its alloys.* Transactions of Institute of Metal Finishing, 1973. 51: p. 85-90.

116. Acharya, N.N. and P.G. Mukunda, *Sintering in the copper-tin system.1. Identification of phases and reactions.* International Journal of Powder Metallurgy, 1995. 31(1): p. 63-71.

117. Chan, Y.C., A.C.K. So, and J.K.L. Lai, *Growth kinetic studies of Cu-Sn intermetallic compound and its effect on shear strength of LCCCSMT solder joints.* Materials Science and Engineering B55, 1998: p. 5-13.

118. Gagliano, R.A., G. Ghosh, and M.E. Fine, *Nucleation kinetics of Cu6Sn5 by reaction of molten tin with a copper substrate.* Journal Of Electronic Materials, 2002. 31(11): p. 1195-1202.

119. Hammam, T. and R. Sundberg. *Heat treatment of tin-coated copper base alloy and the subsequent effect on friction, wear and electrical properties.* in *20th International Conference on Electrical Contacts (ICEC-2000)*. 2000. Stockholm: p. 291-296.

120. Lee, H., M. Chen, H. Jao, and T. Liao, *Influence of interfacial intermetallic compound on fracture behaviour of solder joints*. Materials and Engineering A358, 2003: p. 134-141.

121. Mei, Z., A.J. Sunwoo, and J.W. Morris, *Analysis of Low-Temperature Intermetallic Growth In Copper-Tin Diffusion Couples*. Metallurgical Transactions A-Physical Metallurgy and Materials Science, 1992. 23(3): p. 857-864.

122. Onishi, M. and H. Fujibuchi, *Reaction-Diffusion In Cu-Sn System*. Transactions of The Japan Institute of Metals, 1975. 16(9): p. 539-547.

123. Prakash, K.H. and T. Sritharan, *Effects of solid-state annealing intermetallics between tin- lead on the interfacial solders and copper*. Journal of Electronic Materials, 2003. 32(9): p. 939-947.

124. Pratt, R.E., E.I. Stromswold, and D.J. Quesnel, *Effect of solid-state intermetallic growth on the fracture toughness of Cu/63Sn-37Pb solder joints*. Ieee Transactions On Components Packaging And Manufacturing Technology Part A, 1996. 19(1): p. 134-141.

125. Sunwoo, A.J., J.W. Morris, and G.K. Lucey, *The growth of Cu-Sn intermetallics at a pretinned copper-solder interface*. Metallurgical Transactions A-Physical Metallurgy And Materials Science, 1992. 23(4): p. 1323-1332.

126. Tu, K.N., *Inter-diffusion and reaction in bimetallic Cu-Sn thin films*. Acta Metallurgica, 1973. 21: p. 347-354.

127. Prakash, K.H. and T. Sritharan, *Textured growth of Cu/Sn intermetallic compounds*. Journal of Electronic Materials, 2002. 31(11): p. 1250-1255.

128. Dyson, B.F., T. Anthony, and D. Turnbull, *Interstitial diffusion of copper and silver in lead*. Journal of Applied Physics, 1966. 37(6): p. 2370.

129. Reed-Hill, R.E. and R. Abbaschiam, *Physical Metallurgy Principles*. 1991: PWS Publishing Company. 360-402.

130. Tu, K.N. and R.D. Thompson, *Kinetics of interfacial reaction in bimetallic Cu-Sn thin-films*. Acta Metallurgica, 1982. 30(5): p. 947-952.

131. Anonymous. *Phase diagram and computational thermodynamics*. [cited 2005 08/08/2005];

132. Frederikse, H.P.R., R.J. Fields, and A. Feldman, *Thermal and electrical-properties of copper-tin and nickel-tin intermetallics*. Journal of Applied Physics, 1992. 72(7): p. 2879-2882.

133. Shen, J., *Personal communication*. Grain sizes of Ball milled Cu powder measured by Hall-Williamson method.